Ana Bela Saraiva de Campos

The role of aging-related microglia dysfunction in the neurodegenerative process of Machado-Joseph disease

UMinho | 2022

Universidade do Minho
Escola de Medicina

Ana Bela Saraiva de Campos

The role of aging-related microglia dysfunction in the neurodegenerative process of Machado-Joseph disease

April, 2022

Universidade do Minho
Escola de Medicina

Ana Bela Saraiva de Campos

The role of aging-related microglia dysfunction in the neurodegenerative process of Machado-Joseph disease

Doctoral Thesis

Doctoral Program in Aging and Chronic Diseases

Work supervised by

Patrícia Espinheira de Sá Maciel

António Francisco Rosa Gomes Ambrósio

April, 2022

COPYRIGHT AND TERMS OF USE OF THIS WORK BY A THIRD PARTY

This is an academic work that can be used by third parties as long as internationally accepted rules and good practices regarding copyright and related rights are respected.

Accordingly, this work may be used under the license provided below.

If the user needs permission to make use of the work under conditions not provided for in the indicated licensing, they should contact the author through the RepositoriUM of University of Minho.

License granted to the users of this work

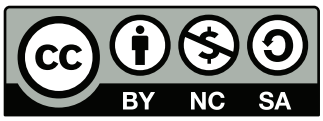

Creative Commons Attribution-NonCommercial-ShareAlike 4.0 International
CC BY-NC-SA 4.0

https://creativecommons.org/licenses/by-nc-sa/4.0/deed.en

Agradecimentos

Life is not easy for any of us. But what of that? We must have perseverance and above all confidence in ourselves. We must believe that we are gifted for something and that this thing must be attained.

— Marie Curie

Agora que chegou a hora de agradecer a todos aqueles que, de alguma forma, me apoiaram durante esta jornada, espero não ficar sem palavras! Devo começar por expressar a minha gratidão à Professora Patrícia Maciel pela oportunidade de integrar o seu grupo de investigação e pela orientação, apoio, disponibilidade, energia e acompanhamento científico ao longo destes 5 anos de doutoramento com o devido grau de exigência e rigor. Quero também agradecer ao Professor Francisco Ambrósio por me permitir trabalhar no seu laboratório, pela sua orientação, comentários, desafios e palavras de incentivo.

Também sou profundamente grata por ter sido acolhida por um grupo de excelência em neurociências: Andreia Carvalho, Andreia Castro, Bruno Almeida, Beatriz Ferreira, Catarina Ferreira, Daniela Campos, Daniela Garcia, Daniela Monteiro, Jorge Silva, Joana Sousa, Joana Correia, Jorge Fernandes, Liliana Costa, Marta Costa, Margarida Sousa, Sara Silva e Stéphanie Oliveira. Um reconhecimento especial à Sara Silva que contribuiu diretamente na minha evolução científica durante este projeto de doutoramento. Obrigado a todos pelo apoio e amizade.

Quero também agradecer aos meus colegas de doutoramento, em especial à Ana Gonçalves, à Gabriela Tavares e ao José Graça, pela vossa extraordinária amizade e por me ajudarem a manter este trabalho no caminho certo.

A minha gratidão é também expressa a toda a comunidade da Escola de Medicina, a todos os NeRD, e à FCT por me fornecerem todos os meios para completar esta jornada, incluindo uma bolsa nacional de doutoramento (com referência PD/BD/127828/2016).

A nível pessoal, devo expressar a minha maior gratidão aos meus amigos e a toda a minha família. Obrigado por estarem sempre ao meu lado. Sou profundamente grata aos meus pais, José e Maria. Por último quero agradecer ao meu companheiro de sempre, Bruno. Obrigada pela partilha incondicional, pela compreensão, pelo apoio desmedido. Por teres orgulho em mim e nunca duvidares que seria capaz. Pelos teus ensinamentos no mundo da informática. Por me ajudares com as tuas criticas construtivas às minhas apresentações e trabalho - por isso esta tese também é tua!

STATEMENT OF INTEGRITY

I hereby declare having conducted this academic work with integrity. I confirm that I have not used plagiarism or any form of undue use of information or falsification of results along the process leading to its elaboration.

I further declare that I have fully acknowledged the Code of Ethical Conduct of University of Minho.

Resumo

O papel da disfunção microglial associada ao envelhecimento nos processos neurodegenerativos da doença de Machado-Joseph

Células microgliais têm sido, cada vez mais, associadas às doenças neurodegenerativas, apresentando diferentes perfis para várias destas doenças. Contudo, o perfil da microglia na doença de Machado-Joseph (DMJ) permanece desconhecido, bem como a contribuição destas células para a doença. Deste modo, este trabalho começou pela caracterização do perfil das células da microglia no modelo de ratinho que mimetiza a DMJ, o modelo CMVMJD135, através do uso das células da microglia obtidas das regiões do cérebro mais afetadas por esta doença. Diversos modelos foram usados para identificar perturbações celulares e moleculares, e potenciais alvos terapêuticos. Mais tarde, perguntamos se a microglia contribuía, ou não, para a patogénese da DMJ. A resposta surgiu pela depleção da microglia nos cérebros dos ratinhos CMVMJD135 usando o fármaco PLX3397. Um conjunto de testes comportamentais foi depois aplicado para avaliar o impacto da depleção destas células no fenótipo motor dos ratinhos CMVMJD135.

Os resultados obtidos revelam alterações morfológicas que apontam para um aumento do estado de ativação da microglia nos ratinhos CMVMJD135 e um perfil transcricional específico da microglia associada à DMJ, abrangendo um total de 101 genes diferencialmente expressos, com enriquecimento em vias relacionadas com o stress oxidativo, resposta imune e metabolismo lipídico. Apesar do tratamento com o fármaco ter promovido uma redução substancial do número de células microgliais, isto não alterou os défices motores presentes neste modelo de ratinho. O fármaco induziu também alterações morfológicas na microglia sobrevivente dos ratinhos de controlo, o que poderá trazer implicações para outros estudos que utilizam este fármaco para reduzir o número de células microgliais.

No geral, estes resultados permitiram-nos definir o perfil celular e molecular da microglia associada à DMJ e identificar genes e vias que podem representar potenciais alvos terapêuticos para combater esta doença. No entanto, estes resultados também sugerem que, apesar das alterações morfológicas, fenotípicas e transcriptómicas observadas na microglia dos ratinhos da DMJ, estas células poderão não ser contribuidores chave para a progressão desta doença.

Palavras-chave: Doença de Machado-Joseph, Fenótipo Motor, Perfil Microglial, Sequenciação de RNA.

Abstract

The role of aging-related microglia dysfunction in the neurodegenerative process of Machado-Joseph disease

Microglia have been increasingly implicated in neurodegenerative diseases (NDs), with non-homeostatic or pathological microglial profiles being defined for several of these NDs. Yet, the microglial profile in Machado-Joseph disease (MJD) remains unexplored as well as their contribution to the disease. Hence, in this study we first characterized the microglial profile in the CMVMJD135 mouse model of MJD, using microglial cells obtained from disease-relevant brain regions. Machine learning models and an RNA-sequencing analysis were used to identify cellular and molecular perturbations and potential therapeutic targets. Afterwards, we asked whether microglia are, or not, actively contributing for MJD pathogenesis. This was addressed by depleting microglia in the brains of CMVMJD135 mice, through the pharmacological inhibition of colony stimulating factor 1 receptor signaling, using PLX3397. A battery of behavioral tests was then applied to evaluate the impact of microglial depletion on the motor phenotype of CMVMJD135 mice.

Our findings reveal morphological alterations that point to an increased activation state of microglia in CMVMJD135 mice and a disease-specific transcriptional profile of MJD microglia, encompassing a total of 101 differentially expressed genes, with enrichment in molecular pathways related to oxidative stress, immune response, cell proliferation, cell death, and lipid metabolism. Although PLX3397 treatment substantially reduced microglia numbers in the affected brain regions, it did not affect the motor deficits seen in this mouse model of MJD. Our results also show that, in addition to reducing the number of microglial cells, the treatment with PLX3397 induces morphological changes in the surviving microglia of wild-type mice that are a finding that has implications for other studies using this drug as a microglia depletion tool.

Overall, these results allowed us to define the cellular and molecular profile of MJD-associated microglia and to identify genes and pathways that might represent potential therapeutic targets for this disorder. However, these results also suggest that despite the morphological, phenotypic, and transcriptomic changes seen in microglia in MJD mice, these cells may not be significant key contributors for MJD progression.

Keywords: Machado-Joseph Disease, Microglial Profile, Motor Phenotype, RNA-sequencing.

Contents

List of Figures

List of Tables

Acronyms

AD Alzheimer's disease

ALS Amyotrophic lateral sclerosis

Atg autophagy-related gene

BBB blood-brain barrier

BDNF brain-derived neurotrophic factor

BSA bovine serum albumin

CAG cytosine-adenine-guanidine

CD200 cluster of differentiation 200

CD200R cluster of differentiation 200 receptor

CD200R1 cluster of differentiation 200 receptor 1

cDNA complementary DNA

CEs cholesterol esters

CMV cytomegalovirus

CNS central nervous system

CR3 complement receptor 3

CSC cervical spinal cord

CSF1 colony stimulating factor-1

CSF1R colony stimulating factor 1 receptor

DAM disease-associated microglia

DAMPS damage-associated molecular patterns

DCN deep cerebellar nuclei

DEGs Differentially Expressed Genes

DGAV Direcção Geral de Alimentação e Veterinária

DIV days *in vitro*

DMEM dulbecco's modified eagle medium

DMSO dimethyl sulfoxide

DRPLA dentatorubral-pallidoluysian atrophy

DUB deubiquitinase

EDTA ethylenediamine tetraacetic acid

EGA exploratory grouping analysis

EMPS erythromyeloid precursors

ERAD endoplasmic reticulum–associated protein degradation

FACS fluorescence activated cell sorting

FBS fetal bovine serum

FDR false discovery rate

FELASA Federation of European Laboratory Animal Science Associations

GBTs gradient boosted trees

GDNF glia cell line-derived neurotrophic factor

GFAP glial fibrillary acid protein

GUI graphical user interface

GWASs genome-wide association studies

HBSS hanks balanced salt solution

HD Huntington's disease

HDL2 Huntington's disease-like 2

HMGB1 high mobility group box 1

ICH intracerebral hemorrhage

IGF-1 insulin-like growth factor-1

IJM ImageJ macro language

IL interleukin

IPA Ingenuity Pathway Analysis

iPSC induced pluripotent stem cell

JD josephin domain

LDAM lipid droplet-accumulating microglia

LDs lipid droplets

LPS lipopolysaccharides

LY6C lymphocyte antigen 6C

MACS magnetic activated cell sorting

Mef2 myocyte enhancer factor-2

MFI mean fluorescent intensity

MGnD microglial neurodegenerative

MHC major histocompatibility complex

MJD Machado-Joseph disease

ML machine learning

mRNA messenger RNA

MS multiple sclerosis

MSE mean squared error

NAMPs neurodegeneration-associated molecular patterns

NDs neurodegenerative diseases

NES nuclear export sequences

NGS normal goat serum

NLS nuclear localization sequence

NNIs neuronal nuclear inclusions

NO nitric oxide

NPCs neural precursor cells

NRS nitrogen reactive species

PAMPS pathogen-associated molecular patterns

PBS phosphate saline buffer

PCA principal component analysis

PCR polymerase chain reaction

PD Parkinson's disease

PE phagocytic efficiency

PET positron emission tomography

PFA paraformaldehyde

PN pontine nuclei

PQC protein quality control

PRRs pattern recognition receptors

RIN RNA integrity number

RNA ribonucleic acid

ROI region of interest

ROS reactive oxygen species

RPM reads per million

RT room temperature

SASP senescence associated secretory phenotype

SBMA spinal and bulbar muscular atrophy

SC spinal cord

SCA1 spinocerebellar ataxia type 1

SCA17 spinocerebellar ataxia type 17

SCA2 spinocerebellar ataxia type 2

SCA3 spinocerebellar ataxia type 3

SCA6 spinocerebellar ataxia type 6

SCA7 spinocerebellar ataxia type 7

SCAs spinocerebellar ataxias

SEM standard error of the mean

SIRP signal-regulatory protein

TAC Transcriptome Analysis Console

TGF transforming growth factor

TLRs toll-like receptors

TNF tumor necrosis factor

TREM2 triggering receptor expressed on myeloid cells-2

UIMS ubiquitin interacting motifs

UPS ubiquitin proteasome system

WT wild-type

YS yolk sac

Chapter 1

Introduction

1.1 Machado-Joseph disease: Historical perspective and Epidemiology

Machado-Joseph disease (MJD) was first recognized in the 1970s in three Portuguese families (Machado, Thomas, and Joseph), originally from São Miguel Island of the Azores that emigrated to the United States of America, being later described in other geographic locations and in families with no Portuguese ancestrality [1, 2].

In 1972, this disorder was described by Nakano and colleagues in William Machado family as an autosomal dominant ataxia and was termed as Machado disease [3]. In the same year, the Thomas family was reported, by Woods and Schaumburg, to suffer from an autosomal dominant illness similar to those described previously but with some particular clinical features. The Thomas family illness was named as Nigro-spino-dentatal degeneration with nuclear ophthalmoplegia [4]. Some years later, in 1976, Rosenberg and collaborators described in the family of Antone Joseph a particular type of autosomal dominant hereditary ataxia associated with striatonigral degeneration, which was entitled as Joseph disease [5]. These studies described the diseases as distinct clinical entities. However, two years later, Coutinho and Andrade proposed the unification of the disease including the previously described phenotypes and suggested that the disease that affected the Machado, the Thomas, and the Joseph families has the same genetic origin with variable phenotypic expression [6]. In the 1980s, this disease was called Machado-Joseph disease (MJD) by the first time by Sequeiros and Coutinho [7], with some clinical criteria for diagnosis being introduced [8].

In the early 1990s, the first dynamic expansions of cytosine-adenine-guanidine (CAG) trinucleotide repeat sequences in the coding region of a given gene, translated into repetitive aminoacid sequences, known as abnormally long polyglutamine (polyQ) tracts, in the corresponding disease proteins, were identified [9, 10]. In particular, MJD was found to be caused by an abnormal expansion of the CAG trinucleotide within the coding region of the *ATXN3* gene [11, 12]. Tandem repeat diseases include the neurodegenerative diseases (NDs) known as polyQ diseases, which share key characteristics that suggest a common toxic mechanism: 1) the CAG expansion is translated into an abnormally long polyglutamine tract; 2) the CAG repeat length is inversely correlated with age at disease onset and directly correlates with severity of disease [13–16]; 3) the CAG repeats present an intergenerational instability, with tendency for disease severity to increase in successive generations of a family (a biological phenomenon named as anticipation) [16–19]; 4) formation of protein aggregates or inclusions bodies largely in the nucleus and/or cytoplasm of the neurons [13]; 5) symptoms typically begin in adulthood and slowly progressing over many years [20–23]; 6) although affecting mainly the central nervous system (CNS), the peripheral nerves and muscles are also affected [24, 25]; and 7) are fatal disorders with no treatments to amend the disease [26].

Currently, ten polyQ disorders have been characterized: Kennedy's disease or spinal and bulbar muscular atrophy (SBMA), dentatorubral-pallidoluysian atrophy (DRPLA), Huntington's disease (HD) and Huntington's disease-like 2 (HDL2), and six types of spinocerebellar ataxias (SCAs) (spinocerebellar ataxia type 1 (SCA1), spinocerebellar ataxia type 2 (SCA2), spinocerebellar ataxia type 3 (SCA3), spinocerebellar ataxia type 6 (SCA6), spinocerebellar ataxia type 7 (SCA7), and spinocerebellar ataxia type 17 (SCA17)) [9, 10]. With exception of the SBMA, which is X-linked, the other polyQ disorders are autosomal dominant [26].

Currently, MJD is also designated as SCA3, and although the SCAs are a group of rare disorders, MJD is the most common dominantly inherited ataxia and the second most common polyQ disease worldwide [21, 27, 28]. Epidemiological data estimates that the prevalence of MJD is 2 per 100.000 inhabitants around the world [10, 27, 28]. Still, it has been reported that the disease prevalence differs significantly between geographic locations and ethnic differences, with the greatest prevalence reported in Portugal and Brazil as well as in East Asian countries such as China, Japan, and Taiwan, being rare in the United Kingdom, Italy, India, and South Africa [18, 29]. In mainland Portugal, the disease prevalence is of 3.1 per 100.000 inhabitants. A higher prevalence is found in the Azores islands and Tejo (Tagus) river valley [30]. Moreover, while studies have shown that Portuguese MJD families arose from two haplotypes, it has been established that the majority of MJD families worldwide result from one single intragenic haplotype [2].

1.1.1 Clinical and neuropathological features of Machado-Joseph disease

MJD is a disorder characterized by the progressive appearance of symptoms that become worse with age. Typically, the symptoms in MJD patients begins between early adolescence and old age, and progress slowly with age [20, 21, 23]. However, the severity of disease is related to the age at onset, an early onset being associated with a more severe and more rapidly progressive form of the disease [23, 31]. The mean survival time is of 21 years after the onset of symptoms, but a failure in brainstem-associated functions generally leads to death earlier, within 10-15 years of symptom onset [7, 32].

The most common clinical hallmark of MJD is the progressive ataxia, which is characterized by motor coordination impairments including abnormal gait, impaired balance, and limb incoordination (Figure 1.1a). MJD patients also exhibit dysfunction of the pyramidal tract, manifesting spasticity (muscle weakness) and hyperreflexia. Other motor-related clinical manifestations are also frequently observed in this progressive disease and include parkinsonism with or without tremor, dystonia (repetitive muscle contractions that cause twisting of the body and limbs, repetitive movements, abnormal postures, and /or rigidity), dysarthria (difficulty with speech articulation), dysphagia (difficulty with swallowing), and oculomotor abnormalities (with nystagmus - involuntary eye movement, bulging eyes due to lid retraction, progressive external ophthalmoplegia, and ophthalmoparesis). Other patients may also experience other clinical symptoms such as facial and lingual fasciculations (muscle twitches), bradykinesia (slowness of movement), loss of proprioception, amyotrophy, as well as corticospinal tract and autonomic nervous system dysfunctions (Figure 1.1a) [6, 8, 18, 23, 26, 33–37]. Non-motor symptoms are less severe and include sleep disorders,

mild cognitive impairments, double vision, frequent urination, weight loss, and psychiatric disturbances [38–41].

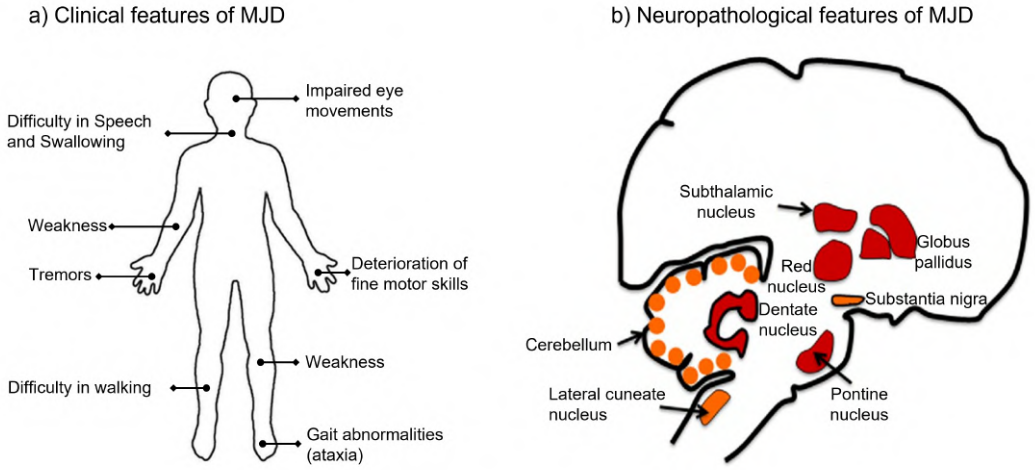

Figure 1.1: **Clinical and neuropathological features of Machado-Joseph disease**. **a)** Machado-Joseph disease (MJD) is characterized by the progressive appearance of symptoms that become worse with age. Adapted from *https://www.ataxia.org/*. **b)** Classical brain regions affected in MJD are showed in red and orange. Red indicates severe or selective neuronal loss and orange indicates moderate or variable cell loss. The circles in the cerebellum represent the relatively mild loss of Purkinje cells in the cerebellar cortex. Adapted from Ross (1995) [38].

The wide phenotypic variability seen in MJD patients led to the classification of the disease into four clinical sub-phenotypes, namely types I, II, III, and IV, mainly distinguishable by differences in age of onset and major symptoms [8, 18, 42]. So, MJD type I is characterized by more severe pyramidal and extra-pyramidal anomalies, in addition to ataxia and other signs, and includes MJD patients with an early age of onset (10-30 years of age) and fast progression. MJD type II includes patients exhibiting cerebellar ataxia, progressive external ophthalmoplegia and pyramidal signs, and is the most frequent form, appearing at an intermediate age (20-50 years of age) with a moderate progression rate. Patients with MJD type III show loss of proprioception and muscle atrophy and present the latest age of onset (40-70 years of age) and a slow disease progression. The fourth type is the rarest form and is characterized by the presence of Parkinsonic signs [6, 8, 18, 42, 43].

Progressive motor dysfunction in MJD results from neuronal dysfunction and neuronal cell loss in the brainstem, cerebellum, midbrain, spinal cord, striatum, and thalamus (Figure 1.1b) [23, 38, 44–46]. Due to the progressive neuronal loss, the brain weight of end-stage MJD patients is lower when compared with the brains of the healthy individuals, an indicator of brain atrophy [18]. Moreover, the presence the gliosis has been described, associated with neuronal loss [43, 47, 48]. Magnetic resonance imaging and neuroimaging studies have revealed an enlargement of the fourth ventricle resulting from atrophy and loss of neuronal cells in the pons and deep cerebellar nuclei (DCN), and loss of pontocerebellar fibers and spinocerebellar tracts [16, 23, 47, 49, 50]. Neurodegeneration also targets the motor neurons of the cranial nerve nuclei, the red nucleus, the subthalamic nucleus, the globus pallidus, and some thalamic

nuclei [23, 46, 51]. In addition, the motor nerve nuclei, Clarke's column nuclei, and the anterior horn of the spinal cord are similarly affected in MJD [52]. Contrarily to other ataxias, in MJD the Purkinje cells of the cerebellar cortex are relatively spared. However, the loss of granule and Purkinje cells has been reported in the cerebellar vermis [16, 53]. The post-mortem analysis of MJD brains also revealed a significant degeneration of dopaminergic neurons of the substantia nigra and of the vestibular nuclei [16, 23, 54] (Figure 1.1b). Other CNS systems affected in MJD patients include the cholinergic and dopaminergic midbrain neurons, the somatosensory (visual, auditory, and vestibular), the cerebellar-cerebral circuitry, and ingestion and urination-related systems [6, 31, 55–57]. Despite the cerebral cortex being another region affected in MJD patients, the extent of damage in this region is much less than in the brainstem and cerebellum [58]. Pathologically, MJD is not limited to the CNS since individuals with this disease also present peripheral neuropathy in the distal limbs, leading to muscle atrophy [24, 25].

The most relevant neuropathological characteristic of MJD is the accumulation of ubiquitinated protein aggregates or inclusions containing the mutant polyQ-expanded ATXN3 in post-mortem brains [59–61]. Neuronal nuclear inclusions (NNIs) make up most of these aggregates and are present both in brain regions affected by neurodegeneration and in regions that are typically spared in this disease [34, 57, 59, 61–63]. This suggest that the occurrence of the intranuclear aggregation is regulated by cellular-specific quality control machinery that maintain the toxicity subthreshold, thus avoiding cell dysfunction and death [53]. Within the ATXN3 neuronal nuclear inclusions (NNIs), other proteins have been detected such as ubiquitin, heat shock proteins, proteasomal components, transcription factors, autophagy-associated chaperones such as p62 and autophagosomal microtubule-associated protein light chain 3 (LC3), other polyQ proteins, and non-expanded ATXN3 [61, 64–66]. In addition to the NNIs, neuronal cytoplasmic inclusions and distal axonal aggregates were also found in MJD patients [67, 68]. Similarly to the intranuclear aggregates, the axonal aggregates were immunopositive for ubiquitin and p62, reinforcing the role of protein quality control (PQC) mechanisms in the regulation of mutant ATXN3 [67, 68]. Currently, even though little is known about the exact role of ATXN3 aggregation in MJD (loss-of-function and/or toxic gain-of-function), it is commonly accepted that the sequestration of critical protein quality control mechanism components into protein aggregates may contribute to dysfunction and loss of neuronal cells [10, 61].

1.1.2 Genetics of Machado-Joseph disease

The genetic mutation in the *MJD1/ATXN3* gene causing MJD was mapped to the long arm of the chromosome 14q32.1 in the 1990's [11, 12, 69]. The *ATXN3* gene spans a genomic region of approximately 48 kb and contains 13 exons, with the (CAG)n tract being located in the exon 10 [12, 70, 71]. In the health population, the number of CAG repeats ranges from 12 to 44, whereas in MJD individuals the CAG size repeat ranges from 56 to 87. Individuals carrying intermediate CAG repeats length ranging from 45 to 55 present incomplete penetrance of MJD symptoms, with possible manifestation of the disease. This evidence allowed the development and improvement of diagnostic methods for MJD, based on the determination of the CAG repeat number in the MJD causative gene (Figure 1.2a) [14, 16, 61, 72–78].

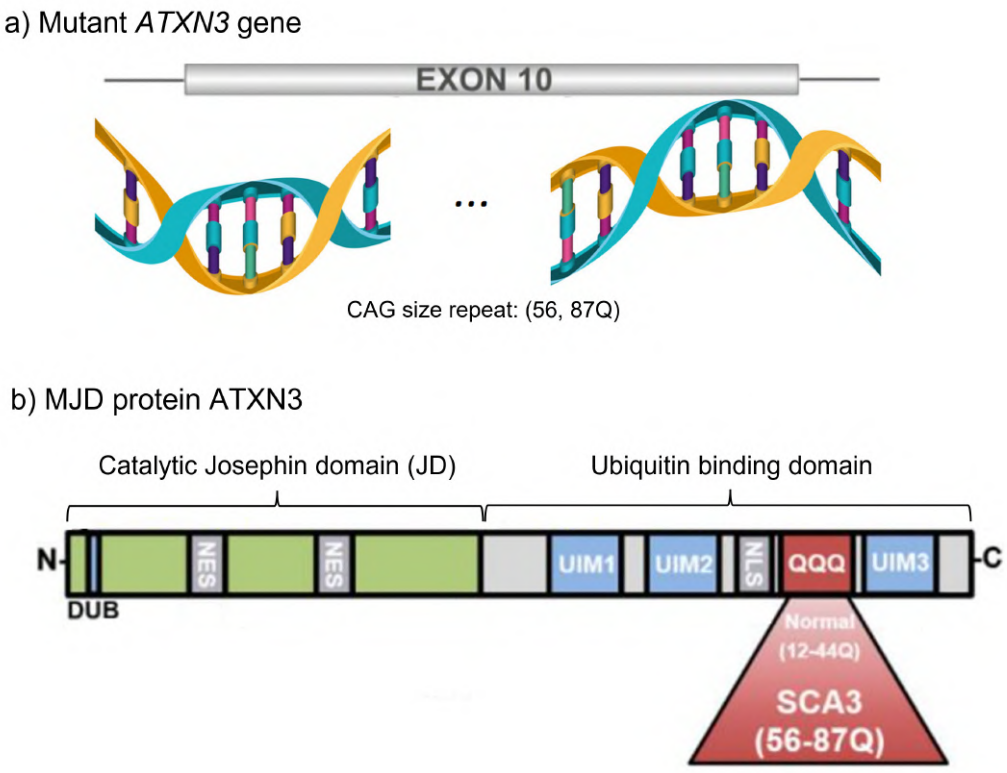

Figure 1.2: **Ataxin-3: Repeat Pathology**. **a)** An expansion of cytosine-adenine-guanidine (CAG) repeats fom 56 to 87 in exon 10 of the *ATXN3* gene is the underlying cause of MJD. Adapted from Da Silva et al. (2019) [53]. **b)** Schematic representation of ATXN3 protein. The N-terminal josephin domain (JD) contains the deubiquitinase (DUB) catalytic sites and nuclear export sites (NES). The C-terminal tail contains two or three ubiquitin-interacting motifs (UIMs), a putative nuclear localization signal (NLS) and the variable polyQ repeat. Repeat lengths of normal and pathogenic polyQ are shown and ranges from 12 to 44 and from 56 to 87, respectively. Adapted from McLoughlin et al. (2020) [10].

The genetic mutation in the *ATXN3* gene is translated into an abnormal polyQ tract near the C-terminus of the ataxin-3 (ATXN3) protein, which has normal expression levels even in the presence of this mutation [11, 79]. Different ATXN3 transcripts, which can result from different splicing and polyadenylation signals, were described to be ubiquitously expressed in neuronal and non-neuronal tissues (such as spleen, liver, heart, kidney, and testis) [12, 59, 71, 79–81].

Like other polyQ diseases, MJD exhibits a clinical phenomenon called “anticipation”, explained by the biological phenomenon of genetic instability, i.e., the tendency for the expanded CAG repeat in mutant *ATXN3* to become increasingly long in successive generations, typically causing more severe, earlier onset disease in offspring [14, 16–19, 74]. Also, as with other polyQ diseases, the size of the expanded CAG repeat number is inversely correlated with the age of disease onset but directly correlated with severity of disease [14, 16, 74, 82]. Thereby, the variability in the CAG repeat length, together with genetic modifiers, contributes to the high variability in the clinical presentation of this disease [10]. Although it is a rare condition, individuals inheriting two copies of the expanded mutant *ATXN3* gene (homozygous MJD individuals) have been reported and present more severe symptoms and earlier onset. Additionally, until

now, no individuals that are haploinsufficient or null for *ATXN3* have been described [10, 83, 84].

Although the genetic cause of MJD is already known for many years, this polyQ disease is still a fatal and untreatable disease [10].

1.1.3 Machado-Joseph disease protein ATXN3

To understand MJD, one is required to understand the MJD disease protein ATXN3, which is a small evolutionary conserved protein in mice, rat, chicken, *C. elegans*, and other organisms [81, 85–90]. The human ATXN3 protein has a molecular weight of 42 kDa, with its size varying slightly according to the length of the polyQ tract, and belongs to the papain-like cysteine proteases family [18, 91, 92]. It is composed of a structured globular amino terminus containing the josephin domain (JD) responsible for catalytic cleavage of ubiquitin chains. The ubiquitin protease activity resides in the putative catalytic triad of amino acids: cysteine (C14), histidine (H119), and asparagine (N134). This domain is followed by a flexible C-terminal tail that contains three ubiquitin interacting motifs (UIMS) that facilitate ATXN3 binding to polyubiquitinated chains. The polyQ tract is located at the C-terminus of the protein (Figure 1.2b) [79, 91, 93, 94]. Although several ATXN3 isoforms have been identified, most studies have focused on two: one expressing all three UIMS (3UIMS), which is the main isoform expressed in the brain of patients and transgenic mice, and one lacking the third UIM (2UIMS). Moreover, the specificity of ATXN3 towards polyubiquitin chains and substrates may change according to the presence or absence of the third UIM (Figure 1.2b) [95, 96].

Regarding its expression, ATXN3 is ubiquitously expressed among different body tissues and cell types, being widely expressed in the brain, with high levels in the cerebellum, hippocampus, and substantia nigra, and intermediate levels in the striatum and cerebral cortex [59, 71, 80, 85]. Also, in terms of subcellular localization, ATXN3 can be found both in the cytoplasm and nucleus, being able to translocate from the cytoplasm to the nucleus and vice-versa, across the nuclear membrane. This ability is associated with the existence of two nuclear export sequences (NES) and a putative nuclear localization sequence (NLS) in the ATXN3 sequence that facilitates active transport across the nuclear membrane (Figure 1.2b). Under normal conditions, ATXN3 is highly present in the cytoplasm of most cell types. However, cellular stressors, such as oxidative stress or heat shock, cause the rapid nuclear localization of ATXN3 [97–100]. In MJD patients, the ATXN3 mutant is expressed predominantly in the neuronal nuclei, a defining feature of this neuropathology. Interestingly, the prevention of the nuclear localization of ATXN3 mutant attenuates the features of the disease, while forcing the abnormal protein inside of the nucleus enhances the disease in MJD mouse models [18, 23, 61, 101]. Moreover, despite its predominance in neurons, in normal and disease brains, expression of *ATXN3* was also found in glial cells [91, 102].

Concerning its physiological function, ATXN3 is a deubiquitinase (DUB) enzyme implicated in protein quality control pathways such as the ubiquitin proteasome system (UPS), and known to regulate the formation of aggresomes [91, 103]. ATXN3 binds to polyubiquitinated proteins (preferentially with four or more ubiquitin moieties) through its ubiquitin interaction motifs (3UIMS) that flank the polyQ track and cleave the ubiquitin chains from proteins [104, 105]. The preference of ATXN3 to wards longer polyubiquitin chain

lengths together with its interaction with several ubiquitin ligases suggest that ATXN3 edits ubiquitin chain length and composition on substrates destined for proteasomal degradation [10, 106]. Furthermore, since ATXN3 preferentially edits polyubiquitin chains with a minimum of length, it may avoid complete removal of the ubiquitinated chain by others DUBs and, hence, facilitate the recognition by the 26S proteasome, which only recognizes chain of at least four ubiquitin moieties (tetraubiquitin) [104, 107, 108]. Alternatively, through its deubiquitylase activity, ATXN3 may inhibit or avoid the delivery to the proteasome of the autophagy-related substrates such as Beclin-1, and DNA damage repair and cell cycle proteins such as Chk1 and p53 [108–111]. As well as playing an important role in the UPS, ATXN3 is involved in other cellular pathways such as DNA damage repair, cytoskeletal organization, transcriptional regulation, and macroautophagy [87, 91, 105, 111–113].

The ATXN3 protein undergoes post-translational modifications such as ubiquitination, SUMOylation, and phosphorylation, which influence its behavior and function [114–119]. Indeed, while ubiquitination potentiates the DUB activity of ATXN3, the phosphorylation may alter the nucleocytoplasmic localization of ATXN3. In regard to SUMOylation, it was described that mutating a SUMO binding site accelerated the degradation of expanded ATXN3 [118–120].

Regarding the mutant ATXN3, the expanded polyQ tract does not impede its enzymatic activity and capacity to bind and cleaves polyubiquitin chains, nevertheless it may modify its substrate specificity or protein-protein interactions [104, 105]. In fact, MJD patients have increased levels of polyubiquitinated proteins due to broad disruptions of the UPS and sequestration of UPS regulators into mutant ATXN3 aggregates. This may suggest some loss of function, contributing to the disease [10, 60, 65].

1.1.4 Mechanisms of Machado-Joseph disease pathogenesis

Several molecular mechanisms and cellular pathways have been identified in MJD pathogenesis [53]. As mentioned above, an expansion of CAG repeats between 56 to 87 in exon 10 of the *ATXN3* gene translates into a protein harboring an expanded polyglutamine segment, which is the underlying cause of MJD [14, 16, 61, 74]. This expansion leads to misfolding of the mutant ATXN3 and subsequent oligomerization and accumulation of the mutant protein in aggregates or amyloid fibers, with consequent deposition of insoluble intracellular inclusions (Figure 1.3) [53, 59, 61, 121].

These alterations affect the PQC mechanisms including the UPS, molecular chaperones, and autophagy, which have been implicated in MJD and other polyQ diseases (Figure 1.3) [10, 60, 122]. These mechanisms are important to avoid the deposition of damaged/dysfunctional proteins and of protein aggregates. However, the aggregation of ATXN3 and other polyQ disease proteins can sequester the components of the PQC network exacerbating the impairment of the protein homeostasis (proteostasis) [10, 53]. Hence, perturbations in proteostasis are thought to represent the initiating factor of pathogenesis in MJD and other polyQ diseases, cells failing to keep up with the continuous production and accumulation of aggregate-prone proteins (Figure 1.3) [53, 123].

Currently, little is known regarding the effect of the polyQ expansion in the role of ATXN3 to regulate

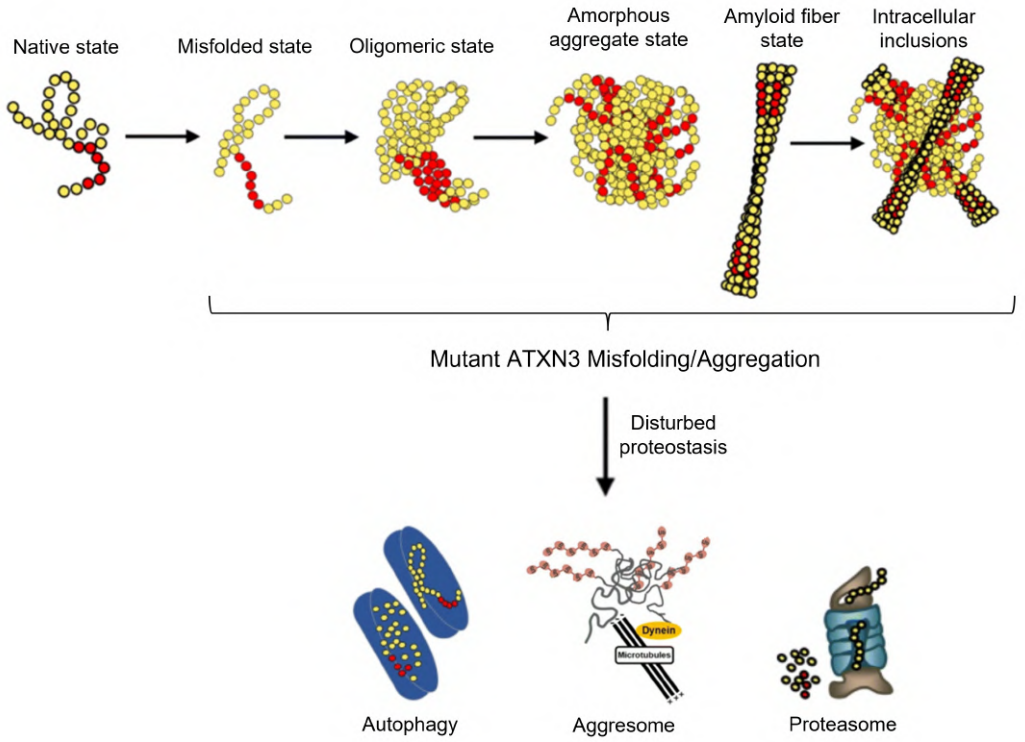

Figure 1.3: **Molecular mechanisms underlying ataxin-3 pathogenesis**. The abnormal expansion (above 56 CAG repeats) leads to misfolding of the mutant ATXN3 and subsequent oligomerization and accumulation of the mutant protein in aggregates or amyloid fibers, with consequent deposition of insoluble intracellular inclusions. These alterations affect the proteostasis including the proteasome, molecular chaperones, autophagy, and the aggresome formation. Adapted from Da Silva et al. (2019) [53].

ubiquitination, the type of chain it can cleave, and the efficiency of delivery of substrates to the proteasome. However, it is known that a toxic gain-of-function of the expanded ATXN3 protein contributes to MJD pathogenesis (both in patients and mouse models), an effect that is widely attributed to the abnormal interactions of these aggregates with the components of the PQC pathways and other proteins such as ubiquitin, proteasomal components, chaperones, transcription factors, and non-expanded ATXN3 [64–66, 124, 125]. The association of the aggregates of ATXN3 with chaperones is seemed to be reversible suggesting that the chaperones recognize the aggregates as targets for refolding and/or disaggregation of toxic misfolded proteins. Also, it has been demonstrated that, when overexpressed, chaperones can alleviate disease features in MJD models. However, unlike the interaction with the chaperones, the association of the aggregates with the proteasomal components appear to be irreversible, implying a permanent sequestration of these proteins [10, 53].

Apart from the sequestration of proteasome components into the aggregates, the mutant ATXN3 can also affect the degradation of other proteins due its own role in the UPS [105, 126, 127]. Indeed, the polyQ-expanded ATXN3 can interfere with the degradation of proteolytic substrates due to its interaction with UPS components [127]. Some studies have suggested that the polyQ expansion and the accumulation of misfolded proteins inhibits the proteasome activity [122]. Furthermore, some chaperones and UPS

components were shown to regulate the degradation of ATXN3, consistent with a positive role of facilitating mutant ATXN3 degradation in counteracting pathogenesis [128, 129]. In addition, it has also been demonstrated that mutant protein is more prone to autophagic degradation [130].

Studies have established a link between MJD and autophagy, with post-mortem MJD patients' brains showing dysregulated levels of key autophagy proteins [60]. Importantly, a function for the polyQ tract of wild-type (WT) ATXN3 in autophagy has been identified. In particular, the polyQ domain of ATXN3 binds to and regulates the levels of beclin-1, a key protein initiator of autophagy. The ATXN3–beclin-1 interaction protects beclin-1 from degradation by the proteasome, thus enabling autophagy [111]. Similarly, the expanded polyQ domain also interacts with beclin-1, but this binding facilitates its delivery and degradation by the proteasome, resulting in reduced levels of beclin-1 [131]. In fact, in post-mortem brains of MJD patients, a strong dysregulation of autophagy was described, particularly the accumulation of autophagy-related gene (Atg) proteins (e.g., ATG-7) and of LC3, in parallel with reduced levels of beclin-1 [60, 132].

ATXN3 also plays an important role in the removal of misfolded proteins by autophagy through its function on aggresome formation. Indeed, ATXN3's DUB-dependent roles are critical to the formation of aggresomes and the capacity of ATXN3 to regulate aggresome formation is disrupted by the removing of the UIMS or by mutations in the catalytic sites [103, 133]. An overwhelming of the UPS and of the chaperone-refolding system can induce the formation of aggresomes containing misfolded disease proteins involved in NDs [133]. The formation of these cytoplasmic juxtanuclear structures is recognized as a protective response, which sequesters toxic misfolded proteins and promotes their removal by autophagy [103, 134].

Hence, the loss of proteostasis in MJD may be the cause of accumulation of mutant ATXN3 aggregates as well as of the sequestration of key UPS and autophagic regulators [10, 61, 64–66]. While mutant ATXN3 misfolding/aggregation and the consequent loss of cells' proteostasis represent the hub of the pathogenic process in MJD (Figure 1.3) [53], transcriptional dysregulation, DNA damage, impairment of mitochondrial function, increased oxidative stress, disruption of the quality control system responsible for degrading misfolded proteins, endoplasmic reticulum–associated protein degradation (ERAD), and changes in cellular communication through potential impairment of axonal transport and synaptic vesicle dynamics, have also been put forward as consequences of the proteostasis impairment, and proposed to also contribute to the disease progression [53, 113, 135–140].

1.1.5 Microglial contribution to Machado-Joseph disease pathogenesis: what do we know until now?

Although most research in polyQ disorders has been following a neuron-centric point of view due to the obvious presence of neuronal degeneration, microglial cells are now recognized as vital components of the CNS that contribute to neuronal health [10].

Microglia, the primary immune cells of the CNS, play multiple roles in neurodevelopment, synaptic plasticity, homeostasis, injury responses, and NDs [141, 142]. Regarding the contribution of microglia to MJD pathogenesis, microgliosis has been observed both in MJD patients' post-mortem brains and in a

mouse model of MJD [143–145]. However, further studies are needed to explore the basis of microglial activation in MJD. In addition, another study found early increased levels of the chemokine eotaxin, in serum of asymptomatic MJD patients when compared with symptomatic MJD patients and normal controls. This chemokine is secreted by astrocytes, with microglia expressing its receptor, suggesting the involvement of both glial cell types in early stages of the disease [10, 146, 147].

Interestingly, studies in mouse models of SCA1, another polyQ disease, suggest that microglia and astrocytes pathology is induced by neuronal dysfunction and is closely associated with the onset and severity of the disease [148]. Also, a reduction in the number of microglial cells during the early stage of SCA1 resulted in the improvement of motor deficits in a mouse model of SCA1 [149]. In addition, it was demonstrated, in asymptomatic HD patients, an association between activated microglia and increased peripheral levels of cytokines [150]. Further, Crotti and their collaborators showed that the expression of the mutant huntingtin protein only in mouse microglia is sufficient to promote neurodegeneration [151].

Overall, it seems that the evaluation of early microglial dysfunction in MJD and other polyQ disorders may provide information about the early pathogenic mechanisms of the disease before symptom onset [10].

1.2 Origin and development of microglia

In 1913, oligodendrocytes and microglia were firstly characterized as the “third element” of the CNS by Santiago Ramón y Cajal. Years later, Pío Del Río-Hortega phenotypically characterized and named the only immune cells in the brain parenchyma, which are now known as microglia [152]. However, despite microglial cells being first described over a century ago, the understanding of these cells has only gained traction in the last decades [153].

The origin of microglia has now been clearly defined and, unlike other CNS glial cells, these cells were shown to relate to the early colonization of the CNS by erythromyeloid precursors (EMPS) that arise from the embryonic yolk sac (YS) primitive macrophages [154, 155]. During fetal development, these microglial precursors migrate and colonize the brain during embryogenesis, before brain vasculature arbonization is complete and before the blood-brain barrier (BBB) is fully formed, and then mature into microglia [156]. The colonization of the CNS by microglial cells is evolutionarily conserved across vertebrate species and takes place even before the formation of the neuroectoderm-derived glial cell types, i.e., astrocytes and oligodendrocytes [157]. Since microglia migrate from the YS to the CNS at approximately the same time that neurons are formed, this led to the conclusion that microglia participate in the development of the CNS [158].

Such as microglial cells, other tissue macrophages and peripheral monocytes arise from EMPS. Thus, little differences differentiate microglial development from that of peripheral monocytes and other hematopoietic cells [155]. While microglial development is dependent on the transcription factors PU.1, interferon regulatory factor 8 (IRF8), and sal-like protein 1 (SALL1), which initiate gene expression gradually during development, the peripheral monocytes and macrophages depend on the Myb1 for development

[159–161]. Other receptors or signalling molecules also dictate microglial development and can partially impact survival, such as the cytokines interleukin (IL)-34 and the colony stimulating factor-1 (CSF1) and its receptor colony stimulating factor 1 receptor (CSF1R) [162]. The Microbiome also influences microglial development and function, its depletion or manipulation through germ-free conditions or antibiotic treatment resulting in sexually dimorphic effects on pre- and postnatal microglial transcriptional identity and function [163, 164].

Peripheral monocytes contribute little to the microglial population in homeostasis. Adult microglia are defined by a transforming growth factor (TGF)-beta- and transcription factor MAFB-dependent transcriptional signature, discriminating them from peripheral monocytes that invade the brain in certain experimental conditions [165, 166].

In the mature brain, microglia are confined by the fully developed BBB and become an autonomous, long-lived cell population that has the ability to divide and self-renew throughout life [167]. In fact, while human microglia turnover at a yearly median rate of 28 %, and live, on average, for 4.2 years, murine microglia have a long life, most recently estimated to be 7.5–15 months [157, 168, 169]. Thus, most of the microglial population is renewed several times over the course of a lifetime [167, 168]. In support of the importance of microglial self-renewal, a recent study demonstrated that the repopulated microglia that rapidly replenish the adult brain's microglial population after microglial depletion are solely derived from the proliferation of residual microglia and not from newly generated progenitors [170]. In contrast, it was demonstrated that depletion-resistant microglia may derive from a microglia-like progenitor cells similar to the EMPS from which microglia arise [169]. Moreover, contrary to monocytes and macrophages, the resident microglial pool receives no significant replenishment from circulation and is internally maintained by self-renewal, even under conditions of acute depletion [167, 171]. However, it has also been demonstrated that peripherally derived macrophages can replace depleted microglia with cells that maintain their own unique identity (distinct from that of microglia), and that these cells may play a distinct role in the progression or resolution of neurological diseases [172].

1.2.1 Microglial transcriptional and molecular signature

Microglia constitute 5-12 % of all CNS-specific cells in the mouse and 0.5-16.6 % of all cell population in the human brain [173]. These cells are the only true CNS parenchymal macrophages, where they can interact with neurons, astrocytes, and oligodendrocytes to mediate developmental programmes, maintain homeostasis, aid in tissue repair, or contribute to disease pathology [158, 166, 174]. In the healthy brain, they exhibit a unique molecular homeostatic signature, consisting of a specific transcriptional profile and surface protein expression pattern, which differs from that of tissue macrophages [166, 174]. Taking advantage of technological advances such as RNA-sequencing, quantitative proteomics, epigenetics, and bioinformatics, several researchers identified a unique transcriptional signature for homeostatic microglia in adult mice [165, 175, 176]. In contrast to the peripheral myeloid cells, microglial cells were shown to express P2Y purinoceptor 12 (*P2ry12*), transmembrane protein 119 (*Tmem119*), sialic acid binding Ig-like

lectin H (*Siglech*), probable G protein coupled receptor 34 (*Gpr34*), suppressor of cytokine signalling 3 (*Socs3*), beta-hexosaminidase subunit beta (*Hexb*), olfactomedin-like protein 3 (*Olfml3*), Fc receptor-like S, scavenger receptor (*Fcrls*), and *Sall1* [165, 175–178]. Identification of this homeostatic microglial transcriptional signature has enabled the generation of novel and much-needed tools for observing and manipulating microglial functions without affecting other cell types [179, 180].

Mature microglia, referred to as homeostatic microglia, use a vast number of surface molecules in order to respond to cytokines, chemokines, purines, hormones, and neurotransmitters, among others [157, 166, 174]. These surface markers include surface glycoproteins, adhesion G protein-coupled receptor E1 (F4/80) and CD68, and the integrin alpha M (ITGAM, also known as CD11b), and are expressed by microglial cells in both mice and humans [157, 166, 174]. Moreover, murine microglia also express other markers, including the CSF1R, the inhibitory immune receptor cell surface glycoprotein cluster of differentiation 200 receptor 1 (CD200R1), the surface enzyme tyrosine-protein phosphatase non-receptor type substrate 1 (CD172a), the fractalkine receptor CX3C-chemokine receptor 1 (CX3CR1), and the calcium binding protein allograft inflammatory factor 1 (Iba-1) [157, 166, 174, 181]. Despite many of these proteins being expressed by all macrophages, the expression levels of some surface proteins can be used to distinguish microglia from non-parenchymal macrophages (which are meningeal, perivascular, and choroid plexus macrophages) [174]. Indeed, and although this means that the identification is less precise than using specific markers, microglia express lower levels of receptor-type tyrosine-protein phosphatase C (CD45) and major histocompatibility complex (MHC) class II molecules than non-parenchymal macrophages [157, 174].

1.2.2 Microglial functions during central nervous system development and homeostasis

Initially, microglial cells were considered to be in a “resting” or “quiescent” state in normal or healthy conditions, eventually acquiring an activated phenotype in pathological conditions [182, 183]. However, this paradigm, which states that microglia retain a resting state under non-pathological or homeostatic conditions and only react to endogenous and exogenous inflammatory stimuli, has been critically evaluated [184, 185]. In fact, studies have shown that microglia constantly survey their surroundings, extending and retracting their processes, to rapidly react and migrate towards impairments such as neuron death, BBB leakage, or extracellular adenosine triphosphate (ATP) accumulation [184–186]. This observation led to the conclusion that microglia might have important functions under normal or healthy conditions and that these cells carry out diverse maintenance tasks to provide a propitious physiological environment [187, 188]. Thus, the term “surveying” is actually used and represents the basal state of activity of microglia. Similarly, microglia are constantly “activated”, but upon detection of changes in the environment, these cells become “reactive” [153, 189].

Microglia in the surveillance state (previously known as the resting state) can be recognized by their ramified morphology and referred to as homeostatic microglia, constantly screening the brain environment,

with their highly motile processes, for various stimuli (e.g., infection, trauma, or stroke) and contribute to its maintenance and plasticity through specific molecular pathways [142, 157, 158, 184, 185, 189]. In particular, homeostatic microglia participate in multiple important events in the development of the CNS as well as in CNS homeostasis, including synaptogenesis and synaptic plasticity [142, 190], neurogenesis [191–193], neuronal and glial trophic support [194, 195], immune surveillance [191, 196, 197], immune regulation and neuronal activity control [198–200], suppression of the destructive inflammation [201–204], immune cell recruitment [166, 174, 205], and angiogenesis [206–208] (Figure 1.4).

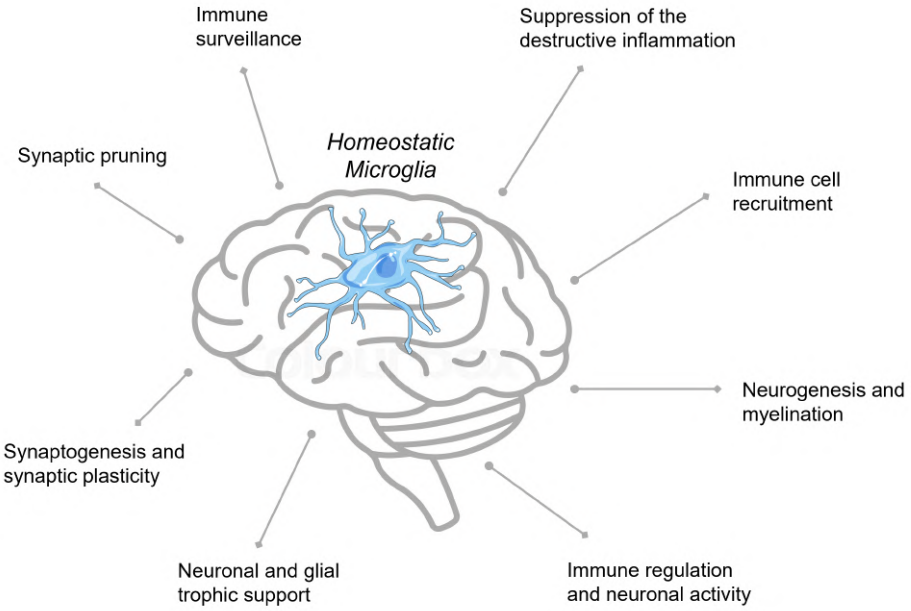

Figure 1.4: **Microglial functions in the central nervous system development and homeostasis**. Homeostatic microglia participate in multiple important events in the brain development and homeostasis including synaptogenesis and synaptic plasticity, synaptic pruning, neurogenesis and myelination, immune surveillance, immune regulation and neuronal activity, among others. Adapted from Angelova et al. (2019) [189].

1.2.2.1 Synaptogenesis and synaptic plasticity

The role of microglia in synaptogenesis and synaptic plasticity during CNS development is well documented (Figure 1.4) [142, 174, 190]. The innate immune system employs the complement, a classical system of proteins and molecules that has a pivotal role in pathogen defence and clearance of cellular debris. Although astrocytes have been shown to express complement components, microglia are the main cells that produce the bulk of complement-related proteins in the brain [174, 209]. During development, microglia play a crucial role in synaptic and axonal pruning through recognition of the complement components C1q or C3, that tag inappropriate synaptic connections and axons, which are then engulfed by microglia via

complement receptor 3 (CR3) [174, 190]. Some studies demonstrated that mice deficient in C1q, C3, or CR3 show reduced microglia-dependent engulfment of synapses as well as defects in synapse elimination or pruning during development [142, 190, 210].

1.2.2.2 Neurogenesis

Microglia contribute to neurogenesis through phagocytosis of excessive newborn cells and by promoting neurogenesis through the secretion of cytokines (Figure 1.4) [166, 174]. Phagocytosis is linked to the homeostatic microglial phenotype and is dependent on the expression of receptor tyrosine kinase MerTK (MERTK), which is responsible for non-inflammatory clearance of dead brain cells in the neurogenic niche [191]. During cerebellar development, microglia actively promote engulfment-mediated Purkinje neuron death, by producing reactive oxygen species (ROS) [211]. Importantly, microglia control the size of the neuronal pool by engulfing neural precursor cells (NPCs) during embryonic and adult neurogenesis, which is mediated by microglial expression of the TYRO3, AXL, and MER (TAM) receptor tyrosine kinases [191, 192]. Hence pharmacological repression of microglia activation or maternal immune challenge in utero can enhance or inhibit phagocytosis of NPCs and modify the cellular composition of the CNS [191]. It is known that a unique molecular signature of microglia is involved in oligodendrocyte development. Interestingly, this signature includes genes that have been described in ageing microglia and in disease models [212, 213]. Inflammation is also important in regulating the influence of microglia on neurogenesis and oligodendrocytes. From adult stem cell progenitor cells, microglia activated by IL-4 or interferon gamma (IFNγ) induced oligodendrogenesis or neurogenesis, respectively [193]. Indeed, high levels of IFNγ induced a microglial phenotype that impeded oligodendrogenesis. IL-4 reduced this impediment and overcame the blockage of insulin-like growth factor-1 (IGF-1) production that was caused by IFNγ [193]. In addition, microglia actively promote injury-induced neurogenesis by producing IGF-1, which is known to supress apoptosis and increase proliferation and differentiation of neural stem cells [214].

1.2.2.3 Neuronal and glial trophic support

Microglia also secrete or produce neurotrophic factors that promote survival and support of neuronal and glial cells during CNS development and homeostasis (Figure 1.4) [158, 207]. For example, microglia secrete IGF-1 to support the survival of certain types of NPCs and oligodendrocytes precursors during embryonic development [194]. In addition, adult mice with IGF-1 deficient microglia show defects in myelination [195]. This finding suggests the importance of microglia-specific IGF-1 in the myelination process [195]. The importance of microglia and the factors that they produce in supporting other glial cells is demonstrated by the fact that microglial ablation decreases oligodendrocytes and oligodendrocyte progenitor cell pool in the mice brain, thus leading to reduced postnatal myelinogenesis [212]. TGF-beta and brain-derived neurotrophic factor (BDNF) are additional microglia-derived factors that promote and regulate the development of the CNS [207]. Microglia also answer to injury through the expression of specific growth factors. In

the injured striatum, activated microglia induce the sprouting of dopaminergic neurons and express both BDNF and glia cell line-derived neurotrophic factor (GDNF) [215].

1.2.2.4 Immune surveillance

Microglia are the primary immune cells of the CNS, quickly responding to changes in the microenvironment due to their surveillant nature. They extend and protract their complex and branched processes expressing surface receptors that detect extracellular signals released by neurons and glial cells (Figure 1.4) [142, 157, 158, 216]. Upon detection of an activating signal, microglia play their role as immune sentinels, through phagocytosis and the secretion of cytokines and mediators of inflammation [166, 174]. Microglial phagocytosis is essential for maintaining CNS homeostasis in healthy and disease since microglia phagocytose pathogens, apoptotic cells, aggregated proteins, myelin debris, and dysfunctional neurons can have a negative impact on brain function [166, 174, 196]. Apoptotic cells, when exposing on their membranes "eat-me" signals, activate surface phagocytic receptors on microglia, such as MER and AXL tyrosine kinase receptors, to initiate phagocytosis through cytoskeletal remodelling [191, 196, 197]. Phagocytosis promotes the release of proinflammatory cytokines and ROS, activating microglia during NDs [207]. Additionally, the triggering receptor expressed on myeloid cells-2 (TREM2), another microglia-specific phagocytic surface receptor, and MERTK and AXL receptors have all been involved in myelin debris clearance during certain NDs [196]. Contrarily, microglia-mediated phagocytosis of apoptotic cells or debris can be blocked by microglial surface receptor signal-regulatory protein (SIRP) alpha, which binds to CD47 expressed by neurons or myelin [217].

1.2.2.5 Immune regulation and neuronal activity control

Microglial receptors and their neuronal signalling molecules are linked to immune regulation and neuronal control during CNS development and homeostasis (Figure 1.4) [207]. Indeed, it has been demonstrated that the CX3CL1-CX3CR1 signalling pathway, where the CX3CR1 is the chemokine receptor expressed by microglia and CX3CL1 (also known as fractalkine) is the neuronal ligand, is involved in preventing neurotoxicity through the inhibition of microglial activation associated with the release of proinflammatory cytokines, which, if prolonged or uncontrolled, can lead to neurotoxicity, synapse loss, or dysregulated neuronal homeostasis [198, 199, 201]. In addition, CX3CL1-CX3CR1 signaling has been proposed to act in microglial migration and synaptic engulfment [142]. Moreover, CX3CR1 knockout in adult mice leads to reduced synaptic plasticity and behavior impairments [218]. Additionally, in adult mice, it was demonstrated that microglia monitor and modulate neuronal activity due, in part, to microglia-specific receptors (e.g., purinergic receptor P2RY12), which recognize levels of metabolites, such as ATP, released by glia and neurons, directly supressing neuronal activity and firing during homeostasis [174, 219]. During CNS development and homeostasis, the TREM2 receptor, expressed mainly in microglia in the CNS, mediates the elimination of synapses by microglia and synapse engulfment via astrocytes [220]. The CSF1R and its ligands, CSF1 and IL-34, are important for the survival of microglia, since knockout adult mice of CSF1R

or ligands show reduced microglial density [162, 221]. Moreover, microglia and other myeloid cell populations can be depleted in adult mice through the administration of certain CSF1R antagonists [169, 222, 223]. The interaction of the glycoprotein cluster of differentiation 200 (CD200), expressed by neurons, and its receptor cluster of differentiation 200 receptor (CD200R), expressed mainly by microglia and myeloid cells, seem to act as a potent immune suppressor, where the triggering of the CD200/CD200R signalling pathway delivers inhibitors signals to block microglia activation and inflammatory responses, thus limiting the production of inflammatory cytokines such as IL-1 beta and IL-6 [200]. In accordance, CD200 knockout mice display severe progression of neuroinflammation, with an enhancement in the production of proinflammatory cytokines by microglia [224]. Likewise, CD200/CD200R signalling was shown to be involved in the recovery of synaptic plasticity after injury through the inhibition of microglia activation and the reduction of inflammatory factors release [225].

1.2.2.6 Neuroinflammation suppression

Neuroinflammation is a defense mechanism within the CNS that, through the activation of the innate immune system, protects the brain by removing, or inhibiting, inflammatory challenges including pathogen-associated molecular patterns (PAMPS) and damage-associated molecular patterns (DAMPS) (Figure 1.4) [201–204]. The recognition of PAMPS and DAMPS is due to the cellular receptors expressed on microglia such as toll-like receptors (TLRs), nuclear oligomerization domain-like receptors, and viral receptors [204]. The inflammatory response of microglia to such stimuli can have beneficial effects by promoting tissue repair and removing cellular debris and pathological agents through the production of proinflammatory cytokines such as tumor necrosis factor (TNF)-alpha, IL-1 beta, IL-6, ROS, and chemokines including the C-C motif chemokine ligand 2 (CCL2) and IL-18. However, despite neuroinflammation being a neuroprotective mechanism, prolonged or uncontrolled inflammatory stimulation due to endogenous (e.g., genetic mutation and misfolded protein aggregates) or environmental (e.g., infection, trauma, and drugs) factors can lead to neurodegenerative diseases [201, 202, 226–228]. Hence, microglia can suppress the destructive neuroinflammation, restore homeostasis, and protect nerve tissues by producing anti-inflammatory mediators such as IL-4, IL-10, and TGF-beta, which supress the exaggerated inflammatory response and the function of pro-inflammatory cytokines [201, 202]. For example, IL-4 is known to supress the release of pro-inflammatory cytokines such as IL-6 and TNF-alpha, and nitric oxide (NO) [229].

1.2.2.7 Immune cell recruitment

Microglia recruit, in a CCL2-dependent manner, circulating myeloid cells such as the monocytes to the brain (Figure 1.4). During certain diseases or injuries involving disruption of the BBB, lymphocyte antigen 6C (LY6C)^{hi} classical inflammatory monocytes may infiltrate the brain parenchyma and differentiate into microglia-like cells, which are blended with the resident microglia pool, to exacerbate or alleviate disease progression [166, 174]. For example, it was demonstrated that microglia-derived from the spinal cord (SC) of a SOD1 mouse model of Amyotrophic lateral sclerosis (ALS) recruited to the CNS splenic monocytes

expressing CC-chemokine receptor 2 (CCR2) and high levels of LY6C^{hi} [230]. Interestingly, the highest levels of CCL2 are expressed when microglia switch from homeostatic to disease-associated phenotypes that facilitate the recruitment of monocytes to the CNS [166, 174].

Furthermore, surrounding the lesion site, it has been described an increase in the number of activated microglia. This intense reaction of microglia to pathogenic insults is designated as "microgliosis". Although the accumulation of microglia has been described in most neuropathological conditions, the source of accumulated microglia involved in microgliosis remains controversial [231]. Evidence suggests that at least three sources for microgliosis may exist in the adult CNS: local proliferation of reactive microglia, infiltration of blood-derived cells, and mobilization of latent progenitors within the CNS [231, 232]. Each or all sources may play a role in microgliosis in different pathological conditions. The predominant origin of microgliosis under a particular pathological condition may depend on the nature of the disease and its pathological manifestations, and may vary when different experimental models are used [231, 232].

1.2.2.8 Angiogenesis

Microglia also play important roles in maintaining and contributing to the homeostasis of the neurovascular system of the brain. During brain regions' development, microglial cells migrate near and along blood vessels [206, 207]. In adulthood, microglia participate in the formation of new blood vessels in the retina and certain regions of the mouse brain, maintaining contact with the vasculature not covered by astrocytic endfeet [206–208].

1.2.3 Phenotypic heterogeneity of microglia between central nervous system regions

Taken together, it is becoming apparent that microglia are involved in a wide range of activities in the development, health, and disease of the CNS. How such a single cell type is capable of mediating multiple functions is unclear and remains to be determined. Strong evidence is now emerging that microglia can be divided into distinct subclasses [153, 233]. Nevertheless, it remains to be determined if these subclasses represent intrinsically distinct cell populations or if intrinsically similar cells are driven into functional heterogeneity imposed by changes in the environment, provided by a highly dynamic CNS [234].

The presence of microglial heterogeneity across different regions in the CNS has also been recognized recently. Microglia differ in their density, morphology, and molecular signatures in different brain regions [153, 233, 234]. The phenotypic heterogeneity of microglia between brain regions is likely the result of their surrounding microenvironment, namely of interaction with neurons, neighboring glia, and stem cells, as well as the infiltrated blood-derived molecules in certain brain regions with an incomplete BBB, and of their intrinsic mechanisms [233, 234]. Hence, understanding microglial regional heterogeneity in the context of their diverse neighboring cells, such as neurons and other glial cells, may provide an important path for the development of therapies for neurodegenerative disorders.

1.2.3.1 Microglial density

Some of the earliest studies on the distribution of microglia in the normal adult mouse brain have observed differences in microglial densities in different brain regions. Studies using antibodies against F4/80 and lipocortin 1 (LC1) reported brain-region specific cell densities, with higher density in the forebrain, hippocampus, basal ganglia, and substantia nigra and lower in the midbrain, fiber tracts, cerebellum, and brainstem [235, 236]. Likewise, recent works using an Iba-1 antibody confirmed a higher microglial number in the frontal cortex and a lower one in the cerebellum and spinal cord [237]. Additionally, earlier evidence using CD68 and MHCII antibodies also demonstrate regional heterogeneity in the human microglia, with less CD68- and MHCII–positive cells in the cerebellum than in the mesencephalon and medulla oblongata. In addition, the numbers of microglia in the white matter are higher when compared to gray matter [238].

Interestingly, heterogeneity in microglial density was found to exist even within the same region, such as within the cerebellum. Indeed, it was demonstrated that microglial density was higher in the cerebellar nuclei than in the cerebellar cortex, and within the cortex the molecular layer was less densely populated by microglial cells than the granular layer and the white matter [239]. Moreover, a microglial depletion study using a genetic approach demonstrated that, in different brain regions, there was diversity in the repopulation of microglia after depletion, with residual microglia recovering more rapidly in the cortex and spinal cord than in the cerebellum [240]. The neuron-microglia crosstalk mechanism may support the regional differences in microglial densities. Microglial depletion studies showed that Il-34, one ligand of the CSF1R expressed mainly by neurons, was important in maintaining microglial numbers in a region dependent manner, as microglia density was reduced in Il-34-deficient mice only in the cortex and striatum, but not in the cerebellum and brainstem [162]. In addition, another study also confirmed that a depletion of the CSF1, another ligand of the CSF1R, affected the number of microglia in the cerebellum but not in the frontal cerebral cortex [241].

It is also important to note that the density of microglia in different brain regions is correlated with the overall glia-to-neuron ratio across the brain. Moreover, different rates of cell proliferation and/or cell death of mature residential microglia or (re)population of different microglial progenitor cells from different embryonic brain regions may also contribute to variations of microglial density in different regions [233].

1.2.3.2 Microglial morphology

The morphology of microglia is one of its most important characteristics. These cells exhibit plasticity and undergo constant morphological changes to engage with other CNS elements for synaptic pruning and clearance of tissue debris under physiological and pathological conditions [183, 242]. Morphological changes are accompanied by an increase in the expression of Iba-1 and CD11b. In addition to these two microglial receptors, microglia activation leads to an increased expression of MHCII and CD68 [243]. According to their shape, microglial cells have been categorized as ramified (numerous thin processes, radial branching), activated or reactive (thickened stout processes with highly reduced branching), or amoeboid

(rounded soma with no branching) [153, 157, 234, 242, 244]. Although microglia is normally ramified in most brain regions, differences in microglial morphologies have been reported in the different brain regions, providing evidence that microglial cells are highly sensitive to the surrounding environment [157, 234].

After colonization of the embryonic CNS, most microglial cells display an amoeboid-like morphology, but with CNS maturation, microglia change their morphology on a brain region-specific manner [153]. In the steady state of the CNS, while amoeboid-like microglia are more abundant in white matter regions, the extent of ramified morphology varies between regions, microglia in the cerebellum presenting a smaller soma and bigger cytoplasm area with lower ramification complexity than those in striatum, hippocampus, and frontal cortex [235, 237]. Even within the same region, such as in the cerebellum, significant heterogeneity in microglial morphology was also found to exist. In fact, studies revealed that microglial cells were ramified in all cerebellar lobules of mice but showed different sizes and ramification patterns as a function of their specific location in the different histological layers [239]. Interestingly, a recent study suggested that differences between cerebral and cerebellar microglial distribution and morphology may underlie a decreased surveillance of Purkinje neurons by cerebellar microglia [237]. Similarly, cortical microglia were found to extend their processes for the site of ATP release faster than microglia in the subventricular zone, which were less branched [245]. Studies have also found that microglia in brain regions with an incomplete BBB displayed an amoeboid form with fewer, or shorter, branched processes [233].

It is widely accepted that the morphology of microglia is closely coupled to their functional state. In the healthy brain, microglia are characterized by their ramified morphology, constantly screening the brain, pruning synapses, and regulating neuronal activity, providing a “fine-tunning” of neural circuits and neurotransmitter signaling/synaptic transmission [184, 210, 246]. However, upon detection of an activating signal or damage, microglia migrate to the site of inflammation or injury and change to an activated or reactive state [182, 242]. Indeed, the morphology of microglia is an important characteristic to identify their activation state [242]. A microglial cell that is in an activated or reactive state but that does not assume the phagocytic phenotype displays a thickening of its branches, up-regulation of MHCI/MHCII, secretion of pro-inflammatory cytokines, and increased ROS production. As they progress in their activation, they can assume a phagocytic state, characterized by large cells that can also exhibit rod-shape or amoeboid-like morphologies, whose processes contain pyknotic fragments and phagocytose material. This state is observed in physiological conditions during brain development, but also in pathological conditions [153, 189, 247, 248]. Moreover, a recent study showed that microglia from the cerebellum present a higher level of clearance activity when compared with those from striatal or cortical zones, associated with an elevated degree of cerebellar neuronal death [249]. Some microglial morphologies are associated to a motility stage, where microglia move to another location within the tissue displaying dynamic cycles of extension and retraction of their processes [158, 250].

Amoeboid and ramified microglia were found to produce equivalent levels of cytokines and chemokines. However, only amoeboid microglia expressed genes involved in cell cycle and migration. This implies that morphologically polarized subtypes of healthy microglia may not differ in their immune properties but may

confer different synaptic modulation functions [251].

1.2.3.3 Microglial molecular signature

In the surveying state, microglia express the Iba-1, CD68, CD11b, CD40, CD45, CD80, CD86, F4/80, TREM2, CXCR3, CCR7, and CCR9 markers [157, 173, 233, 252]. However, regional differences have been described. Regarding the region-specific expression of key microglial receptors, the CD11b, CD45, CD86, and CCR9 markers were found to be more expressed in the spinal cord than the hippocampus [253]. Additionally, it was also found that microglia in the spinal cord express higher levels of CD11b/c and MHCII when compared with the cortical regions [254]. Nevertheless, another study shows no expression of MHCII in the spinal cord [253]. Also, differences between the brain and spinal cord have been reported regarding microglia-mediated neuroinflammation. Higher expression levels of immune molecules were found in microglia from the spinal cord when compared with microglia from brains at the basal state and upon viral infection [254, 255]. Moreover, it was demonstrated by Hart and collaborators that aged mice had greater upregulation of microglial activation markers CD11b, CD68, CD11c, F4/80, and FcyRI in the white matter than in gray matter [256].

Overall, this phenotypic heterogeneity of microglia between CNS regions may lead to diversified responses of microglia towards pathological stimuli at different regions, and possibly also in age- and gender-dependent manners [233]. Given the lack of success of clinical trials on generic immunosuppressants or anti-inflammatory drugs for neurodegenerative diseases [174], targeting only a subclass of microglia in a region-specific manner rather than globally, may have more promising therapeutic efficacy [153].

1.2.4 Microglial involvement in neurodegenerative diseases and aging

The regulation of the microglial phenotype is essentially dependent on its interaction with molecules released by surrounding cells such as neurons, microglia, other glial cells, among others, through the membrane-bound pattern recognition receptors (PRRs) [173, 201, 202, 204]. The classification of these microglial PRRs depend on their affinity for molecules associated to pathogens (PAMPS) or cellular damage (DAMPS) [201, 202, 204, 257]. However, microglial regulation is not only performed by PRRs since microglia are also equipped with a wide variety of receptors to detect other type of molecules, such as hormones and neurotransmitters [204, 257].

1.2.4.1 From a M1/M2 category to a microglial profile

Microglia become activated upon stimulation with a wide variety of signals. Traditionally, and depending on the signals they receive, the microglial activation profiles were referred to as “M1” and “M2”, comparable to those established for peripheral macrophages [153, 173, 183, 201, 207, 258]. This nomenclature categorized “M1” microglia as a proinflammatory state, in which microglial cells, in response to pro-inflammatory factors such as debris from pathogens or damaged cells, produce and release ROS, nitrogen reactive species (NRS) as NO, and pro-inflammatory cytokines such as IL-1 beta, TNF-alpha, and IL-6 [173,

207, 227, 258, 259]. On the other hand, "M2" microglia was considered as an anti-inflammatory sate, in which microglia, in response to anti-inflammatory factors, produce and release anti-inflammatory cytokines and trophic factors associated with immune resolution, phagocytosis, tissue healing and regeneration, and neuroprotection, such as IL-4, IL-13, IL-10, Arginase 1, TGF-beta, and BDNF [173, 201, 227, 259, 260]. However, nowadays, this classification is highly controversial and has been shown not respond to the variety of microglial phenotypes found in the brain. Thus, the scientific community do not longer refers to microglia as M1/M2, but only refers the involved cytokines [173, 183, 207, 258].

Neuroinflammation is defined as an inflammatory response within the CNS, that is mediated in part by the activation of microglial cells that, in response to inflammatory challenges, produce both pro- and anti-inflammatory mediators to protect the brain through tissue repair and by recognizing and removing pathological agents, and dying and dead cells [201, 203, 259]. However, although neuroinflammation is a neuroprotective mechanism, an imbalance between pro- and anti-inflammatory microglial functions, making these cells become mostly pro-inflammatory, might constitute a crucial component onset and progression of NDs [244, 261]. Thus, chronic/persistent neuroinflammation, that can be due, among other factors, to genetic mutations and misfolded protein aggregates, that often accumulate in lesions of neurodegenerative diseases, can induce neurotoxicity and lead to neuronal demise in Alzheimer's disease (AD), HD, Parkinson's disease (PD), and ALS, among others [201, 202, 216, 226–228, 244, 261].

Cumulative evidence also suggested that, during neurodegeneration, microglia can lose beneficial functions and gain neurotoxic ones, in addition to mediating inflammation. Indeed, microglia might over-produce pro-inflammatory mediators and reactive species, which can lead to neuronal damage and, in turn, contribute to sustaining inflammation in the NDs [201, 216]. However, microglial cells are considered to have different phenotypes related to the type and stage of NDs and the regional location. Moreover, the changes in phenotypes of microglia, their loss of neuroprotective role, and gain of detrimental functions may differ with the stage and severity of NDs [173, 216, 262].

1.2.4.2 "Primed microglia" profile

If the imbalance of homeostasis in CNS is continuous, the chronic inflammation could accelerate microglia aging, priming microglia to eventually react with exaggerated responses that contribute to neurodegeneration (Figure 1.5) [204, 263–265].

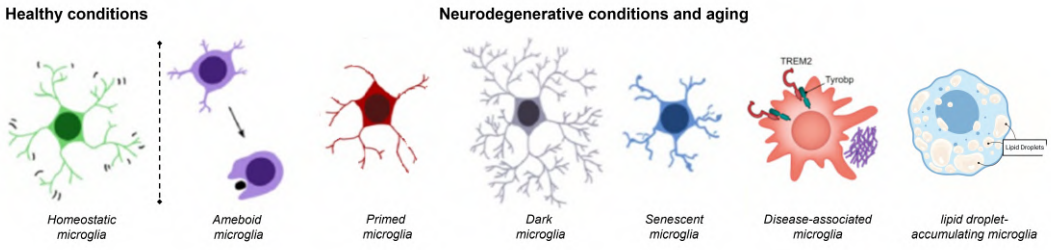

Figure 1.5: **Microglial profiles that could be implicated in the neurodegenerative diseases and aging**. Adapted from Lecours et al. (2018) [216].

With aging, microglia take on a "primed" phenotype, which is characterized by an exaggerated and uncontrolled inflammatory response to an immune stimulus [263, 265, 266]. Primed microglia are vulnerable to subsequent immune stimuli, such as immune challenges, chronic psychological stress, and aging. Thus, upon exposure to these stimuli, primed microglia take on a "hyperactive" state marked by an exaggerated pro-inflammatory response and resistance to regulation [263, 267, 268]. Primed microglia can induce and/or amplify chronic neuroinflammation and inflammatory reactivity, and reduce the release of neurotrophic factors, resulting in loss of healthy neurons in quantity and function that has relationship with NDs [264, 265].

Primed microglia are characterized by a dystrophic morphology including de-ramified processes, spherical cell body, and fragmented cytoplasm [269]. Associated with these morphological alterations are biochemical changes, such as elevated expression of antigen presentation molecules (MHCII), TLRs 2,3, and 4, pro-inflammatory cytokines (IL-1 beta), reduced expression of regulatory molecules (CX3CR1 and CD200R), DNA methylation changes, and telomere shortening [189, 270, 271]. Microglia of the aged brain also show deficient phagocytic activity and impaired mobility [272]. The transcriptional signature of microglial priming seems to be dependent on the high mobility group box 1 (HMGB1) and inhibiting it prevents microglia from entering a primed state [273, 274]. Moreover, microglia show a low rate of mitosis in the surveillance state and a high rate of proliferation after being primed, indicating that microglia possess the ability to counteract cell turnover and resist pro-inflammation stimuli [167, 265]. Although the immunological profile of the aged brain is generally discussed in the context of microglial priming and enhanced pro-inflammatory signalling, some findings indicate that microglia undergo senescence as a function of age [263, 269].

1.2.4.3 Senescent microglial profile

Age-related neurodegenerative diseases have been related with chronic and progressive neuronal loss but also with chronic neuroinflammation involving activated/primed microglia [204, 263–265, 275]. Yet, the increased presence of senescent microglia in different neurodegenerative diseases including, AD, PD, multiple sclerosis (MS), HD, frontotemporal dementia, and ALS, suggests the involvement of microglial senescence in the occurrence, or aggravation, of the pathophysiology of these disorders (Figure 1.5) [189, 269, 275–278].

Cellular senescence, which is characterized by a permanent state of cell cycle arrest, can be induced by several factors including chronic neuroinflammation, DNA damage, oxidative stress and mitochondrial dysfunction, and altered proteostasis [266, 276, 279, 280]. Neuroinflammation and oxidative stress can induce DNA damage and alterations in DNA repair that, in turn, can exacerbate them and contribute to accelerated cell senescence [259, 281–285]. Another important feature associated with senescence is an impaired proteostasis. Due to the disruption in the function and balance of the proteome, the senescence state can modify the proper synthesis, folding, quality control, and degradation rate of proteins producing misfolded proteins or aggregation of abnormal proteins in age-associated neurodegenerative disorders

such as HD, PD, and AD [266, 286–288].

The senescent phenotype has been associated with an increased expression of specific proteins, considered senescence indicators, including some cell cycle regulators and pro-inflammatory cytokines that comprise the so-called senescence associated secretory phenotype (SASP) [276, 279, 280, 289–291]. In the brains of aged mice and in some animal models that mimic NDs, microglia showed senescent features including increased levels of cell cycle regulators, such as $p16^{Ink4a}$ (also known as *Cdkn2a*), $p19^{Arf}$ (also known as *Cdkn2a*), and $p21^{Cip1/Waf1}$ (also known as *Cdkn1a*) and senescence-associated pro-inflammatory cytokines, such as Pai1 (also known as *Serpine1*),Il-6, Il-8, Tnf-alpha, Il-1 alpha and Il-1 beta, and shortened telomeres [277, 280, 290–293]. Some reports have associated a de-ramified morphology and cytoplasmic fragmentation to microglial senescence [189, 266, 278, 294]. The dysmorphic features of aged microglia suggest that, rather than an overactivated state, these cells display a decreased ability to mount a normal response to injury. In fact, reduced migration to sites of injury, reduced ability to phagocytose debris and toxic protein aggregates, reduced production of neurotrophic factors, and the inability to shift from a proinflammatory to an anti-inflammatory phenotype to regulate injury and repair have been observed in aged microglia and related with senescence [266, 272, 275, 278, 295, 296]. Additionally, myelin debris, released from aging myelin sheaths and in some neuropathological conditions, are cleared by microglia. However, with age, this myelin fragmentation increases in microglia and leads to the formation of insoluble, lipofuscin-like lysosomal inclusions that contribute to microglial senescence [297]. These age-related changes in microglia are known to contribute to neurodegeneration [189, 202, 275, 278, 280].

1.2.4.4 “Dark microglia” profile

Another phenotype of microglia, “dark microglia”, was identified based on morphology by electron microscopy in non-homeostatic conditions (Figure 1.5) [153, 216]. Dark microglia display markers of oxidative stress, including a condensed cytoplasm and nucleoplasm, which led to their name, disrupted mitochondria, and dilation of the endoplasmic reticulum and Golgi apparatus. Moreover, these cells are highly ramified extending their processes toward synaptic clefts, suggesting an involvement in synaptic remodeling under pathological or traumatic conditions [216, 298]. Bisht and colleagues proposed that this microglial profile constitute a subclass of hyperactive microglia with dysregulated interactions with synapses, which may contribute to the progression of several NDs with known synaptic loss [153, 298].

1.2.4.5 Disease-associated microglial profile

In the healthy CNS, microglia exhibit a unique homeostatic transcriptional signature that differs from non-CNS tissue macrophages [207]. This homeostatic phenotype is associated with a variety of functions including microglial-mediated neuroprotection, synaptic support, and immune surveillance, and is defined by the expression of “homeostatic” microglial genes such as Cx3cr1, P2ry12, Tmem119, TGF-beta receptor 1 (TGFBR1), Sall1, myocyte enhancer factor-2 (Mef2)a/c, musculoaponeurotic fibrosarcoma oncogene

homolog b (Mafb), and smad family member 3 (Smad3). However, upon neurodegenerative conditions, microglia lose homeostatic molecules and functions, and acquire a unique non-homeostatic transcriptional and functional signature known as disease-associated microglia (DAM) [153, 166, 174, 203, 207, 299]. This DAM phenotype acquires a gene signature associated with a microglial neurodegenerative (MGnD) phenotype (Figure 1.5) [153, 203, 207]. First identified in AD and ALS mouse models, DAM or MGnD profiles have been recently described in tauopathy and MS mouse models, and aging [175, 213, 273, 300–302]. DAM profiles are associated with the expression of genes, many of which were found in human genome-wide association studies (GWASs) as linked to AD and other neurodegenerative diseases. The TREM2 receptor is one of these genes and is required for DAM activation [213, 303]. Indeed, the acquisition of a DAM profile occurs thought a two-step activation process in which homeostatic microglia first transition to an intermediate stage (known as stage 1 DAM) in a TREM2-independent manner, followed by a second TREM2-dependent transition to stage 2 DAM [213]. Typically, the DAM profile is characterized as immune cells expressing microglial markers such as Iba-1, cystatin 3 (Cst3), and Hexb, coincident with the downregulation of the homeostatic genes including Cx3cr1, P2ry12, and Tmem119, and with the upregulation of specific DAM or MGnD-associated genes such as Trem2, apolipoprotein e (Apoe), lipoprotein lipase (Lpl), cystatin-7 (Cst7), secreted phosphoprotein 1 (Spp1), Axl, C-type lectin domain family 7 member a (Clec7a), and transmembrane immune signaling adaptor (Tyrobp), among others [153, 165, 166, 207, 213, 299]. These upregulated genes are involved in lysosomal, phagocytic, clearance of apoptotic cell bodies, and lipid and lipoprotein metabolism pathways [166, 207, 299, 304]. This transcriptional signature represents a preference for lipids as fuel substrates that satisfy the greater bioenergetics needs of activated microglia [304].

Although unique to non-homeostatic conditions, the function of DAM is not known [153, 203]. Some studies have proposed that microglia sense and respond to neuronal damage signals commonly present in various neurodegenerative conditions that are known as neurodegeneration-associated molecular patterns (NAMPs). These NAMPs include misfolded protein aggregates, apoptotic neurons, myelin debris, and lipid degradation products, and are recognized by a battery of receptors expressed on microglia, such as TREM2, which trigger the transition of surveying microglia into DAM [207, 299, 304]. Although NAMPs function in a similar manner to the peripheral immune system signals, PAMPS and DAMPS, detected via PRRs, certain “classical activation” ligands (e.g., bacterial endotoxins, viruses, etc.) do not induce the DAM/MGnD-phenotypic signature in microglia [207, 299, 302]. These findings support the notion that the DAM profile could be the result of microglial reactivity to misfolded protein aggregates, one of the main hallmarks of several neurodegenerative disorders [207, 305]. However, it remains unclear whether the loss of homeostatic function in microglia, or the DAM/MGnD profile, is correlated with the degree of neuronal loss, and whether DAM/MGnD is beneficial, or detrimental, to neurodegenerative diseases [153, 166, 203].

1.2.4.6 Lipid Droplet-Accumulating microglial profile

Healthy microglia clear lipids via cell surface scavenger receptors, such as ApoE, LPL, and TREM2 [304]. Hence, upregulation of the ApoE, TREM2, and LPL genes in microglia during development, damage, and disease, suggest that an increased lipid metabolism is needed to fuel protective cellular functions such as phagocytosis [213, 304]. However, aged or proinflammatory microglia accumulate cholesterol and other myelin-derived lipids, which impairs their ability to phagocytose [304, 306]. Recently, Marschallinger and colleagues discovered a new microglia subclass known as lipid droplet-accumulating microglia (LDAM), which is distinct from previously reported microglial profiles in aging and neurodegeneration, and contributes to neuroinflammation, age-related, and genetic forms of neurodegeneration such as AD, PD, HD, and ALS (Figure 1.5) [304, 307].

With aging, LDAM accumulates lipid droplets (LDs), which are mainly composed of glycerolipids, such as triacylglycerols and diacylglycerols. This profile is defective in phagocytosis, produces increased levels of ROS, releases elevated levels of proinflammatory cytokines, and possesses a gene signature that is similar to that driven by innate immune stimuli, such as bacteria and viruses [306–308]. Neuroinflammation is also a key player for lipid droplet formation in the aged brain. Indeed, lipopolysaccharides (LPS), a commonly proinflammatory stimulus, has been shown to increase the number and size of LDs in microglia that are colocalized with the Perilipin 2 (PLIN2) [308, 309]. This suggests that PLIN2 is an LDs-associated protein and may be considered as a marker of LDs and inflammation in CNS [308]. Marschallinger and colleagues observed that LPS induces lipid droplet formation in murine microglia-derived BV2 cells. Moreover, these authors also showed increased lipid droplet-containing microglia in LPS-treated mice when compared with non-treated mice [307].

A recent study demonstrated that TREM2 receptor regulates microglial cholesterol metabolism and although the TREM2-knochout microglia phagocytose myelin debris, these cells fail to clear myelin-derived cholesterol and upregulate lipid metabolism genes, resulting in cholesterol esters (CEs) accumulation [310]. Increased accumulation of the CEs was also observed in ApoE-deficient glial cells [310, 311]. Curiously, the same authors showed that aged hippocampal microglia are mainly composed of glycerolipids, while CEs are almost absent [307]. Thus, the relationship between composition of lipid droplets and microglial function should be further investigated [306–308].

1.2.5 Microglia as therapeutic targets in neurodegenerative diseases

Given the essential role of microglia in the regulation of CNS homeostasis, the potential therapeutic in targeting microglia is vast, including genetic and degenerative diseases such as AD, PD, HD, SCAs, MS, and ALS [166, 201, 202]. It is now recognized that microglia are resident macrophages of the CNS that are independent from myeloid cells, such as monocytes and macrophages, that migrate into the brain from the periphery [157, 158, 166, 174]. Thus, therapeutic targeting of microglia themselves must target them in the brain. The goal of microglial-targeted therapy is to maintain homeostatic microglial function and to restrain, or inhibit, inflammatory or disease-promoting microglial profiles [166, 189, 207, 264,

299, 306, 308]. Thus, one possible approach could be to agonize molecular targets that enhance the homeostatic signature and antagonize those that drive to diseases [166]. However, the distinction between homeostatic and disease-associated signatures is not absolute in terms of their impact on disease, since some non-homeostatic microglial disease signatures may indeed have neuroprotective effects in halting the disease progress [153, 166, 203, 207]. Thus, it is important to amplify the molecular characterization of homeostatic and disease associated microglia, which will provide one way to identify new microglial-directed therapeutic targets for treatment of NDs [153, 166].

CSF1R signalling is critical for microglial survival and maintenance, and loss-of-function mutations in either of its two natural ligands, CSF1 and IL-34, results in a significant reduction in microglia density [162, 207, 221, 312]. In addition, the CSF1R inhibitor PLX3397 has been widely used in recent studies as a safe research tool to acutely deplete microglia as well as a potential strategy in the treatment of NDs such as AD, PD, HD, ALS, and SCA1 [149, 223, 313–317].

Importantly, despite an increase in the number of therapeutic strategies assessed in mouse models of polyQ diseases in recent years, there is still no effective treatment for theses disorders, including MJD [78, 88, 318–321]. Since the contribution of microglia has already been reported in the pathogenesis of polyQ diseases, including MJD [143–147], SCA1 [148, 149], and HD [150, 151, 315], it is relevant to investigate the potential utility of these cells as potential targets to counteract MJD and other polyQ disorders.

1.3 Objectives

Microglia-mediated inflammation is a significant contributor to NDs pathogenesis as it may occur at an early stage. Yet, some studies suggested that microglia change their characteristics with age, switching to a senescent/dystrophic profile with disease progression, being increasingly involved in the occurrence, or aggravation, of neurodegenerative diseases, including AD, PD, MS, HD, and ALS. MJD pathophysiology appears gradually and progresses over time, pointing to an age-dependent decline in the cells' ability to remove misfolded Ataxin-3, which is expressed ubiquitously in brain cells, including neurons and microglia. These data would support the age-related microglial dysfunction hypothesis, which views the loss of microglial neuroprotection as a central event to the progression of neurodegenerative processes in MJD. Thus, when studying age-associated disorders such as MJD, it is of the utmost importance to characterize the senescent/dystrophic profile of microglia.

Additionally, microglia in neurodegenerative disease mouse models show a loss of homeostatic phenotype and an activation of non-homeostatic or pathological microglial profiles. Even though the contribution of microglia to several neurodegenerative diseases is well recognized, the profile of microglia and their involvement in MJD remains unexplored. Thus, the goal of this study was to characterize the profile of microglia in the CMVMJD135 mouse model of MJD, with a particular focus on the brainstem, cerebellum, and spinal cord, three of the brain areas most affected in this disease. We also aim to explore the contribution of microglia to MJD pathogenesis by evaluating the impact of microglial depletion on the motor phenotype of this mouse model.

To achieve these goals, this study sets four specific aims:

1. **To study if microglia from CMVMJD135 mice show a senescent/dystrophic profile with age and disease progression**, by evaluation of different senescence markers in microglia isolated from adult CMVMJD135 mouse brains and using primary microglial cultures from CMVMJD135 neonatal mice, exploring the differences in functional response characteristics associated to "young" and "aged" microglia phenotypes, by assessing phagocytic activity and morphology (Chapter 2);

2. **To characterize the morphological profile of microglia in the CMVMJD135 mouse model of MJD**, by immunofluorescence assays and confocal microscopy to quantify the number and morphological changes in microglia, and with principal component analysis (PCA) and machine learning (ML) models to identify potential clusters of microglia based on their morphological features as well as those that best characterize microglia from CMVMJD135 and WT mice (Chapter 3);

3. **To characterize gene expression networks in MJD-derived microglia** using RNA-sequencing approaches, thus providing relevant insights into how coordinated gene regulatory programs in microglia underlie MJD pathogenesis (Chapter 4);

4. **To explore the contribution of microglia to disease progression**, by evaluating the impact of microglial depletion on the motor performance of CMVMJD135 mice (Chapter 5).

1.4 Ethics statement and maintenance of the CMVMJD135, a mouse model that mimics the human condition of Machado-Joseph disease

The animal experimentation and reporting were designed and conducted in adherence with the ARRIVE 2.0 guidelines (Animal Research: Reporting *in vivo* Experiments). Animal facilities and the people directly involved in animal experiments are certified by the Portuguese regulatory entity - Direcção Geral de Alimentação e Veterinária (DGAV) (DGAV, license number 020317). All the performed protocols were approved by the Animal Ethics Committee of the Life and Health Sciences Research Institute, University of Minho (SECVS 120/2014).

In recent years, investigation on MJD has been advanced by the development of transgenic mouse models [78, 91, 318, 320, 321]. The CMVMJD135 mouse model, developed by our team, constitutes an excellent model to study the pathogenic mechanisms of MJD and for drug testing, since it mimics the human condition of the disease [88, 322]. Hence, CMVMJD135 and WT littermate mice on a C57BL/6J background, were used. The CMVMJD135 mice express an expanded version of the human MJD1-1 complementary DNA (cDNA) (the 3 UIMS-containing variant of *ATXN3* protein containing 135 glutamines) under the regulation of the cytomegalovirus (CMV) promoter (ubiquitous expression) at near-endogenous levels in the cerebellum, brainstem, forebrain, peripheral tissues, and spinal cord [88].

Regarding the disease symptoms, the CMVMJD135 mice manifests MJD-like motor symptoms that appear gradually and progress slowly over time [88]. Starting as early as 6 weeks of age, the MJD mice present the first symptom, which is loss of muscular strength. Other motor symptoms including motor, balance, and gait deficits appear between 10 and 14 weeks of age. From week 16 onwards, loss of weight gain and reduced exploratory behavior are observed. Later, abnormal neurological reflexes such as limb clasping and grasping, and tremors are detectable. Also, these mice have a reduced lifetime. Neuropathological findings observed in the CMVMJD135 mice at 20-34 weeks of age consist in ATXN3 inclusions in the nucleus of neuronal cells in different regions such as cerebellum, brainstem, forebrain, peripheral tissues, and spinal cord, astrogliosis in the substantia nigra and SC as well as altered inflammatory profile in the brainstem, reduction in the thickness of the molecular layer of the cerebellum, and reduction of the brain weight [88]. DNA extraction, animal genotyping, and CAG repeat size analyses were performed as described in [89].

All animals (Specific Pathogen Free health status) were maintained under standard laboratory conditions: an artificial 12 h light/dark cycle (lights on from 8:00 to 20:00 h), with an ambient temperature of 21 ± 1 °C and a relative humidity of 50-60 %. The mice were given a standard diet (4RF25 during the gestation and postnatal periods, and 4RF21 after weaning; Mucedola SRL, Settimo Milanese, Italy) and water ad libitum. All animal procedures were conducted in consonance with the European Union Directive 2010/63/EU. To minimize discomfort, stress, and pain to the animals, humane endpoints were defined and included a 20 % reduction of the body weight, inability to reach food and water, presence of wounds in the body, and dehydration. Health monitoring was performed according to the Federation of European Laboratory Animal Science Associations (FELASA) guidelines, where the Specified Pathogen Free health status was confirmed by sentinel mice maintained in the same animal housing room.

1.5 Thesis Planning

The present thesis is organized in six chapters and the respective appendices. Chapter 1 provides a general introduction to the research domains; Chapters 2 to 5 characterize the profile of microglia and their contribution to MJD pathogenesis; Chapter 6 presents a general discussion and outlines future perspectives.

Chapter 1 provides a general introduction to the research domains of this thesis, including an historical perspective on MJD, its clinical and neuropathological features, the disease protein ATXN3, and the mechanisms of MJD pathogenesis. The CMVMJD135 mouse model, which mimics the human condition of MJD, is also described. Microglia origin and functions are reviewed, together with the heterogeneity in microglial density, their morphology and molecular signature in the brain, their profile in neurodegenerative diseases and aging, as well as the targeting of microglia as a possible therapeutic approach for neurodegenerative diseases. Objectives, ethics statements, and thesis planning are also provided in this first chapter.

Chapter 2, entitled "*Evidence for a non-senescent microglial profile in a mouse model of*

Machado-Joseph disease", shows a decrease in the expression of senescence markers in microglia isolated from the different affected CNS regions (cerebellum, brainstem, and SC) of adult CMVMJD135 mice. These findings indicate that microglia do not show intrinsic defects nor do they adopt a senescent profile in MJD mice. Additionally, using primary microglial cultures from disease-relevant brain regions of CMVMJD135 neonatal mice, we present evidence suggesting that, early in life, CMVMJD135-derived microglia are mostly similar to WT-derived microglia regarding their morphological characteristics and phagocytic efficiency, and that these cells do not become precociously senescent.

Chapter 3, entitled "*The morphological profiling of microglia in a mouse model of Machado-Joseph disease revealed an activated microglial state*", describes relevant morphological alterations in microglia from the SC of CMVMJD135 mice, which points to an increased activation state of these cells. Microglia from CMVMJD135 mice were found to have less and shorter branches, smaller size, and higher soma thickness when compared with WT mice. Additionally, ML models allowed us to discriminate microglia based on their morphology and identify key features that best characterize each genotype, denoting the impact of the disease in such morphological characteristics. In addition, this chapter describes the design, implementation, and use of a new ImageJ plugin that was conceived during this research task. The plugin, entitled *MorphData*, allows one to automatically collect morphological features for single cells in a matter of minutes, significantly reducing the time spent on the data collection process. This plugin has an increased importance given the lack of solutions for automatic morphological data collection in this field.

Chapter 4, entitled "*Transcriptomic profiling of microglia in the pathogenesis of Machado-Joseph disease*", presents a disease-specific transcriptional profile of MJD microglia encompassing a total of 101 differentially expressed genes, with enrichment in molecular pathways related to oxidative stress, immune response, cell proliferation, cell death, and lipid metabolism. These results allowed us to define the transcriptomic profile of MJD-associated microglia and to identify genes and pathways that might represent potential therapeutic targets for this disorder.

Chapter 5, entitled "*Microglial cell depletion has no impact on disease progression in a mouse model of Machado-Joseph disease*", seeks to answer to whether microglia are, or not, actively contributing for MJD. A battery of behavioral tests was used to evaluate the impact of microglial depletion in motor phenotype of CMVMJD135 mice, our results showing that, despite the treatment substantially reducing microglia numbers in the affected brain regions, it did not affect the motor deficits in CMVMJD135 mice. These results suggest that these cells may not be significant key contributors for MJD.

Chapter 6 provides a general discussion and sets the future perspectives regarding the outcome of the research presented in this thesis.

Still in this thesis, five appendices are included: **Appendix A** corresponds to the supplementary material that support the materials and methods of Chapters 2 to 5; and **Appendix B** consists in the supplementary data that support the results obtained and presented in Chapters 3 to 5. Finally, three manuscripts are also presented in **Appendix C**, **Appendix D**, and **Appendix E**, as follows:

- **Campos AB**, Duarte-Silva S, Fernandes B, das Neves SP, Marques F, Teixeira-Castro A, Neves-Carvalho A, Monteiro-Fernandes D, Portugal CC, Socodato R, Summavielle T, Ambrósio AF, Relvas JB, Maciel P. *Profiling Microglia in a Mouse Model of Machado–Joseph Disease*. Biomedicines. 2022; 10(2):237. https://doi.org/10.3390/biomedicines10020237. Q1 - Research and Experimental Medicine; Q1 - Biochemistry and Molecular Biology. This paper compiles the results obtained and described in Chapters 2, 3, and 4;

- **Campos AB**, Duarte-Silva S, Ambrósio AF, Maciel P, Fernandes B. *MorphData: Automating the data extraction process of morphological features of microglial cells in ImageJ*. Submitted for publication in the Journal of Open Research Software. 2022. https://doi.org/10.1101/2021.08.05.455282. Q2 - Informations Systems; Q2 - Software. This paper presents a new open-source software to facilitate the data collection process that is described in Chapter 3;

- **Campos AB**, Duarte-Silva S, Fernandes B, Coimbra B, Jonas C, Monteiro-Fernandes D, Teixeira-Castro, Ambrósio AF, Maciel P. *Microglial cell depletion has no impact on disease progression in a mouse model of Machado-Joseph disease*. Submitted for publication in the Journal of Biomedical Science. 2022. Q1 - Research and Experimental Medicine; Q1 - Cell Biology. This paper summarizes the results obtained in Chapter 5.

Chapter 2

Evidence for a non-senescent microglial profile in a mouse model of Machado-Joseph disease

2.1 Introduction

Age-related neurodegenerative diseases have been associated with chronic neuroinflammation, with microglia-mediated inflammation as a significant contributor to disease pathogenesis [173, 201, 227, 275]. However, other studies suggest that chronic neuroinflammation occurs only at an early stage of the neurodegenerative diseases, once with aging and disease progression, microglia undergo several changes and adopt an aberrant phenotype, sometimes referred as dystrophic or senescent, which contain a decreased ability to provide a normal response to injury [275, 278, 323, 324]. Cellular senescence is typically characterized by an arrested growth due to elevated DNA damage and oxidative stress that results in increased levels of some proteins seen as senescence indicators, including the cell cycle regulators $p16^{INK4a}$ (also known as *Cdkn2a*), $p19^{Arf}$ (also known as *Cdkn2a*) and $p21^{Cip1/Waf1}$ (also known as *Cdkn1a*), and of senescence-associated pro-inflammatory cytokines, such as Pai1 (also known as *Serpine1*), Il-6, Il-8, Il-1 alpha, and Il-1 beta [276, 291]. A reduced phagocytosis capacity [275, 295], an impaired protein homeostasis (proteostasis) [266], and a dystrophic morphology, typically characterized by de-ramification and shortening of the processes [325], are also consistent age-related changes of microglia. These changes may contribute to an increased susceptibility to neuronal dysfunction and demise during aging, through increased production of inflammatory mediators and impairment of microglia neuroprotective functions [189, 202]. Thus, when studying brain neurodegeneration processes and age-associated disorders, it is of the utmost importance to characterize the senescent/dystrophic microglia profile.

MJD is a neurodegenerative disease of adult onset, caused by an abnormal expansion of a cytosine-adenine-guanine (CAG) triple that encodes the amino acid glutamine in the Ataxin-3 protein [12]. While Ataxin-3 misfolding and the consequent disruption of cells‘ protein homeostasis is considered central to MJD pathogenesis [53], transcriptional dysregulation, increased oxidative stress, and DNA damage have also been proposed to contribute to the disease progression [53]. Predominantly the motor symptoms appear gradually and progress over time, pointing to an age-dependent decline in the cells' ability to remove misfolded proteins [31, 34]. Given that *ATXN3* is expressed in most cell types, including neurons and microglia, it is possible that microglial dysfunction may contribute to the disease process, due to effects of mutant *ATXN3* in microglia themselves or as a consequence of their interaction with neurons. Therefore, we aim to investigate if microglia from CMVMJD135 mice, a mouse model that replicates multiple features of this disease [88, 89], switch to a senescent/dystrophic profile with disease progression. The characterization of senescent microglial profile was performed by evaluation of different senescence markers in microglia isolated from the different affected CNS regions (cerebellum, brainstem, and SC) of CMVMJD135 mice at 48 weeks of age, which corresponds to an advanced disease stage, i.e., when the phenotype is fully established. This characterization was also performed *in vitro*, using primary cultures of microglia from CMVMJD135 and WT neonatal mice, exploring the differences in functional response characteristics

associated to “young” and “aged” microglia phenotypes by assessing phagocytic activity and morphology, as described in [275]. An increased understanding of the physiopathological changes undergone by microglial cells of this neurodegenerative disease may open new avenues for the identification of novel targets for therapy development in this and related diseases.

2.2 Materials and Methods

2.2.1 Animals

All the experiments were performed using male animals with 34-50 weeks of age, corresponding to an advanced disease stage, except for the primary culture of microglial cells that used WT and CMVMJD135 neonatal mice with 3-to-4 day-old (P3-P4).

2.2.2 Flow cytometry analysis

Microglia were collected from the affected brain regions as a whole (cerebellum, brainstem, and SC) of WT and CMVMJD135 littermates using density gradient separation. For characterization of these cells in the samples, the following markers were used: CD45-PE, CD11b-PE/Cy7, and CD11b-Alexa Fluor 647 (Figure A.1 in *Appendix A - Materials and Methods*). Compensation settings were determined using spleen samples of both WT and CMVMJD135 mice, and cell suspensions were evaluated on a fluorescence activated cell sorting (FACS) Canto II analyzer (BD Immunocytometry Systems).

For the intracellular analysis of the $p19^{Arf}$ and $p21^{Cip1/Waf1}$ senescence markers, microglia were fixed, permeabilized and incubated with anti-rat $p19^{Arf}$ and anti-rabbit $p21^{Cip1/Waf1}$ antibodies (Figure A.1 in *Appendix A - Materials and Methods*). Briefly, mice were deeply anesthetized with a mixture of ketamine hydrochloride (150 mg/kg) and medetomidine (0.3 mg/kg) and then transcardially perfused with ice-cold phosphate saline buffer (PBS). For single cell suspensions, tissues were quickly dissected, placed on ice-cold RPMI, and mechanically homogenized. Cell suspension was passed through a 100 μm cell strainer and centrifuged over a discontinuous 70/30 % Percoll (GE Healthcare, Chicago, IL, USA) gradient. Cells on the interface were collected, pelleted, washed, and then counted in a Neubauer chamber using trypan blue exclusion to estimate the number of live cells. Single cell suspensions (5×10^5 cells) were seeded in a U-shape bottom 96-well plate and incubated with CD45-PE, CD11b-Alexa Fluor 647, or CD11b-PE/Cy7 for 30 min at 4 °C in the dark. After antibody washing, cells were fixed in 2 % paraformaldehyde (PFA) for 30 min, washed in PBS and permeabilized with permeabilization buffer (Life Technologies, Carlsbad, CA, USA). Intracellular staining mix using the anti-rat $p19^{Arf}$ and anti-rabbit $p21^{Cip1/Waf1}$ antibodies was prepared in a permeabilization buffer. Microglia were then incubated with this intracellular staining mix overnight, at 4 °C in the dark. After washing with a permeabilization buffer, cells were incubated with Alexa Fluor 488 and 647 secondary antibodies for 1 h at room temperature (RT) in the dark. After that, cells were washed twice in a permeabilization buffer, washed twice in FACS staining buffer (2 % bovine serum albumin (BSA) and 0.1 % sodium azide in PBS), and analyzed in FACS Canto II.

For intracellular detection of Il-8, Il-6, Il-1 alpha, and Il-1 beta, cells were incubated with 10 $\mu g/ml$ of brefeldin A (Sigma-Aldrich, St. Louis, MO, USA) during 3 h in RPMI medium supplemented with 10 % fetal bovine serum (FBS) and 1 % antibiotic-antimycotic solution and maintained at 37 °C in a humidified atmosphere of 5 % CO_2. After staining for the expression of surface molecules, cells were fixed with 2 % PFA and permeabilized with permeabilization buffer. After permeabilization, the cells were stained with anti-rabbit Il-6 and anti-mouse Il-8, or anti-mouse Il-1 alpha and anti-rabbit Il-1 beta antibodies overnight, at 4 °C, followed by Alexa Fluor 488 and 647 secondary antibodies (Figure A.1 in *Appendix A - Materials and Methods*) for 1 h at RT in the dark. Data acquisition was performed in FACS Canto II and analyzed by FlowJo X10 software (TreeStar).

2.2.3 Quantitative Reverse-Transcription PCR

To evaluate the messenger RNA (mRNA) expression levels of human *ATXN3*, ribonucleic acid (RNA) was extracted from CMVMJD135 and WT neonatal mice-derived microglial. To evaluate senescence markers levels, RNA was extracted from CMVMJD135 and WT tissues previously frozen (brainstem, cerebellum, and SC)). TRIZOL (Invitrogen) was used in both cases, following the manufacturer's instructions. Samples were treated with DNase I (ThermoFisher Scientific); RNA concentration was quantified using the NanoDrop™ Spectrophotometer (ThermoFisher Scientific), and RNA quality was tested through electrophoresis. Afterwards, 1 μg first-strand cDNA was synthesized using iScript™ cDNA synthesis kit (Bio-Rad). The quantitative polymerase chain reaction (PCR) was then carried out using the 5× HOT FIREPol® EvaGreen® qPCR Mix Plus (ROX) (Solis BioDyne) with 1 μl of cDNA. Specific primers for different messenger RNAs were obtained either from the literature or previously designed by us, using Primer-BLAST (available at http://www.ncbi.nlm.nih.gov/tools/primer-blast/). The used primers are listed in Figure A.2 in *Appendix A - Materials and Methods*. The housekeeping genes, Beta-2-microglobulin (*B2m*) or mouse endogenous *Atxn3*, were used as an internal standard for the normalization of the expression of selected transcripts. PCR reaction was run in Applied Biosystems™ 7500 Real-Time PCR System (Applied Biosystems) and raw data was extracted using 7500 software v2.3 (7500 Real-Time PCR Software). All melting curves exhibited a single sharp peak at the expected temperature. Statistical analysis was conducted using $2^{-\Delta CT}$ values and plots were reported in Fold Change ($2^{-\Delta\Delta CT}$) or reported as fold change normalized to the mean of the relative expression of the control group.

2.2.4 Primary culture of microglial cells

Primary mixed glial cultures, composed of astrocytes and microglia, were prepared from brainstem and cerebellum together of CMVMJD135 and WT neonatal mice (3-4 days old). Replicating the same methods described by Caldeira et al. (2014) [275], cells (4×10^5 cells/cm^2) were plated on uncoated 12-well tissue culture plates (with 18 mm coverslips) in culture medium (dulbecco's modified eagle medium (DMEM) F12 GlutaMAX-I supplemented with 10 % fetal FBS and 1 % antibiotic-antimycotic solution) and kept at 37

°C in a humidified atmosphere of 5 % CO_2. Medium was replaced every 3 days and maximum confluency and purity of the cultures were achieved after 21 days in mixed culture [275].

Microglia-enriched culture were obtained from both WT and CMVMJD135 mice by mild trypsinization, as previously described by Saura et al. (2003) [326]. Concisely, mild trypsinization was performed with a trypsin-ethylenediamine tetraacetic acid (EDTA) solution diluted 1:3 in DMEM F12 GlutaMAX-I for 45-60 min, which promoted the detachment of cells containing all the astrocytes, while microglia remained at the bottom of the well. The initial mixed glia-conditioned medium was added after the removal of the medium containing the detached cells.

2.2.5 Assessment of microglia culture purity over time

Before proceeding to the characterization of microglia from WT and CMVMJD135 mice over time, the purity of microglia in culture was evaluated using the cells from WT neonatal mice. Briefly, after the mild trypsinization, the purity of these cultures was assessed by immunocytochemistry, in three different time points (4, 10, and 16 days *in vitro* (DIV)), using the anti-ionized calcium binding adaptor molecule 1 (Iba-1) antibody as a microglial marker, and anti-glial fibrillary acid protein (GFAP) antibody as an astrocyte marker, followed by species-specific fluorescent-labelled secondary antibodies, Alexa Fluor 594 goat anti-rabbit and Alexa Fluor 488 goat anti-mouse, respectively (Figure A.1 in *Appendix A - Materials and Methods*). Cells were then incubated with the 4',6-diamidin-2-phenylindol (DAPI, Invitrogen) diluted 1:1000 in PBS. After washing the cells, the coverslips were mounted on microscope Superfrost©Plus slides using an aqueous mounting medium.

Random fluorescence images (11 to 33) were acquired in each coverslip using Olympus Widefield Inverted Microscope IX81 with a resolution of 1024 × 1024 px and a 20× objective. At least 3 coverslips per each independent experiment ($n = 3 - 4$) in each time point (4, 10, and 16 DIV) were used for counting the number of microglia and astrocytes. Total count of Iba-1-positive cells and GFAP-positive cells was obtained using the Point Tool feature of ImageJ software. Quantification was then normalized to the total photo area (624.39 × 624.39 μm).

After the characterization of a microglia-enriched culture in each time point, the cultured microglia from WT and CMVMJD135 mice were characterized over time, exploring the differences in functional response characteristics associated to "young" and "aged" microglia phenotypes by assessing phagocytic activity and morphology, as described by Caldeira et al. (2014) [275], in two conditions: basal and exposed to lipopolysaccharides (LPS) (LPS, E. coli O111:B4, Sigma-Aldrich). To induce reactivity in CMVMJD135 and WT-derived microglia, 100 ng/mL of LPS was added to the culture medium for 24 h before each time point. Microglial cultures of two experimental groups, WT and CMVMJD135, in two different conditions, basal or exposed to LPS, at two different time points, 4 and 16 DIV, were studied as presented in Table 2.1.

With a slight contamination with astrocytes occurring over time, to evaluate microglia phagocytic ability and morphology in culture, only the cells with double staining with Iba-1 and DAPI were included, with cells

Table 2.1: **Organization of the experimental groups to evaluate microglia phagocytic ability and morphology in culture.**

	4 DIV				**16 DIV**			
	WT		**CMVMJD135**		**WT**		**CMVMJD135**	
Condition	Basal	LPS	Basal	LPS	Basal	LPS	Basal	LPS
Nº Animals	3	3	5	5	4	4	3	3
Nº of cells	387	309	597	543	504	318	279	351
Coverslips per animal	3-4				3-4			
Images per coverslip	7-22				7-22			

stained only with DAPI being excluded.

2.2.6 Evaluation of microglia phagocytic ability in culture

To evaluate the phagocytic activity of the primary microglial cultures, the cells, collected at two different time points (4 and 16 DIV), were incubated with 0.0025 % (w/w) of 1 μm green-fluorescent beads latex (Sigma-Aldrich) for 75 min at 37 °C. For immunofluorescence detection, the cells were fixed for 15 min with freshly prepared 4 % PFA in PBS, permeabilized with 0.1 % Triton X-100 for 20 min and then blocked with PBS containing 2 % BSA for 1 h. After this, microglial cells were incubated with anti-Iba-1 (Figure A.1 in *Appendix A - Materials and Methods*) overnight at 4 °C, followed by secondary antibody incubation (anti-rabbit Alexa Fluor 594, Figure A.1 in *Appendix A - Materials and Methods*) for 2 h at RT. Cell nuclei were stained with DAPI for 10 min at RT. Random fluorescence images (7 to 22) were acquired per coverslip, animal, condition, and experimental group (Table 2.1), using an Olympus Widefield Inverted Microscope IX81 (resolution of 1024 × 1024 px and an original magnification of 20×).

To evaluate the phagocytic capacity of the primary microglial cultures, the number of ingested beads per cell was counted using the Point Tool feature in ImageJ. Results are presented as phagocytic efficiency (PE), considering the total number of microglial cells, to obtain the average amount of ingested beads per cell, considering the proportion of cells phagocytosing 1, 2, 3, 4, 5, and more than 5 beads, obtained by the formula described in [327]:

$$\text{Phago Eff (\%)} = \frac{1 \times x_1 + 2 \times x_2 + 3 \times x_3 + \ldots + n \times x_n}{\text{Total Number of Cells}} \times 100 \tag{2.1}$$

where x_n represents the number of cells containing n beads (n = 1, 2, 3, ...up to a maximum of 6 points for more than 5 beads per cell).

2.2.7 Evaluation of microglial morphology in culture

For the morphological analysis, cells were fixed with 4 % PFA in PBS and a standard immunocytochemical technique was performed using a primary antibody against Iba-1 and a secondary antibody, as previously

described, for the evaluation of microglia phagocytic ability. To identify the cells, microglial nuclei were stained with DAPI. The fluorescence images used for evaluation of phagocytic capacity were also used to quantitatively characterize microglia morphology (Table 2.1). For this, using ImageJ, cells were outlined with the Freehand Selection tool and then the particle measurement feature was used to automatically measure the 2D area, perimeter, and the Feret's diameter of at least 3 single microglial cells per image. Feret's diameter, a measure of cell length, is the greatest distance between any two points along the cell perimeter [275]. The transformation index, which categorizes microglia ramification status, was also evaluated as follows [328]:

$$\text{Transformation Index} = \frac{[\text{Perimeter of Cell } (\mu m)]^2}{4\pi[\text{Cell Area } (\mu m^2)]} \tag{2.2}$$

2.2.8 Statistical analysis and graphs

All statistical analyses were performed using the SPSS 22.0, with the Graph-Pad Prism 8.00 software being used to create the graphs. Regarding descriptive statistics, the mean was the considered measure of central tendency, while the measure of variability was the standard error of the mean (SEM). The assumption of normality was assessed by frequency distributions (z-score of skewness and kurtosis) as well as by the Kolmogorov-Smirnov and Shapiro-Wilk tests. The assumption of homogeneity of variances was evaluated by Levene's test. Some of the data were analyzed using the two-tailed unpaired Student's t-test for comparisons between the two groups. For comparisons of more than two groups, the one-way analysis of variance (ANOVA) was used, followed by Tukey HSD or Dunnett T3's test. The critical value for significance was set as $p < 0.05$ throughout the study.

2.3 Results

2.3.1 Senescence markers are decreased in microglia from affected brain regions of CMVMJD135 mice

Growing evidence suggest that microglia change their features with age, switching to a senescent/dystrophic profile, being increasingly involved in the occurrence, or aggravation, of neurodegenerative diseases [189, 275, 278, 323]. Aging-related processes are also thought to explain the mid-life emergence of symptoms in MJD, in spite of mutant gene expression in most cell types since early development. Therefore, aging-related microglial changes could be contributing to disease onset and/or progression. To understand if microglia from CMVMJD135 mice change their features with age and switch to a senescent/dystrophic phenotype with disease progression, we evaluated protein levels of senescence markers by flow cytometry in microglia isolated from the cerebellum, brainstem and SC of mice at 48 weeks of age (that corresponds to an advanced disease stage), as depicted in Figure 2.1a. Contrary to our working hypothesis, we found a decrease in the expression of a senescence indicator, $p19^{Arf}$ ($p = 0.004549$) and

in the expression of senescence-associated pro-inflammatory cytokines, Il-1 alpha ($p = 0.000416$) and Il-1 beta ($p = 0.008074$) in isolated microglia from CMVMJD135 mice when compared with WT mice (Figure 2.1b). Regarding the expression of $p21^{Cip1/Waf1}$, Il-6, and Il-8, no differences were found between WT and CMVMJD135 mice (Figure 2.1b).

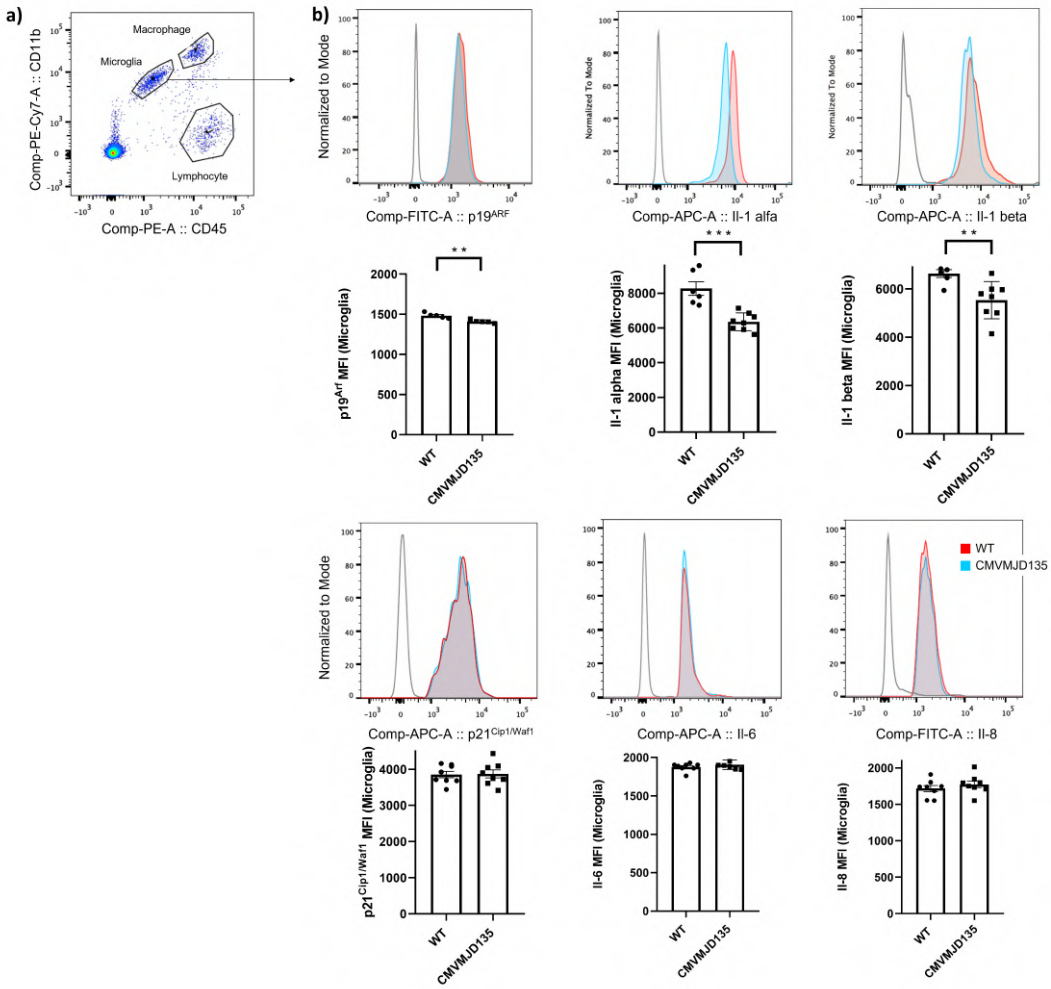

Figure 2.1: **Expression of senescence markers is decreased in microglia of affected central nervous system regions of CMVMJD135 mice**. **a)** Gating strategy used to analyze the flow cytometry data. Microglia, macrophage, and lymphocyte populations were gated using $CD11b^{+}CD45^{mid}$, $CD11b^{+}CD45^{high}$, and $CD11b_{low}/CD45^{low}$, respectively; **b)** Flow cytometry showing expression of $p19^{Arf}$, Il-1 alpha, Il-1 beta, $p21^{Cip1/Waf1}$, Il-6, and Il-8 in microglia (gated using $CD11b^{+}CD45^{mid}$) from wild-type (WT) and CMVMJD135 mice ($n = 5-8$ per group). MFI = Mean Fluorescent Intensity. Data are presented as mean+SEM (Student's t-test). **, ***, represent $p < 0.01$ and $p < 0.001$, respectively.

Additionally, in order to understand if there is a senescent profile in the brain of the CMVMJD135 animals, we also evaluated the mRNA expression levels of several senescence markers, including *p16Ink4a*, *p19Arf*, *p21Cip1/Waf1*, *Pai1*, *Il-6*, *Il-1 beta*, *Icam-1* (senescence-related intercellular adhesion molecule 1) [329], and Hmgb1 (high mobility group box 1) [330] in whole tissue obtained from different affected regions of the CNS (cerebellum, brainstem, and SC). In accordance with the results obtained by flow cytometry, we found a decrease in the expression of *p19Arf* ($p = 0.004019$) in the cerebellum, a decrease

in the expression of *Il-6* ($p = 0.031390$) and *Pai1* ($p = 0.044628$) in the brainstem and a decrease in the expression of the *Icam-1* ($p = 0.015626$) in the SC (Figure 2.2). However, CMVMJD135 mice displayed a similar expression of the $p16^{Ink4a}$, $p21^{Cip1/Waf1}$, *Il-1 beta*, and *Hmgb1* in the cerebellum, brainstem, and SC when compared to WT mice (Figure 2.2). These findings do not support a senescent-like profile of microglia, or other cells, in the nervous system of MJD mice.

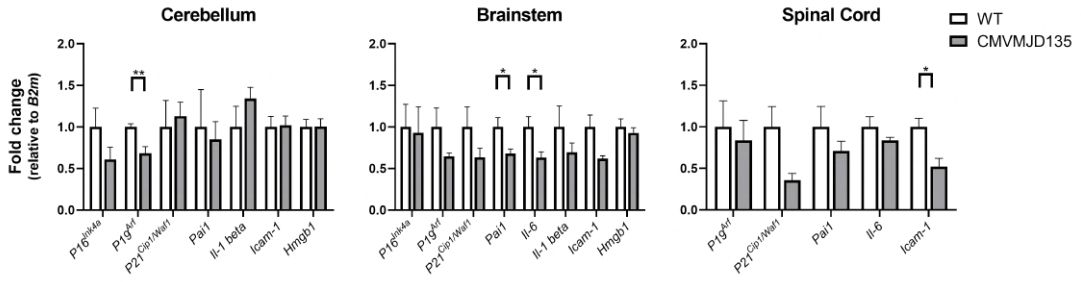

Figure 2.2: **No evidence for a senescence-like gene expression profile in the brain tissue from CMVMJD135 mice**. The expression levels of senescence markers were analysed in the cerebellum, brainstem, and spinal cord (SC) of WT and CMVMJD135 mice. $n = 4 - 5$ per group and two technical replicates were performed. Fold change ($2^{-\Delta\Delta CT}$) is represented using *B2m* as a housekeeping genes. Data are presented as mean+SEM (Student's t-test). *, **, represent $p < 0.05$ and $p < 0.01$, respectively.

2.3.2 Microglia expressing mutant human *ATXN3* showed a less activated phenotype in response to lipopolysaccharides in artificially "aged" primary cultures

To further reinforce our *in vivo* analysis, we used an experimental process, described by Caldeira et al. (2014) [275], to mimic the aging of a microglia-enriched culture and to characterize the cultured cells at 4 and 16 DIV, by assessing phagocytic activity and morphological changes in two conditions: basal and exposed to LPS.

Regarding the purity of these cultures, at 4 DIV, a very high purity was observed (98.4 %). With the increase of DIV, a slight contamination with astrocytes occurred, but the percentage of purity is still high, culminating in a 79 % purity at 16 DIV (Figure 2.3), as described in previously studies [275, 326, 331].

After confirming the purity of the microglia-enriched culture obtained over time (Figure 2.3), and to confirm the relevance of studying cell autonomous processes in microglia in this transgenic model, we evaluated the expression levels of mutant human *ATXN3* in these cells. As expected, expression of mutant *ATXN3* was detected in microglia from CMVMJD135 mice but not in WT mice, in the two different time points: at 4 DIV ($p = 0.027841$) and at 16 DIV ($p = 0.000617$) (Figure 2.4).

To quantitatively evaluate the effect of *in vitro* aging on microglial morphology, the following parameters were measured at 4 and 16 DIV: cell area, cell perimeter, Feret's diameter, and transformation index. As predicted, in LPS conditions an ameboid morphology was verified rather than the ramified morphology seen in basal conditions (Figure 2.5a). In fact, at 4 DIV, microglia from both CMVMJD135 and WT neonatal

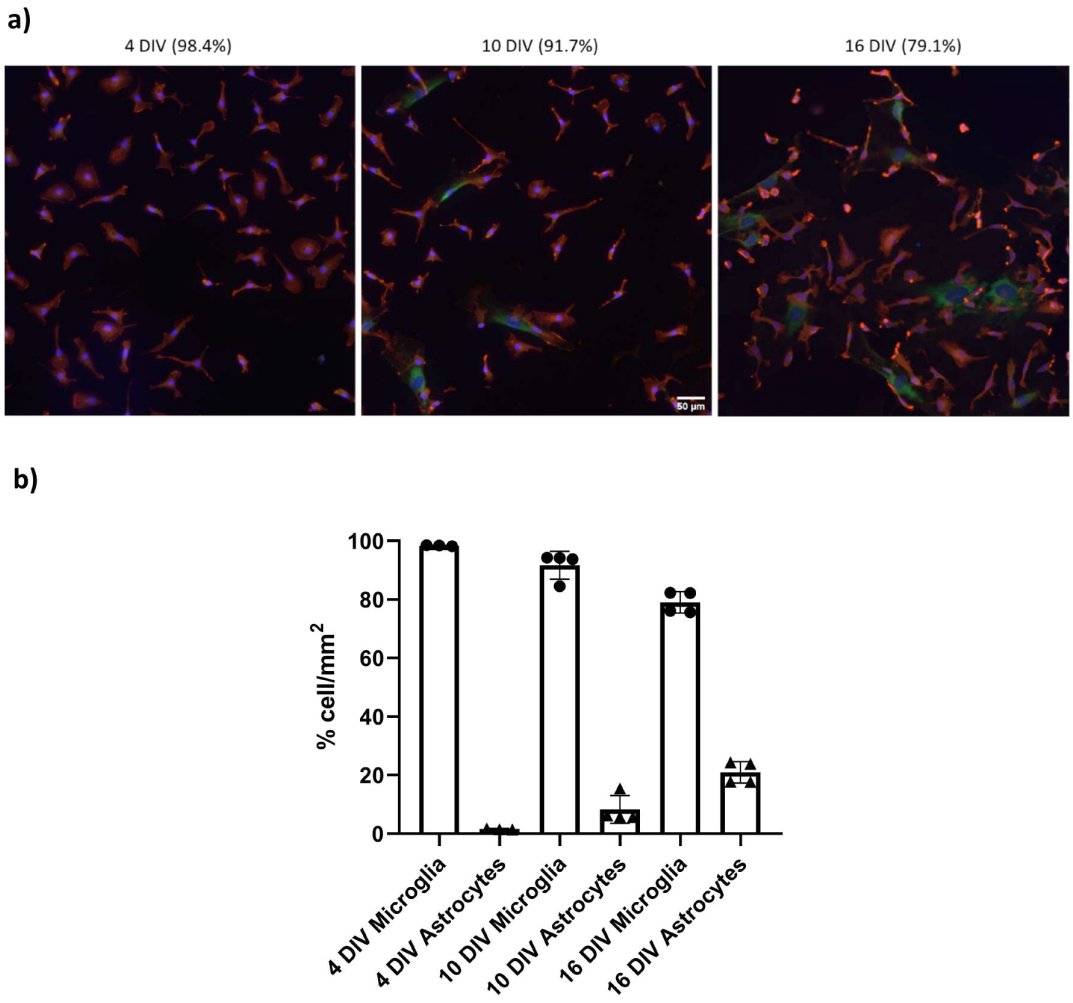

Figure 2.3: **Assessment of microglia culture purity over time**. **a)** Representative images of immunocytochemistry using Iba-1 as a microglial marker (in red) and glial fibrillary acid protein (GFAP) as an astrocyte marker (in green) over time. **b)** At 4 days *in vitro* (DIV), a high purity was observed (98 %) with a slight contamination with astrocytes occurring over time, but maintaining a 79 % purity at 16 DIV. $n = 3 - 4$ independent experiments per each time point (4, 10, and 16 DIV). Each value represents the mean ± SEM. Scale bar 50 μm.

mice, when exposed to LPS, showed a larger cell area, a larger cell perimeter, and a higher Feret's diameter, when compared with microglia in basal conditions (Figure 2.5b-d). The transformation index was also evaluated, with significant differences being found in WT-derived microglia, but not in CMVMJD135-derived microglia (Figure 2.5e).

Curiously, at 16 DIV, corresponding to the artificially "aged" microglia, no differences were found in microglia from neonatal CMVMJD135 mice in both conditions (treated or untreated with LPS) for all analyzed parameters (Figure 2.5f-i). This suggests that, with age, these cells expressing mutant *ATXN3* decrease their ability to respond to LPS. In contrast, microglia from WT mice display a similar response to the previous time point, except for Feret's diameter and Transformation Index, where no differences were found in LPS conditions when compared to basal ones (Figure 2.5f-i).

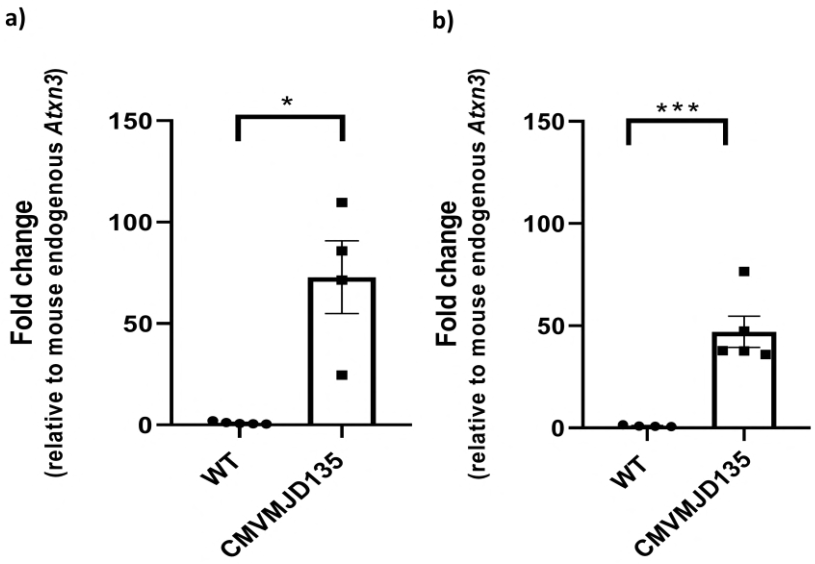

Figure 2.4: **Confirmation of expression of mutant human *ATXN3* in microglia from CMV-MJD135 mice at two different time points in culture**: **a)** at 4 DIV, and **b)** at 16 DIV. Cultures of $n = 4 - 5$ animals per group. Two technical replicates were performed. Fold change ($2^{-\Delta\Delta CT}$) is represented using mouse endogenous *Ataxin-3* mouse as housekeeping gene. Data are presented as mean+SEM (Student's t-test). *, ***, represent $p < 0.05$ and $p < 0.001$, respectively

Nevertheless, when comparing the morphological changes among microglia derived from WT or CMV-MJD135 mice, in basal conditions or exposed to LPS, no statistically significant differences were noted across all studied time points (Figure 2.5).

2.3.3 CMVMJD135 and wild-type-derived microglia showed an increased phagocytic efficiency in the presence of Lipopolysaccharides in culture

To evaluate the phagocytic capacity of microglia derived from CMVMJD135 and WT mice, and to assess if aging in culture could have adverse effects on their phagocytic efficiency, the cells were incubated with fluorescent beads, which are normally engulfed by them. As expected, the exposure to LPS enhanced microglial phagocytic efficiency as shown in Figure 2.6a, with a higher number of beads being engulfed by each cell.

However, at the two time points analyzed, both CMVMJD135 and WT-derived microglia, increased the phagocytic efficiency in the presence of LPS when comparing to basal conditions (Figure 2.6b-c). In agreement with the morphological results, it is worth noting that no significant differences were found in phagocytic efficiency across all studied time points between CMVMJD135 and WT mice, in both conditions (Figure 2.6).

Altogether, our *in vitro* results suggest that early in life CMVMJD135-derived microglia are mostly similar to WT-derived microglia, and that these cells do not become precociously senescent.

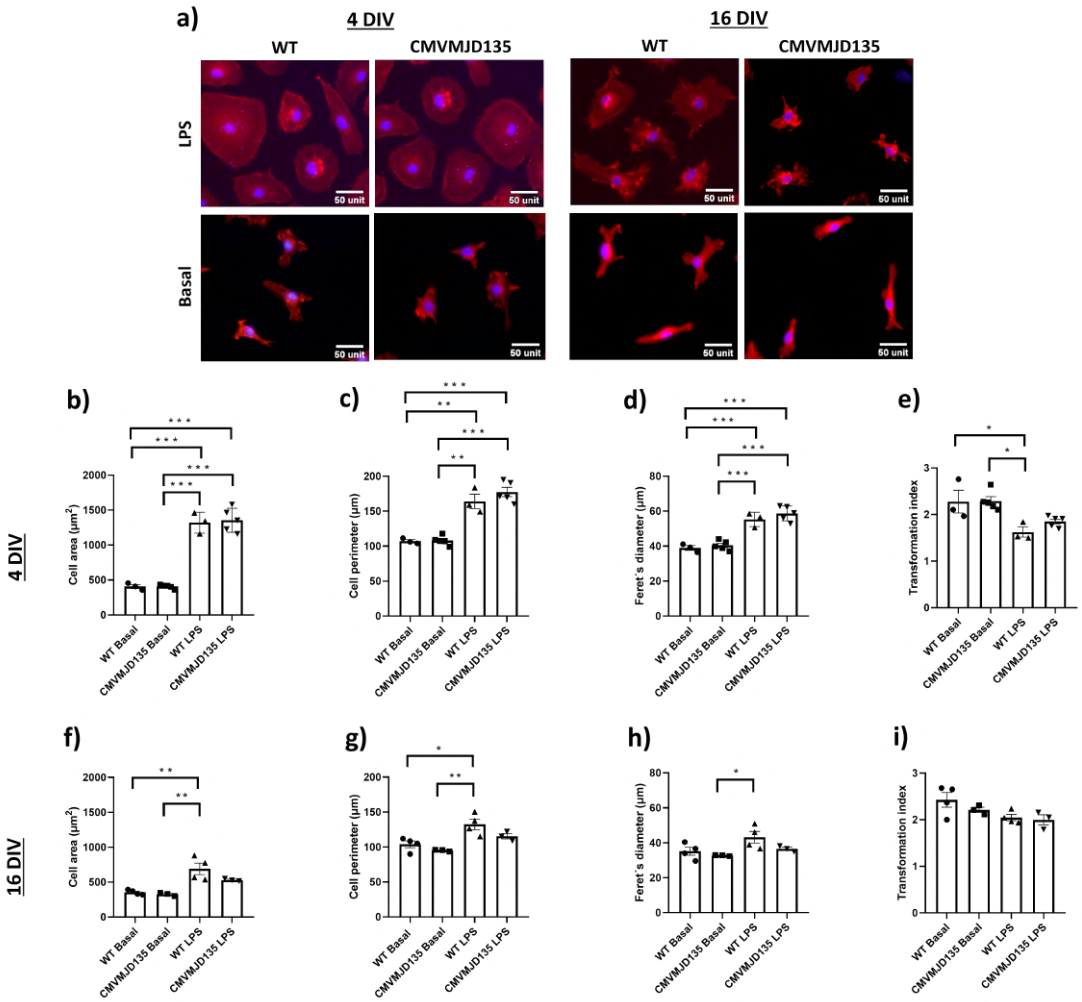

Figure 2.5: **Microglia expressing mutant human *ATXN3* showed a less activated phenotype in response to lipopolysaccharides in artificially "aged" primary cultures**. **a)** Images that represent the morphological changes of microglia, as observed by immunocytochemistry using microglia-specific marker Iba-1 (in red), from CMVMJD135 and WT mice, in the absence/presence of lipopolysaccharides (LPS), over time, in culture; **b)** cell area; **c)** cell perimeter; **d)** Feret's diameter; and **e)** transformation index. **b-e)** measured at 4 DIV and **f, g, h, i)** measured at 16 DIV. Cultures of $n = 3 - 5$ animals per group. Data are presented as mean+SEM, (One-way ANOVA (Post hoc Tukey's test)). *, **, ***, represent $p < 0.05$, $p < 0.01$ and $p < 0.001$, respectively. Scale bar unit as μm.

2.4 Discussion

Because MJD pathophysiology appears gradually and progresses over time [31, 34], and because microglia were described to become senescent/dystrophic in other neurological disorders, including AD, PD, MS, HD, and ALS [189, 275, 278, 280, 323], we first set out to investigate if microglia from CMVMJD135 mice, which express mutant *ATXN3*, as shown in this study, displayed an accelerated senescence profile. For this, the typical signs of cell senescence were further evaluated in microglia from CMVMJD135 mouse brains.

The senescence phenotype has been associated with an increased expression of specific proteins,

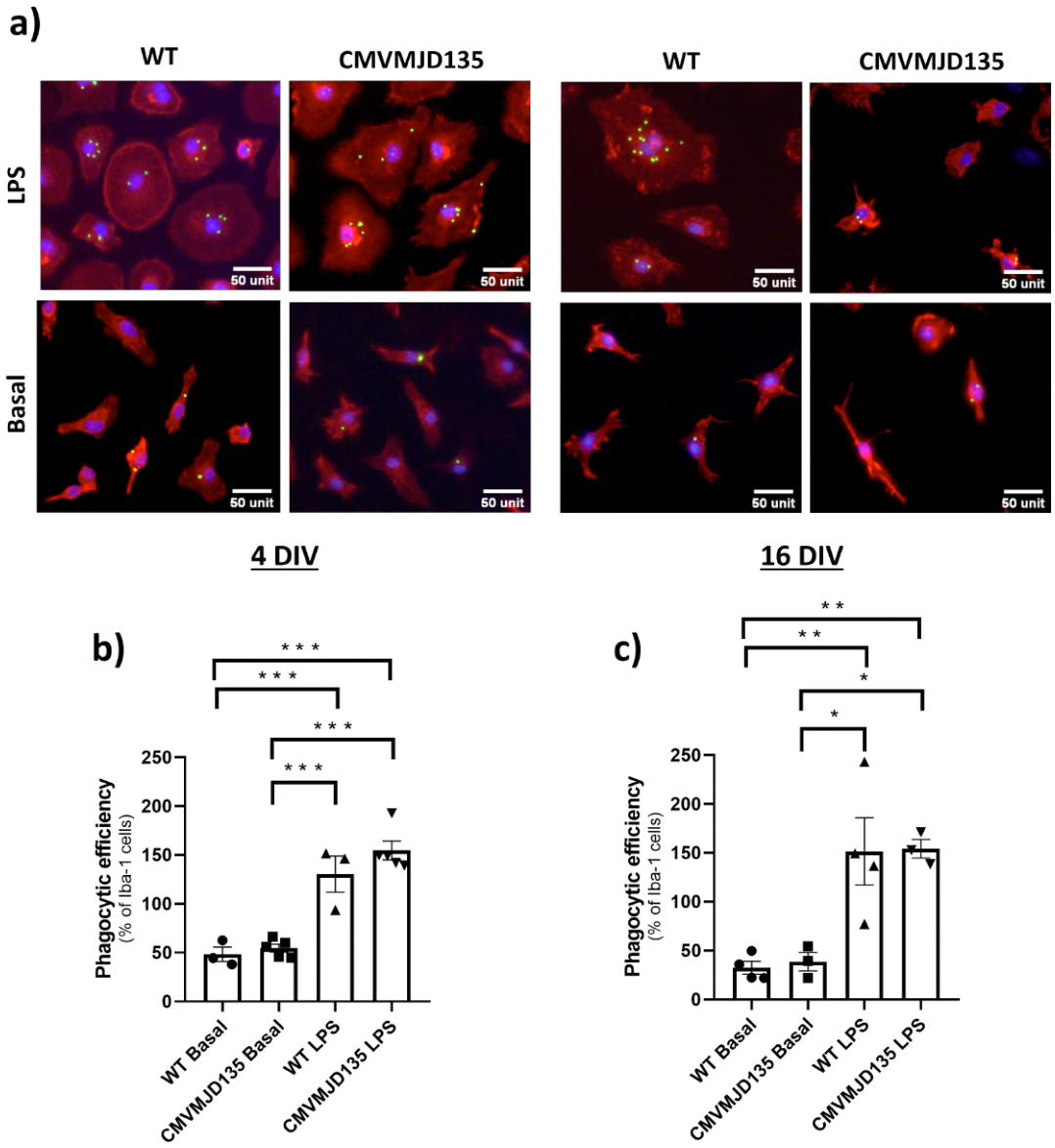

Figure 2.6: **A similarly increased phagocytic efficiency in the presence of lipopolysaccharides was observed in CMVMJD135 and wild-type-derived microglia**. **a)** Representative images of the phagocytic capacity of CMVMJD135 and WT-derived microglia immunostained for Iba-1 (in red) and counterstained with DAPI for nuclei staining (in blue) containing phagocytosed fluorescent beads (in green), in the absence/presence of LPS, over time in culture. **b, c)** Phagocytic efficiency (%) was measured using ImageJ and calculated as previously described. Cultures of $n = 3 - 5$ per group. Data are presented as mean+SEM, (One-way ANOVA (Post hoc Tukey's test)). *, **, ***, represent $p < 0.05$, $p < 0.01$ and $p < 0.001$, respectively. Scale bar unit as μm.

considered senescence indicators, including some cell cycle regulators and senescence-associated pro-inflammatory cytokines [291]. Through these, the so-called SASP may generate an inflammatory environment and induce senescence also in neighbor cells, which may exert a deleterious effect and promote neuronal degeneration [280]. Contrary to what is described in the literature for other neurodegenerative disorders [189, 280, 291], our *in vivo* observations showed a decrease in the protein levels of a senescence indicator, $p19^{Arf}$, and of senescence-associated pro-inflammatory cytokines Il-1 alpha and Il-1 beta

in microglia from CMVMJD135 mice when compared to those of WT animals.

This was consistent with the results of our analysis of senescence-related genes in whole tissue from three affected regions of MJD mice, in which we found a decrease in the expression of $p19^{Arf}$, in the cerebellum, of *Il-6* and *Pai1*, in the brainstem, and of *Icam-1*, in the SC. Overall, our data do not support a significant contribution of cell senescence processes (in microglia or other cell types) to MJD, even at late stages.

To further reinforce our *in vivo* results, an experimental process, described by Caldeira et al. (2014) [275], was used to naturally age microglia and to characterize the cultured cells over time, by assessing phagocytic activity and morphological changes. These *in vitro* models are of interest to gain a broader understanding of microglia and of their contribution for neurodegenerative diseases, further reinforcing a possible correlation between microglial activation and MJD disease progression and other aging-related phenomena.

In this study, and attending to the fact that, in this dataset, animals used to obtain cells differed from time point to time point, it would not be statistically valid to make comparisons between the two different time points and extrapolate about cells aging naturally within a single animal. Still, assuming this limitation, important observations can still be made when examining the data organized by age and genotype of the animal.

Regarding to the phagocytic capacity of microglia, our results show that, as expected, the exposure to LPS enhanced microglial phagocytic efficiency. CMVMJD135 and WT-derived microglia showed an increased phagocytic efficiency in the presence of LPS at all analyzed time points. However, no differences in phagocytic efficiency among microglia derived from WT or from CMVMJD135 mice were detected at any studied time point.

When analyzing each of the morphometric parameters (cell area, perimeter, Feret's diameter, and transformation index) between basal and LPS conditions, an ameboid morphology was verified in LPS-treated cells, in contrast to the more ramified morphology seen in basal conditions. As expected, at 4 DIV, microglia from both CMVMJD135 and WT mice, when exposed to LPS, show a larger cell area, a larger cell perimeter, a higher Feret's diameter, and a lower transformation index when compared with microglia in basal conditions. However, curiously, at 16 DIV, for all analyzed parameters, no differences were found in microglia from CMVMJD135 mice in basal versus LPS conditions. This suggests that with age, these cells decrease their ability to provide response to LPS, which may be indicative of senescent microglia, since the dysfunctional microglial cells are less responsive to stimulation with age [324, 332]. This is in contrast, however, with our observations concerning phagocytic efficiency at 16 DIV, since CMVMJD135-derived microglia show a high phagocytic efficiency in the presence of LPS in culture. In addition, it is worth noting that when analyzing the morphological changes among microglia derived from WT or CMVMJD135 mice, both in basal conditions or when exposed to LPS, no significant differences were noted at any time point. Our results do not replicate the findings described by Caldeira et al. (2014) [275] regarding morphological changes and phagocytic efficiency of the microglial cells upon *in vitro* aging, where the authors describe that, at 16 DIV, cells presented senescent characteristics, such as a more ramified shape and presented

cells with a bipolar shape rather than an amoeboid morphology, and a reduced phagocytosis capacity.

Altogether, our *in vitro* results suggest that CMVMJD135-derived microglia are similar to WT microglia, in regard to their morphology and phagocytic efficiency. However, despite this *in vitro* model being one of the best options to increase insights into the potential role of aged microglia, we cannot ignore the limitations of *in vitro* studies, since they do not replicate the complexity of the brain environment and the variety of signals microglia are exposed to, produced by different cells, as well as due to the fact that microglia from neonatal mice were used.

As a conclusion, our findings reveal a non-senescent profile for microglia or other brain cells in the CMVMJD135 mouse model of MJD, and suggest that the profile of microglia from CMVMJD135 animals should be further investigated.

Chapter 3

The morphological profiling of microglia in a mouse model of Machado-Joseph disease revealed an activated microglial state

3.1 Introduction

Microglial cells are the first line of defense within the CNS, with morphological characterization being widely used to define their activation status [183, 242]. It is known that microglia morphology and function are closely related [331]. Hence, the morphological characterization of these cells is of the utmost importance and can change significantly under different situations of brain disease and pathology [149, 183, 242]. In fact, ramified microglia has been described to transform into an "activated state", characterized by cells with larger cell bodies, shorter and thicker processes [183, 242], or to a "reactive state", typically characterized by smaller, spherical cells, that can also exhibit rod-shaped or amoeboid-like morphologies [183, 242, 333, 334]. This implies that a rigorous analysis of microglia morphology data is of essence for the understanding of the profile of these cells [335–337].

Most methods to evaluate microglia morphological profile are manual, and, therefore, often biased, inaccurate, and time consuming [335, 336]. Yet, a semi-automatic method for microglial morphology analysis was develop by Young et al. (2018) [338], which allows one to obtain multiple morphological features relevant to cell ramification, cell surface and size, soma thickness, and the cylindrical shape of cells. The process to collect morphological data starts with the acquisition of photomicrographs from where images of several single cells are extracted [338]. Then, the researcher collects the morphological features that characterize each cell. However, the process to obtain all morphological features, when performed manually over each cell, is a demanding, repetitive, and laborious task, which can take several weeks to complete. Another potential issue is the human error associated with the data collection process [338, 339]. Thus, it becomes imperative to automate and improve the data collection process of morphological features for single cells, which can then be used to study, understand, and characterize microglia profile in the brain of human patients or of animal models of neurological and psychiatric diseases. Hence, since the manual data collection process from single cells is an almost endless repetitive task, we conceived and developed an open-source ImageJ plugin, *MorphData*, which automatizes the data extraction process of morphological features of single microglial cells, allowing one to obtain all these data in a few minutes, significantly reducing the time spent on the data collection process [339].

Moreover, studies exploring the morphological profiling of microglia in MJD are lacking. Thus, a goal of this study was set to characterize the morphological changes, as well as count the number of microglia, in different affected CNS regions (cerebellum, brainstem, and SC) in a CMVMJD135 mouse model of MJD at 34 weeks of age. A PCA and ML models were implemented to further identify potential clusters of microglia based on their morphological features, as well as to pinpoint those that assume a higher importance in the distinction of microglia from transgenic and WT mice.

3.2 Materials and Methods

3.2.1 Animals

Male CMVMJD135 and WT littermates' mice on a C57BL/6J background with 34 weeks of age, were used for the experiments described below.

3.2.2 Tissue preparation and immunofluorescence staining

CMVMJD135 and WT littermates mice were deeply anesthetized and transcardially perfused with PBS followed by 4 % PFA solution (PFA, 0.1 M, pH 7.4, in PBS). Brain tissue was removed and fixed in a 4 % PFA for 48 h, followed by 30 % sucrose solution for 1 week. Then, coronal, and sagittal sections of 40 μm thickness were sliced using a Leica Vibratome and collected in 0.1 M PBS. Staining was performed with free floating sections in 12-well plates. Tissue slices were hydrated with PBS for 10 min and then permeabilized with 0.3 % PBS-T (0.3 % triton X-100, Sigma Aldrich, in PBS) for 10 min. Antigen retrieval was then performed by immersing the slices in pre-heated citrate buffer (10 mM, pH 6.0; Sigma Aldrich) during 20 min using a thermoblock (D1200, LabNet) set at 80 °C. Once cooled, slices were rinsed in PBS and then blocked with goat serum blocking buffer (10 % normal goat serum (NGS), 0.3 % triton X-100, in PBS) at RT for 90 min. After that, slices were incubated with the primary antibody rabbit anti-Iba-1 diluted in 0.3 % PBS-T, 5 % NGS, overnight at 4 °C. Then, tissue slices were rinsed in PBS and incubated with a secondary antibody, Alexa Fluor 594 anti-rabbit (Figure A.1 in *Appendix A - Materials and Methods*) diluted in 0.3 % PBS-T, 5 % NGS, during 90 min at RT, protected from light. Sections were mounted on microscope slides (Menzel-Glaser Superfrost©Plus, Thermo Fisher Scientific) and covered with a coverslip (Menzel-Glaser 24–60 mm, Wagner und Munz) using aqueous mounting medium (Fluoromount™ Sigma-Aldrich).

3.2.3 Image acquisition for microglial density and morphological analysis

For the analysis of microglial density and morphology, four coronal brain sections per animal ($n = 4$ per genotype) were imaged twice (in both hemispheres), for each region of interest (DCN and cervical spinal cord (CSC)) to yield 4-6 digital photomicrographs per section containing the region for analysis. For the PN, four sagittal brain sections per animal were used ($n = 3$ animals for WT and $n = 4$ animals for CMVMJD135) and 2 photomicrographs per section were taken. The Olympus Confocal FV1000 laser scanning microscope with a resolution of 1024 × 1024 px using a 40× objective (UPlanSApo, N.A. 0.90; dry; field size 624.39 × 624.39 μm; 0.31 $\mu m/px$) was used to obtain all Z-stacked images. The acquisition settings were the following: scanning speed = 4 $\mu m/px$; pinhole aperture = 110 μm; Iba-1, excitation = 559 nm, emission = 618 nm; in a 3-dimensional scenario (X, Y, and Z axis).

3.2.4 Image analysis for microglial density and morphological analysis

Microglial density and morphological analysis were performed using ImageJ software (v1.53c; National Institute of Health, Bethesda, MD, USA) on Z-stacked 3D volume images from sections of the affected brain regions (DCN, CSC, and PN). The total count of Iba-1-positive cells was obtained using the multi-point tool of ImageJ. Quantification was carried out on images acquired with acquisition settings described as above, normalized first to the total photo area (field size 624.39 $\times$ 624.39 μm) and then for volume (40 μm thickness).

For microglial morphology analysis, a semi-automatic method adapted from Young et al. (2018) [338] was used on the same images used for cell counting. To obtain fractal and skeleton data, binary images (white cells on black background) are required, and several steps were followed to apply commands and options to obtain such images. Hence, after stacking the 3D volume images, the double-color image was split to obtain the Iba-1 label in the red channel, and brightness and contrast of this red-channel image were adjusted. The unsharp mask was then applied. Afterwards, the despeckle filter was used to remove salt and pepper noise, with the threshold option being used and adjusted, as needed. Noise was subsequently eliminated using despeckle and by removing outliers. After that, at least 5 cells from both the original and the binary images were selected with the rectangle tool, using the region of interest (ROI) to set the same rectangle dimensions for all the selected cells (field size 296 $\times$ 264). After selecting the cells, the paintbrush tool was used to complete and draw the morphology of the cells (always comparing them with the original ones) and to clean extra signal that is not related to these cells, thus producing a single-cell image without any noise. Finally, the binary single-cell was then converted into an outline or into a skeletonized format for fractal or skeleton analysis, respectively [338] (Figure A.3 in *Appendix A - Materials and Methods*).

To analyze microglia morphology the *skeleton 2D/3D* plugin (developed by and maintained here: https://imagej.net/plugins /analyze-skeleton) was applied to binary single-cells, tagging skeletal features relevant to microglia ramification: number of endpoints voxels (#/cell), number of junctions voxels (#/cell), number of junctions (#/cell), number of slab voxels (#/cell), number of branches (#/cell), number of triple points (#/cell), number of quadruple points (#/cell), Euclidean distance (μm/cell), total branch length (μm/cell), average branch length (μm/cell), and maximum branch length (μm/cell) (Figure A.4 in *Appendix A - Materials and Methods*).

A fractal analysis was carried out using the *FracLac* plugin (Karperien A., FracLac for ImageJ (http: //rsb.info.nih.gov/ij/plugins/fraclac/FL-Help/ Introduction.htm) 1999–2013; available at the ImageJ website, National Institutes of Health) setting the Num G option to 4 and checking the metrics box. Then, the scan was run to obtain the hull and circle results, selecting only the data of interest associated with the cell's surface (cell perimeter (μm) and roughness (ratio)), the soma thickness (cell circularity (ratio) and density (ratio)), the cell's size (mean radius (μm), convex hull perimeter (μm), convex hull circularity (ratio), bounding circle diameter (μm), maximum span across the convex hull (μm), convex hull area (μm^2), and cell area (μm^2)), and the cylindrical shape of the cells (convex hull span ratio and the ratio of convex

hull radii). Data from the box count summary were also obtained, being associated with the complexity of ramifications (fractal dimension - D) and the heterogeneity of the shape (lacunarity - Λ) (Figure A.5 in *Appendix A - Materials and Methods*).

Data were obtained from individual cells of the CSC (310 microglia from WT mice and 389 from CMVMJD135 mice), DCN (349 microglia from WT mice and 445 from CMVMJD135 mice), and PN (152 microglia from WT mice and 180 from CMVMJD135 mice). The grand total is of 1825 microglia that were obtained and stored in the file system, in the TIFF format.

3.2.5 MorphData architecture and implementation

The process to obtain all the morphological features referred to above, when performed manually over each individual cell, would be a demanding and laborious task, which can take several weeks to complete. Hence, to expedite the process, the *MorphData* plugin was conceived and used (https://github.com/anabelacampos/MorphData). This plugin automatizes the data extraction process of morphological features of single microglial cells, collecting, pre-processing, and organizing features associated with cell complexity and ramification in a few minutes [339].

The *MorphData* plugin was developed using ImageJ macro language (IJM), a scripting language that allows a developer to control many features of ImageJ. Plugins written in IJM can be programmed to perform sequences of actions, thus automating repetitive processes. It has a set of basic structures, including variables, conditional statements, loops, and user-defined functions. Importantly, IJM allows the developer to access ImageJ functions that are available from its graphical user interface (GUI). *MorphData* takes advantage of IJM to automatically collect morphological features, working on any operating system in which ImageJ can work. The plugin is open-source and available online to the community. A straightforward architectural diagram is depicted in Figure 3.1.

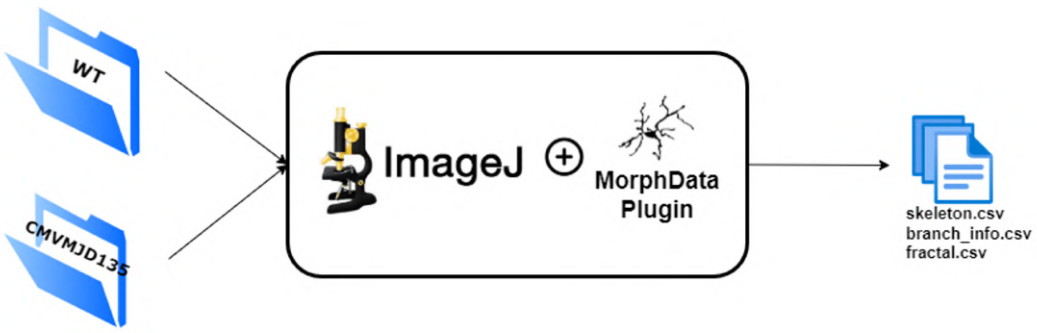

Figure 3.1: ***MorphData*'s architectural diagram.** It receives, as input, the root folders, and producing, as output, three csv files with the morphological features that characterize each single cell.

3.2.5.1 Computational requirements

The *MorphData* plugin requires basic computational resources. The experiments here described were carried out on a personal computer with an 8th generation i7 CPU with 4 cores at 1.80GHz, 8GB of RAM, a SSD disk, and the Windows 10 operating system. ImageJ 1.53c, embedded in Fiji, has been set with 6989MB of maximum heap size.

MorphData runs in any operating system compatible with ImageJ (https://imagej.nih.gov/ij/index.html), which is available, as a downloadable application, for Windows, macOS, and Linux. The plugin is reliant on ImageJ (version 1.52t, or later) and the following ImageJ plugins:

i. *AnalyzeSkeleton (2D/3D)* plugin (version 3.4.2, or later);

ii. *FracLac* plugin (version 2015Sep090313a9330, or later).

ImageJ/Fiji requires a system with a Java 8, or later, virtual machine. *MorphData*'s post-processing script requires Python (version 3.7.10, or later) and the following modules:

i. pandas (version 1.2.3, or later);

ii. tkinter (version 8.6, or later).

3.2.5.2 Installation

To install the *MorphData* plugin the user is required to download ImageJ and associated bundles with preinstalled plugins, such as Fiji, prior to installation (https://imagej.net/Fiji/Downloads). The user is then required to add *MorphData* as a new plugin to ImageJ:

i. Download the *Morph_Data.ijm* file from the code repository;

ii. Put the file in the plugins folder of ImageJ/Fiji itself.

The user can then start ImageJ and the *MorphData* plugin will be available at the Plugins tab. A detailed description on how to install ImageJ plugins can be found online at https://imagej.net/plugins.

MorphData also comes with a post-processing script, which users can run if necessary. To use this script users are required to have a Python environment installed. The easiest way to have such an environment is to download and install Anaconda, a popular open-source Python distribution platform (https://www.anaconda.com/products/individual). To run the post-processing script the user must open the Python console/prompt and execute the command "*python MorphData_PostProcessing.py*".

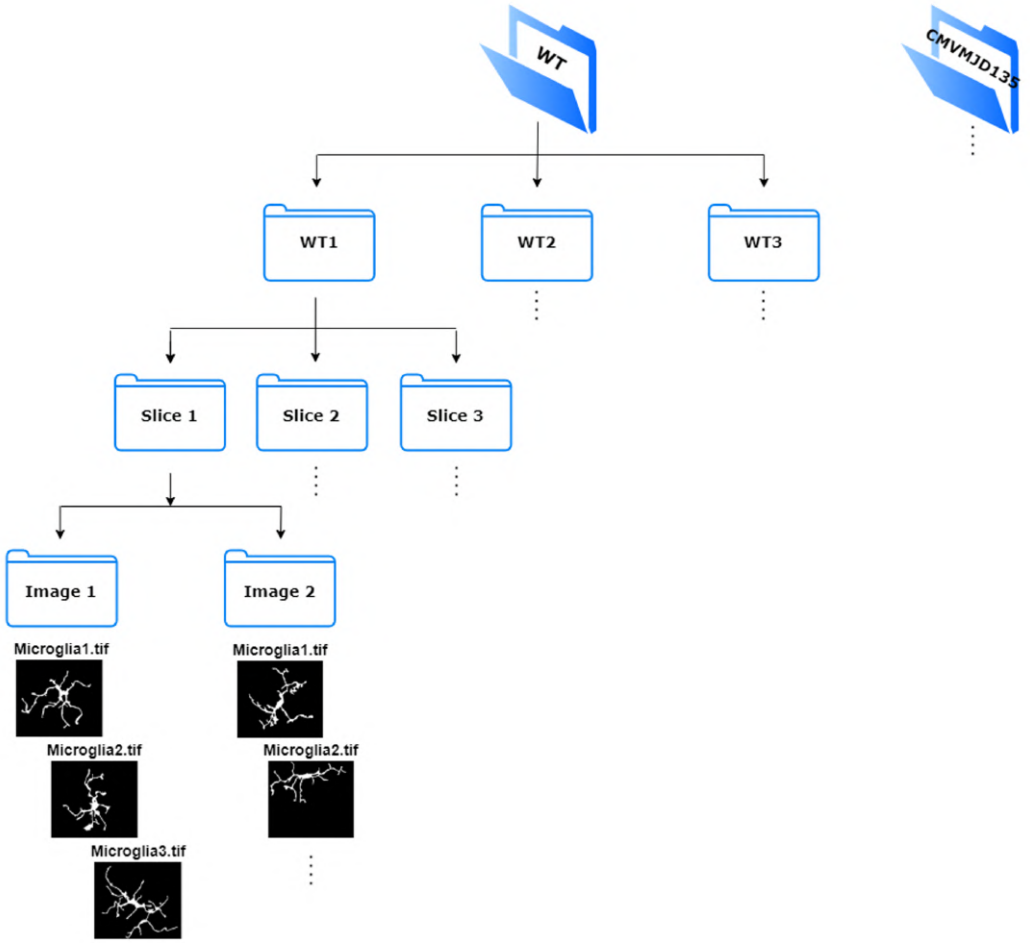

Figure 3.2: **Recommended file system structure to store single cell images.** The root folders, WT and CMVMJD135, hold the images of the corresponding experimental group.

3.2.5.3 Algorithm

Before detailing *MorphData*'s algorithm, it is important to clearly structure the obtained single cell images in the file system. Ideally, the user should create a structure such as the one depicted in Figure 3.2.

To comply with the *MorphData* plugin, while the name of the folders at the two first levels is irrelevant, it is important to guarantee that the last two levels are entitled as "*Slice i*", where *i* identifies different slices, and "*Image j*", where *j* identifies different photomicrographs. Single cells should be placed inside the corresponding image folder, being entitled as "*Microgliak.tif*", where *k* identifies each cell within the image folder. The *MorphData* plugin, when executed, starts by asking the user to indicate the folder containing the single cell images (Figure 3.3a).

Following the file structure defined in Figure 3.2, the user should indicate the WT folder (the root folder). The plugin then creates auxiliary folders to store the collected data and automatically starts navigating the indicated folder looking for single cell images. Then, for each image, the algorithm is summarized as follows:

i. To obtain skeletal features relevant to cell ramification:

a)

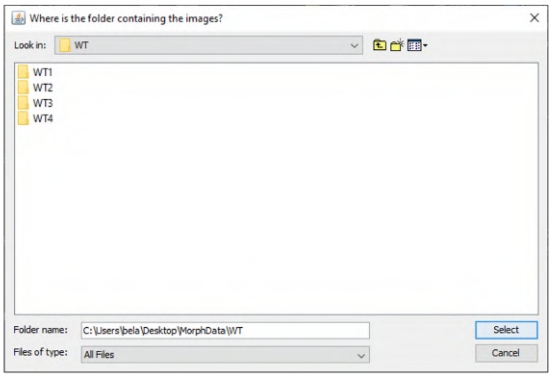

b)

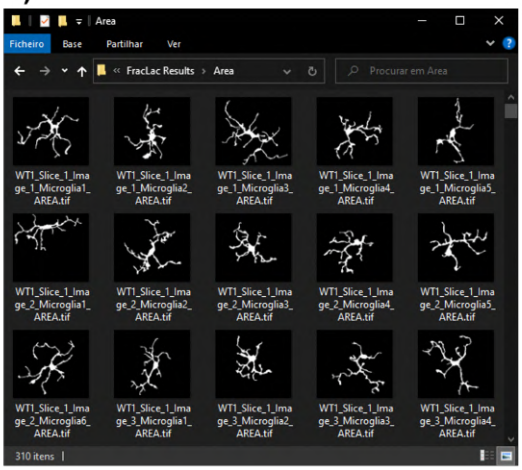

c)

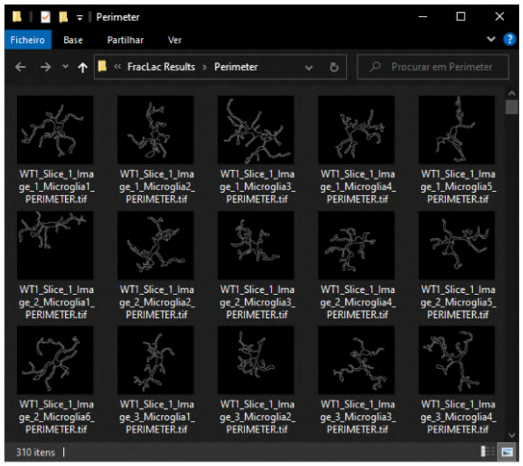

d)

# Branches	# Junctions	# End-point voxels	# Junction voxels	# Slab voxels	Average Branch	# Triple points	# Quadruple points	Maximum Branch	animal	microglia
35	17	19	51	800	17.91	17	0	73.099	WT1	WT1_Slice_1_Image_1_Microglia1
35	17	18	57	693	15.748	16	1	54.153	WT1	WT1_Slice_1_Image_1_Microglia2
47	23	24	83	1039	17.667	22	1	86.705	WT1	WT1_Slice_1_Image_1_Microglia3
37	18	20	58	702	14.87	18	0	47.673	WT1	WT1_Slice_1_Image_1_Microglia4
36	18	18	51	551	12.231	18	0	39.198	WT1	WT1_Slice_1_Image_1_Microglia5
33	16	17	56	692	16.333	15	1	53.98	WT1	WT1_Slice_1_Image_2_Microglia1
60	30	29	97	755	10.528	29	1	52.342	WT1	WT1_Slice_1_Image_2_Microglia2
38	19	18	54	637	13.285	18	1	39.45	WT1	WT1_Slice_1_Image_2_Microglia3
39	19	20	48	666	13.397	18	1	37.116	WT1	WT1_Slice_1_Image_2_Microglia4
33	16	18	49	686	16.07	16	0	66.034	WT1	WT1_Slice_1_Image_2_Microglia5

Figure 3.3: **Execution and results of the *MorphData* plugin. a)** *MorphData* dialog graphical user interface (GUI) asking the user where the single cell images are located. **b)** Shaped images, produced by *MorphData*, stored in the "*Area*" folder. **c)** Outlined images, produced by *MorphData*, stored in the "*Perimeter*" folder. Both shaped and outlined images are ready to be passed to the *FracLac* plugin for batch mode execution. **d)** A sample of the *skeleton_final_results.csv* file, produced by *MorphData*. This file contains 11 features relevant to cell ramification and cell identification.

a) Open a single cell;

b) Run the command "*Process* > *Binary* > *Skeletonize*" to create a skeletonized image;

c) Run the *Analyze Skeleton (2D/3D)* plugin;

d) Run the "*saveAs*" command to collect and store, in a csv file, skeletal data;

e) Run the "*saveAs*" command to collect and store, in a csv file, branch information data.

ii. To obtain features relevant to cell complexity:

a) Open a single cell;

b) Run the "*saveAs*" command to store a shaped single cell, in TIFF format, in a folder entitled as "*Area*";

c) Run the "*Process > Binary > Outline*" and "*saveAs*" commands to store an outlined single cell, in TIFF format, in a folder entitled as "*Perimeter*".

iii. Repeat steps 1. and 2. for each single cell;

iv. At the end, the algorithm indicates the number of analyzed cells.

Finally, contrary to the *Analyze Skeleton (2D/3D)* plugin, which is automatically executed by *MorphData*, the *FracLac* plugin cannot be directly executed from within another plugin. This limitation requires the user to manually execute the *FracLac* plugin itself after the *MorphData* plugin has finished. Fortunately, since the "*Area*" and the "*Perimeter*" folders, which were automatically created by *MorphData*, already contain all shaped and outlined cells (Figure 3.3b,c), the user can execute the *FracLac* plugin in batch mode. Hence, with a batch execution of this plugin, the user obtains fractal data for all cells almost immediately (avoiding the need to execute *FracLac* for each cell individually).

3.2.5.4 Post-processing script

Up to this point, all morphological data are now available, for all single cells, in multiple csv files in auxiliary "*results*" folders. In total, the *MorphData* plugin gathers 221 features (from skeleton to fractal ones), and some of them may be irrelevant to the characterization of microglial cells. Hence, the post-processing step is useful to join all data, cleaning irrelevant features, and performing a feature engineering process to create new ones, including the *cell_area*, *cell_perimeter*, *roughness*, and *cell_circularity*, among others.

Due to the potential high number of rows (cells) and columns (morphological features), an ImageJ plugin is unsuitable for the task, as it would eventually run out of memory. Hence, a Python script, entitled as *MorphData_PostProcessing.py*, was conceived and released as part of the *MorphData* plugin. This script requires a simple python environment to execute, again asking the user to indicate the location of the root folder. It will then automatically apply the post-processing procedures, creating three final files, containing the following 46 features:

i. **skeleton_final_results.csv:**

- *# Branches*, *# Junctions*, *# End-point voxels*, *# Junction voxels*, *# Slab voxels*, *Average Branch Length*, *# Triple points*, *# Quadruple points*, *Maximum Branch Length*, *animal*, *microglia_id*.

ii. **branch_info_final_results.csv:**

- *Skeleton ID*,*Total branch length*,*V1 x*,*V1 y*,*V1 z*,*V2 x*,*V2 y*,*V2 z*, *Euclidean distance*, *running average length*, *average intensity (inner 3rd)*, *average intensity*, *animal*, *microglia_id*.

iii. **fraclac_final_results.csv:**

- *fractal_dimension*, *lacunarity*, *outline_mean_fg*, *density*, *span_ratio_major_minor*, *convex_hull_area*, *convex_hull_perimeter*, *convex_hull_circularity*, *diameter_ bounding_circle*, *mean_radius*, *max_span_across_convex_hull*, *max_min_radii*, *shape _mean_fg*, *1_pixel_side_micron*, *1_pixel_area_micron_sq*, *cell_area*, *cell_perimeter*, *roughness*, *cell_circularity*, *animal*, *microglia_id*.

Figure 3.3d contains a graphical perspective of part of the content of the *skeleton_final_results.csv* file, which contains 11 features relevant for cell ramification. The remaining two files are similar, varying only on the quantified features. Sample input and output data are available at *MorphData*'s code repository.

3.2.6 Machine Learning modeling

To further process the obtained data and to identify potential clustering of microglia concerning their morphological features, an open-source data science and ML modeling platform was used. KNIME is a data-flow centric platform, enabling the assembly of visual and interactive flows. It integrates multiple components, including data loading modules, interactive widgets and views, data transformation operations, and statistical and ML models. Using the KNIME platform, two flows were conceived. The first is responsible for loading the obtained data and applying functions to arrange identical data into groups. These data are then used for statistical analysis, as explained in subsequent lines. The second flow is responsible for applying a PCA on the obtained data. This flow is also used to apply an unsupervised ML model, the k-means, which is a clustering method that is able to find groups, or clusters, with similar characteristics within the entire dataset. This method partitions the data into k clusters, with each observation belonging to a single cluster, i.e., each observation belongs to the nearer cluster, represented by its centroid. To find the ideal number of clusters, i.e., the ideal number for k, the flow applies the elbow method, experimenting and plotting the mean squared error (MSE) associated to each cluster, with k varying between 1 to 12. The ideal k is found by picking the "elbow" of the curve as a function that minimizes the error of k. This flow is also used to generate 3D plots.

$$\text{Mean squared error (MSE)} = \frac{1}{n}\sum(y-\sigma)^2 \tag{3.1}$$

where n is the number of parameters, y is the parameter value, and σ is the value of the centroid on the corresponding parameter space.

Finally, gradient boosted trees (GBTs) were used to obtain estimates of parameter importance, i.e., a score that measures how valid each parameter was for the model. GBTs are a supervised ML model,

being used to convert weak learners, typically decision trees, into strong ones. GBTs train the learners in a gradual, additive, and sequential manner, with a gradient descent procedure being performed. The importance was estimated using gain as importance type. A higher value for a parameter when compared to another, implies it is more important for classifying the label [340]. In this case, the label was set as the parameter identifying WT and CMVMJD135 cells, this being a binary classification problem.

3.2.7 Statistical analysis

SPSS V22.0 was used for all statistical analyses, with the Graph-Pad Prism 8.00 software being used to create the graphs. Regarding descriptive statistics, the mean was the considered measure of central tendency, while the measure of variability was the SEM. The assumption of normality was assessed by frequency distributions (z-score of skewness and kurtosis) as well as by the Kolmogorov-Smirnov and Shapiro-Wilk tests. The assumption of homogeneity of variances was evaluated by Levene's test. All data were analyzed using the two-tailed unpaired Student's t-test for comparisons between the two groups. The critical value for significance was set as $p < 0.05$ throughout the study.

3.3 Results

3.3.1 Numerical changes are observed in microglia from CMVMJD135 mice in a region-dependent manner

To better characterize the alterations in the profile of microglia from CMVMJD135 animals, we first counted the number of microglia (Iba-1-positive cells). These numerical analysis was performed in the affected brain regions of CMVMJD135 mice, namely in the DCN, at the cerebellum, the PN, at the brainstem, and in the CSC, at an age when the motor phenotype of this animal model is fully established. A significant reduction in the number of microglia was found in the PN ($p = 0.020384$) of CMVMJD135 mice when compared with WT mice (Figure 3.4a,d). This suggests the possibility of mutant *ATXN3* causing glia toxicity, eventually leading to microglial death processes. No differences were found in the DCN or CSC (Figure 3.4b,e; c,f, respectively).

3.3.2 MorphData's performance evaluation for automating the data extraction process of morphological features

Regarding the morphological profiling of microglia, we first developed and evaluated *MorphData*'s ability to automatically collect the morphological features that describe microglia in the PN, DCN, and CSC of WT and CMVMJD135 mice. For this, skeleton data was used to evaluate changes in features relevant to microglia ramification, while fractal data was used to evaluate characteristics associated with cell surface, soma thickness, cell size, the cylindrical shape of cells, the complexity of their ramifications, and the heterogeneity of their shape.

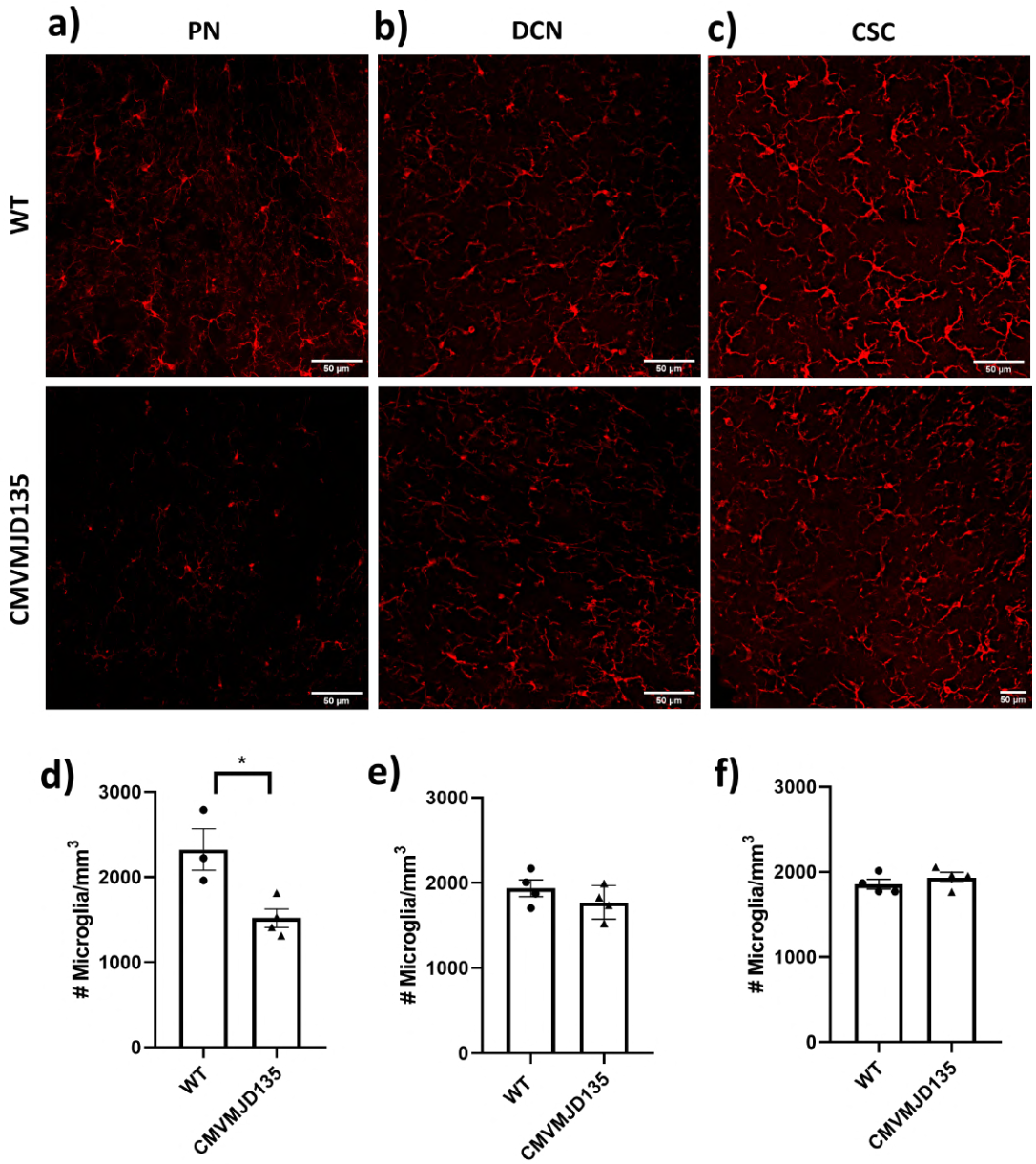

Figure 3.4: **Reduction of the number of microglial cells in the pontine nuclei of CMVMJD-135 mice.** Representative images of microglial cells, using Iba-1 as a microglia marker (in red), in the **a)** Pontine nuclei (PN), **b)** Deep cerebellar nuclei (DCN), and **c)** Cervical spinal cord (CSC) of CMVMJD135 and WT mice. **d, e, f)** Quantitative analysis of the number of Iba-1-positive cells in the PN, DCN, and CSC of WT and CMVMJD135 mice ($n = 4 - 5$ per group), using ImageJ software. Data are presented as mean+SEM (Student's t-test). *, represent $p < 0.05$. Scale bar 50 μm.

The performance of *MorphData* was evaluated based on the validity and on the time it took to collect the morphological features for a subset of 699 single cells from both experimental groups, when compared to a manual collection of such data. Totally, in a computer with limited computing power, it took less than 14 minutes to collect 46 morphological features associated with these 699 single cells. In particular, 6.5 minutes were spent handling the WT group by the *MorphData* plugin. Of those, nearly 3 minutes were spent collecting skeleton data, 3.25 minutes by the *FracLac* plugin on batch mode, and 10 seconds by

the post-processing script. On the other hand, 7.5 minutes were spent handling the CMVMJD135 group. Of those, 3.5 minutes were spent collecting skeleton data, 3.8 minutes by the *FracLac* plugin on batch mode, and 11 seconds by the post-processing script.

The same process was performed manually, by a skilled user of ImageJ, for a subset of ten single cells of the WT group. To ease the process, the same file system structure (as required by the *MorphData* plugin) was used. The goal was to mimic the processes that are automatically performed by *MorphData*, and manually collect 46 morphological features for the ten cells. The mean time to collect such morphological features was of 13 minutes per cell. Skeleton data were faster to collect (around 1.5 minutes), since the *AnalyzeSkeleton (2D/3D)* plugin only opens two results' windows that the user can immediately save in two distinct files in the file system, in csv format, and then close the opened windows. However, fractal data were considerably harder to collect (around 11.5 minutes). On the one hand, for each cell, the *FracLac* plugin must be executed twice - one for a shaped cell and one for an outlined cell, which the user must prepare. On the other hand, for each execution, this plugin opens multiple results' windows. The ones to keep opened are the "Hull and Circle Results" and the "Box Count Summary" windows. However, these windows are not user-friendly and, besides providing the user with an overwhelming amount of 173 features (most of them formulas and unwanted columns), it does not allow the user to copy only the desired features - the user must manually write each value of each desired feature to a csv, or excel, file. In fact, the process of selecting features from the *FracLac* plugin is extremely exhausting and error-prone. Finally, it is up to the user to calculate the value of non-existing features such as *cell_area*, *cell_perimeter*, *roughness*, and *cell_circularity*.

A couple more obstacles emerged with the manual process. First, the user was required to edit each stored file, for each cell, to identify the animal and the microglia of each row of data. Secondly, the user was required to copy the contents of each file to an overall file, aggregating the data for the experimental group. Since each cell is made of three files (two skeleton files and one fractal file) this would require the user to open and copy 699×3 files, which would, again, be a time-consuming task that would have to be performed after collecting all data. Overall, the manual process for ten single cells of the WT group took more than 2 hours to complete. On the other hand, the *MorphData* plugin and its post-processing script took less than 14 minutes to collect, process, and organize the morphological features of 699 cells. Assuming a mean value of 13 minutes per cell, the manual process to collect the morphological features of all cells would take 151 hours, which corresponds to almost 19 working days (8 hours/day) collecting data without stopping.

3.3.3 Morphological changes are observed in microglia from CMVMJD135 mice in a region-dependent manner

With *MorphData* properly validated, it was used to collect the morphological features of a grand-total of 1825 single microglial cells from the PN, DCN, and CSC of WT and CMVMJD135 mice. Data were collected in a matter of minutes, significantly reducing the time that would be required to perform the data collection

process.

The skeleton and fractal analysis showed no differences between the groups, neither in the PN (Figure B.1 and B.2 in *Appendix B - Results*) nor in the DCN (Figure B.3 and B.4 in *Appendix B - Results*). Interestingly, in the CSC, skeleton data showed significant differences in microglia from CMVMJD135 mice when compared with those from WT mice. The number of slab voxels ($p = 0.012917$), the maximum branch length ($p = 0.031432$), the total branch length ($p = 0.016352$), and the Euclidean distance ($p = 0.020316$) were lower in microglia from CMVMJD135 mice (Figure 3.5). On the other hand, the number of branches, the number of junction voxels, the number of endpoint voxels, the average branch length, and the triple and quadruple points, were similar between groups (Figure B.5 in *Appendix B - Results*).

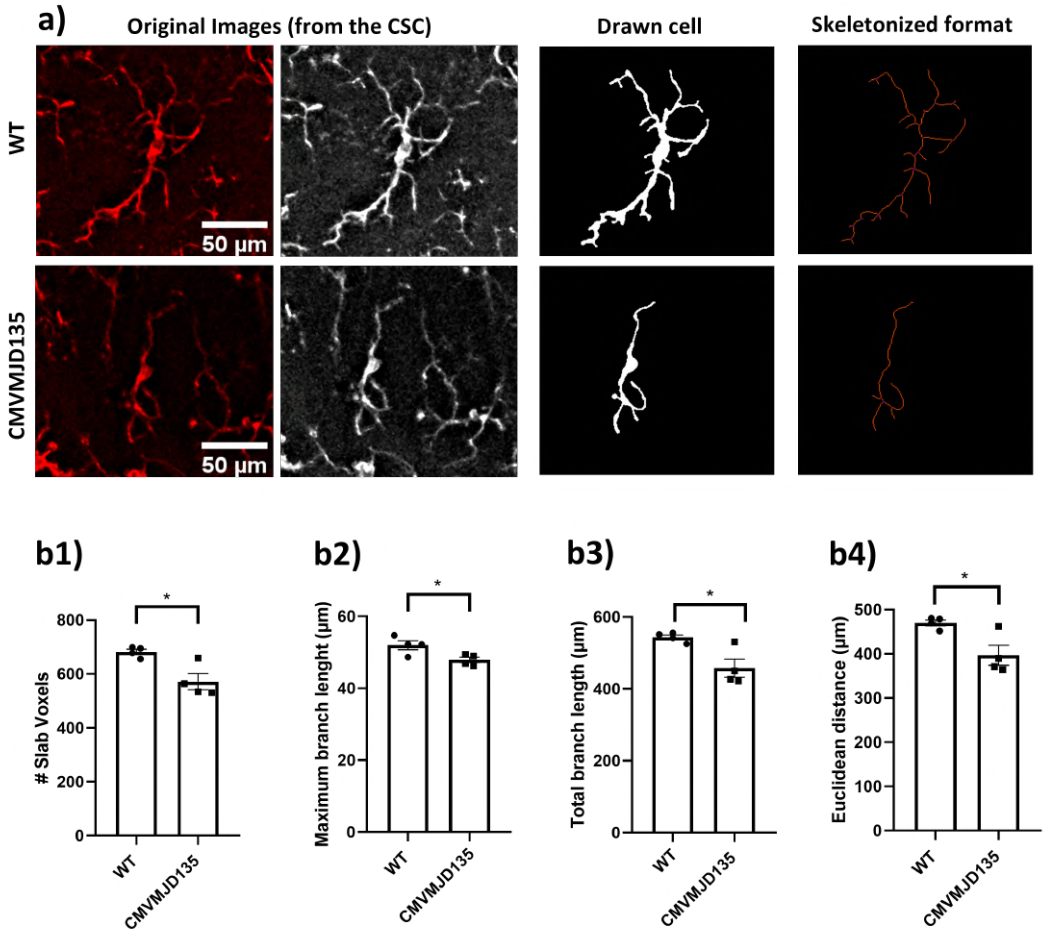

Figure 3.5: **Microglia in the cervical spinal cord of CMVMJD135 mice show less morphological complexity. a)** Representation of the process to prepare the images for skeleton analysis of microglia morphology. **b)** Quantification of the morphometric features associated to microglia ramification, including: **b1)** # slab voxels, **b2)** maximum branch length, **b3)** total branch length, and **b4)** Euclidean distance. Data of all these features were obtained from 310 microglial cells from WT mice ($n = 4$) and 389 microglial cells from 34 weeks-old CMVMJD135 mice ($n = 4$) of the CSC. Data are presented as mean+SEM (Student's t-test). *, represent $p < 0.05$. Scale bar 50 μm.

Additionally, alterations in several parameters associated with the heterogeneity of the shape, cell size, cell surface, and soma thickness were observed in CMVMJD135 mice. In fact, the lacunarity ($p =$

0.017934), the convex hull area ($p = 0.003983$), the convex hull perimeter ($p = 0.001963$), the diameter of the bounding circle ($p = 0.000753$), the mean radius ($p = 0.001132$), the maximum span across the convex hull ($p = 0.000757$), the cell area ($p = 0.021343$), and the cell perimeter ($p = 0.011744$) were found to be decreased in microglia from CMVMJD135 mice when compared to WT ones. On the other hand, density ($p = 0.000798$) and cell circularity ($p = 0.014008$) were increased in the CMVMJD135 group (Figure 3.6).

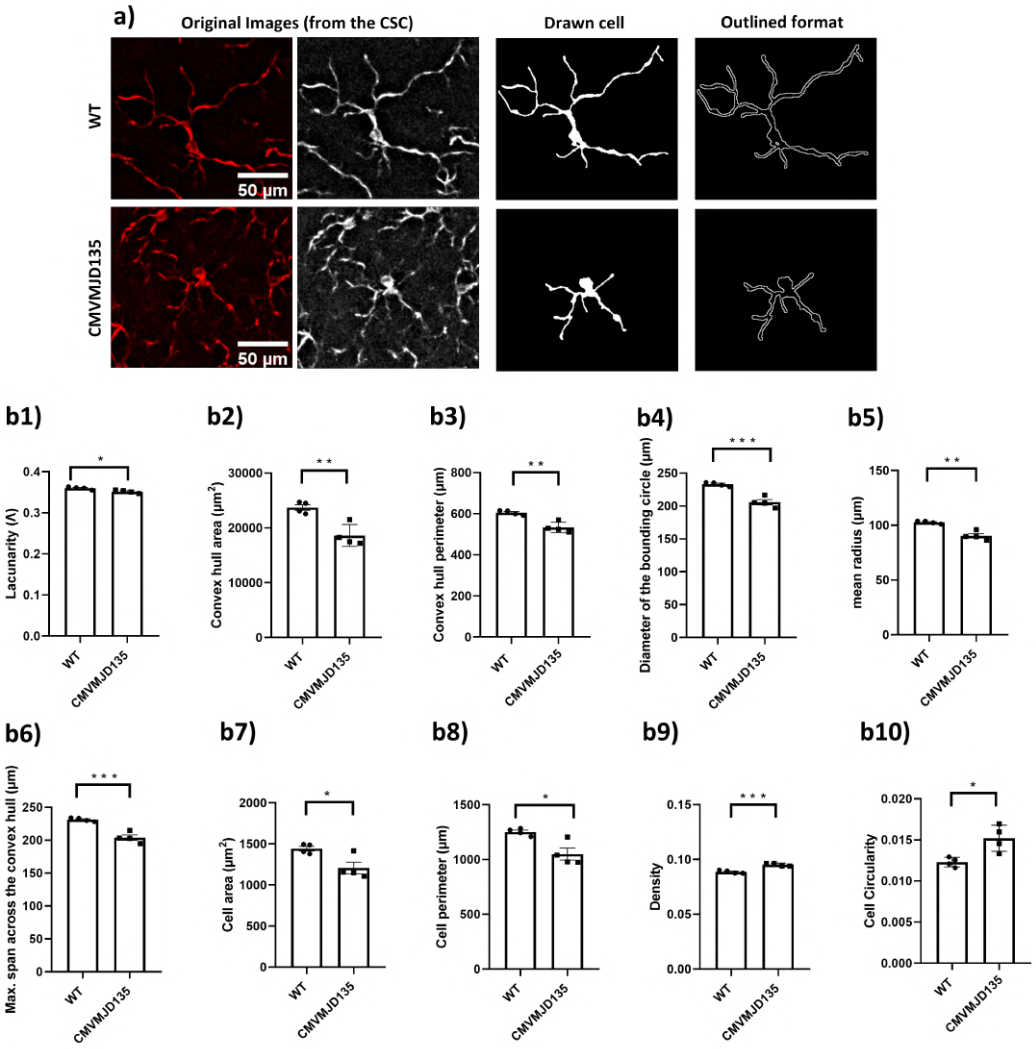

Figure 3.6: **Microglia in the cervical spinal cord of CMVMJD135 mice showed distinct activation-associated morphological features. a)** Representation of the process to prepare the images for fractal analysis of microglia morphology. These images show differences regarding the convex hull area, the mean radius, and the maximum span across the convex hull in microglia from CMVMJD135 mice. **b)** Quantification of the morphometric features associated with heterogeneity of the shape: **b1)** lacunarity; Associated with cell size: **b2)** convex hull area, **b3)** convex hull perimeter, **b4)** diameter of the bounding circle, **b5)** the mean radius, **b6)** the maximum span across the convex, and **b7)** the cell area; Associated with cell surface: **b8)** cell perimeter; Associated with soma thickness: **b9)** density and **b10)** cell circularity. Data of all these features were obtained from 310 microglial cells from WT mice ($n = 4$) and 389 microglial cells from 34 weeks-old CMVMJD135 mice ($n = 4$) of the CSC. Data are presented as mean+SEM (Student's t-test). *, **, ***, represent $p < 0.05$, $p < 0.01$ and $p < 0.001$, respectively. Scale bar 50 μm.

Regarding the parameters associated with the complexity of ramifications and with the cylindrical shape of the cells, no differences were observed between groups (Figure B.6 in *Appendix B - Results*). These observations suggest that microglia in the CSC of CMVMJD135 mice are more activated when compared with WT mice, since microglia from CMVMJD135 mice were found to be less tortuous and to have less and shorter branches, with smaller size, and higher soma thickness.

3.3.4 Morphological features that best characterize spinal cord microglia of Machado-Joseph disease mice

Since our initial analysis revealed changes in microglia in the SC, a region that is affected since early stages in MJD patients and in the CMVMJD135 mouse model, PCA and ML models were implemented to further characterize the morphological changes between CMVMJD135- and WT-derived microglia, allowing the identification of potential clusters of cells based on their morphological features as well as to pinpoint those that assume a higher importance. A morphological analysis of microglia from the CSC of CMVMJD135 and WT mice was performed by measuring a total of twenty-six different features related to microglia ramification, complexity, and cell shape. Regarding microglia ramification features, four were found to be statistically different in microglia from CMVMJD135 mice (Figure 3.5). On the other hand, from the fifteen features associated with complexity and cell shape, ten were found to be significantly different between the groups (Figure 3.6). Considering the number of significantly altered features, a PCA was performed to reduce this dimensionality. A 3D space was computed based on three principal components, the PCA being able to preserve 99.1 % of the entire information present in the fourteen significant features (PC0 = 91.7 %, PC1 = 5.8 %, and PC2 = 1.6 %; Figure 3.7a).

A scatter plot was designed, plotting each animal as a point in a 3D space on the principal components plane. Figure 3.7a depicts a clear separation between CMVMJD135 and WT animals, based on the three principal components that are grounded on the statistically different features. The exception was one CMVMJD135 mouse, which was closer to the WT group. To better visualize the relationships between multiple significant features found to be altered between both groups, two more 3D scatter plots were conceived. Figure 3.7b,c show a clear distinction between the two groups based on cell ramification and cell size features, respectively. Both plots show a clear distinction of CMVMJD135 and WT animals based on the morphological features of their microglia.

With the PCA showing promising prospects, an unsupervised Machine Learning model, the k-means, was used to identify clusters of data with similar characteristics. The used dataset comprised 310 microglia from the CSC of WT mice and 389 from the CSC of CMVMJD135 ones. Using all fourteen statistically significant features, the elbow method, as depicted in Figure 3.7d, identifies the largest drop in the error for k = 2, i.e., identifies two clusters in the dataset, which is in accordance with expectations since these data originated from two groups (CMVMJD135 and WT). Once the ideal number of clusters was found, these clusters were plotted in a 4D space, with color as the fourth dimension. One cluster, in green, is grouping more ramified cells, with longer branches, larger area and perimeter, and lower circularity and

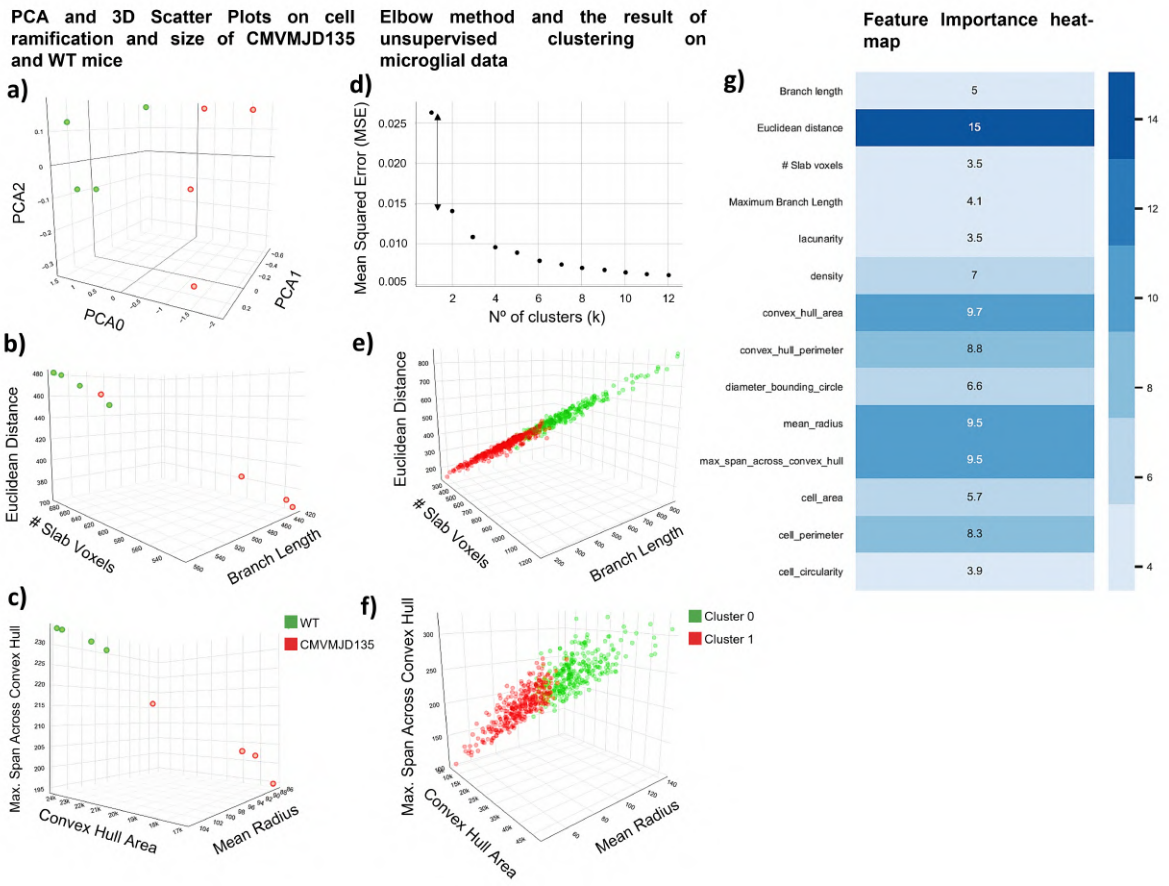

Figure 3.7: **A clear separation of microglia in the cervical spinal cord of CMVMJD135 and wild-type mice regarding features associated with cell ramification and cell size. a)** 3D scatter plot showing the distribution of CMVMJD135 mice (in red) and WT animals (in green) on a principal components plane. **b)** 3D scatter plot showing a clear separation between CMVMJD135 and WT mice regarding the number of slab voxels, total branch length, and Euclidean distance; and **c)** 3D scatter plot showing a clear separation between CMVMJD135 and WT mice regarding their convex hull area, mean radius, and maximum span across the convex hull. **d)** Graphical result of the elbow method applied on the dataset comprised of 310 cells from WT mice and 389 from CMVMJD135 ones. **e, f)** Data points of a total of 310 microglial cells from WT mice and 389 microglial cells from CMVMJD135 mice were plotted as a function of the significant features, belonging to one of two clusters: cluster 0, in green, or cluster 1, in red. **e)** 3D scatter plot showing the relationship between the number of slab voxels, total branch length, and Euclidean distance; and **f)** 3D scatter plot showing the relationship between the convex hull area, mean radius, and maximum span across the convex hull of all microglia. **g)** Feature importance heatmap for each parameter used to classify microglia from CMVMJD135 and WT mice. The higher the color tone, the higher the importance of the parameter.

density. This cluster is mainly composed of microglia from WT mice. Conversely, the second cluster, in red, is mainly composed of CMVMJD135 microglia, which have less and shorter branches, lower size, and higher soma thickness, characteristics typically found in activated microglia (Figure 3.7e,f).

To complement this analysis, GBTs were conceived, otimized, and evaluated, the goal being to use a supervised ML model that can distinguish microglia from CMVMJD135 and WT mice, in the CSC. Four independent trials were run, using nested k-fold cross-validation (5 outer and 5 inner folds). While the input

data are all the significant features, the label was set as the parameter identifying WT and CMVMJD135 cells, this being a binary classification problem. The candidate models were tuned regarding the number of estimators, learning rate, tree's max depth, and fraction of columns to be sub-sampled, being evaluated by its accuracy, precision, and recall. The best candidate model attained an accuracy of approximately 70 % using one-fifth of the total number of columns per estimator, 100 estimators, a tree's max depth of 2, and a learning rate of 0.1. Since GBTs provide the ability to obtain estimates of feature importance, Figure 3.7g depicts the importance attained by each feature. While the ML model allocates lower importance to features such as the cell's lacunarity and circularity, and the number of slab voxels, features such as the Euclidean distance, convex hull area, mean radius, and maximum span across the convex hull have an increased importance when identifying microglia based on their morphological features. This further reinforces the significance of these morphological features to characterize SC microglia of MJD mice, denoting the impact of the disease in these morphological characteristics.

3.4 Discussion

Morphological characterization of microglial cells is highly relevant in the sciences field, and particularly in neurosciences. However, when performed manually, the process for obtaining morphological features from single cells is a demanding, repetitive, and laborious task; it is error-prone and can take several weeks to be completed. Thus, this work describes the design, implementation, and use of a new plugin that automatically runs and collects morphological features for single cells in a matter of minutes, significantly reducing the time spent on the data collection process. This plugin has an increased importance given the lack of solutions for automatic data collection. Indeed, one example is provided by Heindl et al. (2018) [341], where the authors propose a morphological analysis method outside ImageJ, using a closed and proprietary programming language and numeric computing environment. However, *MorphData* is not only free but also open-source, setting its goal on optimizing the data collection process of morphological features.

MorphData brings obvious advantages, mainly by significantly reducing the time it takes to collect morphological data. These values could be further reduced by a computer with higher computation power. In addition, the automation of the data collection process completely removes the risk of human error. It is worth mentioning that since *MorphData* is using well established plugins to collect morphological features, it produces the same exact results as when performing the data collection process manually. In fact, *MorphData*'s collected values were further compared and validated with multiple cells data that were manually collected, without a single collection error. Even though the plugin was optimized for microglial cells, it is likely to be performant for other glial cells, such as astrocytes and oligodendrocytes, and non-glial cells, such as neurons. Likewise, *MorphData* can also be used to automate the data extraction process of morphological features of *in vitro* cells.

Once collected, processed, and organized successfully all morphological features associated with cell

complexity and ramification of several microglial cells, we characterized the morphological profiling of microglia from CMVMJD135 mice in different affected CNS regions (PN, DCN, and CSC) at a late disease stage. Since dystrophic cells can display some of the features typically associated with activation, mostly de-ramification and shortening of the processes, it is difficult to distinguish, with certainty, "activated" from "dystrophic" microglia [342]. However, other abnormal morphological features, such as gnarled, beaded, unusually tortuous, or fragmented cytoplasmic processes, are typically signs of senescent microglia [189, 269, 278, 343]. These allow us to distinguish between an "activated state", which is characterized by ramified cells with a larger cell body and shorter, thick processes, and a "reactive state", typically characterized by smaller, spherical cells, which can also exhibit rod-shaped or amoeboid-like morphologies [183, 242]. These microglial states, which display inflammatory and phagocytic features, are most often observed in pathological situations [242]. However, in some neurological conditions, and depending on the stage of the pathological process, microglia can play both a toxic or a protective role. Hence, the extent of microglial activation and, thereby, their contribution to the pathogenesis may depend on the type and duration of injury [149, 183, 186, 216, 275, 331] and on the CNS region under study. A better comprehension of MJD-associated microglia based on the characterization of their morphological profile may help to unravel the relevance of these cells in MJD pathogenesis.

Of the three analyzed areas, only microglia from the SC (one of the earliest affected CNS regions in this mouse model) showed significant differences in features associated with microglia ramification, heterogeneity of the shape, cell size, cell surface, and soma thickness. Indeed, microglia from CMVMJD135 mice showed a decreased number of slab voxels, a decrease of the maximum branch length and total branch length, and lower Euclidean distance, which is an indicator of the cell's tortuosity [344]. This suggests that these cells are less ramified, with shorter processes, and less tortuous when compared with microglia from WT mice. In addition, we found an increased density and circularity of microglia from CMVMJD135 mice. As described in [334], circularity determines the cell's roundness, which is increased in amoeboid-like cells. On the other hand, an increased density occurs during the morphological shift from a ramified to an amoeboid shape upon neuroinflammatory insults, a phenotype seen upon exposure to stress [333]. Features associated with cell size such as convex hull area, convex hull perimeter, diameter of the bounding circle, the convex hull area, the mean radius, the maximum span convex hull, and the cell area, were lower in microglia from CMVMJD135 mice when compared to WT ones. Previous studies have demonstrated that decreased values of these features are associated with an amoeboid-like shape [183, 242, 334]. Finally, the lacunarity, which refers to the degree of inhomogeneity, was found to be decreased in microglia from CMVMJD135 mice, implying that these cells have a more homogeneous outline when compared with cells from WT mice [334]. These results were complemented with the PCA and ML models outcome, which depicted a clear structure on the morphological data, with two clusters being identified. While one is mainly composed of WT-derived microglia (more ramified cells, with longer branches, larger area and perimeter, and lower circularity and density), the other is mainly grouping CMVMJD135-derived microglia (with less and shorter branches, lower size, and higher soma thickness). The supervised ML model, which was otimized to identify the cells' genotype based on their morphological features, allowed

us to further identify those that best characterize SC microglia of MJD mice (Euclidean distance, convex hull area, mean radius, and maximum span across the convex hull), being these the features that are most affected by this disease. Overall, these observations are particularly relevant and may indicate that microglia in the SC of CMVMJD135 mice are more activated than WT-derived microglia. Even though the morphological changes point to an increased activation state of microglia, and other studies showing microgliosis in MJD patients [10, 143, 144] and MJD mice [145], further mechanistic studies are required to understand if these microglial cells actively contribute to MJD onset and/or progression.

Chapter 4

Transcriptomic profiling of microglia in the pathogenesis of Machado-Joseph disease

4.1 Introduction

Microglia are the main immune cells of the CNS with multiple roles in neurodevelopment, homeostasis, synaptic plasticity, and injury responses [141, 142], being increasingly recognized as implicated in NDs [345]. In healthy conditions, these cells are continuously scanning their environment, pruning synapses, and regulating neuronal activity [184, 331]. It is thought that, depending on the received stimulus, microglia can polarize to different states, like the initially proposed M1 and M2 phenotypes, where M1 is a pro-inflammatory phenotype, associated with tissue damage induced by inflammation, and M2 is an anti-inflammatory phenotype, corresponding to microglia prone to remove cellular debris and promote tissue regeneration [189, 346]. However, the M1/M2 model does not properly describe the brain microglia complexity and the possible patterns of response when facing to the enormous quantity of signals microglia are exposed to. Defining the microglial transcriptomic signatures in different states has contributed to reveal that their activation status is quite heterogeneous and, thus, hard to clearly characterize [183]. Inflammation is an important component of the NDs and disequilibrium between the production of the both pro- and anti-inflammatory microglial mediators, becoming mainly pro-inflammatory, may constitute a crucial component of the NDs onset and progression [203, 216, 275]. Accumulating evidence also suggests that, upon neurodegenerative conditions, microglia may lose beneficial roles and gain destructive ones, in addition to mediating inflammation [203, 216, 275]. Additionally, it was observed in neurodegenerative diseases including AD, ALS, and frontotemporal dementia, and aging, that the microglia adopt a collective signature significantly different from the homeostatic transcriptional signature [166, 203, 207, 213, 299]. These “DAM” acquire a gene signature collectively associated with a “MGnD” phenotype [207]. Nonetheless, it remains unclear whether DAM or MGnD phenotypes are harmful or beneficial to neurodegenerative diseases [203, 207].

Currently, little is known about gene expression and molecular pathways that underlie microglial changes in the context of MJD. Since transcriptomic studies have highlighted the role of microglia in the pathogenesis of several NDs, mapping crucial pathological processes that aid the identification of new therapeutic targets [345, 347], we characterized gene expression networks in MJD-derived microglia, providing relevant insights into how coordinated gene regulatory programs in microglia underlie MJD pathogenesis. Thus, an RNA-sequencing analysis was performed on microglia isolated from relevant brain regions, cerebellum and brainstem, known to be highly affected in MJD, in CMVMJD135 mice, to define their transcriptional signature and to investigate the potential utility of therapeutically targeting these cells to counteract MJD. In summary, we were able to better define the cellular and molecular profile of MJD-associated microglia, contributing with new insights on MJD pathogenesis.

4.2 Materials and Methods

4.2.1 Animals

Two groups, CMVMJD135 and WT mice on a C57BL/6J background with 34 weeks of age, were considered.

4.2.2 Brain tissue dissociation and Magnetic Activated Cell Sorting isolation of adult microglia

4.2.2.1 Cellular suspension preparation

Microglia were isolated from the brainstem and cerebellum of WT and CMVMJD135 mice as described by Holt et al. (2016) [348]. The isolation was performed by pooling these 2 brain areas from 3 animals for each experiment. Hence, $n = 5$ implies the use of 15 animals WT and 15 CMVMJD135 mice. Mice were transcardially perfused under deep anesthesia with PBS, and then the brainstem and cerebellum were removed, dissected, and rinsed in cold hanks balanced salt solution (HBSS) without calcium chloride or magnesium chloride (HBSS-$CaCl_2$/[-]$MgCl_2$, ThermoFisher Scientific). Then, the regions of interest were cut into small pieces by using a sterile scalpel, and the samples were centrifuged at 300 $\times$ g for 2 min at 4 °C and the supernatant was discarded carefully. Enzymatic cell dissociation was performed using a neural tissue dissociation Kit (Miltenyi Biotec), according to the manufacturer's instructions. Briefly, the enzyme mix 1 (50 μL of enzyme P and 1950 μL of buffer x), previously vortexed and pre-heated at 37 °C for 15 min, was transferred to the tissue pieces (up to 400 mg of tissue per sample), and then we proceeded to incubation for another 15 min at 37 °C under slow rotation to allow the digestion of the tissue. The enzyme mix 2 (10 μL of enzyme A and 20 μL of buffer Y) was then added and the tissue was dissociated mechanically using a 1 mL syringe and a 20 G needle. After that, the samples were resuspended with cold HBSS with calcium chloride and magnesium chloride (HBSS+$CaCl_2$/[+]$MgCl_2$, ThermoFisher Scientific) and filtered through a 70 μm cell strainer (Sigma-Aldrich) to remove cell clumps followed by a centrifugation at 300 $\times$ g for 10 min at 4 °C.

4.2.2.2 Myelin and debris removal

After centrifugation, cells were resuspended in magnetic activated cell sorting (MACS) solution (0.5 % BSA in PBS, pH 7.2) and incubated for 15 min at 4 °C with myelin removal beads II (Miltenyi Biotec Myelin removal kit) for myelin and debris removal. After that, cells were washed by adding blocking solution and centrifuged at 300 $\times$ g for 10 min at 4 °C. The supernatant was removed and the pellet was resuspended in MACS solution. Then, the autoMACS® Pro Separator, using a reusable autoMACS® Column for separation, was prepared to automatically isolate the cells. Briefly, the tube containing the sample (row A of the rack), the tubes for collecting the labelled (myelin positive fraction; row C of the rack), and the unlabeled cell fractions (myelin negative fraction - mixed glial population, row B of the rack) were placed in

the autoMACS®. For the separation of these two different fractions, the following program was chosen: "Depletion: Depletes - collect negative fraction in row B of the rack".

4.2.2.3 MACS sorting of adult microglial cells

After myelin and debris removal, the myelin negative fraction was used to obtain the microglial cells. After centrifugation of the cell suspension at 300 × g for 10 min at 4 °C, the cell population was resuspended in MACS solution and incubated with anti-CD11b Magnetic Microbeads (Miltenyi Biotec CD11b Microbeads) for 15 min at 4 °C. The cells were washed by adding MACS solution, and the unbound beads and debris were discarded after centrifugation at 300 × g for 10 min at 4 °C. The pellet were resuspended and put in row A of the rack as well as the tubes for collecting the labelled cell fractions (microglia positive fraction in row C of the rack) were placed in the autoMACS® Pro Separator using the following program: "Positive selection: Possel - collect positive fraction in row C of the rack". After centrifugation at 300 × g for 10 min at 4 °C, the microglia pellets were used for RNA extraction.

4.2.3 RNA extraction, library preparation, and targeted RNA-sequencing

The microglia pellets were resuspended in buffer RLT plus with β-mercaptoethanol for RNA extraction using the RNeasy Plus Mini Kit, along with the recommended on-column DNase digestion (Qiagen 74136). RNA quality and concentrations were measured using an Agilent Technologies Bioanalyzer (Agilent RNA 2100 Pico) and samples having RNA integrity number (RIN) scores higher than 8 were used.

The AmpliSeq Library preparation kit protocol, described by Li et al. (2015) [205], was used to prepare Ion Torrent sequencing libraries. Briefly, 0.5 ng of total RNA was converted to cDNA and amplified for 16 cycles by adding PCR Master Mix and the AmpliSeq Mouse transcriptome gene expression primer pool (targeting 20767 well-annotated RefSeq genes + 3163 XM and XR genes, based on GRCm38/mm10). The proprietary FuPa enzyme was used for digestion of amplicons, and then barcoded adapters were ligated onto the target amplicons. The library amplicons were bound to magnetic beads, and residual reaction components were washed off. Libraries were amplified, re-purified, and individually quantified using Agilent TapeStation High Sensitivity tape. Individual libraries were diluted to a 50 pM concentration and pooled equally, with eight individual samples ($n = 4$ for WT and CMVMJD135 mice) per pool for further processing. Emulsion PCR, templating, and 540 chip loading were performed with an Ion Chef Instrument (Thermo-Fisher). Ion S5XL™ sequencer (Thermo-Fisher) was used for sequencing. Automated data analysis was done with Torrent Suite™ Software using the Ion AmpliSeq™ RNA plug-in v.5.12 and target region AmpliSeq_Mouse_Transcriptome_V1_Designed.

4.2.4 Analysis of differentially expressed genes and pathways

For the analysis of Differentially Expressed Genes (DEGs), RNA expression levels were recorded as reads per million (RPM), normalized for the number of sequences reads per sample. Before the DEGs analysis, to verify the enrichment of microglial cells in the samples, a list of several cell-type specific genes

known to be expressed specifically in microglia, astrocytes, neurons, endothelial cells, oligodendrocytes and macrophages was prepared [178, 347, 349–351], being described in (Figure A.6 and Figure A.7 in *Appendix A - Materials and Methods*). An heatmap containing the cell-specific markers was created using the Clue Morpheus software.

The Transcriptome Analysis Console (TAC) software, version 4.0.2 (Applied Biosystems by Thermo Fisher Scientific), was used to analyze and compare the gene expression profile from microglia of WT and CMVMJD135 mice. exploratory grouping analysis (EGA), a tool from TAC for analyzing the relationships among a group of samples, was used to identify the distribution of samples using PCA and a clustering analysis. TAC software provides the LIMMA Bioconductor package for determining differential expression based on linear models. LIMMA uses an Empirical Bayes method that corrects the variance of the ANOVA analysis. Genes were considered significantly differentially expressed if they showed a |fold change| > 1, $p < 0.05$, and a false discovery rate (FDR)<0.1. Genes overlapping between published gene sets and enriched genes in microglia of CMVMJD135 mice when compared with WT littermates were found by contingency analysis using the Fisher's exact test and the Baptista-Pike method to calculate the odds-ratio. Significance was set at $p < 0.05$.

For pathways analysis, the TAC software and the Ingenuity Pathway Analysis (IPA) (QIAGEN Inc) were used. Pathways were considered significantly altered in microglial cells from CMVMJD135 mice when compared with WT mice if they had $p < 0.05$ and a significance value >1.3, calculated as $-log10$ of the p value.

The validation of RNA-sequencing data was performed trough quantitative RT-PCR using the same RNA used for RNA-sequencing. cDNA synthesis and quantitative RT-PCR was performed as described in the chapter 2. The primers were designed using NCBI Primer-BLAST and are listed in Figure A.2 in *Appendix A - Materials and Methods*.

4.2.5 Statistics

SPSS software V22.0 was used for all statistical analyses, with a significance level of 0.05 being used throughout the study. Regarding descriptive statistics, the mean was the considered measure of central tendency, while the measure of variability was the SEM. The assumption of normality was assessed by frequency distributions (z-score of skewness and kurtosis) as well as by the Kolmogorov-Smirnov and Shapiro-Wilk tests. The assumption of homogeneity of variances was evaluated by Levene's test. All data were analyzed using the two-tailed unpaired Student's t-test for comparisons between the two groups. Comparisons by contingency analysis used the Fisher's exact test and the Baptista-Pike method to calculate the odds-ratio. Graph-Pad Prism 8.00 software was used to create the graphs.

4.3 Results

4.3.1 Transcriptomic profiling of microglia in the pathogenesis of Machado-Joseph disease

To further explore the molecular profile of MJD-associated microglia, and in the attempt to identify potential targets to counteract this disease, a RNA-sequencing analysis was performed on microglia isolated from WT and CMVMJD135 animals at 34 weeks of age. The analysis of the transcriptomic data confirmed that specific markers for microglia were expressed at high levels. In contrast, other cell-type markers were expressed at shallow levels, indicating that the microglial samples from CMVMJD135 and WT mice presented high purity (Figure 4.1a-d), even though a residual expression of some oligodendrocyte-specific genes was found (Figure 4.1e).

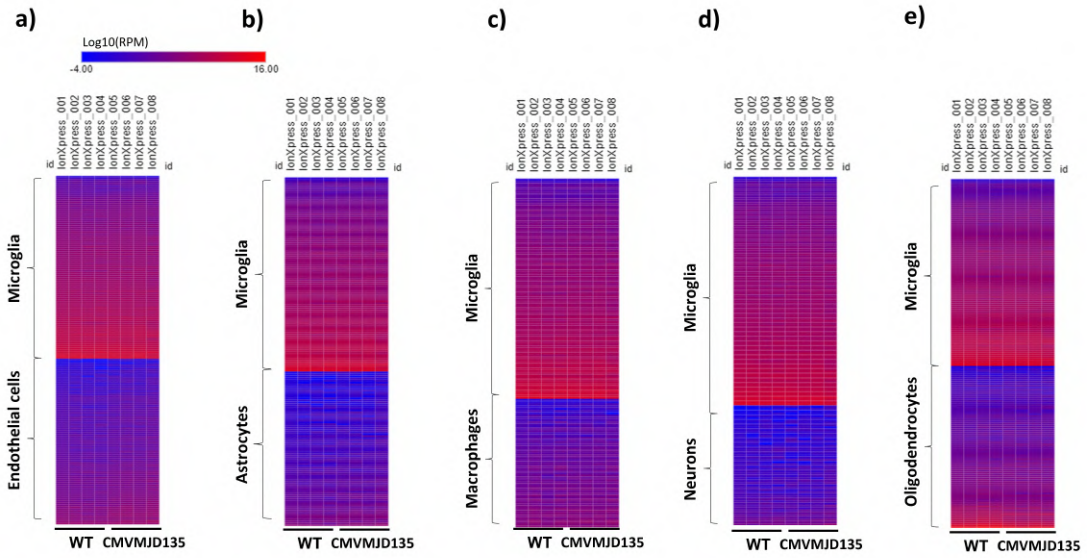

Figure 4.1: **Evaluation of microglial enrichment in RNA-sequencing samples.** Heatmaps showing high levels of expression for specific markers of microglia when compared with markers of other cell types. **a)** Microglia versus endothelial cells; **b)** microglia versus astrocytes; **c)** microglia versus macrophages; **d)** microglia versus neurons; and **e)** microglia versus oligodendrocytes. Four biological replicates for WT and CMVMJD135 mice were used. A heatmap containing the cell-specific markers was generated using the Clue Morpheus software.

The PCA and hierarchical clustering heatmap confirmed that CMVMJD135 and WT mice showed distinct profiles (Figure 4.2a,b), revealing a non-overlapping clustering of samples in each group, with exception of one sample from the WT group, the PCA being able to preserve 68.8 % of the entire information (PC1 = 41.2 %, PC2 = 16.2 %, and PC3 = 11.4 %). This WT outlier, which was overlapping with samples of CMVMJD135 mice instead of WT (Figure 4.2a), was discarded from the analysis to remove overlapping clusters, thus improving the amount of information captured by the PCA, which rose to 73.7 % (PC1 = 44.8 %, PC2 = 16.9 %, and PC3 = 12.0 %). Figure 4.2b depicts the non-overlapping clusters of samples in each group, indicating a distinct profile among genotypes.

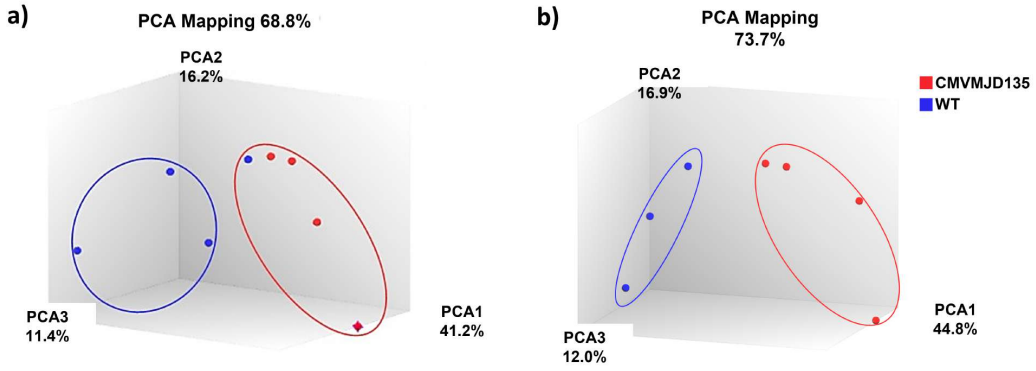

Figure 4.2: **Principal Component Analysis and hierarchical clustering heatmap depicting the distinct profiles between CMVMJD135 and wild-type.** Before the analysis of the Differentially Expressed Genes (DEGs) and of the molecular pathways altered, a principal component analysis (PCA) was conceived to evaluate if CMVMJD135 and WT mice showed distinct profiles. **a)** The PCA sets one WT sample within the vicinity of the CMVMJD135 cluster. WT cluster presents a sparser configuration. **b)** PCA shows a clear separation between CMVMJD135 and WT expression profiles when excluding sample WT1. WT cluster presents a denser configuration. Three biological replicates for WT mice and four biological replicates for CMVMJD135 mice were included in the analysis.

The number of DEGs in microglia from CMVMJD135 mice when compared to WT ones was then determined using the TAC software. A total of 101 DEGs were identified: 83 up-regulated and 18 down-regulated genes. The full list of DEGs is provided in Figure 4.3.

4.3.2 Transcriptional changes seen in CMVMJD135 microglia overlap those in Amyotrophic lateral sclerosis and are symmetric to those seen in Alzheimer's disease mouse models

Next, we compared the list of transcripts found to be differentially expressed in CMVMJD135 mice with 40 different datasets of previously reported DEGs, which include, among others, data on the microglial signature program [249, 352] on other neurodegenerative disorders [151, 175, 203, 273, 315, 353–359], aging [273, 350, 360], DAM [213], and injury-related microglia [273, 350] (Figure B.7 in *Appendix B - Results*). We found a significant overlap with only 3 of the 40 published gene sets, namely with the DEGs seen in microglia of a mouse model of ALS, the $SOD1^{G93A}$ mouse model [203]; of a mouse model of AD, the $App^{NL\text{-}G\text{-}F/NL\text{-}G\text{-}F}$ mouse model [203]; and with a list of microglial genes highly expressed and/or affected in different neuroinflammatory conditions [165] (Figure 4.4a-c).

The $SOD1^{G93A}$ mouse model of ALS shared 27 deregulated genes with CMVMJD135 mice. Of these 27 overlapping genes, 17 displayed a similarly altered gene expression profile: *Lamc1*, *Hipk3*, *Lrrc58*, *Bmpr2*, *Nav1*, *St8sia4*, *Cpd*, *Fmnl2*, *Atp6v0a1*, *Klhl24*, *Cnot1*, *Tmem106b*, *Xpr1*, and *Rnh1*, are up-regulated in both $SOD1^{G93A}$ and CMVMJD135 mice; and *Bend6*, *Ups11*, and *Tbkbp* are down-regulated in both models. However, *Ncam1*, *Arhgef15*, *Abcb1a*, *Alpl*, *Foxf2*, *Caskin2*, *Fbxl12*, *Gpld1*, and *Csad* genes were found to be up-regulated in CMVMJD135 mice but down-regulated in

a)

ID count: 83	Fold Chan...	P-val	FDR P-val	Public Gene IDs	Gene Symbol
Ufl1	1,72	1,63E-06	0,0097	NM_026194	Ufl1
Lrrc58	1,49	3,44E-06	0,0137	NM_177093	Lrrc58
Lamc1	2,5	4,34E-06	0,0149	NM_010683	Lamc1
Cdyl	1,95	8,26E-06	0,0247	NM_001123386	Cdyl
Rnf144b	1,54	1,37E-05	0,0364	NM_001170643	Rnf144b
Ncam1	2	1,55E-05	0,0367	NM_001081445	Ncam1
Ddb1	1,47	1,75E-05	0,0367	NM_015735	Ddb1
Cux2	2,36	1,84E-05	0,0367	NM_001312908	Cux2
A2m	1,97	2,29E-05	0,0391	NM_175628	A2m
Epsti1	1,28	3,46E-05	0,0552	NM_029495	Epsti1
Hipk3	1,71	3,88E-05	0,0581	NM_001145824	Hipk3
Ccdc151	2,36	4,16E-05	0,0581	NM_001163787	Ccdc151
Arhgef12	1,79	4,49E-05	0,0581	NM_027144	Arhgef12
Pcdhb21	2,83	4,77E-05	0,0581	NM_053146	Pcdhb21
Mef2c	1,43	5,24E-05	0,0597	NM_001170537	Mef2c
Mira	1,67	5,88E-05	0,0639	NR_045199	Mira
L3mbtl3	1,98	6,73E-05	0,0686	NM_172787	L3mbtl3
Fam188b	1,62	6,88E-05	0,0686	NM_001142781	Fam188b
Gm6548	2,33	7,64E-05	0,0697	NR_003363	Gm6548
Tmem136	2,02	7,78E-05	0,0697	NM_001034863	Tmem136
4930564C03Rik	1,72	7,86E-05	0,0697	NM_029257	4930564C03Rik
Pcnx3	1,82	0,0001	0,0817	NM_144868	Pcnx3
Scd2	1,74	0,0001	0,0817	NM_009128	Scd2
Haghl	1,48	0,0001	0,0817	NM_001271433	Haghl
Zfp568	2,01	0,0001	0,0850	NM_001033355	Zfp568
Ak8	1,98	0,0001	0,0850	NM_001033874	Ak8
Mpg	1,69	0,0001	0,0850	NM_010822	Mpg
Ap3m2	1,61	0,0001	0,0850	NM_001122820	Ap3m2
Sox8	2,07	0,0001	0,0850	NM_011447	Sox8
Rbbp6	1,56	0,0001	0,0850	NM_011247	Rbbp6
Ptpn4	1,78	0,0001	0,0850	NM_019933	Ptpn4
Nav1	1,9	0,0002	0,0850	NM_173437	Nav1
Abcb1a	2,25	0,0002	0,0850	NM_011076	Abcb1a
Igfbp3	5,15	0,0002	0,0850	NM_008343	Igfbp3
Celsr1	2,81	0,0002	0,0850	NM_009886	Celsr1
Dok7	4,17	0,0002	0,0850	NM_172708	Dok7
Zc3h6	2,97	0,0002	0,0850	NM_178404	Zc3h6
Hydin	2,39	0,0002	0,0850	NM_172916	Hydin
Alpl	2,13	0,0002	0,0850	NM_001287172	Alpl
Abca7	1,7	0,0002	0,0850	NM_013850	Abca7
Syt3	1,48	0,0002	0,0850	NM_001114116	Syt3
St8sia4	1,63	0,0002	0,0850	NM_001159745	St8sia4
Gsk3b	1,59	0,0002	0,0850	NM_019827	Gsk3b
Acsl4	1,41	0,0002	0,0850	NM_001033600	Acsl4
Csad	1,27	0,0002	0,0850	NM_144942	Csad
Tanc1	1,43	0,0002	0,0850	NM_001290659	Tanc1
St5	1,5	0,0002	0,0867	NM_001001326	St5
Tmem106b	1,33	0,0002	0,0867	NM_027992	Tmem106b
Prrc2a	1,76	0,0002	0,0906	NM_001199044	Prrc2a
Klhl24	1,39	0,0002	0,0906	NM_029436	Klhl24
Sh2d5	1,56	0,0002	0,0906	NM_001099631	Sh2d5
Rad54l2	1,57	0,0002	0,0906	NM_030730	Rad54l2
Zfp882	1,26	0,0003	0,0930	NM_001166645	Zfp882
Degs2	2,15	0,0003	0,0930	NM_001171002	Degs2
Vps37c	1,3	0,0003	0,0930	NM_181403	Vps37c
Bmpr2	1,99	0,0003	0,0930	NM_007561	Bmpr2
Arhgap20	1,94	0,0003	0,0930	NM_175535	Arhgap20
Xpr1	1,23	0,0003	0,0930	NM_011273	Xpr1
Caskin2	1,85	0,0003	0,0934	NM_080643	Caskin2
Gpld1	1,55	0,0003	0,0935	NM_008156	Gpld1
Ola1	1,27	0,0003	0,0954	NM_025942	Ola1
Foxf2	2,13	0,0003	0,0961	NM_010225	Foxf2
Cpd	1,62	0,0003	0,0961	NM_007754	Cpd
Cpsf7	1,63	0,0003	0,0961	NM_001164272	Cpsf7
1110004F10Rik	1,56	0,0003	0,0961	NM_019772	1110004F10Rik
Kat6a	1,22	0,0003	0,0961	NM_001081149	Kat6a
Mkl2	3,3	0,0003	0,0961	NM_001122667	Mkl2
Map3k19	1,64	0,0004	0,0995	NM_011737	Map3k19
Tyro3	2,17	0,0004	0,0995	NM_001290800	Tyro3
Fmnl2	1,59	0,0004	0,0995	NM_172409	Fmnl2
Atp2b4	1,72	0,0004	0,0995	NM_001167949	Atp2b4
Junb	1,45	0,0004	0,0995	NM_008416	Junb
Atp6v0a1	1,46	0,0004	0,0995	NM_001243049	Atp6v0a1
Atg101	1,41	0,0004	0,0995	NM_026566	Atg101
Frmd4b	1,36	0,0004	0,0995	NM_145148	Frmd4b
Cnot1	1,34	0,0004	0,0995	NM_001205226	Cnot1
Ahnak	1,97	0,0004	0,0995	NM_001039959	Ahnak
Arhgef15	2,48	0,0004	0,0995	NM_177566	Arhgef15
Ntn1	2,78	0,0004	0,0995	NM_008744	Ntn1
Fos	1,47	0,0004	0,0995	NM_010234	Fos
Rnh1	1,21	0,0004	0,0995	NM_001172100	Rnh1
Fbxl12	1,76	0,0004	0,0995	NM_001002846	Fbxl12
Stard13	2,16	0,0004	0,0995	NM_001163493	Stard13

b)

ID count: 18	Fold Chan...	P-val	FDR P-val	Public Gene IDs	Gene Symbol
4921530L21Rik	-1,09	1,98E-08	0,0002	NM_025733	4921530L21Rik
Cpsf1	-1,09	1,98E-08	0,0002	NM_001164173	Cpsf1
Olfr791	-1,09	1,98E-08	0,0002	NM_146930	Olfr791
Zfp62	-1,98	2,04E-06	0,0097	NM_001024846	Zfp62
Bend6	-1,97	2,16E-05	0,0391	NM_001310484	Bend6
Usp11	-1,28	4,85E-05	0,0581	NM_145628	Usp11
Gm2694	-6,97	9,62E-05	0,0817	NR_033430	Gm2694
LOC108169012	-4,19	0,0001	0,0841	XR_001784563	LOC108169012
Akap7	-3,22	0,0001	0,0850	NM_018747	Akap7
Fbxw4	-1,68	0,0002	0,0850	NM_013907	Fbxw4
Nek9	-1,22	0,0002	0,0850	NM_145138	Nek9
Hoxb8	-1,63	0,0002	0,0906	NM_010461	Hoxb8
Phlpp1	-1,67	0,0003	0,0930	NM_133821	Phlpp1
Plin2	-1,41	0,0003	0,0930	NM_007408	Plin2
Pnpla3	-1,63	0,0003	0,0930	NM_054088	Pnpla3
Rbfox1	-2,21	0,0003	0,0930	NM_021477	Rbfox1
Tasp1	-1,72	0,0003	0,0930	NM_001159640	Tasp1
Tbkbp1	-1,34	0,0003	0,0954	NM_198100	Tbkbp1

c)

Figure 4.3: **Differential gene expression between microglial cells from CMVMJD135 and wild-type mice. a, b, and c)** Up-regulated and down-regulated genes were determined using the Transcriptome Analysis Console (TAC) software, between CMVMJD135 and WT mice. **a)** Heatmap of 83 up-regulated genes in microglial cells from CMVMJD135 mice, in ascending order of false discovery rate (FDR) value. **b)** Heatmap of 18 down-regulated genes in microglial cells from CMVMJD135 mice, in ascending order of FDR value. **c)** Volcano plot view of CMVMJD135 versus WT genes. Red for up-regulated genes and green for down-regulated genes. |fold change| > 1, $p < 0.05$, and a FDR<0.1 was considered to determine genes significantly differentially expressed.

SOD1^{G93A} mice, while the *Plin2* gene was found to be down-regulated in CMVMJD135 mice but up-regulated in SOD1^{G93A} mice (Figure 4.4a).

Most of the genes (19 out of 31 genes) that showed an overlap with the App$^{NL\text{-}G\text{-}F/NL\text{-}G\text{-}F}$ mouse model of AD were discordant regarding their altered gene expression profile. In fact, while that in CMVMJD135 mice the *Cux2*, *Ncam1*, *Arhgef12*, *Mkl2*, *Arhgef15*, *Abcb1a*, *Tyro3*, *Alpl*, *Foxf2*, *Sox8*, *Ahnak*, *Caskin2*, *Scd2*, *Atp2b4*, *Sh2d5*, *Gpld1*, and *Syt3* genes were found to be up-regulated and the *Fbxw4* and *Plin2* genes were down-regulated, in App$^{NL\text{-}G\text{-}F/NL\text{-}G\text{-}F}$ mice the same genes were found to be down-regulated and up-regulated, respectively. Regarding the remaining overlapping genes, some were found to be up-regulated in both App$^{NL\text{-}G\text{-}F/NL\text{-}G\text{-}F}$ and CMVMJD135 mice (*Gm6548*, *Rnf144b*, *Epsti1*, *St8sia4*, *Cpd*, *Fos*, *Junb*, *Acsl4*, and *Klhl24*) while others were found to be down-regulated in

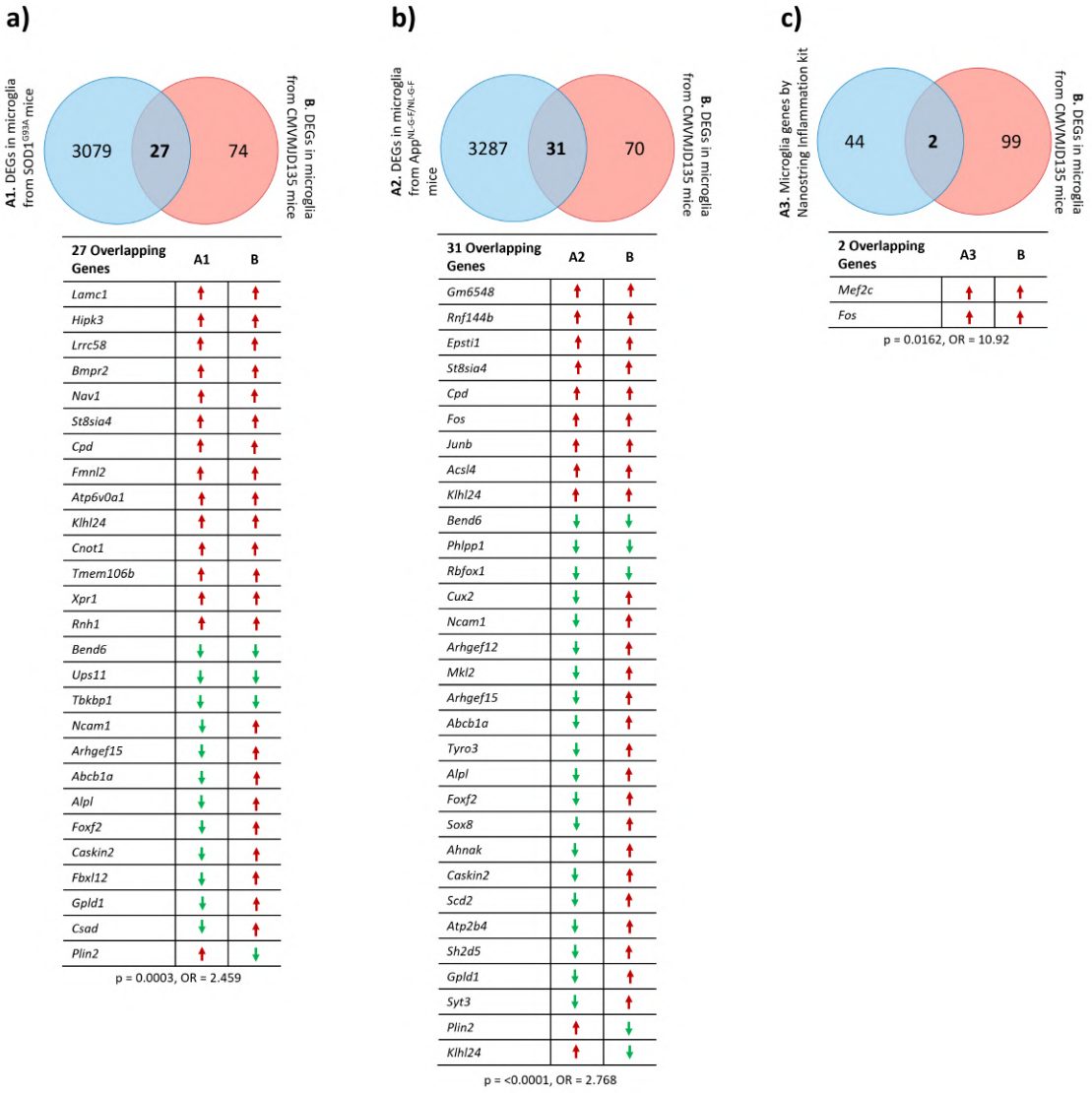

Figure 4.4: **Transcriptional changes seen in CMVMJD135 microglia overlap those in Amyotrophic lateral sclerosis and are symmetric to those seen in Alzheimer's disease mouse models.** Venn diagrams and table overview representing the overlapping genes between the 101 CMVMJD135-altered genes found in our RNA-sequencing analysis, with **a)** 3106 DEGs previously reported in the microglia of a mouse model of Amyotrophic lateral sclerosis (ALS), $SOD1^{G93A}$ mouse [203]; with **b)** 318 DEGs previously reported in the microglia of a mouse model of Alzheimer's disease (AD), $App^{NL\text{-}G\text{-}F/NL\text{-}G\text{-}F}$ mouse [203]; and with **c)** 46 microglial genes highly expressed and/or affected in microglia in different neuroinflammatory conditions, as detected by the Nanostring inflammation kit [165]. Red arrows represent the up-regulated genes and green arrows represent the down-regulated genes. Comparisons were conducted by contingency analysis, using the Fisher's exact test and the Baptista-Pike method to calculate the odds-ratio. Significance was set at $p < 0.05$.

both models (*Bend6*, *Phlpp1*, and *Rbfox1*) (Figure 4.4b). We also found a positive association of two CMVMJD135-altered genes with the cluster of microglial genes highly expressed in neuroinflammatory conditions. In particular, *Mefc2* and *Fos*, two of the up-regulated genes found in CMVMJD135-derived microglia, are implicated in neuroinflammation conditions [165] (Figure 4.4c).

Overall, these results suggest a path of disease with higher similarity to that of ALS, a motor neuron

disease, than with that of AD and other more "neuroinflammatory diseases".

4.3.3 Genes found to be up-regulated in CMVMJD135-derived microglia are associated with immune response, oxidative stress, cell growth, cell proliferation, cell death, and lipid metabolism pathways

An analysis on the involvement of the DEGs found in CMVMJD135-derived microglia in different biological pathways was performed. Interestingly, this analysis revealed eight DEGs associated with cellular processes such as immune response, oxidative stress, cell growth, cell proliferation, and cell death. The pathways found to be significantly altered in microglia from CMVMJD135 mice when compared with WT mice were as follows: oxidative stress (*Junb* and *Fos* (also known as *c-Fos*)); TGF-β Receptor Signaling Pathway (*Fos*, *Junb*, and *Mef2c*); TNF-α NF-kβ Signaling Pathway (*Gsk3β*, *Usp11*, and *Alpl*); Role of NFAT in Regulation of the Immune Response (*Fos*, *Gsk3β*, and *Mef2c*); the Novel Jun-Dmp1 Pathway (*Junb* and *Fos*); FAT10 Cancer Signaling Pathway (*Bmpr2* and *Gsk3β*); ERK5 Signaling (*Fos* and *Mef2c*); Wnt/β-catenin Signaling (*Bmpr2*, *Gsk3β*, and *Sox8*); and Delta-Notch Signaling Pathway (*Gsk3β* and *Mef2c*). All the indicated genes showed an increased expression in microglia from CMVMJD135 mice, except for *Usp11*, which showed a decreased expression (Figure 4.5a).

Interestingly, the altered gene expression also suggested changes in microglial lipid metabolism. These include the Omega-9 FA synthesis pathway, Cholesterol metabolism (includes both Bloch and Kandutsch-Russell pathways), and PPAR signaling pathway. The *Acsl4* and *Scd2* DEGs were found to be involved in these lipid metabolism pathways (Figure 4.5b). It was also found that the expression of genes related to oxidative stress, particularly the synthesis of NO, was increased in CMVMJD135 mice, as seen by the up-regulation of *Gsk3β*, *Junb*, *Cpd*, *Igfbp3*, and *Ntn1*.

The RNA-sequencing results were further validated through qPCR. Five DEGs, *Fos*, *Junb*, *Bmpr2*, *Hipsk3*, and *Epsti1*, were validated with acceptable cycle threshold (CT) values. While no statistically significant differences were found in the expression of *Junb* and *Epsti1*, the results were similar to those obtained by RNA-sequencing, with an increase in the expression of *Fos* ($p = 0.019$), *Bmpr2* ($p = 0.006$), and *Hipsk3* ($p = 0.003$) in microglia from CMVMJD135 mice (Figure 4.5c).

4.4 Discussion

To define the cellular and molecular profile of MJD-associated microglia, which, currently, is largely unknown, RNA-sequencing analysis was performed on microglia isolated from the cerebellum and brainstem (as a whole), of WT and CMVMJD135 animals, and allowed us to identify significantly altered genes and molecular pathways in CMVMJD135 mice. From the 101 DEGs found in CMVMJD135-derived microglia, eight (*Junb*, *Fos*, *Bmpr2*, *Gsk3β*, *Mef2c*, *Usp11*, *Alpl*, and *Sox8*) were found to be overlapping several significantly altered pathways related to the immune response, oxidative stress, cell growth, cell

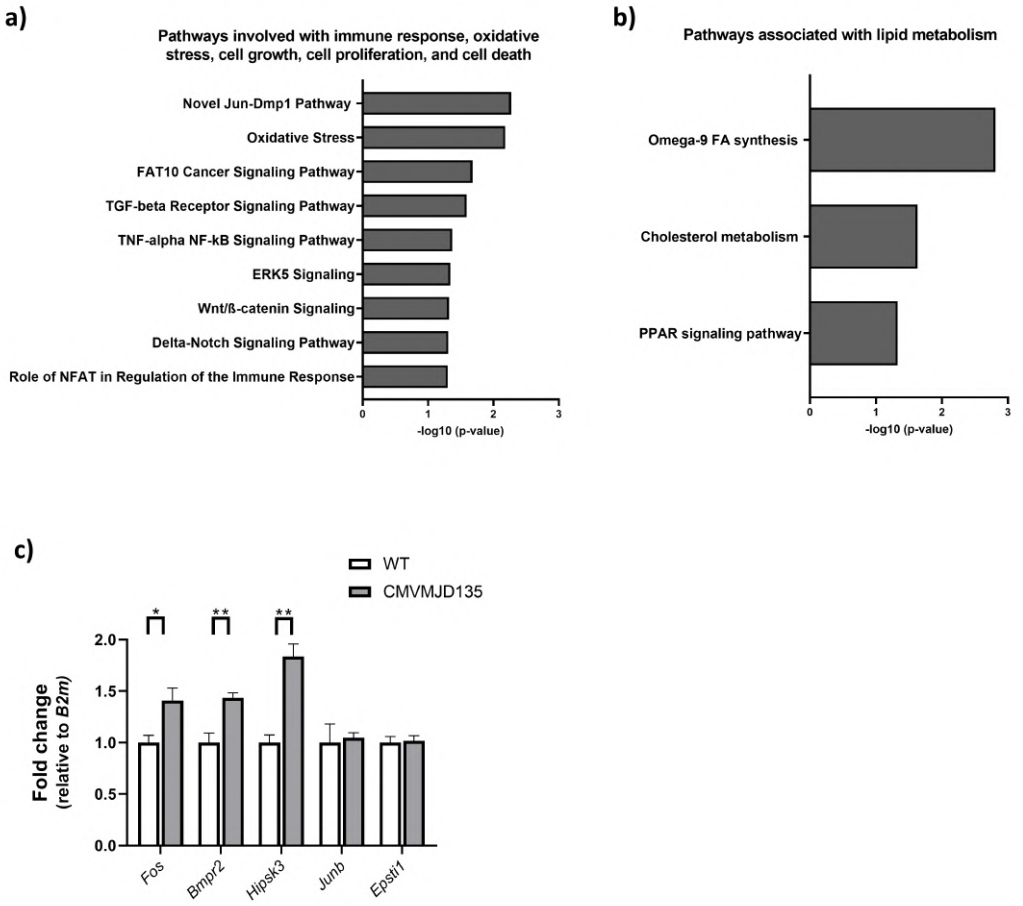

Figure 4.5: **Genes found to be up-regulated in CMVMJD135-derived microglia are associated with immune response, oxidative stress, cell growth, cell proliferation, cell death, and lipid metabolism pathways.** Pathways significantly altered were found in microglia from CMVMJD135 mice compared with WT mice. **a)** Pathways associated with immune response, oxidative stress, cell growth, cell proliferation, and cell death and **b)** pathways associated with lipid metabolism. All pathways are presented in descending order of significance based on p value. **c)** Expression analysis performed on the selected genes confirmed the results obtained from RNA-sequencing analysis of microglia. An increase in the expression of *Fos*, *Bmpr2*, and *Hipsk3* genes was confirmed by an orthogonal method (qRT-PCR) in microglia from CMVMJD135 mice. $n = 3$-4 per group and two technical replicates were performed. Fold change ($2^{-\Delta\Delta CT}$) is represented using *B2m* as a housekeeping gene. Data are presented as mean+SEM (Student's t-test). *, **, represent $p < 0.05$ and $p < 0.01$, respectively.

proliferation, and cell death. Other cellular pathways were also found to be altered, namely some associated with the lipid metabolism.

The relevance of several of these individual DEGs in microglia and/or neurological conditions has been demonstrated in the literature. In a mouse model of ALS, microglial transcriptional factor *c-Fos* was found to be significantly down-regulated. This alteration is associated with restoring the abnormal microglial phenotype and attenuation of the disease [361]. While some studies show that *c-Fos* suppresses the expression of pro-inflammatory phenotype-associated genes, such as inducible NO synthase (*iNOS*) [362], tumor necrosis factor alpha (*Tnf*α), and *Il-6* through the suppression of NF-kβ activity [363], suggesting that it acts as an anti-inflammatory transcription factor essential for microglia survival [361, 363],

other studies show that blockade of c-Fos with dexmedetomidine halts microglia inflammation and inhibits postoperative cognitive dysfunction in AD patients, thus setting c-Fos as a potential anti-inflammatory therapeutic target for NDs [364]. Additionally, it was also demonstrated that monocytes incubated with fibrillar amyloid β or amylin displayed an elevated expression of *c-Fos* and *Junb*, and of pro-inflammatory cytokines [365]. Regarding the *Gsk3*β, its activation has been associated with increased neuroinflammation and microglial activation. In fact, some studies have demonstrated that Gsk3β promotes microglial responses to inflammation, and that the use of Gsk3β inhibitors such as lithium, SB216763, kenpaullone, and indirubin-3'-monoxime, provides a mean to limit the inflammatory actions of microglia and provides protection from inflammation-induced neuronal toxicity [366]. Another study reinforces Gsk3β-mediated neuroinflammation, partially by enhancing nuclear factor kappa b subunit 1 (Nfkb1) signaling, where the inhibition of Gsk3β with the SB216763 inhibitor reduces Nfkb1 signaling and inflammation levels, in a mouse model of Rett syndrome [367]. The expression of the *BMPR2* gene by microglia is scarcely referred in the literature, being found to be increased in active multiple sclerosis lesions, suggesting a possible role for this gene in MS pathogenesis [368]. Regarding the *Alpl* gene encoding the Alkaline phosphatase, tissue-nonspecific isozyme protein, known to have a role in brain development and function [369], it has been demonstrated that its activity is increased in both brain and plasma of AD patients, inducing neuronal toxicity via tau dephosphorylation [370, 371]. On the other hand, the transcription factor *Mef2c* has been reported to be expressed in both mouse and human microglia, being known to be involved in microglial specification [174, 372]. Recently, a study demonstrated that a decreased function of Mef2c is associated with a possible microglial activation that is sufficient to induce autism-like symptoms in mice [373]. Additionally, it was shown that Mef2c normally restrains microglial inflammatory response, and its expression is lost in aged brains in a type I interferon (IFN-I)-dependent manner [374]. These facts demonstrate that the activity of Mef2c becomes critical under pathological conditions and with aging, when the levels of inflammatory cytokines are increased. The *Usp11* gene, on the other hand, was demonstrated to regulate microglial activation and neuroinflammation in intracerebral hemorrhage (ICH). Thus, silencing *Usp11* was put forward as a novel anti-inflammatory method for ICH treatment since it blocks the release of pro-inflammatory cytokines by microglia, leading to protection from neurological impairment [375]. Hence, the decreased expression of *Usp11* in the brain of MJD mice could indicate a similar adaptive and protective response.

The role of lipid metabolism in the polarization of microglial inflammatory status has recently been explored and may highlight novel approaches that modulate metabolism to ameliorate neuroinflammation and NDs [304, 307, 308, 376]. In fact, regarding the specific MJD DEGs here identified and known to be involved in the lipid metabolism, *Acsl4* was found to be a novel regulator of neuroinflammation in ischemic stroke, and the knockdown of *Acsl4* expression was proposed to provide a potential therapeutic target through the inhibition of pro-inflammatory cytokine production in microglia [377]. Meanwhile, the *Scd2* gene was found to be down-regulated upon activation of microglia induced by LPS [378].

The expression of genes related to synthesis of NO was found to be increased in microglia from

CMVMJD135 mice, namely of *Gsk3β*, *Junb*, *Cpd*, *Igfbp3*, and *Ntn1*. This pathway is known to be implicated in the pathogenesis of NDs, in which elevated NO provokes either neuroinflammation or apoptosis in microglia [379]. As mentioned above, Gsk3β and Junb have been associated with increased neuroinflammation and microglial activation [365–367]. However, an increase of *Igfbp3* expression was seen in an ischemic injury mouse model to lead to increased microglial apoptosis and to a reduction of activated microglia. These findings imply that *Igfbp3* can act as an anti-inflammatory factor [380]. In addition, Ntn1 was put forward as a novel therapeutic agent to ameliorate early brain injury via its anti-inflammation effect, by suppression of microglia activation, peroxisome proliferator-activated receptor (PPARγ) activation, inhibition of factor nuclear kappa β (NF-kβ), and decrease of Tnfα, Il-6, and Icam-1 [381].

Interestingly, we also found multiple deregulated genes that are common in both CMVMJD135-derived microglia and microglia of the neurodegenerative mouse models of ALS and AD. However, while some of them displayed a similarly altered gene expression profile, others were discordant. To the best of our knowledge, apart from nine genes (*Atp6v0a1*, *Tmem106b*, *Bmpr2*, *Ups11*, *Fos*, *Junb*, *Acsl4*, *Tyro3*, and *Scd2*), the overlapping of the remaining forty-nine genes with datasets of DEGs from neurodegenerative mouse models of ALS and AD, is here reported for the first time. From the nine genes identified above, only three remain to be described (*Atp6v0a1*, *Tmem106b*, and *Tyro3*). Regarding the *Atp6v0a1* gene, it was found that the attenuation of the human microglial inflammation and suppression of the expression *IL-1 beta* and *IL-6* by the increase of *ATP6V0A1* expression with rifampicin, improved the lysosomal function, which may be a novel therapeutic strategy for PD [382]. The *TMEM106B* gene was found to be involved in the pathological processes of AD, whose expression is reduced in AD brains [383]. On the other hand, it was demonstrated that the TAM (Tyro3, Axl, Mer) family of receptor tyrosine kinases limit inflammatory responses upon Toll-like receptors stimulation in microglia, with a positive impact on AD progression [384]. Another study reported that the loss of TAM receptors affects adult brain neurogenesis, which was attributed to exaggerated inflammatory responses by microglia characterized by increased Mitogen Activated Protein Kinases (MAPK) and NF-kβ activation, as well as to an increased production of pro-inflammatory cytokines [385].

As described above, we found genes (such as the *Fos*, *Junb*, *Gsk3β*, *Acsl4*, and *Bmpr2*) that, when up-regulated promote pro-inflammatory microglial responses. The use of inhibitors of these genes and the protein they encode may provide a mean to offer protection from inflammation-induced neuronal toxicity, i.e., these genes could be potential targets to counteract MJD. However, we also found genes (such as the *Mefc2*, *Scd2*, *Igfbp3*, *Ntn1*, *Usp11*, *Atp6v0a1*, and *Tyro3*) that promote the inhibition of inflammation in microglia through the inhibition of pro-inflammatory cytokine production, which could correspond to an endogenous neuroprotective response and explain the decrease in expression of genes encoding pro-inflammatory cytokines, such as *Il-6*, *Il-1 alpha*, *Il-1 beta*, and *Icam-1* in CMVMJD135 mice. Overall, the profile of MJD microglia is mixed, regarding pro- and anti-inflammatory molecule expression, and the overlapping results suggest a higher similarity of MJD with ALS than AD, which is not unexpected given the shared involvement of motor systems in these two disorders.

In summay, the results obtained from the transcriptional profile analysis of MJD-associated microglia

provided the identification of genes and molecular pathways that might represent potential targets for the treatment of this disorder, and suggest that, among others, lipid metabolism should be further investigated in these cells.

Chapter 5

Microglial depletion has no impact on disease progression in a mouse model of Machado-Joseph disease

5.1 Introduction

MJD, also known as SCA3, represents the most common dominantly inherited ataxia and the second most common polyglutamine disease (polyQ) [6] worldwide. This neurodegenerative disease is caused by an expansion of a CAG repeat tract in exon 10 of the Ataxin-3 (*ATXN3*) gene located in chromosome 14q32.1, which encodes an abnormally long polyglutamine (polyQ) segment in the ATXN3 protein, making it prone to self-assembly, and to form aggregates that are toxic to neurons [12, 14, 53]. While in healthy individuals this CAG repeat tract ranges from 12 to 44 units, in the affected patients the CAG repeat ranges from 56 to 87, the age of symptom onset being inversely correlated with repeat length [18]. MJD symptoms reflect the involvement of multiple neurological systems, including a wide range of progressive motor impairments such as cerebellar ataxia with abnormal gait, loss of limb coordination, impaired balance, dystonia, dysarthria, dysphagia, spasticity, and oculomotor abnormalities [7, 31]. Post-mortem analysis of MJD patients' brains reveals that the progressive motor impairment results from neuronal dysfunction and neuronal cell loss in several regions of the CNS, such as in the DCN, in the cerebellum, in the PN, in the brainstem, and in spinocerebellar tracts, although in some patients, the involvement of the peripheral nerves may also be present [34]. Although most research in polyQ disorders has been following a neuron-centric point of view, due to the neuronal degeneration, microglial cells are now recognized as vital components of the CNS that contribute to neuronal health [10].

Microglial cells are resident macrophages of myeloid origin in the CNS, being considered the first line of defense within the brain and the major orchestrators of the brain inflammatory response [141, 142, 173]. Their morphology is one of its more outstanding characteristics and can change upon different situations of brain disease and pathology, including enlargement of cell bodies and thickening of their processes [183, 242]. In some neurological pathologies, microglial cells can play either a toxic or a protective role because the extent of microglial activation and, thus, their contribution to pathogenesis depends on the type and duration of injury [149, 183, 331]. Indeed, while some studies report chronically activated microglia to be harmful and worsen the disease outcome in HD [150, 151], PD [386], AD [387], and ALS [388], other studies suggest that activated microglia may be beneficial in these diseases [389–392].

Recent studies suggested that microglia might also play a role in the MJD pathogenesis. In fact, reactive microgliosis was observed in MJD patients' brains [10, 143, 144] and in a mouse model of MJD [145]. Additionally, morphological alterations that point to an increased activation state, as well as molecular perturbations related with oxidative stress, immune response, and lipid metabolism were seen significantly altered in microglial cells derived from CMVMJD135 mice [393], an MJD mouse model that replicates motor symptoms and neuropathology of the human condition [88]. Although the onset of the symptoms occurs very early in this mouse model, the onset of the neuropathological features occurs later in life [88, 322]. Because most brain cells express *ATXN3*, microglial dysfunction may contribute to the disease

process due to the effects of mutant *ATXN3* in microglia or as a consequence of their interaction with neurons. However, it is yet unknown whether, and how, microglia contribute to disease onset and progression in MJD. A strategy widely used to clarify these important questions in NDs has been the depletion of microglial cells in the brains of animal models, through pharmacological inhibition of CSF1R signalling, which is essential for microglial survival and maintenance [149, 222, 315, 316, 394].

PLX3397, an orally bioavailable selective CSF1R inhibitor that crosses the blood-brain barrier [395], has been shown to cause microglial depletion within several days of administration [223, 314, 315, 396, 397], albeit to different extents in different studies. While depletion efficiency varies, full microglial ablation has never been reported [396–402]. In fact, it is known that a small subset of microglia in adult mouse brains can survive without CSF1R signaling [169].

In this study, we addressed the contribution of microglial cells to MJD pathogenesis through the administration of PLX3397 to the CMVMJD135 mouse model at an mid-stage of disease and evaluated the impact of microglial depletion on the motor phenotype of this mouse model.

5.2 Materials and Methods

5.2.1 Transgenic mouse model and administration of PLX3397

Male mice on a C57BL/6J background were considered and the transgenic mouse model used in this work was the CMVMJD135 mouse model. The mean CAG repeat size [±SD] for all CMVMJD135 mice used in this study was of 138.2 ± 4.4). Age-matched WT littermate animals were used as controls. Animals (CMVMJD135 and WT, PLX3397- and vehicle treated) were housed at weaning in groups of five animals, in filter-topped polysulfone cages 267 × 207 × 140 mm (370 cm^2 floor area) (Tecniplast, Buguggiate, Italy), with corncob bedding (Scobis Due, Mucedola SRL, Settimo Milanese, Italy), in a conventional animal facility.

A total of 81 animals (all littermates) were used in this study. Groups of 4-5 animals per genotype/treatment were used for microglia density and morphological analysis as shown in Figure 5.1a, and groups of 14-18 animals were used per genotype/treatment for behavioral tests (Figure 5.1b). The treatment with PLX3397 (MedChemExpress, Sollentuna, Sweden) was initiated at a mid-stage of the disease (18 weeks of age) and ended at 21 weeks of age. PLX3397 was delivered to CMVMJD135 ($n = 18$ mice) and WT ($n = 15$ mice) littermates every day via oral gavage at a dose of 40 mg/kg for 3 weeks and dissolved in 5 % dimethyl sulfoxide (DMSO) and 25 % PEG300 in ddH2O as previously described by Merry et al. (2020) [403]. Control littermate animals (CMVMJD135 ($n = 16$ mice) and WT ($n = 14$ mice)) were given vehicle (5 % DMSO and 25 % PEG300 in ddH2O), with the same frequency [403].

5.2.2 Immunofluorescence staining

Four experimental groups were considered for microglial cell staining: CMVMJD135 PLX3397- and vehicle treated animals (CMVMJD135 + PLX3397 ($n = 3 - 4$ mice) and CMVMJD135 + vehicle ($n = 4$ mice)),

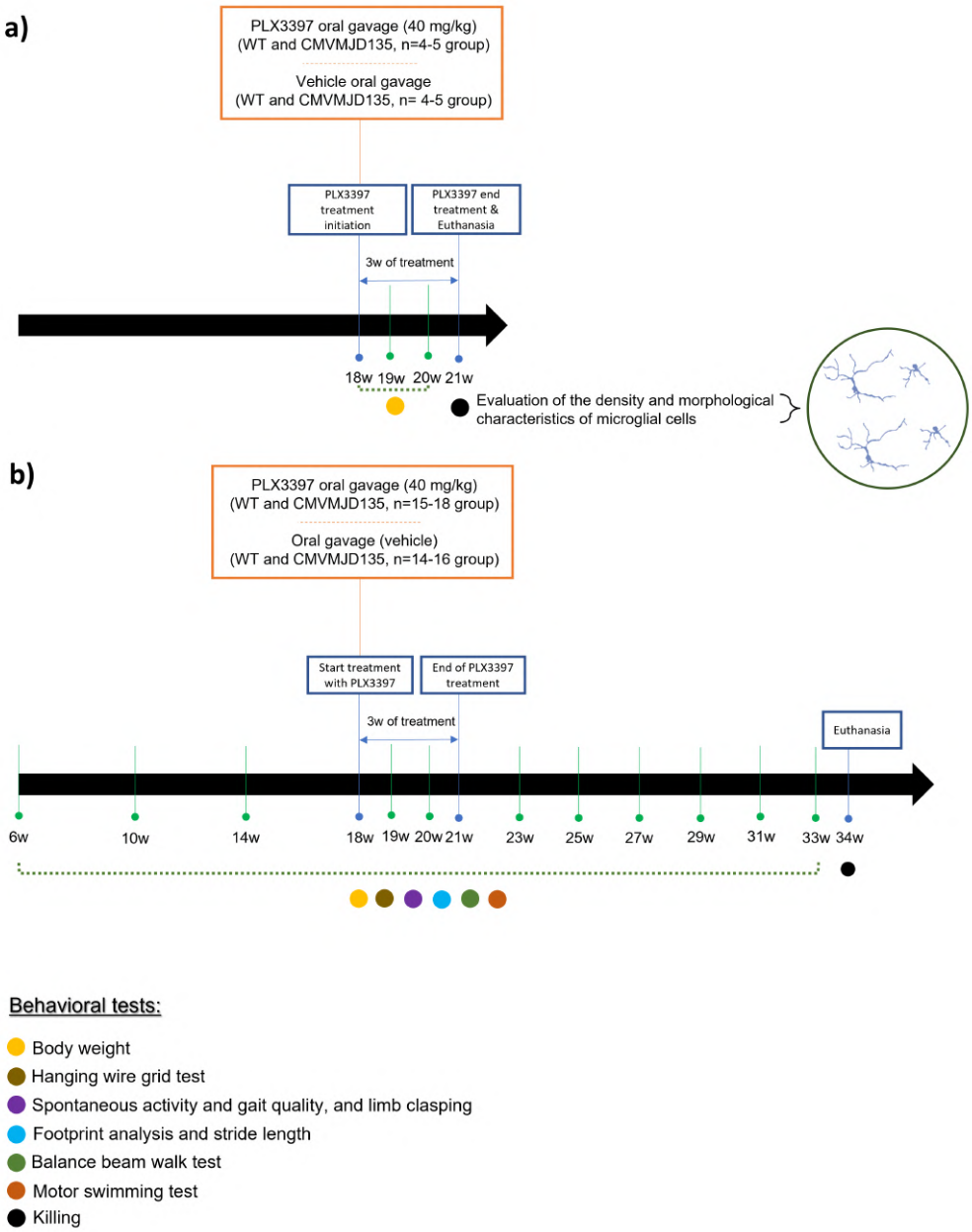

Figure 5.1: **Schematic representation of the experimental design.** The administration of PLX3397 was delivered to CMVMJD135 and WT mice every day by oral gavage at a dose of 40 mg/kg dissolved in 5 % dimethyl sulfoxide (DMSO) and 25 % PEG300 in ddH2O, from 18 to 21 weeks of age. Control animals (CMVMJD135 and WT) were given vehicle (5 % (DMSO) and 25 % PEG300 in ddH2O) with the same frequency and route of administration.Three weeks after treatment, groups of **a)** 4-5 animals per genotype-/treatment were submitted to evaluation of density and morphological characteristics of microglial cells; and of **b)** 14-18 animals per genotype/treatment were used for behavioral analyze, that were performed from week 6 to week 33 of age.

and WT PLX3397- and vehicle treated animals (WT + PLX3397 ($n = 5$ mice) and WT + vehicle ($n = 5$ mice)). All animals were deeply anesthetized with a mixture of ketamine hydrochloride (150 mg/kg) and medetomidine (0.3 mg/kg), and transcardially perfused with PBS followed by 4 % PFA solution (0.1 M PFA, pH 7.4, in PBS). Brains were removed and immersed in 4 % PFA (48 h, in agitation), followed by 1

week in a 30 % sucrose PBS buffer (at 4 °C). Sagittal sections were obtained using a vibratome (VT1000S, Leica, Germany) with 40 μm of thickness, followed by the permeabilization, in the free-floating sections, with 0.3 % PBS-T (0.3 % triton X-100, Sigma Aldrich, in PBS) for 10 min. Then, antigen retrieval was performed by immersing the slices in a pre-heated citrate buffer (10 mM, pH 6.0; Sigma Aldrich) during 20 min using a thermoblock (D1200, LabNet) set at 80 °C. Once cooled, slices were blocked with goat serum blocking buffer (10 % NGS, 0.3 % triton X-100, in PBS) at RT for 90 min. After this, the sections were incubated with the primary antibody anti-Iba-1 (rabbit polyclonal IgG anti-Iba-1, 1:600; Wako; Figure A.1 in *Appendix 1 - Materials and Methods*) overnight at 4 °C. In the next day, sections were incubated with a secondary antibody (Alexa Fluor 594 goat anti-rabbit, 1:1000; ThermoFisher Scientific; Figure A.1 in *Appendix 1 - Materials and Methods*) during 90 min at RT, protected from light, followed by 4',6-Diamidin-2-phenylindol (DAPI, 1:1000; Invitrogen) for nuclei staining. Afterwards, on microscope slides (Menzel-Glaser Superfrost©Plus, Thermo Fisher Scientific), the sections were mounted and covered with a coverslip (Menzel-Glaser 24–60 mm, Wagner und Munz) using aqueous mounting medium (Fluoromount TM, Sigma-Aldrich).

5.2.3 Image acquisition for evaluation of density and morphological characteristics of microglial cells

For microglial density analysis, mosaic imaging was acquired by stitching of several images taken in a 3-dimensional plane (X, Y, and Z axis) using Olympus Confocal FV3000 laser scanning microscope with a resolution of 1024 × 1024 px and a 20× objective, for each region of interest (DCN and lobules, in the cerebellum, and PN, in the brainstem). Each image of the mosaic imaging consisted of 40-μm Z-stacks, composed of 5 μm thick image slices. 3-5 sagittal brain sections per animal were used ($n = 3 - 5$ animals per group) and one mosaic imaging per section of region of interest was taken. The total count of Iba-1-positive cells was obtained using the multi-point tool of ImageJ software (v1.53c; National Institute of Health, Bethesda, MD, USA) on Z-stacked 3D volume mosaic from sections of the affected brain regions (DCN, lobules, and PN). Quantification was performed on mosaic images acquired with acquisition settings described as above, normalized first to the total mosaic area and then for volume (40 μm thickness).

For the morphological analysis of microglial cells, four sagittal brain sections per animal were used ($n = 4 - 5$ animals per group) and 2 photomicrographs per section were taken in each region of interest (DCN and PN). The Olympus Confocal FV1000 laser scanning microscope with a resolution of 1024 × 1024 px and a 40× objective was used to obtain all 40-μm Z-stacked images composed of 0.31 μm thick image slices, which include two distinct channels (red, Iba-1; blue, DAPI). Using ImageJ software on Z-stacked 3D volume images from sections of the affected brain regions, a morphological analysis was performed based on a semi-automatic method adapted from [338]. Several steps were followed to apply commands and options to obtain binary images (white cells on black background), which are required to obtain fractal and skeleton data. Briefly, the double-color image was split to obtain the Iba-1 label in the red channel, whose brightness and contrast were adjusted. Then, the despeckle filter was used to remove salt

and pepper noise. To convert the image into binary format, the threshold option was used and adjusted, as needed. Noise was subsequently eliminated using despeckle and by removing outliers. After that, at least 5 cells from both the original and the binary images were selected with the rectangle tool, using the ROI to set the same rectangle dimensions for all the selected cells. Afterwards, the single-cell images without any noise were obtained by using the paintbrush tool. This tool allowed us to complete and draw the morphology of the selected cells and to clean extra signal that is not related to these cells. Then, each binary single-cell was converted into an outlined and skeletonized format, to carry out a fractal or skeleton analysis, respectively (Figure A.3 in *Appendix 1 - Materials and Methods*).

Features relevant to microglia ramification were obtained by the application of the *AnalyzeSkeleton 2D/3D* plugin (developed by and maintained at https://imagej.net/plugins/analyze-skeleton) over each binary single-cell. These skeletal features include the number of endpoints voxels, number of junctions voxels, number of junctions, number of slab voxels, number of branches, number of triple points, number of quadruple points, Euclidean distance, total branch length, average branch length, and maximum branch length (Figure A.4 in *Appendix 1 - Materials and Methods*).

A fractal analysis was performed using the *FracLac* plugin (Karperien A., FracLac for ImageJ, available at https://imagej.nih.gov/ij/plugins/fraclac/FLHelp/Introduction.htm) to evaluate characteristics associated with cell surface (cell perimeter and roughness), soma thickness (cell circularity and density), cell size (mean radius, convex hull perimeter, convex hull circularity, bounding circle diameter, maximum span convex hull, convex hull area, and cell area), the cylindrical shape of cells (convex hull span ratio and the ratio of convex hull radii), the complexity of their ramifications (fractal dimension - D), and the heterogeneity of their shape (lacunarity - Λ) (Figure A.5 in *Appendix 1 - Materials and Methods*).

5.2.4 MorphData plugin for morphological data acquisition and pre-processing

The *MorphData* plugin (available at https://github.com/anabelacampos/MorphData) was used to automatize the data extraction process of morphological features of single microglial cells [339]. Data were obtained from single-cells of the DCN (number of microglial cells: 263 from CMVMJD135 + PLX3397 mice, 256 from CMVMJD135 + vehicle mice, 475 from WT + PLX3397 mice, and 387 from WT + vehicle mice) and of the PN (number of microglial cells: 235 from CMVMJD135 + PLX3397 mice, 217 from CMVMJD135 + vehicle mice, 248 from WT + PLX3397 mice, and 210 from WT + vehicle mice). The total number of microglial cells used was of 1381 for the DCN, and 910 for the PN.

5.2.5 Machine Learning modeling

KNIME, a data-flow centric and ML platform, was used to process the obtained data and to identify potential clustering of microglial cells concerning their morphological features. This platform integrates several modules responsible for processes such as data loading, data transformation, and the application of statistical and ML models. Using the KNIME platform, one workflow was conceived for each region of interest

(DCN and PN). The workflows are similar, except for the used data. In fact, these are used to conceive and apply a PCA on the used data as well as to apply an unsupervised ML model, the k-means, which is a clustering method that is able to cluster data points with similar characteristics. The k-means partitions the dataset into k clusters, with each observation belonging to a single cluster, i.e., each observation belongs to the nearer cluster, represented by its centroid. On the other hand, the elbow method was used to find the ideal number of clusters, experimenting and plotting the MSE associated to each cluster, with k varying between 1 to 6. The ideal k is found by picking the "elbow" of the curve as a function that minimizes the error.

5.2.6 Behavioral analysis

CMVMJD135 mice and WT littermates treated with PLX3397 ($n = 15 - 18$ animals per group) or with vehicle ($n = 14 - 16$ animals per group) were used for behavioral assessment (Figure 5.1b). All behavioral tests were performed during the diurnal period. Before PLX3397 treatment, animals were tested in several motor behavioral paradigms monthly (at 6, 10, and 14 weeks of age) to make the animals get used to the tests and acquire the learning curve, and following PLX3397 administration, the behavioral assessment was conducted every two weeks until 33 weeks of age, that corresponds to an advanced disease stage, when the phenotype is fully established (Figure 5.1b). At endpoint, at 34 weeks of age, animals were euthanized accordingly. These neurological/motor tests included (1) a general health and neurological assessment using a selection of tests from the SHIRPA protocol, namely assessment of body weight, strength to grab, spontaneous activity and gait quality, and limb clasping [404, 405]; (2) footprinting analysis and stride length measurement; (3) balance beam walk (12-mm square, and 11-mm and 17-mm round beams); and (4) motor swimming tests. All behavioral tests used in this study were performed as previously described [88, 89, 319] and are briefly described below.

5.2.6.1 SHIRPA Protocol

A protocol for phenotypic assessment based on the primary screen of SHIRPA protocol was established in this study. This protocol mimics the diagnostic process of general neurological and psychiatric examination in humans [404]. A detailed description of the SHIRPA protocol is available online at https://www.mousephenotype.org/impress/protocol/82. A brief description of the tests follows below.

Body weight All mice were weighed throughout the study from 6 weeks of age until the end of the trial (33 weeks of age).

Hanging wire grid test Each animal was placed on the top of a metallic horizontal grid, which was slowly inverted and suspended at approximately 30 cm to the floor. The time it took each mouse to fall from the cage top was recorded. After 120 seconds (the maximum time of the test), any animal still gripping the cage top was removed.

Spontaneous activity and gait quality Mice were transferred to a 15-labelled-squares open arena (55×33×18 cm), and the number of squares travelled for 1 minute was counted. The gait quality was also assessed by the same researcher, where freely moving animals were scored as: normal, fluid but abnormal movement (incorrect posture of the body and tail, with decreased distance over the ground), limited (very limited movement), and unable to walk.

Limb clasping To determine limb clasping, mice were picked by the tail and slowly descended towards a horizontal surface. The extension/contraction of the limbs was observed by the researcher and scored as absent (extension of the hindlimbs), mild (contraction in one of the hindlimbs), or severe (contraction in both hindlimbs).

5.2.6.2 Footprint analysis and stride length quantification

The footprint test was used to evaluate motor performance. To register footprint patterns of each mouse, the hind- and forepaws were coated with black or red non-toxic ink, respectively. A clean paper sheet was placed on the floor of the runway for each mouse run, and then the animals were encouraged to walk along a 100 cm long×4.2 cm width×10 cm height inclined runway in the direction of an enclosed safe black box. Since animals tend to run upwards to escape, an inclined runway was used, instead of a horizontal one. The stride length was obtained by measuring manually the distance between two pawprints. Three values were measured for six consecutive steps and the mean of the three values was used. To evaluate severity of footdragging, the same six consecutive steps were used, and the dragging was scored as absent = 0, mild = 1 (up to three steps), and severe = 2 (more than three steps out of six).

5.2.6.3 Balance beam walk test

This test was performed as previously described [406] and assesses the ability of the animals to stay upright and to walk on an elevated beam (50 cm above the bench surface) without falling to sponges that are used to protect mice from falls. The beams (12-mm square, and 11-mm and 17-mm round beams) were placed horizontally with one end mounted on narrow support and the other end attached to an enclosed dark box, into which the mouse could escape. Mice were trained for 3 days (three trials per animal) in the square beam (12 mm), and in the fourth day, they were tested in the 12-mm square, and in the 11-mm and 17-mm round beams (two trials per animal were scored). The time each animal took to traverse the beams was scored and time was discounted whenever the animals stopped in the beam. The trial was considered invalid if the animal fell or turned around in the beam. Each animal was given the opportunity to fail twice.

5.2.6.4 Motor swimming test

To analyze voluntary locomotion in the water environment, each mouse was trained for two consecutive days (three trials per mouse) to traverse a clear perspex water tank (100 cm long) to a safe (black perspex-made) platform at the end, with the water temperature being monitored at 23 °C using a thermostat. Animals were tested for three consecutive days (two trials per mouse), and the latency to cross the tank was registered by the researcher from a 60 cm distance (the initiation position was marked with a blue line) [406].

5.2.7 Statistical Analysis

Mouse sample size was previously calculated, using the G-Power 3.1.9.2 software (University of Kiel, Germany), assuming a power of 0.95 and 0.8, for each behavioral test and histopathological analyses, respectively [319]. All statistical analyses were performed using SPSS 22.0 (SPSS Inc., Chicago, IL, USA), and a significance level of $p < 0.05$ was used throughout this study. The assumption of normality was tested for all continuous variables through evaluation of the qualitative analysis of Q-Q plots and of the frequency distributions (z-score of skewness and kurtosis) as well as by the Kolmogorov-Smirnov and Shapiro-Wilk tests. Continuous variables with normal distributions were analysed with repeated-measures ANOVA for longitudinal multiple comparisons, using genotype and treatment as factors. The one-way analysis of variance (ANOVA), followed by Tukey HSD test, was used when data passed on the assumption of homogeneity of variances (evaluated by Levene's test). However, Dunnett T3's test was applied instead of the Tukey HSD test when the populations variances were not equal. Concerning non-normally distributed data and/or for the comparison of medians of discrete variables across time-points, a Friedman's ANOVA was carried out, with pairwise comparisons through the Kruskal-Wallis statistic test. GraphPad Prism 8 was used to create graphs, the mean being the considered measure of central tendency, while the measure of variability was the SEM.

5.3 Results

5.3.1 PLX3397 treatment promoted a partial reduction of microglial cells in CMVMJD135 mice

To further understand the role of microglia in MJD, we applied a protocol to deplete microglia in the CMVMJD135 mice at a mid-stage of disease using PLX3397, an inhibitor of CSF1R signaling. Beginning at 18 weeks of age, the CSF1R inhibitor PLX3397 or vehicle were delivered to CMVMJD135 and WT littermates every day by oral gavage for three weeks, thus generating four experimental groups: WT + vehicle, WT + PLX3397, CMVMJD135 + vehicle, and CMVMJD135 + PLX3397.

At 21 weeks of age, a significant decrease was found in the number of microglial cells in the cerebellar lobules (1593±536 microglia per mm^3; $p = 0.047085$) (Figure 5.2e,f,n) and in the PN (2743±748

microglia per mm^3; $p = 0.019112$) (Figure 5.2i,j,o) but not in the DCN (Figure 5.2a,b,m) of vehicle-treated CMVMJD135 mice when compared with vehicle-treated WT mice. This suggests the possibility of mutant *ATXN3* causing glial toxicity, eventually leading to microglial death processes.

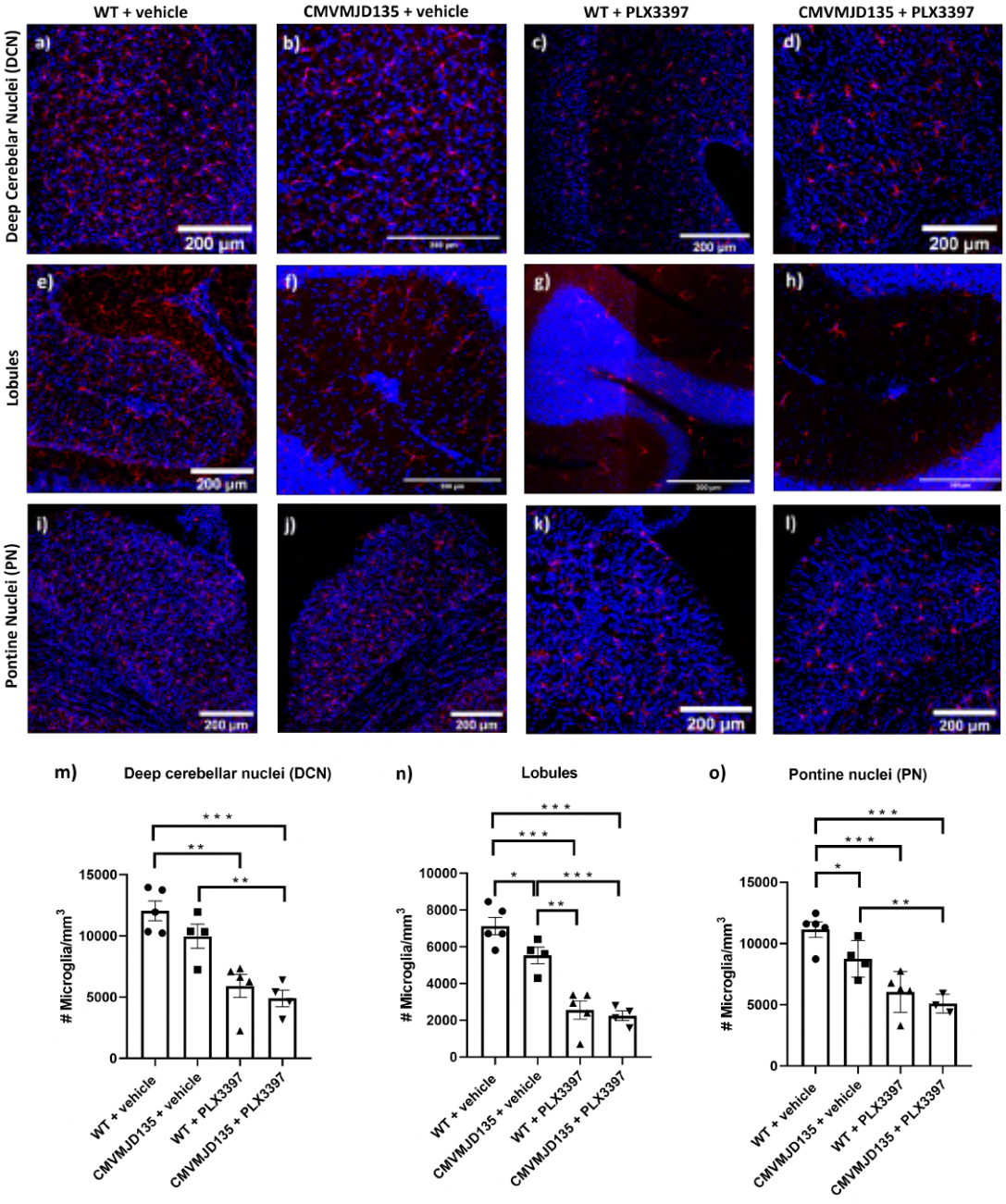

Figure 5.2: **Partial microglial reduction by PLX3397 in CMVMJD135 mice. a-l)** Representative images of microglial cells, using Iba-1 as a microglia marker (in red), from the DCN **a-d)** and lobules **e-h)**, of the cerebellum, and from the PN **i-l)**, in the brainstem of WT and CMVMJD135 mice treated with PLX3397 **c, d, g, h, k, l)** or vehicle **a, b, e, f, i, j)**. **m-o)** Quantitative analysis of the number of microglial cells per mm^3 in the **m)** DCN, **n)** lobules, and **o)** PN from PLX3397 or vehicle-treated WT and CMVMJD135 mice ($n = 3 - 5$ animals per group). Data are presented as mean+SEM (One-way ANOVA (Post hoc Tukey's test)). *, **, ***, represent the $p < 0.05$, $p < 0.01$, and $p < 0.001$, respectively. Scale bar 200 μm.

The treatment of both CMVMJD135 and WT mice with PLX3397 led to a decrease in the number

of microglia in the DCN, lobules, and PN when compared to vehicle-treated CMVMJD135 and WT animals, respectively. In fact, the PLX3397 treatment resulted in (1) a 59 % reduction in the lobules of both CMVMJD135 (3285 ± 565 microglia per mm^3; $p = 0.000313$) and WT (4105 ± 536 microglia per mm^3; $p = 0.000019$) groups; (2) a 42 % reduction in the PN of both CMVMJD135 (3652 ± 748 microglia per mm^3; $p = 0.003001$) and WT (4756 ± 748 microglia per mm^3; $p = 0.000402$) groups; and (3) a 51 % reduction in microglial density in the DCN of CMVMJD135 mice (5072 ± 1086 microglia per mm^3; $p = 0.002164$) and in a 43 % reduction in WT mice (5207 ± 1030 microglia per mm^3; $p = 0.001106$). No significant differences were found in the proportion of microglial cells lost upon PLX3397 treatment between CMVMJD135 and WT mice in the affected brain regions, suggesting that microglial mutant *ATXN3* expression does not alter the dependence of these cells on CSF1R signaling for survival.

5.3.2 PLX3397 treatment did not promote morphological changes in microglia from CMVMJD135 mice

In addition to the partial depletion observed, we determined the effects of PLX3397 on the morphology of the remaining microglial cells in the DCN and PN of CMVMJD135 and WT mice at 21 weeks of age.

Regarding the skeleton data of the 2291 single microglial cells analyzed, only four out of ten parameters (number of branches, junctions voxels, triple points, and quadruple points) were not found to be statistically different between the four groups (CMVMJD135 + vehicle and CMVMJD135 + PLX3397, and WT + vehicle and WT + PLX3397) in the PN (Figure B.8 in *Appendix 2 - Results*)

On the other hand, regarding the fifteen fractal parameters, only four (density, convex hull circularity, ratio of convex hull radii, and convex hull span ratio) were not found to be statistically different between the four groups in the DCN (Figure B.9 in *Appendix 2 - Results*), while two more (fractal dimension, and lacunarity) were not found to be statistically different in the PN (Figure B.10 in *Appendix 2 - Results*).

Hence, significant morphological changes were found, in both DCN and PN brain regions, in parameters relevant to cell ramification, size, surface, and soma thickness (Figure 5.3 and Figure 5.6, respectively), suggesting that microglia from CMVMJD135 + vehicle mice are more activated when compared with those from WT + vehicle mice.

Indeed, when compared with microglial cells from WT + vehicle mice, those from CMVMJD135 + vehicle mice were found to (1) have less and shorter branches; (2) to be less tortuous; (3) to be less ramified; (Figure 5.4 and Figure 5.7); (4) to have smaller size and surface; and (5) with higher soma thickness (Figure 5.5 and Figure 5.8) and Table 5.1.

Curiously, CSF1R inhibition by PLX3397 treatment on CMVMJD135 mice did not induce further morphological changes in the features associated to cell ramification, size, surface, and soma thickness, because no differences being found between CMVMJD135 + vehicle and CMVMJD135 + PLX3397 mice, in both regions (Figure 5.4, Figure 5.5, Figure 5.7, and Figure 5.8). Nevertheless, like CMVMJD135 + vehicle-derived microglia, CMVMJD135 + PLX3397-derived microglia, when compared with WT + vehicle, were also found to have less and shorter branches, to be less tortuous, to be less ramified, with smaller

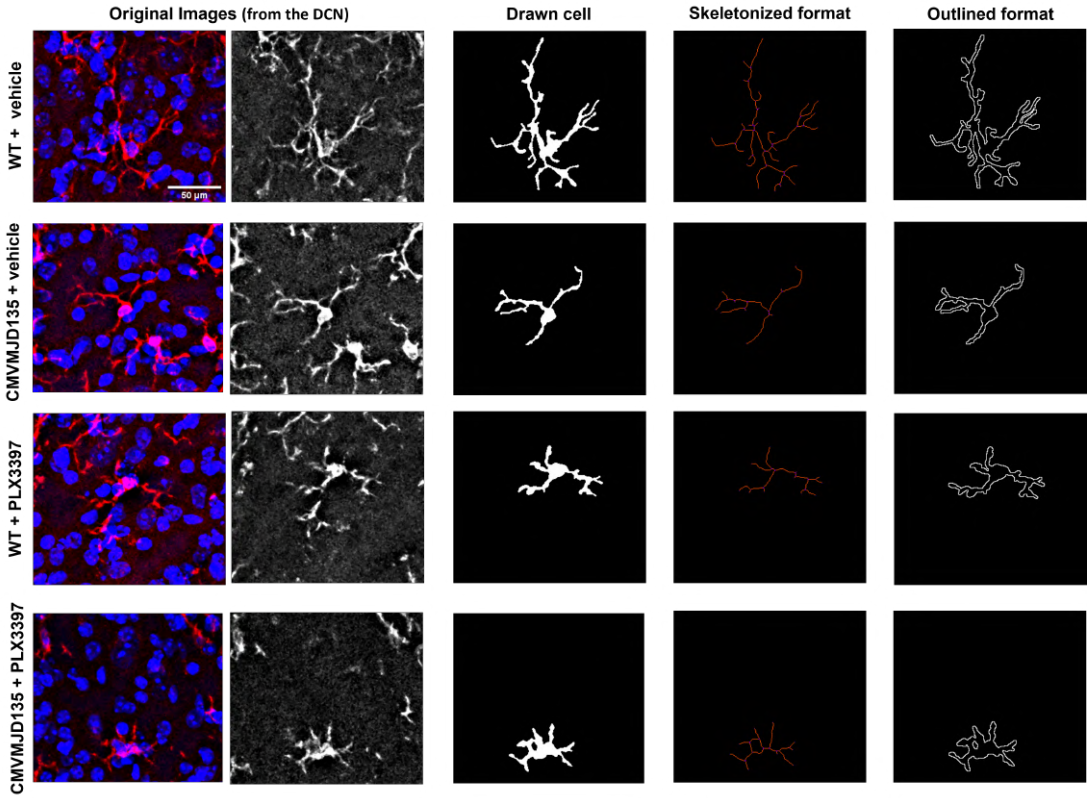

Figure 5.3: **Treatment with PLX3397 did not induce morphological changes in the microglia in the deep cerebellar nuclei of CMVMJD135 mice.** Representation of the process to prepare the images for skeleton and fractal analysis of microglia morphology. These images show differences regarding the features relevant to cell ramification (from skeleton data) and relevant to cell size, surface, and soma thickness (from fractal data).

size and surface, and with higher soma thickness. In fact, in both regions, multiple parameters were found to be decreased in CMVMJD135 + PLX3397-derived microglia when compared with WT + vehicle, namely: total branch length; number of branches; Euclidean distance; number of slab voxels; number of junctions voxels; number of endpoints voxels; number of triple points; and the number of quadruple points (Figure 5.4 and Figure 5.7) and Table 5.1. On the other hand, in contrast to the cell circularity, which was found to be increased in the CMVMJD135 + PLX3397 group when compared with WT + vehicle group, the features associated with cell size and surface were found to be decreased, namely: convex hull area; convex hull perimeter; diameter of the bounding circle; mean radius; maximum span across the convex hull; cell perimeter; and roughness (Figure 5.5 and 5.8) and Table 5.1. These alterations suggest that microglial cells from CMVMJD135 + vehicle and the surviving microglia from CMVMJD135 + PLX3397 mice are similar and show an activation profile which is not apparently dependent on CSF1R signaling.

In contrast, in both regions, treatment with PLX3397 on WT mice promoted morphological changes associated with microglial cells becoming more activated, being similar to those of CMVMJD135 animals (PLX3397-treated and vehicle-treated) in some of the analyzed parameters, namely, the total branch length, Euclidean distance, number of slab voxels, convex hull area, convex hull perimeter, diameter of the bounding circle, mean radius, maximum span across the convex hull, cell perimeter, roughness, and

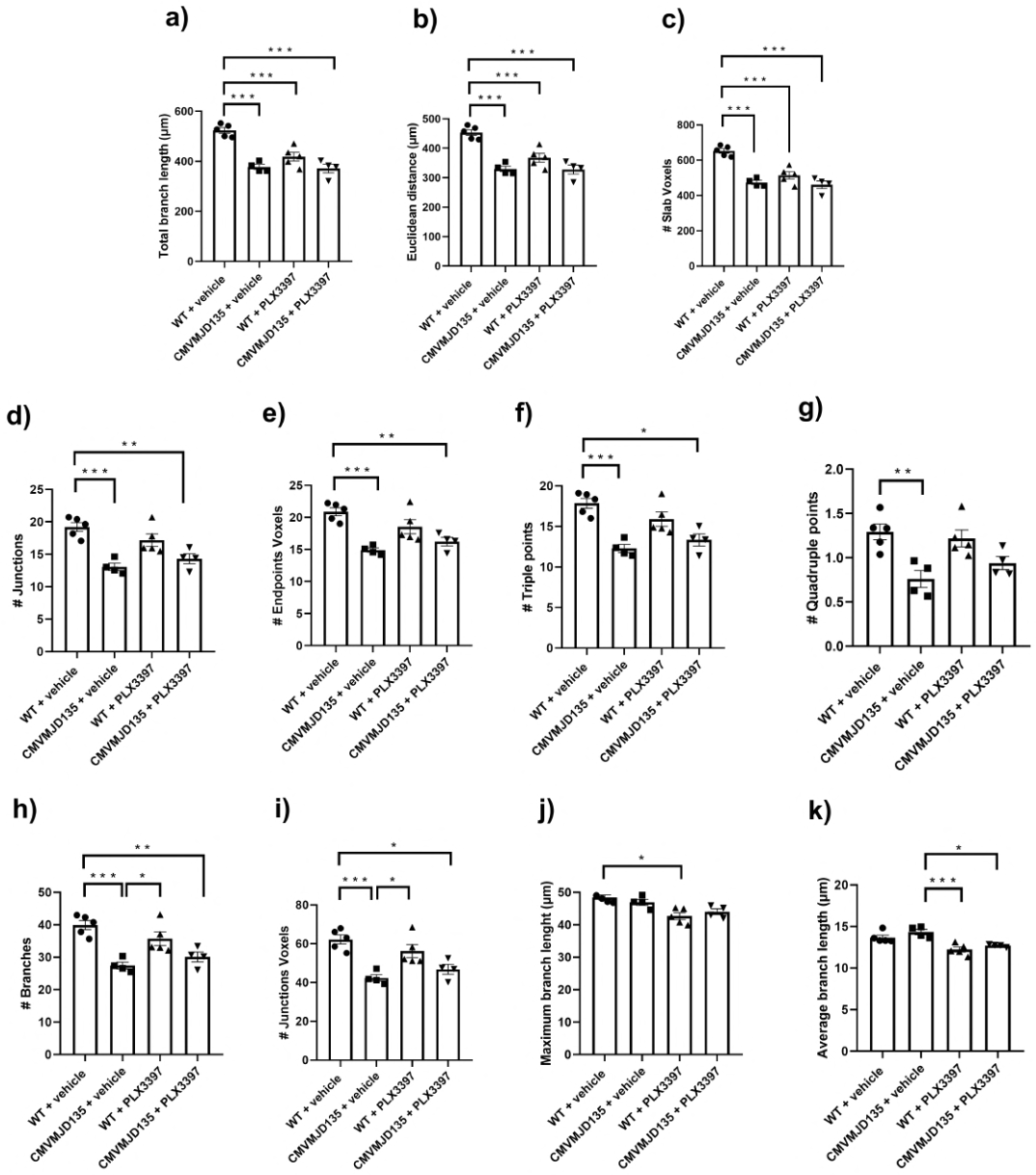

Figure 5.4: **Treatment with PLX3397 did not induce morphological changes in the features relevant to microglia ramification in the deep cerebellar nuclei of CMVMJD135 mice.** Quantification of the morphometric parameters associated to microglia ramification, including: **a)** total branch length, **b)** euclidean distance, **c)** # slab voxels, **d)** # junctions, **e)** # endpoints voxels, **f)** # triple points, **g)** # quadruple points, **h)** # branches, **i)** # junctions voxels, **j)** maximum branch length, and **k)** average branch length. Data of all these parameters were obtained from: 387 microglial cells from WT + vehicle mice ($n = 5$); 256 microglial cells from CMVMJD135 + vehicle mice ($n = 4$); 475 microglial cells from WT + PLX3397 mice ($n = 5$); and 263 microglial cells from CMVMJD135 + PLX3397 mice ($n = 4$). Data are presented as mean+SEM, (One-way ANOVA (Post hoc Tukey's test)). *, **, ***, represent $p < 0.05$, $p < 0.01$, and $p < 0.001$, respectively. Scale bar 50 μm.

cell circularity (Figure 5.4, Figure 5.7, Figure 5.5, and Figure 5.8). In fact, in both regions, skeleton data showed significant differences in microglial cells from WT + PLX3397 mice when compared with those from WT + vehicle mice. The total branch length, Euclidean distance, number of slab voxels, and maximum branch length were lower in microglial cells from WT + PLX3397 mice (Figure 5.4, Figure 5.7,

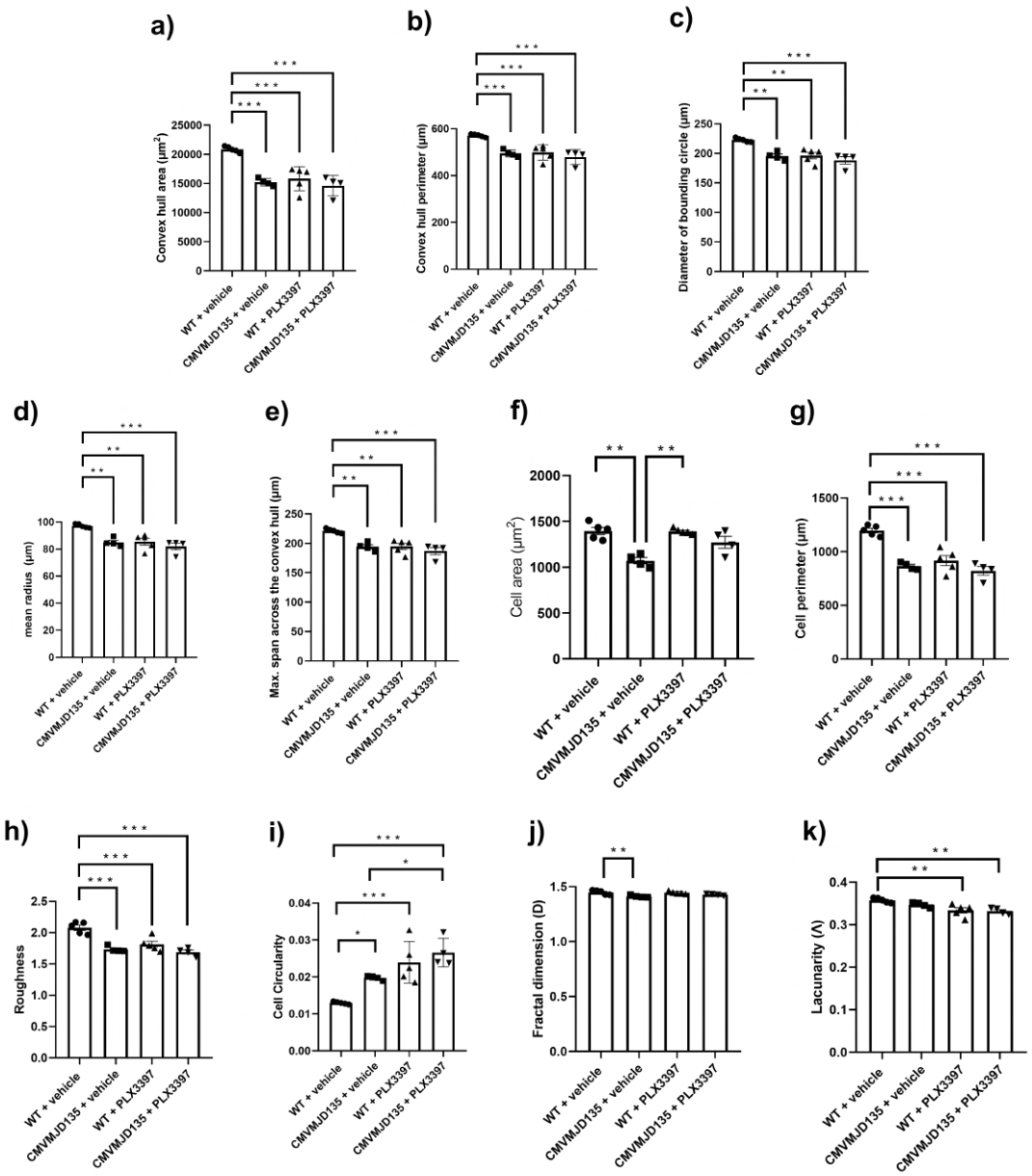

Figure 5.5: **Treatment with PLX3397 did not induce morphological changes in the features relevant to complexity and microglia shape in the deep cerebellar nuclei of CMV-MJD135 mice.** Quantification of the morphometric parameters associated with cell size: **a)** convex hull area, **b)** convex hull perimeter, **c)** diameter of the bounding circle, **d)** mean radius, **e)** maximum span across the convex hull, and **f)** cell area. Associated with cell surface: **g)** cell perimeter, and **h)** roughness. Associated with soma thickness: **i)** cell circularity. Associated with complexity of the ramifications: **j)** fractal dimension. Associated with heterogeneity of the shape: **k)** lacunarity. Data of all these parameters were obtained from: 387 microglial cells from WT + vehicle mice ($n = 5$); 256 microglial cells from CMVMJD135 + vehicle mice ($n = 4$); 475 microglial cells from WT + PLX3397 mice ($n = 5$); and 263 microglial cells from CMVMJD135 + PLX3397 mice ($n = 4$). Data are presented as mean+SEM, (One-way ANOVA (Post hoc Tukey's test)). *, **, ***, represent $p < 0.05$, $p < 0.01$, and $p < 0.001$, respectively. Scale bar 50 μm.

and Table 5.1). Additionally, alterations in parameters associated with the heterogeneity of the shape, cell size, cell surface, and soma thickness were also observed, namely a decreased convex hull area, convex hull perimeter, diameter of the bounding circle, mean radius, maximum span across the convex hull,

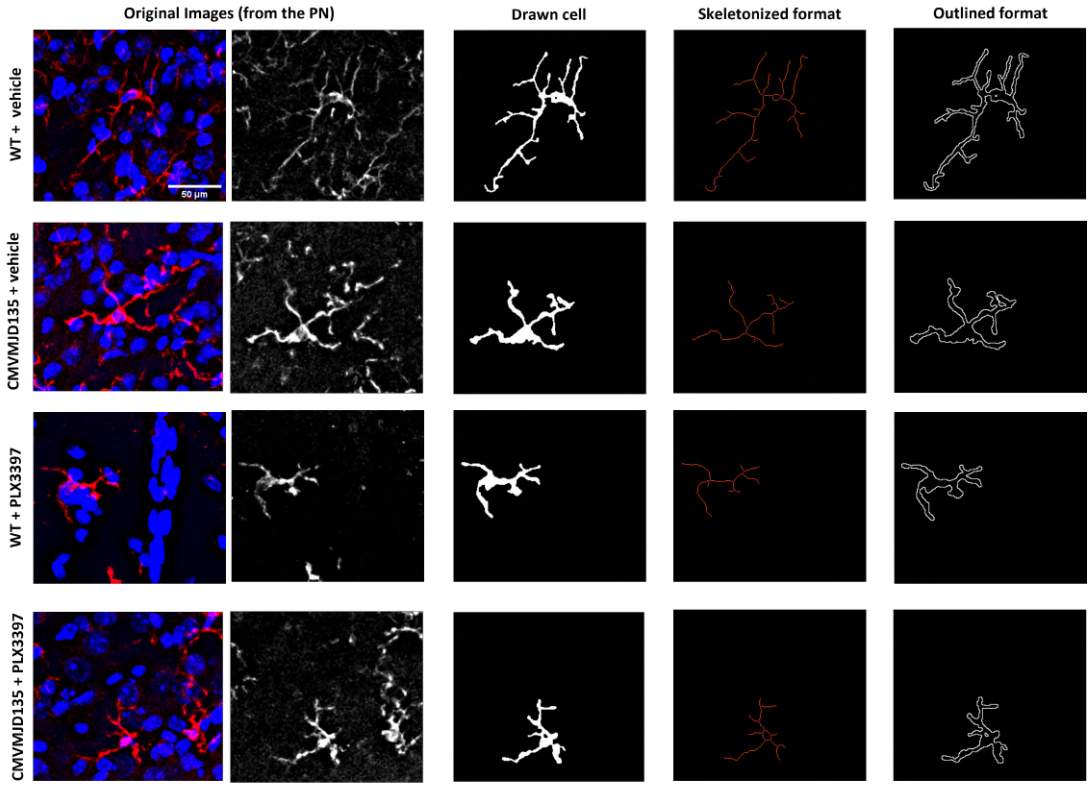

Figure 5.6: **Morphological features of microglial activation were not altered by PLX3397 treatment in the pontine nuclei of CMVMJD135 mice.** Representation of the process to prepare the images for skeleton and fractal analysis of microglia morphology. These images show differences regarding the features relevant to cell ramification (from skeleton data) and relevant to cell size, surface, and soma thickness (from fractal data).

cell perimeter, roughness, and lacunarity (Figure 5.5, Figure 5.8, and Table 5.1). On the other hand, an increased cell circularity was observed in the WT + PLX3397 group (Figure 5.5, Figure 5.8, and Table 5.1).

5.3.3 PLX3397-treated WT-derived microglia showed an activation profile similar to CMVMJD135-derived microglia

The morphological analysis of microglial cells from the DCN and PN of CMVMJD135 (PLX3397- and vehicle-treated) and WT (PLX3397- and vehicle-treated) mice was performed by measuring a total of twenty-six different parameters to evaluate microglia ramification, complexity, cell size, cell surface, and soma thickness. Hence, considering all statistically different parameters that were found between the four groups, in both regions, a PCA was performed to reduce the parameters' dimensionality to a two-dimensional space, obtained based on two principal components. In the DCN, the PCA preserves 96.1 % of the entire information present in the twenty-two statistically different parameters (PC0 = 76.7 % and PC1 = 19.4 %). On the other hand, in the PN the PCA preserves 93.1 % of the entire information present in the sixteen statistically different parameters (PC0 = 71.4 % and PC1 = 21.7 %).

For both brain regions, scatter plots were designed, plotting each animal as a point in a two-dimensional

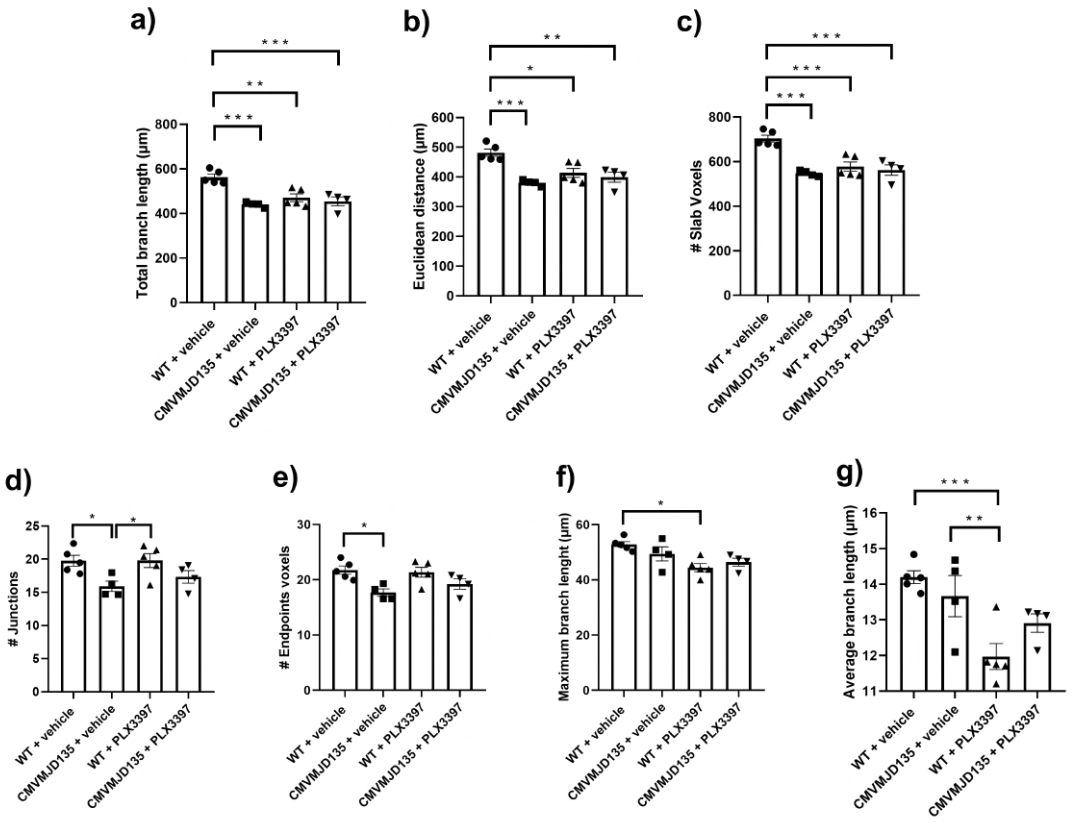

Figure 5.7: **Treatment with PLX3397 did not induce changes in the morphological features relevant to microglia ramification in the pontine nuclei of CMVMJD135 mice.** Quantification of the morphometric parameters associated to microglia ramification, including: **a)** total branch length, **b)** euclidean distance, **c)** # slab voxels, **d)** # junctions, **e)** # endpoints voxels, **f)** maximum branch length, and **g)** average branch length. Data of all these parameters were obtained from: 210 microglial cells from WT + vehicle mice ($n = 4$); 217 microglial cells from CMVMJD135 + vehicle mice ($n = 4$); 248 microglial cells from WT + PLX3397 mice ($n = 5$); and 235 microglial cells from CMVMJD135 + PLX3397 mice ($n = 5$). Data are presented as mean+SEM, (One-way ANOVA (Post hoc Tukey's test)). *, **, ***, represent $p < 0.05$, $p < 0.01$ and $p < 0.001$, respectively. Scale bar 50 μm.

space on the principal components plane. Figure 5.9a and Figure 5.10a display the two-dimensional space of WT + vehicle and CMVMJD135 + vehicle mice for the DCN and PN, respectively, with a clear separation between these two groups being easily noticeable (established by the first principal component - PC0), which strengthens the assumption that microglia from CMVMJD135 + vehicle mice are different from those of WT + vehicle mice. The remaining groups (WT + PLX3397 and CMVMJD135 + PLX3397) were plotted closer to the CMVMJD135 + vehicle mice in both regions (Figure 5.9b,c for the DCN and Figure 5.10b,c for the PN), suggesting that these three groups share similarities among them. Treatment with PLX3397 has reduced impact on the profile of microglia of CMVMJD135 mice, whereas it brings WT-derived microglia into a state of activation that resembles the one of MJD mice.

To further visualize the relationships between multiple significant parameters found to be altered in WT + vehicle mice when compared to the remaining groups (WT + PLX3397, CMVMJD135 + vehicle, and CMVMJD135 + PLX3397 mice), scatter plots on a three-dimensional space were designed for both

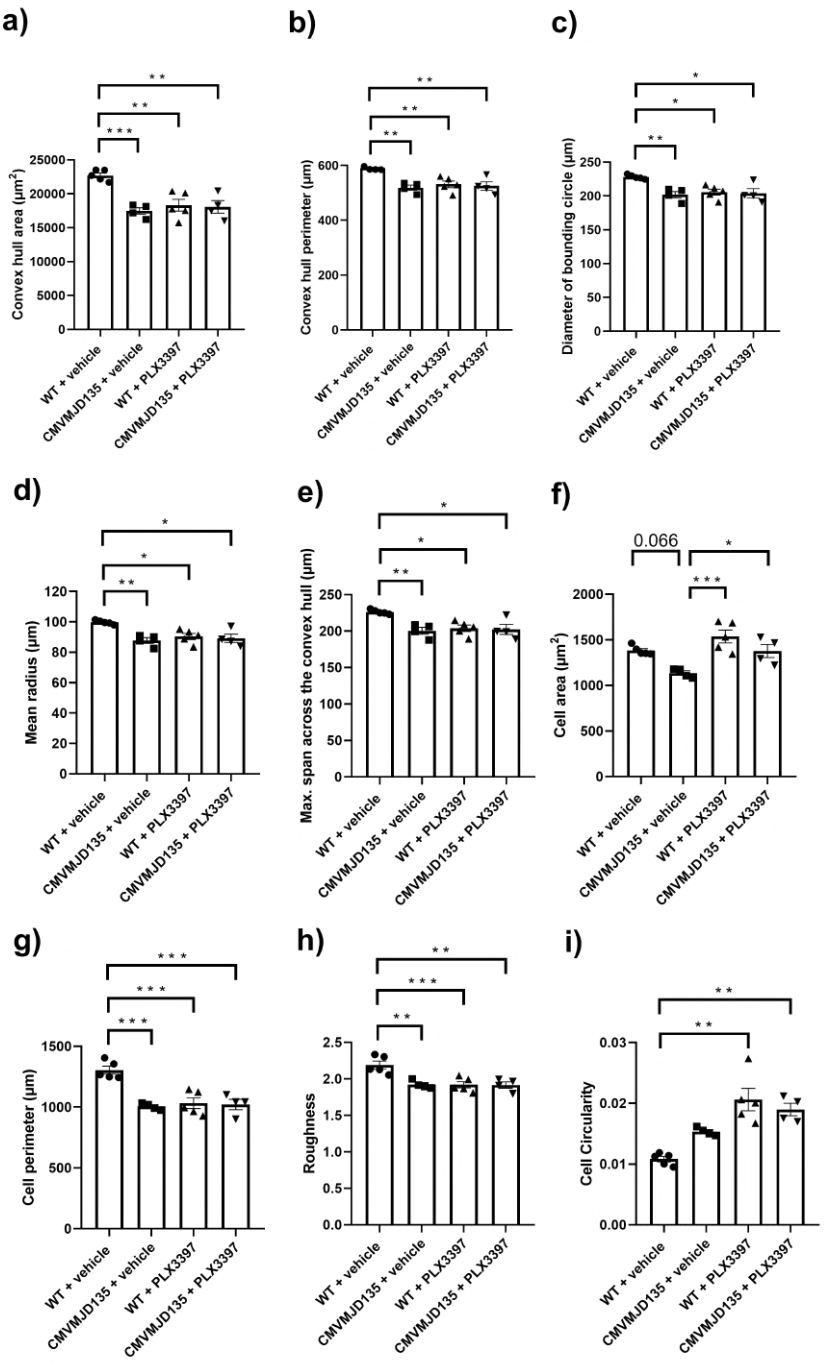

Figure 5.8: **Treatment with PLX3397 did not induce changes in the morphological features relevant to complexity and microglia shape in the pontine nuclei of CMVMJD135 mice.** Quantification of the morphometric parameters associated with cell size: **a)** convex hull area, **b)** convex hull perimeter, **c)** diameter of the bounding circle, **d)** mean radius, **e)** maximum span across the convex hull, and **f)** cell area. Associated with cell surface: **g)** cell perimeter, and **h)** roughness. Associated with soma thickness: **i)** cell circularity. Data of all these parameters were obtained from: 210 microglial cells from WT + vehicle mice ($n = 4$); 217 microglial cells from CMVMJD135 + vehicle mice ($n = 4$); 248 microglial cells from WT + PLX3397 mice ($n = 5$); and 235 microglial cells from CMVMJD135 + PLX3397 mice ($n = 5$). Data are presented as mean+SEM, (One-way ANOVA (Post hoc Tukey's test)). *, **, ***, represent $p < 0.05$, $p < 0.01$ and $p < 0.001$, respectively. Scale bar 50 μm.

Table 5.1: **Significant morphological changes found in both brain regions, deep cerebellar nuclei and pontine nuclei, in features relevant to cell ramification, size, surface, and soma thickness**. A stands for WT + vehicle mice; B for CMVMJD135 + vehicle mice; C for CMVMJD135 + PLX3397 mice; and D for WT + PLX3397 mice. A significance level of $p < 0.05$ was used. N. S. stands for non significant values.

	A vs B		A vs C		A vs D	
	DCN	PN	DCN	PN	DCN	PN
Cell ramification features (p-values)						
N° of branches	0.000477	N.S.	0.00800	N.S.	N.S.	N.S.
Total branch length	0.000004	0.000074	0.000002	0.000074	0.000312	0.001628
Euclidean distance	0.000007	0.000174	0.000005	0.002507	0.000788	0.011000
N° of slab voxels	0.000003	0.000027	0.000007	0.000127	0.000074	0.000298
N° of junctions	0.000248	0.039256	0.004317	N.S.	N.S.	N.S.
N° of junctions voxels	0.000593	N.S.	0.011179	N.S.	N.S.	N.S.
N° of endpoints voxels	0.000361	0.025005	0.007278	N.S.	N.S.	N.S.
N° of triple points	0.000949	N.S.	0.010280	N.S.	N.S.	N.S.
N° of quadruple points	0.001122	N.S.	0.018000	N.S.	N.S.	N.S.
Max. branch length	N.S.	N.S.	N.S.	N.S.	0.028847	0.001628
Average branch length	N.S.	N.S.	N.S.	N.S.	N.S.	0.000738
Cell complexity and shape features (p-values)						
Convex hull area	0.000080	0.000246	0.000016	0.001212	0.000186	0.001170
Convex hull perimeter	0.000738	0.001747	0.000054	0.004893	0.000692	0.007210
Diameter bounding circle	0.004057	0.005877	0.000203	0.013184	0.002651	0.015690
Mean radius	0.003004	0.003518	0.000158	0.013447	0.002305	0.023623
Max. span across convex hull	0.004383	0.006752	0.000197	0.014309	0.002723	0.014764
Cell area	0.001454	N.S.	N.S.	N.S.	N.S.	N.S.
Cell perimeter	0.000010	0.000056	0.000001	0.000136	0.000064	0.000096
Roughness	0.000042	0.001423	0.000006	0.001110	0.000208	0.000584
Cell circularity	0.017501	N.S.	0.000001	0.002756	0.000019	0.002997
Lacunarity	N.S.	N.S.	N.S.	N.S.	0.002194	N.S.
Fractal dimension	0.007317	N.S.	N.S.	N.S.	N.S.	N.S.

regions (Figure 5.9d,e,f for the DCN and Figure 5.10d,e,f for the PN). Again, a clear separation between WT + vehicle mice and the remaining groups is noticeable, reinforcing the previous observations. Finally, scatter plots were conceived over 1381 single microglial cells for the DCN (Figure 5.9g,h,i) and 910 for the PN (Figure 5.10g,h,i), displaying all these cells on a three-dimensional space for three additional significant morphological parameters. Once more, it is possible to visualize that microglial cells from the WT + vehicle group is clustered together in higher values of convex hull area, total branch length, and number of slab voxels, whereas microglia from the three remaining groups are overlapping with each other, assuming lower values for the referred parameters.

The PCA showing promising prospects regarding the existence of two distinct clusters, an unsupervised ML model, the k-means, was used to validate and identify clusters of data with similar characteristics within the entire dataset of microglial cells. Using all the statistically significant parameters found in microglial cells from the DCN (twenty-two parameters) and from the PN (sixteen parameters), the elbow method was implemented to identify the ideal number of clusters. As depicted in Figure 5.11a,d, the largest drop in the

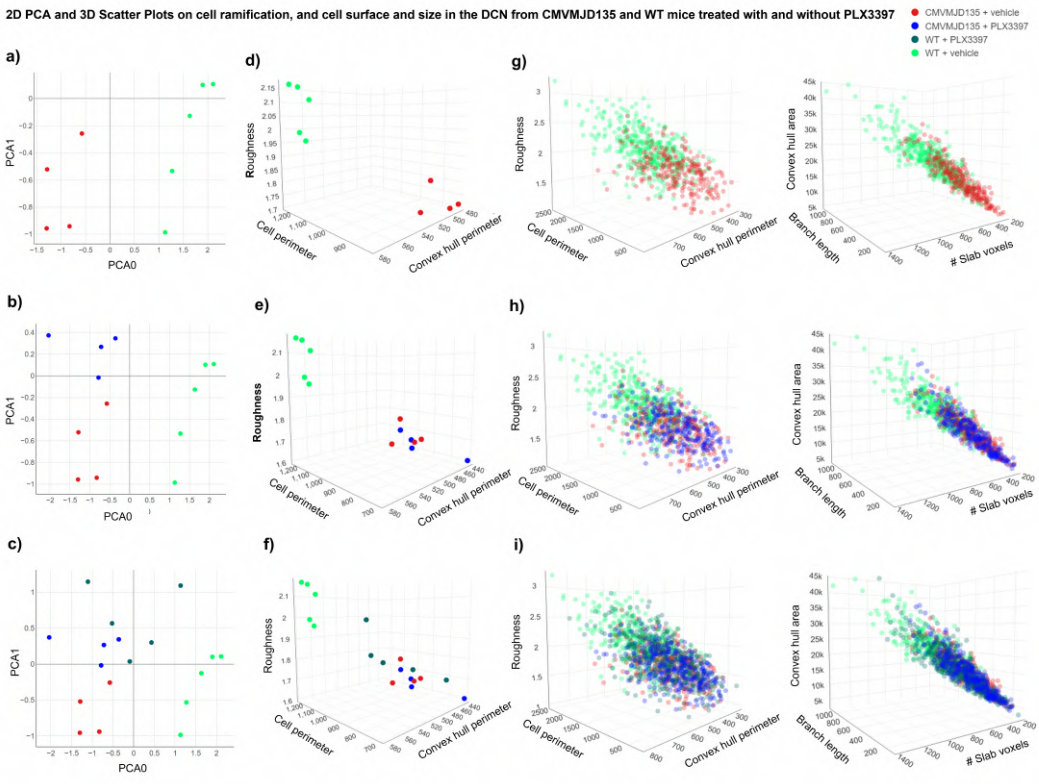

Figure 5.9: **Separation of wild-type + vehicle group and all the remaining groups, including wild-type + PLX3397, CMVMJD135 + vehicle, and CMVMJD135 + PLX3397 mice, regarding the twenty-two significant morphological parameters found in deep cerebellar nuclei microglial cells. a)** 2D scatter plot showing the distribution of WT + vehicle mice (in green) and CMVMJD135 + vehicle (in red) on a principal components plane. **b, c)** 2D scatter plots showing that the remaining groups (WT + PLX3397 and CMVMJD135 + PLX3397) were plotted closer to CMVMJD135 + vehicle mice, regarding the twenty-two significant morphological parameters found in the DCN. **d, e, f)** 3D scatter plots showing a separation between WT + vehicle mice and the remaining groups regarding their roughness, cell perimeter, and convex hull perimeter. **g, h, i)** Data points of a total of 387 microglial cells from WT + vehicle mice, 256 microglial cells from CMVMJD135 + vehicle mice, 475 microglial cells from WT + PLX3397 mice, and 263 microglial cells from CMVMJD135 + PLX3397 mice were plotted on a 3D space, showing the relationship between roughness, cell perimeter, and convex hull perimeter, and between convex hull area, total branch length, and number of slab voxels.

error is found when defining two clusters for both regions, which reinforces the assumption that CSF1R inhibition with PLX3397 promoted morphological changes that led to microglial cells of WT mice becoming similar to those of CMVMJD135 mice (PLX3397-treated and vehicle-treated).

Once the ideal number of clusters was found, these clusters were plotted in a four-dimensional space, with the color, which defines the clusters, as a fourth dimension. Figure 5.11b,c,e,f show the relationship between multiple significant morphological parameters for both regions. An analysis on the two conceived clusters shows that cluster 1, in green, is mainly composed of microglial cells from WT + vehicle mice, which are more ramified, have longer branches, and higher size and surface. The exception is two WT + PLX3397 mice that are clustered together with WT + vehicle mice in the DCN, and two WT + PLX3397 mice plus one CMVMJD135 + PLX3397 mouse in the PN. Conversely, cluster 0, in red, contains the majority of

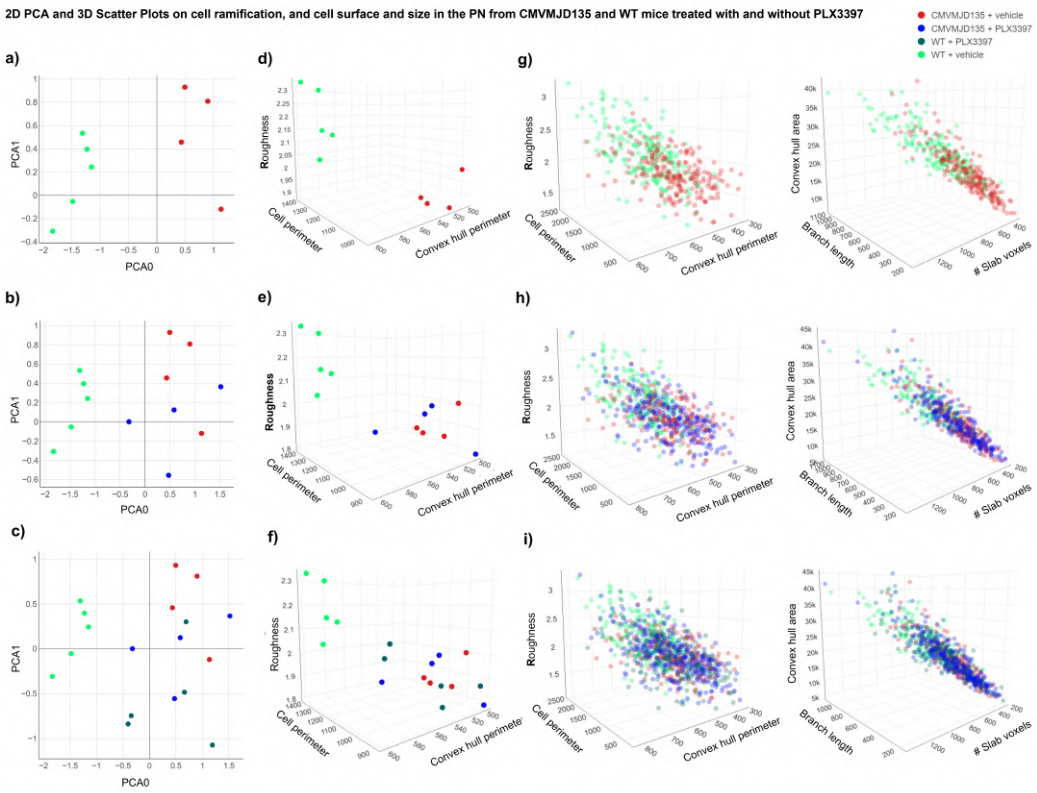

Figure 5.10: **Separation of wild-type + vehicle group and all the remaining groups, including wild-type + PLX3397, CMVMJD135 + vehicle, and CMVMJD135 + PLX3397 mice, regarding the sixteen significant morphological parameters found in the microglial cells from the pontine nuclei. a)** 2D scatter plot showing the distribution of WT + vehicle mice (in green) and CMVMJD135 + vehicle (in red) on a principal components plane. **b, c)** 2D scatter plots showing that the remaining groups (WT + PLX3397 and CMVMJD135 + PLX3397) were plotted closer to CMVMJD135 + vehicle mice as a function of the sixteen significant parameters found in the PN. **d, e, f)** 3D scatter plots showing a separation between WT + vehicle mice and the remaining groups regarding their roughness, cell perimeter, and convex hull perimeter. **g, h, i)** Data points of a total of 210 microglial cells from WT + vehicle mice, 217 microglial cells from CMVMJD135 + vehicle mice, 248 microglial cells from WT + PLX3397 mice, and 235 microglial cells from CMVMJD135 + PLX3397 mice were plotted on a 3D space, showing the relationship between roughness, cell perimeter, and convex hull perimeter, and the relationship between convex hull area, total branch length, and number of slab voxels.

the animals of the remaining groups, which have typically smaller values regarding parameters associated with cell ramification, size, and surface.

Altogether, these alterations suggest that, in addition to partial microglial depletion, CSF1R inhibition by PLX3397 promotes activation of the remaining microglial cells being these cells, from WT + PLX3397 mice, similar to those of CMVMJD135 animals (PLX3397-treated and vehicle-treated), both showing an activated state.

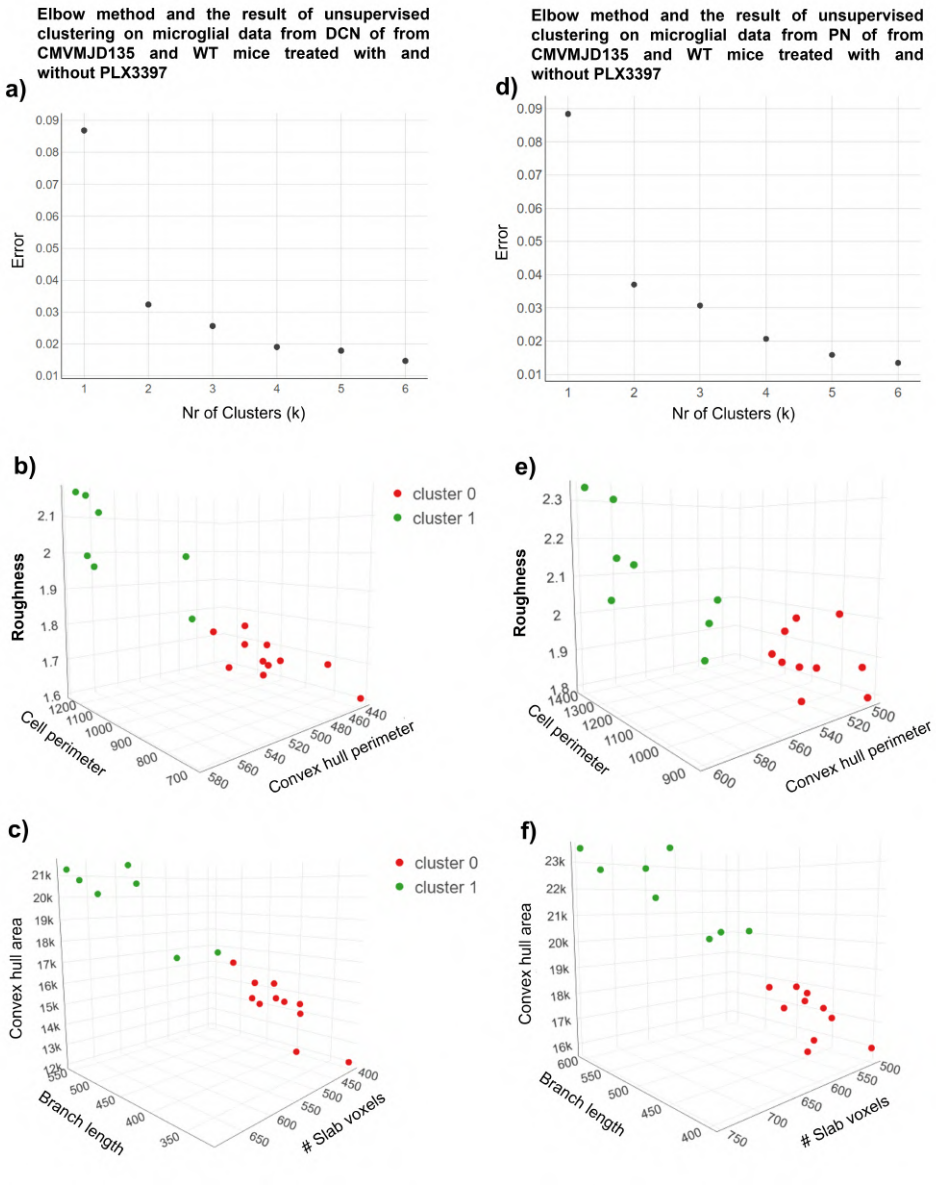

Figure 5.11: **In both affected brain regions, colony stimulating factor 1 receptor inhibition by PLX3397 on wild-type mice promoted morphological changes that led to microglial cells becoming similar to those of CMVMJD135 mice (PLX3397-treated and vehicle-treated). a,d)** Graphical result of the elbow method applied on the dataset comprised of **a)** 1381 single microglial cells for the DCN and **d)** of 910 for the PN, using all statistically significant parameters found in microglial cells from the DCN (twenty-two parameters) and from the PN (sixteen parameters). **b, c, e, f)** All mice of four groups were plotted on a 3D space, belonging to one of two clusters: cluster 0, in red, or cluster 1, in green. **b, e)** 3D scatter plots showing the relationship between roughness, cell perimeter, and convex hull perimeter. **c, f)** 3D scatter plots showing the relationship between convex hull area, total branch length, and number of slab voxels. **b, c)** Except for the two WT + PLX3397 mice that are clustered together with WT + vehicle mice in the DCN, and **e, f)** for the two WT + PLX3397 mice plus one CMVMJD135 + PLX3397 mouse in the PN, cluster 1 is composed of WT + vehicle mice, while cluster 0 is composed of animals of the remaining groups (CMVMJD135 + vehicle, WT + PLX3397, and CMVMJD135 + PLX3397).

5.3.4 PLX3397 treatment had no impact on the motor phenotype of CMVMJD135 mice

We have recently shown morphological alterations that point to an increased activation state as well as molecular pathways involved with oxidative stress, immune response, and lipid metabolism significantly altered in microglia from CMVMJD135 mice [393]. However, it is unknown if they are, or not, actively contributing to the progression of MJD. Hence, to study this contribution, we evaluated the impact of microglial cells depletion with PLX3397 on the motor phenotype of CMVMJD135 mice. For this, we submitted the CMVMJD135 mice (PLX3397-treated and vehicle-treated) to various tests to evaluate different components of the behavioral motor dimension, such as motor coordination and balance, muscular strength, and gait, at 6, 10, 14, 18, 21, 23, 25, 27, 29, 31, and 33 weeks of age.

To understand whether the treatment with PLX3397 has impact on the motor (un)coordination of this animal model, we used the motor swimming test. No significant differences were found between CMVMJD135 + PLX3397 and CMVMJD135 + vehicle mice, and between WT + PLX3397 and WT + vehicle mice throughout age (Figure 5.12a), suggesting that the treatment with PLX3397 had no impact on swimming performance of CMVMJD135 or WT mice. However, the CMVMJD135 mice (PLX3397-treated and vehicle-treated) displayed swimming impairments over time given by a significant increase in the time spent to cross the 60 cm distance when compared with WT mice (PLX3397-treated and vehicle-treated)(Figure 5.12a).

Because CMVMJD135 mice have difficulties in maintaining balance and show progressive impairments in fine motor control, we aimed to understand if PLX3397 treatment modified this phenotype. For this, we tested the ability of the mice to maintain balance while traversing a narrow beam to reach a safe platform. In the 12-mm square beam test, no significant differences were found between CMVMJD135 + PLX3397 and CMVMJD135 + vehicle mice, and between WT + PLX3397 and WT + vehicle mice over time (Figure 5.12b), although, as expected, CMVMJD135 mice (PLX3397-treated and vehicle-treated) showed a significantly worse performance traversing the 12-mm square beam when compared with WT mice (PLX3397-treated and vehicle-treated) (Figure 5.12b). With disease progression, CMVMJD135 mice (PLX3397-treated and vehicle-treated) showed a worsening of the phenotype that affected their ability to perform this task, causing them to fall off the beams frequently. We analyzed these data by attributing performance scores to the animals as follows: 0 – able to perform the task (can walk on the beam), and 1 – Unable to perform the task (cannot walk on the beam). Again, PLX3397 treatment had no impact on the performance of the animals traversing the 12 mm-square beam (at 29, 31, and 33 weeks of age) and the 17 mm-round beam (from 18 weeks of age onwards), as no significant differences were found between CMVMJD135 + PLX3397 and CMVMJD135 + vehicle mice, and between WT + PLX3397 and WT + vehicle mice (Figure 5.12c,d). Once more, and as expected, significant differences were found between CMVMJD135 + vehicle mice and WT + vehicle mice, the former performing significantly worse than the latter, when traversing both the 12-mm square and 17 mm-round beams (Figure 5.12c,d).

Difficulties in traversing the 11 mm-round beam were observed in CMVMJD135 + vehicle mice from 14

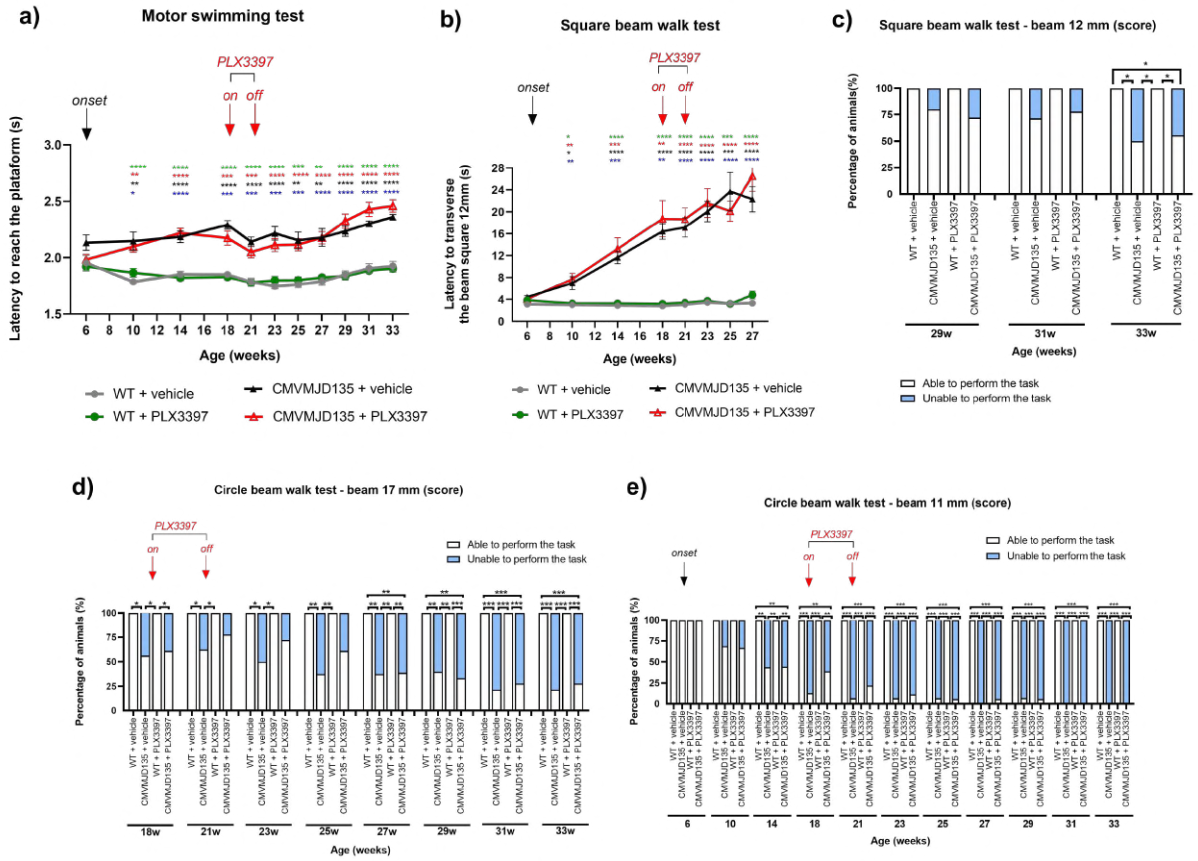

Figure 5.12: **PLX3397 treatment had no impact on the motor coordination and balance deficits of CMVMJD135 mice. a)** Motor swimming test showed that CMVMJD135 mice (PLX3397- and vehicle-treated) spent more time swimming to reach the safe platform than WT mice (PLX3397- and vehicle-treated), throughout age. No significant differences were found between PLX3397-treated and vehicle-treated mice (curve comparison over time $p > 0.05$, 6–33 weeks). *One-way ANOVA (Post hoc Dunnett T3 test)*. **b)** In the square beam test, no differences were found between CMVMJD135 + PLX3397 and CMVMJD135 + vehicle mice, and between WT + PLX3397 and WT + vehicle mice (curve comparison over time $p > 0.05$, 6–27weeks). *One-way ANOVA (Post hoc Dunnett T3 test)*. In both motor swimming and square beam tests, asterisks indicate significant differences which were found between: * WT + vehicle and CMVMJD135 + vehicle; * WT + vehicle and CMVMJD135 + PLX3397; * WT + PLX3397 and CMVMJD135 + vehicle; and * WT + PLX3397 and CMVMJD135 + PLX3397. The 12 mm-square beams walk test (at 29, 31, and 33 weeks of age) and the 17 mm-round beams walk test (from 18 weeks of age onwards), were analysed by scoring the animals. **c)** In the square beam (score) and **d)** in the circle beam of 17 mm-round (score), significant differences were found between CMVMJD135 + vehicle mice and WT + vehicle mice, but no differences were found between CMVMJD135 + PLX3397 and CMVMJD135 + vehicle mice, and between WT + PLX3397 and WT + vehicle mice. *Friedman test with Kruskal-Wallis analysis*. **e)** In the circle beam of 11 mm-round (score), results showed significant differences between WT + vehicle and CMVMJD135 + vehicle, but not between PLX3397-treated and vehicle-treated mice, from 14 weeks to 33 weeks of age. *Friedman test with Kruskal-Wallis analysis*. Values are presented as mean ± SEM or as percentage of animals (%) (for the continuous and non-continuous variables, respectively). Means were considered statistically significant at a p-value * $p < 0.05$, ** $p < 0.01$, *** $p < 0.001$, **** $p < 0.0001$.

weeks of age onwards when compared with WT + vehicle mice. Consistently with the previous results, the difficulty in performing this task was similar for CMVMJD135 + PLX3397 and CMVMJD135 + vehicle mice,

and all animals from both WT + PLX3397 and WT + vehicle groups were able to complete the task in all timepoints analysed (Figure 5.12e), suggesting that motor and balance deficits observed in CMVMJD135 + PLX3397 animals can be attributed to their genotype, not being affected by microglial depletion.

5.3.5 Partial microglial depletion in CMVMJD135 mouse showed no effect on gait quality

The footprint test, used to evaluate motor impairment related to peripheral neuropathy, also revealed that the treatment with PLX3397 had no impact in the gait quality of CMVMJD135 or WT animals, as no significant differences were found between CMVMJD135 + PLX3397 and CMVMJD135 + vehicle mice, and between WT + PLX3397 and WT + vehicle mice, in the distance between the front and hind footprint (stride length) throughout age (Figure 5.13a). However, and in agreement with previous observations, from 14 until 33 weeks of age, CMVMJD135 mice (PLX3397- and vehicle-treated) displayed reduced stride length when compared with WT mice (PLX3397- and vehicle-treated) (Figure 5.13a). In addition, PLX3397 treatment had no impact in the severity of the footdragging phenotype observed in CMVMJD135 animals, CMVMJD135 + PLX3397 mice not differing significantly from CMVMJD135 + vehicle mice throughout age. WT mice (PLX3397- and vehicle-treated) did not show footdragging in all timepoints analysed (Figure 5.13b). No significant difference in spontaneous activity, as exploratory measured in an open arena, was found between vehicle-treated transgenic mice and the PLX3397-treated transgenic mice. Although, curiously, the vehicle-treated WT mice travelled significantly less than the PLX3397-treated WT mice (Figure 5.13c). The gait quality was also assessed in the open arena, onset of an abnormal gait being observed at 10 weeks in both CMVMJD135 + PLX3397 and CMVMJD135 + vehicle mice (Figure 5.13d). We also observed no therapeutic or deleterious effect of the PLX3397 treatment on this abnormal gait throughout age (Figure 5.13d).

5.3.6 Muscular strength and general well-being of Machado-Joseph disease mice were not affected by microglial depletion

Some parameters of the SHIRPA protocol were also used to assess the impact of PLX3397 treatment in the motor and neurological dysfunction of CMVMJD135 mice. CMVMJD135 mice (PLX3397- and vehicle-treated) displayed significantly lower body weight gain than WT mice (PLX3397- and vehicle-treated) throughout time (Figure 5.14a). No differences were found among PLX3397- and vehicle-treated mice, regarding this parameter (Figure 5.14a).

Loss of muscular strength is a very early and severe symptom observed in CMVMJD135 mice [88, 89]. However, a similar performance in the hanging wire grid test was observed between CMVMJD135 + PLX3397 and CMVMJD135 + vehicle mice, suggesting that the PLX3397 treatment does not impact the muscular strength of CMVMJD135 animals (Figure 5.14b).

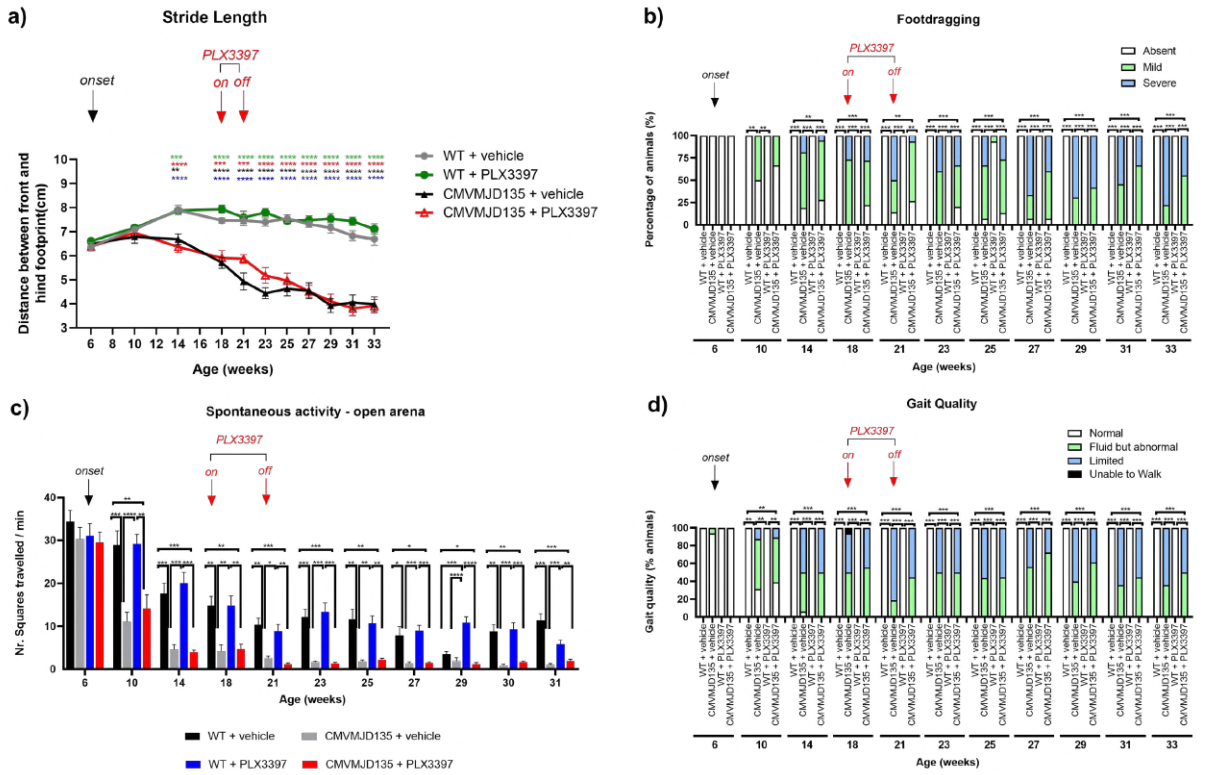

Figure 5.13: **Abnormal stride length and footdragging phenotype observed in CMVMJD135 animals were not affected by PLX3397 treatment. a)** The treatment with PLX3397 had no impact on the gait quality of CMVMJD135 mice, which displayed an abnormal stride length when compared with WT mice. Asterisks indicate significant differences which were found between: * WT + vehicle and CMVMJD135 + vehicle; * WT + vehicle and CMVMJD135 + PLX3397; * WT + PLX3397 and CMVMJD135 + vehicle; and * WT + PLX3397 and CMVMJD135 + PLX3397. *One-way ANOVA (Post hoc Tukey's test)*. **b)** PLX3397 treatment had no impact on the severity of the footdragging phenotype that is observed in CMVMJD135 animals, which displayed a worsening of the footdragging phenotype with age. *Friedman test with Kruskal-Wallis analysis*. **c)** and **d)** no therapeutic effect of the PLX3397 treatment on abnormal gait observed in CMVMJD135 mice throughout age. *Friedman test with Kruskal-Wallis analysis*. Values are presented as mean ± SEM or as percentage of animals (%) (for the continuous and non-continuous variables, respectively). Means were considered statistically significant at a p-value ** $p < 0.01$, *** $p < 0.001$, **** $p < 0.0001$.

Abnormal reflexes (limb clasping) are another phenotypic characteristic of the CMVMJD135 mouse model, starting at 10 weeks of age in both groups of transgenic animals (CMVMJD135 + PLX3397 and CMVMJD135 + vehicle mice) (Figure 5.14c). However, this phenotypic characteristic was not significantly modified by PLX3397 treatment, as no differences were observed between CMVMJD135 + PLX3397 and CMVMJD135 + vehicle mice, from 10 until 33 weeks of age (Figure 5.14c).

5.4 Discussion

We have previously demonstrated morphological, phenotypic, and transcriptomic alterations that point to an increased activation state of microglial cells during the late stages of disease in CMVMJD135 mice [393].

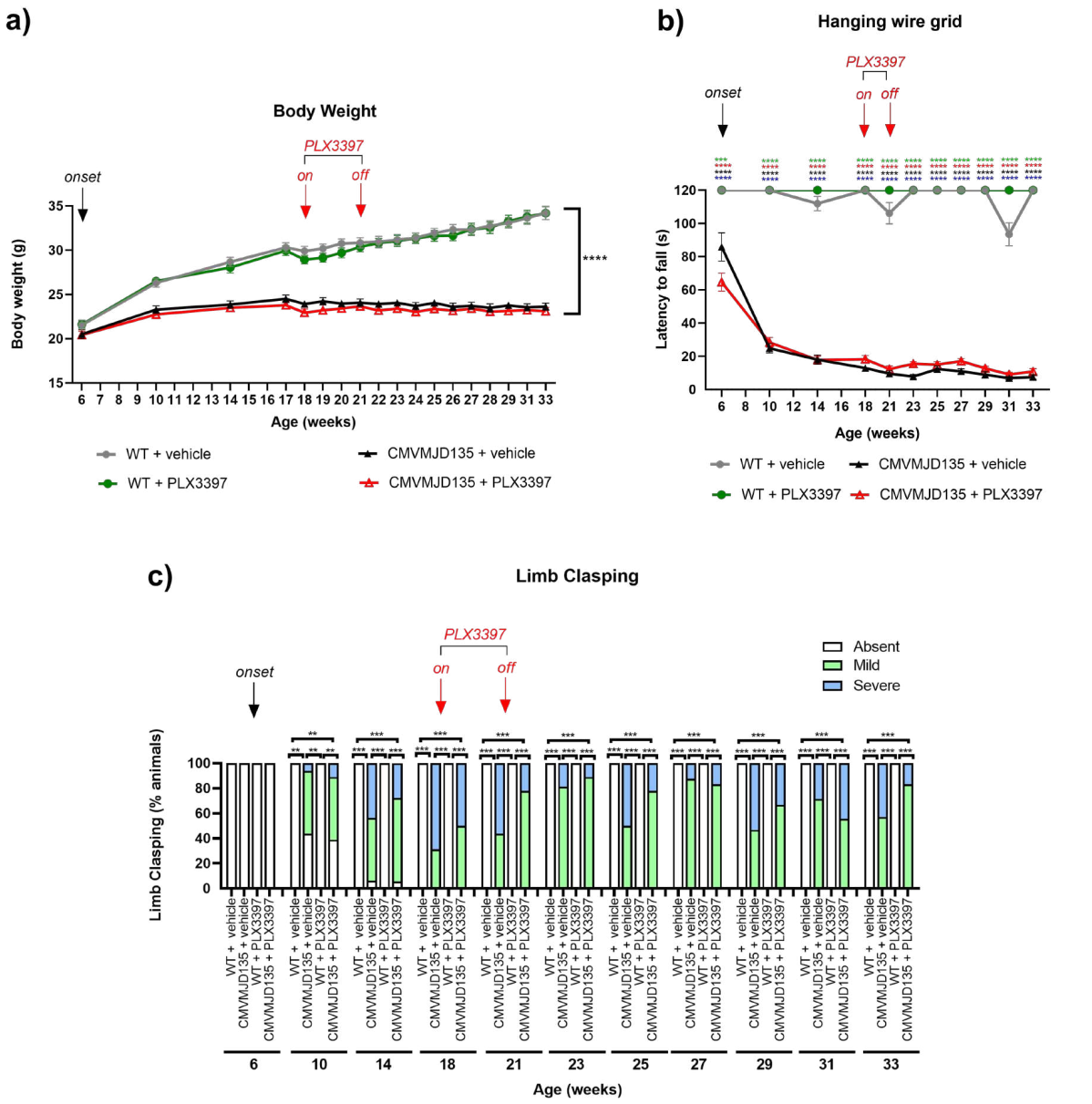

Figure 5.14: **PLX3397-treatment did not modify the loss of muscular strength and abnormal reflexes seen in CMVMJD135 mice. a)** Assessment of body weight showed significant differences between CMVMJD135 mice (PLX3397- and vehicle-treated) and WT mice (PLX3397- and vehicle-treated) throughout time. *One-way ANOVA (Post hoc Tukey's test)*. **b)** In the hanging wire grid test, in all the analysed timepoints, CMVMJD135 mice (PLX3397- and vehicle-treated) showed a significantly lower latency to fall from the grid when compared to WT mice (PLX3397- and vehicle-treated). Asterisks indicate significant differences which were found between: * WT + vehicle and CMVMJD135 + vehicle; * WT + vehicle and CMVMJD135 + PLX3397; * WT + PLX3397 and CMVMJD135 + vehicle; and * WT + PLX3397 and CMVMJD135 + PLX3397. *Friedman test with Kruskal-Wallis analysis*. **c)** Abnormal reflexes observed in the transgenic mice were not significantly improved by the PLX3397 treatment. *Friedman test with Kruskal-Wallis analysis*. Values are presented as mean ± SEM or as percentage of animals (%) (for the continuous and non-continuous variables, respectively). Means were considered statistically significant at a p-value * $p < 0.05$, ** $p < 0.01$, *** $p < 0.001$, **** $p < 0.0001$.

Here, we aimed to understand if these alterations are, or not, actively contributing for disease onset and progression in MJD. Hence, to study the contribution of these cells during early to mid stages of disease,

we evaluated the impact of microglial depletion with PLX3397 in motor phenotype of CMVMJD135 mice. The administration of PLX3397 was made at a mid-stage of the disease since (1) studies suggested that it is hard to treat neurodegenerative diseases, including MJD, during the late stages after neuronal loss had already occurred [149, 407] and (2) a decrease in the number of microglia during an early stage of the disease resulted in the amelioration of motor deficits in a mouse model of SCA1, another spinocerebellar ataxia caused by a polyQ expansion [149]. Although PLX3397 treatment was able of substantially reduce the microglia numbers in two of the key affected regions in this disease, the cerebellum and the brainstem, it did not have an impact on the motor deficits of CMVMJD135 mice, suggesting that the contribution of microglia for MJD progression may not be relevant, and its activate state may be a consequence of the disease establishment.

In this study, CMVMJD135 and WT mice treated with PLX3397 were found to have a 42-59 % reduction in the number of microglia in the lobules and DCN, from the cerebellum, and in the PN, from the brainstem. In general, our results are similar to those obtained by Merry et al. (2020) [403], who reported a 55 % reduction in macrophages (CSF1R is also expressed by these peripheral monocytes [408]) between treated and untreated mice with PLX3397 using a similar experimental approach (method, dose, time of the administration, and age of treatment initiation). In fact, multiple studies have reported different results regarding the extent of depletion of microglia using PLX3397. While some have found a depletion of around 90 % of microglial cells [315, 396–398], others report depletion between 30 and 60 % [399–402]. To the best of our knowledge, complete microglial ablation has never been reported [169]. Although it is unknown if sensitivity to CSF1R blockade changes with age [400], it is known that a small subset of microglia in adult mouse brains can survive without CSF1R signaling, which may explain the variation in depletion efficiency between different studies [169, 315, 396–398]. Therefore, additional experiments are needed to understand if the remaining microglia observed in the DCN and PN of CMVMJD135 and WT mice belong to these cell populations resistant to CSF1R inhibition.

With a partial depletion being found, we also evaluated the effects of PLX3397 on the morphology of the remaining microglial cells in the DCN and PN of CMVMJD135 and WT mice. PLX3397 treatment did not promote morphological changes in the microglia of CMVMJD135 mice in the two affected regions. Both CMVMJD135 + vehicle and CMVMJD135 + PLX3397 microglia, when compared with that of WT + vehicle, were found to have less and shorter branches, to be less tortuous, to be less ramified, with smaller size and surface, and with higher soma thickness. Previous studies have demonstrated that decreased values of these features and increased circularity are associated with an “activated state”, characterized by cells with larger cell bodies, and shorter and thicker processes [183, 242, 334]. These alterations, typically found in different situations of brain disease and pathology [149, 183, 242, 333, 334], suggest that microglia from CMVMJD135 + vehicle and CMVMJD135 + PLX3397 mice are similar and showed an activation profile, which was not dependent on CSF1R signaling. Because mutant *ATXN3* is expressed in microglia [393], we hypothesize that this activation profile may be due to mutant *ATXN3* in microglial cells themselves or/and emerge as a consequence of their interaction with neurons undergoing degenerative processes. This, however, remains to be explored.

Interestingly, in both regions, it seems that the treatment with PLX3397 on WT mice promoted morphological changes that led to microglial cells becoming more activated, and thus more similar to those observed for CMVMJD135 animals. In fact, the PCA showed the existence of a clear structure on these morphological data, with two clusters being identified. Our analysis show that one cluster is grouping more ramified cells, with longer branches, and higher size and surface. This cluster is mainly composed of microglia from WT + vehicle mice. On the other hand, the second cluster is mainly composed of microglia from animals of the remaining groups, which have typically smaller values regarding parameters associated with cell ramification, size, and surface, characteristics typically found in activated microglia. These findings are in accordance with other studies that used PLX3397, which have also found that the remaining microglia exhibited shorter and thicker processes, smaller cell size and an increased circularity [222, 409], a consequence that needs to be taken into account when interpreting the results of such experiments in the context of neurological diseases.

The neuroprotective effects of PLX3397 have been described in several models of neurodegenerative diseases [313, 315, 316, 410], and this compound was already shown to have beneficial effects in motor performance in a transgenic mouse model of SCA1, without major adverse events [149]. In this study, we submitted the CMVMJD135 mice (PLX3397- and vehicle-treated) to various tests to evaluate different components of the behavioral motor dimension, such as motor coordination and balance, muscular strength, and gait, throughout age. The general health of all animals used in this study suggests that the administration of PLX3397 is safe, as it did not cause any major behavioral alterations, weight loss, or sign of illness in mice treated with PLX3397 for 3 weeks. Since a depletion of ≈50 % of microglial cells was seen in brain regions relevant for motor function in WT mice treated with PLX3397 and this did not impact the motor phenotype of the animals, we conclude that these cells may not be highly relevant for motor performance. Additionally, and contrarily to our hypothesis, the partial reduction of microglia induced in CMVMJD135 mice had no impact on their motor phenotype. In fact, PLX3397-treated and vehicle CMVMJD135 mice displayed a similar loss of muscular strength, abnormal gait, reflexes, and stride length, and motor and balance deficits. This does not support the hypothesis that microglia is a relevant contributor for MJD pathogenesis or symptoms progression, despite the morphological, phenotypic and transcriptomic changes seen in microglia of MJD mice [393].

In conclusion, this study demonstrates that reducing the number of microglial cells, after the onset of motor deficits, is not an effective strategy to counteract disease progression in MJD: in fact, halving the microglial population did not change the phenotypic outcome in CMVMJD135 mice. While it is possible that a more severe depletion of microglia could lead to a change in neurodegeneration-related phenotype, or that the effect of microglial depletion would be more marked at earlier phases of the disease, prior to the appearance of motor symptoms, overall our data does not support a central role for microglial cells in this disease.

Chapter 6

General Discussion and Future Perspectives

The contribution of microglia to several NDs is well recognized. It is known that these cells play a pivotal role in NDs pathogenesis, often with different contributions at different disease stages and in distinct brain regions [173, 201, 261]. A major feature of neurodegeneration is the disruption of CNS homeostasis during which microglia play diverse roles [173, 216, 244]. Non-homeostatic microglial profiles have been described in several neurodegenerative disorders and aging [189, 203, 204, 207, 213, 216, 263, 264, 275, 291, 298, 304, 307]. Moreover, changes in microglia phenotypes, their loss of neuroprotective role, and the gain of detrimental functions may differ with the stage and severity of different NDs [173, 216, 262].

Yet, little is known about the profile of microglia in MJD. Hence, we characterized the profile of microglia in a mouse model of MJD at late stages of the disease, with a particular focus on the brainstem, cerebellum, and spinal cord, three of the CNS areas most affected in this polyglutamine disease [23, 44–46]. To the best of our knowledge, this was the first study to characterize the functional and morphological features of microglia in an *in vivo* model of MJD and to provide new insights into the transcriptomic profile of these cells in the context of this disorder.

It is known that MJD pathophysiology appears gradually and progresses over time, pointing to an age-dependent decline in the cells' ability to remove misfolded Ataxin-3, which is expressed ubiquitously in brain cells, including neurons and microglia [31, 34, 91, 102]. Ataxin-3 misfolding and the consequent disruption of cells' proteostasis are considered central to MJD pathogenesis. However, transcriptional dysregulation, increase of oxidative stress and mitochondrial dysfunction, and DNA damage also contribute to disease progression [10, 53]. Additionally, it is known that cellular senescence can be induced by DNA damage, oxidative stress and mitochondrial dysfunction, and altered proteostasis [266, 276, 279, 280]. Also, microglia were described to become senescent/dystrophic in other neurological disorders, including AD, PD, MS, HD, and ALS [189, 275, 276, 278, 280, 323]. Hence, we first set out to investigate if microglia from CMVMJD135 mice displayed an accelerated senescence profile. For this, the typical signs of cellular senescence were evaluated in microglia isolated from the affected brain regions of CMVMJD135 mice (Figure 6.1). Contrary to what is described in the literature for other neurodegenerative disorders [189, 216, 280, 291], our observations showed a decrease in the protein levels of a senescence indicator and of senescence-associated pro-inflammatory cytokines in microglia from CMVMJD135 mice. This was consistent with the results of our analysis of senescence-related genes in the whole tissue from three affected regions of MJD mice, in which we found a decrease in the expression of $p19^{Arf}$ in the cerebellum, of *Il-6* and *Pai1* in the brainstem, and of *Icam-1* in the spinal cord. Our findings reveal a non-senescent profile for microglia, or other brain cells, in the CMVMJD135 mouse model of MJD, and do not support a significant contribution of cell senescence processes to MJD, even at late stages (Figure 6.1).

To further reinforce our *in vivo* analysis, we also used an experimental process, described by Caldeira et al. (2014), to mimic the aging of a microglia-enriched culture and to characterize the cultured cells at 4 and 16 DIV, by assessing its phagocytic activity and existing morphological changes [275]. It is known that

reduced ability to phagocytose debris and toxic protein aggregates have been observed in aged microglia and related with senescence [275, 295]. Also, some reports have associated a de-ramified morphology and cytoplasmic fragmentation to microglial senescence [189, 266, 278, 294]. Our *in vitro* results suggest that, early in life, CMVMJD135-derived microglia are mostly similar with WT microglia in regard to their phagocytic activity and morphological features, and that these cells do not become precociously senescent (Figure 6.1).

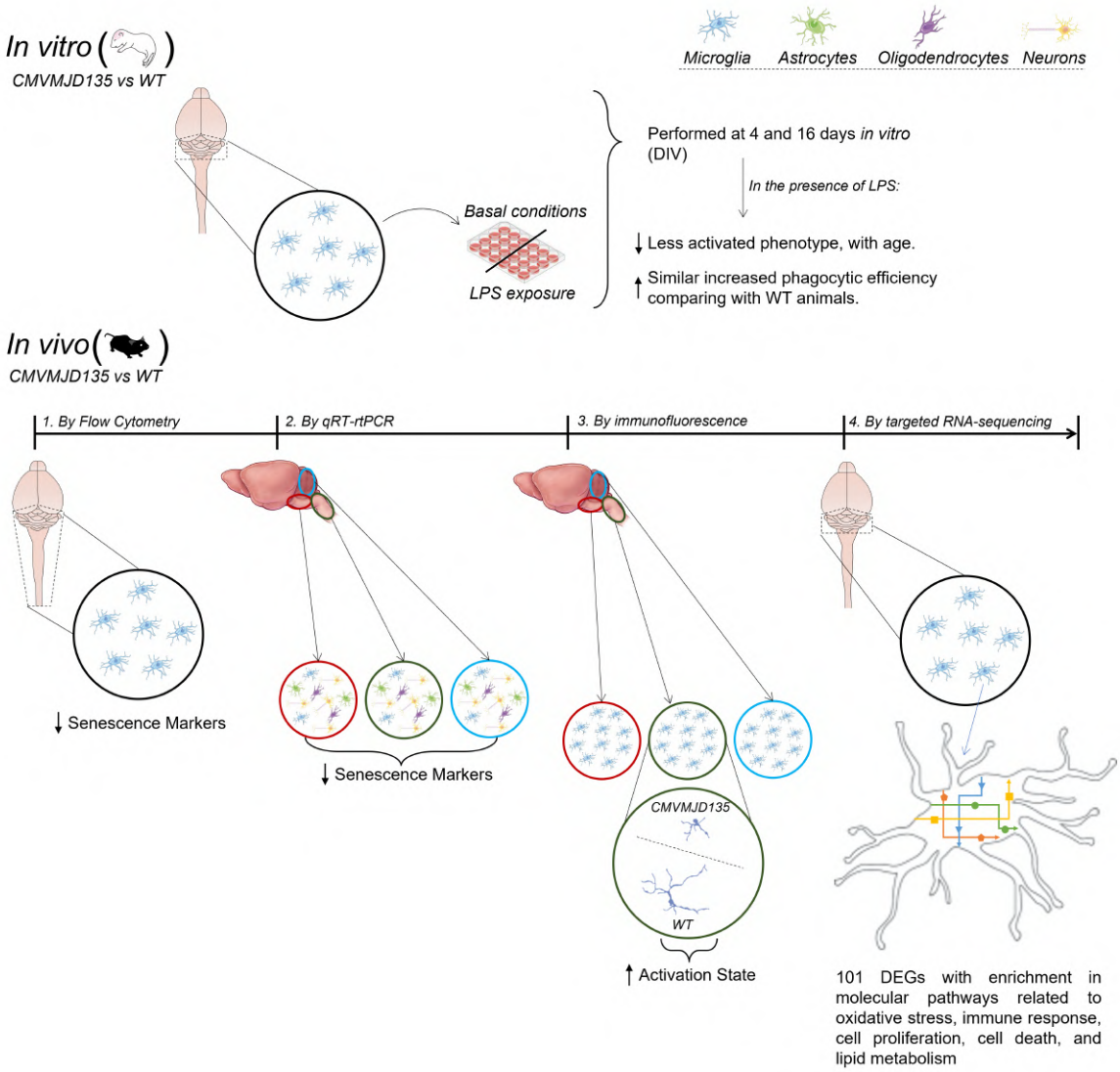

Figure 6.1: **Schematic representation of microglia profile in a mouse model of Machado-Joseph disease.** The expression of senescence markers is decreased in CMVMJD135-derived microglia, with an increased activation state of CMVMJD135-derived microglia. One hundred and one DEGs with enrichment in molecular pathways related to oxidative stress, immune response, cell proliferation and death, and lipid metabolism.

The study of aged microglia is not only relevant to understand their phenotype but also their gene expression, allowing one to deepen the knowledge on their role in both the aging of the CNS and in neurodegenerative diseases [189]. Hence, it becomes imperative to have the means to assess the role of

aged microglia when studying advanced brain neurodegeneration processes and age-associated related disorders [275]. However, since there are no adequate means to isolate degenerating microglia or to cultivate microglia from adult brains effectively, most research is done using microglia from newborns [189, 275, 332, 411]. Indeed, only a few studies have reported using primary culture of microglial cells from aged animals, using either short-term cultures or high concentrations of mitogens in the culture medium, which induces microglia reactivity and have an impact on the conclusions drawn [189, 412]. Nonetheless, even though these *in vitro* models are one of the best option to increase insights into the potential role of aged microglia, we cannot ignore the limitations of *in vitro* studies, since they do not replicate the complexity of the brain environment and the variety of signals microglia are exposed to, which are produced by different cells. Additionally, even at 16 DIV this model is very short lived, thus making it limited for the study of neurodegeneration [189]. It is also worth highlighting that the implementation of these primary cell cultures raises several issues, mainly in terms of the optimization of the protocol required to establish them. Indeed, during this research work, several months were spent optimizing the protocol in order to have cell cultures with high purity, mainly in the last timepoint (16 DIV). This was crucial since after the trypsinization process, which promoted the detachment of non-microglial cells, a slight contamination with astrocytes occurs over time, lowering the purity of these cultures, which can also bias the obtained results.

As discussed in different chapters of this thesis, the morphological characterization of microglia is key for the understanding of its profile. Thus, and since studies exploring the morphological profiling of microglia in MJD are lacking, a better comprehension of MJD-associated microglia based on the characterization of their morphological profile could help to unravel the relevance of these cells for MJD pathogenesis. However, it is clear that a major reason why such studies are lacking is due to the fact that the manual data collection process of morphological features from single microglial cells, and others, is an almost endless and repetitive task, which can take several weeks to complete. Indeed, the current methods besides being manual, are often biased, inaccurate, and time consuming, which increases the possibility of human error associated with the data collection process [335, 336, 338, 339]. It soon became obvious to us that we would need to automate and improve the data collection process of morphological features from single cells, which may then be used to study, understand, and characterize microglia profile in the brain of human patients or of animal models of neurological and psychiatric diseases. *MorphData* emerged to fill this gap, allowing us to collect, in a matter of minutes, a set of morphological features from several thousand cells, significantly reducing the time spent on the data collection process, allowing us to characterize the morphological profile of microglia in this mouse model of MJD [339, 393]. It is also worth pointing that we have been notified that *MorphData* is currently being used by researchers to characterize brain cells in AD animal models (Chrysoula Dioli 2021, personal communication, 11 September).

In this study, the characterization of morphological changes of microglia from CMVMJD135 mice was performed in affected CNS regions (cerebellum, brainstem, and cervical spinal cord) at a late disease stage. Of the three analyzed regions, only microglia from the CSC (one of the earliest affected CNS regions in this mouse model) showed to be more activated when compared with WT mice, since microglia from

CMVMJD135 mice were found to be less tortuous and to have less and shorter branches, with smaller size, and higher soma thickness [183, 242, 333, 334]. In order to better characterize the differences in morphological features, we went further than current studies, which only perform a statistical analysis to characterize morphological profiles. Besides the corresponding statistical analysis, we applied a set of ML models, which allowed us to understand the features that best characterize microglial cells from CMVMJD135 mice [393]. This is specially relevant since clustering single cell measurements is an important undertaking in computational biology and data-driven bioinformatics, which is now becoming the trend.

It is widely accepted that the morphology of microglia is closely coupled to their functional state. Upon detection of an activating signal, or damage, microglia migrate to the site of inflammation or injury and change to an activated state [182, 242]. A microglial cell that is in an activated state but that does not assume the phagocytic phenotype displays a thickening of its branches, up-regulation of MHCI/MHCII, secretion of pro-inflammatory cytokines, and increased ROS production. As they progress in their activation, they can assume a phagocytic state, characterized by large cells that can also exhibit rod-shape or amoeboid-like morphologies. These microglial states are most often observed in pathological conditions [153, 189, 247, 248]. Even though the morphological changes detected point to an increased activation state of microglia, and other studies showing microgliosis in MJD patients [10, 143, 144] and MJD mice [145], other types of studies, as seen in the chapter 5 of this thesis, are required to understand if these microglial cells actively contribute to MJD onset and/or progression. In addition, we also found a significant reduction in the number of microglia in the PN at mid and late stages of disease in the CMVMJD135 mice. This suggests the possibility of mutant ATXN3 causing glia toxicity or/and a consequence of their interaction with neurons and/or other cells, which can eventually lead to microglial death processes.

We then proceeded to characterize gene expression networks in MJD-derived microglia, providing relevant insights into how coordinated gene regulatory programs in microglia underlie MJD pathogenesis. Our findings revealed a disease-specific transcriptional profile of MJD microglia isolated from the cerebellum and brainstem (as a whole), encompassing a total of 101 DEGs. From the 101 DEGs found in CMVMJD135-derived microglia, eight (*Junb*, *Fos*, *Bmpr2*, *Gsk3β*, *Mef2c*, *Usp11*, *Alpl*, and *Sox8*) were found to be overlapping several significantly altered pathways related to the immune response, oxidative stress, cell growth, cell proliferation, and cell death. Other cellular pathways were also changed, including those associated with the lipid metabolism. The *Acsl4* and *Scd2* DEGs were found to be involved in these lipid metabolism pathways. It was also found that the expression of genes related to oxidative stress, particularly the synthesis of NO, was increased in CMVMJD135 mice, as seen by the up regulation of *Gsk3β*, *Junb*, *Cpd*, *Igfbp3*, and *Ntn1*. Interestingly, we also found multiple deregulated genes that are common in both CMVMJD135-derived microglia and microglia of the neurodegenerative mouse models of ALS and AD [203]. However, these results suggest a path of disease with higher similarity to that of ALS, a motor neuron disease, than with that of AD, which is not unexpected given the shared involvement of motor systems in these two disorders.

The relevance of these individual DEGs in microglia and/or neurological conditions has been demonstrated in the literature. We found genes (such as the *Fos*, *Junb*, *Gsk3β*, *Acsl4*, and *Bmpr2*) that, when up-regulated, promote pro-inflammatory microglial responses. The use of inhibitors of these genes and the proteins they encode may provide a mean to offer protection from inflammation-induced neuronal toxicity, i.e., these genes could be potential targets to counteract MJD [361, 363–366, 368, 377]. However, we also found genes (such as the *Mefc2*, *Scd2*, *Igfbp3*, *Ntn1*, *Usp11*, *Atp6v0a1*, and *Tyro3*) that encode proteins which themselves promote the inhibition of inflammation in microglia through the inhibition of pro-inflammatory cytokine production [372, 373, 375, 378, 380–384]. This could correspond to an endogenous neuroprotective response and explain the decrease in the expression of genes encoding pro-inflammatory cytokines in CMVMJD135 mice. Overall, the profile of MJD microglia is mixed regarding pro- and anti-inflammatory molecules expression, and the overlapping results suggest a higher similarity of MJD with ALS than AD, which is not unexpected, given the shared involvement of motor systems in these two disorders. Furthermore, and since microgliosis has been observed in MJD patients' post-mortem brains, it would be interesting to explore, hereafter, whether the genes and pathways identified in the CMVMJD135 mouse model of MJD are also altered in the brains of MJD patients, at the mRNA or protein level. Also, the results here obtained allowed us to define the transcriptional profile of MJD-associated microglia providing the identification of genes and molecular pathways that might represent potential targets for the treatment of this disorder. However, the distinction between homeostatic and disease-associated signatures is not absolute in terms of their impact on disease, since some non-homeostatic microglial disease signatures may indeed have neuroprotective effects in halting the disease progress [153, 166, 203, 207]. Thus, it is important to broaden the molecular characterization of homeostatic and disease associated microglia, which will provide one way to identify new microglia directed therapeutic targets for treatment of NDs [153, 166].

In this work, the transcriptional profile of MJD microglia was performed using the affected brain regions as a whole (cerebellum and brainstem) at an advanced disease stage, which prevented us from exploring spatio-temporal characteristics of microglia and their heterogeneity in certain nuclei that are more affected in this disease. In fact, previous studies demonstrated that microglia isolated from different regions of the brain have age- and region-dependent differences in transcriptomic profiles [153, 173, 233]. In addition, region-specific biochemical cues, which establish different microglial phenotypes, may be restricted to the level of individual nuclei at an anatomical structure [173, 262]. In addition, the process of isolating microglial cells may disrupt their activation state and, with that, influence the results obtained from transcriptomic analyses. In that perspective, single-cell RNA-seq analysis is an emerging technology that could provide the ability to explore the spatio-temporal characteristics of microglia and their heterogeneity in different physiological and pathological conditions at a single-cell level [413–415]. Also, we used bulk RNA sequencing of microglial cells isolated based only on CD11b, a known marker. It is possible that some sub-types of microglia were missed.

Despite the morphological, phenotypic, and transcriptomic alterations pointing to an increased activation state of microglia at late stages of the disease in CMVMJD135 mice, it is unknown whether microglia

are, or not, actively contributing for MJD pathogenesis. One approach widely used to study the role of microglia in NDs has been the depletion of these cells in the brains of animal models using PLX3397, a CSF1R inhibitor. The CSF1R-inhibitor PLX3397 has been widely used in recent studies as a safe research tool to acutely deplete microglia as well as a potential strategy in the treatment of NDs such as AD, PD, HD, ALS, and SCA1 [149, 223, 313–317]. The administration of this drug may follow different approaches [149, 396, 397, 403]. In the conducted study, the option was to use oral gavage as administration method since it allowed us to carefully control the concentration of drug administered to each mouse. Other options, which include supplemented food, would not guarantee that the dosage would be the same among all animals. The experimental approach (method, dose, and time of the administration) was chosen based on multiple studies [313, 397, 403, 416] and proved to allow a good proportion of depletion, albeit not complete elimination of microglial cells.

In our study, no significant differences were found in the proportion of microglial cells lost upon PLX3397 treatment between CMVMJD135 and WT mice in the affected brain regions, suggesting that microglial mutant *ATXN3* expression does not alter the dependence of these cells on CSF1R signaling for survival. Currently, it is not clear if the microglial cells that are resistant to depletion rely on other signals aside from CSF1R for survival, but evidence suggests that other receptors, such as TREM2, may contribute with compensatory survival pathways [207]. Additionally, a recent study suggested that depletion-resistant microglia may arise from a microglia-like progenitor cell similar to the EMPS from which microglia arise [169]. Either way, the proportion of depletion-resistant cells was not different between WT and MJD mice, suggesting that these pathways are not altered in the disease.

It would also be interesting to study whether the effect of microglial depletion would be more relevant at earlier stages of the disease, prior to the appearance of motor symptoms. It is also possible that a more severe depletion of microglia, achievable by increasing the concentration and/or the time of PLX3397 administration, might lead to a change in neurodegeneration-related phenotype. A complementary approach could be to use targeted therapy, using genetic or pharmacological approaches, for targeting specific regions, allowing us to better understand the contribution of microglia in each specific region. For example, a study confirmed that the depletion of CSF1, a ligand of the CSF1R, affected the number of microglia in the cerebellum but not in the frontal cerebral cortex [241]. In addition, microglial depletion studies showed that Il-34, another ligand of CSF1R mainly expressed by neurons, was important for maintaining microglial numbers in a region-dependent manner, as microglia density was reduced in Il-34-deficient mice only in the cortex and striatum, but not in the cerebellum and brainstem [162].

Overall, although the PLX3397 treatment was able to substantially reduce microglia numbers in two of the key affected regions in this disease, the cerebellum and the brainstem, it did not have an impact on the motor deficits of CMVMJD135 mice, suggesting that the contribution of microglia for MJD progression may not be significant. In fact, PLX3397-treated and vehicle CMVMJD135 mice displayed a similar loss of muscular strength, abnormal gait, reflexes, stride length, and motor and balance deficits. In addition, and as expected, PLX3397 treatment did not have an impact in WT mice; indeed, it has been demonstrated that microglia depletion during adulthood in mice and rats does not negatively affect behavior or cognition

[222, 396].

Our results also show that, in addition to reducing the number of microglial cells, the treatment with PLX3397 induced morphological changes suggestive of activation in the surviving microglia, making the surviving cells from WT mice become more similar to those of CMVMJD135 animals, which were found to have less and shorter branches, to be less tortuous, to be less ramified, with smaller size and surface, and with higher soma thickness, in both, the cerebellum and the brainstem. This leads to the assumption that CSF1R inhibition with PLX3397 promoted these morphological changes in the WT-derived microglial cells. However, microglial cells from CMVMJD135 + vehicle and the surviving microglia from CMVMJD135 + PLX3397 mice are similar, and both show an activation profile, apparently not dependent on CSF1R signaling. Thus, we hypothesize that this activation profile may be due to mutant *ATXN3* in microglial cells themselves or/and emerge as a consequence of their interaction with neurons undergoing degenerative processes.

Interestingly, our findings in chapter 5 revealed morphological alterations in microglia from the cerebellum and brainstem of CMVMJD135 mice at mid-stage of the disease, which points to an increased activation state of these cells when compared with those of WT animals. However, these alterations were not found at a late stage of the disease (chapter 3). This suggests a functional adaptation of these cells to the characteristics of their microenvironment, which may differ with the stage and severity of the disease. Indeed, microglia are considered to have multiple phenotypes related to the stage and severity of NDs, with different proportions of each phenotype depending on the stage of the disease [173, 216, 262]. Again, a single-cell RNA sequencing analysis could help us define the proportions of these sub-phenotypes.

It is also worth noting that most published studies of microglia to the date use rodent microglia. However, there is increasing evidence that rodent microglia may not faithfully mirror the biology of human microglia [417, 418]. Indeed, recent transcriptomic studies have demonstrated that a number of immunity-related genes were abundantly expressed in human microglia but were not identified as part of the mouse microglial signature [360, 419]. Moreover, a small overlap was observed in microglial genes during aging and neurodegeneration between humans and mice, which may indicate that human and mouse microglia age differently under normal and disease conditions [301, 360]. Such findings clearly set the need for the development of species-specific tools to investigate microglial functions in human brain aging and neurodegeneration [166, 417]. This could be done using post-mortem brain samples (with their own intrinsic limitations), *in vivo* imaging using positron emission tomography (PET) markers [420], or using human induced pluripotent stem cell (iPSC)-derived microglial cells [417].

Overall, our results suggest that microglia may not be significant key contributors for MJD progression despite the morphological, phenotypic, and transcriptomic changes seen in microglia from MJD mice. These findings also indicate that MJD-associated microglia found in this mouse model may result as a consequence of prolonged exposure to the toxic stimuli that result from the expression of the mutant *ATXN3* in other cell types (neurons or, less likely, astrocytes). As main conclusions, we found that microglial cells:

1. were not senescent from an MJD mouse model;
2. showed a less activated phenotype in response to LPS in artificially aged primary cultures;
3. showed an increased phagocytic efficiency in the presence of LPS in culture;
4. displayed morphological alterations pointing to an increased activation state in the spinal cord;
5. revealed key morphological features most affected by the disease, including the Euclidean distance, convex hull area, mean radius, and maximum span across the convex hull;
6. showed transcriptomic changes in molecular pathways that may constitute potential targets to counteract this disease, including those related to oxidative stress, immune response, cell proliferation and death, and lipid metabolism;
7. showed transcriptional changes that overlap those seen in ALS models and are opposite to those seen in AD mouse models;
8. were not differentially affected by PLX3397 treatment, which promoted a partial reduction of microglial cells in both, WT and CMVMJD135 mice;
9. did not undergo morphological changes upon PLX3397 treatment in contrast to WT-derived microglial cells;
10. were not main contributors to the motor phenotype of CMVMJD135 mice, as on this phenotype PLX3397 treatment had no impact.

Future perspectives are vast and spread along several axes. Indeed, our findings raise several questions of great interest, which should be addressed in the near future to further clarify the meaning and origin of the multiple alterations that were found in this mouse model of MJD. For instance, it becomes relevant to assert if all these observed morphological and transcriptomic changes are due to the mutant *ATXN3* in microglial cells themselves or/and if they are a consequence of the interaction with other brain cells. A possible approach focuses the co-culturing of microglia from affected CNS regions of CMVMJD135 mice with other brain cells, such as neurons, astrocytes, or oligodendrocytes, namely exposing microglia from WT mice to neurons, astrocytes, or oligodendrocytes from MJD mice and vice-versa, to test the possibility of a disturbed signaling between microglia and other cells. Also, since these morphological changes point to an increased activation state of microglia from the cerebellum and brainstem, at a mid-stage of the disease, and from the spinal cord, at a late-stage of the disease, it would be relevant to explore the transcriptomic profile of these MJD-associated microglia separately by region and during disease progression, to identify genes and pathways that might represent potential therapeutic targets for this disorder. To complete the characterization of the morphological profile of MJD-associated microglia, it would also be important to analyze the morphology of microglia from the spinal cord of CMVMJD135 mice at a mid-stage of the disease. This would allow one to further understand if the morphological changes seen in this affected

region at a late-stage of the disease, also appear before this stage or if are dependent on the stage of the disease. Finally, additional research approaches to further deepen our knowledge about MJD may involve the replication of these morphological, phenotypic, and transcriptomic studies for other brain cells in other models of MJD, or even of other polyQ diseases.

Bibliography

[1] A. T. Meira, J. L. Pedroso, F. Boller, G. L. Franklin, O. G. P. Barsottini, and H. A. G. Teive. "Reconstructing the History of Machado-Joseph Disease." *European Neurology* 83.1 (2020), pp. 99–104. doi: 10.1159/000507191.

[2] C. Gaspar, I. Lopes-Cendes, S. Hayes, J. Goto, K. Arvidsson, A. Dias, I. Silveira, P. Maciel, P. Coutinho, M. Lima, Y.-X. Zhou, B.-W. Soong, M. Watanabe, P. Giunti, G. Stevanin, O. Riess, H. Sasaki, M. Hsieh, G. A. Nicholson, E. Brunt, J. J. Higgins, M. Lauritzen, L. Tranebjaerg, V. Volpini, N. Wood, L. Ranum, S. Tsuji, A. Brice, J. Sequeiros, and G. A. Rouleau. "Ancestral Origins of the Machado-Joseph Disease Mutation: A Worldwide Haplotype Study." *The American Journal of Human Genetics: Cell Press* 68.2 (2001), pp. 523–528. doi: 10.1086/318184.

[3] K. K. Nakano, D. M. Dawson, and A. Spence. "Machado disease. A hereditary ataxia in Portuguese emigrants to Massachusetts." *Neurology* 22.1 (1972), pp. 45–55. doi: 10.1212/wnl.22.1.49.

[4] B. T. Woods and H. H. Schaumburg. "Nigro-spino-dentatal degeneration with nuclear ophthalmoplegia. A unique and partially treatable clinico-pathological entity." *Journal of the Neurological Sciences* 17.2 (1972), pp. 149–66. doi: 10.1016/0022-510x(72)90137-2.

[5] R. N. Rosenberg, W. L. Nyhan, C. Bay, and P. Shore. "Autosomal dominant striatonigral degeneration. A clinical, pathologic, and biochemical study of a new genetic disorder." *Neurology* 26.8 (1976), pp. 703–14. doi: 10.1212/wnl.26.8.703.

[6] P. Coutinho and C. Andrade. "Autosomal dominant system degeneration in Portuguese families of the Azores Islands. A new genetic disorder involving cerebellar, pyramidal, extrapyramidal and spinal cord motor functions." *Neurology* 28.7 (1978), pp. 703–9. doi: 10.1212/wnl.28.7.703.

[7] P. Coutinho and J. Sequeiros. "Clinical, genetic and pathological aspects of Machado-Joseph disease." *Journal de Genetie Humaine* 29.3 (1981), pp. 203–9.

[8] L. Lima and P. Coutinho. "Clinical criteria for diagnosis of Machado-Joseph disease: report of a non-Azorena Portuguese family." *Neurology* 30.3 (1980), pp. 319–22. doi: 10.1212/wnl.30.3.319.

[9] T. Klockgether, C. Mariotti, and H. L. Paulson. "Spinocerebellar ataxia." *Nature Reviews Disease Primers* 5.1 (2019), p. 24. doi: 10.1038/s41572-019-0074-3.

[10] H. S. McLoughlin, L. R. Moore, and H. L. Paulson. “Pathogenesis of SCA3 and implications for other polyglutamine diseases.” *Neurobiology Disease* 134.104635 (2020). doi: 10.1016/j.nbd.2019.104635.

[11] Y. Takiyama, M. Nishizawa, H. Tanaka, S. Kawashima, H. Sakamoto, Y. Karube, H. Shimazaki, M. Soutome, K. Endo, S. Ohta, and et al. “The gene for Machado-Joseph disease maps to human chromosome 14q.” *Nature Genetics* 4.3 (1993), pp. 300–4. doi: 10.1038/ng0793-300.

[12] Y. Kawaguchi, T. Okamoto, M. Taniwaki, M. Aizawa, M. Inoue, S. Katayama, H. Kawakami, S. Nakamura, M. Nishimura, and I. Akiguchi. “CAG expansions in a novel gene for Machado-Joseph disease at chromosome 14q32.1.” *Nature Genetics* 8.3 (1994), pp. 221–8. doi: 10.1038/ng1194-221.

[13] H. Y. Zoghbi and H. T. Orr. “Glutamine repeats and neurodegeneration.” *Annual Review of Neuroscience* 23 (2000), pp. 217–47. doi: 10.1146/annurev.neuro.23.1.217.

[14] P. Maciel, C. Gaspar, A. L. DeStefano, I. Silveira, P. Coutinho, J. Radvany, D. M. Dawson, L. Sudarsky, J. Guimaraes, J. E. L. Loureiro, M. M. Nezarati, L. I. Corwin, I. Lopes-Cendes, K. Rooke, R. Rosenberg, P. MacLeod, L. A. Farrer, J. Seeiros, and G. A. Rouleau. “Correlation between CAG Repeat Length and Clinical Features in Machado-Joseph Disease.” *American Journal of Human Genetics* 57.1 (1995), pp. 54–61.

[15] L. P. Ranum, J. K. Lundgren, L. J. Schut, M. J. Ahrens, S. Perlman, J. Aita, T. D. Bird, C. Gomez, and H. T. Orr. “Spinocerebellar ataxia type 1 and Machado-Joseph disease: incidence of CAG expansions among adult-onset ataxia patients from 311 families with dominant, recessive, or sporadic ataxia.” *American Journal of Human Genetics* 57.3 (1995), pp. 603–8.

[16] A. Durr, G. Stevanin, G. Cancel, C. Duyckaerts, N. Abbas, O. Didierjean, H. Chneiweiss, A. Benomar, O. Lyon-Caen, J. Julien, M. Serdaru, C. Penet, Y. Agid, and A. Brice. “Spinocerebellar ataxia 3 and Machado-Joseph disease: clinical, molecular, and neuropathological features.” *Annals of Neurology* 39.4 (1996), pp. 490–9. doi: 10.1002/ana.410390411.

[17] S. Tsuji. “Molecular genetics of triplet repeats: unstable expansion of triplet repeats as a new mechanism for neurodegenerative diseases.” *Internal Medicine* 36.1 (1997), pp. 3–8. doi: 10.2169/internalmedicine.36.3.

[18] C. Bettencourt and M. Lima. “Machado-Joseph Disease: from first descriptions to new perspectives.” *Orphanet Journal of Rare Diseases* 6.35 (2011), pp. 1009–1031. doi: 10.1186/1750-1172-6-35.

[19] H. Paulson. “Repeat expansion diseases.” *Handbook of Clinical Neurology* 147 (2019), pp. 105–123. doi: 10.1016/B978-0-444-63233-3.00009-9.

[20] C. M. Everett and N. W. Wood. “Trinucleotide repeats and neurodegenerative disease.” *Brain* 127.11 (2004), pp. 2385–405. doi: 10.1093/brain/awh278.

[21] L. Schols, P. Bauer, T. Schmidt, T. Schulte, and O. Riess. "Autosomal dominant cerebellar ataxias: clinical features, genetics, and pathogenesis." *Lancet Neurology* 3.5 (2004), pp. 291–304. doi: 10.1016/S1474-4422(04)00737-9.

[22] M. C. F. Jr, V. E. Emmel, A. D. Abreu, C. V. Maurer-Morelli, R. Secolin, L. C. Bonadia, M. S. da Silva, A. Nucci, L. B. Jardim, M. L. Saraiva-Pereira, W. M. Jr, H. Paulson, and I. Lopes-Cendes. "Normal ATXN3 Allele but Not CHIP Polymorphisms Modulates Age at Onset in Machado-Joseph Disease." *Frontiers in Neurology* 3.164 (2012). doi: 10.3389/fneur.2012.00164.

[23] U. Rub, L. Schols, H. Paulson, G. Auburger, P. Kermer, J. C. Jen, K. Seidel, H.-W. Korf, and T. Deller. "Clinical features, neurogenetics and neuropathology of the polyglutamine spinocerebellar ataxias type 1, 2, 3, 6 and 7." *Progress in Neurobiology* 104 (2013), pp. 38–66. doi: 10.1016/j.pneurobio.2013.01.001.

[24] N. Suga, M. Katsuno, H. Koike, H. Banno, K. Suzuki, A. Hashizume, T. Mano, M. Iijima, Y. Kawagashira, M. Hirayama, T. Nakamura, H. Watanabe, F. Tanaka, and G. Sobue. "Schwann cell involvement in the peripheral neuropathy of spinocerebellar ataxia type 3." *Neuropathology and Applied Neurobiology* 40.5 (2014), pp. 628–39. doi: 10.1111/nan.12055.

[25] C. Linnemann, S. T. du Montcel, M. Rakowicz, T. Schmitz-Hubsch, S. Szymanski, J. Berciano, B. P. van de Warrenburg, K. Pedersen, C. Depondt, R. Rola, T. Klockgether, A. Garcia, G. Mutlu, and L. Schols. "Peripheral Neuropathy in Spinocerebellar Ataxia Type 1, 2, 3, and 6." *Cerebellum* 15.2 (2016), pp. 165–73. doi: 10.1007/s12311-015-0684-6.

[26] H. L. Paulson, V. G. Shakkottai, H. B. Clark, and H. T. Orr. "Polyglutamine spinocerebellar ataxias - from genes to potential treatments." *Nature Reviews Neuroscience* 18.10 (2017), pp. 613–626. doi: 10.1038/nrn.2017.92.

[27] A. Durr. "Autosomal dominant cerebellar ataxias: polyglutamine expansions and beyond." *Lancet Neurology* 9.9 (2010), pp. 885–94. doi: 10.1016/S1474-4422(10)70183-6.

[28] S. L. Gardiner, M. W. Boogaard, S. Trompet, R. de Mutsert, F. R. Rosendaal, J. Gussekloo, J. W. Jukema, R. A. C. Roos, and N. A. Aziz. "Prevalence of Carriers of Intermediate and Pathological Polyglutamine Disease-Associated Alleles Among Large Population-Based Cohorts." *JAMA Neurology* 76.6 (2019), pp. 650–656. doi: 10.1001/jamaneurol.2019.0423.

[29] R. A. M. Buijsen, L. J. A. Toonen, S. L. Gardiner, and W. M. C. v. Roon-Mom. "Genetics, Mechanisms, and Therapeutic Progress in Polyglutamine Spinocerebellar Ataxias." *Neurotherapeutics* 16.2 (2019), pp. 263–286. doi: 10.1007/s13311-018-00696-y.

[30] P. Coutinho. "Machado-Joseph Disease Revisited." *V International Workshop on Machado-Joseph disease* (2009).

[31] J. Sequeiros and P. Coutinho. "Epidemiology and clinical aspects of Machado-Joseph disease." *Advances in Neurology* 61 (1993), pp. 139–53.

[32] A. Diallo, H. Jacobi, A. Cook, R. Labrum, A. Durr, A. Brice, P. Charles, C. Marelli, C. Mariotti, L. Nanetti, M. Panzeri, M. Rakowicz, A. Sobanska, A. Sulek, T. Schmitz-Hubsch, L. Schols, H. Hengel, B. Melegh, A. Filla, A. Antenora, J. Infante, J. Berciano, B. P. van de Warrenburg, D. Timmann, S. Boesch, M. Pandolfo, J. B. Schulz, P. Bauer, P. Giunti, J.-S. Kang, T. Klockgether, and S. T. du Montcel. "Survival in patients with spinocerebellar ataxia types 1, 2, 3, and 6 (EUROSCA): a longitudinal cohort study." *Lancet Neurology* 17.4 (2018), pp. 327–334. doi: 10.1016/S1474-4422(18)30042-5.

[33] K. Gwinn-Hardy, A. Singleton, P. O'Suilleabhain, M. Boss, D. Nicholl, A. Adam, J. Hussey, P. Critchley, J. Hardy, and M. Farrer. "Spinocerebellar ataxia type 3 phenotypically resembling parkinson disease in a black family." *Archives of Neurology* 58.2 (2001), pp. 296–9. doi: 10.1001/archneur.58.2.296.

[34] U. Rub, E. R. Brunt, and T. Deller. "New insights into the pathoanatomy of spinocerebellar ataxia type 3 (Machado-Joseph disease)." *Current Opinion in Neurology* 21.2 (2008), pp. 111–6. doi: 10.1097/WCO.0b013e3282f7673d.

[35] I. Klinke, M. Minnerop, T. Schmitz-Hubsch, M. Hendriks, T. Klockgether, U. Wullner, and C. Helmstaedter. "Neuropsychological features of patients with spinocerebellar ataxia (SCA) types 1, 2, 3, and 6." *Cerebellum* 9.3 (2010), pp. 433–42. doi: 10.1007/s12311-010-0183-8.

[36] A. D'Abreu, M. C. F. Jr, H. L. Paulson, and I. Lopes-Cendes. "Caring for Machado-Joseph disease: current understanding and how to help patients." *Parkinsonism Related disorders* 16.1 (2010), pp. 2–7. doi: 10.1016/j.parkreldis.2009.08.012.

[37] H. Park, H.-J. Kim, and B. S. Jeon. "Parkinsonism in spinocerebellar ataxia." *BioMed Research International* 2015.125273 (2015). doi: 10.1155/2015/125273.

[38] C. A. Ross. "When more is less: pathogenesis of glutamine repeat neurodegenerative diseases." *Neuron* 15.3 (1995), pp. 493–6. doi: 10.1016/0896-6273(95)90138-8.

[39] T. M. Lopes, A. D'Abreu, M. C. F. Jr, C. L. Yasuda, L. E. Betting, A. B. Samara, G. Castellano, J. C. Somazz, M. L. F. Balthazar, I. Lopes-Cendes, and F. Cendes. "Widespread neuronal damage and cognitive dysfunction in spinocerebellar ataxia type 3." *Journal of Neurology* 260.9 (2013), pp. 2370–9. doi: 10.1007/s00415-013-6998-8.

[40] J. L. Pedroso, P. Braga-Neto, A. C. Felicio, L. A. Dutra, W. A. C. Santos, G. F. do Prado, and O. G. P. Barsottini. "Sleep disorders in machado-joseph disease: frequency, discriminative thresholds, predictive values, and correlation with ataxia-related motor and non-motor features." *Cerebellum* 10.2 (2011), pp. 291–5. doi: 10.1007/s00415-013-6998-8.

[41] D. V. Seshagiri, R. Botta, A. Sasidharan, P. K. Pal, S. Jain, R. Yadav, and B. M. Kutty. "Assessment of Sleep Spindle Density among Genetically Positive Spinocerebellar Ataxias Types 1, 2, and 3 Patients." *Annals of Neuroscience* 25.2 (2018), pp. 106–111. doi: 10.1159/000484516.

[42] A. M., R. P. Munhoz, W. O. Arruda, S. Raskin, M. Moscovich, and H. A. G. Teive. “Spinocerebellar ataxia type 3: subphenotypes in a cohort of Brazilian patients.” *Arquivos de Neuropsiquiatria* 72.9 (2014), pp. 659–62. doi: 10.1590/0004-282x20140129.

[43] R. N. Rosenberg. “Machado-Joseph disease: an autosomal dominant motor system degeneration.” *Movement Disorders* 7.3 (1992), pp. 193–202. doi: 10.1002/mds.870070302.

[44] K. Burk, M. Abele, M. Fetter, J. Dichgans, M. Skalej, F. Laccone, O. Didierjean, A. Brice, and T. Klockgether. “Autosomal dominant cerebellar ataxia type I clinical features and MRI in families with SCA1, SCA2 and SCA3.” *Brain* 119.5 (1996), pp. 1497–505. doi: 10.1093/brain/119.5.1497.

[45] O. Onodera, J. Idezuka, S. Igarashi, Y. Takiyama, K. Endo, H. Takano, M. Oyake, H. Tanaka, T. Inuzuka, T. Hayashi, T. Yuasa, J. Ito, T. Miyatake, and S. Tsuji. “Progressive atrophy of cerebellum and brainstem as a function of age and the size of the expanded CAG repeats in the MJD1 gene in Machado-Joseph disease.” *Annals of Neurology* 43.3 (1998), pp. 288–96. doi: 10.1002/ana.410430305.

[46] U. Rub, D. D. Turco, K. D. Tredici, R. A. I. de Vos, E. R. Brunt, G. Reifenberger, C. Seifried, C. Schultz, G. Auburger, and H. Braak. “Thalamic involvement in a spinocerebellar ataxia type 2 (SCA2) and a spinocerebellar ataxia type 3 (SCA3) patient, and its clinical relevance.” *Brain* 126.10 (2003), pp. 2257–72. doi: 10.1093/brain/awg234.

[47] T. Klockgether, M. Skalej, D. Wedekind, A. R. Luft, D. Welte, J. B. Schulz, M. Abele, K. Burk, F. Laccone, A. Brice, and J. Dichgans. “Autosomal dominant cerebellar ataxia type I. MRI-based volumetry of posterior fossa structures and basal ganglia in spinocerebellar ataxia types 1, 2 and 3.” *Brain* 121.9 (1998), pp. 1687–93. doi: 10.1093/brain/121.9.1687.

[48] Y. Horimoto, M. Matsumoto, H. Akatsu, A. Kojima, M. Yoshida, K. Nokura, H. Yuasa, E. Katada, T. Yamamoto, K. Kosaka, Y. Hashizume, H. Yamamoto, and S. Mitake. “Longitudinal study on MRI intensity changes of Machado-Joseph disease: correlation between MRI findings and neuropathological changes.” *Journal of Neurology* 258.9 (2011), pp. 1657–64. doi: 10.1007/s00415-011-5992-2.

[49] E. C. Etchebehere, F. Cendes, I. Lopes-Cendes, J. A. Pereira, M. C. Lima, C. R. Sansana, C. A. Silva, M. F. Camargo, A. O. Santos, C. D. Ramos, and E. E. Camargo. “Brain single-photon emission computed tomography and magnetic resonance imaging in Machado-Joseph disease.” *Archives of Neurology* 58.8 (2001), pp. 1257–63. doi: 10.1001/archneur.58.8.1257.

[50] T. Yoshizawa, M. Watanabe, K. Frusho, and S. Shoji. “Magnetic resonance imaging demonstrates differential atrophy of pontine base and tegmentum in Machado–Joseph disease.” *Journal of the Neurological Sciences* 215 (2003), pp. 45–50. doi: 10.1016/S0022-510X(03)00185-0.

[51] U. Rub, R. A. I. de Vos, E. R. Brunt, C. Schultz, H. Paulson, K. D. Tredici, and H. Braak. "Degeneration of the external cuneate nucleus in spinocerebellar ataxia type 3 (Machado-Joseph disease)." *Brain Research* 953 (2002), pp. 126–34. doi: 10.1016/s0006-8993(02)03278-x.

[52] C. N. Fahl, L. M. T. Branco, F. P. G. Bergo, A. D'Abreu, I. Lopes-Cendes, and M. C. F. Jr. "Spinal cord damage in Machado-Joseph disease." *Cerebellum* 14.8 (2015), pp. 128–32. doi: 10.1007/s12311-014-0619-7.

[53] J. D. Da Silva, A. Teixeira-Castro, and P. Maciel. "From pathogenesis to novel therapeutics for Spinocerebellar Ataxia type 3: Evading potholes on the way to translation." *Neurotherapeutics* 16.4 (2019), pp. 1009–1031. doi: 10.1007/s13311-019-00798-1.

[54] U. Rub, E. R. Brunt, R. A. I. de Vos, D. D. Turco, K. D. Tredici, K. Gierga, C. S. adn E. Ghebremedhin, K. Burk, G. Auburger, and H. Braak. "Degeneration of the central vestibular system in spinocerebellar ataxia type 3 (SCA3) patients and its possible clinical significance." *Neuropathology and Applied Neurobiology* 30.4 (2004), pp. 402–14. doi: 10.1111/j.1365-2990.2004.00554.x.

[55] U. Wullner, M. Reimold, M. Abele, K. Burk, M. Minnerop, B.-M. Dohmen, H.-J. Machulla, R. Bares, and T. Klockgether. "Dopamine Transporter Positron Emission Tomography in Spinocerebellar Ataxias Type 1, 2, 3, and 6." *Archives of Neurology* 62.8 (2005), pp. 1280–5. doi: 10.1001/archneur.62.8.1280.

[56] T.-H. Yeh, C.-S. Lu, Y.-H. W. Chou, C.-C. Chong, T. Wu, N.-H. Han, and R.-S. Chen. "Autonomic dysfunction in Machado-Joseph disease." *Archives of Neurology* 62.4 (2005), pp. 630–6. doi: 10.1001/archneur.62.4.630.

[57] U. Rub, E. R. Brunt, E. Petrasch-Parwez, L. Schols, D. Theegarten, G. Auburger, K. Seidel, C. Schultz, K. Gierga, H. Paulson, C. van Broeckhoven, T. Deller, and R. A. I. de Vos. "Degeneration of ingestion-related brainstem nuclei in spinocerebellar ataxia type 2, 3, 6 and 7." *Neuropathology and Applied Neurobiology* 32.6 (2006), pp. 635–49. doi: 10.1111/j.1365-2990.2006.00772.x.

[58] M. Yamada, S. Hayashi, S. Tsuji, and H. Takahashi. "Involvement of the cerebral cortex and autonomic ganglia in Machado-Joseph disease." *Acta Neuropathologica* 101.2 (2001), pp. 140–4. doi: 10.1007/s004010000277.

[59] T. Schmidt, G. B. Landwehrmeyer, I. Schmitt, Y. Trottier, G. Auburger, F. Laccone, T. Klockgether, M. Volpel, J. T. Epplen, L. Schols, and O. Riess. "An isoform of ataxin-3 accumulates in the nucleus of neuronal cells in affected brain regions of SCA3 patients." *Brain Pathology* 8.4 (1998), pp. 669–79. doi: 10.1111/j.1750-3639.1998.tb00193.x.

[60] A. Sittler, M.-P. Muriel, M. Marinello, A. Brice, W. den Dunnen, and S. Alves. "Deregulation of autophagy in postmortem brains of Machado-Joseph disease patients." *Neuropathology* 38.2 (2018), pp. 113–124. doi: 10.1111/neup.12433.

[61] H. L. Paulson, M. K. Perez, Y. Trottier, J. Q. Trojanowski, S. H. Subramony, S. S. Das, P. Vig, J. L. Mandel, K. H. Fischbeck, and R. N. Pittman. "Intranuclear inclusions of expanded polyglutamine protein in spinocerebellar ataxia type 3." *Neuron* 19.2 (1997), pp. 333–44. doi: 10.1016/s0896-6273(00)80943-5.

[62] M. Yamada, C.-F. Tan, C. Inenaga, S. Tsuji, and H. Takahashi. "Sharing of polyglutamine localization by the neuronal nucleus and cytoplasm in CAG-repeat diseases." *Neuropathology and Applied Neurobiology* 30.6 (2004), pp. 665–75. doi: 10.1111/j.1365-2990.2004.00583.x.

[63] U. Rub, K. Seidel, I. Ozerden, K. Gierga, E. R. Brunt, L. Schols, R. A. I. de Vos, W. den Dunnen, C. Schultz, G. Auburger, and T. Deller. "Consistent affection of the central somatosensory system in spinocerebellar ataxia type 2 and type 3 and its significance for clinical symptoms and rehabilitative therapy." *Brain Research Reviews* 53.2 (2007), pp. 235–49. doi: 10.1016/j.brainresrev.2006.08.003.

[64] Y. Chai, S. L. Koppenhafer, N. M. Bonini, and H. L. Paulson. "Analysis of the role of heat shock protein (Hsp) molecular chaperones in polyglutamine disease." *The Journal of Neuroscience* 19.23 (1999), pp. 10338–47. doi: 10.1523/JNEUROSCI.19-23-10338.1999.

[65] Y. Chai, S. L. Koppenhafer, S. J. Shoesmith, M. K. Perez, and H. L. Paulson. "Evidence for proteasome involvement in polyglutamine disease: localization to nuclear inclusions in SCA3/MJD and suppression of polyglutamine aggregation in vitro." *Human Molecular Genetics* 8.4 (1999), pp. 673–82. doi: 10.1093/hmg/8.4.673.

[66] T. Uchihara, H. Fujigasaki, S. Koyano, A. Nakamura, S. Yagishita, and K. Iwabuchi. "Non-expanded polyglutamine proteins in intranuclear inclusions of hereditary ataxias–triple-labeling immunofluorescence study." *Acta Neuropathologica* 102.2 (2001), pp. 149–52. doi: 10.1007/s004010100364.

[67] K. Seidel, W. F. A. den Dunnen, C. Schultz, H. Paulson, S. Frank, R. A. de Vos, E. R. Brunt, T. Deller, H. H. Kampinga, and U. Rub. "Axonal inclusions in spinocerebellar ataxia type 3." *Acta Neuropathologica* 120.4 (2010), pp. 449–60. doi: 10.1007/s00401-010-0717-7.

[68] K. Seidel, S. Siswanto, M. Fredrich, M. Bouzrou, W. F. A. den Dunnen, I. Ozerden, H.-W. Korf, B. Melegh, J. J. de Vries, E. R. Brunt, G. Auburger, and U. Rub. "On the distribution of intranuclear and cytoplasmic aggregates in the brainstem of patients with spinocerebellar ataxia type 2 and 3." *Brain Pathology* 27.3 (2017), pp. 345–355. doi: 10.1111/bpa.12412.

[69] S. Gispert, R. Twells, G. Orozco, A. Brice, J. Weber, L. Heredero, K. Scheufler, B. Riley, R. Allotey, C. Nothers, and et al. "Chromosomal assignment of the second locus for autosomal dominant cerebellar ataxia (SCA2) to chromosome 12q23-24.1." *Nature Genetics* 4.3 (1993), pp. 295–9. doi: 10.1038/ng0793-295.

[70] G. Haberhausen, M. S. Damian, F. Leweke, and U. Muller. “Spinocerebellar ataxia, type 3 (SCA3) is genetically identical to Machado-Joseph disease (MJD).” *Journal of the Neurological Sciences* 132.1 (1995), pp. 71–5. doi: 10.1016/0022-510x(95)90927-i.

[71] Y. Ichikawa, J. Goto, M. Hattori, A. Toyoda, K. Ishii, S.-Y. Jeong, H. Hashida, N. Masuda, K. Ogata, F. Kasai, M. Hirai, P. Maciel, G. A. Rouleau, Y. Sakaki, and I. Kanazawa. “The genomic structure and expression of MJD, the Machado-Joseph disease gene.” *Journal of Human Genetics* 46 (2001), pp. 413–422. doi: 10.1007/s100380170060.

[72] P. Maciel, M. C. Costa, A. Ferro, M. Rousseau, C. S. Santos, C. Gaspar, J. Barros, G. A. Rouleau, P. Coutinho, and J. Sequeiros. “Improvement in the molecular diagnosis of Machado-Joseph disease.” *Archives of Neurology* 58.11 (2001), pp. 1821–7. doi: 10.1001/archneur.58.11.1821.

[73] M. Drusedau, J. C. F. M. Dreesen, C. D. Die-Smulders, K. Hardy, M. Bras, J. C. M. Dumoulin, J. L. H. Evers, H. J. M. Smeets, J. P. M. Geraedts, and J. Herbergs. “Preimplantation genetic diagnosis of spinocerebellar ataxia 3 by (CAG)(n) repeat detection.” *Molecular Human Reproduction* 10.1 (2004), pp. 71–5. doi: 10.1093/molehr/gah008.

[74] H. Maruyama, S. Nakamura, Z. Matsuyama, T. Sakai, M. Doyu, G. Sobue, M. Seto, M. Tsujihata, T. Oh-i, T. Nishio, and et al. “Molecular features of the CAG repeats and clinical manifestation of Machado-Joseph disease.” *Human Molecular Genetics* 4.5 (1995), pp. 807–12. doi: 10.1093/hmg/4.5.807.

[75] K. Lindblad, A. Lunkes, P. Maciel, G. Stevanin, C. Zander, T. Klockgether, T. Ratzlaff, A. Brice, G. A. Rouleau, T. Hudson, G. Auburger, and M. Schalling. “Mutation detection in Machado-Joseph disease using repeat expansion detection.” *Molecular Medicine* 2.1 (1996), pp. 77–85.

[76] I. Lopes-Cendes, I. Silveira, P. Maciel, C. Gaspar, J. Radvany, D. Chitayat, R. Babul, J. Stewart, M. Dolliver, Y. Robitaille, G. A. Rouleau, and J. Sequeiros. “Limits of clinical assessment in the accurate diagnosis of Machado-Joseph disease.” *Archives of Neurology* 53.11 (1996), pp. 1168–74.

[77] J. Sequeiros, P. Maciel, F. Taborda, S. Ledo, J. C. Rocha, A. Lopes, F. Reto, A. M. Fortuna, M. Rousseau, M. Fleming, P. Coutinho, G. A. Rouleau, and C. S. Jorge. “Prenatal diagnosis of Machado-Joseph disease by direct mutation analysis.” *Prenatal Diagnosis* 18.6 (1998), pp. 611–7.

[78] T. Ashizawa, G. Oz, and H. L. Paulson. “Spinocerebellar ataxias: prospects and challenges for therapy development.” *Nature Reviews Neurology* 14.10 (2018), pp. 590–605. doi: 10.1038/s41582-018-0051-6.

[79] J. Goto, M. Watanabe, Y. Ichikawa, S. B. Yee, N. Ihara, K. Endo, S. Igarashi, Y. Takiyama, C. Gaspar, P. Maciel, S. Tsuji, G. A. Rouleau, and I. Kanazawa. "Machado-Joseph disease gene products carrying different carboxyl termini." *Neuroscience Research* 28.4 (1997), pp. 373–7. doi: 10.1016/s0168-0102(97)00056-4.

[80] H. L. Paulson, S. S. Das, P. B. Crino, M. K. Perez, S. C. Patel, D. Gotsdiner, K. H. Fischbeck, and R. N. Pittman. "Machado-Joseph disease gene product is a cytoplasmic protein widely expressed in brain." *Annals of Neurology* 41.4 (1997), pp. 453–62. doi: 10.1002/ana.410410408.

[81] I. Schmitt, T. Brattig, M. Gossen, and O. Riess. "Characterization of the rat spinocerebellar ataxia type 3 gene." *Neurogenetics* 1.2 (1997), pp. 103–12. doi: 10.1007/s100480050015.

[82] A. L. DeStefano, L. A. Cupples, P. Maciel, C. Gaspar, J. Radvany, D. M. Dawson, L. Sudarsky, L. Corwin, P. Coutinho, P. MacLeod, and et al. "A familial factor independent of CAG repeat length influences age at onset of Machado-Joseph disease." *American Journal of Human Genetics* 59.1 (1996), pp. 119–27.

[83] G. Sobue, M. Doyu, N. Nakao, N. Shimada, T. Mitsuma, H. Maruyama, and S. Kawakami. "Homozygosity for Machado-Joseph disease gene enhances phenotypic severity." *Journal of Neurology, Neurosurgery, and Psychiatry* 60.3 (1996), pp. 354–6. doi: 10.1136/jnnp.60.3.354-a.

[84] D. R. Carvalho, A. L. Rocque-Ferreira, I. M. Rizzo, E. U. Imamura, and C. E. Speck-Martins. "Homozygosity enhances severity in spinocerebellar ataxia type 3." *Pediatric Neurology* 38.4 (2008), pp. 296–9. doi: 10.1016/j.pediatrneurol.2007.12.006.

[85] M. d. C. Costa, J. G. da Silva, C. J. Miranda, J. Sequeiros, M. M. Santos, and P. Maciel. "Genomic structure, promoter activity, and developmental expression of the mouse homologue of the Machado-Joseph disease (MJD) gene." *Genomics* 84.2 (2004), pp. 361–73. doi: 10.1016/j.ygeno.2004.02.012.

[86] I. Linhartova, M. Repitz, P. Draber, M. Nemec, G. Wiche, and F. Propst. "Conserved domains and lack of evidence for polyglutamine length polymorphism in the chicken homolog of the Machado-Joseph disease gene product ataxin-3." *Biochimica Biophysica Acta* 1444.2 (1999), pp. 299–305. doi: 10.1016/s0167-4781(99)00004-4.

[87] A. J. Rodrigues, G. Coppola, C. Santos, M. do Carmo Costa, M. Ailion, J. Sequeiros, D. H. Geschwind, and P. Maciel. "Functional genomics and biochemical characterization of the C. elegans orthologue of the Machado-Joseph disease protein ataxin-3." *Federation of American Societies for Experimental Biology* 21.4 (2007), pp. 1126–36. doi: 10.1096/fj.06-7002com.

[88] A. Silva-Fernandes, S. Duarte-Silva, A. Neves-Carvalho, M. Amorim, C. Soares-Cunha, P. Oliveira, K. Thirstrup, A. Teixeira-Castro, and P. Maciel. "Chronic treatment with 17-DMAG improves balance and coordination in a new mouse model of Machado-Joseph disease." *Neurotherapeutics* 11.2 (2014), pp. 433–49. doi: 10.1007/s13311-013-0255-9.

[89] A. Silva-Fernandes, M. d. C. Costa, S. Duarte-Silva, P. Oliveira, C. M. Botelho, L. Martins, J. A. Mariz, T. Ferreira, F. Ribeiro, M. Correia-Neves, C. Costa, and P. Maciel. "Motor uncoordination and neuropathology in a transgenic mouse model of Machado-Joseph disease lacking intranuclear inclusions and ataxin-3 cleavage products." *Neurobiology of Disease* 40.1 (2010), pp. 163–76. doi: 10.1016/j.nbd.2010.05.021.

[90] A. Teixeira-Castro, M. Ailion, A. Jalles, H. R. Brignull, J. L. Vilaça, N. Dias, P. Rodrigues, J. F. Oliveira, A. Neves-Carvalho, R. I. Morimoto, and P. Maciel. "Neuron-specific proteotoxicity of mutant ataxin-3 in C. elegans: rescue by the DAF-16 and HSF-1 pathways." *Human Molecular Genetics* 20.15 (2011), pp. 2996–3009. doi: 10.1093/hmg/ddr203.

[91] M. d. C. Costa and H. L. Paulson. "Toward understanding Machado-Joseph Disease." *Progress in Neurobiology* 97.2 (2012), pp. 239–257. doi: 10.1016/j.pneurobio.2011.11.006.

[92] M. M. Evers, L. J. A. Toonen, and W. M. C. van Roon-Mom. "Ataxin-3 Protein and RNA Toxicity in Spinocerebellar Ataxia Type 3: Current Insights and Emerging Therapeutic Strategies." *Molecular Neurobiology* 49.3 (2014), pp. 1513–1531. doi: 10.1007/s12035-013-8596-2.

[93] L. Masino, V. Musi, R. P. Menon, P. Fusi, G. Kelly, T. A. Frenkiel, Y. Trottier, and A. Pastore. "Domain architecture of the polyglutamine protein ataxin-3: a globular domain followed by a flexible tail." *FEBS Letters* 549.1-3 (2003), pp. 21–5. doi: 10.1016/s0014-5793(03)00748-8.

[94] G. Nicastro, L. Masino, V. Esposito, R. P. Menon, A. D. Simone, F. Fraternali, and A. Pastore. "Josephin domain of ataxin-3 contains two distinct ubiquitin-binding sites." *Biopolymers* 91.12 (2009), pp. 1203–14. doi: 10.1002/bip.21210.

[95] G. M. Harris, K. Dodelzon, L. Gong, P. Gonzalez-Alegre, and H. L. Paulson. "Splice isoforms of the polyglutamine disease protein ataxin-3 exhibit similar enzymatic yet different aggregation properties." *PLoS One* 5.10 (2010). doi: 10.1371/journal.pone.0013695.

[96] D. Weishaupl, J. Schneider, B. P. Pinheiro, C. Ruess, S. M. Dold, F. von Zweydorf, C. J. Gloeckner, J. Schmidt, O. Riess, and T. Schmidt. "Physiological and pathophysiological characteristics of ataxin-3 isoforms." *Journal of Biological Chemistry* 294.2 (2019), pp. 644–661. doi: 10.1074/jbc.RA118.005801.

[97] P. M. A. Antony, S. Mantele, P. Mollenkopf, J. Boy, R. H. Kehlenbach, O. Riess, and T. Schmidt. "Identification and functional dissection of localization signals within ataxin-3." *Neurobiology of Disease* 36.2 (2009), pp. 280–92. doi: 10.1016/j.nbd.2009.07.020.

[98] A. S. Sowa, E. Martin, I. M. Martins, J. Schmidt, R. Depping, J. J. Weber, F. Rother, E. Hartmann, M. Bader, O. Riess, H. Tricoire, and T. Schmidt. "Karyopherin -3 is a key protein in the pathogenesis of spinocerebellar ataxia type 3 controlling the nuclear localization of ataxin-3." *Proceedings of the National Academy of Sciences of the United States of America* 115.11 (2018), pp. 2624–2633. doi: 10.1073/pnas.1716071115.

[99] C. P. Reina, X. Zhong, and R. N. Pittman. "Proteotoxic stress increases nuclear localization of ataxin-3." *Human Molecular Genetics* 19.2 (2010), pp. 235–49. doi: 10.1093/hmg/ddp482.

[100] S. Macedo-Ribeiro, L. Cortes, P. Maciel, and A. L. Carvalho. "Nucleocytoplasmic shuttling activity of ataxin-3." *PLoS One* 4.6 (2009). doi: 10.1371/journal.pone.0005834.

[101] U. Bichelmeier, T. Schmidt, J. Hubener, J. Boy, L. Ruttiger, K. Habig, S. Poths, M. Bonin, M. Knipper, W. J. Schmidt, J. Wilbertz, H. Wolburg, F. Laccone, and O. Riess. "Nuclear localization of ataxin-3 is required for the manifestation of symptoms in SCA3: in vivo evidence." *Journal of Neuroscience* 27.28 (2007), pp. 7418–28. doi: 10.1523/JNEUROSCI.4540-06.2007.

[102] J. Boy, T. Schmidt, H. Wolburg, A. Mack, S. Nuber, M. Bottcher, I. Schmitt, C. Holzmann, F. Zimmermann, A. Servadio, and O. Riess. "Reversibility of symptoms in a conditional mouse model of spinocerebellar ataxia type 3." *Human Molecular Genetics* 18.22 (2009), pp. 4282–4295. doi: 10.1093/hmg/ddp381.

[103] B. Burnett and R. N. Pittman. "The polyglutamine neurodegenerative protein ataxin 3 regulates aggresome formation." *Proceedings of the National Academy of Sciences of the United States of America* 102.12 (2005), pp. 4330–5. doi: 10.1073/pnas.0407252102.

[104] B. J. Winborn, S. M. Travis, S. V. Todi, K. M. Scaglione, P. Xu, A. J. Williams, R. E. Cohen, J. Peng, and H. L. Paulson. "The deubiquitinating enzyme ataxin-3, a polyglutamine disease protein, edits Lys63 linkages in mixed linkage ubiquitin chains." *Journal of Biological Chemistry* 283.39 (2008), pp. 26436–43. doi: 10.1074/jbc.M803692200.

[105] B. Burnett, F. Li, and R. N. Pittman. "The polyglutamine neurodegenerative protein ataxin-3 binds polyubiquitylated proteins and has ubiquitin protease activity." *Human Molecular Genetics* 12.23 (2003), pp. 3195–205. doi: 10.1093/hmg/ddg344.

[106] K. D. Wilsinson. "Ubiquitination and deubiquitination: targeting of proteins for degradation by the proteasome." *Seminars in Cell and Developmental Biology* 11.3 (2000), pp. 141–8. doi: 10.1006/scdb.2000.0164.

[107] J. S. Thrower, L. Hoffman, M. Rechsteiner, and C. M. Pickart. "Recognition of the polyubiquitin proteolytic signal." *EMBO Journal* 19.1 (2000), pp. 94–102. doi: 10.1093/emboj/19.1.94.

[108] X. Li, H. Liu, P. L. Fischhaber, and T.-S. Tang. "Toward therapeutic targets for SCA3: Insight into the role of Machado-Joseph disease protein ataxin-3 in misfolded proteins clearance." *Progress in Neurobiology* 132 (2015), pp. 34–58. doi: 10.1016/j.pneurobio.2015.06.004.

[109] Y. Tu, H. Liu, X. Zhu, H. Shen, X. Ma, F. Wang, M. Huang, J. Gong, X. Li, Y. Wang, C. Guo, and T.-S. Tang. "Ataxin-3 promotes genome integrity by stabilizing Chk1." *Nucleic Acids Research* 45.8 (2017), pp. 4532–4549. doi: 10.1093/nar/gkx095.

[110] H. Liu, X. Li, G. Ning, S. Zhu, X. Ma, X. Liu, C. Liu, M. Huang, I. Schmitt, U. Wullner, Y. Niu, C. Guo, Q. Wang, and T.-S. Tang. "The Machado-Joseph Disease Deubiquitinase Ataxin-3 Regulates the Stability and Apoptotic Function of p53." *PLoS Biology* 14.11 (2016). doi: 10.1371/journal.pbio.2000733.

[111] A. Ashkenazi, C. F. Bento, T. Ricketts, M. Vicinanza, F. Siddiqi, M. Pavel, F. Squitieri, M. C. Hardenberg, S. Imarisio, F. M. Menzies, and D. C. Rubinsztein. "Polyglutamine tracts regulate beclin 1-dependent autophagy." *Nature* 545.7652 (2017), pp. 108–111. doi: 10.1038/nature22078.

[112] A. J. Rodrigues, M. d. C. Costa, T. L. Silva, D. Ferreira, F. Bajanca, E. Logarinho, and P. Maciel. "Absence of ataxin-3 leads to cytoskeletal disorganization and increased cell death." *Biochimica Biophysica Acta* 1803.10 (2010), pp. 1154–63. doi: 10.1016/j.bbamcr.2010.07.004.

[113] R. Gao, Y. Liu, A. Silva-Fernandes, X. Fang, A. Paulucci-Holthauzen, A. Chatterjee, H. L. Zhang, T. Matsuura, S. C. abd T. Ashizawa, A. H. Koeppen, P. Maciel, T. K. Hazra, and P. S. Sarkar. "Inactivation of PNKP by mutant ATXN3 triggers apoptosis by activating the DNA damage-response pathway in SCA3." *PLoS Genetics* 11.1 (2015). doi: 10.1371/journal.pgen.1004834.

[114] C. A. Matos, C. Nobrega, S. R. Louros, B. Almeida, E. Ferreiro, J. Valero, L. P. de Almeida, S. Macedo-Ribeiro, and A. L. Carvalho. "Ataxin-3 phosphorylation decreases neuronal defects in spinocerebellar ataxia type 3 models." *Journal of Cell Biology* 212.4 (2016), pp. 465–480. doi: 10.1083/jcb.201506025.

[115] E. Fei, N. Jia, T. Zhang, X. Ma, H. Wang, C. Liu, W. Zhang, L. Ding, N. Nukina, and G. Wang. "Phosphorylation of ataxin-3 by glycogen synthase kinase 3beta at serine 256 regulates the aggregation of ataxin-3." *Biochemical and Biophysical Research Communications* 357.2 (2007), pp. 487–92. doi: 10.1016/j.bbrc.2007.03.160.

[116] S. V. Todi, B. J. Winborn, K. M. Scaglione, J. R. Blount, S. M. Travis, and H. L. Paulson. "Ubiquitination directly enhances activity of the deubiquitinating enzyme ataxin-3." *EMBO Journal* 28.4 (2009), pp. 372–382. doi: 10.1038/emboj.2008.289.

[117] W.-L. Tsou, A. A. Burr, M. Ouyang, J. R. Blount, K. M. Scaglione, and S. V. Todi. "Ubiquitination regulates the neuroprotective function of the deubiquitinase ataxin-3 in vivo." *Journal of Biological Chemistry* 288.48 (2013), pp. 34460–9. doi: 10.1074/jbc.M113.513903.

[118] B. Almeida, I. A. Abreu, C. A. Matos, J. S. Fraga, S. Fernandes, M. G. Macedo, R. Gutierrez-Gallego, P. J. B. Pereira, A. L. Carvalho, and S. Macedo-Ribeiro. "SUMOylation of the brain-predominant Ataxin-3 isoform modulates its interaction with p97." *Biochimica Biophysica Acta* 1852.9 (2015), pp. 1950–9. doi: 10.1016/j.bbadis.2015.06.010.

[119] Y.-F. Zhou, S.-S. Liao, Y.-Y. Luo, J.-G. Tang, J.-L. Wang, L.-F. Lei, J.-W. Chi, J. Du, H. Jiang, K. Xia, B.-S. Tang, and L. Shen. "SUMO-1 modification on K166 of polyQ-expanded ataxin-3 strengthens its stability and increases its cytotoxicity." *PLoS One* 8.1 (2013). doi: 10.1371/journal.pone.0054214.

[120] T. Mueller, P. Breuer, I. Schmitt, J. Walter, B. O. Evert, and U. Wullner. "CK2-dependent phosphorylation determines cellular localization and stability of ataxin-3." *Human Molecular Genetics* 18.17 (2009), pp. 3334–3343. doi: 10.1093/hmg/ddp274.

[121] M. Hayashi, K. Kobayashi, and H. Furuta. "Immunohistochemical study of neuronal intranuclear and cytoplasmic inclusions in Machado-Joseph disease." *Psychiatry and Clinical Neurosciences* 57.2 (2003), pp. 205–13. doi: 10.1046/j.1440-1819.2003.01102.x.

[122] N. F. Bence, R. M. Sampat, and R. R. Kopito. "Impairment of the ubiquitin-proteasome system by protein aggregation." *Science* 292.5521 (2001), pp. 1552–5. doi: 10.1126/science.292.5521.1552.

[123] M. S. Hipp, S.-H. Park, and F. U. Hartl. "Proteostasis impairment in protein-misfolding and -aggregation diseases." *Trends in Cell Biology* 24.9 (2014), pp. 506–14. doi: 10.1016/j.tcb.2014.05.003.

[124] T. Schmidt, K. S. Lindenberg, A. Krebs, L. Schols, F. Laccone, J. Herms, M. Rechsteiner, O. Riess, and G. B. Landwehrmeyer. "Protein surveillance machinery in brains with spinocerebellar ataxia type 3: redistribution and differential recruitment of 26S proteasome subunits and chaperones to neuronal intranuclear inclusions." *Annals of Neurology* 51.3 (2002), pp. 302–10. doi: 10.1002/ana.10101.

[125] H. Yang, J.-J. Li, S. Liu, J. Zhao, Y.-J. Jiang, A.-X. Song, and H.-Y. Hu. "Aggregation of polyglutamine-expanded ataxin-3 sequesters its specific interacting partners into inclusions: Implication in a loss-of-function pathology." *Scientific Reports* 4.6410 (2014). doi: 10.1038/srep06410.

[126] K. M. Donaldson, W. Li, K. A. Ching, S. Batalov, C.-C. Tsai, and C. A. P. Joazeiro. "Ubiquitin-mediated sequestration of normal cellular proteins into polyglutamine aggregates." *Proceedings of the National Academy of Sciences of the United States of America* 100.15 (2003), pp. 8892–7. doi: 10.1038/srep06410.

[127] E. W. Doss-Pepe, E. S. Stenroos, W. G. Johnson, and K. Madura. "Ataxin-3 interactions with rad23 and valosin-containing protein and its associations with ubiquitin chains and the proteasome are consistent with a role in ubiquitin-mediated proteolysis." *Molecular and Cellular Biology* 23.18 (2003), pp. 6469–83. doi: 10.1128/MCB.23.18.6469-6483.2003.

[128] Y. C. Tsai, P. S. Fishman, N. V. Thakor, and G. A. Oyler. "Parkin facilitates the elimination of expanded polyglutamine proteins and leads to preservation of proteasome function." *Journal of Biological Chemistry* 278.24 (2003), pp. 22044–55. doi: 10.1074/jbc.M212235200.

[129] N. R. Jana, P. Dikshit, A. Goswami, S. Kotliarova, S. Murata, K. Tanaka, and N. Nukina. "Co-chaperone CHIP associates with expanded polyglutamine protein and promotes their degradation by proteasomes." *Journal of Biological Chemistry* 280.12 (2005), pp. 11635–40. doi: 10.1074/jbc.M412042200.

[130] F. M. Menzies, J. Huebener, M. Renna, M. Bonin, O. Riess, and D. C. Rubinsztein. "Autophagy induction reduces mutant ataxin-3 levels and toxicity in a mouse model of spinocerebellar ataxia type 3." *Brain* 133.1 (2010), pp. 93–104. doi: 10.1093/brain/awp292.

[131] I. Onofre, N. Mendonca, S. Lopes, R. Nobre, J. B. de Melo, I. M. Carreira, C. Januario, A. F. Goncalves, and L. P. de Almeida. "Fibroblasts of Machado Joseph Disease patients reveal autophagy impairment." *Scientific Reports* 6.28220 (2016). doi: 10.1038/srep28220.

[132] I. Nascimento-Ferreira, T. Santos-Ferreira, L. Sousa-Ferreira, G. Auregan, I. Onofre, S. Alves, N. Dufour, V. F. C. Gould, A. Koeppen, N. Deglon, and L. P. de Almeida. "Overexpression of the autophagic beclin-1 protein clears mutant ataxin-3 and alleviates Machado-Joseph disease." *Brain* 134.5 (2011), pp. 1400–15. doi: 10.1038/srep28220.

[133] R. R. Kopito. "Aggresomes, inclusion bodies and protein aggregation." *Trends in Cell Biology* 10.12 (2000), pp. 524–30. doi: 10.1016/s0962-8924(00)01852-3.

[134] J. A. Olzmann, L. Li, and C. L. S. "Aggresome formation and neurodegenerative diseases: therapeutic implications." *Current Medicinal Chemistry* 15.1 (2008), pp. 47–60. doi: 10.2174/092986708783330692.

[135] A.-H. Chou, T.-H. Yeh, P. Ouyang, Y.-L. Chen, S.-Y. Chen, and H.-L. Wang. "Polyglutamine-expanded ataxin-3 causes cerebellar dysfunction of SCA3 transgenic mice by inducing transcriptional dysregulation." *Neurobiology of Disease* 31.1 (2008), pp. 89–101. doi: 10.1016/j.nbd.2008.03.011.

[136] A. Chatterjee, S. Saha, A. Chakraborty, A. Silva-Fernandes, S. M. Mandal, A. Neves-Carvalho, Y. Liu, R. K. Pandita, M. L. Hegde, P. M. Hegde, I. Boldogh, T. Ashizawa, A. H. Koeppen, T. K. Pandita, P. Maciel, P. S. Sarkar, and T. K. Hazra. "The role of the mammalian DNA end-processing enzyme polynucleotide kinase 3'-phosphatase in spinocerebellar ataxia type 3 pathogenesis." *PLoS Genetics* 11.1 (2015). doi: 10.1371/journal.pgen.1004749.

[137] N. Kazachkova, M. Raposo, R. Montiel, T. Cymbron, C. Bettencourt, A. Silva-Fernandes, S. Silva, P. Maciel, and M. Lima. "Patterns of mitochondrial DNA damage in blood and brain tissues of a transgenic mouse model of Machado-Joseph disease." *Neurodegenerative Diseases* 11.4 (2013), pp. 206–14. doi: 10.1159/000339207.

[138] A. M. de Assis, J. A. M. Saute, A. Longoni, C. B. Haas, V. R. Torrez, A. W. Brochier, G. N. Souza, G. V. Furtado, T. C. Gheno, A. Russo, T. L. Monte, R. M. Castilhos, A. Shumacher-Schuh, R. D Avila, K. C. Donis, C. R. d. M. Rieder, D. O. Souza, S. Camey, V. B. Leotti, L. B. Jardim, and

L. V. Portela. “Peripheral Oxidative Stress Biomarkers in Spinocerebellar Ataxia Type 3/Machado-Joseph Disease.” *Frontiers in Neurology* 8.485 (2017). doi: 10.3389/fneur.2017.00485.

[139] J. Hubener, F. Vauti, C. Funke, H. Wolburg, Y. Ye, T. Schmidt, K. Wolburg-Buchholz, I. Schmitt, A. Gardyan, S. Driessen, H.-H. Arnold, H. P. Nguyen, and O. Riess. “N-terminal ataxin-3 causes neurological symptoms with inclusions, endoplasmic reticulum stress and ribosomal dislocation.” *Brain* 134.7 (2011), pp. 1925–42. doi: 10.1093/brain/awr118.

[140] R. Y. Hampton. “ER-associated degradation in protein quality control and cellular regulation.” *Current Opinion in Cell Biology* 14.4 (2002), pp. 476–82. doi: 10.1016/s0955-0674(02)00358-7.

[141] Y. He, X. Yao, N. Taylor, Y. Bai, T. Lovenberg, and A. Bhattacharya. “RNA sequencing analysis reveals quiescent microglia isolation methods from postnatal mouse brains and limitations of BV2 cells.” *Journal of Neuroinflammation* 15.153 (2018). doi: 10.1186/s12974-018-1195-4.

[142] D. P. Schafer and B. Stevens. “Microglia function in central nervous system development and plasticity.” *Cold Spring Harbor Perspectives in Bioloy* 7.10 (2015). doi: 10.1101/cshperspect.a020545.

[143] B. O. Evert, I. R. Vogt, C. Kindermann, L. Ozimek, R. A. de Vos, I. Schmitt, T. Klockgether, and U. Wullner. “Inflammatory genes are upregulated in expanded ataxin-3-expressing cell lines and Spinocerebellar Ataxia type 3 brains.” *Journal of Neuroscience* 21.15 (2001), pp. 5389–96. doi: 10.1523/JNEUROSCI.21-15-05389.2001.

[144] D. Duarte-Lobo, R. J. Nobre, C. O. Miranda, D. Pereira, J. Castelhano, J. Sereno, A. Koeppen, M. Castelo-Branco, and L. P. de Almeida. “The blood-brain barrier is disrupted in Machado-Joseph disease/spinocerebellar ataxia type 3: evidence from transgenic mice and human post-mortem samples.” *Acta Neuropathologica Communications* 8.152 (2020). doi: 10.1186/s40478-020-00955-0.

[145] J. Cunha-Santos, J. Duarte-Neves, V. Carmona, L. Guarente, L. P. de Almeida, and C. Cavadas. “Caloric restriction blocks neuropathology and motor deficits in Machado–Joseph disease mouse models through SIRT1 pathway.” *Nature Communications* 7.11445 (2016). doi: 10.1038/ncomms11445.

[146] G. da Silva Carvalho, J. A. M. Saute, C. B. Haas, V. R. Torrez, A. W. Brochier, G. N. Souza, G. V. Furtado, T. Gheno, A. Russo, T. L. Monte, A. Schumacher-Schuh, R. D Avila, K. C. Donis, R. M. Castilhos, D. O. Souza, M. L. Saraiva-Pereira, V. L. Torman, S. Camey, L. V. Portela, and L. B. Jardim. “Cytokines in Machado Joseph Disease/Spinocerebellar Ataxia 3.” *Cerebellum* 15.4 (2016), pp. 518–25. doi: 10.1007/s12311-015-0719-z.

[147] B. Parajuli, H. Horiuchi, T. Mizuno, H. Takeuchi, and A. Suzumura. “CCL11 enhances excitotoxic neuronal death by producing reactive oxygen species in microglia.” *Glia* 63.12 (2015), pp. 2274–84. doi: 10.1002/glia.22892.

[148] M. Cvetanovic, M. Ingram, H. Orr, and P. Opal. "Early activation of microglia and astrocytes in mouse models of spinocerebellar ataxia type 1." *Neuroscience* 289 (2015), pp. 289–99. doi: 10.1016/j.neuroscience.2015.01.003.

[149] W. Qu, A. Johnson, J. H. Kim, A. Lukowicz, D. Svedberg, and M. Cvetanovic. "Inhibition of colony-stimulating factor 1 receptor early in disease ameliorates motor deficits in SCA1 mice." *Journal of Neuroinflammation* 14.107 (2017). doi: 10.1186/s12974-017-0880-z.

[150] M. Politis, N. Lahiri, F. Niccolini, P. Su, K. Wu, P. Giannetti, R. I. Scahill, F. E. Turkheimer, S. J. Tabrizi, and P. Piccini. "Increased central microglial activation associated with peripheral cytokine levels in premanifest Huntington's disease gene carriers." *Neurobiology of disease* 83 (2015), pp. 115–21. doi: 10.1016/j.nbd.2015.08.011.

[151] A. Crotti, C. Benner, B. E. Kerman, D. Gosselin, C. Lagier-Tourenne, C. Zuccato, E. Cattaneo, F. H. Gage, D. W. Cleveland, and C. K. Glass. "Mutant Huntingtin promotes autonomous microglia activation via myeloid lineage-determining factors." *Nature Neuroscience* 17.4 (2014), pp. 513–21. doi: 10.1038/nn.3668.

[152] F. Perez-Cerda, M. V. Sanchez-Gomez, and C. Matute. "Pío del Río Hortega and the discovery of the oligodendrocytes." *Frontiers in Neuroanatomy* 9.92 (2015). doi: 10.3389/fnana.2015.00092.

[153] S. D. Benusa, N. M. George, and J. L. Dupree. "Microglial heterogeneity: distinct cell types or differential functional adaptation?" *Neuroimmunology and Neuroinflammation* 7 (2020), pp. 248–63. doi: 10.20517/2347-8659.2020.03.

[154] F. Ginhoux, M. Greter, M. Leboeuf, S. Nandi, P. See, S. Gokhan, M. F. Mehler, S. J. Conway, L. G. Ng, E. R. Stanley, I. M. Samokhvalov, and M. Merad. "Fate mapping analysis reveals that adult microglia derive from primitive macrophages." *Science* 330.6005 (2010), pp. 841–5. doi: 10.1126/science.1194637.

[155] E. G. Perdiguero, K. Klapproth, C. Schulz, K. Busch, E. Azzoni, L. Crozet, H. Garner, C. Trouillet, M. F. de Bruijn, F. Geissmann, and H.-R. Rodewald. "Tissue-resident macrophages originate from yolk-sac-derived erythro-myeloid progenitors." *Nature* 518 (2014), pp. 547–551. doi: 10.1038/nature13989.

[156] Z. Chen and B. D. Trapp. "Microglia and neuroprotection." *Journal of Neurochemistry* 136 (2015), pp. 10–17. doi: 10.1111/jnc.13062.

[157] T. L. Tay, J. C. Savage, C. W. Hui, K. Bisht, and M.-E. Tremblay. "Microglia across the lifespan: from origin to function in brain development, plasticity and cognition." *Journal of Physiology* 595.6 (2017), pp. 1929–1945. doi: 10.1113/JP272134.

[158] D. Nayak, T. L. Roth, and D. B. McGavern. "Microglia Development and function." *Annual Review of Immunology* 32 (2014), pp. 367–402. doi: 10.1146/annurev-immunol-032713-120240.

[159] K. Kierdorf, D. Erny, T. Goldmann, V. Sander, C. Schulz, E. G. Perdiguero, P. Wieghofer, A. Heinrich, P. Riemke, C. Holscher, D. N. Muller, B. Luckow, T. Brocker, K. Debowski, G. Fritz, G. Opdenakker, A. Diefenbach, K. Biber, M. Heikenwalder, F. Geissmann, F. Rosenbauer, and M. Prinz. "Microglia emerge from erythromyeloid precursors via Pu.1- and Irf8-dependent pathways." *Nature Neuroscience* 16 (2013), pp. 273–280. doi: 10.1038/nn.3318.

[160] A. Buttgereit, I. Lelios, X. Yu, M. Vrohlings, N. R. Krakoski, E. L. Gautier, R. Nishinakamura, B. Becher, and M. Greter. "Sall1 is a transcriptional regulator defining microglia identity and function." *Nature Immunology* 17.12 (2016), pp. 1397–1406. doi: 10.1038/ni.3585.

[161] C. Schulz, E. G. Perdiguero, L. Chorro, H. Szabo-Rogers, N. Cagnard, K. Kierdorf, M. Prinz, B. Wu, S. E. W. Jacobsen, J. W. Pollard, J. Frampton, K. J. Liu, and F. Geissmann. "A lineage of myeloid cells independent of Myb and hematopoietic stem cells." *Science* 336.6077 (2012), pp. 86–90. doi: 10.1126/science.1219179.

[162] Y. Wang, K. J. Szretter, W. Vermi, S. Gilfillan, C. Rossini, M. Cella, A. D. Barrow, M. S. Diamond, and M. Colonna. "IL-34 is a tissue-restricted ligand of CSF1R required for the development of Langerhans cells and microglia." *Nature Immunology* 13 (2012), pp. 753–760. doi: 10.1038/ni.2360.

[163] D. Erny, A. L. H. de Angelis, D. Jaitin, P. Wieghofer, O. Staszwski, E. David, H. Keren-Shaul, T. Mahlakoiv, K. Jakobshagen, T. Buch, V. Schwierzeck, O. Utermohlen, E. Chun, W. S. Garrett, K. D. McCoy, A. Diefenbach, P. Staeheli, B. Stecher, I. Amit, and M. Prinz. "Host microbiota constantly control maturation and function of microglia in the CNS." *Nature Neuroscience* 18 (2015), pp. 965–977. doi: 10.1038/nn.4030.

[164] M. S. Thion, D. Low, A. Silvin, J. Chen, P. Grisel, J. Schulte-Schrepping, R. Blecher, T. Ulas, P. Squarzoni, G. Hoeffel, F. Coulpier, E. Siopi, F. S. David, C. Scholz, F. Shihui, J. Lum, A. A. Amoyo, A. Larbi, M. Poidinger, A. Buttgereit, P.-M. Lledo, M. Greter, J. K. Y. Chan, I. Amit, M. Beyer, J. L. Schultze, A. Schlitzer, S. Pettersson, F. Ginhoux, and S. Garel. "Microbiome Influences Prenatal and Adult Microglia in a Sex-Specific Manner." *Cell* 172.3 (2018), pp. 500–516. doi: 10.1016/j.cell.2017.11.042.

[165] O. Butovsky, M. P. Jedrychowski, C. S. Moore, R. Cialic, A. J. Lanser, G. Gabriely, T. Koeglsperger, B. Dake, P. M. Wu, C. E. Doykan, Z. Fanek, L. Liu, Z. Chen, J. D. Rothstein, R. M. Ransohoff, S. P. Gygi, J. P. Antel, and H. L. Weiner. "Identification of a unique TGF-β-dependent molecular and functional signature in microglia." *Nature Neuroscience* 17.1 (2014), pp. 131–43. doi: 10.1038/nn.3599.

[166] O. Butovsky and H. L. Weiner. "Microglial signatures and their role in health and disease." *Nature Reviews Neuroscience* 19.10 (2018), pp. 622–635. doi: 10.1038/s41583-018-0057-5.

[167] B. Ajami, J. L. Bennett, C. Krieger, W. Tetzlaff, and F. M. V. Rossi. “Local self-renewal can sustain CNS microglia maintenance and function throughout adult life.” *Nature Neuroscience* 10 (2007), pp. 1538–1543. doi: 10.1038/nn2014.

[168] P. Reu, A. Khosravi, S. Bernard, J. E. Mold, M. Salehpour, K. Alkass, S. Perl, J. Tisdale, G. Possnert, H. Druid, and J. Frisen. “The Lifespan and Turnover of Microglia in the Human Brain.” *Cell Reports* 20.4 (2017), pp. 779–784. doi: 10.1016/j.celrep.2017.07.004.

[169] L. Zhan, L. Fan, L. Kodama, P. D. Sohn, M. Y. Wong, G. A. Mousa, Y. Zhou, Y. Li, and L. Gan. “A MAC2-positive progenitor-like microglial population is resistant to CSF1R inhibition in adult mouse brain.” *Elife* 9 (2020). doi: 10.7554/eLife.51796.

[170] Y. Huang, Z. Xu, S. Xiong, F. Sun, G. Qin, G. Hu, J. Wang, L. Zhao, Y.-X. Liang, T. Wu, Z. Lu, M. S. Humayun, K.-F. So, Y. Pan, N. Li, T.-F. Yuan, Y. Rao, and B. Peng. “Repopulated microglia are solely derived from the proliferation of residual microglia after acute depletion.” *Nature Neuroscience* 21 (2018), pp. 530–540. doi: 10.1038/s41593-018-0090-8.

[171] A. Mildner, H. Schmidt, M. Nitsche, D. Merkler, U.-K. Hanisch, M. Mack, M. Heikenwalder, W. Bruck, J. Priller, and M. Prinz. “Microglia in the adult brain arise from Ly-6ChiCCR2+ monocytes only under defined host conditions.” *Nature Neuroscience* 10.12 (2007), pp. 1544–53. doi: 10.1038/nn2015.

[172] J. C. Cronk, A. J. Filiano, A. Louveau, I. Marin, R. Marsh, E. Ji, D. H. Goldman, I. Smirnov, N. Geraci, S. Acton, C. C. Overall, and J. Kipnis. “Peripherally derived macrophages can engraft the brain independent of irradiation and maintain an identity distinct from microglia.” *Journal of Experimental Medicine* 215.6 (2018), pp. 1627–1647. doi: 10.1084/jem.20180247.

[173] S. Bachiller, I. Jiménez-Ferrer, A. Paulus, Y. Yang, M. Swanberg, T. Deierborg, and A. Boza-Serrano. “Microglia in Neurological Diseases: A Road Map to Brain-Disease Dependent-Inflammatory Response.” *Frontiers in Cellular Neuroscience* 12.488 (2018). doi: 10.3389/fncel.2018.00488.

[174] Q. Li and B. A. Barres. “Microglia and macrophages in brain homeostasis and disease.” *Nature Reviews Immunology* 18 (2018), pp. 225–242. doi: 10.1038/nri.2017.125.

[175] I. M. Chiu, E. T. A. Morimoto, H. Goodarzi, J. T. Liao, S. O. Keeffe, H. P. Phatnani, M. Muratet, M. C. Carrol, S. Levy, S. Tavazoie, R. M. Myers, and T. Maniatis. “A neurodegeneration-specific gene-expression signature of acutely isolated microglia from an amyotrophic lateral sclerosis mouse model.” *Cell Reports* 4.2 (2013), pp. 385–401. doi: 10.1016/j.celrep.2013.06.018.

[176] S. E. Hickman, N. D. Kingery, T. K. Ohsumi, M. L. Borowsky, L.-C. Wang, T. K. Means, and J. E. Khoury. “The microglial sensome revealed by direct RNA sequencing.” *Nature Neuroscience* 16 (2013), pp. 1896–1905. doi: 10.1038/nn.3554.

[177] C. Zhu, J. M. Kros, M. v. der Weiden, P. Zheng, C. Cheng, and D. A. M. Mustafa. "Expression site of P2RY12 in residential microglial cells in astrocytomas correlates with M1 and M2 marker expression and tumor grade." *Acta Neuropathologica Communications* 5.4 (2017). doi: 10.1186/s40478-016-0405-5.

[178] M. L. Bennett, F. C. Bennett, S. A. Liddelow, B. Ajami, J. L. Zamaniam, N. B. Fernhoff, S. B. Mulinyawe, C. J. Bohlen, A. Adil, A. Tucker, I. L. Weissman, E. F. Chang, G. Li, G. A. Grant, M. G. H. Gephart, and B. A. Barres. "New tools for studying microglia in the mouse and human CNS." *PNAS* 113.12 (2016), pp. 1738–1746. doi: 10.1073/pnas.1525528113.

[179] J. Muffat, Y. Li, B. Yuan, M. Mitalipova, A. Omer, S. Corcoran, G. Bakiasi, L.-H. Tsai, P. Aubourg, R. M. Ransohoff, and R. Jaenisch. "Efficient derivation of microglia-like cells from human pluripotent stem cells." *Nature Medicine* 22 (2016), pp. 1358–1367. doi: 10.1038/nm.4189.

[180] E. M. Abud, R. N. Ramirez, E. S. Martinez, L. M. Healy, C. H. H. Nguyen, S. A. Newman, A. V. Yeromin, V. M. Scarfone, S. E. Marsh, C. Fimbres, C. A. Caraway, G. M. Fote, A. M. Madany, A. Agrawal, R. Kayed, K. H. Gylys, M. D. Cahalan, B. J. Cummings, J. P. Antel, A. Mortazavi, M. J. Carson, W. W. Poon, and M. Blurton-Jones. "iPSC-derived human microglia-like cells to study neurological diseases." *Neuron* 94.2 (2017), pp. 278–293. doi: 10.1016/j.neuron.2017.03.042.

[181] F. Ginhoux and M. Prinz. "Origin of microglia: current concepts and past controversies." *Cold Spring Harbor perspectives in Biology* 7.8 (2015). doi: 10.1101/cshperspect.a020537.

[182] E. J. Davis, T. D. Foster, and W. E. Thomas. "Cellular forms and functions of brain microglia." *Brain Research Bulletin* 34.1 (1994), pp. 73–78. doi: 10.1016/0361-9230(94)90189-9.

[183] M. d. M. Fernández-Arjona, J. M. Grondona, P. Fernández-Llebrez, and M. D. Lopez-Ávalos. "Microglial morphometric parameters correlate with the expression level of IL-1B, and allow identifying different activated morphotypes." *Frontiers in Cellular Neuroscience* 13.472 (2019). doi: 10.3389/fncel.2019.00472.

[184] A. Nimmerjahn, F. Kirchhoff, and F. Helmchen. "Resting microglial cells are highly dynamic surveillants of brain parenchyma in vivo." *Science* 308.5726 (2005), pp. 1314–8. doi: 10.1126/science.1110647.

[185] A. Nimmerjahn. "Two-Photon Imaging of Microglia in the Mouse Cortex In Vivo." *Cold Spring Harbor Protocols* 2012.5 (2012). doi: 10.1101/pdb.prot069294.

[186] K. Biber and M. L. Block. "Neuroprotection Versus Neurotoxicity." *In M. Tremblay & A. Sierra (Eds.), Microglia in Health and Disease* (2014), pp. 145–172. doi: 10.1007/978-1-4939-1429-6_6.

[187] D. Gomes-Nicola and V. H. Perry. "Microglial dynamics and role in the healthy and diseased brain: a paradigm of functional plasticity." *Neuroscientist* 21.2 (2015), pp. 169–84. doi: 10.1177/1073858414530512.

[188] U. B. Eyo and M. E. Dailey. “Microglia: Key Elements in Neural Development, Plasticity, and Pathology.” *Journal Neuroimmune Pharmacology* 8.3 (2013), pp. 494–509. doi: 10.1007/s11481-013-9434-z.

[189] D. M. Angelova and D. R. Brown. “Microglia and the aging brain: are senescent microglia the key to neurodegeneration?” *Journal of Neurochemistry* 151.6 (2019), pp. 676–688. doi: 10.1111/jnc.14860.

[190] B. Stevens, N. J. Allen, L. E. Vazquez, G. R. Howell, K. S. Christopherson, N. Nouri, K. D. Micheva, A. K. Mehalow, A. D. Huberman, B. Stafford, A. Sher, A. M. Litke, J. D. Lambris, S. J. Smith, S. W. M. John, and B. A. Barres. “The classical complement cascade mediates CNS synapse elimination.” *Cell* 131.6 (2007), pp. 1164–78. doi: 10.1016/j.cell.2007.10.036.

[191] L. Fourgeaud, P. G. Traves, Y. Tufail, H. Leal-Bailey, E. D. Lew, P. G. Burrola, P. Callaway, A. Zagorska, C. V. Rothlin, A. Nimmerjahn, and G. Lemke. “TAM receptors regulate multiple features of microglial physiology.” *Nature* 532.7598 (2016), pp. 240–244. doi: 10.1038/nature17630.

[192] A. Sierra, J. M. Encinas, J. J. P. Deudero, J. H. Chancey, G. Enikolopov, L. S. Overstreet-Wadiche, S. E. Tsirka, and M. Maletic-Savatic. “Microglia shape adult hippocampal neurogenesis through apoptosis-coupled phagocytosis.” *Cell Stem Cell* 7.4 (2010), pp. 483–95. doi: 10.1016/j.stem.2010.08.014.

[193] O. Butovsky, Y. Ziv, A. Schwartz, G. Landa, A. E. Talpalar, S. Pluchino, G. Martino, and M. Schwartz. “Microglia activated by IL-4 or IFN-gamma differentially induce neurogenesis and oligodendrogenesis from adult stem/progenitor cells.” *Molecular and Cellular Neurosciences* 31.1 (2006), pp. 149–60. doi: 10.1016/j.mcn.2005.10.006.

[194] V. Nieto-Estevez, C. Defterali, and C. Vicario-Abejon. “IGF-I: A Key Growth Factor that Regulates Neurogenesis and Synaptogenesis from Embryonic to Adult Stages of the Brain.” *Frontiers in Neuroscience* 10.52 (2016). doi: 10.3389/fnins.2016.00052.

[195] A. Wlodarczyk, I. R. Holtman, M. Krueger, N. Yogev, J. Bruttger, R. Khorooshi, A. Benmamar-Badel, J. J. d. Boer-Bergsma, N. A Martin, K. Karram, I. Kramer, E. W. Boddeke, A. Waisman, B. J. Eggen, and T. Owens. “A novel microglial subset plays a key role in myelinogenesis in developing brain.” *EMBO Journal* 36.22 (2017), pp. 3292–3308. doi: 10.15252/embj.201696056.

[196] D. A. Galloway, A. E. M. Phillips, D. R. J. Owen, and C. S. Moore. “Phagocytosis in the Brain: Homeostasis and Disease.” *Frontiers in Immunology* 10.790 (2019). doi: 10.3389/fimmu.2019.00790.

[197] G. C. Brown and J. J. Neher. “Microglial phagocytosis of live neurons.” *Nature Reviews Neuroscience* 15.4 (2014), pp. 209–16. doi: 10.1038/nrn3710.

[198] D. J. Finneran and K. R. Nash. “Neuroinflammation and fractalkine signaling in Alzheimer’s disease.” *Journal of Neuroinflammation* 16.30 (2019). doi: 10.1186/s12974-019-1412-9.

[199] C. Limatola and R. M. Ransohoff. “Modulating neurotoxicity through CX3CL1/CX3CR1 signaling.” *Frontiers in Cellular Neuroscience* 8.229 (2014). doi: 10.3389/fncel.2014.00229.

[200] G. Manich, M. Recasens, T. Valente, B. Almolda, B. Gonzalez, and B. Castellano. “Role of the CD200-CD200R Axis During Homeostasis and Neuroinflammation.” *Neuroscience* 405 (2019), pp. 118–136. doi: 10.1016/j.neuroscience.2018.10.030.

[201] H. S. Kwon and S.-H. Koh. “Neuroinflammation in neurodegenerative disorders: the roles of microglia and astrocytes.” *Translational Neurodegeneration* 9.42 (2020). doi: 10.1186/s40035-020-00221-2.

[202] W.-W. Chen, X. Zhang, and W.-J. Huang. “Role of neuroinflammation in neurodegenerative diseases.” *Molecular Medicine Reports* 13.4 (2016), pp. 3391–3396. doi: 10.3892/mmr.2016.4948.

[203] A. Sobue, O. Komine, Y. Hara, F. Endo, H. Mizoguchi, S. Watanabe, S. Murayama, T. Saito, T. C. Saido, N. Sahara, M. Higuchi, T. Ogi, and K. Yamanaka. “Microglial gene signature reveals loss of homeostatic microglia associated with neurodegeneration of Alzheimer´s disease.” *Acta Neuropathologica Communications* 9.1 (2021). doi: 10.1186/s40478-020-01099-x.

[204] B. Spittau. “Aging Microglia—Phenotypes, Functions and Implications for Age-Related Neurodegenerative Diseases.” *Frontiers in Aging Neuroscience* 9.194 (2017). doi: 10.3389/fnagi.2017.00194.

[205] W. Li, A. Turner, P. Aggarwal, A. Matter, E. Storvick, D. K. Arnett, and U. Broeckel. “Comprehensive evaluation of AmpliSeq transcriptome, a novel targeted whole transcriptome RNA seencing methodology for global gene expression analysis.” *BMC Genomics* 16.1069 (2015). doi: 10.1186/s12864-015-2270-1.

[206] L.-R. Liu, J.-C. Liu, J.-S. Bao, Q.-Q. Bai, and G.-Q. Wang. “Interaction of Microglia and Astrocytes in the Neurovascular Unit.” *Frontiers in Immunology* 11.1024 (2021). doi: 10.3389/fimmu.2020.01024.

[207] B. T. Casali and E. G. Reed-Geaghan. “Microglial Function and Regulation during Development, Homeostasis and Alzheimer’s Disease.” *Cells* 10.4 (2021). doi: 10.3390/cells10040957.

[208] E. Mondo, S. C. Becker, A. G. Kautzman, M. Schifferer, C. E. Baer, J. Chen, E. J. Huang, M. Simons, and D. P. Schafer. “A Developmental Analysis of Juxtavascular Microglia Dynamics and Interactions with the Vasculature.” *The Journal of Neuroscience* 40.34 (2020), pp. 6503–6521. doi: 10.1523/JNEUROSCI.3006-19.2020.

[209] S. A. Liddelow and B. A. Barres. “Reactive Astrocytes: Production, Function, and Therapeutic Potential.” *Immunity* 46.6 (2017), pp. 957–967. doi: 10.1016/j.immuni.2017.06.006.

[210] D. P. Schafer, E. K. Lehrman, A. G. Kautzman, R. Koyama, A. R. Mardinly, R. Yamasaki, R. M. Ransohoff, M. E. Greenberg, B. A. Barres, and B. Stevens. "Microglia sculpt postnatal neural circuits in an activity and complement-dependent manner." *Neuron* 74.4 (2012), pp. 691–705. doi: 10.1016/j.neuron.2012.03.026.

[211] J. L. Marin-Teva, I. Dusart, C. Colin, A. Gervais, N. van Rooijen, and M. Mallat. "Microglia Promote the Death of Developing Purkinje Cells." *Neuron* 41.4 (2004), pp. 535–547. doi: 10.1016/S0896-6273(04)00069-8.

[212] N. Hagemeyer, K.-M. Hanft, M.-A. Akriditou, N. Unger, E. S. Park, E. R. Stanley, O. Staszwski, L. Dimou, and M. Prinz. "Microglia contribute to normal myelinogenesis and to oligodendrocyte progenitor maintenance during adulthood." *Acta Neuropathologica* 134.3 (2017), pp. 441–458. doi: 10.1007/s00401-017-1747-1.

[213] H. Keren-Shaul, A. Spinrad, A. Weiner, O. Matcovitch-Natan, R. Dvir-Szternfeld, T. K. Ulland, E. David, K. Baruch, D. Lara-Astaiso, B. Toth, S. Itzkovitz, M. Colonna, M. Schwartz, and I. Amit. "A Unique Microglia Type Associated with Restricting Development of Alzheimer's Disease." *Cell* 169.7 (2017), pp. 1276–1290. doi: 10.1016/j.cell.2017.05.018.

[214] C. A. McPherson, A. D. Kraft, and G. J. Harry. "Injury-induced neurogenesis: consideration of resident microglia as supportive of neural progenitor cells." *Neurotoxicity Research* 19.2 (2011), pp. 341–52. doi: 10.1007/s12640-010-9199-6.

[215] P. E. Batchelor, G. T. Liberatore, J. Y. Wong, M. J. Porritt, F. Frerichs, G. A. Donnan, and D. W. Howells. "Activated macrophages and microglia induce dopaminergic sprouting in the injured striatum and express brain-derived neurotrophic factor and glial cell line-derived neurotrophic factor." *Journal of Neuroscience* 19.5 (1999), pp. 1708–16. doi: 10.1523/JNEUROSCI.19-05-01708.1999.

[216] C. Lecours, M. Bordeleau, L. Cantin, M. Parent, T. D. Paolo, and M.-V. Tremblay. "Microglial Implication in Parkinson's Disease: Loss of Beneficial Physiological Roles or Gain of Inflammatory Functions?" *Frontiers in Cellular Neuroscience* 12.282 (2018). doi: 10.3389/fncel.2018.00282.

[217] E. K. Lehrman, D. K. Wilton, E. Y. Litvina, C. A. Welsh, S. T. Chang, A. Frouin, A. J. Walker, M. D. Heller, H. Umemori, C. Chen, and B. Stevens. "CD47 Protects Synapses from Excess Microglia-Mediated Pruning during Development." *Neuron* 100.1 (2018), pp. 120–134. doi: 10.1016/j.neuron.2018.09.017.

[218] J. T. Rogers, J. M. Morganti, A. D. Bachstetter, C. E. Hudson, M. M. Peters, B. A. Grimming, E. J. Weeber, P. C. Bickford, and C. Gemma. "CX3CR1 Deficiency Leads to Impairment of Hippocampal Cognitive Function and Synaptic Plasticity." *Journal of Neuroscience* 31.45 (2011), pp. 16241–16250. doi: 10.1523/JNEUROSCI.3667-11.2011.

[219] S. E. Haynes, G. Hollopeter, G. Yang, D. Kurpius, M. E. Dailey, W.-B. Gan, and D. Julius. "The P2Y12 receptor regulates microglial activation by extracellular nucleotides." *Nature Neuroscience* 9.12 (2006), pp. 1512–9. doi: 10.1038/nn1805.

[220] T. R. Jay, V. E. v. Saucken, B. Munoz, J. F. Codocedo, B. K. Atwood, B. T. Lamb, and G. E. Landreth. "TREM2 is required for microglial instruction of astrocytic synaptic engulfment in neurodevelopment." *Glia* 67.10 (2019), pp. 1873–1892. doi: 10.1002/glia.23664.

[221] B. Erblich, L. Zhu, A. M. Etgen, K. Dobrenis, and J. W. Pollard. "Absence of Colony Stimulation Factor-1 Receptor Results in Loss of Microglia, Disrupted Brain Development and Olfactory Deficits." *PLoS One* 6.10 (2011). doi: 10.1371/journal.pone.0026317.

[222] M. R. P. Elmore, A. R. Najafi, M. A. Koike, N. N. Dagher, E. E. Spangenberg, R. A. Rice, M. Kitazawa, B. Matusow, H. Nguyen, B. L. West, and K. N. Green. "Colony-stimulating factor 1 receptor signaling is necessary for microglia viability, unmasking a microglia progenitor cell in the adult brain." *Neuron* 82.2 (2014), pp. 380–97. doi: 10.1016/j.neuron.2014.02.040.

[223] J. Sosna, S. Philipp, R. Albay, J. M. Reyes-Ruiz, D. Baglietto-Vargas, F. M. LaFerla, and C. G. Glabe. "Early long-term administration of the CSF1R inhibitor PLX3397 ablates microglia and reduces accumulation of intraneuronal amyloid, neuritic plaque deposition and pre-fibrillar oligomers in 5XFAD mouse model of Alzheimer's disease." *Molecular Neurodegeneration* 13.11 (2018). doi: 10.1186/s13024-018-0244-x.

[224] R. M. Hoek, S. R. Ruuls, C. A. Murphy, G. J. Wright, R. Goddard, S. M. Zurawski, B. Blom, M. E. Homola, W. J. Streit, M. H. Brown, A. N. Barclay, and J. D. Sedgwick. "Down-regulation of the macrophage lineage through interaction with OX2 (CD200)." *Science* 290.5497 (2000), pp. 1768–71. doi: 10.1126/science.290.5497.1768.

[225] H. Sun, X. He, X. Tao, T. Hou, M. Chen, M. He, and H. Liao. "The CD200/CD200R signaling pathway contributes to spontaneous functional recovery by enhancing synaptic plasticity after stroke." *Journal of Neuroinflammation* 17.171 (2020). doi: 10.1186/s12974-020-01845-x.

[226] D. Kempuraj, R. Thangavel, P. A. Natteru, G. P. Selvakumar, D. Saeed, H. Zahoor, S. Zaheer, S. S. Iyer, and A. Zaheer. "Neuroinflammation Induces Neurodegeneration." *Journal of Neurology, Neurosurgery and Spine* 1.1 (2017).

[227] C. K. Glass, K. Saijo, B. Winner, M. C. Marchetto, and F. H. Gage. "Mechanisms underlying inflammation in neurodegeneration." *Cell* 140.6 (2010), pp. 918–34. doi: 10.1016/j.cell.2010.02.016.

[228] J. Stephenson, E. Nutma, P. van der Valk, and S. Amor. "Inflammation in CNS neurodegenerative diseases." *Immunology* 154.2 (2018), pp. 204–219. doi: 10.1111/imm.12922.

[229] W. Zhao, W. Xie, Q. Xiao, D. R. Beers, and S. H. Appel. "Protective effects of an anti-inflammatory cytokine, interleukin-4, on motoneuron toxicity induced by activated microglia." *Journal of Neurochemistry* 99.4 (2006), pp. 1176–87. doi: 10.1111/j.1471-4159.2006.04172.x.

[230] O. Butovsky, S. Siddiqui, G. Gabriely, A. J. Lanser, B. Dake, G. Murugaiyan, C. E. Doykan, P. M. Wu, R. R. Gali, L. K. Iyer, R. Lawson, J. Berry, A. M. Krichevsky, M. E. Cudkowicz, and H. L. Weiner. "Modulating inflammatory monocytes with a unique microRNA gene signature ameliorates murine ALS." *Journal of Clinical Investigation* 122.9 (2012), pp. 3063–87. doi: 10.1172/JCI62636.

[231] T. Li and S. Zhang. "Microgliosis in the Injured Brain: Infiltrating Cells and Reactive Microglia Both Play a Role." *Neuroscientist* 22.2 (2015), pp. 165–70. doi: 10.1177/1073858415572079.

[232] A. Navarro-Sempere, P. Martinez-Peinado, A. S. Rodrigues, P. V. Garcia, R. Camarinho, M. Garcia, and Y. Segovia. "The Health Hazards of Volcanoes: First Evidence of Neuroinflammation in the Hippocampus of Mice Exposed to Active Volcanic Surroundings." *Mediators of Inflammation* 2021.5891095 (2021). doi: 10.1155/2021/5891095.

[233] Y.-L. Tan, Y. Yuan, and L. Tian. "Microglial regional heterogeneity and its role in the brain." *Molecular Psychiatry* 25 (2019), pp. 351–367. doi: 10.1038/s41380-019-0609-8.

[234] V. Stratoulias, J. L. Venero, M.-E. Tremblay, and B. Joseph. "Microglial subtypes: diversity within the microglial community." *EMBO Journal* 38.17 (2019). doi: 10.15252/embj.2019101997.

[235] L. J. Lawson, V. H. Perry, P. Dri, and S. Gordon. "Heterogeneity in the distribution and morphology of microglia in the normal adult mouse brain." *Neuroscience* 39.1 (1990), pp. 151–70. doi: 10.1016/0306-4522(90)90229-w.

[236] V. L. Savchenko, I. R. Nikonenko, G. G. Skibo, and J. A. McKanna. "Distribution of microglia and astrocytes in different regions of the normal adult rat brain." *Neurophysiology* 29 (1997), pp. 343–351. doi: 10.1007/BF02463354.

[237] R. D. Stowell, E. L. Wong, H. N. Batchelor, M. S. Mendes, C. E. Lamantia, B. S. Whitelaw, and A. K. Majewska. "Cerebellar microglia are dynamically unique and survey Purkinje neurons in vivo." *Developmental Neurobiology* 78.6 (2018), pp. 627–644. doi: 10.1002/dneu.22572.

[238] M. Mittelbronn, K. Dietz, H. J. Schluesener, and R. Meyermann. "Local distribution of microglia in the normal adult human central nervous system differs by up to one order of magnitude." *Acta Neuropathologica* 101.3 (2001), pp. 249–55. doi: 10.1007/s004010000284.

[239] J. M. Vela, I. Dalmau, B. Gonzalez, and B. Castellano. "Morphology and distribution of microglial cells in the young and adult mouse cerebellum." *The Journal of Comparative Neurology* 361.4 (1995), pp. 602–16. doi: 10.1002/cne.903610405.

[240] J. Bruttger, K. Karram, S. Wortge, T. Regen, F. Marini, N. Hoppmann, M. Klein, T. Blank, S. Yona, Y. Wolf, M. Mack, E. Pinteaux, W. Muller, F. Zipp, H. Binder, T. Bopp, M. Prinz, S. Jung, and A. Waisman. "Genetic Cell Ablation Reveals Clusters of Local Self-Renewing Microglia in the Mammalian Central Nervous System." *Immunity* 43.1 (2015), pp. 92–106. doi: 10.1016/j.immuni.2015.06.012.

[241] V. Kana, F. A. Desland, M. Casanova-Acebes, P. Ayata, A. Badimon, N. E, K. Yamamuro, M. Sneeboer, I.-L. Tan, M. E. Flanigan, S. A. Rose, C. Chang, A. Leader, H. L. Bourhis, E. S. Sweet, N. Tung, A. Wroblewska, Y. Lavin, P. See, A. Baccarini, F. Ginhoux, V. Chitu, E. R. Stanley, S. J. Russo, Z. Yue, B. D. Brown, A. L. Joyner, L. D. D. Witte, H. Morishita, A. Schaefer, and M. Merad. "CSF-1 controls cerebellar microglia and is required for motor function and social interaction." *Journal of Experimental Medicine* 216.10 (2019), pp. 2265–2281. doi: 10.1084/jem.20182037.

[242] M. d. M. Fernández-Arjona, J. M. Grondona, P. Granados-Duran, P. Fernandez-Llebrez, and M. D. Lopez-Avalos. "Microglia morphological categorization in a rat model of neuroinflammation by hierarchical cluster and principal components analysis." *Frontiers in Cellular Neuroscience* 11.235 (2017). doi: 10.3389/fncel.2017.00235.

[243] M. V. Pinto and A. Fernandes. "Microglial Phagocytosis-Rational but Challenging Therapeutic Target in Multiple Sclerosis." *International Journal of Molecular Sciences* 21.17 (2020). doi: 10.3390/ijms21175960.

[244] Y. Xu, M.-Z. Jin, Z.-Y. Yang, and W.-L. Jin. "Microglia in neurodegenerative diseases." *Neural Regeneration Research* 16.2 (2021), pp. 270–280. doi: 10.4103/1673-5374.290881.

[245] A. L. R. Xavier, B. T. Kress, S. A. Goldman, J. R. L. de Menezes, and M. Nedergaard. "A distinct population of microglia supports adult neurogenesis in the subventricular zone." *Journal of Neurosciences* 35.34 (2015), pp. 11848–11861. doi: 10.1523/JNEUROSCI.1217-15.2015.

[246] C. Bechade, Y. Cantaut-Belarif, and A. Bessis. "Microglial control of neuronal activity." *Frontiers in Cellular Neuroscience* 7.32 (2013). doi: 10.3389/fncel.2013.00032.

[247] R. B. Rock, G. Gekker, S. Hu, W. S. Sheng, M. Cheeran, J. R. Lokensgard, and P. K. Peterson. "Role of Microglia in Central Nervous System Infections." *Clinical Microbiology Reviews* 17.4 (2004), pp. 942–964. doi: 10.1128/CMR.17.4.942-964.2004.

[248] C. A. Colton. "Heterogeneity of Microglial Activation in the Innate Immune Response in the Brain." *Journal of Neuroimmune Pharmacology* 4.4 (2009), pp. 399–418. doi: 10.1007/s11481-009-9164-4.

[249] P. Ayata, A. Badimon, H. J. Strasburger, M. K. Duff, S. E. Montgomery, Y.-H. E. Loh, A. Ebert, A. A. Pimenova, B. R. Ramirez, A. T. Chan, J. M. Sullivan, I. Purushothaman, J. R. Scarpa, A. M. Goate, M. Busslinger, L. Shen, B. Losic, and A. Schaefer. "Epigenetic regulation of brain region-specific microglia clearance activity." *Nature Neuroscience* 21.8 (2018), pp. 1049–1060. doi: 10.1038/s41593-018-0192-3.

[250] M. A. Petersen and M. E. Dailey. “Diverse microglial motility behaviors during clearance of dead cells in hippocampal slices.” *Glia* 46.2 (2004), pp. 195–206. doi: 10.1002/glia.10362.

[251] R. Parakalan, B. Jiang, B. Nimmi, M. Janani, M. Jayapal, J. Lu, S. S. W. Tay, E.-A. Ling, and S. T. Dheen. “Transcriptome analysis of amoeboid and ramified microglia isolated from the corpus callosum of rat brain.” *BMC Neuroscience* 13.64 (2012). doi: 10.1186/1471-2202-13-64.

[252] A. M. Jurga, M. Paleczna, and K. Z. Kuter. “Overview of General and Discriminating Markers of Differential Microglia Phenotypes.” *Frontiers in Cellular Neuroscience* 14.198 (2020). doi: 10.3389/fncel.2020.00198.

[253] A. H. de Haas, H. W. G. M. Boddeke, and K. Biber. “Region-specific expression of immunoregulatory proteins on microglia in the healthy CNS.” *Glia* 56.8 (2008), pp. 888–94. doi: 10.1002/glia.20663.

[254] O. Matcovitch-Natan, D. R. Winter, A. Giladi, S. V. Aguilar, A. Spinrad, S. Sarrazin, H. Ben-Yehuda, E. David, F. Z. Gonzalez, P. Perrin, H. Keren-Shaul, M. Gury, D. Lara-Astaiso, C. A. Thaiss, M. Cohen, K. B. Halpern, K. Baruch, A. Deczkowska, E. Lorenzo-Vivas, S. Itzkovitz, E. Elinav, M. H. Sieweke, M. Schwartz, and I. Amit. “Microglia development follows a stepwise program to regulate brain homeostasis.” *Science* 353.6301 (2016). doi: 10.1126/science.aad8670.

[255] J. K. Olson. “Immune response by microglia in the spinal cord.” *Annals of the New York Academy of Sciences* 1198 (2010), pp. 271–8. doi: 10.1111/j.1749-6632.2010.05536.x.

[256] A. D. Hart, A. Wyttenbach, V. H. Perry, and J. L. Teeling. “Age related changes in microglial phenotype vary between CNS regions: grey versus white matter differences.” *Brain Behavior and Immunity* 26.5 (2012), pp. 754–65. doi: 10.1016/j.bbi.2011.11.006.

[257] H. Kettenmann, U.-K. Hanisch, M. Noda, and A. Verkhratsky. “Physiology of microglia.” *Physiological Reviews* 91.2 (2011), pp. 461–553. doi: 10.1152/physrev.00011.2010.

[258] F. O. Martinez and S. Gordon. “The M1 and M2 paradigm of macrophage activation: time for reassessment.” *F1000Prime Reports* 6.13 (2014). doi: 10.12703/P6-13.

[259] R. von Bernhardi, L. E. v. Bernhardi, and J. Eugenin. “Microglial cell dysregulation in brain aging and neurodegeneration.” *Frontiers in Aging Neuroscience* 7.124 (2015). doi: 10.3389/fnagi.2015.00124.

[260] F. O. Martinez, L. Helming, and S. Gordon. “Alternative activation of macrophages: an immunologic functional perspective.” *Annual Review of Immunology* 27 (2009), pp. 451–83. doi: 10.1146/annurev.immunol.021908.132532.

[261] S. Hickman, S. Izzy, P. Sen, L. Morsett, and J. E. Khoury. “Microglia in neurodegeneration.” *Nature Neuroscience* 21 (2018), pp. 1359–1369. doi: 10.1038/s41593-018-0242-x.

[262] L. M. D. Biase, K. E. Schuebel, Z. H. Fusfeld, K. Jair, I. A. Hawes, R. Cimbro, H.-Y. Zhang, Q.-R. Liu, H. Shen, Z.-X. Xi, D. Goldman, and A. Bonci. "Local Cues Establish and Maintain Region-Specific Phenotypes of Basal Ganglia Microglia." *Neuron* 95.2 (2017), pp. 341–356. doi: 10.1016/j.neuron.2017.06.020.

[263] A. Niraula, J. F. Sheridan, and J. P. Godbout. "Microglia Priming with Aging and Stress." *Neuropsychopharmacology* 42.1 (2017), pp. 318–333. doi: 10.1038/npp.2016.185.

[264] J.-W. Li, Y. Zong, X.-P. Cao, L. Tan, and L. Tan. "Microglial priming in Alzheimer's disease." *Annals of Translational Medicine* 6.10 (2018), p. 176. doi: 10.21037/atm.2018.04.22.

[265] V. H. Perry and C. Holmes. "Microglial priming in neurodegenerative disease." *Nature Reviews Neurology* 10 (2014), pp. 217–224. doi: 10.1038/nrneurol.2014.38.

[266] K. I. Mosher and T. Wyss-Coray. "Microglial Dysfunction in Brain Aging and Alzheimer's Disease." *Biochemical Pharmacology* 88.4 (2014), pp. 594–604. doi: 10.1016/j.bcp.2014.01.008.

[267] J. P. Godbout, J. Chen, J. Abraham, A. F. Richwine, B. M. Berg, K. W. Kelley, and R. W. Johnson. "Exaggerated neuroinflammation and sickness behavior in aged mice following activation of the peripheral innate immune system." *FASEB Journal* 19.10 (2005), pp. 1329–31. doi: 10.1096/fj.05-3776fje.

[268] M. G. Frank, R. M. Barrientos, L. R. Watkins, and S. F. Maier. "Aging sensitizes rapidly isolated hippocampal microglia to LPS ex vivo." *Journal of Neuroimmunology* 226 (2010), pp. 181–184. doi: 10.1016/j.jneuroim.2010.05.022.

[269] W. J. Streit, N. W. Sammons, A. J. Kuhns, and D. L. Sparks. "Dystrophic microglia in the aging human brain." *Glia* 45.2 (2004), pp. 208–12. doi: 10.1002/glia.10319.

[270] M. G. Frank, R. M. Barrientos, J. C. Biedenkapp, J. W. Rudy, L. R. Watkins, and S. F. Maier. "mRNA up-regulation of MHC II and pivotal pro-inflammatory genes in normal brain aging." *Neurobiology of Aging* 27.5 (2006), pp. 717–22. doi: 10.1016/j.neurobiolaging.2005.03.013.

[271] B. E. Ianary and W. J. Streit. "Telomeres Shorten with Age in Rat Cerebellum and Cortex in vivo." *Journal of Anti-Aging Medicine* 6.4 (2004). doi: 10.1089/109454503323028894.

[272] M. R. Damani, L. Zhao, A. M. Fontainhas, J. Amaral, R. N. Fariss, and W. T. Wong. "Age-related alterations in the dynamic behavior of microglia." *Aging Cell* 10.2 (2011), pp. 263–76. doi: 10.1111/j.1474-9726.2010.00660.x.

[273] I. R. Holtman, D. D. Raj, J. A. Miller, W. Schaafsma, Z. Yin, N. Brouwer, P. D. Wes, T. Moller, M. Orre, W. Kamphuis, E. M. Hol, E. W. G. M. Boddeke, and B. J. L. Eggen. "Induction of a common microglia gene expression signature by aging and neurodegenerative conditions: a co-expression meta-analysis." *Acta Neuropathologica Communications* 3.31 (2015). doi: 10.1186/s40478-015-0203-5.

[274] L. K. Fonken, M. D. Weber, R. A. Daut, M. M. Kitt, M. G. Frank, L. R. Watkins, and S. F. Maier. "Stress-induced neuroinflammatory priming is time of day dependent." *Psychoneuroendocrinology* 66 (2016), pp. 82–90. doi: 10.1016/j.psyneuen.2016.01.006.

[275] C. Caldeira, A. F. Oliveira, C. Cunha, A. V. Vaz, A. S. Falcao, A. Fernandes, and D. Brites. "Microglia change from a reactive to an age-like phenotype with the time in culture." *Frontiers in Cellular Neuroscience* 8.152 (2014). doi: 10.3389/fncel.2014.00152.

[276] C. Martinez-Cue and N. Rueda. "Cellular Senescence in Neurodegenerative Diseases." *Frontiers in Cellular Neuroscience* 14.16 (2020). doi: 10.3389/fncel.2020.00016.

[277] D. J. Baker, T. Wijshake, T. Tchkonia, N. K. LeBrasseur, B. G. Childs, B. v. de Sluis, J. L. Kirkland, and J. M. van Deursen. "Clearance of p16Ink4a-positive senescent cells delays ageing-associated disorders." *Nature* 479 (2011), pp. 232–236. doi: 10.1038/nature10600.

[278] W. J. Streit and Q.-S. Xue. "Alzheimer's Disease, Neuroprotection, and CNS Immunosenescence." *Frontiers in Pharmacology* 3.138 (2012). doi: 10.3389/fphar.2012.00138.

[279] L. Roger, F. Tomas, and V. Gire. "Mechanisms and Regulation of Cellular Senescence." *International Journal of Molecular Sciences* 22.23 (2011). doi: 10.3390/ijms222313173.

[280] Z. Si, L. Sun, and X. Wang. "Evidence and perspectives of cell senescence in neurodegenerative diseases." *Biomedicine and Pharmacotherapy* 137 (2021). doi: 10.1016/j.biopha.2021.111327.

[281] I. Liguori, G. Russo, F. Curcio, G. Bulli, L. Aran, D. Della-Morte, G. Gargiulo, G. Testa, F. Cacciatore, D. Bonaduce, and P. Abete. "Oxidative stress, aging, and diseases." *Clinical Interventions in Aging* 13 (2018), pp. 757–772. doi: 10.2147/CIA.S158513.

[282] G. Nelson, J. Wordsworth, C. Wang, D. Jurk, C. Lawless, C. Martin-Ruiz, and T. von Zglinicki. "A senescent cell bystander effect: senescence-induced senescence." *Aging Cell* 11.2 (2012), pp. 345–349. doi: 10.1111/j.1474-9726.2012.00795.x.

[283] H.-C. Chow and K. Herrup. "Genomic integrity and the ageing brain." *Nature Reviews Neuroscience* 16 (2015), pp. 672–684. doi: 10.1038/nrn4020.

[284] G. Hewitt, D. Jurk, F. D. M. Marques, C. Correia-Melo, T. Hardy, A. Gackowska, R. Anderson, M. Taschuk, J. Mann, and J. F. Passos. "Telomeres are favoured targets of a persistent DNA damage response in ageing and stress-induced senescence." *Nature Communications* 3.708 (2012). doi: 10.1038/ncomms1708.

[285] J. P. Jackon and J. Bartek. "The DNA-damage response in human biology and disease." *Nature* 461 (2009), pp. 1071–1078. doi: 10.1038/nature08467.

[286] H. T. Kang, K. B. Lee, S. Y. Kim, H. R. Choi, and S. C. Park. "Autophagy Impairment Induces Premature Senescence in Primary Human Fibroblasts." *PLoS One* 6.8 (2011). doi: 10.1371/journal.pone.0023367.

[287] R. C. Taylor and A. Dillin. “Aging as an Event of Proteostasis Collapse.” *Cold Spring Harbor Perspectives in Biology* 3.5 (2011). doi: 10.1101/cshperspect.a004440.

[288] K. Montague-Cardoso. “Cellular proteostasis decline in human senescence.” *Communications Biology* 4.17 (2021). doi: 10.1038/s42003-020-01578-w.

[289] W. J. Streit and Q.-S. Xue. “Human CNS immune senescence and neurodegeneration.” *Current Opinion in Immunology* 29 (2014), pp. 93–96. doi: 10.1016/j.coi.2014.05.005.

[290] A. Sierra, A. C. Gottfried-Blackmore, B. S. McEwen, and K. Bulloch. “Microglia derived from aging mice exhibit an altered inflammatory profile.” *Glia* 55.4 (2007), pp. 412–24. doi: 10.1002/glia.20468.

[291] T. J. Bussian, A. Aziz, C. F. Meyer, B. L. Swenson, J. M. van Deursen, and D. J. Baker. “Clearance of senescent glial cells prevents tau-dependent pathology and cognitive decline.” *Nature* 562 (2018), pp. 578–582. doi: 10.1038/s41586-018-0543-y.

[292] E. Trias, P. R. Beilby, M. Kovacs, S. Ibarburu, V. Varela, R. Barreto-Nunez, S. C. Bradford, J. S. Beckman, and L. Barbeito. “Emergence of Microglia Bearing Senescence Markers During Paralysis Progression in a Rat Model of Inherited ALS.” *Frontiers Aging Neuroscience* 11.42 (2019). doi: 10.3389/fnagi.2019.00042.

[293] B. E. Flanary, N. W. Sammons, C. Nguyen, D. Walker, and W. J. Streit. “Evidence that aging and amyloid promote microglial cell senescence.” *Rejuvenation Research* 10.1 (2007), pp. 61–74. doi: 10.1089/rej.2006.9096.

[294] W. J. Streit, Q.-S. Xue, J. Tischer, and I. Bechmann. “Microglial pathology.” *Acta Neuropathologica Communications* 2.142 (2014). doi: 10.1186/s40478-014-0142-6.

[295] W. Li. “Phagocyte dysfunction, tissue aging and degeneration.” *Ageing Research Reviews* 12.4 (2013), pp. 1005–12. doi: 10.1016/j.arr.2013.05.006.

[296] M. Orre, W. Kamphuis, L. M. Osborn, J. Melief, L. Kooijman, I. Huitinga, J. Klooster, K. Bossers, and E. M. Hol. “Acute isolation and transcriptome characterization of cortical astrocytes and microglia from young and aged mice.” *Neurobiology of Aging* 35.1 (2014), pp. 1–14. doi: 10.1016/j.neurobiolaging.2013.07.008.

[297] S. Safaiyan, N. Kannaiyan, N. Snaidero, S. Brioschi, K. Biber, S. Yona, A. L. Edinger, S. Jung, M. J. Rossner, and M. Simons. “Age-related myelin degradation burdens the clearance function of microglia during aging.” *Nature Neuroscience* 19.8 (2016), pp. 995–8. doi: 10.1038/nn.4325.

[298] K. Bisht, K. P. Sharma, C. Lecours, M. G. Sanchez, H. E. Hajj, G. Milior, A. Olmos-Alonso, D. Gomez-Nicola, G. Luheshi, L. Vallieres, I. Branchi, L. Maggi, C. Limatola, O. Butovsky, and M.-E. Tremblay. “Dark microglia: A new phenotype predominantly associated with pathological states.” *Glia* 64.5 (2016), pp. 826–839. doi: 10.1002/glia.22966.

[299] A. Deczkowska, H. Keren-Shaul, A. Weiner, M. Colonna, M. Schwartz, and I. Amit. "Disease-Associated Microglia: A Universal Immune Sensor of Neurodegeneration." *Cell* 173.5 (2018), pp. 1073–1081. doi: 10.1016/j.cell.2018.05.003.

[300] C. E. G. Leyns, J. D. Ulrich, M. B. Finn, F. R. Stewart, L. J. K. amd J. R. Serrano, G. O. Robinson, E. Anderson, M. Colonna, and D. M. Holtzman. "TREM2 deficiency attenuates neuroinflammation and protects against neurodegeneration in a mouse model of tauopathy." *Proceedings of the National Academy of Sciences of the United States of America* 114.43 (2017), pp. 11524–11529. doi: 10.1073/pnas.1710311114.

[301] B. A. Friedman, K. Srinivasan, G. Ayalon, W. J. Meilandt, H. Lin, M. A. Huntley, Y. Cao, S.-H. Lee, P. C. G. Haddick, H. Ngu, Z. Modrusan, J. L. Larson, J. S. Kaminker, M. P. van der Brug, and D. V. Hansen. "Diverse Brain Myeloid Expression Profiles Reveal Distinct Microglial Activation States and Aspects of Alzheimer's Disease Not Evident in Mouse Models." *Cell Reports* 22.3 (2018), pp. 832–847. doi: 10.1016/j.celrep.2017.12.066.

[302] S. Krasemann, C. Madore, R. Cialic, C. Baufeld, N. Calcagno, R. E. Fatimy, L. Beckers, E. O Loughlin, Y. Xu, Z. Fanek, D. J. Greco, S. T. Smith, G. Tweet, Z. Humulock, T. Zrzavy, P. Conde-Sanroman, M. Gacias, Z. Weng, H. Chen, E. Tjon, F. Mazaheri, K. Hartmann, A. Madi, J. D. Ulrich, M. Glatzel, A. Worthmann, J. Heeren, B. Budnik, C. Lemere, T. Ilezu, F. L. Heppner, V. Litvak, D. M. Holtzman, H. Lassmann, H. L. Weiner, J. Ochando, C. Haass, and O. Butovsky. "The TREM2-APOE Pathway Drives the Transcriptional Phenotype of Dysfunctional Microglia in Neurodegenerative Diseases." *Immunity* 47.3 (2017), pp. 566–581. doi: 10.1016/j.immuni.2017.08.008.

[303] F. L. Yeh, D. V. Hansen, and M. Sheng. "TREM2, Microglia, and Neurodegenerative Diseases." *Trends in Molecular Medicine* 23.6 (2017), pp. 512–533. doi: 10.1016/j.molmed.2017.03.008.

[304] B. A. Loving and K. D. Bruce. "Lipid and lipoprotein metabolism in microglia." *Frontiers in Physiology* 11.393 (2020). doi: 10.3389/fphys.2020.00393.

[305] K. A. Clayton, A. A. V. Enoo, and T. Ikezu. "Alzheimer's Disease: The Role of Microglia in Brain Homeostasis and Proteopathy." *Frontiers in Neuroscience* 11.680 (2017). doi: 10.3389/fnins.2017.00680.

[306] E. S. Jung and I. Mook-Jung. "New Microglia on the Block." *Cell Metabolism* 31.4 (2020), pp. 664–667. doi: 10.1016/j.cmet.2020.03.015.

[307] J. Marschallinger, T. Iram, M. Zardeneta, S. E. Lee, B. Lehallier, M. S. Haney, J. V. Pluvinage, V. Mathur, O. Hahn, D. W. Morgens, J. Kim, J. Tevini, T. K. Felder, H. Wolinski, C. R. Bertozzi, M. C. Bassik, L. Aigner, and T. Wyss-Coray. "Lipid-droplet-accumulating microglia represent a dysfunctional and proinflammatory state in the aging brain." *Nature Neuroscience* 23 (2020), pp. 194–208. doi: 10.1038/s41593-019-0566-1.

[308] B. C. Farmer, A. E. Walsh, J. C. Kluemper, and L. A. Johnson. “Lipid Droplets in Neurodegenerative Disorders.” *Frontiers in Neuroscience* 14.742 (2020). doi: 10.3389/fnins.2020.00742.

[309] A. Khatchadourian, S. D. Bourque, V. R. Richard, V. I. Titorenko, and D. Maysinger. “Dynamics and regulation of lipid droplet formation in lipopolysaccharide (LPS)-stimulated microglia.” *Biochimica Biophysica Acta* 1821.4 (2012), pp. 607–17. doi: 10.1016/j.bbalip.2012.01.007.

[310] A. A. Nugent, K. Lin, B. van Lengerich, S. Lianoglou, L. Przybyla, S. S. Davis, C. Llapashtica, J. Wang, D. J. Kim, D. Xia, A. Lucas, S. Baskaran, P. C. G. Haddick, M. Lenser, T. K. Earr, J. Shi, J. C. Dugas, B. J. Andreone, T. Logan, H. O. Solanoy, H. Chen, A. Srivastava, S. B. Poda, P. E. Sanchez, R. J. Watts, T. Sandmann, G. Astarita, J. W. Lewcock, K. M. Monroe, and G. D. Paolo. “TREM2 Regulates Microglial Cholesterol Metabolism upon Chronic Phagocytic Challenge.” *Neuron* 105.5 (2020), pp. 837–854. doi: 10.1016/j.neuron.2019.12.007.

[311] E. P. de Chaves and V. Narayanaswami. “Apolipoprotein E and cholesterol in aging and disease in the brain.” *Future Lipidology* 3.5 (2009), pp. 505–530.

[312] C. Easley-Neal, O. Foreman, N. Sharma, A. A. Zarrin, and R. M. Weimer. “CSF1R Ligands IL-34 and CSF1 Are Differentially Required for Microglia Development and Maintenance in White and Gray Matter Brain Regions.” *Frontiers in Immnunology* 10.2199 (2019). doi: 10.3389/fimmu.2019.02199.

[313] S. J. Oh, H. Ahn, K.-H. Jung, S. J. Han, K. R. Nam, K. J. Kang, J.-A. Park, K. C. Lee, Y. J. Lee, and J. Y. Choi. “Evaluation of the Neuroprotective Effect of Microglial Depletion by CSF-1R Inhibition in a Parkinson’s Animal Model.” *Molecular Imaging and Biology* 22.4 (2020), pp. 1031–1042. doi: 10.1007/s11307-020-01485-w.

[314] K. J. Spiller, C. R. Restrepo, T. Khan, M. A. Dominique, T. C. Fang, R. G. Canter, C. Roberts, K. R. Miller, R. M. Ransohoff, J. Q. Trojanowski, and C. M.-Y. Lee. “Microglia-mediated recovery from ALS-relevant motor neuron degeneration in a mouse model of TDP-43 proteinopathy.” *Nature Neuroscience* 21.3 (2018), pp. 329–340. doi: 10.1038/s41593-018-0083-7.

[315] J. D. Crapser, J. Ochaba, N. Soni, J. C. Reidling, L. M. Thompson, and K. N. Green. “Microglial depletion prevents extracellular matrix changes and striatal volume reduction in a model of Huntington’s disease.” *Brain* 143.1 (2020), pp. 266–288. doi: 10.1093/brain/awz363.

[316] E. E. Spangenberg, R. J. Lee, A. R. Najafi, R. A. Rice, M. R. P. Elmore, M. Blurton-Jones, B. L. West, and K. N. Green. “Eliminating microglia in Alzheimer’s mice prevents neuronal loss without modulating amyloid-B pathology.” *Brain* 139.4 (2016), pp. 1265–81. doi: 10.1093/brain/aww016.

[317] H. Asai, S. Ikezu, S. Tsunoda, M. Medalla, J. Luebke, T. Haydar, B. Wolozin, O. Butovsky, S. Kugler, and T. Ikezu. “Depletion of microglia and inhibition of exosome synthesis halt tau propagation.” *Nature Neuroscience* 18 (2015), pp. 1584–1593. doi: 10.1038/nn.4132.

[318] P. O. Bauer and N. Nukina. “The pathogenic mechanisms of polyglutamine diseases and current therapeutic strategies.” *Journal of Neurochemistry* 110.6 (2009), pp. 1737–1765. doi: 10.1111/j.1471-4159.2009.06302.x.

[319] A. Teixeira-Castro, A. Jalles, S. Esteves, S. Kang, L. d. S. Santos, A. Silva-Fernandes, M. F. Neto, R. M. Brielmann, C. Bessa, S. Duarte-Silva, A. Miranda, S. Oliveira, A. Neves-Carvalho, J. Bessa, T. Summavielle, R. B. Silverman, P. Oliveira, R. I. Morimoto, and P. Maciel. “Serotonergic signalling suppresses ataxin 3 aggregation and neurotoxicity in animal models of Machado-Joseph disease.” *Brain* 138.11 (2015), pp. 3221–37. doi: 10.1093/brain/awv262.

[320] S. Duarte-Silva and P. Maciel. “Pharmacological Therapies for Machado-Joseph Disease.” *Advances in Experimental Medicine and Biology* 1049 (2018), pp. 369–394. doi: 10.1007/978-3-319-71779-1_19.

[321] A. Neves-Carvalho, S. Duarte-Silva, A. Teixeira-Castro, and P. Maciel. “Polyglutamine spinocerebellar ataxias: emerging therapeutic targets.” *Expert Opinion on Therapeutic Targets* 24.11 (2020), pp. 1099–1119. doi: 10.1080/14728222.2020.1827394.

[322] J. S. Correia, A. Neves-Carvalho, B. Mendes-Pinheiro, J. Pires, F. G. Teixeira, R. Lima, S. Monteiro, N. A. Silva, C. Soares-Cunha, S. C. Serra, S. Duarte-Silva, A. Teixeira-Castro, A. J. Salgado, and P. Maciel. “Preclinical Assessment of Mesenchymal-Stem-Cell-Based Therapies in Spinocerebellar Ataxia Type 3.” *Biomedicines* 9.12 (2021). doi: 10.3390/biomedicines9121754.

[323] M. B. Graeber and W. J. Streit. “Microglia: biology and pathology.” *Acta Neuropathologica* 119.1 (2010), pp. 89–105. doi: 10.1007/s00401-009-0622-0.

[324] E. G. Njie, E. Boelen, F. R. Stassen, H. W. M. Steinbusch, D. R. Borchelt, and W. J. Streit. “Ex vivo cultures of microglia from young and aged rodent brain reveal age-related changes in microglial function.” *Neurobiology of aging* 33.1 (2012), pp. 1–12. doi: 10.1016/j.neurobiolaging.2010.05.008.

[325] W. J. Streit and Q.-S. Xue. “Life and death of microglia.” *Journal of Neuroimmune Pharmacology* 4.4 (2009), pp. 371–379. doi: 10.1007/s11481-009-9163-5.

[326] J. Saura, J. M. Tusell, and J. Serratosa. “High-yield isolation of murine microglia by mild trypsinization.” *Glia* 44.3 (2003), pp. 183–9. doi: 10.1002/glia.10274.

[327] M. H. Madeira, A. Ortin-Martinez, F. Nadal-Nicolas, A. F. Ambrosio, M. Vidal-Sanz, M. Agudo-Barriuso, and A. R. Santiago. “Caffeine administration prevents retinal neuroinflammation and loss of retinal ganglion cells in an animal model of glaucoma.” *Scientific Reports* 6.27532 (2016). doi: 10.1038/srep27532.

[328] H. Fujita, J. Tanaka, K. Toku, N. Tateishi, Y. Suzuki, S. Matsuda, M. Sakanaka, and N. Maeda. “Effects of GM-CSF and ordinary supplements on the ramification of microglia in culture: A morphometrical study.” *Glia* 18.4 (1996), pp. 269–281. doi: 10.1002/(SICI)1098-1136(199612).

[329] V. G. Gorgoulis, H. Pratsinis, P. Zacharatos, C. Demoliou, F. Sigala, P. J. Asimacopoulos, A. G. Papavassiliou, and D. Kletsas. "p53-dependent ICAM-1 overexpression in senescent human cells identified in atherosclerotic lesions." *Laboratory Investigation* 85.4 (2005), pp. 502–11. doi: 10.1038/labinvest.3700241.

[330] J.-J. Lee, I. H. Park, M. S. Kwak, W. J. Rhee, S. H. Kim, and J.-S. Shin. "HMGB1 orchestrates STING-mediated senescence via TRIM30 modulation in cancer cells." *Cell Death Discovery* 7.28 (2021). doi: 10.1038/s41420-021-00409-z.

[331] R. Socodato, C. C. Portugal, T. Canedo, A. Rodrigues, T. O. Almeida, J. F. Henries, S. H. Vaz, J. Magalhaes, C. M. Silva, F. I. Baptista, R. L. Alves, V. Coelho-Santos, A. P. Silva, R. P. de Carvalho, A. Magalhaes, C. Brakebusch, A. M. Sebastiao, T. Summavielle, A. F. Ambrosio, and J. B. Relvas. "Microglia Dysfunction Caused by the Loss of Rhoa Disrupts Neuronal Physiology and Leads to Neurodegeneration." *Cell Reports* 31.12 (2020), p. 107796. doi: 10.1016/j.celrep.2020.107796.

[332] C. Caldeira, C. Cunha, A. R. Vaz, A. S. Falcao, A. Barateiro, E. Seixas, A. Fernandes, and D. Brites. "Key Aging-Associated Alterations in Primary Microglia Response to Beta-Amyloid Stimulation." *Frontiers in Aging Neuroscience* 9.277 (2017). doi: 10.3389/fnagi.2017.00277.

[333] M. Bordeleau, C. Lacabanne, L. F. d. Cossio, N. Vernoux, J. C. Savage, F. Gonzalez-Ibanez, and M.-E. Tremblay. "Microglial and peripheral immune priming is partially sexually dimorphic in adolescent mouse offspring exposed to maternal high-fat diet." *Journal of Neuroinflammation* 17.264 (2020). doi: 10.1186/s12974-020-01914-1.

[334] A. Vargas-Caraveo, A. Sayd, J. Robledo-Montana, J. R. Caso, J. L. M. Madrigal, B. Garcia-Bueno, and J. C. Leza. "Toll-like receptor 4 agonist and antagonist lipopolysaccharides modify innate immune response in rat brain circumventricular organs." *Journal of Neuroinflammation* 17.1 (2020), p. 6. doi: 10.1186/s12974-019-1690-2.

[335] H. W. Morrison and J. A. Filosa. "A quantitative spatiotemporal analysis of microglia morphology during ischemic stroke and reperfusion." *Journal of Neuroinflammation* 10.782 (2013). doi: 10.1186/1742-2094-10-4.

[336] R. Kongsui, S. B. Beynon, S. J. Johnson, and F. R. Walker. "Quantitative assessment of microglial morphology and density reveals remarkable consistency in the distribution and morphology of cells within the healthy prefrontal cortex of the rat." *Journal of Neuroinflammation* 11.182 (2014). doi: 10.1186/s12974-014-0182-7.

[337] B. M. Davis, M. Salinas-Navarro, M. F. Cordeiro, L. Moons, and L. D. Groef. "Characterizing microglia activation: a spatial statistics approach to maximize information extraction." *Scientific Reports* 7.1576 (2017). doi: 10.1038/s41598-017-01747-8.

[338] K. Young and H. Morrison. “Quantifying Microglia Morphology from Photomicrographs of Immunohistochemistry Prepared Tissue Using ImageJ.” *Journal of Visualized Experiments* 136.57648 (2018). doi: 10.3791/57648.

[339] A. B. Campos, S. Duarte-Silva, A. F. Ambrósio, P. Maciel, and B. Fernandes. “MorphData: Automating the data extraction process of morphological features of microglial cells in ImageJ.” *bioRxiv* (2021). doi: 10.1101/2021.08.05.455282.

[340] B. Fernandes, A. Gonzalez-Briones, P. Novais, M. Calafate, C. Analide, and J. Neves. “An Adjective Selection Personality Assessment Method Using Gradient Boosting Machine Learning.” *Processes* 8.5 (2020). doi: 10.3390/pr8050618.

[341] S. Heindl, B. Gesierich, C. Benakis, G. Llovera, M. Duering, and A. Liesz. “Automated Morphological Analysis of Microglia After Stroke.” *Frontiers in Cellular Neuroscience* 12.106 (2018). doi: 10.3389/fncel.2018.00106.

[342] W. J. Streit. “Microglial senescence: does the brain’s immune system have an expiration date?” *Trends in Neuroscience* 29.9 (2006), pp. 506–10. doi: 10.1016/j.tins.2006.07.001.

[343] R. K. Shahidehpour, R. E. Higdon, N. G. Crawford, J. H. Neltner, E. T. Ighodaro, E. Patel, D. Price, P. T. Nelson, and A. D. Bachstetter. “Dystrophic microglia are associated with neurodegenerative disease and not healthy aging in the human brain.” *Neurobiology of Aging* 99 (2021), pp. 19–27. doi: 10.1016/j.neurobiolaging.2020.12.003.

[344] I. Arganda-Carreras, R. Fernandez-Gonzalez, A. Munoz-Barrutia, and C. Ortiz-De-Solorzano. “3D reconstruction of histological sections: Application to mammary gland tissue.” *Microscopy Research and Technie* 73.11 (2010), pp. 1019–29. doi: 10.1002/jemt.20829.

[345] G. Chew and E. Petretto. “Transcriptional Networks of Microglia in Alzheimer’s Disease and Insights into Pathogenesis.” *Genes (Basel)* 10.10 (2019). doi: 10.3390/genes10100798.

[346] I. Napoli and H. Neumann. “Microglial clearance function in health and disease.” *Neuroscience* 158.3 (2009), pp. 1030–1038. doi: 10.1016/j.neuroscience.2008.06.046.

[347] J. Pan, N. Ma, B. Yu, W. Zhang, and J. Wan. “Transcriptomic profiling of microglia and astrocytes throughout aging.” *Journal of Neuroinflammation* 17.97 (2020). doi: 10.1186/s12974-020-01774-9.

[348] L. M. Holt and M. L. Olsen. “Novel Applications of Magnetic Cell Sorting to Analyze Cell-Type Specific Gene and Protein Expression in the Central Nervous System.” *PLOS ONE* 11.2 (2016). doi: 10.1371/journal.pone.0150290.

[349] A. B. DePaula-Silva, C. Gorbea, D. J. Doty, J. E. Libbey, J. M. S. Sanchez, T. J. Hanak, D. Cazalla, and R. S. Fujinami. “Differential transcriptional profiles identify microglial- and macrophage-specific gene markers expressed during virus-induced neuroinflammation.” *Journal of Neuroinflammation* 16.152 (2019). doi: 10.1186/s12974-019-1545-x.

[350] T. R. Hammond, C. Dufort, L. Dissing-Olesen, S. Giera, A. Young, A. Wysoker, A. J. Walker, F. Gergits, M. Segel, J. Nemesh, S. E. Marsh, A. Saunders, E. Macosko, F. Ginhoux, J. Chen, R. J. M. Franklin, X. Piao, S. A. McCarroll, and B. Stevens. "Single-Cell RNA Sequencing of Microglia throughout the Mouse Lifespan and in the Injured Brain Reveals Complex Cell-State Changes." *Immunity* 50.1 (2019), pp. 253–271. doi: 10.1016/j.immuni.2018.11.004.

[351] N. Itoh, Y. Itoh, A. Tassoni, E. Ren, M. Kaito, A. Ohno, Y. Ao, V. Farkhondeh, H. Johnsonbaugh, J. Burda, M. V. Sofroniew, and R. R. Voskuhl. "Cell-specific and region-specific transcriptomics in the multiple sclerosis model: Focus on astrocytes." *PNAS* 115.2 (2018), pp. 302–309. doi: 10.1073/pnas.1716032115.

[352] A. S. Mendiola, J. K. Rysu, S. Bardehle, A. Meyer-Franke, K. K.-H. Ang, C. Wilson, K. M. Baeten, K. Hanspers, M. Merlini, S. Thomas, M. A. Petersen, A. Williams, R. Thomas, V. A. Rafalski, R. Meza-Acevedo, R. Tognatta, Z. Yan, S. J. Pfaff, M. R. Machado, C. Bedard, P. E. R. Coronado, X. Jiang, J. Wang, M. A. Pleiss, A. J. Green, S. S. Zamvil, A. R. Pico, B. G. Bruneau, M. R. Arkin, and K. Akassoglou. "Transcriptional profiling and therapeutic targeting of oxidative stress in neuroinflammation." *Nature Immunology* 21 (2020), pp. 513–524. doi: 10.1038/s41590-020-0654-0.

[353] K. Srinivasan, B. A. Friedman, A. Etxeberria, M. A. Huntley, M. P. V. D. Brug, O. Foreman, J. S. Paw, Z. Modrusan, T. G. Beach, G. E. Serrano, and D. V. Hansen. "Alzheimer's Patient Microglia Exhibit Enhanced Aging and Unique Transcriptional Activation." *Cell Reports* 31.13 (2020). doi: 10.1016/j.celrep.2020.107843.

[354] M. Orre, W. Kamphuis, L. M. Osborn, A. H. P. Jansen, L. Kooijman, K. Bossers, and E. M. Hol. "Isolation of glia from Alzheimer's mice reveals inflammation and dysfunction." *Neurobiology of aging* 35.12 (2014). doi: 10.1016/j.neurobiolaging.2014.06.004.

[355] H. Wang, Y. Li, J. W. Ryder, J. T. Hole, P. J. Ebert, D. C. Airey, H. R. Qian, B. Logsdon, A. Fisher, Z. Ahmed, T. K. Murray, A. Cavallini, S. Bose, B. J. Eastwood, D. A. Collier, J. L. Dage, B. B. Miller, K. M. Merchant, M. J. O'Neill, and R. B. Demattos. "Genome-wide RNAseq study of the molecular mechanisms underlying microglia activation in response to pathological tau perturbation in the rTg4510 tau transgenic animal model." *Molecular Neurodegeneration* 13.1 (2018). doi: 10.1186/s13024-018-0296-y.

[356] H. N. Noristani, J. C. Sabourin, Y. N. Gerber, M. Teigell, A. Sommacal, M. D. Vivanco, M. Weber, and E. Perrin. "Brca1 is expressed in human microglia and is dysregulated in human and animal model of ALS." *Molecular Neurodegeneration* 10.34 (2015), pp. 385–401. doi: 10.1186/s13024-015-0023-x.

[357] O. Al-Dalahmah, A. A. Sosunov, A. Shaik, K. Ofori, Y. Liu, P. Vonsattel, I. Adorjan, V. Menon, and J. E. Goldman. "Single-nucleus RNA-seq identifies Huntington disease astrocyte states." *Acta Neuropathologica Communications* 8.19 (2020). doi: 10.1186/s40478-020-0880-6.

[358] J. Lai, J. Kim, A. M. Jeffries, A. Tolles, T. W. Chittenden, P. G. Buckley, T. W. Yu, M. A. Lodato, and E. A. Lee. "Single-nucleus transcriptomic analyses reveal microglial activation underlying cerebellar degeneration in Ataxia Telangiectasia." *bioRxiv* (2021). doi: 10.1101/2021.09.09.459619.

[359] J. Zhong, G. Tang, J. Zhu, W. Wu, G. Li, X. Lin, L. Liang, C. Chai, Y. Zeng, F. Wang, L. Luo, J. Li, F. Chen, Z. Huang, X. Zhang, Y. Zhang, H. Liu, X. Qiu, S. Tang, and D. Chen. "Single-cell brain atlas of Parkinson's disease mouse model." *Journal of Genetics and Genomics* 48.4 (2021), pp. 277–288. doi: 10.1016/j.jgg.2021.01.003.

[360] T. F. Galatro, I. R. Holtman, A. M. Lerario, I. D. Vainchtein, N. Brouwe, P. R. Sola, M. M. Veras, T. F. Pereira, R. E. P. Leite, T. Moller, P. D. Wes, M. C. Sogayar, J. D. Laman, W. D. Dunnen, C. A. Pasqualucci, S. M. Oba-Shinjo, E. W. G. M. Boddeke, S. K. N. Marie, and B. J. L. Eggen. "Transcriptomic analysis of purified human cortical microglia reveals age-associated changes." *Nature Neuroscience* 20.8 (2017), pp. 1162–1171. doi: 10.1038/nn.4597.

[361] O. Butovsky, M. P. Jedrychowski, R. Cialic, S. Krasemann, G. Murugaiyan, Z. Fanek, D. J. Greco, P. Wu, C. E. Doykan, O. Kiner, R. J. Lawson, M. P. Frosch, N. Pochet, R. E. Fatimy, A. M. Krichevsky, S. P. Gygi, H. Lassmann, J. Berry, M. E. Cudkowicz, and H. L. Weiner. "Targeting mir-155 restores abnormal microglia and attenuates disease in SOD1 mice." *Annals of Neurology* 77.1 (2015), pp. 75–99. doi: 10.1002/ana.24304.

[362] S. Okada, S. Obata, M. Hatano, and T. Tokuhisa. "Dominant-negative effect of the c-fos family gene products on inducible NO synthase expression in macrophages." *International Immunology* 15.11 (2003), pp. 1275–82. doi: 10.1093/intimm/dxg126.

[363] N. Ray, M. Kuwahara, Y. Takada, K. Maruyama, T. Kawaguchi, H. Tsubone, H. Ishikawa, and K. Matsuo. "c-Fos suppresses systemic inflammatory response to endotoxin." *International Immunology* 18.5 (2006), pp. 671–7. doi: 10.1093/intimm/dxl004.

[364] H. Li, X. Zhang, M. Chen, J. Chen, T. Gao, and S. Yao. "Dexmedetomidine inhibits inflammation in microglia cells under stimulation of LPS and ATP by c-Fos/NLRP3/caspase-1 cascades." *EXCLI Journal* 17 (2018), pp. 302–311. doi: 10.17179/excli2017-1018.

[365] S. L. Yates, L. H. Burgess, J. Kocsis-Angle, J. M. Antal, M. D. Dority, P. B. Embury, A. M. Piotrkowski, and K. R. Brunden. "Amyloid beta and amylin fibrils induce increases in proinflammatory cytokine and chemokine production by THP-1 cells and murine microglia." *Journal of Neurochemistry* 74.3 (2000), pp. 1017–1025. doi: 10.1046/j.1471-4159.2000.0741017.x.

[366] C. J. Yuskaitis and R. S. Jope. "Glycogen synthase kinase-3 regulates microglial migration, inflammation, and inflammation-induced neurotoxicity." *Cellular Signalling* 21.2 (2009), pp. 264–273. doi: 10.1016/j.cellsig.2008.10.014.

[367] O. C. Jorge-Torres, K. Szczesna, L. Roa, C. Casal, L. Gonzalez-Somermeyer, M. Soler, C. D. Velasco, P. M.-S. Segundo, P. Petazzi, M. A. Saez, R. Delgado-Morales, S. Fourcade, A. Pujol, D. Huertas, A. Llobet, S. Guil, and M. Esteller. "Inhibition of Gsk3b reduces Nfkb1 signaling and rescues synaptic activity to improve the Rett Syndrome phenotype in Mecp2-knockout mice." *Cell Reports* 23.6 (2018), pp. 1665–1677. doi: 10.1016/j.celrep.2018.04.010.

[368] C. Costa, H. Eixarch, E. Martinez-Saez, L. Calvo-Barreiro, M. Calucho, Z. Castro, A. Ortega-Aznar, S. R. y Cajal, X. Montalban, and C. Espejo. "Expression of bone morphogenetic proteins in Multiple Sclerosis lesions." *The American Journal of Pathology* 189.3 (2019), pp. 665–676. doi: 10.1016/j.ajpath.2018.11.007.

[369] C. Fonta, P. Barone, L. R. Martinez, and L. Negyessy. "Rediscovering TNAP in the Brain: A Major Role in Regulating the Function and Development of the Cerebral Cortex." *Sub-cellular Biochemistry* 76 (2015), pp. 85–106. doi: 10.1007/978-94-017-7197-9_5.

[370] K. A. B. Kellett and N. M. Hooper. "The role of tissue non-specific alkaline phosphatase (TNAP) in neurodegenerative diseases: Alzheimer's disease in the focus." *Sub-cellular Biochemistry* 76 (2015), pp. 363–374. doi: 10.1007/978-94-017-7197-9_17.

[371] E. R. L. C. Vardy, K. A. B. Kellett, S. L. Cocklin, and N. M. Hooper. "Alkaline phosphatase is increased in both brain and plasma in Alzheimer's disease." *Neurodegenerative Diseases* 9.1 (2012), pp. 31–37. doi: 10.1159/000329722.

[372] Y. Lavin, D. Winter, R. Blecher-Gonen, E. David, H. Keren-Shaul, M. Merad, S. Jung, and I. Amit. "Tissue-resident macrophage enhancer landscapes are shaped by the local microenvironment." *Cell* 159.6 (2014), pp. 1312–26. doi: 10.1016/j.cell.2014.11.018.

[373] A. J. Harrington, C. M. Bridges, S. Berto, K. Blankenship, J. Y. Cho, A. Assali, B. M. Siemsen, H. W. Moore, E. Tsvetkov, A. Thielking, G. Konopka, D. B. Everman, M. D. Scofield, S. A. Skinner, and C. W. Cowan. "MEF2C hypofunction in neuronal and neuroimmune populations produces MEF2C haploinsufficiency syndrome–like behaviors in mice." *Biological Psychiatry* 88.6 (2020), pp. 488–499. doi: 10.1016/j.biopsych.2020.03.011.

[374] A. Deczkowska, O. Matcovitch-Natan, A. Tsitsou-Kampeli, S. Ben-Hamo, R. Dvir-Szternfeld, A. Spinrad, O. Singer, E. David, D. R. Winter, L. K. Smith, A. Kertser, K. Baruch, N. Rosenzweig, A. Terem, M. Prinz, S. Villeda, A. Citri, I. Amit, and M. Schwartz. "Mef2c restrains microglial inflammatory response and is lost in brain ageing in an IFN-I-dependent manner." *Nature Communications* 8.717 (2017). doi: 10.1038/s41467-017-00769-0.

[375] X. Zhang, T. Liu, S. Xu, P. Gao, W. Dong, W. Liu, M. Gao, L. Song, L. Cui, and X. Dong. "A pro-inflammatory mediator USP11 enhances the stability of p53 and inhibits KLF2 in intracerebral hemorrhage." *Molecular therapy. Methods and clinical development* 21 (2021), pp. 681–692. doi: 10.1016/j.omtm.2021.01.015.

[376] A. Folick, S. K. Koliwad, and M. Valdearcos. "Microglial lipid biology in the hypothalamic regulation of metabolic homeostasis." *Frontiers in Endocrinology* 12.668396 (2021). doi: 10.3389/fendo.2021.668396.

[377] Y. Cui, Y. Zhang, X. Zhao, L. Shao, G. Liu, C. Sun, R. Xu, and Z. Zhang. "ACSL4 exacerbates ischemic stroke by promoting ferroptosis-induced brain injury and neuroinflammation." *Brain, Behavior, and Immunity* 93 (2021), pp. 312–321. doi: 10.1016/j.bbi.2021.01.003.

[378] E. B. Button, A. S. Mitchell, M. M. Domingos, J. H.-J. Chung, R. M. Bradley, A. Hashemi, P. M. Marvyn, A. C. Patterson, K. D. Stark, J. adrilatero, and R. E. Duncan. "Microglial cell activation increases saturated and decreases monounsaturated fatty acid content, but both lipid species are proinflammatory." *Lipids* 49 (2014), pp. 305–316. doi: 10.1007/s11745-014-3882-y.

[379] J. E. Yuste, E. Tarragon, C. M. Campuzano, and F. Ros-Bernal. "Implications of glial nitric oxide in neurodegenerative diseases." *Frontiers in Cellular Neuroscience* 9.322 (2015). doi: 10.3389/fncel.2015.00322.

[380] J. L. Kielczewski, P. Hu, L. C. Shaw, S. L. Calzi, R. N. Mames, T. A. Gardiner, E. McFarland, T. Chan-Ling, and M. B. Grant. "Novel protective properties of IGFBP-3 result in enhanced pericyte ensheathment, reduced microglial activation, increased microglial apoptosis, and neuronal protection after ischemic retinal injury." *The American Journal of Pathology* 178.4 (2011), pp. 1517–28. doi: 10.1016/j.ajpath.2010.12.031.

[381] Z. Xie, L. Huang, B. Enkhjargal, C. Reis, W. Wan, J. Tang, Y. Cheng, and J. H. Zhang. "Recombinant Netrin-1 binding UNC5B receptor attenuates neuroinflammation and brain injury via PPARγ/NFkB signaling pathway after subarachnoid hemorrhage in rats." *Brain, Behavior, and Immunity* 69 (2018), pp. 190–202. doi: 10.1016/j.bbi.2017.11.012.

[382] Y. Liang, D. Zheng, S. Peng, D. Lin, X. Jing, Z. Zeng, Y. Chen, K. Huang, Y. Xie, T. Zhou, and E. Tao. "Rifampicin attenuates rotenone-treated microglia inflammation via improving lysosomal function." *Toxicology in Vitro* 63.104690 (2020). doi: 10.1016/j.tiv.2019.104690.

[383] J. Satoh, Y. Kino, N. Kawana, Y. Yamamoto, T. Ishida, Y. Saito, and K. Arima. "TMEM106B expression is reduced in Alzheimer's disease brains." *Alzheimer's Research and Therapy* 6.17 (2014). doi: 10.1186/alzrt247.

[384] M. Herrera-Rivero, F. Santarelli, F. Brosseron, M. P. Kummer, and M. T. Heneka. "Dysregulation of TLR5 and TAM Ligands in the Alzheimer's Brain as Contributors to Disease Progression." *Molecular Neurobiology* 56.9 (2019), pp. 6539–6550. doi: 10.1007/s12035-019-1540-3.

[385] R. Ji, S. Tian, H. J. Lu, Q. Lu, Y. Zheng, X. Wang, J. Ding, Q. Li, and Q. Lu. "TAM receptors affect adult brain neurogenesis by negative regulation of microglial cell activation." *Journal of Immunology* 191.12 (2013), pp. 6165–77. doi: 10.4049/jimmunol.1302229.

[386] P. L. McGeer and E. G. McGeer. "Glial reactions in Parkinson's disease." *Movement disorders* 23.4 (2008), pp. 474–83. doi: 10.1002/mds.21751.

[387] H. Lian, L. Yang, A. Cole, L. Sun, A. C. A. Chiang, S. W. Fowler, D. J. Shim, J. Rodriguez-Rivera, G. Taglialatela, J. L. Jankowsky, H.-C. Lu, and H. Zheng. "NFkB-activated astroglial release of complement C3 compromises neuronal morphology and function associated with Alzheimer's disease." *Neuron* 85.1 (2015), pp. 101–115. doi: 10.1016/j.neuron.2014.11.018.

[388] S. Boillee, K. Yamanaka, C. S. Lobsiger, N. G. Copeland, N. A. Jenkins, G. Kassiotis, G. Kollias, and D. W. Cleveland. "Onset and progression in inherited ALS determined by motor neurons and microglia." *Science* 312.5778 (2006), pp. 1389–92. doi: 10.1126/science.1123511.

[389] D. R. Beers, J. S. Henkel, Q. Xiao, W. Zhao, J. Wang, A. A. Yen, L. Siklos, S. R. McKercher, and S. H. Appel. "Wild-type microglia extend survival in PU.1 knockout mice with familial amyotrophic lateral sclerosis." *Proceedings of the National Academy of Sciences of the United States of America* 103.43 (2006), pp. 16021–6. doi: 10.1073/pnas.0607423103.

[390] G. Gowing, T. Philips, B. V. Wijmeersch, J.-N. Audet, M. Dewil, L. V. D. Bosch, A. D. Billiau, W. Robberecht, and J.-P. Julien. "Ablation of proliferating microglia does not affect motor neuron degeneration in amyotrophic lateral sclerosis caused by mutant superoxide dismutase." *Journal of Neuroscience* 28.41 (2008), pp. 10234–44. doi: 10.1523/JNEUROSCI.3494-08.2008.

[391] W. J. Streit. "Microglia as neuroprotective, immunocompetent cells of the CNS." *Glia* 40.2 (2002), pp. 133–139. doi: 10.1002/glia.10154.

[392] C. N. Parkhurst, G. Yang, I. Ninan, J. N. Savas, J. R. Y. 3rd, J. J. Lafaille, B. L. Hempstead, D. R. Littman, and W.-B. Gan. "Microglia promote learning-dependent synapse formation through brain-derived neurotrophic factor." *Cell* 155.7 (2013), pp. 1596–609. doi: 10.1016/j.cell.2013.11.030.

[393] A. B. Campos, S. Duarte-Silva, B. Fernandes, S. P. das Neves, F. Marques, A. Teixeira-Castro, A. Neves-Carvalho, D. Monteiro-Fernandes, C. C. Portugal, R. Socodato, T. Summavielle, A. F. Ambrosio, J. B. Relvas, and P. Maciel. "Profiling Microglia in a Mouse Model of Machado–Joseph Disease." *Biomedicines* 10.2 (2022). doi: 10.3390/biomedicines10020237.

[394] N. N. Dagher, A. R. Najafi, K. M. N. Kayala, M. R. P. Elmore, T. E. White, R. Medeiros, B. L. West, and K. N. Green. "Colony-stimulating factor 1 receptor inhibition prevents microglial plae association and improves cognition in 3xTg-AD mice." *Journal of Neuroinflammation* 12.139 (2015). doi: 10.1186/s12974-015-0366-9.

[395] C.-C. Lin. "Clinical Development of Colony-Stimulating Factor 1 Receptor (CSF1R) Inhibitors." *Journal of Immunotherapy and Precision Oncology* 4.2 (2014), pp. 105–114. doi: 10.36401/JIPO-20-32.

[396] M. R. P. Elmore, R. J. Lee, B. L. West, and K. N. Green. "Characterizing Newly Repopulated Microglia in the Adult Mouse: Impacts on Animal Behavior, Cell Morphology, and Neuroinflammation." *PLOS ONE* 10.4 (2015). doi: 10.1371/journal.pone.0122912.

[397] M. Li, Z. Li, H. Ren, W.-N. Jin, K. Wood, Q. Liu, K. N. Sheth, and F.-D. Shi. "Colony stimulating factor 1 receptor inhibition eliminates microglia and attenuates brain injury after intracerebral hemorrhage." *Journal of Cerebral Blood Flow and Metabolism* 37.7 (2016). doi: 10.1177/0271678X16666551.

[398] W.-N. Jin, S. X.-Y. Shi, Z. Li, M. Li, K. Wood, R. J. Gonzales, and Q. Liu. "Depletion of microglia exacerbates postischemic inflammation and brain injury." *Journal of Cerebral Blood Flow and Metabolism* 37.6 (2017), pp. 2224–2236. doi: 10.1177/0271678X17694185.

[399] Y. Son, Y. J. Jeong, N.-R. Shin, S. J. Oh, K. R. Nam, H.-D. Choi, J. Y. Choi, and H.-J. Lee. "Inhibition of Colony-Stimulating Factor 1 Receptor by PLX3397 Prevents Amyloid Beta Pathology and Rescues Dopaminergic Signaling in Aging 5xFAD Mice." *International Journal of Molecular Sciences* 21.15 (2020), p. 5553. doi: 10.3390/ijms21155553.

[400] R. E. Bennett, A. Bryant, M. Hu, A. B. Robbins, S. C. Hopp, and B. T. Hyman. "Partial reduction of microglia does not affect tau pathology in aged mice." *Journal of Neuroinflammation* 15.311 (2018). doi: 10.1186/s12974-018-1348-5.

[401] B. Yegla, J. Boles, A. Kumar, and T. C. Foster. "Partial microglial depletion is associated with impaired hippocampal synaptic and cognitive function in young and aged rats." *Glia* 69.6 (2021), pp. 1494–1514. doi: 10.1002/glia.23975.

[402] Z. Cai, T. Ye, X. Xu, M. Gao, Y. Zhang, D. Wang, Y. Gu, H. Zhu, L. Tong, J. Lu, Z. Chen, and C. Huang. "Antidepressive properties of microglial stimulation in a mouse model of depression induced by chronic unpredictable stress." *Progress in Neuro-Pyschopharmacology and Biological Psychiatry* 101.109931 (2020). doi: 10.1016/j.pnpbp.2020.109931.

[403] T. L. Merry, A. E. S. Brooks, S. W. Masson, S. E. Adams, J. K. Jaiswal, S. M. F. Jamieson, and P. R. Shepherd. "The CSF1 receptor inhibitor pexidartinib (PLX3397) reduces tissue macrophage levels without affecting glucose homeostasis in mice." *International Journal of Obesity* 44.1 (2020), pp. 245–253. doi: 10.1038/s41366-019-0355-7.

[404] D. C. Rogers, E. M. Fisher, S. D. Brown, J. Peters, A. J. Hunter, and J. E. Martin. "Behavioral and functional analysis of mouse phenotype: SHIRPA, a proposed protocol for comprehensive phenotype assessment." *Mammalian Genome* 8.10 (1997), pp. 711–3. doi: 10.1007/s003359900551.

[405] J. A. Rafael, Y. Nitta, and J. P. K. E. Davies. "Testing of SHIRPA, a mouse phenotypic assessment protocol, on Dmd(mdx) and Dmd(mdx3cv) dystrophin-deficient mice." *Mammalian Genome* 11.9 (2000), pp. 725–8. doi: 10.1007/s003350010149.

[406] R. J. Carter, L. A. Lione, T. Humby, L. Mangiarini, A. Mahal, G. P. Bates, S. B. Dunnett, and A. J. Morton. "Characterization of progressive motor deficits in mice transgenic for the human Huntington's disease mutation." *The Journal of Neuroscience* 19.8 (1999), pp. 3248–57. doi: 10.1523/JNEUROSCI.19-08-03248.1999.

[407] M. Banez-Coronel, F. Ayhan, A. D. Tarabochia, T. Zu, B. A. Perez, S. K. Tusi, O. Pletnikova, D. R. Borchelt, C. A. Ross, R. L. Margolis, A. T. Yachnis, J. C. Troncoso, and L. P. W. Ranum. "RAN Translation in Huntington Disease." *Neuron* 88.4 (2015), pp. 667–77. doi: 10.1016/j.neuron.2015.10.038.

[408] F. Lei, N. Cui, C. Zhou, J. Chodosh, D. G. Vavvas, and E. I. Paschalis. "CSF1R inhibition by a small-molecule inhibitor is not microglia specific; affecting hematopoiesis and the function of macrophages." *Proceedings of the National Academy of Sciences of the United States of America* 117.38 (2020), pp. 23336–23338. doi: 10.1073/pnas.1922788117.

[409] S. Kasihara, K. Shinohara, and H. Tsutsui. "Effects of Intracerebroventricular Administration of Colony Stimulating Factor 1 Receptor Inhibitor on Microglia." *Federation of American Societies for Experimental Biology* 33.S1 (2019), pp. 621–621. doi: 10.1096/fasebj.2019.33.1_supplement.lb621.

[410] F. Tahmasebi, P. Pasbakhsh, K. Mortezaee, S. Madadi, S. Barati, and I. R. Kashani. "Effect of the CSF1R inhibitor PLX3397 on remyelination of corpus callosum in a cuprizone-induced demyelination mouse model." *Journal of Cellular Biochemistry* 120.6 (2019), pp. 10576–10586. doi: 10.1002/jcb.28344.

[411] M.-J. Park, H.-S. Park, M.-J. You, J. Yoo, S. H. Kim, and M.-S. Kwon. "Dexamethasone Induces a Specific Form of Ramified Dysfunctional Microglia." *Molecular Neurobiology* 56 (2019), pp. 1421–1436. doi: 10.1007/s12035-018-1156-z.

[412] R. von Bernhardi, J. Tichauer, and L. E. von Bernhardi. "Proliferating culture of aged microglia for the study of neurodegenerative diseases." *Journal of Neuroscience Methods* 202.1 (2011), pp. 65–9. doi: 10.1016/j.jneumeth.2011.08.027.

[413] T. Masuda, R. Sankowski, O. Staszewski, and M. Prinz. "Microglia Heterogeneity in the Single-Cell Era." *Cell Reports* 30.5 (2020), pp. 1271–1281. doi: 10.1016/j.celrep.2020.01.010.

[414] T. Masuda, R. Sankowski, O. Staszewski, C. Bottcher, L. Amann, Sagar, C. Scheiwe, S. Nessler, P. Kunz, G. van Loo, V. A. Coenen, P. C. Reinacher, A. Michel, U. Sure, R. Gold, D. Grun, J. Priller, C. Stadelmann, and M. Prinz. "Spatial and temporal heterogeneity of mouse and human microglia at single-cell resolution." *Nature* 566 (2019), pp. 388–392. doi: 10.1038/s41586-019-0924-x.

[415] J. Zheng, W. Ru, J. R. Adolacion, M. S. Spurgat, X. Liu, S. Yuan, R. X. Liang, J. Dong, A. S. Potter, S. S. Potter, K. Chen, R. Chen, N. Varadarajan, and S.-J. Tang. "Single-cell RNA-seq analysis reveals compartment-specific heterogeneity and plasticity of microglia." *Cell Press* 24.3 (2021). doi: 10.1016/j.isci.2021.102186.

[416] H.-D. Li, M. Li, E. Shi, W.-N. Jin, K. Wood, R. Gonzales, and Q. Liu. "A translocator protein 18 kDa agonist protects against cerebral ischemia/reperfusion injury." *Journal of Neuroinflammation* 14.151 (2017). doi: 10.1186/s12974-017-0921-7.

[417] R. Xu, X. Li, A. J. Boreland, A. Posyton, K. Kwan, R. P. Hart, and P. Jiang. “Human iPSC-derived mature microglia retain their identity and functionally integrate in the chimeric mouse brain.” *Nature Communications* 11.1 (2020). doi: 10.1038/s41467-020-15411-9.

[418] A. M. Smith and M. Dragunow. “The human side of microglia.” *Trends in Neuroscience* 37.3 (2014), pp. 125–35. doi: 10.1016/j.tins.2013.12.001.

[419] D. Gosselin, D. Skola, N. G. Coufal, I. R. Holtman, J. C. M. Schlachetzki, E. Sajti, B. N. Jaeger, C. O Connor, C. Fitzpatrick, M. P. Pasillas, M. Pena, A. Adair, D. D. Gonda, M. L. Levy, R. M. Ransohoff, F. H. Gage, and C. K. Glass. “An environment-dependent transcriptional network specifies human microglia identity.” *Science* 356.6344 (2017). doi: 10.1126/science.aal3222.

[420] C. Tronel, B. Largeau, M. J. S. Ribeiro, D. Guilloteau, A.-C. Dupont, and N. Arlicot. “Molecular Targets for PET Imaging of Activated Microglia: The Current Situation and Future Expectations.” *International Journal of Molecular Sciences* 18.4 (2017). doi: 10.3390/ijms18040802.

Appendix A

Materials and Methods of Chapters 2 to 5

Antibodies	Supplier	Dilution	Technique
Primary antibodies			
PE anti-mouse CD45 antibody	BioLegend Catalog nº 103106	1:200	Flow cytometry
PE/Cy7 anti-mouse/human CD11b antibody	BioLegend Catalog nº Cat#101215	1:200	Flow cytometry
Alexa Fluor 647 anti-mouse/human CD11b antibody	BioLegend Catalog nº 101218	1:200	Flow cytometry
Anti-rat CDKN2A/p19ARF antibody	Santa Cruz biotechnology Catalog nº sc -32748	1:200	Flow cytometry
Anti-rabbit Cdkn1a/p21Cip1/Waf1 antibody	Abcam Catalog nº ab188224	1:50	Flow cytometry
Anti-mouse CXCL8/IL-8 antibody	GeneTex Catalog nº GTX15763	2µg/ml	Flow cytometry
Anti-rabbit IL-6 antibody	Cell Signalling Catalog nº #12912	1:400	Flow cytometry
Anti-rabbit IL-1 beta antibody	Abcam Catalog nº ab9722	1:100	Flow cytometry
Anti-rabbit IL-1 alpha antibody	Abcam Catalog nº ab7632	1:100	Flow cytometry
Anti-rabbit Iba-1 antibody	Wako Catalog nº 019-19741	1:600	Immunofluorescence
Anti-mouse GFAP antibody	EMD Millipore Catalog nº MAB360	1:500	Immunofluorescence
Secondary antibodies			
Goat Anti-Rabbit IgG (H+L) Cross-Adsorbed Secondary Antibody, Alexa Fluor 594	Thermo Fisher Scientific Catalog nº # A-11012	1:1000	Immunofluorescence
Goat Anti-mouse IgG (H+L) Cross-Adsorbed Secondary Antibody, Alexa Fluor 488	Thermo Fisher Scientific Catalog nº # A-11001	1:1000	Immunofluorescence
Goat anti-Rabbit IgG (H+L) Cross-Adsorbed Secondary Antibody, Alexa Fluor 647	Thermo Fisher Scientific Catalog nº #A-21244	1:1000	Flow cytometry
Goat anti-mouse IgG (H+L) Cross-Adsorbed Secondary Antibody, Alexa Fluor 488	Thermo Fisher Scientific Catalog nº #A-11001	1:1000	Flow cytometry
Goat anti-rat IgG (H+L) Cross-Adsorbed Secondary Antibody, Alexa Fluor 488	Thermo Fisher Scientific Catalog nº #A-11006	1:1000	Flow cytometry

Figure A.1: **List of primary and secondary antibodies used in flow cytometry and immunofluorescence.**

Gene	Sequence		Reference
	Forward (5´to 3´)	Reverse (5´to 3´)	
p16^{INK4a}	5′- CCCAACGCCCCGAACT- 3′	5′- GCAGAAGAGCTGCTACGTGAA- 3′	[14]
p19^{Arf}	5′- AGGCCGGCAAATGATCATAGA - 3′	5′- ACTTCCAAACATCATGAC CTGC - 3′	Primer-BLAST
p21$^{Cip1/Waf1}$	5′- GTCCAATCCTGGTGATGTCC - 3′	5′- GTTTTCGGCCCTGAGATGT - 3′	[14]
Pai1	5′- GCACTGCAAAAGGTCAGGAT - 3′	5′- TGGCCCATGAAGAGGATTGT - 3′	[14]
Icam-1	5′- CCATCACCGTGTATTCGTTTC - 3′	5′- AGGTCCTTGCCTACTTGCT - 3′	Primer-BLAST
Hmgb1	5′- CCATTGGTGATGTTGCAAAG - 3′	5′- CTTTTTCGCTGCATCAGGTT - 3′	Primer-BLAST
Il-1 beta	5′- ACCTTCCAGGATGAGGACATGA - 3′	5′- AACGTCACACACCAGCAGGTTA - 3′	Primer-BLAST
Il-6	5′- ACACATGTTCTCTGG GAAATCGT- 3′	5′-AAGTGCATCATCGTTGTTCATACA - 3′	Primer-BLAST
Fos	5′- ATGGTGAAGACCGTGTCAGG - 3′	5′- GTTGATCTGTCTCCGCTTGGA - 3′	Primer-BLAST
Bmpr2	5′- GAGCACAGAGGCCCAATTCT - 3′	5′- ATCTTGTGTTGACTCACCTATCTGT - 3′	Primer-BLAST
Hipk3	5′- AGAAAGCGGGTGTGAGACTG - 3′	5′- GGCTGGCATGTAGAATCCGT - 3′	Primer-BLAST
Junb	5′- AGGCAGCTACTTTTCGGGTC - 3′	5′- TTGCTGTTGGGGACGATCAA - 3′	Primer-BLAST
Epsti1	5′- CGAGAGCATCATCAGTCCAAAAC - 3′	5′- GTCCATCCCTCGTCTTTTGC - 3′	Primer-BLAST
human ataxin-3	5′- GGAACAATGCGTCGGTTG - 3′	5′- GCCCTAACTTTAGACATGTTAC - 3′	[29]
mouse ataxin-3	5′- TGTCTTGTTACAGAAAGATCAG - 3′	5′- GTTACAAGAACAGAGCTGACT - 3′	[29]
B2m	5′- CCTTCAGCAAGGACTGGTCT - 3′	5′- TCTCGATCCCAGTAGACGGT - 3′	Primer-BLAST

Figure A.2: **List of primers used in reverse-transcription quantitative real-time PCR.**

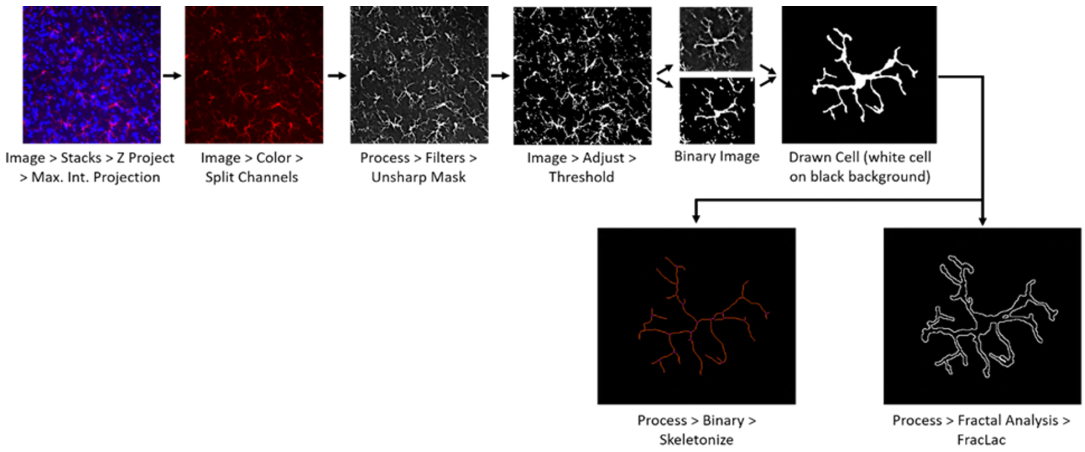

Figure A.3: **The process to prepare binary (black and white) images for fractal and skeleton analysis.** Several steps were followed to apply commands and options to obtain single-cell binary of microglia from original Z-stacks images with double-color image (Iba-1 labels the microglia in the red channel and DAPI labels the nuclei in the blue channel). Binary single-cells were then converted into an outline or into a skeletonized format, to carry out a fractal or skeleton analysis, respectively. Adapted from Young et al. (2018) [338].

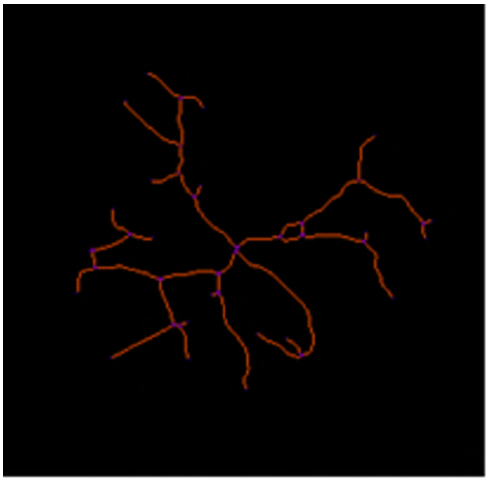

Figure A.4: **The MorphData and Skeleton 2D/3D plugins were applied to the skeletonized images, which tag skeletal features relevant to microglia ramification:** total branch length and slab voxels as orange, endpoints as blue, and junctions as purple. Adapted from Young et al. (2018) [338].

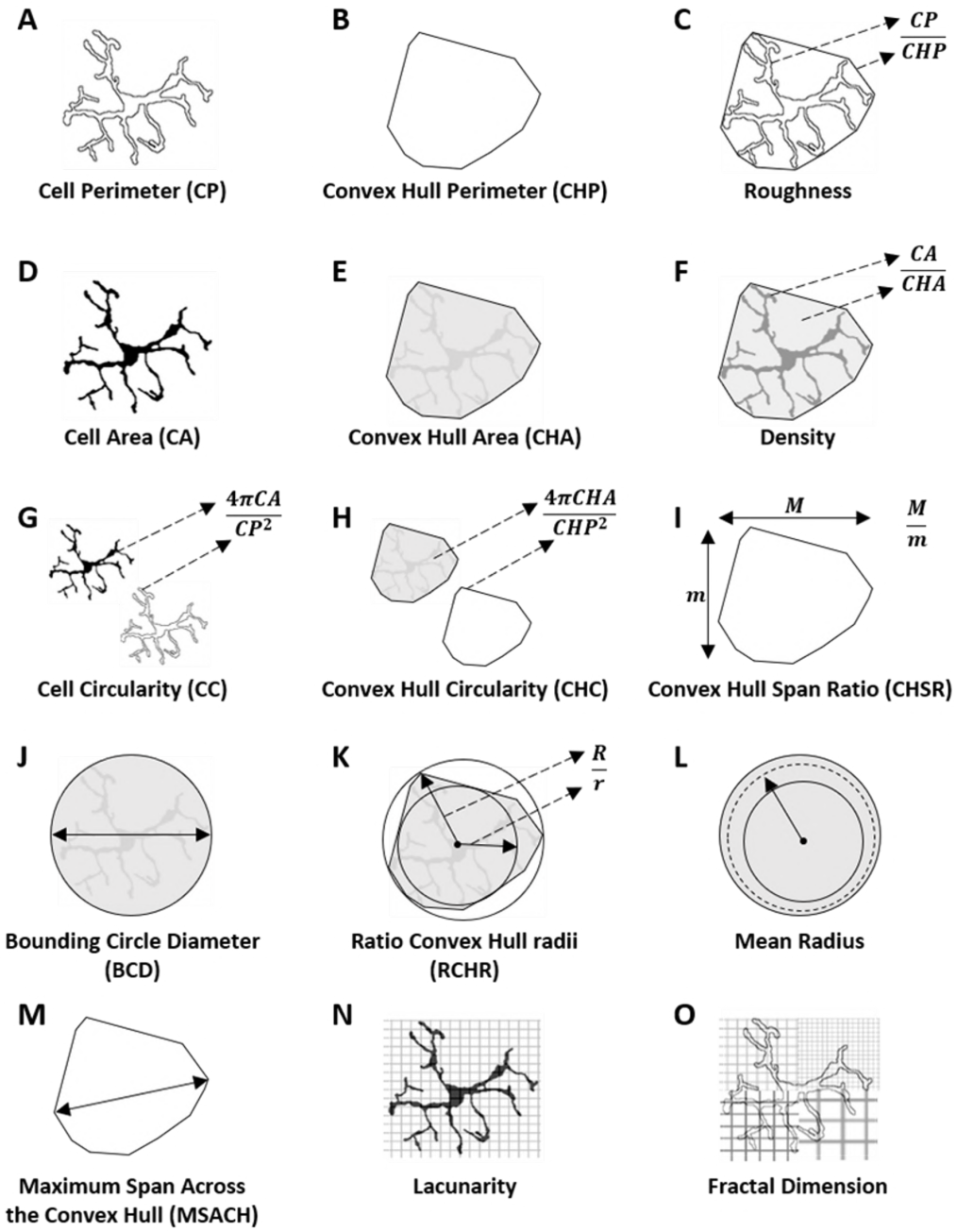

Figure A.5: **The outline images were processed using the *MorphData* and *FracLac* plugins to obtain data regarding the hull and circle results such as a)** cell perimeter, **b)** convex hull perimeter, **c)** roughness, **d)** cell area, **e)** convex hull area, **f)** density, **g)** cell circularity, **h)** convex hull circularity, **i)** convex hull span ratio, **j)** bounding circle diameter, **k)** ratio convex hull radii, **l)** mean radius, and **m)** maximum span across the convex hull. Regarding the box count summary, **n)** lacunarity and **o)** fractal dimension were the obtained data. Adapted from Fernández-Arjona et al. (2019) [183].

Cell Type	Gene	WT_1	WT_2	WT_3	WT_4
Astrocytes	P4ha3	-2.736965594	-1.184424571	-2.473931188	-0.535331733
Astrocytes	Slc25a34	-2.184424571	-0.200912694	0.214124805	-0.943416472
Astrocytes	Chrdl1	-2.184424571	-1.184424571	-1.473931188	-3.473931188
Astrocytes	Glis3	-1.785875195	0.070389328	-3.473931188	-3.473931188
Astrocytes	Cybrd1	-1.184424571	-1.943416472	-2.473931188	0.378511623
Astrocytes	Kcnn3	-1.184424571	-3.473931188	-1.473931188	-3.473931188
Astrocytes	Gdpd2	-0.971430848	-0.200912694	0.214124805	-0.074000581
Astrocytes	Trim9	-0.971430848	-1.184424571	-1.152003093	0.056583528
Astrocytes	Mlc1	-0.971430848	-0.713118852	-1.473931188	-0.943416472
Astrocytes	Slc7a2	-0.971430848	0.565597176	-0.029146346	-2.556393349
Astrocytes	Ranbp3l	-0.76121314	0.070389328	0.970853654	0.275007047
Astrocytes	Gm5089	-0.76121314	-1.943416472	-0.888968688	-2.556393349
Astrocytes	Rgs20	-0.76121314	-1.943416472	-0.49410907	-2.556393349
Astrocytes	Grhl1	-0.59946207	-3.473931188	-0.49410907	1.111031312
Astrocytes	Fzd2	-0.59946207	-0.058893689	-2.473931188	-2.556393349
Astrocytes	Vnn1	-0.321928095	-3.473931188	0.516015147	-0.943416472
Astrocytes	Ttpa	-0.321928095	0.389566812	-3.473931188	-0.535331733
Astrocytes	2900005J15Rik	-0.184424571	1.339137385	-1.152003093	0.925999419
Astrocytes	Pm20d1	0.22650853	0.070389328	1.599317794	1.22650853
Astrocytes	Pamr1	0.310340121	0.475084883	-0.49410907	-1.943416472
Astrocytes	Frem2	0.310340121	-0.713118852	0.604071324	-0.200912694
Astrocytes	Rorb	0.310340121	0.731183242	1.799087306	1.895302621
Astrocytes	Gli1	0.40053793	-1.514573173	0.604071324	0.555816155
Astrocytes	Mamdc2	0.40053793	-0.200912694	0.321928095	0.713695815
Astrocytes	Pipox	0.40053793	1.182692298	1.682573297	-0.074000581
Astrocytes	Cyp4f15	0.475084883	-1.184424571	-1.888968688	-2.556393349
Astrocytes	Gli3	0.545968369	-0.358453971	1.15704371	1.859969548
Astrocytes	Cbs	0.545968369	0.286881148	0.604071324	1.056583528
Astrocytes	Itih3	0.687060688	0.176322773	-0.49410907	0.86393845
Astrocytes	Atp13a4	0.748461233	0.176322773	-0.321928095	-0.074000581
Astrocytes	Grm3	0.748461233	0.176322773	2.15704371	-0.074000581
Astrocytes	Tnc	0.807354922	-0.713118852	0.757023247	0.790772038
Astrocytes	Ccdc80	0.871843649	1.726831217	1.510961919	1.859969548
Astrocytes	Cldn10	1.03562391	0.176322773	1.510961919	1.275007047
Astrocytes	Elovl2	1.03562391	1.608809243	1.555816155	1.111031312
Astrocytes	Entpd2	1.13093087	1.124328135	1.269033146	0.86393845
Astrocytes	Crb2	1.182692298	1.063502942	0.604071324	0.641546029
Astrocytes	Dio2	1.182692298	0.871843649	2.003602237	2.752748591
Astrocytes	Itga7	1.182692298	1.063502942	1.761285273	0.86393845
Astrocytes	Paqr6	1.316145742	1.384049807	2.066950244	1.372952098
Astrocytes	Cth	1.475084883	0.565597176	0.757023247	0.713695815
Astrocytes	Sorcs2	1.510961919	1.432959407	0.90303827	-0.358453971
Astrocytes	Plcd4	1.618238656	0.799087306	2.6622055	2.422233001
Astrocytes	Hgf	1.687060688	1.687060688	1.214124805	1.22650853
Astrocytes	Aqp9	1.748461233	2.336283388	1.970853654	3.209453366
Astrocytes	Slc14a2	1.839959587	1.232660757	2.904965719	1.327687364
Astrocytes	Ephx2	1.867896464	2.003602237	1.372952098	0.275007047
Astrocytes	Celsr1	2.13093087	0.070389328	0.604071324	0.555816155
Astrocytes	Aqp4	2.13093087	2.456806149	3.08236197	2.771885579
Astrocytes	Fam20a	2.201633861	2.150559677	0.970853654	2.422233001
Astrocytes	Bmpr1b	2.247927513	2.871843649	2.778208576	2.825785627
Astrocytes	Slc15a2	2.435628594	2.853995647	3.599317794	3.182692298

Cell Type	Gene	WT_1	WT_2	WT_3	WT_4
Astrocytes	AI464131	2.510961919	2.17951105	1.90303827	1.469885976
Astrocytes	Adhfe1	2.634593268	2.063502942	1.835924074	2.250961574
Astrocytes	Fgfr3	2.669026766	2.587364991	2.887525271	2.944858446
Astrocytes	Gm973	2.939226578	2.608809243	3.112700133	3.399171094
Astrocytes	Egfr	3.203201156	1.871843649	2.682573297	2.22342255
Astrocytes	Fmo1	3.385431037	3.311793718	3.198494154	1.992768431
Astrocytes	Lrig1	3.444932049	3.577730931	3.280956314	3.097610797
Astrocytes	Nwd1	3.529820947	3.444932049	3.22650853	3.350497247
Astrocytes	Ppp1r3c	3.600507645	3.49057013	4.09000653	4.083213368
Astrocytes	Slc14a1	3.733354341	3.456806149	3.588564737	3.301587647
Astrocytes	Aldh1l1	3.772941338	3.679198571	3.641546029	3.523561956
Astrocytes	Prdm16	3.839959587	3.444932049	3.465974465	1.992768431
Astrocytes	Slc4a4	3.847996907	3.165107985	3.407352751	2.698218478
Astrocytes	Tmem82	3.919340082	3.512226887	3.769771739	3.638073837
Astrocytes	Slc7a11	4.150559677	4.572283367	4.351204277	4.873321063
Astrocytes	Slc39a12	4.34978987	4.056583528	4.29351763	3.434294618
Astrocytes	Slc6a11	4.35473424	4.299391206	4.702103407	4.381283373
Astrocytes	Notch3	4.370164281	3.818646083	3.929790998	3.534808661
Astrocytes	Aifm3	4.622344723	4.698218478	4.820689561	4.363171077
Astrocytes	Sox9	5.029452886	4.193771743	4.615298579	3.456806149
Astrocytes	Vcam1	5.171126747	5.849999259	5.865176497	5.262658655
Astrocytes	Gja1	5.397802962	5.621465834	5.880685525	5.75141016
Astrocytes	Abcd2	5.542877099	5.075532631	4.904484098	5.348019909
Astrocytes	Daam2	5.745237332	5.037821465	5.469234794	5.9800253
Astrocytes	Slc7a10	5.874796966	5.467931546	5.260402093	3.860962798
Astrocytes	Slc1a3	6.955940451	6.662917555	6.499367566	6.007419784
Endothelia	Fgfbp1	-2.184424571	-0.358453971	-3.473931188	-3.473931188
Endothelia	Sox17	-1.785875195	-3.473931188	-3.473931188	-3.473931188
Endothelia	Kcnq1	-1.785875195	-0.713118852	-0.888968688	-2.556393349
Endothelia	Megf6	-1.434402824	-0.058893689	-0.49410907	-1.514573173
Endothelia	Hmgcs2	-0.454031631	-0.514573173	-0.168122759	-3.473931188
Endothelia	Angpt2	-0.184424571	-0.514573173	-0.888968688	-3.473931188
Endothelia	Abcc6	-0.074000581	0.286881148	-0.321928095	0.713695815
Endothelia	Hrct1	0.028569152	0.475084883	0.097610797	-1.217591435
Endothelia	Gimap4	0.137503524	-0.200912694	0.422233001	0.641546029
Endothelia	Myct1	0.310340121	0.799087306	-2.473931188	1.372952098
Endothelia	Slco1a4	0.475084883	0.799087306	1.321928095	-0.074000581
Endothelia	C130074G19Rik	0.687060688	0.475084883	0.516015147	1.169925001
Endothelia	Clec14a	0.748461233	1.232660757	0.097610797	0.378511623
Endothelia	Hmcn1	0.748461233	1.232660757	0.604071324	-0.535331733
Endothelia	Adh1	0.748461233	-0.713118852	0.831877241	-0.358453971
Endothelia	Sigirr	1.084064265	1.937344392	1.03562391	1.275007047
Endothelia	4930578C19Rik	1.35614381	-0.514573173	0.678071905	1.056583528
Endothelia	Adamtsl2	1.510961919	1.124328135	1.269033146	1.056583528
Endothelia	Igsf5	1.584962501	-0.200912694	1.416839742	0.713695815
Endothelia	Gimap8	1.687060688	1.937344392	0.604071324	0.555816155
Endothelia	Asb4	1.839959587	2.765534746	2.370164281	3.007195501
Endothelia	Nostrin	1.839959587	2.939226578	2.922197848	1.925999419
Endothelia	AU021092	1.981852653	2.629939409	2.266036894	2.422233001
Endothelia	Stap2	2.007195501	1.937344392	2.097610797	1.555816155
Endothelia	Csrp2	2.060047384	1.726831217	2.066950244	1.599317794
Endothelia	Ly75	2.17951105	1.650764559	0.678071905	1.056583528

Cell Type	Gene	WT_1	WT_2	WT_3	WT_4
Endothelia	Flt4	2.313245852	2.456806149	0.422233001	0.713695815
Endothelia	Mmrn2	2.35614381	2.336283388	2.23878686	1.718087584
Endothelia	Mfsd7c	2.414135533	2.23572706	1.90303827	2.195347598
Endothelia	Cd40	2.414135533	2.970853654	2.599317794	3.534808661
Endothelia	Scarf1	2.510961919	1.687060688	1.321928095	1.275007047
Endothelia	Icam2	2.548436625	3.324810603	3.294253136	3.140778656
Endothelia	Mecom	2.548436625	3.608809243	1.937344392	2.87774425
Endothelia	Sema3g	2.582556003	3.033863452	2.742006211	2.195347598
Endothelia	Nos3	2.748461233	1.937344392	1.599317794	1.718087584
Endothelia	Rnf125	2.794935663	3.27351589	2.62058641	3.697106574
Endothelia	Ctsw	2.794935663	2.09423607	2.003602237	3.209453366
Endothelia	Trim16	2.811471031	3.545968369	2.513490746	2.169925001
Endothelia	Foxf2	2.811471031	2.23572706	1.871843649	2.301587647
Endothelia	Rassf9	2.811471031	2.063502942	2.555816155	2.735522177
Endothelia	Serpinb6b	2.869871406	2.587364991	2.887525271	1.372952098
Endothelia	Mmp25	2.925999419	3.726831217	2.12763328	3.399171094
Endothelia	Slc19a3	2.939226578	3.260025656	2.759155834	3.196921734
Endothelia	Tie1	2.994579724	3.017921908	2.722466024	2.250961574
Endothelia	Ptgis	2.994579724	3.207892852	3.267535798	2.350497247
Endothelia	Ctla2a	2.994579724	3.311793718	3.896271849	3.22342255
Endothelia	Dll4	3.132576843	2.629939409	3.198494154	2.46727948
Endothelia	Robo4	3.17951105	2.904965719	2.641546029	2.513490746
Endothelia	Higd1b	3.280956314	3.311793718	3.419538892	1.992768431
Endothelia	Foxq1	3.280956314	1.565597176	1.799087306	2.111031312
Endothelia	Egfl7	3.435628594	3.27351589	3.169925001	3.007195501
Endothelia	Akr1c14	3.444932049	3.234194723	3.798050515	3.411426246
Endothelia	Ushbp1	3.473786912	3.361768359	3.3950628	3.422233001
Endothelia	Adcy4	3.557042415	3.764473551	3.9800253	3.375734539
Endothelia	Slc38a5	3.764473551	3.374343989	2.815575429	2.657640005
Endothelia	Kdr	3.794935663	3.152183419	2.49057013	2.715893371
Endothelia	8430408G22Rik	3.854993017	4.8928767	4.376429311	3.301587647
Endothelia	Erg	4.077242999	4.444932049	4.357552005	4.351204277
Endothelia	Cyyr1	4.083213368	3.649615459	4.260025656	3.983677695
Endothelia	Cd93	4.161887682	4.06436554	3.887525271	3.968090752
Endothelia	Slc16a4	4.302319051	4.267535798	4.27351589	3.313245852
Endothelia	Tm4sf1	4.329123596	4.8928767	5.570159302	5.093813673
Endothelia	She	4.334139179	3.649615459	4.10433666	4.06091205
Endothelia	Itga4	4.482848283	4.456806149	3.77925972	3.512226887
Endothelia	Emcn	4.556429415	4.917909074	4.721372659	5.316869805
Endothelia	Wfdc1	4.622344723	5.00270252	4.860962798	4.501439145
Endothelia	Gm694	4.717539343	5.00270252	4.589164237	5.068240861
Endothelia	Slc39a8	4.721372659	5.101397952	5.066950244	5.123086751
Endothelia	Slc22a8	4.741466986	4.361768359	4.126807703	4.097610797
Endothelia	Tek	4.74899785	4.717539343	4.833902077	4.307428525
Endothelia	Esam	4.764473551	4.659353759	4.212569339	4.169123281
Endothelia	Cgnl1	4.810443104	4.618825953	4.615298579	4.404630684
Endothelia	Slfn5	4.876762491	4.618825953	4.760220946	5.545041683
Endothelia	Lsr	4.953265239	5.093813673	4.72628629	4.692092375
Endothelia	Ocln	4.967168608	5.126807703	4.860962798	4.622930351
Endothelia	Abcb1a	5.070818638	5.053111336	4.847495884	4.702103407
Endothelia	Cldn5	5.214124805	4.974988112	4.019701914	4.512858954
Endothelia	Car4	5.328764672	5.220716892	5.382667253	5.442611804

Cell Type	Gene	WT_1	WT_2	WT_3	WT_4
Endothelia	Igfbp7	5.405311683	5.427606173	5.564683017	5.316869805
Endothelia	Stra6	5.782146424	5.504302583	5.3323499	4.422233001
Endothelia	Pglyrp1	5.983677695	7.031880366	5.575614878	6.428276414
Endothelia	Ptprb	6.168120505	5.582556003	6.102658131	5.871350841
Endothelia	Flt1	6.260402093	6.304145941	5.689578726	5.907131025
Endothelia	Cdh5	6.43496176	5.838951767	5.181102551	5.531693361
Endothelia	Fn1	6.443440891	6.531849286	5.506525779	5.758356483
Endothelia	Ly6a	6.591858905	6.744833837	6.625854931	6.561020578
Endothelia	Fam129a	6.669452026	6.450881315	5.743353391	6.106641452
Endothelia	Itm2a	6.970393538	6.462215955	6.727648222	6.432625411
Endothelia	Pecam1	7.323550215	7.508507884	7.253611152	7.420297118
Endothelia	Cd34	7.82635781	7.688739868	7.397802962	6.967053298
Microglia	Ptafr	-0.184424571	-0.943416472	-0.321928095	0.275007047
Microglia	Ch25h	1.432959407	1.384049807	1.15704371	-0.074000581
Microglia	Fcgr2b	2.669026766	3.862947248	2.292781749	3.386810946
Microglia	Ccr7	3.007195501	4.343407822	3.140778656	3.678071905
Microglia	Myo1g	3.313245852	3.628773595	3.003602237	3.678071905
Microglia	Angptl7	3.385431037	3.649615459	3.155425432	2.375734539
Microglia	C1qc	3.64385619	3.689299161	3.489286023	3.326249701
Microglia	Ccl7	3.74092756	3.432959407	3.344828497	2.513490746
Microglia	Tnf	3.749534268	3.311793718	2.987320866	2.596935142
Microglia	Gdf15	3.960697039	3.658782734	4.03562391	3.648465443
Microglia	Hmha1	3.987320866	3.746312766	3.577730931	3.648465443
Microglia	Tnfaip8l2	4.799087306	4.577126661	4.506525779	4.776630423
Microglia	Arhgap9	4.904965719	5.148120631	4.599912842	4.972233124
Microglia	Tlr2	5.176721693	5.302684614	5.145269857	5.126394738
Microglia	Rac2	5.456806149	6.123086751	4.925999419	5.147713722
Microglia	Asb2	5.576522138	5.086613947	4.59454855	5.137093609
Microglia	Myo1f	5.655924213	5.746043983	5.059182199	5.498889087
Microglia	Ccl4	5.67468662	5.045268215	5.357552005	4.94016675
Microglia	Rhoh	5.731454808	5.759954742	6.066735029	5.892391026
Microglia	C5ar1	5.741197299	5.807870078	5.335569006	5.605257263
Microglia	Ncf4	5.764738923	6.12122267	5.567423758	5.96208625
Microglia	Csf2rb	5.764738923	6.086613947	5.394719913	5.966015097
Microglia	Slamf8	5.934516502	6.257387843	6.041549645	6.324630615
Microglia	Tbxas1	6.005175391	5.6441447	5.027684877	5.007644031
Microglia	Psd4	6.060047384	6.071676874	5.322649262	5.526381863
Microglia	Fermt3	6.303598117	6.203788453	6.064796646	5.854245054
Microglia	Ccdc88b	6.349612972	6.453682186	5.967399199	6.147713722
Microglia	Gpr157	6.371384614	5.981167667	6.09148828	6.309067021
Microglia	H2-Oa	6.405481882	6.534497434	6.234961095	6.432625411
Microglia	Csf3r	6.463851293	6.208868371	5.66448284	5.929790998
Microglia	Hk3	6.586314394	7.064257744	6.908692838	6.932746251
Microglia	Pik3r5	6.676662335	6.972118218	6.286881148	6.229780167
Microglia	H2-DMb1	6.687060688	6.671576448	6.393175914	6.391630262
Microglia	Nlrp3	6.744161096	6.69474093	6.892633883	6.871227612
Microglia	Gpr183	6.836555368	6.651625784	7.264536431	7.029563314
Microglia	Slc15a3	6.886428211	7.07264178	6.977737849	7.027574304
Microglia	Nfam1	7.015024705	6.923268053	6.257010618	6.307428525
Microglia	Parvg	7.028016544	7.113117036	6.965437996	6.888256181
Microglia	Cd83	7.134631671	6.92943596	8.191602128	7.749601306
Microglia	Slamf9	7.15916495	7.110405007	6.909773104	7.012233436

Cell Type	Gene	WT_1	WT_2	WT_3	WT_4
Microglia	Card9	7.16138386	7.386897147	7.510724614	7.681378984
Microglia	Snx20	7.192687344	7.258141996	7	7.365360097
Microglia	Ncf2	7.242983516	7.568716189	7.559950613	7.734438666
Microglia	Il21r	7.271276259	7.341896821	7.160476536	7.303506793
Microglia	Hck	7.282161767	7.328674927	7.208185577	7.298749947
Microglia	Was	7.322198575	7.489767697	7.272863023	7.303506793
Microglia	Ccl2	7.399769244	7.371036052	7.510012465	6.649471757
Microglia	Abcc3	7.458529652	7.336461928	6.854245054	6.850874416
Microglia	Cd300a	7.462706751	7.726013749	7.531069493	7.889777722
Microglia	Slfn2	7.533251852	7.859721129	7.453929061	7.868575655
Microglia	Cbr2	7.611393726	7.73782194	7.64911244	7.650046479
Microglia	Plau	7.710324307	6.852123719	6.533096079	6.319943024
Microglia	Alox5ap	7.746648675	7.882826431	7.442114122	7.864867085
Microglia	Cxcl16	7.79298546	7.631540867	7.632995197	7.539003674
Microglia	Ltc4s	7.824958741	7.939226578	7.73430317	7.724445639
Microglia	Rasal3	7.877928255	7.794415866	7.661279302	7.526929538
Microglia	P2ry6	7.955533674	8.247452865	8.151016539	8.060263599
Microglia	Ccr5	8.025582548	8.353852559	8.219071692	8.209697044
Microglia	Sash3	8.084648965	8.251577088	7.625197417	7.858416225
Microglia	Lag3	8.202809492	8.026634096	7.860280012	7.845490051
Microglia	Pik3ap1	8.264067216	7.924278073	7.775379826	7.885574364
Microglia	Kcnk6	8.299299615	8.537606691	8.12820059	7.734438666
Microglia	Il1b	8.422401216	8.832130501	8.454998363	9.130029933
Microglia	Irf5	8.454011343	8.301450467	7.461970494	7.524894265
Microglia	Ccrl2	8.466300829	8.482404631	8.528922886	8.392317423
Microglia	Ptpn6	8.46837967	8.498490233	8.151473257	8.570235215
Microglia	Cd37	8.49988574	8.475733431	8.467768557	8.295998462
Microglia	Blnk	8.587440004	8.822443365	8.764506725	8.806710718
Microglia	Vav1	8.708325207	8.768118145	8.644937806	8.853559081
Microglia	Nckap1l	8.720346877	8.61176256	8.713352144	8.435128498
Microglia	Tlr9	8.746379954	8.492574264	8.193377511	8.587515014
Microglia	Cd52	8.816567709	9.227447479	8.900414008	9.569077102
Microglia	Ccl9	8.838605166	8.967341555	9.060236574	9.483654573
Microglia	Itgb2	9.075693064	9.425069003	8.644649454	9.071650062
Microglia	Slc11a1	9.092387172	9.174276573	9.173477269	9.114367025
Microglia	Nfkbid	9.125232638	8.886001351	9.058316496	8.52320908
Microglia	Cd14	9.330267071	9.606608786	9.396690399	9.763162561
Microglia	Ncf1	9.502931228	9.818550224	9.45318831	9.665762267
Microglia	Siglech	9.534127764	9.536907693	9.784324027	9.53954658
Microglia	Irf8	9.557119022	9.103130415	8.173926932	8.280446011
Microglia	Pla2g15	9.627460927	9.470597871	8.954312652	9.211815306
Microglia	Cx3cr1	9.980910713	9.856067534	9.619192892	9.535683629
Microglia	Tmem119	10.16948662	10.22724289	9.807612523	9.817799107
Microglia	Selplg	10.23734143	10.42231711	10.24366194	10.23021262
Microglia	Ccl3	10.25557154	9.954603465	9.863892003	9.289212003
Microglia	Fcgr3	10.2598727	10.69971125	10.51415186	10.77879173
Microglia	Tyrobp	10.33092808	10.36027648	10.52379716	10.72651621
Microglia	Il10ra	10.37890172	10.24163762	10.03544521	10.27750826
Microglia	Olfml3	10.45522446	10.23945533	9.439727015	9.739561236
Microglia	Pld4	10.53782021	10.64800698	10.59361521	10.70366137
Microglia	Cd68	10.57982503	10.62884649	10.47159393	10.35699109
Microglia	Fcer1g	10.8798053	11.00556841	10.77349365	11.04065275

Cell Type	Gene	WT_1	WT_2	WT_3	WT_4
Microglia	Csf1r	11.34630873	11.38252676	11.18201563	11.07291639
Microglia	Itgam	11.3811157	11.34048995	11.3011532	11.46806905
Microglia	Itgam	11.3811157	11.34048995	11.3011532	11.46806905
Microglia	Lyz2	11.7300455	12.09746924	11.55485741	12.52860306
Microglia	Cd74	12.20983409	12.32351925	11.7945702	11.7570024
Microglia	C1qb	12.53898913	12.47343179	12.37042859	12.43472986
Microglia	Laptm5	13.23444773	13.23874059	12.91005617	12.83751953
Neurons	Trank1	-3.836501268	-2.556393349	-0.49410907	-1.514573173
Neurons	Igfbpl1	-3.836501268	-3.473931188	-3.473931188	-0.358453971
Neurons	Amy1	-2.736965594	-1.943416472	-0.49410907	-2.556393349
Neurons	March4	-2.184424571	-2.556393349	-1.888968688	-0.074000581
Neurons	Crmp1	-1.785875195	-0.713118852	0.321928095	-1.217591435
Neurons	Dpysl5	-1.184424571	-3.473931188	-1.152003093	-1.943416472
Neurons	Ankrd35	-1.184424571	-0.514573173	0.757023247	-2.556393349
Neurons	Srrm4	-0.76121314	-1.514573173	0.097610797	-0.713118852
Neurons	Islr2	-0.454031631	-0.200912694	1.03562391	0.163498732
Neurons	Robo2	-0.321928095	-1.184424571	1.269033146	0.056583528
Neurons	Fam183b	-0.184424571	0.389566812	-0.689659879	-1.217591435
Neurons	Fibin	-0.184424571	-0.058893689	0.422233001	-0.200912694
Neurons	Mab21l1	-0.184424571	-2.556393349	-0.168122759	-1.943416472
Neurons	Clstn2	-0.074000581	-2.556393349	1.15704371	-1.514573173
Neurons	Cdh8	0.137503524	-0.058893689	-1.888968688	-0.200912694
Neurons	St8sia2	0.137503524	1.063502942	-1.473931188	-1.514573173
Neurons	Ina	0.22650853	0.070389328	-3.473931188	-0.358453971
Neurons	Mme	0.22650853	-1.184424571	0.321928095	0.056583528
Neurons	Dync1i1	0.545968369	1.063502942	0.90303827	2.327687364
Neurons	Syt1	0.545968369	1.339137385	1.641546029	2.44625623
Neurons	Sphkap	0.687060688	0.871843649	0.831877241	1.056583528
Neurons	Celsr3	0.687060688	-0.358453971	-0.321928095	0.275007047
Neurons	Cacng2	0.687060688	1.803227036	1.269033146	2.275007047
Neurons	Scube3	0.687060688	0.286881148	1.097610797	0.275007047
Neurons	Tmem130	0.687060688	1.124328135	-0.888968688	-3.473931188
Neurons	Myt1l	0.97819563	1.687060688	-0.49410907	1.555816155
Neurons	Ccbe1	1.03562391	-0.943416472	0.90303827	0.275007047
Neurons	L1cam	1.03562391	0.475084883	-0.321928095	2.140778656
Neurons	Nxph3	1.182692298	1.937344392	0.90303827	-0.074000581
Neurons	Slc10a4	1.182692298	1.182692298	0.831877241	1.327687364
Neurons	Trp73	1.22650853	1.608809243	0.757023247	0.378511623
Neurons	Npy	1.35614381	-0.358453971	0.097610797	1.752748591
Neurons	Nos1	1.432959407	0.650764559	1.416839742	1.63691458
Neurons	Reln	1.510961919	2.456806149	1.835924074	2.250961574
Neurons	Penk	1.510961919	-0.200912694	0.516015147	-1.217591435
Neurons	Igsf9	1.545968369	1.906890596	0.321928095	2.084064265
Neurons	Gap43	1.687060688	1.182692298	2.3950628	1.111031312
Neurons	Ripk4	1.748461233	0.389566812	-0.168122759	-0.200912694
Neurons	Rgs8	1.811471031	2.063502942	2.370164281	1.678071905
Neurons	Celf4	1.89917563	1.526068812	1.555816155	2.350497247
Neurons	Tubb3	2.007195501	2.801158656	3.465974465	3.155425432
Neurons	Cacna2d2	2.17951105	1.835924074	2.066950244	0.713695815
Neurons	Elavl2	2.292781749	2.500802053	3.672425342	2.859969548
Neurons	Snhg11	2.650764559	1.835924074	2.370164281	2.555816155
Neurons	Rian	2.825785627	2.480265122	3.267535798	2.735522177

Cell Type	Gene	WT_1	WT_2	WT_3	WT_4
Neurons	Mrap2	2.939226578	2.765534746	2.6622055	1.111031312
Neurons	Bmp5	3.19061486	3.152183419	3.651912745	3.168321116
Neurons	Ebf3	3.529820947	2.523561956	2.702657543	3.155425432
Neurons	Calb2	3.987320866	3.871843649	4.260025656	4.597531174
Neurons	Stmn2	4.203201156	4.048759312	4.460742564	4.856487779
Neurons	Cd274	4.385431037	5.207111961	4.512226887	4.984133595
Neurons	Meg3	5.299757512	4.056583528	5.74092756	5.390254956
Oligodendrocyte	S1pr5	-0.971430848	-1.943416472	-0.49410907	-1.217591435
Oligodendrocyte	Slc45a3	-0.971430848	0.389566812	0.097610797	-0.713118852
Oligodendrocyte	Rab37	-0.59946207	0.176322773	2.03562391	1.169925001
Oligodendrocyte	Gng13	0.137503524	-0.058893689	-0.029146346	0.86393845
Oligodendrocyte	Pkd2l1	0.622930351	-0.058893689	-0.168122759	-0.943416472
Oligodendrocyte	Tmem151a	0.748461233	0.286881148	1.372952098	0.163498732
Oligodendrocyte	Bace2	1.182692298	1.182692298	1.871843649	0.992768431
Oligodendrocyte	D7Ertd443e	1.269033146	1.384049807	0.604071324	0.056583528
Oligodendrocyte	Acy3	1.650764559	1.565597176	1.321928095	1.275007047
Oligodendrocyte	Hist1h4h	1.748461233	1.835924074	0.214124805	0.275007047
Oligodendrocyte	Adssl1	1.811471031	2.629939409	2.722466024	2.771885579
Oligodendrocyte	Ldb3	1.839959587	1	1.03562391	0.464668267
Oligodendrocyte	Gjc2	2.007195501	1.124328135	1.970853654	2.397802962
Oligodendrocyte	Nol3	2.17951105	2.313245852	2.266036894	2.350497247
Oligodendrocyte	Nkain2	2.22650853	2.386810946	2.833902077	2.752748591
Oligodendrocyte	Adamtsl4	2.269033146	2.063502942	1.214124805	1.422233001
Oligodendrocyte	Phlda3	2.435628594	2.746312766	2.292781749	2.250961574
Oligodendrocyte	Srd5a1	2.454175893	1.526068812	1.097610797	0.790772038
Oligodendrocyte	Aspa	2.472487771	2.819668183	3.500802053	3.068670811
Oligodendrocyte	Gpr62	2.472487771	1.765534746	2.266036894	1.790772038
Oligodendrocyte	Wnt3	2.510961919	1.937344392	2.23878686	2.169925001
Oligodendrocyte	Itgb4	2.634593268	1.871843649	1.682573297	1.22650853
Oligodendrocyte	Slco3a1	2.718087584	3.09423607	3.019701914	2.843983844
Oligodendrocyte	Stmn4	2.748461233	2.545968369	3.22650853	3.053111336
Oligodendrocyte	Tmem88b	2.780310099	1.871843649	2.851998837	2.596935142
Oligodendrocyte	Cdc42ep2	2.839959587	2.801158656	3.382667253	3.275007047
Oligodendrocyte	Dock5	3.007195501	3.979110755	2.939226578	4.126807703
Oligodendrocyte	Rhou	3.17951105	3.386810946	3.69265037	3.648465443
Oligodendrocyte	Tmod1	3.17951105	3.17951105	3.051372102	2.555816155
Oligodendrocyte	Fbxo36	3.424922088	3.09423607	3.319039816	2.021479727
Oligodendrocyte	B3galt5	3.592158002	3.456806149	3.442280035	3.350497247
Oligodendrocyte	Larp6	3.626439137	2.904965719	4.286881148	3.851998837
Oligodendrocyte	Mog	3.634593268	2.987320866	4.545350645	3.576522138
Oligodendrocyte	Pigz	3.669026766	3.502075956	3.672425342	3.607626221
Oligodendrocyte	Lgi3	3.749534268	2.819668183	3.523561956	2.275007047
Oligodendrocyte	Plekhh1	3.757023247	3.286881148	4.051372102	3.350497247
Oligodendrocyte	Gpr37	3.780310099	3.311793718	4.219555769	3.125981654
Oligodendrocyte	Cldn11	3.780310099	3.502075956	3.711494907	2.596935142
Oligodendrocyte	Ctnna3	3.803227036	2.765534746	3.08236197	2.111031312
Oligodendrocyte	Fa2h	3.832890014	3.17951105	4.096767855	2.87774425
Oligodendrocyte	Ermn	4.019701914	4.06436554	4.869871406	4.860466259
Oligodendrocyte	Pla2g16	4.259272487	4.221103725	4.615298579	4.399171094
Oligodendrocyte	Galnt6	4.307428525	3.801158656	3.815575429	3.991861931
Oligodendrocyte	Gamt	4.313245852	4.484782623	4.692092375	4.075532631
Oligodendrocyte	Cmtm5	4.334139179	3.746312766	4.666756592	3.90303827

Cell Type	Gene	WT_1	WT_2	WT_3	WT_4
Oligodendrocyte	Tmeff2	4.344828497	4.200064862	4.260025656	4.730096466
Oligodendrocyte	Josd2	4.464014725	4.324810603	4.802193217	4.534186139
Oligodendrocyte	Gss	4.506525779	4.963011648	4.682011391	4.898692073
Oligodendrocyte	Tprn	4.506525779	4.416164165	4.534808661	4.643278996
Oligodendrocyte	Car14	4.60940039	4.260778432	4.712045449	3.288358562
Oligodendrocyte	Slain1	4.741466986	4.796493929	4.842978832	4.771885579
Oligodendrocyte	Aplp1	5.182692298	4.769242795	5.672142433	4.856487779
Oligodendrocyte	Cntn2	5.194165869	4.260778432	4.74092756	4.512858954
Oligodendrocyte	Arsg	5.267161218	5.312156888	5.523248293	4.906890596
Oligodendrocyte	Ppp1r14a	5.336640446	5.283551423	6.390254956	5.974070367
Oligodendrocyte	Rftn1	5.375387027	5.352617299	4.625854931	5.154615611
Oligodendrocyte	Anln	5.397802962	5.621465834	5.919340082	5.828072998
Oligodendrocyte	Nkain1	5.412781525	4.922197848	5.942514505	4.9800253
Oligodendrocyte	Prr5l	5.542877099	5.427606173	5.419201774	5.605257263
Oligodendrocyte	Slc48a1	5.643278996	5.72955277	5.74819285	5.459759467
Oligodendrocyte	Efhd1	5.727375939	5.498889087	6.390254956	5.665335917
Oligodendrocyte	Mag	5.741197299	5.639232163	6.14689956	5.730368236
Oligodendrocyte	Tppp3	5.862203399	6.052894047	6.503666755	6.299574371
Oligodendrocyte	Inf2	5.885574364	5.564073256	5.651625784	5.653060017
Oligodendrocyte	Adi1	5.913846824	5.886550147	5.906650126	5.323009711
Oligodendrocyte	Mal	5.932864335	5.959074601	6.674545394	5.85623876
Oligodendrocyte	Cryab	5.992088609	5.85224859	6.210817432	6.242983516
Oligodendrocyte	Sh3gl3	6.06307145	5.603477988	6.878480131	6.62058641
Oligodendrocyte	Gsn	6.191207302	6.515384461	6.117695043	6.229780167
Oligodendrocyte	Pdlim2	6.208478242	6.169323753	6.507953169	6.221490455
Oligodendrocyte	Padi2	6.242411963	5.924337464	5.388533979	5.37816478
Oligodendrocyte	Ndrg1	6.372778017	5.975217457	5.840714991	5.685099172
Oligodendrocyte	Sept4	6.602735976	6.372603915	7.279471296	6.822475232
Oligodendrocyte	Synj2	7.008540672	6.417346217	6.640100298	6.880807948
Oligodendrocyte	Kif5a	8.273329387	8.258989947	8.983563697	8.560332834
Oligodendrocyte	Cnp	8.34251919	7.886001351	7.788228924	7.418105597
Oligodendrocyte	Prr18	8.373343703	7.995936704	8.603885933	8.364572432
Oligodendrocyte	Trp53inp2	8.938903252	8.729246852	9.258024185	9.092598594
Oligodendrocyte	Apod	9.03609117	9.142821844	9.284662185	9.554876595
Oligodendrocyte	Scd1	9.321386983	8.8008999	9.615592857	9.607792642
Oligodendrocyte	Lpar1	9.694009578	9.431267758	10.35948603	9.945370676
Oligodendrocyte	Qdpr	9.986738008	10.05029762	10.94734472	10.4023939
Oligodendrocyte	Trak2	10.44407275	10.01063999	10.63641618	10.76494621
Oligodendrocyte	Mobp	11.54118376	11.61892687	12.51459571	12.48265924
Oligodendrocyte	Plekhb1	12.85325302	12.69505425	13.56629074	13.28059825
Macrophages	Ifitm1	-0.971430848	-0.713118852	0.097610797	-0.535331733
Macrophages	Relb	-0.76121314	-0.713118852	-1.473931188	-0.943416472
Macrophages	S100a6	-0.321928095	1.063502942	-0.49410907	0.641546029
Macrophages	Msr1	-0.184424571	-0.058893689	0.321928095	0.925999419
Macrophages	Traf3ip2	0.310340121	-0.058893689	-0.49410907	-2.556393349
Macrophages	Ly6i	0.925999419	2.09423607	-0.168122759	1.859969548
Macrophages	Fut7	0.97819563	-0.200912694	-0.888968688	-0.713118852
Macrophages	Ms4a8a	1.475084883	2.746312766	0.90303827	0.790772038
Macrophages	Tnfsf14	1.748461233	2.286881148	0.321928095	2.843983844
Macrophages	Trim56	1.778208576	0.650764559	1.321928095	0.713695815
Macrophages	Slfn4	1.981852653	3.566815154	2.15704371	3.952333566
Macrophages	Il18rap	2.15704371	1.565597176	0.422233001	1.599317794

Cell Type	Gene	WT_1	WT_2	WT_3	WT_4
Macrophages	Kynu	2.17951105	1.339137385	1.970853654	2.375734539
Macrophages	Gpr141	2.22650853	3.422233001	2.887525271	3.968090752
Macrophages	Gch1	2.493134922	3.311793718	3.577730931	3.339137385
Macrophages	Scarf1	2.510961919	1.687060688	1.321928095	1.275007047
Macrophages	Cxcl1	2.548436625	2.207892852	2.682573297	1.275007047
Macrophages	Slco3a1	2.718087584	3.09423607	3.019701914	2.843983844
Macrophages	Ccl22	2.748461233	3.386810946	2.003602237	2.195347598
Macrophages	Ms4a4c	2.748461233	3.523561956	2.3950628	3.959770155
Macrophages	Nedd4	2.794935663	2.669026766	2.6622055	2.513490746
Macrophages	Fam26f	3.258518925	3.545968369	3.500802053	4.015247774
Macrophages	Usp18	3.375734539	3.669026766	3.721372659	4
Macrophages	Cxcl2	3.463360886	4.331275267	3.344828497	4.288358562
Macrophages	Plscr1	3.519793486	3.608809243	3.382667253	3.789729251
Macrophages	Antxr2	3.557042415	4.561326136	3.599317794	4.479618608
Macrophages	Cfp	3.608809243	4.361768359	3.477677328	4.428276414
Macrophages	Vegfa	3.716990894	4.04176865	3.12763328	3.444932049
Macrophages	Alcam	3.74092756	4.137503524	3.824767853	4.189033824
Macrophages	Ms4a7	3.904965719	3.888499736	4.219555769	4.375039431
Macrophages	Clec4e	4	5.289834465	4.03562391	5.62556274
Macrophages	Clec4e	4	5.289834465	4.03562391	5.62556274
Macrophages	Clec4n	4.026800059	4.392317423	4.111865964	4.148120631
Macrophages	Kcnn4	4.032982417	3.658782734	3.500802053	2.859969548
Macrophages	Lilra6	4.058316496	4.849999259	2.577730931	5.307428525
Macrophages	Ecm1	4.339137385	4.539779192	2.815575429	3.399171094
Macrophages	Pdpn	4.339137385	4.507160349	4.523561956	3.607626221
Macrophages	Cd274	4.385431037	5.207111961	4.512226887	4.984133595
Macrophages	Jak2	4.506525779	4.379898164	4.90014226	4.931683057
Macrophages	Fgr	4.569855608	5.090430042	4.436961338	5.140778656
Macrophages	Lgals3	4.578938713	5.734167661	5.059182199	5.91336816
Macrophages	Iqgap2	4.713145902	4.410069692	3.938285792	4.140778656
Macrophages	Ccr2	4.854993017	4.845490051	3.609991295	4.386810946
Macrophages	Bst1	5.036063689	6.084702108	4.051372102	6.145881211
Macrophages	Tlr8	5.083638879	4.792334806	3.74092756	4.28169825
Macrophages	Clec4d	5.083638879	6.324810603	5.170325694	6.391630262
Macrophages	Il15	5.219942914	5.082787732	5.270528942	5.348019909
Macrophages	Gpr132	5.331275267	5.049195106	3.824767853	4.711494907
Macrophages	Polr3c	5.589763487	5.731997787	5.397802962	5.275752049
Macrophages	Trem1	5.607034346	6.430619811	5.111865964	6.663059924
Macrophages	Crip1	5.664198369	6.112283109	5.669593751	5.970163425
Macrophages	Ccr1	5.733354341	6.265474403	6.132371199	6.409221197
Macrophages	Ms4a6d	5.757023247	6.346602375	6.322649262	6.280399611
Macrophages	Psen2	5.897966432	5.998872454	5.586164246	5.436961338
Macrophages	Pglyrp1	5.983677695	7.031880366	5.575614878	6.428276414
Macrophages	Ifitm6	6.018367116	7.234194723	5.778997006	7.138015753
Macrophages	Wfdc17	6.451870479	6.401050159	6.01189812	6.640678764
Macrophages	Myd88	6.746178381	6.91910168	6.621905346	6.872336288

Figure A.6: **Cell-type specific genes known to be expressed in microglia, astrocytes, neurons, endothelial cells, oligodendrocytes and macrophages in wild-type samples.**

Cell Type	Gene	CMVMJD135_1	CMVMJD135_2	CMVMJD135_3	CMVMJD135_4
Astrocytes	P4ha3	0.765534746	0.35614381	-1.943416472	-1.888968688
Astrocytes	Slc25a34	-0.234465254	-1.217591435	-1.943416472	-0.184424571
Astrocytes	Chrdl1	-0.556393349	-3.184424571	-1.514573173	0.310340121
Astrocytes	Glis3	-0.971430848	0.678071905	0.495695163	-1.184424571
Astrocytes	Cybrd1	-0.377069649	-0.217591435	-1.184424571	0.82374936
Astrocytes	Kcnn3	-0.971430848	-3.184424571	-1.943416472	-1.514573173
Astrocytes	Gdpd2	0.028569152	0.678071905	-0.915935735	1.500802053
Astrocytes	Trim9	-0.234465254	-1.64385619	-0.689659879	-0.915935735
Astrocytes	Mlc1	-1.556393349	-1.217591435	-2.473931188	-0.915935735
Astrocytes	Slc7a2	0.443606651	0.097610797	0.815575429	-0.321928095
Astrocytes	Ranbp3l	-0.377069649	0.941106311	-1.943416472	0.669026766
Astrocytes	Gm5089	-0.736965594	0.35614381	-0.340075442	1.304511042
Astrocytes	Rgs20	-0.556393349	0.097610797	-2.473931188	-0.043943348
Astrocytes	Grhl1	-0.971430848	-3.184424571	0.084064265	0.411426246
Astrocytes	Fzd2	-1.556393349	0.23878686	-0.184424571	0.669026766
Astrocytes	Vnn1	0.5360529	-0.915935735	-0.340075442	1.545968369
Astrocytes	Ttpa	-1.943416472	-1.64385619	-1.184424571	0.201633861
Astrocytes	2900005J15Rik	0.150559677	-0.415037499	-1.184424571	0.669026766
Astrocytes	Pm20d1	-0.089267338	0.773996325	-0.340075442	1.40599236
Astrocytes	Pamr1	-0.377069649	-1.217591435	0.298658316	1.021479727
Astrocytes	Frem2	1.695993813	2.475084883	0.956056652	2.084064265
Astrocytes	Rorb	0.5360529	1.163498732	0.659924558	1.304511042
Astrocytes	Gli1	0.90303827	0.23878686	-1.943416472	1.992768431
Astrocytes	Mamdc2	1.695993813	2.580145484	2.350497247	2.477677328
Astrocytes	Pipox	0.695993813	1.232660757	0.40053793	0.669026766
Astrocytes	Cyp4f15	-0.234465254	-0.217591435	0.815575429	1.35614381
Astrocytes	Gli3	-1.943416472	0.584962501	-0.043943348	1.35614381
Astrocytes	Cbs	0.970853654	0.941106311	0.084064265	1.304511042
Astrocytes	Itih3	1.028569152	0.23878686	0.584962501	1.925999419
Astrocytes	Atp13a4	1.769771739	1.298658316	0.084064265	2.280956314
Astrocytes	Grm3	1.575312331	-0.217591435	0.815575429	1.021479727
Astrocytes	Tnc	0.839959587	1.773996325	-2.473931188	-1.888968688
Astrocytes	Ccdc80	1.304511042	1.475084883	3.17951105	2.765534746
Astrocytes	Cldn10	0.613531653	0.23878686	-0.689659879	1.084064265
Astrocytes	Elovl2	1.803227036	1.981852653	1.66448284	2.908812908
Astrocytes	Entpd2	2.117695043	0.475084883	1.298658316	2.974529312
Astrocytes	Crb2	2.375734539	2.839959587	1.887525271	2.358958826
Astrocytes	Dio2	1.695993813	0.475084883	1.077242999	1.925999419
Astrocytes	Itga7	1.769771739	1.819668183	0.739848103	1.992768431
Astrocytes	Paqr6	1.09085343	1.35614381	0.495695163	1.40599236
Astrocytes	Cth	0.970853654	1.298658316	1.952333566	2.543495883
Astrocytes	Sorcs2	1.40053793	2.817623258	2.375734539	2.608809243
Astrocytes	Plcd4	0.90303827	1.097610797	2.516015147	2.333423734
Astrocytes	Hgf	2.533563348	2.655351829	2.195347598	2.253989266
Astrocytes	Aqp9	2.353323291	2.839959587	1.887525271	2.477677328
Astrocytes	Slc14a2	2.767654798	3.784503983	2.220329955	3.158660175
Astrocytes	Ephx2	1.769771739	2.680324357	1.739848103	2.430285273
Astrocytes	Celsr1	2.655351829	2.528571319	2.327687364	3.099295204
Astrocytes	Aqp4	2.937344392	2.963474124	2.601696516	3.649615459
Astrocytes	Fam20a	2.693765712	0.584962501	1.952333566	2.72900887
Astrocytes	Bmpr1b	2.277984747	1.944858446	1.66448284	2.14404637
Astrocytes	Slc15a2	3.29130886	3.077242999	3.001802243	2.942983598

Cell Type	Gene	CMVMJD135_1	CMVMJD135_2	CMVMJD135_3	CMVMJD135_4
Astrocytes	AI464131	2.596935142	2.580145484	2.247927513	2.608809243
Astrocytes	Adhfe1	2.937344392	3.727920455	3.137503524	3.847996907
Astrocytes	Fgfr3	3.174725988	2.981852653	2.702657543	4.069530325
Astrocytes	Gm973	3.82984956	3.828834649	4.071247819	4.306699707
Astrocytes	Egfr	2.95419631	3.372952098	2.516015147	3.054848477
Astrocytes	Fmo1	3.803227036	2.963474124	3.326249701	4.114367025
Astrocytes	Lrig1	3.279471296	3.44625623	2.66448284	4.185866545
Astrocytes	Nwd1	3.468583317	4.173926932	3.760220946	4.798569004
Astrocytes	Ppp1r3c	2.922197848	2.13093087	2.424922088	3.430285273
Astrocytes	Slc14a1	4.484782623	4.289096702	3.911691582	3.975446766
Astrocytes	Aldh1l1	4.023255352	4.521678952	3.919340082	5.015247774
Astrocytes	Prdm16	4.067810784	4.917909074	3.77925972	5.14689956
Astrocytes	Slc4a4	3.665620164	3.416839742	3.447579197	4.234194723
Astrocytes	Tmem82	3.160274831	3.860962798	3.166715445	3.587364991
Astrocytes	Slc7a11	4.260025656	4.887037791	3.960697039	5.132576843
Astrocytes	Slc39a12	4.846994687	5.257010618	4.87282876	5.360715425
Astrocytes	Slc6a11	4.358958826	3.892391026	3.71259578	4.247927513
Astrocytes	Notch3	4.146492307	4.92314918	4.071247819	4.87036472
Astrocytes	Aifm3	4.790250739	5.528258743	4.702657543	5.796493929
Astrocytes	Sox9	5.376776572	5.574101508	4.702657543	5.726013749
Astrocytes	Vcam1	5.65047737	6.101818134	6.342163583	6.147103144
Astrocytes	Gja1	6.10433666	5.680042993	5.586164246	6.594996337
Astrocytes	Abcd2	5.554588852	5.521364878	5.717539343	5.023255352
Astrocytes	Daam2	5.462706751	4.424250286	5.515699838	4.925999419
Astrocytes	Slc7a10	5.585563498	6.519793486	5.844486088	6.675815931
Astrocytes	Slc1a3	6.79363582	6.831243897	6.616328288	7.506605116
Endothelia	Fgfbp1	0.150559677	0.773996325	-0.915935735	0.82374936
Endothelia	Sox17	-1.943416472	-0.915935735	-0.514573173	-1.888968688
Endothelia	Kcnq1	-1.556393349	-3.184424571	-1.184424571	-0.321928095
Endothelia	Megf6	0.695993813	0.584962501	-0.184424571	1.500802053
Endothelia	Hmgcs2	-1.217591435	0.475084883	-0.340075442	-0.321928095
Endothelia	Angpt2	-1.943416472	-0.415037499	1.014355293	1.084064265
Endothelia	Abcc6	0.695993813	1.773996325	1.195347598	2.22650853
Endothelia	Hrct1	0.250961574	1.416839742	0.887525271	1.891419187
Endothelia	Gimap4	-0.971430848	0.475084883	0.495695163	0.584962501
Endothelia	Myct1	1.350497247	0.678071905	0.584962501	0.956056652
Endothelia	Slco1a4	2.201633861	2.295723025	1.350497247	2.500802053
Endothelia	C130074G19Rik	1.49057013	2.198494154	1.495695163	2.454175893
Endothelia	Clec14a	1.09085343	2.750606505	1.250961574	2.689299161
Endothelia	Hmcn1	0.443606651	0.678071905	0.189033824	2.381283373
Endothelia	Adh1	1.448900951	1.580145484	1.298658316	1.891419187
Endothelia	Sigirr	1.201633861	1.859969548	1.580145484	1.891419187
Endothelia	4930578C19Rik	1.655351829	2.726831217	1.851998837	2.500802053
Endothelia	Adamtsl2	-0.234465254	0.584962501	0.739848103	0.956056652
Endothelia	Igsf5	1.028569152	2.327687364	1.887525271	2.839959587
Endothelia	Gimap8	2.375734539	2.060047384	1.014355293	2.253989266
Endothelia	Asb4	2.803227036	3.200064862	3.548436625	2.99095486
Endothelia	Nostrin	2.555816155	2.963474124	3.001802243	2.669026766
Endothelia	AU021092	2.693765712	3.372952098	3.326249701	3.618238656
Endothelia	Stap2	2.201633861	1.944858446	2.682573297	3.476381688
Endothelia	Csrp2	2.277984747	3.264536431	2.815575429	3.565597176
Endothelia	Ly75	2.060047384	3.112700133	2.469885976	1.819668183

Cell Type	Gene	CMVMJD135_1	CMVMJD135_2	CMVMJD135_3	CMVMJD135_4
Endothelia	Flt4	2.837943242	3.580145484	2.375734539	3.59812696
Endothelia	Mmrn2	2.693765712	2.859969548	3.137503524	2.974529312
Endothelia	Mfsd7c	2.803227036	3.040892431	3.001802243	3.418189948
Endothelia	Cd40	2.693765712	3.403267722	3.313245852	3.200064862
Endothelia	Scarf1	1.803227036	2.839959587	2.682573297	2.784503983
Endothelia	Icam2	3.40053793	3.655351829	3.868884273	3.812498225
Endothelia	Mecom	3.522306893	3.568032105	3.960697039	4.247927513
Endothelia	Sema3g	3.016139703	4.021479727	2.797012978	3.576522138
Endothelia	Nos3	2.786596362	3.44625623	3.683696454	3.344828497
Endothelia	Rnf125	3.340562269	2.963474124	3.653060017	3.892391026
Endothelia	Ctsw	2.032100843	1.90303827	1.704871964	2.959770155
Endothelia	Trim16	2.904965719	4.058316496	3.107687869	3.709290636
Endothelia	Foxf2	3.329123596	3.297191417	3.74092756	3.679198571
Endothelia	Rassf9	3.329123596	3.148934105	3.247927513	3.554588852
Endothelia	Serpinb6b	2.713695815	2.90303827	2.64385619	3.628773595
Endothelia	Mmp25	3.49057013	4.182692298	2.560714954	3.200064862
Endothelia	Slc19a3	3.160274831	3.817623258	3.722466024	4.586764743
Endothelia	Tie1	3.512226887	4.207892852	4.300855871	4.241077458
Endothelia	Ptgis	3.478971805	4.030336078	3.559491813	3.803227036
Endothelia	Ctla2a	3.44625623	3.43162296	3.339137385	4.576522138
Endothelia	Dll4	3.478971805	3.343407822	3.275007047	3.71918344
Endothelia	Robo4	3.512226887	4.715893371	3.769771739	3.85698569
Endothelia	Higd1b	2.555816155	2.817623258	2.64385619	3.476381688
Endothelia	Foxq1	3.304511042	3.715893371	3.275007047	4.106850796
Endothelia	Egfl7	3.456806149	4.784503983	4.122672719	5.011227255
Endothelia	Akr1c14	3.49057013	3.327687364	3.447579197	4.332707934
Endothelia	Ushbp1	3.522306893	4.077242999	3.548436625	4.602884409
Endothelia	Adcy4	3.703765179	4.265286858	4.40053793	4.766595162
Endothelia	Slc38a5	3.316145742	3.182692298	3.504620392	3.908812908
Endothelia	Kdr	3.961623328	3.953265239	4.287620044	4.516645558
Endothelia	8430408G22Rik	3.575312331	4.806839582	4.526694846	4.406672716
Endothelia	Erg	4.527946099	4.957914599	4.381975479	5.546585829
Endothelia	Cyyr1	4.40599236	5.030777472	4.575917361	5.165107985
Endothelia	Cd93	4.272769732	4.43162296	4.430285273	4.319762428
Endothelia	Slc16a4	4.689299161	4.709842019	4.287620044	5.027242536
Endothelia	Tm4sf1	5.227278994	5.912889336	5.607330314	6.027021315
Endothelia	She	4.763411574	5.13093087	4.750606505	5.752213368
Endothelia	Itga4	4.631104282	5.316145742	5.036503334	4.628773595
Endothelia	Emcn	5.237257771	5.335569006	5.21800615	5.814806743
Endothelia	Wfdc1	5.187451054	5.804001915	5.570159302	5.906890596
Endothelia	Gm694	5.310340121	5.445594291	5.447579197	6.47118746
Endothelia	Slc39a8	4.689299161	5.099715999	4.997292408	4.917431755
Endothelia	Slc22a8	5.638363506	5.655924213	5.130107179	6.00337736
Endothelia	Tek	4.909773104	5.304511042	5.21451341	5.766330131
Endothelia	Esam	5.214124805	5.46662712	5.28132733	5.917431755
Endothelia	Cgnl1	5.170726276	5.709842019	5.231509211	6.19298317
Endothelia	Slfn5	5.5360529	5.747655933	5.316869805	5.382321407
Endothelia	Lsr	5.075532631	5.831117195	5.554281863	5.979339446
Endothelia	Ocln	5.300855871	6.269033146	5.999323578	6.218974857
Endothelia	Abcb1a	6.012121673	6.088311236	5.785812075	6.152386258
Endothelia	Cldn5	5.884842094	5.817623258	6.327866971	6.191404729
Endothelia	Car4	5.77925972	6.318136041	5.959074601	6.882153917

Cell Type	Gene	CMVMJD135_1	CMVMJD135_2	CMVMJD135_3	CMVMJD135_4
Endothelia	Igfbp7	5.598424761	6.141800612	5.967168608	6.660780334
Endothelia	Stra6	5.630813152	6.816215688	5.8899602	6.614562623
Endothelia	Pglyrp1	6.553206886	7.121947877	6.533719071	6.891905188
Endothelia	Ptprb	6.635899466	7.027021315	6.450551443	6.988457473
Endothelia	Flt1	6.835166157	7.207892852	6.753149879	7.328495421
Endothelia	Cdh5	6.805808349	6.908932967	6.773073253	7.220716892
Endothelia	Fn1	7.274913895	7.54303182	7.030667136	7.375300136
Endothelia	Ly6a	7.118422024	7.161283075	7.189528084	7.35834351
Endothelia	Fam129a	6.597084173	6.454504938	6.515857501	5.961160258
Endothelia	Itm2a	6.929790998	7.482283612	7.19564288	8.230885073
Endothelia	Pecam1	7.716922324	8.097400107	7.688180359	8.379551653
Endothelia	Cd34	7.62592797	7.449148645	7.761418259	7.276031325
Microglia	Ptafr	0.443606651	-0.058893689	-0.514573173	-1.184424571
Microglia	Ch25h	1.304511042	1.35614381	1.137503524	1.500802053
Microglia	Fcgr2b	3.060047384	3.568032105	3.944858446	2.477677328
Microglia	Ccr7	3.961623328	3.870857864	4.617651119	3.71918344
Microglia	Myo1g	3.929790998	3.992768431	3.876762491	3.3950628
Microglia	Angptl7	2.46727948	3.514753498	3.001802243	2.873813198
Microglia	C1qc	3.340562269	3.403267722	3.247927513	3.054848477
Microglia	Ccl7	2.513490746	2.680324357	3.590961241	3.465974465
Microglia	Tnf	3.29130886	3.541019153	3.63343121	3.307428525
Microglia	Gdf15	4.139142019	3.762348816	3.885574364	4.43629512
Microglia	Hmha1	4.358958826	4.216454865	4.622930351	3.865918815
Microglia	Tnfaip8l2	4.859472667	4.767654798	4.698218478	4.879215637
Microglia	Arhgap9	4.961623328	4.692092375	5.093391153	4.654206378
Microglia	Tlr2	5.263034406	5.331633567	5.545968369	5.030777472
Microglia	Rac2	5.355791547	5.362119167	5.551516018	5.189429246
Microglia	Asb2	5.564987801	5.273142859	5.447579197	4.803227036
Microglia	Myo1f	5.496014873	5.49441561	6.044175513	5.128870759
Microglia	Ccl4	5.493134922	5.764738923	6.022811651	5.812498225
Microglia	Rhoh	5.816599707	5.955591792	5.993221467	5.706530553
Microglia	C5ar1	5.715069679	5.551208374	5.999323578	5.244506551
Microglia	Ncf4	5.722192761	6.417008587	5.705425039	5.991408467
Microglia	Csf2rb	6.036723106	6.006746832	5.850999395	5.605553595
Microglia	Slamf8	6.13422094	6.280956314	5.969242604	5.488322191
Microglia	Tbxas1	5.861707287	5.58044702	5.95489422	5.069530325
Microglia	Psd4	6.040454121	5.879215637	6.078524445	5.406332578
Microglia	Fermt3	6.672425342	6.207892852	6.594100624	5.861459166
Microglia	Ccdc88b	6.24697806	6.549669171	6.113742166	6.359134582
Microglia	Gpr157	6.741736624	6.534808661	6.469234794	6.427438564
Microglia	H2-Oa	6.200849575	5.82858081	6.106222673	5.573798644
Microglia	Csf3r	6.155020578	6.195347598	6.515857501	6.061776198
Microglia	Hk3	6.683275373	6.785812075	6.638073837	6.116031993
Microglia	Pik3r5	6.798050515	6.675533686	6.672142433	5.967168608
Microglia	H2-DMb1	6.702241961	6.610877199	6.879338185	6.290756138
Microglia	Nlrp3	7.040344523	7.42609699	7.084064265	7.118006651
Microglia	Gpr183	6.822092774	6.803872798	6.944624223	7.197413299
Microglia	Slc15a3	6.876516947	6.92552477	6.899659026	6.911092332
Microglia	Nfam1	6.824258697	6.709842019	7.042316017	6.215484464
Microglia	Parvg	7.155121802	7.171927354	7.083106971	6.535741941
Microglia	Cd83	7.071676874	7.187945856	6.789207575	7.787314917
Microglia	Slamf9	6.992881703	7.065550771	7.24583789	7.344295908

Cell Type	Gene	CMVMJD135_1	CMVMJD135_2	CMVMJD135_3	CMVMJD135_4
Microglia	Card9	7.622783966	7.654349609	7.260778432	7.623076721
Microglia	Snx20	7.097926773	6.978996396	7.202515674	6.854868383
Microglia	Ncf2	7.570766497	7.919161284	7.607848111	7.611983815
Microglia	Il21r	7.056149961	7.002027365	7.347577079	6.702934532
Microglia	Hck	7.581727841	7.24688308	7.273982042	7.034853974
Microglia	Was	7.512147859	7.443855256	7.691254979	6.863690714
Microglia	Ccl2	6.821072391	6.881786959	7.088735246	7.384481583
Microglia	Abcc3	7.690417096	7.300672869	7.444020969	6.698079537
Microglia	Cd300a	7.412527507	7.43496176	7.622710768	7.361417467
Microglia	Slfn2	7.975446766	8.116967695	7.866846175	8.105960874
Microglia	Cbr2	7.443192215	7.023477152	8.156133652	7.4325419
Microglia	Plau	7.637059538	7.446504379	7.759089238	6.956985925
Microglia	Alox5ap	8.104231809	8.234194723	8.020424415	7.811920518
Microglia	Cxcl16	7.571449285	7.50199637	7.950293432	7.786138913
Microglia	Ltc4s	7.942397208	7.920412408	7.817623258	7.491772944
Microglia	Rasal3	7.612794795	7.556199473	8.018979052	7.309339922
Microglia	P2ry6	8.046851165	8.04990299	7.972233124	7.176422513
Microglia	Ccr5	8.163247124	7.780244473	8.164102412	7.627533884
Microglia	Sash3	8.248923768	7.876516947	8.141340821	7.198297695
Microglia	Lag3	8.203396949	8.022312324	7.907070921	7.668884984
Microglia	Pik3ap1	8.429030064	8.05343721	8.2277122	7.882765306
Microglia	Kcnk6	8.346513733	8.43721109	8.409687931	7.938344609
Microglia	Il1b	9.112022407	8.904423884	9.007672059	9.301084591
Microglia	Irf5	8.39145842	7.915341628	8.364572432	7.742747316
Microglia	Ccrl2	8.524149891	8.403054643	8.704733663	8.748092193
Microglia	Ptpn6	8.580748492	8.263081368	8.359178518	8.170676209
Microglia	Cd37	8.590025581	8.549245602	8.481759076	8.079858076
Microglia	Blnk	8.688879711	8.884689491	8.7977912	8.320168738
Microglia	Vav1	8.814806743	8.962751439	8.73809226	8.402713651
Microglia	Nckap1l	8.533135023	8.362864349	8.411934625	8.265708801
Microglia	Tlr9	8.67093945	8.561517078	8.208136793	8.2956312
Microglia	Cd52	9.179038235	8.87682387	9.076762163	9.349369701
Microglia	Ccl9	9.179461288	8.927096446	9.350254125	9.313948704
Microglia	Itgb2	9.223470819	9.158003705	8.891935558	8.671045636
Microglia	Slc11a1	8.994608008	8.909263079	8.966909148	8.636552121
Microglia	Nfkbid	8.791423397	8.803872798	8.807193898	9.111292193
Microglia	Cd14	9.735319081	9.924560158	9.755838966	9.4993875
Microglia	Ncf1	9.496034853	9.801126314	9.563234413	9.46913302
Microglia	Siglech	9.573855436	9.505811554	9.482122236	9.102264444
Microglia	Irf8	9.329415156	9.077563467	9.487799847	8.665122695
Microglia	Pla2g15	9.446008039	9.179436406	9.240171198	8.401178188
Microglia	Cx3cr1	9.941253062	9.81419791	9.957102042	9.034853974
Microglia	Tmem119	10.13262825	10.2502155	10.40043119	9.159341579
Microglia	Selplg	10.24225713	9.879782334	10.11995268	9.420107599
Microglia	Ccl3	10.25467435	10.0633816	10.5243752	10.25706957
Microglia	Fcgr3	10.41666032	10.33415035	10.55076602	10.31164615
Microglia	Tyrobp	10.50308035	10.34899366	10.45471055	10.62845465
Microglia	Il10ra	10.48107286	10.34355217	10.37627736	9.889336641
Microglia	Olfml3	9.593054922	9.509200979	10.1842059	8.786694368
Microglia	Pld4	10.44195856	10.23930017	10.41584738	9.984019633
Microglia	Cd68	10.40448167	10.10832843	10.23302043	9.992173604
Microglia	Fcer1g	10.80721	10.38908276	10.70267486	10.14421211

Cell Type	Gene	CMVMJD135_1	CMVMJD135_2	CMVMJD135_3	CMVMJD135_4
Microglia	Csf1r	11.35201583	10.99019617	11.06193817	10.50930986
Microglia	Itgam	11.41171223	11.29469541	11.18371601	10.67629209
Microglia	Itgam	11.41171223	11.29469541	11.18371601	10.67629209
Microglia	Lyz2	11.96571215	12.05068874	12.20841728	12.2771101
Microglia	Cd74	12.34685996	12.00376736	12.28201114	11.30350108
Microglia	C1qb	12.10581686	11.983129	12.4490506	11.71191643
Microglia	Laptm5	13.08602009	12.76154915	12.8965746	12.22706535
Neurons	Trank1	0.443606651	-1.64385619	-3.473931188	0.82374936
Neurons	Igfbpl1	-3.473931188	0.097610797	0.084064265	1.40599236
Neurons	Amy1	-1.217591435	-3.184424571	-1.514573173	-0.915935735
Neurons	March4	-3.473931188	-1.64385619	-1.514573173	-0.689659879
Neurons	Crmp1	-1.217591435	-0.64385619	-1.943416472	1.084064265
Neurons	Dpysl5	-3.473931188	-0.217591435	0.084064265	-1.888968688
Neurons	Ankrd35	0.765534746	0.23878686	-0.340075442	-0.689659879
Neurons	Srrm4	1.09085343	0.097610797	-0.514573173	0.82374936
Neurons	Islr2	-2.556393349	0.941106311	0.40053793	1.14404637
Neurons	Robo2	0.028569152	0.773996325	-0.915935735	-2.473931188
Neurons	Fam183b	1.350497247	1.232660757	1.40053793	0.895302621
Neurons	Fibin	0.028569152	-0.058893689	0.739848103	0.495695163
Neurons	Mab21l1	-1.943416472	-0.217591435	-0.340075442	0.495695163
Neurons	Clstn2	-0.971430848	-0.915935735	0.298658316	0.310340121
Neurons	Cdh8	1.906890596	-3.184424571	1.298658316	-1.184424571
Neurons	St8sia2	2.422233001	1.232660757	0.084064265	0.748461233
Neurons	Ina	-0.736965594	-0.915935735	-0.184424571	-0.915935735
Neurons	Mme	-0.556393349	0.097610797	-0.915935735	0.895302621
Neurons	Dync1i1	1.731183242	0.678071905	1.350497247	0.411426246
Neurons	Syt1	1.40053793	0.23878686	0.189033824	1.40599236
Neurons	Sphkap	-0.971430848	-0.415037499	1.014355293	0.584962501
Neurons	Celsr3	-1.943416472	-1.217591435	-0.340075442	0.201633861
Neurons	Cacng2	-1.556393349	0.475084883	0.084064265	-0.49410907
Neurons	Scube3	1.575312331	2.922197848	1.952333566	2.477677328
Neurons	Tmem130	-1.556393349	-3.184424571	0.659924558	-1.514573173
Neurons	Myt1l	1.14404637	-1.217591435	1.195347598	0.82374936
Neurons	Ccbe1	0.028569152	2.060047384	0.084064265	1.891419187
Neurons	L1cam	1.731183242	1.682573297	1.298658316	1.454175893
Neurons	Nxph3	0.5360529	1.163498732	0.189033824	2.608809243
Neurons	Slc10a4	0.35614381	1.819668183	1.298658316	1.627606838
Neurons	Trp73	-0.234465254	1.580145484	1.580145484	2.333423734
Neurons	Npy	1.250961574	1.475084883	-0.915935735	2.381283373
Neurons	Nos1	1.304511042	2.881664619	2.301587647	2.748461233
Neurons	Reln	2.40053793	1.90303827	1.250961574	3.476381688
Neurons	Penk	1.970853654	0.35614381	1.077242999	0.084064265
Neurons	Igsf9	1.970853654	1.580145484	2.137503524	2.333423734
Neurons	Gap43	-0.089267338	0.475084883	0.298658316	1.454175893
Neurons	Ripk4	-0.377069649	2.13093087	1.704871964	2.608809243
Neurons	Rgs8	1.350497247	0.23878686	0.887525271	1.709290636
Neurons	Celf4	1.839959587	1.726831217	0.659924558	1.669026766
Neurons	Tubb3	3.316145742	3.13093087	3.063502942	3.331991778
Neurons	Cacna2d2	2.117695043	3.311793718	2.601696516	2.839959587
Neurons	Elavl2	2.353323291	1.298658316	2.077242999	1.201633861
Neurons	Snhg11	2.855989697	2.327687364	2.538538164	4.581953751
Neurons	Rian	3	1.021479727	2.469885976	3.084064265

Cell Type	Gene	CMVMJD135_1	CMVMJD135_2	CMVMJD135_3	CMVMJD135_4
Neurons	Mrap2	1.970853654	3.849999259	2.885574364	3.607626221
Neurons	Bmp5	3.731183242	3.750606505	4.100977648	4.803227036
Neurons	Ebf3	3.646162657	3.992768431	3.137503524	4.023255352
Neurons	Calb2	3.880685525	2.555816155	3.301587647	3.649615459
Neurons	Stmn2	4.146492307	4.3950628	4.944858446	5.424250286
Neurons	Cd274	4.40053793	4.942983598	4.648465443	4.7473874
Neurons	Meg3	5.403267722	5.58044702	5.859721129	7.131651214
Oligodendrocyte	S1pr5	-1.217591435	-3.184424571	-1.943416472	-2.473931188
Oligodendrocyte	Slc45a3	0.443606651	0.23878686	0.887525271	1.304511042
Oligodendrocyte	Rab37	-0.377069649	-0.64385619	0.659924558	-1.888968688
Oligodendrocyte	Gng13	0.250961574	-0.915935735	0.739848103	0.895302621
Oligodendrocyte	Pkd2l1	1.14404637	0.941106311	0.189033824	-0.184424571
Oligodendrocyte	Tmem151a	1.448900951	1.163498732	0.815575429	1.14404637
Oligodendrocyte	Bace2	1.695993813	1.944858446	1.014355293	2.201633861
Oligodendrocyte	D7Ertd443e	0.90303827	0.86393845	0.887525271	1.14404637
Oligodendrocyte	Acy3	2	2.475084883	2.220329955	2.821710215
Oligodendrocyte	Hist1h4h	2.060047384	1.632268215	1.014355293	1.40599236
Oligodendrocyte	Adssl1	2.675815931	3.388189537	2.580145484	2.280956314
Oligodendrocyte	Ldb3	1.201633861	1.021479727	0.189033824	0.669026766
Oligodendrocyte	Gjc2	2.871843649	2.580145484	3.09423607	2.025028794
Oligodendrocyte	Nol3	1.871843649	1.981852653	1.448900951	1.786596362
Oligodendrocyte	Nkain2	1.695993813	1.859969548	2.469885976	0.584962501
Oligodendrocyte	Adamtsl4	2.855989697	2.327687364	2.815575429	2.925999419
Oligodendrocyte	Phlda3	2.173127433	2.942983598	2.469885976	3.007195501
Oligodendrocyte	Srd5a1	2.327687364	1.90303827	2.722466024	1.584962501
Oligodendrocyte	Aspa	1.937344392	1.981852653	2.424922088	2.748461233
Oligodendrocyte	Gpr62	2.44625623	1.726831217	1.815575429	1.35614381
Oligodendrocyte	Wnt3	3.060047384	2.44625623	3.247927513	2.839959587
Oligodendrocyte	Itgb4	3.10433666	3.148934105	2.682573297	3.727920455
Oligodendrocyte	Slco3a1	3.187451054	3.703765179	3.339137385	3.975446766
Oligodendrocyte	Stmn4	2.09085343	1.232660757	2.761285273	1.35614381
Oligodendrocyte	Tmem88b	2.969012308	1.773996325	2.867896464	1.786596362
Oligodendrocyte	Cdc42ep2	2.767654798	2.90303827	1.298658316	3.054848477
Oligodendrocyte	Dock5	3.500802053	3.870857864	3.702657543	3.847996907
Oligodendrocyte	Rhou	3.388189537	2.680324357	2.702657543	3.171527106
Oligodendrocyte	Tmod1	3.575312331	3.021479727	3.40053793	3.699329526
Oligodendrocyte	Fbxo36	2.655351829	3.43162296	3.570462931	3.727920455
Oligodendrocyte	B3galt5	4.352617299	4.296457407	4.032982417	3.465974465
Oligodendrocyte	Larp6	3.731183242	2.386810946	3.221877081	3.522306893
Oligodendrocyte	Mog	4.207892852	3.680324357	4.173127433	2.873813198
Oligodendrocyte	Pigz	3.253989266	2.981852653	3.760220946	3.90014226
Oligodendrocyte	Lgi3	4.328405659	4.173926932	3.769771739	3.488000771
Oligodendrocyte	Plekhh1	3.95419631	3.112700133	3.953265239	3.679198571
Oligodendrocyte	Gpr37	4.43496176	4.030336078	4.144862143	3.737686761
Oligodendrocyte	Cldn11	3.938285792	3.881664619	3.581351247	3.709290636
Oligodendrocyte	Ctnna3	3.377123749	2.606442228	3.137503524	2.40599236
Oligodendrocyte	Fa2h	4.377123749	3.297191417	3.969012308	3.659924558
Oligodendrocyte	Ermn	4.310340121	3.165107985	4.122672719	3.331991778
Oligodendrocyte	Pla2g16	4.517275693	5.09085343	4.663344619	5.441948191
Oligodendrocyte	Galnt6	4.590961241	4.265286858	4.234961095	4.453517579
Oligodendrocyte	Gamt	3.684818738	3.606442228	4.115199749	3.958842675
Oligodendrocyte	Cmtm5	4.297925053	3.933572638	3.581351247	3.967168608

Cell Type	Gene	CMVMJD135_1	CMVMJD135_2	CMVMJD135_3	CMVMJD135_4
Oligodendrocyte	Tmeff2	4.10433666	3.357552005	4.055716264	4.106850796
Oligodendrocyte	Josd2	4.303780748	3.715893371	4.381975479	4.516645558
Oligodendrocyte	Gss	5.128870759	4.680324357	4.673556424	4.879215637
Oligodendrocyte	Tprn	4.544114402	4.631104282	4.783456654	4.742545234
Oligodendrocyte	Car14	5.100557221	5.674121633	5.316869805	5.865918815
Oligodendrocyte	Slain1	4.605849867	4.232660757	4.596935142	4.388189537
Oligodendrocyte	Aplp1	5.585563498	5.739037979	5.760220946	5.415488271
Oligodendrocyte	Cntn2	5.696272084	4.992315252	5.070818638	4.613531653
Oligodendrocyte	Arsg	5.417515003	6.318136041	5.412442825	5.997518235
Oligodendrocyte	Ppp1r14a	4.925999419	4.438292852	4.424250286	4.66448284
Oligodendrocyte	Rftn1	5.648177796	5.244887059	5.727103604	4.942514505
Oligodendrocyte	Anln	5.674969031	4.917909074	5.767125077	5.217230716
Oligodendrocyte	Nkain1	5.765799923	4.586764743	4.877253454	4.69432306
Oligodendrocyte	Prr5l	5.585563498	5.244887059	5.473462236	5.110613806
Oligodendrocyte	Slc48a1	5.640678764	6.014132087	6.048105374	5.814806743
Oligodendrocyte	Efhd1	4.921721947	4.43162296	5.02103548	4.848497755
Oligodendrocyte	Mag	6.200849575	6.438625538	6.067165427	5.6441447
Oligodendrocyte	Tppp3	6.086189313	5.631104282	5.804001915	6.090218302
Oligodendrocyte	Inf2	5.925762114	6.083851588	5.801676029	6.391286558
Oligodendrocyte	Adi1	5.712870868	5.841973119	5.804001915	5.977279923
Oligodendrocyte	Mal	5.94976836	6.141800612	5.932155684	6.054197294
Oligodendrocyte	Cryab	5.814550423	5.261154673	6.130107179	6.009436756
Oligodendrocyte	Sh3gl3	5.240314329	3.838951767	5.017031081	4.185866545
Oligodendrocyte	Gsn	6.782539618	6.695019442	6.496334513	6.772149591
Oligodendrocyte	Pdlim2	5.907611763	5.689019541	5.668459557	5.605553595
Oligodendrocyte	Padi2	5.989139007	5.514753498	6.137298581	5.237640195
Oligodendrocyte	Ndrg1	6.331633567	6.242793024	6.617504198	6.227471546
Oligodendrocyte	Sept4	6.684397984	6.176322773	6.665904355	6.259460816
Oligodendrocyte	Synj2	6.656639374	6.350674037	6.133604623	6.698079537
Oligodendrocyte	Kif5a	7.062531903	5.992315252	7.209453366	6.201829866
Oligodendrocyte	Cnp	8.378598321	8.090641752	8.367676837	7.610729587
Oligodendrocyte	Prr18	6.883742991	6.28503225	7.06619685	6.101397952
Oligodendrocyte	Trp53inp2	8.217085276	7.767588594	8.228145276	7.471106152
Oligodendrocyte	Apod	9.976549804	9.527907014	9.722568485	10.08158996
Oligodendrocyte	Scd1	8.877774919	8.22650853	8.710496514	8.283412518
Oligodendrocyte	Lpar1	8.459349645	7.841344192	8.39394812	8.110143966
Oligodendrocyte	Qdpr	8.985898847	8.326384543	8.78891405	8.271042764
Oligodendrocyte	Trak2	9.804808638	9.384244122	9.918266959	9.584887358
Oligodendrocyte	Mobp	10.93749153	10.3958447	11.16210805	10.22547257
Oligodendrocyte	Plekhb1	12.06563491	11.07386039	11.9429836	11.28359193
Macrophages	Ifitm1	-1.556393349	0.097610797	1.137503524	1.992768431
Macrophages	Relb	-0.971430848	-0.915935735	-0.915935735	-1.514573173
Macrophages	S100a6	0.695993813	1.981852653	0.887525271	1.627606838
Macrophages	Msr1	1.14404637	0.475084883	1.195347598	0.895302621
Macrophages	Traf3ip2	-1.217591435	0.475084883	0.189033824	1.14404637
Macrophages	Ly6i	0.443606651	1.981852653	-0.043943348	-1.184424571
Macrophages	Fut7	0.150559677	0.097610797	0.084064265	-3.473931188
Macrophages	Ms4a8a	1.695993813	1.580145484	2.247927513	1.669026766
Macrophages	Tnfsf14	1.970853654	1.944858446	1.778208576	2.430285273
Macrophages	Trim56	0.90303827	1.580145484	1.918386234	2.114367025
Macrophages	Slfn4	1.655351829	1.944858446	0.739848103	3.618238656
Macrophages	Il18rap	2.904965719	3.09592442	1.704871964	2.629939409

Cell Type	Gene	CMVMJD135_1	CMVMJD135_2	CMVMJD135_3	CMVMJD135_4
Macrophages	Kynu	1.769771739	2.981852653	2.275007047	2.40599236
Macrophages	Gpr141	3.316145742	4.173926932	3.09423607	3.039138394
Macrophages	Gch1	2.937344392	3.580145484	3.351910961	3.554588852
Macrophages	Scarf1	1.803227036	2.839959587	2.682573297	2.784503983
Macrophages	Cxcl1	1.906890596	0.35614381	1.778208576	3.068670811
Macrophages	Slco3a1	3.187451054	3.703765179	3.339137385	3.975446766
Macrophages	Ccl22	3.615887074	2.704871964	3.927896454	2.114367025
Macrophages	Ms4a4c	3.423578171	3.680324357	4.100977648	3.917431755
Macrophages	Nedd4	2.922197848	3.528571319	3.207892852	3.991861931
Macrophages	Fam26f	3.10433666	3.912649865	4.100977648	3.488000771
Macrophages	Usp18	4.554588852	4.148120631	4.683134985	4.023255352
Macrophages	Cxcl2	3.767654798	4.011674533	4.228049048	4.623515741
Macrophages	Plscr1	3.543495883	3.762348816	3.936402378	3.917431755
Macrophages	Antxr2	4.37086174	4.721372659	4.268284667	4.613531653
Macrophages	Cfp	4.118525849	3.870857864	4.165911939	3.228049048
Macrophages	Vegfa	2.713695815	3.593353771	3.516015147	4.453517579
Macrophages	Alcam	4.253232939	4.001802243	4.085764554	4.40053793
Macrophages	Ms4a7	3.837943242	4.13996057	4.828834649	4.448240225
Macrophages	Clec4e	4.153805336	4.049630768	4.017031081	5.335569006
Macrophages	Clec4e	4.153805336	4.049630768	4.017031081	5.335569006
Macrophages	Clec4n	4.468583317	3.593353771	4.702657543	4.7473874
Macrophages	Kcnn4	4.000901403	3.715893371	3.74092756	2.974529312
Macrophages	Lilra6	4.872336288	5.220329955	4.778734244	4.785027362
Macrophages	Ecm1	4.905447179	3.92314918	4.570462931	4.47118746
Macrophages	Pdpn	4.358958826	5.169925001	4.815575429	5.628773595
Macrophages	Cd274	4.40053793	4.942983598	4.648465443	4.7473874
Macrophages	Jak2	4.888986721	4.844486088	4.570462931	4.975446766
Macrophages	Fgr	4.794935663	5.354381632	4.537917249	4.807870078
Macrophages	Lgals3	5.462706751	5.884353707	5.255123015	5.608217853
Macrophages	Iqgap2	4.468583317	4.917909074	4.376429311	4.865918815
Macrophages	Ccr2	5.423241996	5.178316272	5.158660175	4.227278994
Macrophages	Bst1	5.414812061	5.18705509	4.532316959	5.801158656
Macrophages	Tlr8	4.71259578	5.420549772	5.537917249	4.789729251
Macrophages	Clec4d	5.575312331	5.945560886	5.470862199	6.65692534
Macrophages	Il15	4.884597921	5.117695043	5.074676686	5.468257468
Macrophages	Gpr132	5.420549772	4.927896454	5.097189387	4.757023247
Macrophages	Polr3c	5.426264755	5.747655933	5.513174885	5.513490746
Macrophages	Trem1	6.10076745	6.122051448	5.467931546	6.534341795
Macrophages	Crip1	6.521521924	6.501120634	6.466463984	6.698079537
Macrophages	Ccr1	5.996840648	5.697940583	6.069100632	6.077029314
Macrophages	Ms4a6d	6.212569339	5.759155834	6.394376945	5.95070169
Macrophages	Psen2	6.256633295	6.211985606	6.160476536	5.433293326
Macrophages	Pglyrp1	6.553206886	7.121947877	6.533719071	6.891905188
Macrophages	Ifitm6	6.835166157	7.466708681	6.506049668	7.579089615
Macrophages	Wfdc17	6.476705707	6.077029314	6.648321627	6.782670659
Macrophages	Myd88	6.655494946	6.714245518	6.759022639	6.492494152

Figure A.7: **Cell-type specific genes known to be expressed in microglia, astrocytes, neurons, endothelial cells, oligodendrocytes and macrophages in CMVMJD135 samples.**

Appendix B

Results of Chapters 3 to 5

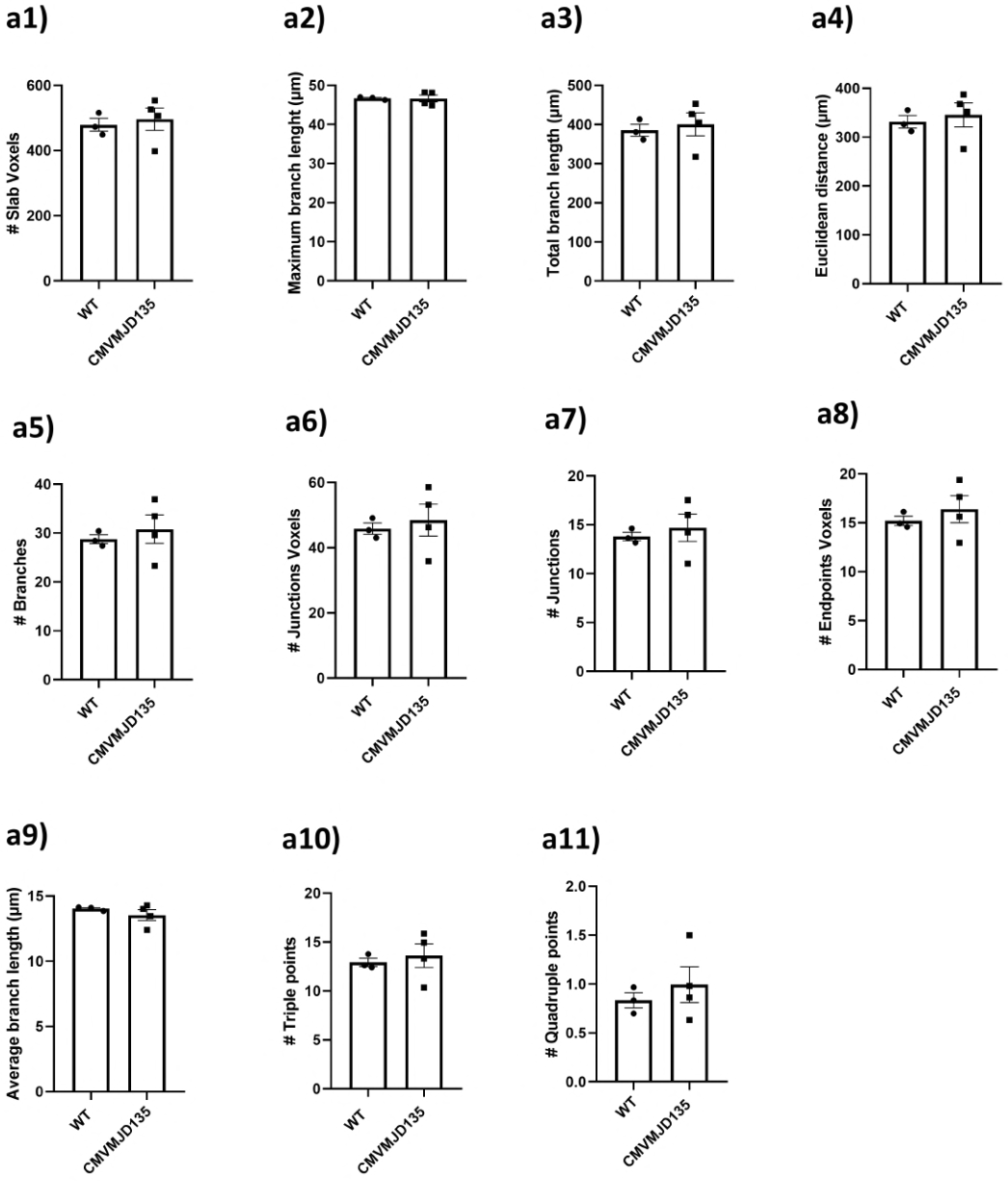

Figure B.1: **The ramification state of microglia in the pontine nuclei of the CMVMJD135 mice is similar to that of microglia from wild-type mice.a)** Quantification of the morphometric parameters associated with microglia ramification, including: **a1)** # slab voxels, **a2)** maximum branch length, **a3)** total branch length, **a4)** euclidean distance, **a5)** # branches, **a6)** # junctions voxels, **a7)** # junctions, **a8)** # endpoints voxels, **a9)** average branch length, **a10)** # triple points, **a11)** # quadruple points. Values for all these parameters were obtained from 152 microglial cells from WT mice ($n = 3$) and 180 microglial cells from CMVMJD135 mice ($n = 4$) of the PN. Data are presented as mean+SEM (Student's t-test).

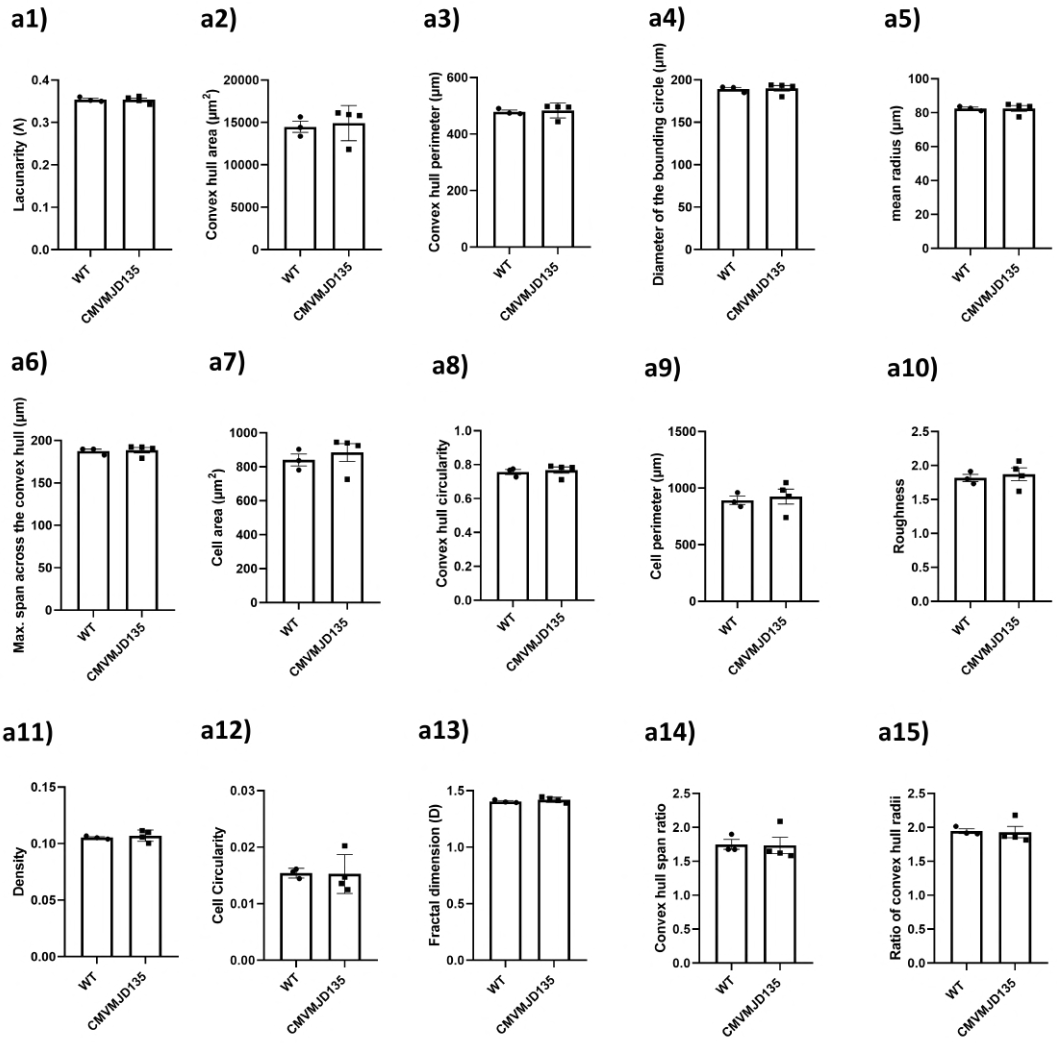

Figure B.2: **The complexity and shape of microglia in the pontine nuclei of CMVMJD135 mice are similar to those of microglia from wild-type mice. a)** Quantification of the morphometric parameters associated with the heterogeneity of the shape: **a1)** lacunarity (Λ); associated with cell size: **a2)** convex hull area, **a3)** the convex hull perimeter, **a4)** the diameter of bounding circle, **a5)** the mean radius, **a6)** the maximum span across the convex hull, **a7)** the cell area, and **a8)** the convex hull circularity; associated with cell surface **a9)** cell perimeter and **a10)** roughness; associated with soma thickness: **a11)** density and **a12)** cell circularity; associated with the complexity of ramifications: **a13)** fractal dimension (D); and associated with the cylindrical shape of cells: **a14)** convex hull span ratio and **a15)** the ratio of convex hull radii. Values for all these parameters were obtained from 152 microglial cells from WT mice ($n = 3$) and 180 microglial cells from CMVMJD135 mice ($n = 4$) of the PN. Data are presented as mean+SEM (Student's t-test).

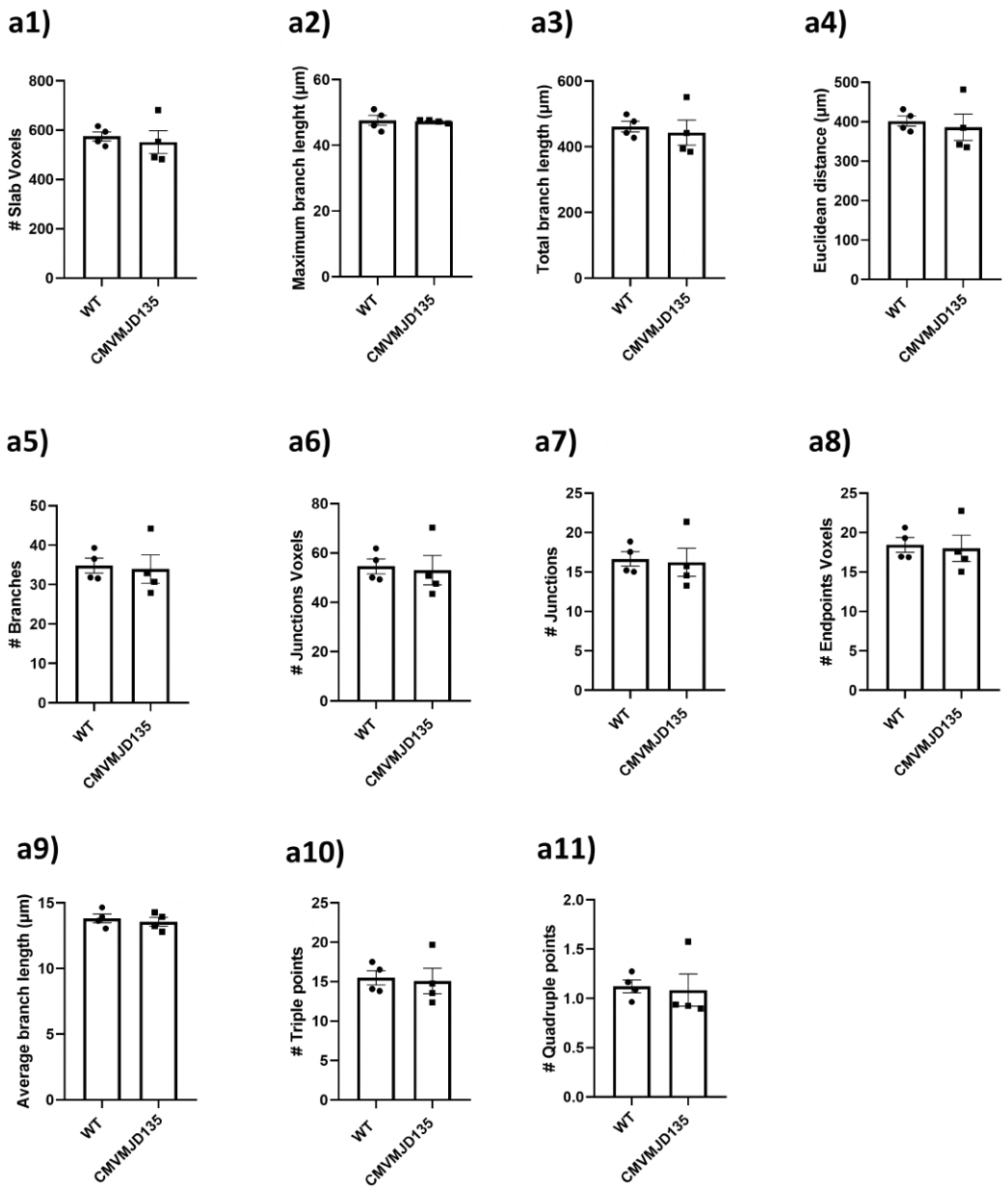

Figure B.3: **Microglia in the deep cerebellar nuclei of CMVMJD135 mice showed no differences in features relevant to microglia ramification.a)** Quantification of the morphometric parameters associated with microglia ramification including: **a1)** # slab voxels, **a2)** maximum branch length, **a3)** total branch length, **a4)** euclidean distance, **a5)** # branches, **a6)** # junctions voxels, **a7)** # junctions, **a8)** # endpoints voxels, **a9)** average branch length, **a10)** # triple points, and **a11)** # quadruple points. Values for all these parameters were obtained from 349 microglial cells from WT mice ($n = 4$) and 445 microglial cells from CMVMJD135 mice ($n = 4$) of the DCN. Data are presented as mean+SEM (Student's t-test).

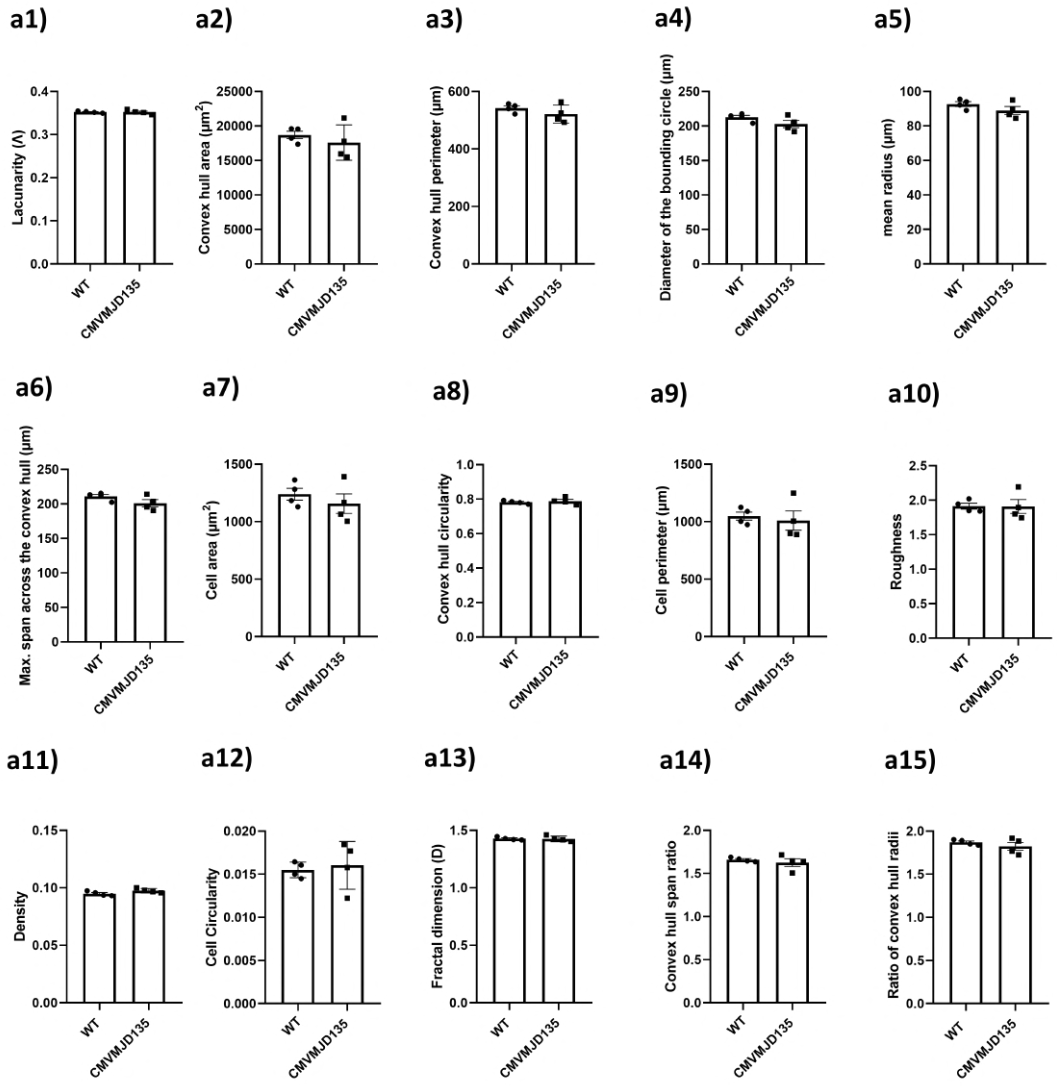

Figure B.4: **Microglia in the deep cerebellar nuclei of CMVMJD135 mice showed no changes in the complexity and shape. a)** Quantification of the morphometric parameters associated with the heterogeneity of the shape: **a1)** lacunarity (Λ); associated with cell size: **a2)** convex hull area, **a3)** the convex hull perimeter, **a4)** the diameter of bounding circle, **a5)** the mean radius, **a6)** the maximum span across the convex hull, **a7)** the cell area, and **a8)** the convex hull circularity; associated with cell surface **a9)** cell perimeter and **a10)** roughness; associated with soma thickness: **a11)** density and **a12)** cell circularity; associated with the complexity of ramifications: **a13)** fractal dimension (D); and associated with the cylindrical shape of the cells: **a14)** convex hull span ratio and **a15)** the ratio of convex hull radii. Values for all these parameters were obtained from 349 microglial cells from WT mice ($n = 4$) and 445 microglial cells from CMVMJD135 mice ($n = 4$) of the DCN. Data are presented as mean+SEM (Student's t-test).

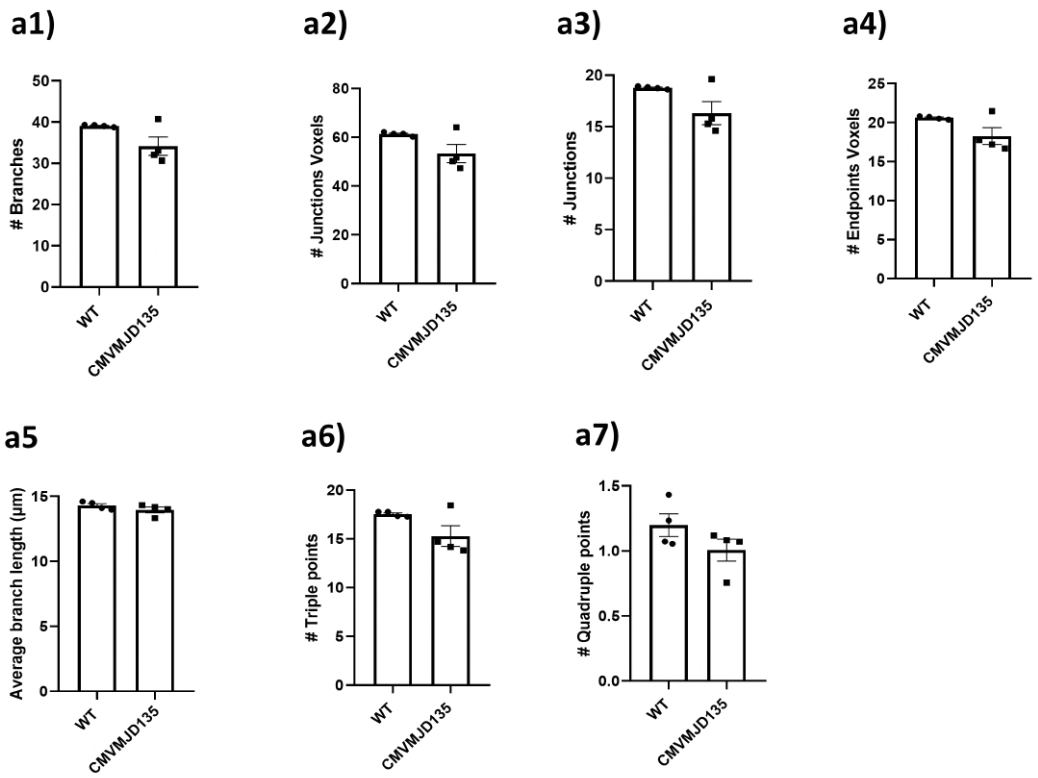

Figure B.5: **Some parameters associated with microglia ramification were similar between CMVMJD135 and wild-type mice in the cervical spinal cord. a)** Quantification of the morphometric parameters associated with microglia ramification including: **a1)** # branches, **a2)** # junctions voxels, **a3)** # junctions, **a4)** # endpoints voxels, **a5)** average branch length, **a6)** # triple points, and **a7)** # quadruple points. Values for all these parameters were obtained from 310 microglial cells from WT mice ($n = 4$) and 389 microglial cells from CMVMJD135 mice ($n = 4$) of the CSC. Data are presented as mean+SEM (Student's t-test).

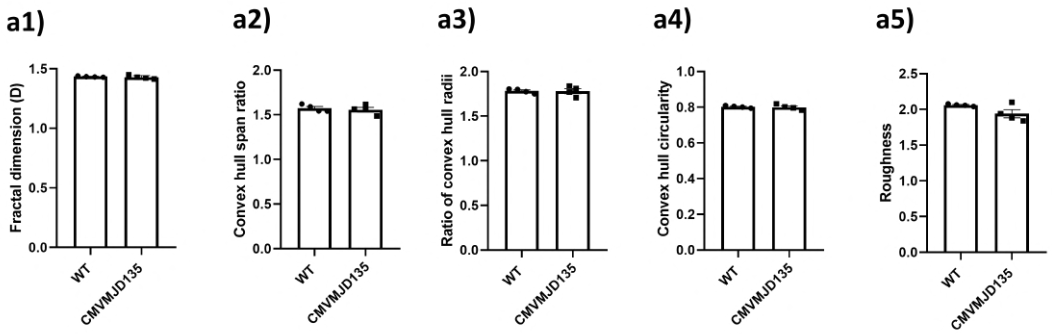

Figure B.6: **No changes were observed in the parameters related to the complexity of ramifications and with the cylindrical shape of the cells between groups in the cervical spinal cord. a)** Quantification of the morphometric parameters associated with the complexity of ramifications: **a1)** fractal dimension (D); associated with cylindrical shape of the cells: **a2)** convex hull span ratio and **a3)** the ratio of convex hull radii; one of the parameters associated with cell size: **a4)** the convex hull circularity; and one of the parameters associated with cell surface: **a5)** roughness. Values for all these parameters were obtained from 310 microglial cells from WT mice ($n = 4$) and 389 microglial cells from CMVMJD135 mice ($n = 4$) of the CSC. Data are presented as mean+SEM (Student's t-test).

Dataset	Total nº of compared genes	Overlapping genes	Fisher's exact test (p-value)	Odds ratio	Intersection genes
[HUMAN] Human postmortem Aging *Ref.: Galatro et al., 2017*	572	0	0.1812	0.2001	
[MICE] Aging DBA and Aging BL6-SJL mice *Ref.: Holtman et al., 2015*	1093	5	0.809	1.089	*Cdyl; Epsti1; 1110004F10Rik; Xpr1; Nek9*
[MICE] Aging C57BL/6J mice Cluster 2(AO) (P540) *Ref.: Hammond et al., 2019*	136	0	> 0.9999	0	
[MICE] Aging C57BL/6J mice Cluster 3(AO) (P540) *Ref.: Hammond et al., 2019*	37	0	> 0.9999	0	
[MICE] Adult C57BL/6J mice cluster 1a (P100) *Ref.: Hammond et al., 2019*	23	0	> 0.9999	0	
[MICE] Adult C57BL/6J mice cluster 1b (P100) *Ref.: Hammond et al., 2019*	12	0	> 0.9999	0	
[MICE] Transgenic accelerated aged ERCC1 microglia *Ref.: Holtman et al., 2015*	2713	13	0.6358	1.156	*Lamc1; Zfp62; Epsti1; Cpsf1; Fbxw4; Ap3m2; 1110004F10Rik; Fos; Atp6v0a1; Klhl24; Frmd4b; Csad; Ola1*
[HUMAN] Human Alzheimer Microglia (HAM) Cluster *Ref.: Srinivasan et al., 2020*	66	0	> 0.9999	0	
[MICE] App-Ps1 Alzheimer's disease transgenic mice *Ref.: Holtman et al., 2015; Orre et al., 2014*	3235	19	0.1424	1.485	*Lamc1; Cpsf1; Zfp568; Scd2; Abca7; Fbxw4; St8sia4; Ap3m2; Gpld1; Haghl; Atp6v0a1; Junb; Klhl24; Frmd4b; Tbkbp1; Csad; Ola1; Nek9*
[MICE] Homozygous AppNL-G-F/NL-G-F (mouse model of Alzheimer disease) *Ref.: Sobue et al., 2021*	3318	31	**<0.0001**	2.768	*Cux2; Gm6548; Ncam1; Bend6; Arhgef12; Rnf144b; Epsti1; Mkl2; Arhgef15; Abcb1a; Rbfox1; Tyro3; Alpl; Foxf2; Sox8; Ahnak; Caskin2; Scd2; Atp2b4; Fbxw4; Phlpp1; St8sia4; Cpd; Sh2d5; Gpld1; Syt3; Fos; Junb; Acsl4; Plin2; Klhl24*
[MICE] rTg4510 mouse model of Taupathology (Cerebral cortex microglia). *Ref.: Sobue et al., 2021*	2630	16	0.1482	1.528	*Cux2; Ncam1; Bend6; Tyro3; Nav1; Ptpn4; Scd2; Atp2b4; St8sia4; Cpd; Sh2d5; Gpld1; Fos; Junb; Plin2; Tbkbp1*
[MICE] rTg4510 mouse model of Taupathology (Forebrain microglia) *Ref.: Wang et al., 2018*	2950	12	>0.9999	0.9587	*Arhgef15; Rbfox1; Degs2; Alpl; Nav1; Caskin2; St8sia4; Cpd; Fmnl2; Plin2; Ola1; Zfp882*
[MICE] 5xFAD mice model (Hippocampi and cortices microglia) *Ref.: Wang et al., 2018*	715	5	0.2312	1.696	*Scd2; St8sia4; Cpd; Plin2; Ola1*
[MICE] App-Ps1 Alzheimer's disease transgenic mice. *Ref.: Orre et al., 2014; Wang et al., 2018*	947	5	0.6026	1.265	*Scd2; St8sia4; Cpd; Plin2; Frmd4b*
[MICE] DAM Cluster for Alzheimer's disease (5XFAD transgenic mice) *Ref.: Keren-Shaul et al., 2017*	102	1	0.351	2.349	*Scd2*
[MICE] Transgenic neurodegeneration Sod1-mice (SOD1(G93A)) *Ref.: Holtman et al., 2015; Chiu et al., 2013*	1766	6	0.7049	0.7919	*Lamc1; Scd2; Gpld1; Frmd4b; Csad; Ola1*
[MICE] Transgenic neurodegeneration Sod1-mice (SOD1(G93A)) *Ref.: Sobue et al., 2021*	3106	27	**0.0003**	2.459	*Lamc1; Ncam1; Bend6; Hipk3; Lrrc58; Usp11; Arhgef15; Abcb1a; Alpl; Bmpr2; Nav1; Caskin2; Fbxl12; St8sia4; Cpd; Fmnl2; Gpld1; Atp6v0a1; Plin2; Klhl24; Tbkbp1; Cnot1; Tmem106b; Csad; Xpr1; Rnh1; Foxf2*

Dataset	Total nº of compared genes	Overlapping genes	Fisher's exact test (p-value)	Odds ratio	Intersection genes
[MICE] Transgenic neurodegeneration Sod1-mice (SOD1(G93A)) *Ref.: Noristani et al., 2015*	630	3	0.7502	1.133	*Ncam1; Ahnak; Cpd*
[MICE] DAM Cluster for Amyotrophic lateral sclerosis (SOD1(G93A)) *Ref.: Keren-Shaul et al., 2017*	836	3	> 0.9999	0.8451	*Scd2; Cpd; Sh2d5*
[MICE] R62 mouse model of Huntington disease *Ref.: Crasper et al., 2020*	45	1	0.1735	5.406	*Abca7*
[HUMAN] Human postmortem control versus Huntington disease *Ref.: Al-Dalahmah et al., 2020*	149	0	>0.9999	0.7803	
BV2 microglia cell lines transduced with lentivirus expressing mHTT N548 *Ref.: Crotti et al., 2014*	81	0	>0.9999	1.435	
[MICE] Intreperitoneal LPS injected microglia mice *Ref.: Holtman et al., 2015*	4202	23	0.1886	1.387	*Zfp62; L3mbtl3; Hipk3; Mef2c; Olfr791; Akap7; Fbxl12; Scd2; Fbxw4; St8sia4; Ap3m2; Gsk3b; Rbbp6; 1110004F10Rik; St5; Haghl; Atp6v0a1; Klhl24; Frmd4b; Tbkbp1; Csad; Ola1; Xpr1*
[MICE] Injury cluster IR1 (Injury-Responsive Microglia) (saline injected) *Ref.: Hammond et al., 2019*	201	0	> 0.9999	0	
[MICE] Injury cluster IR2 (Injury-Responsive Microglia) (LPC injected, promote myelin loss) *Ref.: Hammond et al., 2019*	197	0	> 0.9999	0	
[HUMAN] Human postmortem tissues Ataxia Telangiectasia (Cerebellum microglia) *Ref.: Lai et al., 2021*	1577	6	>0.9999	0.8948	*MEF2C; ST8SIA4; RNF144B; A2M; PTPN4; TYRO3*
[HUMAN] Human postmortem tissues Ataxia Telangiectasia (Prefrontal cortex microglia) *Ref.: Lai et al., 2021*	1222	4	0.8201	0.7655	*ST8SIA4; FOS; ABCA7; NCAM1*
[MICE] Parkinson's disease mouse model α-syn-A53T (midbrain microglia) *Ref.: Zhong et al., 2021*	85	0	>0.9999	1.368	
[MICE] Parkinson's disease mouse model α-syn-A53T (striatum microglia) *Ref.: Zhong et al., 2021*	39	1	0.1522	6.261	*Atp6v0a1*
[MICE] Experimental autoimmune encephalomyelitis mice (Oxidative Stress Gene Cluster) *Ref.: Mendiola et al., 2020*	639	4	0.3488	1.506	*Ahnak; Cpd; Plin2; Rnh1*
[MICE] Experimental autoimmune encephalomyelitis mice (onset EAE Cluster 2) *Ref.: Mendiola et al., 2020*	791	5	0.3909	1.527	*Mef2c; Fbxw4; Cpd; Fos; Junb*
Genes Enriched in cerebellum microglia over striatum microglia *Ref.: Ayata et al., 2018*	297	2	0.3574	1.612	*Tmem136; Zfp568*
Genes Enriched in striatum microglia over cerebellum microglia *Ref.: Ayata et al., 2018*	733	4	0.5545	1.307	*Mef2c; Epsti1; Frmd4b; Csad*
Genes equally expressed in both striatum and cerebellum microglia *Ref.: Ayata et al., 2018*	250	2	0.2847	1.921	*Rnf144b; Nek9*

Dataset	Total nº of compared genes	Overlapping genes	Fisher's exact test (p-value)	Odds ratio	Intersection genes
Engulfment Cluster *Ref.: Ayata et al., 2018*	48	0	> 0.9999	0	
Catabolism Cluster *Ref.: Ayata et al., 2018*	45	0	> 0.9999	0	
Transcription regulation Cluster *Ref.: Ayata et al., 2018*	47	0	> 0.9999	0	
Chromatin modification Cluster *Ref.: Ayata et al., 2018*	13	0	> 0.9999	0	
Proinflammatory Cluster *Ref.: Ayata et al., 2018*	21	0	> 0.9999	0	
Microglial genes expressed in neuroinflammatory conditions *Ref.: Butovsky et al., 2014*	46	2	**0.0162**	10.92	*Mef2c; Fos*

Figure B.7: **Overlap between published microglial gene sets and enriched genes in CMV-MJD135 and WT-derived microglia.**

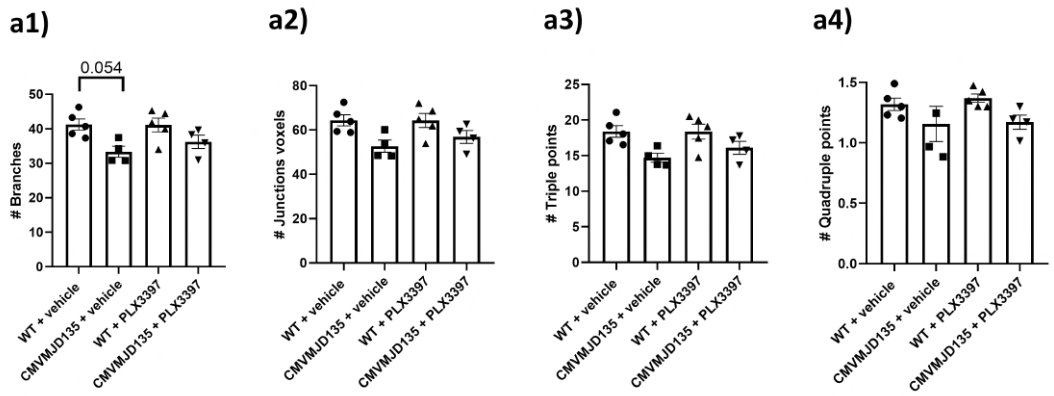

Figure B.8: **Features associated with microglial ramification in the pontine nuclei were found to be similar between the four groups. a)** Quantification of the morphometric parameters associated with microglia ramification including: **a1)** # branches, **a2)** # junctions voxels, **a3)** # triple points, and **a4)** # quadruple points. Data of all these parameters were obtained from: 210 microglial cells from WT + vehicle mice ($n = 4$); 217 microglial cells from CMVMJD135 + vehicle mice ($n = 4$); 248 microglial cells from WT + PLX3397 mice ($n = 5$); and 235 microglial cells from CMVMJD135 + PLX3397 mice ($n = 5$). Data are presented as mean+SEM, *(One-way ANOVA (Post hoc Tukey's test))*.

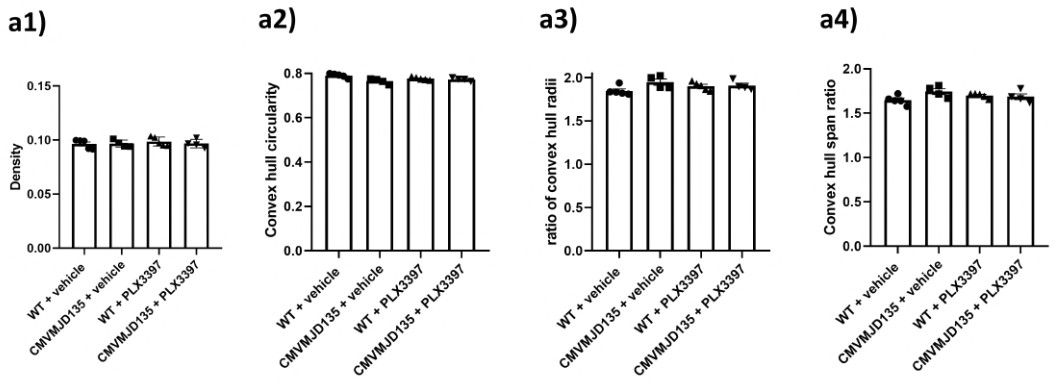

Figure B.9: **Features associated with complexity and shape of microglial cells in the deep cerebellar nuclei found not to be different between the four groups. a)** Quantification of the morphometric parameters associated with soma thickness: **a1)** density. Associated with cell size: **a2)** convex hull circularity. Associated with the cylindrical shape of cells: **a3)** ratio of convex hull radii, and **a4)** convex hull span ratio. Data of all these parameters were obtained from: 387 microglial cells from WT + vehicle mice ($n = 5$); 256 microglial cells from CMVMJD135 + vehicle mice ($n = 4$); 475 microglial cells from WT + PLX3397 mice ($n = 5$); and 263 microglial cells from CMVMJD135 + PLX3397 mice ($n = 4$). Data are presented as mean+SEM, *(One-way ANOVA (Post hoc Tukey's test))*.

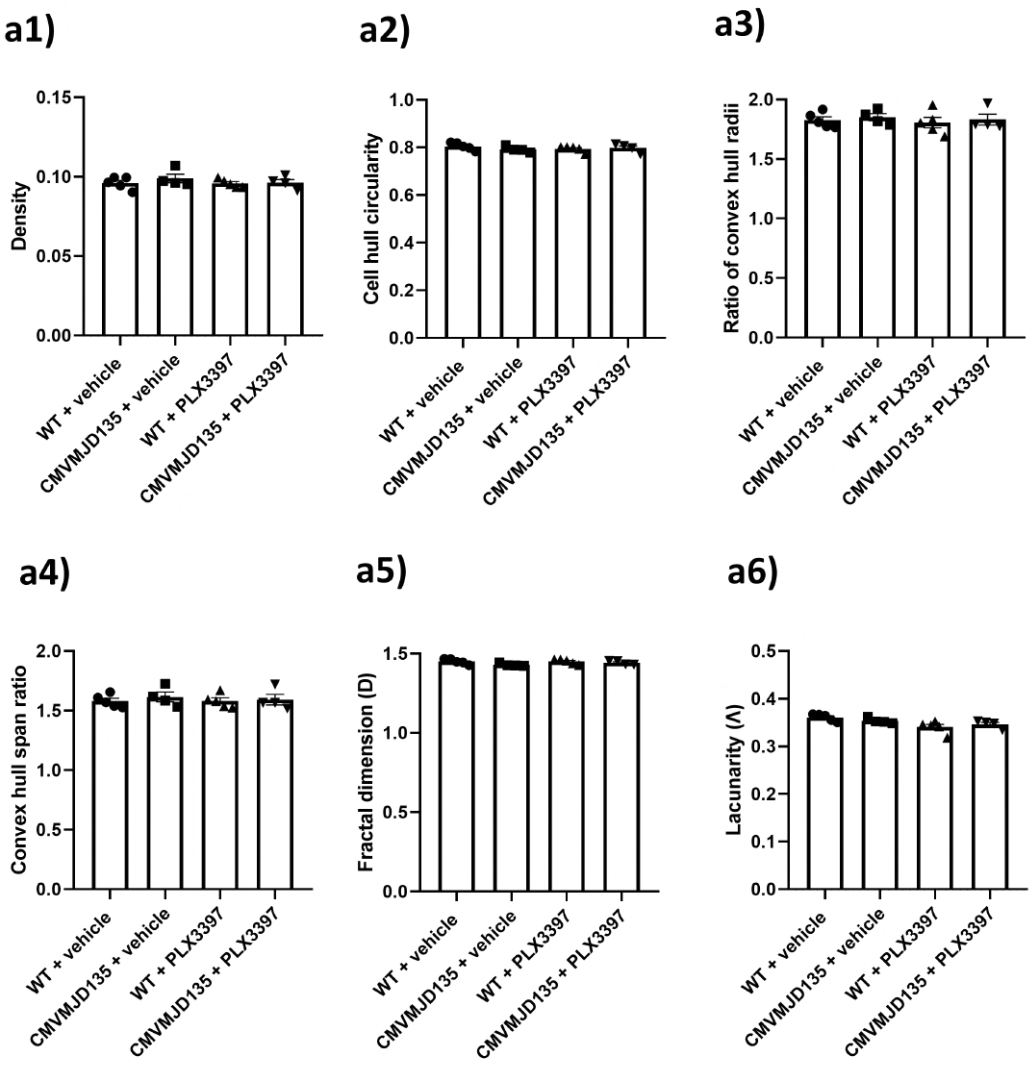

Figure B.10: **Features associated with complexity and shape of microglial cells in the pontine nuclei found to be similar between the four groups. a)** Quantification of the morphometric parameters associated with soma thickness: **a1)** density. Associated with cell size: **a2)** convex hull circularity. Associated with the cylindrical shape of cells: **a3)** ratio of convex hull radii; and **a4)** convex hull span ratio. Associated with the complexity of their ramifications: **a5)** fractal dimension. Associated with the heterogeneity of their shape: **a6)** lacunarity. Data of all these parameters were obtained from: 210 microglial cells from WT + vehicle mice ($n = 4$); 217 microglial cells from CMVMJD135 + vehicle mice ($n = 4$); 248 microglial cells from WT + PLX3397 mice ($n = 5$); and 235 microglial cells from CMVMJD135 + PLX3397 mice ($n = 5$). Data are presented as mean+SEM, *(One-way ANOVA (Post hoc Tukey's test))*.

Appendix C

Published article: Profiling Microglia in a Mouse Model of Machado–Joseph Disease

biomedicines

MDPI

Article

Profiling Microglia in a Mouse Model of Machado–Joseph Disease

Ana Bela Campos [1,2,†], Sara Duarte-Silva [1,2,†], Bruno Fernandes [3], Sofia Pereira das Neves [1,2], Fernanda Marques [1,2], Andreia Teixeira-Castro [1,2], Andreia Neves-Carvalho [1,2], Daniela Monteiro-Fernandes [1,2], Camila Cabral Portugal [4], Renato Socodato [4], Teresa Summavielle [5,6], António Francisco Ambrósio [7,8,9], João Bettencourt Relvas [4,10] and Patrícia Maciel [1,2,*]

1 Life and Health Sciences Research Institute (ICVS), School of Medicine, University of Minho, 4710-057 Braga, Portugal; ana.bela.campos.88@gmail.com (A.B.C.); sarasilva@med.uminho.pt (S.D.-S.); pereiradasneves.sofia@mayo.edu (S.P.d.N.); fmarques@med.uminho.pt (F.M.); accastro@med.uminho.pt (A.T.-C.); andreiacarvalho@med.uminho.pt (A.N.-C.); id8942@alunos.uminho.pt (D.M.-F.)
2 ICVS/3B's, PT Government Associate Laboratory, 4710-057 Braga, Portugal
3 Department of Informatics, ALGORITMI Center, University of Minho, 4710-057 Braga, Portugal; bruno.fernandes@algoritmi.uminho.pt
4 Glial Cell Biology Group, Instituto de Investigação e Inovação em Saúde (i3S), Instituto de Biologia Molecular e Celular (IBMC), University of Porto, 4200-135 Porto, Portugal; camila.portugal@ibmc.up.pt (C.C.P.); renato.socodato@ibmc.up.pt (R.S.); jrelvas@ibmc.up.pt (J.B.R.)
5 Addiction Biology Group, Instituto de Investigação e Inovação em Saúde (i3S), Instituto de Biologia Molecular e Celular (IBMC), University of Porto, 4200-135 Porto, Portugal; tsummavi@ibmc.up.pt
6 ESS.PP, Escola Superior de Saúde do Politécnico do Porto, 4200-072 Porto, Portugal
7 Coimbra Institute for Clinical and Biomedical Research (iCBR), Faculty of Medicine, Univiversity of Coimbra, 3004-504 Coimbra, Portugal; afambrosio@fmed.uc.pt
8 Center for Innovative Biomedicine and Biotechnology (CIBB), Univiversity of Coimbra, 3004-504 Coimbra, Portugal
9 Clinical Academic Center of Coimbra (CACC), 3004-561 Coimbra, Portugal
10 Faculty of Medicine, University of Porto, 4200-319 Porto, Portugal
* Correspondence: pmaciel@med.uminho.pt
† These authors contributed equally to this work.

check for updates

Citation: Campos, A.B.; Duarte-Silva, S.; Fernandes, B.; das Neves, S.P.; Marques, F.; Teixeira-Castro, A.; Neves-Carvalho, A.; Monteiro-Fernandes, D.; Portugal, C.C.; Socodato, R.; et al. Profiling Microglia in a Mouse Model of Machado–Joseph Disease. *Biomedicines* **2022**, *10*, 237. https://doi.org/10.3390/biomedicines10020237

Academic Editors: Cristina Carvalho, Sónia Correia and Susana Cardoso

Received: 31 December 2021
Accepted: 19 January 2022
Published: 23 January 2022

Publisher's Note: MDPI stays neutral with regard to jurisdictional claims in published maps and institutional affiliations.

Copyright: © 2022 by the authors. Licensee MDPI, Basel, Switzerland. This article is an open access article distributed under the terms and conditions of the Creative Commons Attribution (CC BY) license (https://creativecommons.org/licenses/by/4.0/).

Abstract: Microglia have been increasingly implicated in neurodegenerative diseases (NDs), and specific disease associated microglia (DAM) profiles have been defined for several of these NDs. Yet, the microglial profile in Machado–Joseph disease (MJD) remains unexplored. Here, we characterized the profile of microglia in the CMVMJD135 mouse model of MJD. This characterization was performed using primary microglial cultures and microglial cells obtained from disease-relevant brain regions of neonatal and adult CMVMJD135 mice, respectively. Machine learning models were implemented to identify potential clusters of microglia based on their morphological features, and an RNA-sequencing analysis was performed to identify molecular perturbations and potential therapeutic targets. Our findings reveal morphological alterations that point to an increased activation state of microglia in CMVMJD135 mice and a disease-specific transcriptional profile of MJD microglia, encompassing a total of 101 differentially expressed genes, with enrichment in molecular pathways related to oxidative stress, immune response, cell proliferation, cell death, and lipid metabolism. Overall, these results allowed us to define the cellular and molecular profile of MJD-associated microglia and to identify genes and pathways that might represent potential therapeutic targets for this disorder.

Keywords: microglia; Machado–Joseph disease; cell morphology; RNA-sequencing; machine learning

1. Introduction

Microglia, the primary immune cells of the central nervous system (CNS), play multiple roles in neurodevelopment, synaptic plasticity, homeostasis, injury responses [1,2],

and neurodegenerative diseases (NDs) [3]. Microglia can polarize into different activation states depending on the gamut of environmental cues they are exposed to [4,5]. However, defining microglial transcriptomic signatures in different states has revealed that their activation profile is quite heterogeneous and, to a large extent, context dependent [6].

The morphological characterization of microglia is of the utmost importance, as it is widely used to define their activation status and changes substantially under brain disease and pathology. Ramified microglia can undergo morphological transformations into an "activated state" (characterized by larger cell bodies with shorter and thicker processes) [6,7] or a "reactive state" (characterized by smaller, spherical cells that can also exhibit rod-shaped or amoeboid-like morphologies) [6–9].

Age-related neurodegenerative diseases are associated with chronic neuroinflammation, and microglia-mediated inflammation is a significant contributor to disease pathogenesis [10–14]. Aging causes microglia to adopt an aberrant phenotype, sometimes referred to as dystrophic or senescent, usually associated with a decreased ability to provide a normal response to injury [11]. Cellular senescence is typically characterized by an arrested growth due to elevated DNA damage and oxidative stress that increases the amounts of senescence indicators, including the cell cycle regulators $P16^{Ink4a}$ (also known as *Cdkn2a*), $P19^{Arf}$ (also known as *Cdkn2a*) and $P21^{Cip1/Waf1}$ (also known as *Cdkn1a*), and pro-inflammatory cytokines, such as Pai1 (also known as *Serpine1*), Il-6, Il-8, Il-1 alpha, and Il-1 beta [15]. Reduced phagocytic capacity [11,16], impaired protein homeostasis (proteostasis) [17], and dystrophic morphology, characterized by de-ramification and shortening of the processes [18], are also consistent age-related changes in microglia. These changes may contribute to an increased susceptibility to neuronal dysfunction and demise during aging, through increased production of inflammatory mediators and impairment of microglia neuroprotective functions [4,14].

Little is known about the profile of microglia and their involvement in Machado–Joseph disease (MJD), a neurodegenerative disorder caused by an abnormal expansion of a CAG triplet that encodes the amino acid glutamine in the ataxin-3 protein [19]. The CAG repeat size in the *ATXN3* gene translates into a polyglutamine tract of 61 to 87 glutamines that renders ataxin-3 prone to self-assembly and thus to the formation of aggregates that are toxic to neurons [19,20]. While ataxin-3 misfolding and the consequent disruption of cells' proteostasis are considered central to MJD pathogenesis [20], transcriptional dysregulation, oxidative stress, and DNA damage also contribute to disease progression [20]. Neuropathological analyses of MJD patients' brains reveal significant neuronal loss in the deep cerebellar nuclei (DCN) within the cerebellum, pontine nuclei (PN) within the brainstem, and in spinocerebellar tracts. The motor symptoms appear gradually and progress over time, pointing to an age-dependent decline in the cells' ability to remove misfolded proteins [21,22]. Although microgliosis has been observed both in MJD patients' post-mortem brains [23–25] and a mouse model of MJD [26], further studies are required to fully understand the basis of microglial activation in MJD [25]. Because most brain cells express *ATXN3*, microglial dysfunction may contribute to the disease process due to the effects of mutant *ATXN3* in microglia or as a consequence of their interaction with neurons.

In this study, we used the CMVMJD135 mouse model [27] to characterize the profile of microglia in the context of MJD. Combining principal components analysis (PCA), machine learning models, and RNA sequencing, we characterized morphological clusters and mapped gene expression networks in MJD-derived microglia, providing relevant novel insights into how coordinated microglia morphology and gene regulatory programs might contribute to MJD pathogenesis.

2. Materials and Methods

2.1. Animal Maintenance

CMVMJD135 and wild-type (WT) littermates' mice on a C57BL/6J background were used. The CMVMJD135 mouse expresses an expanded version of the human MJD1-1 cDNA (the 3 UIMs-containing a variant of ataxin-3) under the regulation of the CMV promoter

(ubiquitous expression) at near-endogenous levels and manifests MJD-like motor symptoms that appear gradually and progress over time [27,28]. All animals (specific pathogen-free health status) were maintained under standard laboratory conditions: an artificial 12 h light/dark cycle (lights on from 8:00 to 20:00 h), with an ambient temperature of 21 ± 1 °C and a relative humidity of 50–60%. All animal procedures were conducted following the European Union Directive 2010/63/EU. Health monitoring was performed according to the Federation of European Laboratory Animal Science Associations (FELASA) guidelines. The specified pathogen-free health status was confirmed by sentinel mice maintained in the same animal housing room. Except for the primary culture of microglial cells that used 3-to-4-day-old (P3-P4) WT and CMVMJD135 mice, all the remaining experiments were performed using animals of 34–50 weeks of age, corresponding to an advanced disease stage.

2.2. Evaluation of Microglia Phagocytic Ability in Culture

After the characterization of a microglia-enriched culture (detailed protocol in Supplementary Materials and Methods), their phagocytic activity and morphology were assessed, as described in [11], in two conditions: basal and exposed to lipopolysaccharide (LPS, E. coli O111:B4, Sigma-Aldrich, St. Louis, MO, USA), and at two different time points, 4 and 16 days in vitro (DIV), as presented in Table S1 in Supplementary Materials and Methods.

To evaluate the phagocytic activity of the primary microglial cultures, the cells, collected at two different time points (4 and 16 DIV), were incubated with 0.0025% (*w*/*w*) of 1 µm green fluorescent latex beads (Sigma-Aldrich, St. Louis, MO, USA). For immunofluorescence detection, the cells were fixed for 15 min with freshly prepared 4% paraformaldehyde (PFA) in phosphate saline buffer (PBS), permeabilized with 0.1% Triton X-100 for 20 min, and then blocked with PBS containing 2% bovine serum albumin (BSA) for 1 h. After this, the microglial cells were incubated with an anti-ionized calcium binding adaptor molecule 1 (Iba-1) antibody (Table S2 in Supplementary Materials and Methods) overnight at 4 °C, followed by secondary antibody incubation (anti-rabbit Alexa Fluor 594, Table S2 in Supplementary Materials and Methods) for 2 h at room temperature (RT). Cell nuclei were stained with 4',6-diamidin-2-phenylindol (DAPI, Invitrogen, Waltham, MA, USA) for 10 min at RT. Random fluorescence images (7 to 22) were acquired per coverslip, animal, condition, and experimental group (Table S2 in Supplementary Materials and Methods), using an Olympus Widefield Inverted Microscope IX81 (Olympus Corporation, Tokyo, Japan) (resolution of 1024 × 1024 px and an original magnification of 20×).

To evaluate the phagocytic capacity of the primary microglial cultures, the number of ingested beads per cell was counted using the Point Tool feature in ImageJ software (v1.53c). Results are presented as phagocytic efficiency, considering the total number of microglial cells, to obtain the average amount of ingested beads per cell, considering the proportion of cells phagocytosing 1, 2, 3, 4, 5, and more than 5 beads, obtained by the formula described in [29].

2.3. Evaluation of Microglial Morphology in Culture

For the morphological analysis, cells were fixed with 4% PFA in PBS, and a standard immunolabeling technique was performed using a primary antibody against Iba-1 to evaluate the microglia phagocytic ability. To identify the cells, microglial nuclei were stained with DAPI. Using ImageJ software, cells were outlined with the Freehand Selection tool. Then the particle measurement feature was used to automatically measure the 2D area, perimeter, and the Feret's diameter of at least 3 single microglial cells per image [11]. The fluorescence images used to evaluate phagocytic capacity were also used to characterize the microglia morphology, quantitatively. The transformation index, which categorizes the microglia ramification status, was also assessed as described previously [30].

2.4. Quantitative Reverse-Transcription PCR (qRT-PCR)

To evaluate the mRNA expression levels of human *ATXN3*, RNA was extracted from CMVMJD135 and WT neonatal mice-derived microglial. To evaluate senescence marker levels, RNA was extracted from CMVMJD135 and WT tissues previously frozen (brainstem, cerebellum, and spinal cord). TRIZOL (Invitrogen, Waltham, MA, USA) was used in both cases, following the manufacturer's instructions. Samples were treated with DNase I (ThermoFisher Scientific, Waltham, MA, USA); RNA concentration was quantified using the NanoDrop™ Spectrophotometer (ThermoFisher Scientific, Waltham, MA, USA), and RNA quality was tested through electrophoresis. Afterwards, 1 µg first-strand complementary DNA (cDNA) was synthesized using the iScript™ cDNA synthesis kit (Bio-Rad, Hercules, CA, USA). The quantitative polymerase chain reaction (PCR) was then carried out using the 5× HOT FIREPol® EvaGreen® qPCR Mix Plus (ROX) (Solis BioDyne, Tartu, Estonia) with 1 µL of cDNA. Specific primers for different messenger RNAs were obtained either from the literature or those previously designed by us, using Primer-BLAST. The used primers are listed in Table S3 of Supplementary Materials and Methods. The housekeeping genes, Beta-2-microglobulin (*B2m*) or endogenous mouse *Atxn3*, were used as an internal standard to normalize the expression of selected transcripts. PCR reaction was run in Applied Biosystems™ 7500 Real-Time PCR System, and raw data were extracted using 7500 Real-Time PCR software v2.3 (Applied Biosystems by ThermoFisher, Waltham, MA, USA). All melting curves exhibited a single sharp peak at the expected temperature. Statistical analysis was conducted using $2^{-\Delta CT}$ values, and plots were reported in fold change ($2^{-\Delta\Delta CT}$) or reported as fold change normalized to the mean of the relative expression of the control group.

2.5. Flow Cytometry Analysis

Microglia were collected from the affected brain regions as a whole (cerebellum, brainstem, and spinal cord) of WT and CMVMJD135 littermates, using density gradient separation. The following markers were used to characterize these cells in the samples: CD45-PE, CD11b-PE/Cy7, and CD11b-Alexa Fluor 647.

For the intracellular analysis of the $P19^{Arf}$ and $P21^{Cip1/Waf1}$ senescence markers, microglia were fixed, permeabilized, and incubated with anti-rat $P19^{Arf}$ and anti-rabbit $P21^{Cip1/Waf1}$ antibodies (Table S2 in Supplementary Materials and Methods). Briefly, mice were deeply anesthetized with a mixture of ketamine hydrochloride (150 mg/kg) and medetomidine (0.3 mg/kg) and perfused with ice-cold PBS. The tissues were quickly dissected and mechanically homogenized. The cell suspension was passed through a 100 µm cell strainer and centrifuged over a discontinuous 70/30% Percoll (GE Healthcare, Chicago, IL, USA) gradient. Single-cell suspensions (5×10^5 cells) were seeded in a U-shape bottom 96-well plate and incubated with CD45-PE, CD11b-Alexa Fluor 647, or CD11b-PE/Cy7 for 30 min at 4 °C in the dark. After antibody washing, cells were fixed in 2% PFA for 30 min and permeabilized with a permeabilization buffer (Life Technologies, Carlsbad, CA, USA). Intracellular staining mix using the anti-rat $P19^{Arf}$ and anti-rabbit $P21^{Cip1/Waf1}$ antibodies was prepared in a permeabilization buffer. Microglia were then incubated with this intracellular staining mix overnight, at 4 °C in the dark. After that, cells were incubated with Alexa Fluor 488 and 647 secondary antibodies for 1 h at RT in the dark.

For intracellular detection of Il-8, Il-6, Il-1 alpha, and Il-1 beta, cells were incubated with 10 µg/mL of brefeldin A (Sigma-Aldrich, St. Louis, MO, USA) over 3 h, in an RPMI medium supplemented with 10% FBS and 1% antibiotic–antimycotic solution, and maintained at 37 °C in a humidified atmosphere of 5% CO_2. After staining for the expression of surface molecules, cells were fixed with 2% PFA and permeabilized with a permeabilization buffer. After permeabilization, the cells were stained with anti-rabbit Il-6 and anti-mouse Il-8, or anti-mouse Il-1 alpha and anti-rabbit Il-1 beta antibodies overnight, at 4 °C, followed by Alexa Fluor 488 and 647 secondary antibodies (Table S2 in Supplementary Materials and Methods) for 1 h at RT in the dark.

Data acquisition was performed in Fluorescence-Activated Cell Sorting (FACS) Canto II analyzer (BD Immunocytometry Systems, San Jose, CA, USA) and data were analyzed by FlowJo X10 software (FlowJo, Ashland, OR, USA).

2.6. Tissue Preparation and Immunofluorescence Staining

CMVMJD135 and WT littermates were deeply anesthetized and transcardially perfused with PBS followed by 4% PFA solution (PFA, 0.1 M, pH 7.4, in PBS). Brain tissue was removed and fixed in a 4% PFA for 48 h, followed by 30% sucrose solution for 1 week. Then, coronal, and sagittal sections of 40 µm thickness were sliced using a Leica Vibratome. Tissue slices were permeabilized with PBS-T 0.3% (0.3% Triton X-100; Sigma Aldrich, St. Louis, MO, USA) for 10 min. Antigen retrieval was then performed by immersing the slices in pre-heated citrate buffer (10 mM, pH 6.0; Sigma Aldrich, St. Louis, MO, USA) for 20 min using a thermoblock (D1200, LabNet, Cary, NC, USA) set at 80 °C. Once cooled, the slices were rinsed in PBS and then blocked with goat serum blocking buffer (10% normal goat serum (NGS), 0.3% Triton X-100, in PBS) at RT for 90 min. After that, the slices were incubated with the primary antibody rabbit anti-Iba-1 diluted in PBS-T 0.3%, 5% NGS, overnight at 4 °C. Then, the tissue slices were rinsed in PBS and incubated with a secondary antibody, Alexa Fluor 594 anti-rabbit (Table S2 in Supplementary Materials and Methods) diluted in PBS-T 0.3%, 5% NGS, for 90 min at RT, protected from light. The sections were mounted on microscope slides (Menzel Gläser Superfrost©Plus, ThermoFisher Scientific, Waltham, MA, USA) and covered with a coverslip (Menzel Gläser 24–60 mm, Wagner & Munz, Munchen, Germany) using an aqueous mounting medium (Fluoromount™ Sigma-Aldrich, St. Louis, MO, USA).

2.7. Image Acquisition for Microglial Density and Morphological Analysis

For the analysis of microglial density and morphology, four coronal brain sections per animal ($n = 4$ per genotype) were imaged twice (in both hemispheres) for each region of interest (DCN and cervical spinal cord (CSC)) to yield 4–6 digital photomicrographs per section containing the region for analysis. For the PN, four sagittal brain sections per animal were used ($n = 3$ animals for WT and $n = 4$ animals for CMVMJD135), and 2 photomicrographs per section were taken. The Olympus Confocal FV1000 laser scanning microscope with a resolution of 1024 × 1024 px using a 40× objective (UPlanSApo, N.A. 0.90; dry; field size 624.39 × 624.39 µm; 0.31 µm/px) was used to obtain all Z-stacked images. The acquisition settings were the following: scanning speed = 4 µm/px; pinhole aperture = 110 µm; Iba-1, excitation = 559 nm, emission = 618 nm; in a 3-dimensional scenario (X, Y, and Z axes).

The ImageJ software was used on Z-stacked 3D volume images from sections of the affected brain regions (DCN, CSC, and PN). The total count of Iba-1-positive cells was obtained using the multi-point tool of ImageJ. Quantification was performed on images acquired with acquisition settings described as above, normalized first to the total image area and then for volume. For morphological analysis, a semi-automatic method adapted from [31] was used (detailed protocol in Supplementary Materials and Methods and Figure S1 in Supplementary Materials and Methods).

2.8. Morphological Data Acquisition and Pre-Processing

When performed manually over every cell, obtaining all morphological features is demanding and laborious. Hence, to expedite the process, the *MorphData* plugin was used [32]. This plugin automatizes the data extraction process of morphological features of single microglial cells, collecting, pre-processing, and organizing features associated with cell complexity and ramification (detailed protocol in Supplementary Materials and Methods and Figures S2 and S3 in Supplementary Materials and Methods).

Data were obtained from individual cells of the CSC (310 microglial cells from WT mice and 389 from CMVMJD135 mice), DCN (349 microglial cells from WT mice and

445 from CMVMJD135 mice), and PN (152 microglial cells from WT mice and 180 from CMVMJD135 mice). The total number of analyzed microglia was 1825.

2.9. Machine Learning Modeling

An open-source data science and machine learning modeling platform was used to further process the obtained data and identify potential microglia clustering, concerning their morphological features. KNIME is a data-flow-centric platform, enabling visual and interactive flows.

Using the KNIME platform, two flows were conceived. The first is responsible for loading the obtained data and applying functions to arrange identical data into groups. As explained in subsequent lines, these data are then used for statistical analysis. The second flow is responsible for applying a PCA to the obtained data. This flow is also used to apply an unsupervised machine learning model, the k-means, a clustering method that finds groups or clusters with similar characteristics within the entire dataset. This method partitions the data into k clusters, with each observation belonging to a single cluster, represented by its centroid. To find the ideal number of clusters, i.e., the ideal number for k, the flow applies the elbow method, experimenting and plotting the mean squared error (MSE) associated with each cluster, with k varying between 1 and 12. The ideal k is found by picking the "elbow" of the curve as a function that minimizes the error of k. This flow is also used to generate 3D plots.

Finally, gradient boosted trees were used to obtain estimates of parameter importance, i.e., a score that measures how valid each parameter is for the model. Gradient boosted trees are a supervised machine learning model used to convert weak learners, typically decision trees, into strong ones. Gradient boosted trees train the learners gradually, additively, and sequentially, performing a gradient descent procedure. The importance was estimated using gain as the importance type. A higher value for a parameter, when compared to another, implies it is more important for classifying the label [33]. In this case, the label was set as the parameter identifying WT and CMVMJD135 cells, a binary classification problem.

2.10. Brain Dissociation for Magnetic Activated Cell Sorting Isolation of Adult Microglia

2.10.1. Cellular Suspension Preparation

Microglia were isolated from the brainstem and cerebellum of WT and CMVMJD135 mice as described in [34]. The isolation was performed by pooling these 2 brain areas from 3 animals for each experiment. Hence, $n = 5$ implies the use of 15 WT animals and 15 CMVMJD135 ones. Mice were transcardially perfused under deep anesthesia with PBS. Then the brainstem and cerebellum were removed, dissected, and rinsed in cold Hanks' Balanced Salt solution without calcium chloride or magnesium chloride (HBSS[-]$CaCl_2$/[-]$MgCl_2$; ThermoFisher Scientific). The regions of interest were cut into small pieces using a sterile scalpel, and the samples were centrifuged at 300× g for 2 min at 4 °C, and the supernatant was discarded carefully. According to the manufacturer's instructions, enzymatic cell dissociation was performed using a neural tissue dissociation Kit (Miltenyi Biotec, Cologne, Germany). Briefly, the enzyme mix 1 (50 µL of enzyme P and 1950 µL of buffer x), previously vortexed and pre-heated at 37 °C for 15 min, was transferred to the tissue pieces (up to 400 mg of tissue per sample). Then we proceeded to incubate for another 15 min at 37 °C under slow rotation to allow the digestion of the tissue. The enzyme mix 2 (10 µL of enzyme A and 20 µL of buffer Y) was then added, and the tissue was dissociated mechanically using a 1 mL syringe and a 20 G needle. After that, the samples were resuspended with cold Hanks' Balanced Salt solution with calcium chloride and magnesium chloride (HBSS[+]$CaCl_2$/[+]$MgCl_2$; ThermoFisher Scientific, Waltham, MA, USA) and filtered through a 70 µm cell strainer (Sigma-Aldrich, St. Louis, MO, USA) to remove cell clumps followed by centrifugation at 300× g for 10 min at 4 °C.

2.10.2. Myelin and Debris Removal

After centrifugation, cells were resuspended in a magnetically activated cell sorting (MACS) solution (0.5% BSA in PBS, pH 7.2) and incubated for 15 min at 4 °C with myelin removal beads II (Miltenyi Biotec, Cologne, Germany) for myelin and debris removal. After that, cells were washed by adding blocking solution and centrifuged at 300× *g* for 10 min at 4 °C. The supernatant was removed, and the pellet was resuspended in MACS solution. Then, the autoMACS® Pro Separator, using a reusable autoMACS® Column for separation, was prepared to isolate the cells automatically. Briefly, the tube containing the sample (row A of the rack), the tubes for collecting the labeled (myelin positive fraction; row C of the rack), and the unlabeled cell fractions (myelin negative fraction—mixed glial population, row B of the rack) were placed in the autoMACS®. The following program was chosen to separate these two fractions: "Depletion: Depletes—collect negative fraction in row B of the rack".

2.10.3. MACS Sorting of Adult Microglia

After myelin and debris removal, the myelin negative fraction was used to obtain the microglia. After centrifugation of the cell suspension at 300× *g* for 10 min at 4 °C, the cell population was resuspended in MACS solution and incubated with anti-CD11b Magnetic Microbeads (Miltenyi Biotec, Cologne, Germany) for 15 min at 4 °C. The cells were washed by adding MACS solution, and the unbound beads and debris were discarded after centrifugation at 300× *g* for 10 min at 4 °C. The pellets were resuspended and put in row A of the rack, and the tubes for collecting the labeled cell fractions (microglia positive fraction in row C of the rack) were placed in the autoMACS® Pro Separator using the following program: "Positive selection: Possel—collect positive fraction in row C of the rack". After centrifugation at 300× *g* for 10 min at 4 °C, the microglia-enriched pellets were used for RNA extraction.

2.11. RNA Extraction, Library Preparation, and Targeted RNA-Sequencing

The microglia-enriched pellets were resuspended in buffer RLT plus with β- mercaptoethanol for RNA extraction using the RNeasy Plus Mini Kit, along with the recommended on-column DNase digestion (Qiagen Inc., Venlo, The Netherlands). RNA quality and concentration were measured using Agilent Tech. Bioanalyzer, with samples having RNA integrity number (RIN) scores higher than 8.

The AmpliSeq Library preparation kit protocol, described in [35], was used to prepare Ion Torrent sequencing libraries. Briefly, 0.5 ng of total RNA was converted to cDNA and amplified for 16 cycles by adding PCR Master Mix and the AmpliSeq Mouse transcriptome gene expression primer pool (targeting 20,767 well-annotated RefSeq genes + 3163 XM and XR genes, based on GRCm38/mm10). The proprietary FuPa enzyme was used to digest amplicons, and then barcoded adapters were ligated onto the target amplicons. The library amplicons were bound to magnetic beads, and residual reaction components were washed off. Libraries were amplified, re-purified, and individually quantified using Agilent TapeStation High Sensitivity tape. Individual libraries were diluted to a 50 pM concentration and pooled equally, with eight individual samples ($n = 4$ for WT and CMVMJD135 mice) per pool for further processing. Emulsion PCR, templating, and 540 chip loading were performed with an Ion Chef Instrument (ThermoFisher, Waltham, MA, USA). Ion S5XL™ sequencer (ThermoFisher, Waltham, MA, USA) was used for sequencing. Automated data analysis was performed with Torrent Suite™ Software using the Ion AmpliSeq™ RNA plugin v.5.12 and target region AmpliSeq_Mouse_Transcriptome_V1_Designed (ThermoFisher, Waltham, MA, USA).

2.12. Analysis of Differentially Expressed Genes and Pathways

To analyze the differentially expressed genes (DEGs), RNA expression levels were recorded as reads per million (RPM), normalized for the number of sequences reads per sample. To verify the enrichment of microglia in the samples, a list of several cell-type-

specific genes was prepared [36–40], being described in Supplementary Data 1. A heatmap containing the cell-specific markers was achieved using the Clue Morpheus software (Broad Institute, Cambridge, MA, USA).

The Transcriptome Analysis Console (TAC) software, version 4.0.2 (Applied Biosystems by ThermoFisher, Waltham, MA, USA), was used to analyze and compare the gene expression profiles from the microglia of WT and CMVMJD135 mice. Exploratory grouping analysis was performed to identify the distribution of samples using PCA and a clustering analysis. TAC software provides the LIMMA Bioconductor package for determining differential expression based on linear models. LIMMA uses an empirical Bayes method that corrects the variance of the ANOVA analysis. Genes were considered significantly differentially expressed if they showed a $|\text{fold change}| > 1$, $p < 0.05$, and a false discovery rate (FDR) < 0.1. Genes overlapping between published gene sets and enriched genes in microglia of CMVMJD135 mice when compared with WT littermates were found by contingency analysis using the Fisher's exact test and the Baptista–Pike method to calculate the odds ratio. Significance was set at $p < 0.05$.

The TAC software and the ingenuity pathway analysis (IPA) (Qiagen Inc., Venlo, Netherlands) were used for pathways analysis. Pathways were considered significantly altered if $p < 0.05$ and a significance value > 1.3, calculated as $-log10$ of the p value.

The validation of RNA-sequencing data was performed through quantitative RT-PCR using the same RNA used for RNA-sequencing. cDNA synthesis and quantitative RT-PCR were performed as described above. The primers were designed using NCBI Primer-BLAST and are listed in Table S3 in Supplementary Materials and Methods.

2.13. Statistical Analysis and Graphs

All statistical analyses were performed using the SPSS 22.0 (IBM, Armonk, NY, USA), with the GraphPad Prism 8.00 software (GraphPad Software, San Diego, CA, USA) being used to create the graphs. Regarding descriptive statistics, the mean was the considered measure of central tendency, while the extent of variability was the standard error of the mean (SEM). The normality assumption was assessed by frequency distributions (z-score of skewness and kurtosis) as well as by the Kolmogorov–Smirnov and Shapiro–Wilk tests. Levene's test evaluated the assumption of homogeneity of variances. Most data were analyzed using the two-tailed unpaired Student's *t*-test for comparisons between the two groups. For comparisons of more than two groups, the one-way analysis of variance (ANOVA) was used, followed by Tukey HSD or Dunnett T3's test. Comparisons by contingency analysis used Fisher's exact test and the Baptista–Pike method to calculate the odds ratio. The critical value for significance was set as $p < 0.05$ throughout the study.

3. Results

3.1. Evidence of a Non-Senescent Microglial Profile in the CMVMJD135 Mouse Model of Machado–Joseph Disease

Growing evidence suggests that microglia change their features with age, switching to a senescent/dystrophic profile, increasingly involved in the occurrence or aggravation, of neurodegenerative diseases [4,11,41,42]. Aging-related processes are also thought to explain the mid-life emergence of symptoms in MJD, in spite of mutant gene expression in most cell types since early development. Therefore, aging-related microglial changes could be contributing to disease onset and/or progression. To understand if microglia from CMVMJD135 mice change their features with age and switch to a senescent/dystrophic phenotype with disease progression, we evaluated protein levels of senescence markers by flow cytometry in microglia isolated from the cerebellum, brainstem, and spinal cord of these transgenic mice at 48 weeks of age (which corresponds to an advanced disease stage, Figure 1a).

Our results showed a decrease in the expression of a senescence indicator, $P19^{Arf}$ ($p = 0.004549$), and in the expression of senescence-associated pro-inflammatory cytokines Il-1 alpha ($p = 0.000416$) and Il-1 beta ($p = 0.008074$) in microglia isolated from CMVMJD135

Biomedicines **2022**, *10*, 237

mice compared with that of WT mice (Figure 1b). No significant differences were found in the expression of $P21^{Cip1/Waf1}$, Il-6, and Il-8 between WT and CMVMJD135 mice (Figure 1b).

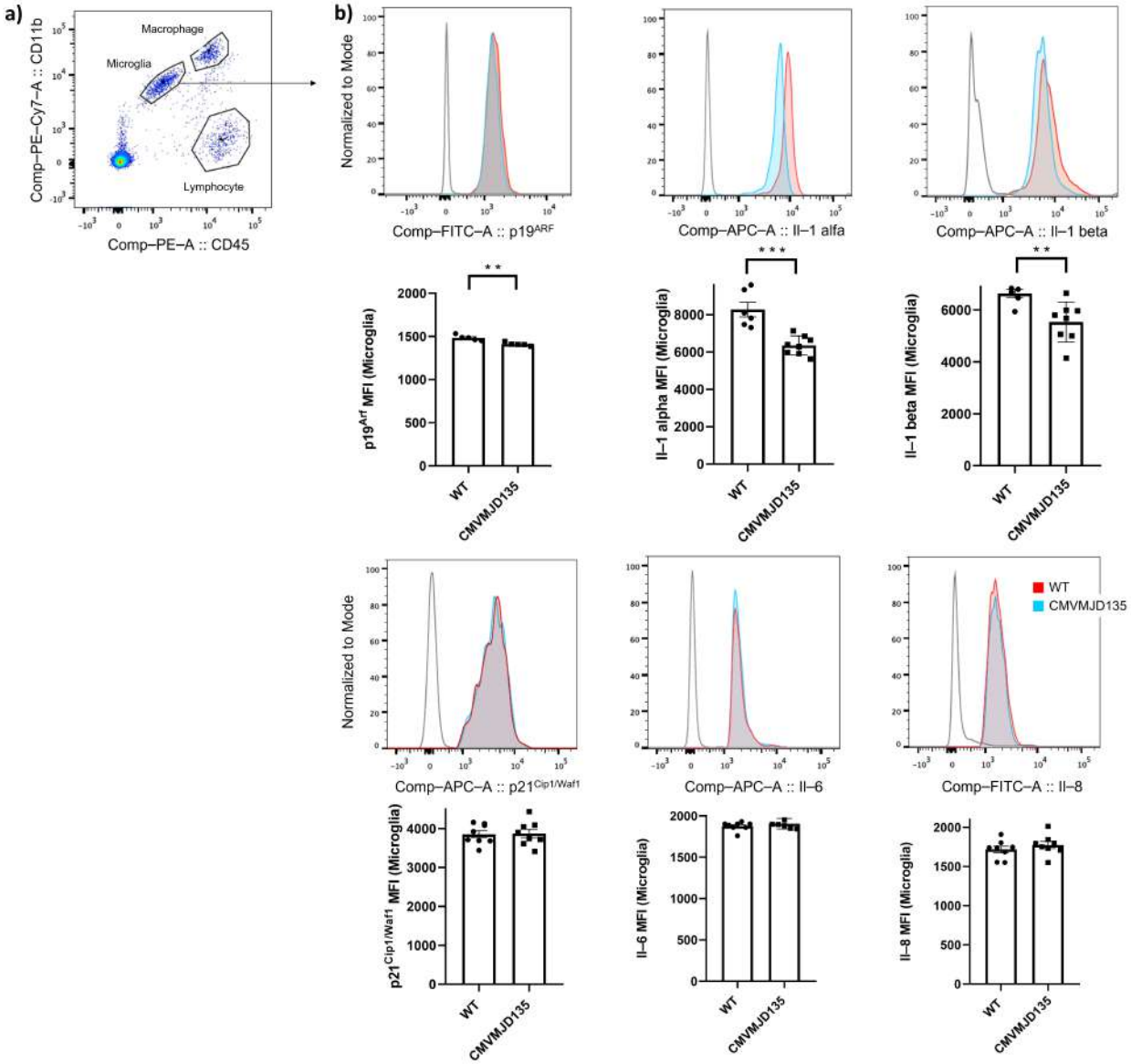

Figure 1. Expression of senescence markers is decreased in microglia of affected central nervous system (CNS) regions of CMVMJD135 mice. (**a**) Gating strategy used to analyze the flow cytometry data. Microglia, macrophage, and lymphocyte populations were gated using $CD11b^{+}CD45^{mid}$, $CD11b^{+}CD45^{high}$, and $CD11b^{low}CD45^{low}$, respectively; (**b**) Flow cytometry showing expression of $P19^{Arf}$, Il-1 alpha, Il-1 beta, $P21^{Cip1/Waf1}$, Il-6, and Il-8 in microglia (gated using $CD11b^{+}CD45^{mid}$) from wild-type (WT) and CMVMJD135 mice (n = 5–8 per group). MFI = mean fluorescent intensity. Data are presented as mean + SEM (Student's t-test). **, ***, represent $p < 0.01$ and $p < 0.001$, respectively.

To understand if a senescent profile was present in the brain of the CMVMJD135 animals, we also evaluated the mRNA expression levels of several senescence markers, including *P16*^{Ink4a}, *P19*^{Arf}, *P21*$^{Cip1/Waf1}$, *Pai1*, *Il-6*, *Il-1 beta*, *Icam-1* (senescence-related intercellular adhesion molecule 1) [43], and *Hmgb1* (high mobility group box 1) [44], in whole tissue obtained from different affected regions of the CNS. In line with the results obtained by flow cytometry, we found a decrease in the expression of *P19*^{Arf} ($p = 0.004019$) in the cerebellum, a decrease in the expression of *Il-6* ($p = 0.031390$) and *Pai1* ($p = 0.044628$)

in the brainstem, and a decrease in the expression of *Icam-1* ($p = 0.015626$) in the spinal cord (Figure 2). However, CMVMJD135 mice displayed similar expression of $P16^{Ink4a}$, $P21^{Cip1/Waf1}$, *Il-1 beta*, and *Hmgb1* in the cerebellum, brainstem, and spinal cord, compared to WT mice (Figure 2). These findings indicate that microglia do not adopt a senescent-like profile in the MJD mice.

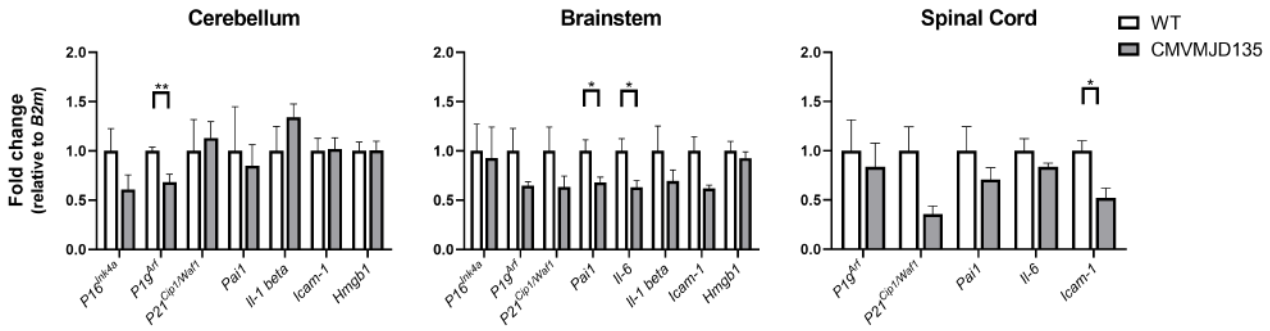

Figure 2. No evidence for a senescence gene expression profile in affected CNS regions of CMVMJD135 mice. The expression levels of senescence markers were analyzed in the cerebellum, brainstem, and spinal cord of 48 weeks-old WT and CMVMJD135 mice. $n = 4$–5 per group and two technical replicates were performed. Fold change ($2^{-\Delta\Delta CT}$) is represented using *B2m* as a housekeeping gene. Data are presented as mean + SEM (Student's *t*-test). *, **, represent $p < 0.05$ and $p < 0.01$, respectively.

To complement our in vivo analysis, we used an experimental process, described in [11], to mimic the aging of a microglia-enriched culture (Figure S1 in Supplementary Results) and characterized the cultured cells at 4 and 16 DIV by assessing phagocytic activity and morphological changes in basal conditions or when exposed to LPS. After confirming the purity of the microglia-enriched culture obtained over time, as described in previous studies [11,45,46] (Figure S1 in Supplementary Results), and to confirm the relevance of studying cell autonomous processes in microglia in this transgenic model, we evaluated the expression levels of mutant human *ATXN3* in these cells. As expected, the expression of mutant *ATXN3* was detected in microglia from CMVMJD135 mice but not in WT mice (Figure S2 in Supplementary Results). Curiously, at 16 DIV, corresponding to the artificially "aged" microglia, no differences were found in microglia from neonatal CMVMJD135 mice upon LPS treatment (when compared to untreated cells) for all analyzed parameters (Figure S3f–i in Supplementary Results). This suggests that, with age, microglia expressing mutant *ATXN3* might show less activation in response to LPS, which could be interpreted as being indicative of senescent microglia, as dysfunctional microglia are less responsive to stimulation with age [47,48]. However, this is in contrast with our observations in the same system concerning phagocytic efficiency at 16 DIV because, like those of WT, CMVMJD135-derived microglia showed a higher phagocytic efficiency in the presence of LPS, a response that was maintained with age (Figure S4 in Supplementary Results). In addition, when analyzing the morphological changes and phagocytic efficiency among microglia derived from WT or CMVMJD135 mice, no significant differences were noted at any time point. Altogether, our in vitro results suggest that early in life, CMVMJD135-derived microglia are mostly similar to WT microglia, and that these cells do not become precociously senescent upon repeated passaging.

3.2. Numerical and Morphological Changes Are Observed in Microglia from CMVMJD135 Mice in a Brain Region-Dependent Manner

To better characterize the profile of microglia from CMVMJD135 mice, the next step was to evaluate the microglia density and morphology (Iba-1-positive cells), and to analyze their morphological features in the affected brain regions of CMVMJD135 mice, namely in the DCN, (cerebellum), the PN (brainstem), and in the cervical spinal cord (CSC), at

Biomedicines **2022**, *10*, 237

an age when the motor phenotype of this animal model is fully established. A significant reduction in the number of microglia was found in the PN ($p = 0.020384$) of CMVMJD135 mice compared with WT mice (Figure 3a,d). No differences were found in the DCN nor the CSC (Figures 3b,e and 3c,f, respectively).

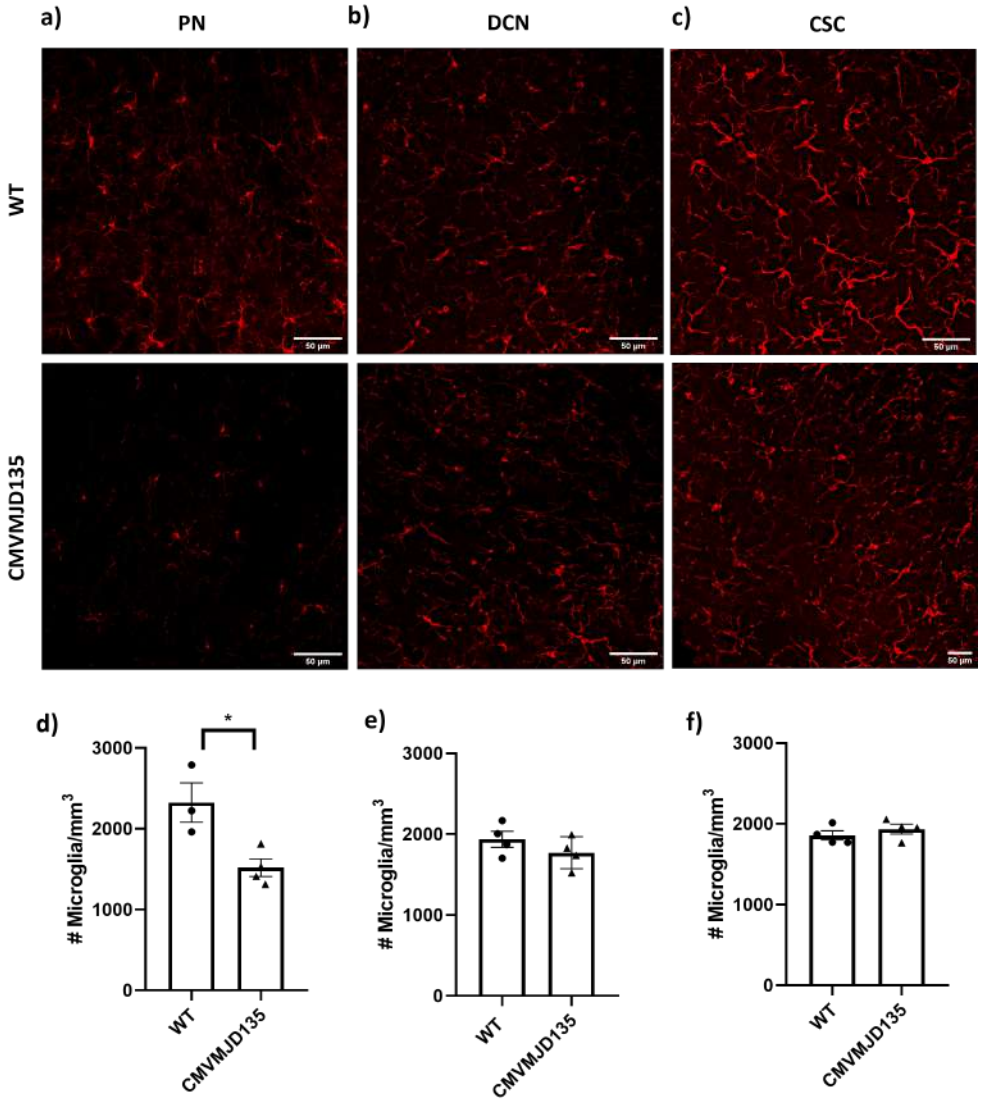

Figure 3. Reduction of the number of microglia in the pontine nuclei (PN) of CMVMJD135 mice. Representative images of microglial cells, using Iba-1 as a microglial marker (in red), in the (**a**) PN, (**b**) deep cerebellar nuclei (DCN), and (**c**) cervical spinal cord (CSC) of 34 weeks-old CMVMJD135 and WT mice. (**d**–**f**) Quantitative analysis of the number of Iba-1-positive cells in the PN, DCN, and CSC of WT and CMVMJD135 mice ($n = 4$–5 per group), using ImageJ software. Data are presented as mean + SEM (Student's *t*-test). *, represent $p < 0.05$. Scale bar: 50 µm.

Immunostaining of the microglial marker Iba-1 was used to evaluate whether morphological alterations occur in microglia from the PN, DCN, and CSC of CMVMJD135 mice. A skeleton analysis was used to assess changes in features relevant to microglia ramification, whereas fractal analysis was used to evaluate characteristics associated with cell surface, soma thickness, cell size, the cylindrical shape of cells, the complexity of their ramifications, and the heterogeneity of their shape. The skeleton and fractal analyses showed no differences between the groups, neither in the PN nor the DCN (Figures S5–S8 in Supplementary Results).

Biomedicines **2022**, *10*, 237

Interestingly, the skeleton data showed significant differences in microglia from CMV-MJD135 mice in the CSC compared with WT mice. The number of slab voxels ($p = 0.012917$), the maximum branch length ($p = 0.031432$), the total branch length ($p = 0.016352$), and the Euclidean distance ($p = 0.020316$) were lower in microglia from CMVMJD135 mice (Figure 4).

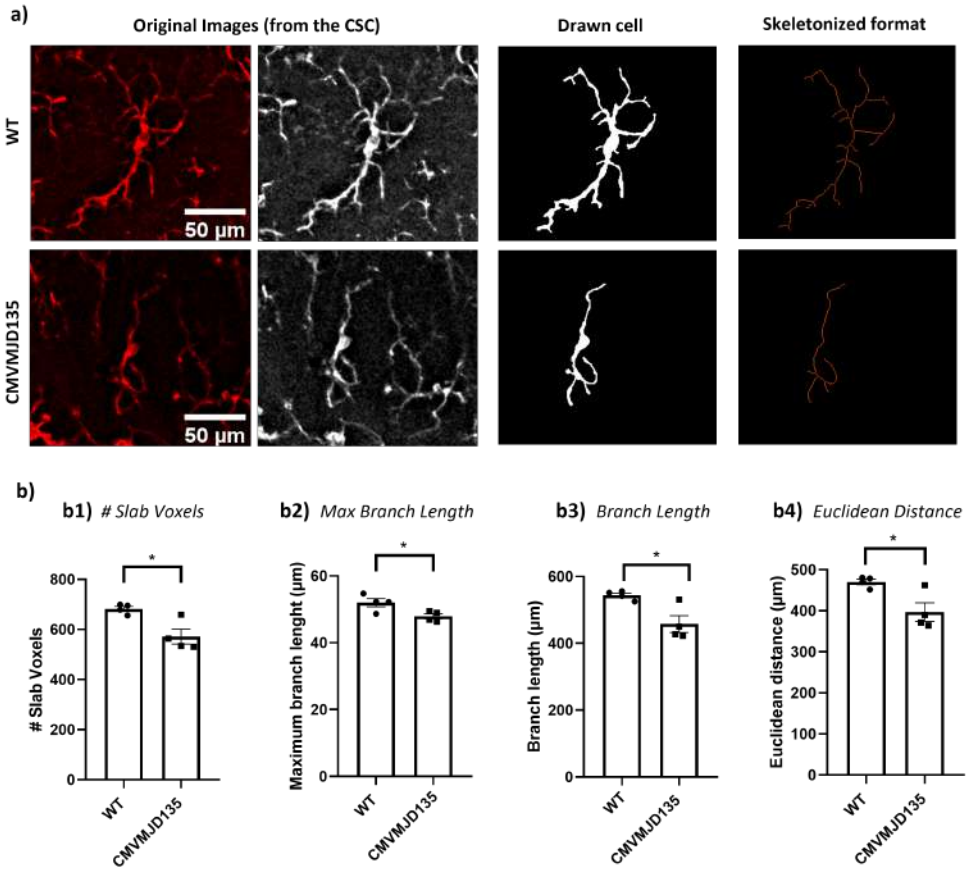

Figure 4. Microglia in the CSC of CMVMJD135 mice show less morphological complexity. (**a**) Representation of the process to prepare the images for skeleton analysis of microglia morphology. These images show differences regarding the number of slab voxels, the maximum branch length, the branch length, and the Euclidean distance. (**b**) Quantification of the morphometric features associated with microglia ramification, including: (**b1**) # slab voxels; (**b2**) maximum branch length; (**b3**) branch length; and (**b4**) Euclidean distance. Data of all these features were obtained from 310 microglial cells from WT mice ($n = 4$) and 389 microglial cells from 34-week-old CMVMJD135 mice ($n = 4$) of the CSC. Data are presented as mean + SEM (Student's *t*-test). *, represent $p < 0.05$. Scale bar: 50 µm.

On the other hand, the number of branches, the number of junction voxels, the number of endpoint voxels, the average branch length, and the triple and quadruple points were similar between groups (Figure S9 in Supplementary Results). Additionally, alterations in several features associated with the heterogeneity of the shape, cell size, cell surface, and soma thickness were observed in CMVMJD135 mice. In fact, the lacunarity ($p = 0.017934$), the convex hull area ($p = 0.003983$), the convex hull perimeter ($p = 0.001963$), the diameter of the bounding circle ($p = 0.000753$), the mean radius ($p = 0.001132$), the maximum span across the convex hull ($p = 0.000757$), the cell area ($p = 0.021343$), and the cell perimeter ($p = 0.011744$) were found to be decreased in microglia from CMVMJD135 mice, whereas density ($p = 0.000798$) and cell circularity ($p = 0.014008$) were increased in this group (Figure 5).

Biomedicines **2022**, *10*, 237

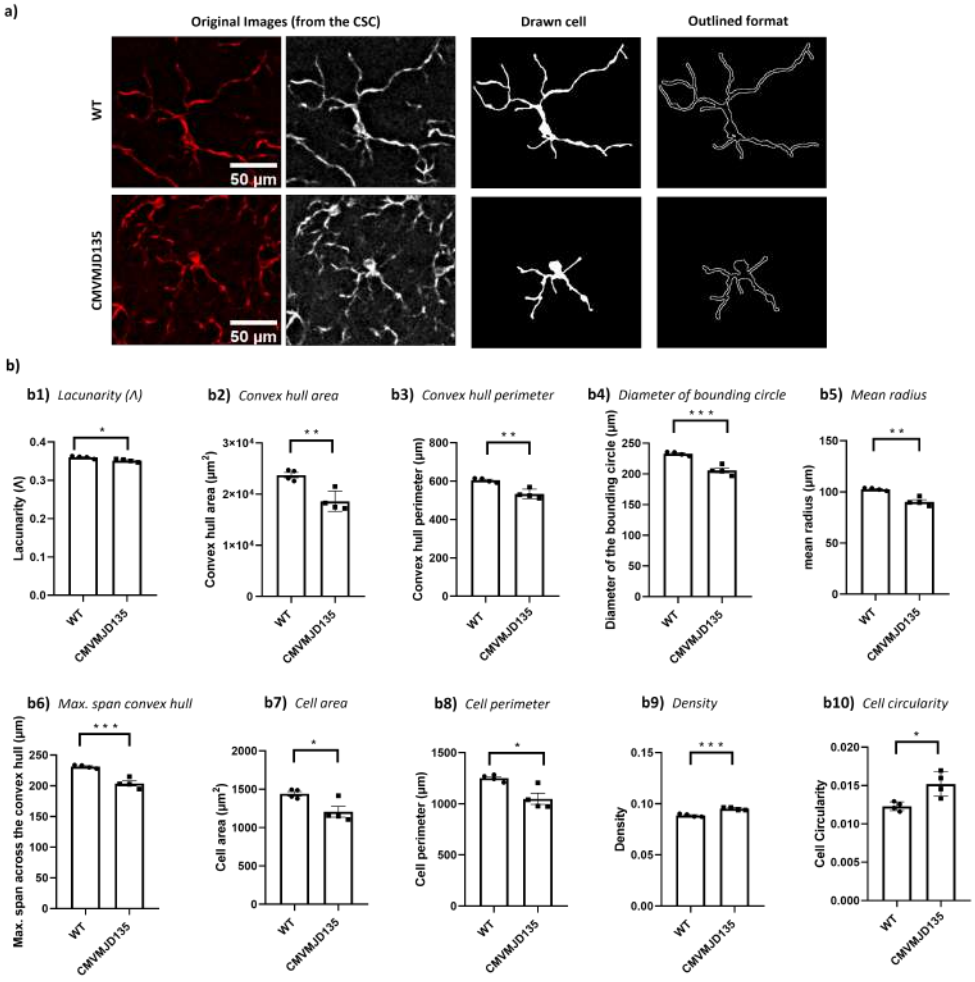

Figure 5. Microglia in the CSC of CMVMJD135 mice showed distinct activation-associated morphological features. (**a**) Representation of the process to prepare the images for fractal analysis of microglia morphology. These images show differences regarding the convex hull area, the mean radius, and the maximum span across the convex hull in microglia from CMVMJD135 mice. (**b**) Quantification of the morphometric features associated with heterogeneity of the shape: (**b1**) lacunarity. Associated with cell's size: (**b2**) convex hull area, (**b3**) convex hull perimeter, (**b4**) diameter of the bounding circle, (**b5**) the mean radius, (**b6**) the maximum span across the convex hull, and (**b7**) the cell area. Associated with cell's surface: (**b8**) cell perimeter. Associated with soma thickness: (**b9**) density and (**b10**) cell circularity. Data of all these features were obtained from 310 microglial cells from WT mice ($n = 4$) and 389 microglial cells from 34-week-old CMVMJD135 mice ($n = 4$) of the CSC. Data are presented as mean + SEM (Student's *t*-test). *, **, ***, represent $p < 0.05$, $p < 0.01$ and $p < 0.001$, respectively. Scale bar: 50 µm.

Regarding the features associated with the complexity of ramifications and with the cylindrical shape of the cells, no differences were observed between groups (Figure S10 in Supplementary Results). These observations suggest that microglia in the CSC of CMVMJD135 mice are more activated when compared with WT mice since these microglia have fewer and shorter branches, with smaller size and higher soma thickness.

3.3. Euclidean Distance, Convex Hull Area, Mean Radius, and Maximum Span across the Convex Hull Are the Features That Best Characterize Spinal Cord Microglia of MJD Mice

Since our initial analysis revealed changes in microglia in the spinal cord, a region that is affected since early stages in MJD patients and in the CMVMJD135 mouse model, PCA and machine learning models were implemented to further characterize the morphological changes between CMVMJD135- and WT-derived microglia, allowing the identification of

potential clusters of cells based on their morphological features and pinpointing those features that assume higher importance. A morphological analysis of microglia from the CSC of CMVMJD135 and WT mice was performed by measuring a total of 25 different features related to microglia ramification, complexity, and cell shape. Regarding microglial ramification features, four were statistically different in microglia from CMVMJD135 mice (Figure 4). On the other hand, from the 15 features associated with complexity and cell shape, 10 were found to be significantly different between the groups (Figure 5). Considering the number of significantly altered features, a PCA was performed to reduce this dimensionality. A 3D space was computed based on three principal components, the PCA being able to preserve 99.1% of all information present in the 14 significant features (PC0 = 91.7%, PC1 = 5.8%, and PC2 = 1.6%; Figure 6a). A scatter plot was designed, plotting each animal as a point in a 3D space on the principal components plane. Figure 6a depicts a clear separation between CMVMJD135 and WT animals, based on the three principal components that are grounded on the statistically different features. The exception was one CMVMJD135 mouse, which was closer to the WT group. To better visualize the relationships between multiple significant features found to be altered between both groups, two more 3D scatter plots were conceived. Figure 6b,c shows a clear distinction between the two groups based on cell ramification and cell size features, respectively. Both plots show a clear distinction between CMVMJD135 and WT animals based on the morphological features of their microglia.

With the PCA showing promising prospects, an unsupervised machine learning model, the k-means, was used to identify clusters of data with similar characteristics. The used dataset comprised 310 microglial cells from the CSC of WT mice and 389 from the CSC of CMVMJD135 ones. Using all 14 statistically significant features, the elbow method, as depicted in Figure 6d, identified the largest drop in the error for $k = 2$, i.e., identified two clusters in the dataset, which is in accordance with the expectations since these data originated from two groups (CMVMJD135 and WT). Once the ideal number of clusters was found, these clusters were plotted in a 4D space, with color as the fourth dimension. One cluster, in green, groups more ramified cells, with longer branches, larger area and perimeter, and lower circularity and density. This cluster is mainly composed of microglia from WT mice. Conversely, the second cluster, in red, is primarily composed of CMVMJD135 microglia, which have fewer and shorter branches, smaller size, and higher soma thickness, characteristics typically found in activated microglia (Figure 6e,f).

To complement this analysis, gradient boosted trees were conceived, optimized, and evaluated, the goal being to use a machine learning model that is able to distinguish microglia from CMVMJD135 and WT mice, in the CSC. Four independent trials were run, using nested k-fold cross-validation (5 outer and 5 inner folds). While the input data are all the significant features, the label was set as the parameter identifying WT and CMVMJD135 cells, this being a binary classification problem. The candidate models were tuned regarding the number of estimators, learning rate, tree's max depth, and fraction of columns to be sub-sampled, being evaluated by its accuracy, precision, and recall. The best candidate model attained an accuracy of approximately 70% using one-fifth of the total number of columns per estimator, 100 estimators, a tree's max depth of 2, and a learning rate of 0.1. Since gradient boosted trees provide the ability to obtain estimates of feature importance, Figure 6g depicts the importance attained by each feature. While the machine learning model allocates lower importance to features such as the cell's lacunarity and circularity, and the number of slab voxels, features such as the Euclidean distance, convex hull area, mean radius, and maximum span across the convex hull have increased importance when identifying microglia based on their morphological features. This further reinforces the significance of these morphological features to characterize spinal cord microglia of MJD mice, denoting the impact of the disease in these morphological characteristics.

Biomedicines **2022**, *10*, 237

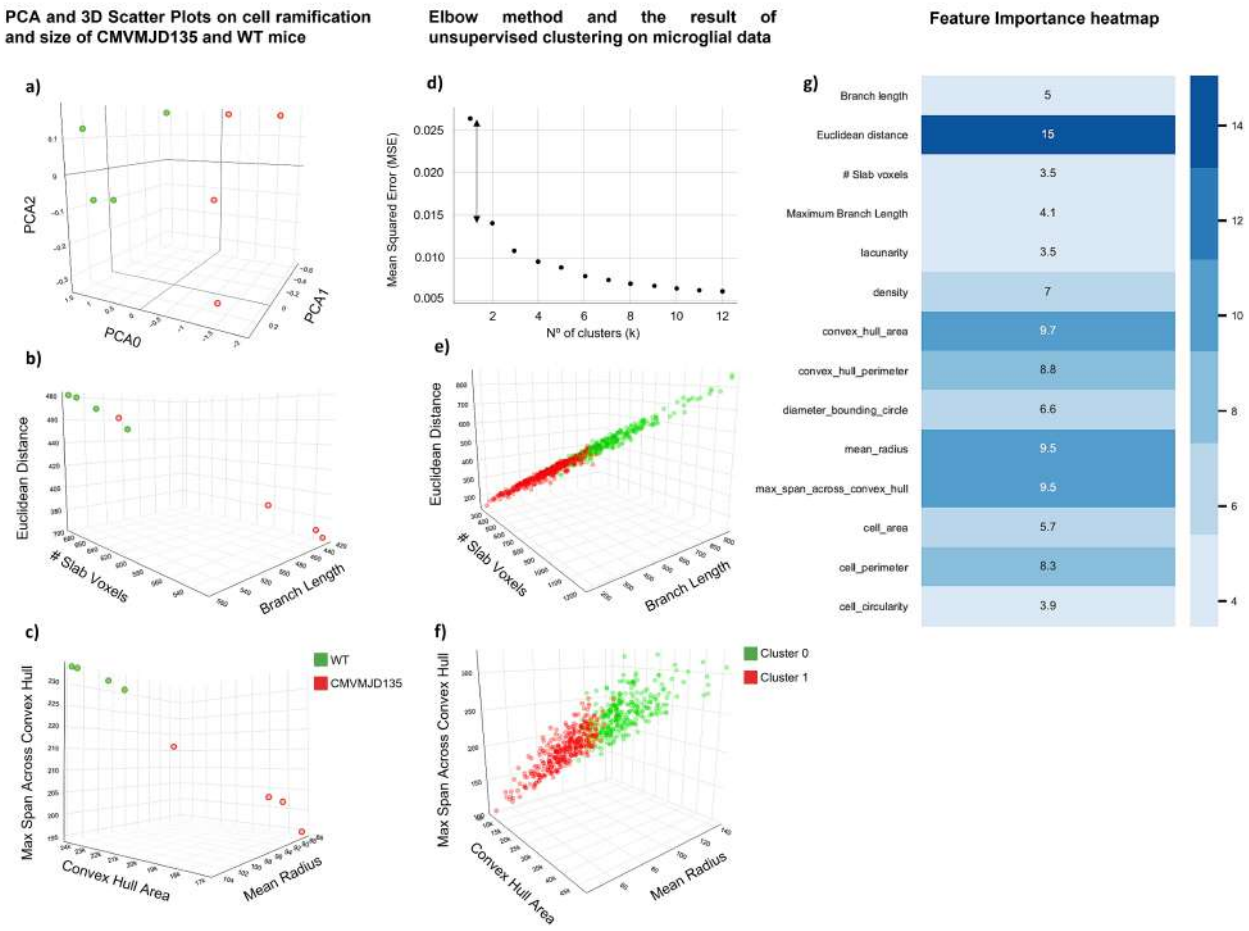

Figure 6. A clear separation of microglia in the CSC of CMVMJD135 and WT mice regarding features associated with cell ramification and cell size. (**a**) A 3D scatter plot showing the distribution of CMVMJD135 mice (in red) and WT animals (in green) on a principal components plane. (**b**) A 3D scatter plot showing a clear separation between CMVMJD135 and WT mice regarding the number of slab voxels, branch length, and Euclidean distance; and (**c**) a 3D scatter plot showing a clear separation between CMVMJD135 and WT mice regarding their convex hull area, mean radius, and maximum span across the convex hull. (**d**) Graphical result of the elbow method applied on the dataset comprised of 310 cells from WT mice and 389 from CMVMJD135 ones. (**e**,**f**) Data points of a total of 310 microglial cells from WT mice and 389 microglial cells from CMVMJD135 mice were plotted as a function of the significant features, belonging to one of two clusters: cluster 0, in green, or cluster 1, in red. (**e**) A 3D scatter plot showing the relationship between the number of slab voxels, branch length, and Euclidean distance; and (**f**) a 3D scatter plot showing the relationship between the convex hull area, mean radius, and maximum span across the convex hull of all microglia. (**g**) Feature importance heatmap for each parameter used to classify microglia from CMVMJD135 and WT mice. The higher the color tone, the higher the importance of the parameter.

3.4. Transcriptomic Profiling of Microglia in the Pathogenesis of MJD

To further explore the molecular profile of MJD-associated microglia, RNA-sequencing analysis was performed on microglia isolated from WT and CMVMJD135 animals at 34 weeks of age. The analysis of the transcriptomic data confirmed that specific markers for microglia were expressed at high levels. In contrast, other cell-type markers were expressed at shallow levels, indicating that the microglial samples from CMVMJD135 and WT mice presented high purity (Figure S11a–d in Supplementary Results), even though

Biomedicines **2022**, *10*, 237

a residual expression of some oligodendrocyte-specific genes was found (Figure S11e in Supplementary Results).

The PCA and hierarchical clustering heatmap confirmed that CMVMJD135 and WT mice showed distinct transcriptional profiles (Figure 7a,b), revealing a non-overlapping clustering of samples in each group, with the exception of one sample from the WT group, the PCA being able to preserve 68.8% of all information (PC1 = 41.2%, PC2 = 16.2%, and PC3 = 11.4%). This WT outlier, which overlapped with samples of CMVMJD135 mice instead of WT (Figure 7a), was discarded from the analysis to remove overlapping clusters, thus improving the amount of information captured by the PCA, which rose to 73.7% (PC1 = 44.8%, PC2 = 16.9%, and PC3 = 12.0%). Figure 7b depicts the non-overlapping clusters of samples in each group, indicating a distinct profile among genotypes.

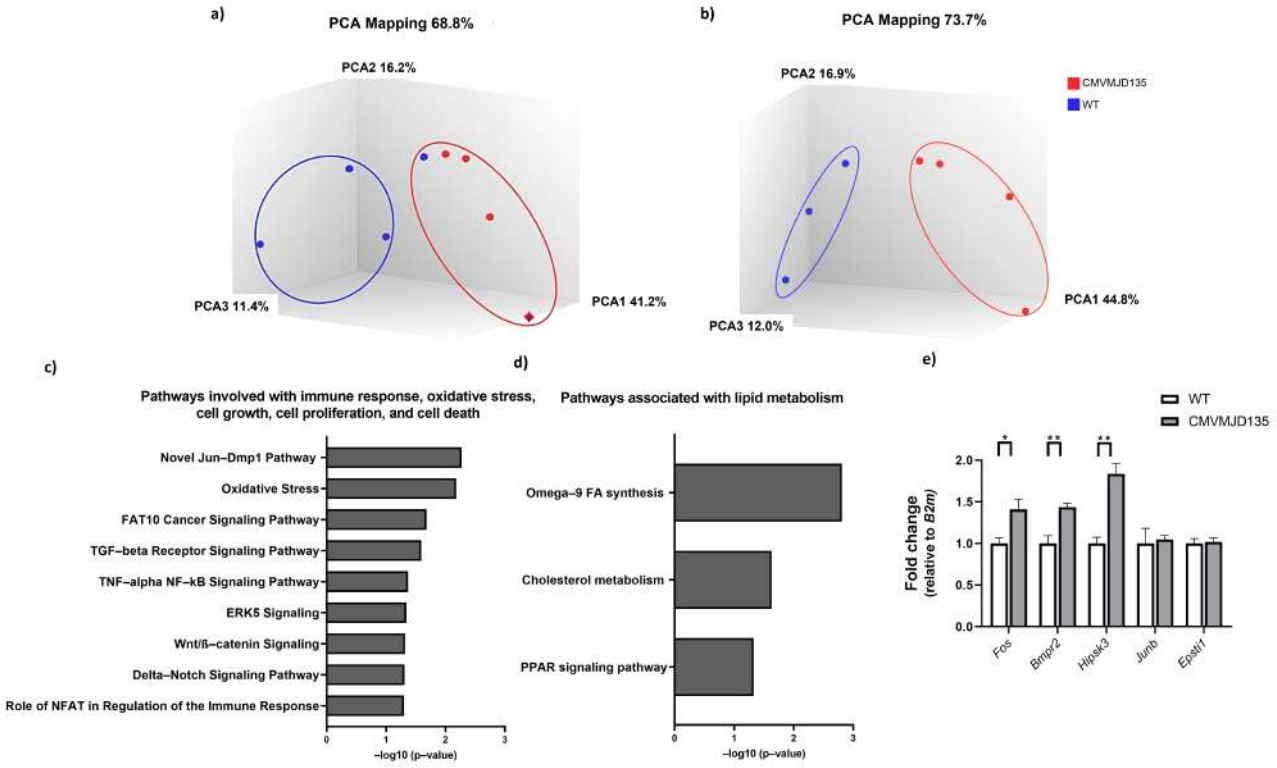

Figure 7. Up-regulated differentially expressed genes (DEGs) found in CMVMJD135-derived microglia are associated with immune response, oxidative stress, cell growth, cell proliferation, cell death, and lipid metabolism pathways. Before the analysis of the DEGs, and of the molecular pathways altered, a principal components analysis (PCA) was conceived to evaluate if CMVMJD135 and WT mice showed distinct profiles. (**a**) The PCA sets one WT sample within the vicinity of the CMVMJD135 cluster. WT cluster presents a sparser configuration. (**b**) PCA shows a clear expression separation between CMVMJD135 and WT without sample WT1. WT cluster presents a denser configuration. Three biological replicates for WT mice and four biological replicates for CMVMJD135 mice. Pathways significantly altered were found in microglia from CMVMJD135 mice compared with WT mice. (**c**) Pathways associated with immune response, oxidative stress, cell growth, cell proliferation, and cell death. (**d**) Pathways associated with lipid metabolism. All pathways are presented in descending order of significance. (**e**) Expression analysis performed on the selected genes confirmed the results obtained from RNA-sequencing analysis of microglia. An increase in the expression of *Fos*, *Bmpr2*, and *Hipsk3* was found in microglia from CMVMJD135 mice. $n = 3$–4 per group, and two technical replicates were performed. Fold change ($2^{-\Delta\Delta CT}$) is represented using *B2m* as a housekeeping gene. Data are presented as mean + SEM (Student's *t*-test). *, **, represent $p < 0.05$ and $p < 0.01$, respectively.

The TAC software then determined the number of DEGs in microglia from CMVMJD135 mice. In total, 101 DEGs were identified: 83 up-regulated and 18 down-regulated genes. The complete list of DEGs is provided in Figure S12 in Supplementary Results.

3.5. Transcriptional Changes Seen in CMVMJD135 Microglia Overlap Those in Amyotrophic Lateral Sclerosis and Alzheimer Disease Mouse Models

Next, we compared the list of transcripts found to be differentially expressed in CMVMJD135 mice with 40 different datasets of previously reported DEGs, which include, among others, data on the microglial signature program [49,50] on other neurodegenerative disorders [51–62], aging [38,51,63], disease-associated microglia (DAM) [64], and injury-related microglia [38,51]. We found a significant overlap with only 3 of the 40 published gene sets, namely with the DEGs seen in microglia of a mouse model of amyotrophic lateral sclerosis (ALS), the $SOD1^{G93A}$ mouse model [52]; of a mouse model of Alzheimer disease (AD), the $App^{NL\text{-}G\text{-}F/NL\text{-}G\text{-}F}$ mouse model [52]; and with a list of microglial genes highly expressed and/or affected in different neuroinflammatory conditions [65] (Figure S13 in Supplementary Results and Supplementary Data 2).

The $SOD1^{G93A}$ mouse model of ALS shared 27 deregulated genes with CMVMJD135 mice. Of these 27 overlapping genes, 17 displayed a similarly altered gene expression profile: *Lamc1*, *Hipk3*, *Lrrc58*, *Bmpr2*, *Nav1*, *St8sia4*, *Cpd*, *Fmnl2*, *Atp6v0a1*, *Klhl24*, *Cnot1*, *Tmem106b*, *Xpr1*, and *Rnh1* are up-regulated in both $SOD1^{G93A}$ and CMVMJD135 mice; and *Bend6*, *Ups11*, and *Tbkbp1* are down-regulated in both models. However, *Ncam1*, *Arhgef15*, *Abcb1a*, *Alpl*, *Foxf2*, *Caskin2*, *Fbxl12*, *Gpld1*, and *Csad* genes were found to be up-regulated in CMVMJD135 mice but down-regulated in $SOD1^{G93A}$ mice. In contrast, the *Plin2* gene was found to be down-regulated in CMVMJD135 mice but up-regulated in $SOD1^{G93A}$ mice (Figure S13 in Supplementary Results and Supplementary Data 2).

Most of the genes (19 out of 31) that showed an overlap with the $App^{NL\text{-}G\text{-}F/NL\text{-}G\text{-}F}$ mouse model of AD were discordant regarding their altered gene expression profile. In fact, while that in CMVMJD135 mice the *Cux2*, *Ncam1*, *Arhgef12*, *Mkl2*, *Arhgef15*, *Abcb1a*, *Tyro3*, *Alpl*, *Foxf2*, *Sox8*, *Ahnak*, *Caskin2*, *Scd2*, *Atp2b4*, *Sh2d5*, *Gpld1*, and *Syt3* genes were found to be up-regulated and the *Fbxw4* and *Plin2* genes were down-regulated, in $App^{NL\text{-}G\text{-}F/NL\text{-}G\text{-}F}$ mice, the same genes were found to be down-regulated and up-regulated, respectively. Regarding the remaining overlapping genes, some were found to be up-regulated in both $App^{NL\text{-}G\text{-}F/NL\text{-}G\text{-}F}$ and CMVMJD135 mice (*Gm6548*, *Rnf144b*, *Epsti1*, *St8sia4*, *Cpd*, *Fos*, *Junb*, *Acsl4*, and *Klhl24*), while others were found to be down-regulated in both models (*Bend6*, *Phlpp1*, and *Rbfox1*). We also found a positive association of two CMVMJD135-altered genes with the cluster of microglial genes highly expressed in neuroinflammatory conditions. In particular, *Mefc2* and *Fos*, two of the up-regulated genes found in CMVMJD135-derived microglia, were implicated in neuroinflammation conditions [65] (Figure S13 in Supplementary Results and Supplementary Data 2).

Overall, these results suggest a path of disease with higher similarity to that of ALS, a motor neuron disease, than with that of AD and other more "neuroinflammatory diseases".

3.6. Up-Regulated DEGs Found in CMVMJD135-Derived Microglia Are Associated with Immune Response, Oxidative Stress, Cell Growth, Cell Proliferation, Cell Death, and Lipid Metabolism Pathways

An analysis of the involvement of the DEGs found in CMVMJD135-derived microglia in different biological pathways was performed. This analysis revealed eight DEGs associated with cellular processes, such as immune response, oxidative stress, cell growth, cell proliferation, and cell death. The pathways found to be significantly altered in microglia from CMVMJD135 mice when compared with WT mice were as follows: oxidative stress (*Junb* and *Fos* (also known as *c-Fos*)); TGF-β receptor signaling pathway (*Fos*, *Junb*, and *Mef2c*); TNF-α NF-kβ signaling pathway (*Gsk3β*, *Usp11*, and *Alpl*); role of NFAT in regulation of the immune response (*Fos*, *Gsk3β*, and *Mef2c*); the novel Jun-Dmp1 pathway (*Junb* and *Fos*); FAT10 cancer signaling pathway (*Bmpr2* and *Gsk3β*); ERK5 signaling (*Fos* and *Mef2c*); Wnt/β-catenin signaling (*Bmpr2*, *Gsk3β*, and *Sox8*); and delta-notch signaling path-

way (*Gsk3β* and *Mef2c*). All the indicated genes showed increased expression in microglia from CMVMJD135 mice, except for *Usp11*, which showed decreased expression (Figure 7c).

Interestingly, the altered gene expression also suggested changes in the microglial lipid metabolism. These include the Omega-9 FA synthesis pathway, cholesterol metabolism (consists of both Bloch and Kandutsch–Russell pathways), and PPAR signaling pathway. The *Acsl4* and *Scd2* DEGs were found to be involved in these lipid metabolism pathways (Figure 7d). It was also found that the expression of genes related to oxidative stress, particularly the synthesis of nitric oxide (NO), was increased in CMVMJD135 mice, as seen by the up-regulation of *Gsk3β*, *Junb*, *Cpd*, *Igfbp3*, and *Ntn1*.

The RNA-sequencing results were further validated through qPCR. Five DEGs—*Fos*, *Junb*, *Bmpr2*, *Hipsk3*, and *Epsti1*—were validated with acceptable cycle threshold (CT) values. While no statistically significant differences were found in the expression of *Junb* and *Epsti1*, the results were similar to those obtained by RNA-sequencing, with an increase in the expression of *Fos* ($p = 0.019$), *Bmpr2* ($p = 0.006$), and *Hipsk3* ($p = 0.003$) in microglia from CMVMJD135 mice (Figure 7e).

4. Discussion

The contribution of microglia to several neurodegenerative diseases is well recognized, and these cells play a pivotal role in their pathogenesis, often with different contributions at different disease stages and in distinct brain regions [10,13,66]. Microglial subpopulations called DAM have been defined for several neurodegenerative diseases, chronic neuroinflammatory states, and aging [52,64,67]. Yet, little is known about the profile of microglia and their involvement in MJD. In this study, we characterized the profile of microglia in a mouse model of MJD, with a particular focus on the brainstem, cerebellum, and spinal cord, three of the CNS areas most affected in this polyglutamine disease [21,22].

Because MJD pathophysiology appears gradually and progresses over time [21,22], and microglia were described to become senescent/dystrophic in other neurological disorders, including AD, Parkinson's disease (PD), multiple sclerosis (MS), Huntington's disease (HD), and ALS [4,11,41,42,68,69], we first set out to investigate if microglia from CMVMJD135 mice displayed an accelerated senescence profile. For this, the typical signs of cellular senescence were further evaluated in brain microglia from CMVMJD135 mice.

The senescence phenotype is associated with an increased expression of specific proteins, considered senescence indicators, including some cell cycle regulators and senescence-associated pro-inflammatory cytokines [15]. Through these, the so-called senescence-associated secretory phenotype (SASP) may generate an inflammatory environment and induce senescence in neighbor cells, which may exert a deleterious effect and promote neuron degeneration [68]. Contrary to what is described in the literature for other neurodegenerative disorders [4,15,67,68], our observations showed a decrease in the protein levels of a senescence indicator, $P19^{Arf}$ and of senescence-associated pro-inflammatory cytokines Il-1 alpha and Il-1 beta in microglia from CMVMJD135 mice when compared to those of WT animals. This was consistent with the results of our analysis of senescence-related genes in whole tissue from three affected regions of MJD mice, in which we found a decrease in the expression of $P19^{Arf}$ in the cerebellum, of *Il-6* and *Pai1* in the brainstem, and of *Icam-1* in the spinal cord. Overall, our data do not support a significant contribution of cell senescence processes (in microglia or other cell types) to MJD, even at late stages.

The characterization of morphological changes of microglia from CMVMJD135 mice was also performed in affected CNS regions at a late disease stage. Since dystrophic cells can display some of the features typically associated with activation, mostly deramification and shortening of the processes, it is difficult to distinguish, with certainty, "activated" from "dystrophic" microglia [70]. However, other abnormal morphological features, such as gnarled, beaded, unusually tortuous, or fragmented cytoplasmic processes, are usual signs of senescent microglia [4,42,71,72]. These allow us to distinguish between an "activated state", which is characterized by ramified cells with a larger cell body and shorter, thick processes, and a "reactive state", typically characterized by smaller, spherical cells,

which can also display amoeboid-like morphologies [6,7]. These microglial states, which display inflammatory and phagocytic features, are most often observed in pathological situations [7]. However, in some neurological conditions, and depending on the stage of the pathological process, microglia can play both a toxic or a protective role. Hence, the extent of microglial activation and, thereby, their contribution to the pathogenesis may depend on the type and duration of injury [6,11,45,67,73,74] and on the CNS region under study [67]. A better comprehension of MJD-associated microglia based on the characterization of their morphological profile may help to unravel the relevance of these cells in MJD pathogenesis.

Of the three analyzed regions, only microglia from the spinal cord (one of the earliest affected CNS regions in this mouse model) showed significant differences in features associated with ramification, heterogeneity of the shape, cell size, cell surface, and soma thickness. Indeed, microglia from CMVMJD135 mice showed a decreased number of slab voxels, a decrease in the maximum branch length and branch length, and lower Euclidean distance, which is an indicator of the cell's tortuosity [75]. Thus, these microglia are less ramified, with shorter processes, and less tortuous when compared with microglia from WT mice. In addition, we found an increased density and circularity of microglia from CMVMJD135 mice. As described in [9], circularity determines the cell's roundness, which is increased in amoeboid-like cells. On the other hand, an increased density occurs during the morphological shift from a ramified to an amoeboid shape upon neuroinflammatory insults, a phenotype seen upon exposure to stress [8]. Features associated with cell size, such as convex hull area, convex hull perimeter, diameter of the bounding circle, the convex hull area, the mean radius, the maximum span across the convex hull, and the cell area, were lower in microglia from CMVMJD135 mice. Previous studies show that decreased values of such features are associated with amoeboid-like shapes [6,7,9]. Finally, the lacunarity, which refers to the degree of inhomogeneity, was found to be decreased in microglia from CMVMJD135 mice, implying that these cells have a more homogeneous outline when compared with cells from WT mice [9]. These results were complemented with the PCA and machine learning models outcome, which depicted a clear structure on the morphological data, with two clusters being identified. While one is mainly composed of WT-derived microglia (more ramified cells, with longer branches, larger area and perimeter, and lower circularity and density), the other mainly groups CMVMJD135-derived microglia (with fewer and shorter branches, smaller size, and higher soma thickness). The supervised machine learning model, which was tuned to identify the cells' genotype based on their morphological features, allowed us to further identify those that best characterize spinal cord microglia of MJD mice (Euclidean distance, convex hull area, mean radius, and maximum span across the convex hull), these being the features that are most affected by this disease. Overall, these observations are particularly relevant and may indicate that microglia in the spinal cord of CMVMJD135 mice are more activated than WT-derived microglia. Even though the morphological changes point to an increased activation state of microglia, and other studies show microgliosis in MJD patients [23–25] and MJD mice [26], further mechanistic studies are required to understand whether these microglial cells actively contribute to MJD onset and/or progression.

The RNA-sequencing analysis on microglia isolated from the cerebellum and brainstem (as a whole), of WT and CMVMJD135 animals, identified significantly altered genes and molecular pathways in CMVMJD135 mice. From the 101 DEGs found in CMVMJD135-derived microglia, 8 (*Junb*, *Fos*, *Bmpr2*, *Gsk3β*, *Mef2c*, *Usp11*, *Alpl*, and *Sox8*) were found to be overlapping several significantly altered pathways related to the immune response, oxidative stress, cell growth, cell proliferation, and cell death. Other cellular pathways were also changed, namely, some associated with lipid metabolism.

In a mouse model of ALS, the microglial transcriptional factor *c-Fos* was significantly down-regulated. This alteration is associated with restoring the abnormal microglial phenotype and attenuation of the disease [76]. While some studies show that *c-Fos* suppresses the expression of pro-inflammatory phenotype-associated genes, such as inducible NO synthase (*iNOS*) [77], tumor necrosis factor-alpha (*Tnfα*), and *Il-6* through the suppression

of NF-kβ activity [78], suggesting that it acts as an anti-inflammatory transcription factor essential for microglia survival [76,78], other studies show that the blockade of c-Fos with dexmedetomidine halts microglia inflammation and inhibits postoperative cognitive dysfunction in AD patients, thus setting c-Fos as a potential anti-inflammatory therapeutic target for NDs [79]. Regarding the Gsk3β, its activation is associated with increased neuroinflammation and microglial activation. Some studies have demonstrated that Gsk3β promotes microglial responses to inflammation, and that the use of Gsk3β inhibitors, such as lithium, SB216763, kenpaullone, and indirubin-3'-monoxime, provides a means to limit the inflammatory actions of microglia and provides protection from inflammation-induced neuronal toxicity [80]. Another study reinforces Gsk3β-mediated neuroinflammation, partially by enhancing nuclear factor kappa b subunit 1 (Nfkb1) signaling, where the inhibition of Gsk3β with the SB216763 inhibitor reduces Nfkb1 signaling and inflammation levels, in a mouse model of Rett syndrome [81]. The expression of the *BMPR2* gene by microglia is scarcely referred to in the literature. Still, it is increased in active multiple sclerosis lesions, suggesting a possible role for this gene in MS pathogenesis [82]. Regarding the *Alpl* gene encoding the Alkaline phosphatase, tissue-nonspecific isozyme protein, known to have a role in brain development and function [83], it was demonstrated that its activity is increased in both brain and plasma of AD patients, inducing neuronal toxicity via tau dephosphorylation [84,85]. On the other hand, the transcription factor *Mef2c* was reported to be expressed in both mouse and human microglia and is known to be involved in microglial specification [86,87]. Moreover, decreased function of Mef2c is associated with a possible microglial activation that is sufficient to induce autism-like symptoms in mice [88]. Additionally, *Mef2c* normally restrains the microglial inflammatory response, and its expression is lost in aged brains in a type I interferon (IFN-I)-dependent manner [89]. These facts demonstrate that the activity of Mef2c becomes critical under pathological conditions and with aging, when the levels of inflammatory cytokines are increased. The *Usp11* gene, on the other hand, was demonstrated to regulate microglial activation and neuroinflammation in intracerebral hemorrhage (ICH). Thus, silencing *Usp11* was put forward as a novel anti-inflammatory method for ICH treatment since it blocks the release of pro-inflammatory cytokines by microglia, leading to protection from neurological impairment [90]. Hence, the decreased expression of *Usp11* in the brain of MJD mice could indicate a similar adaptive and protective response.

The role of lipid metabolism in the polarization of microglial inflammatory status was recently explored and may inspire novel approaches that modulate metabolism to ameliorate neuroinflammatory and NDs [91–94]. In fact, regarding the specific MJD DEGs here identified and known to be involved in the lipid metabolism, *Acsl4* was found to be a novel regulator of neuroinflammation in ischemic stroke, and the knockdown of *Acsl4* expression was proposed to provide a potential therapeutic target through the inhibition of pro-inflammatory cytokine production in microglia [95]. Meanwhile, the *Scd2* gene was found to be down-regulated upon activation of microglia induced by LPS [96].

The expression of genes related to the synthesis of nitric oxide (NO) was found to be increased in microglia from CMVMJD135 mice, namely of *Gsk3β*, *Junb*, *Cpd*, *Igfbp3*, and *Ntn1*. This pathway is known to be implicated in the pathogenesis of NDs, in which elevated NO provokes either neuroinflammation or apoptosis in microglia [97]. As mentioned above, Gsk3β and Junb are associated with increased neuroinflammation and microglial activation [80,81,98]. However, an increase in *Igfbp3* expression was seen in an ischemic injury mouse model to lead to increased microglial apoptosis and to a reduction of activated microglia. These findings imply that *Igfbp3* can act as an anti-inflammatory factor [99]. In addition, Ntn1 was put forward as a novel therapeutic agent to ameliorate early brain injury via its anti-inflammation effect, by suppression of microglia activation, peroxisome proliferator-activated receptor (PPARγ) activation, inhibition of factor nuclear kappa β (NF-kβ), and decrease in Tnfα, Il-6, and Icam-1 [100].

Interestingly, we also found multiple deregulated genes that are common in both CMVMJD135-derived microglia and microglia of the neurodegenerative mouse models of

ALS and AD. However, while some of them displayed a similarly altered gene expression profile, others were discordant. To the best of our knowledge, apart from nine genes (*Atp6v0a1*, *Tmem106b*, *Bmpr2*, *Ups11*, *Fos*, *Junb*, *Acsl4*, *Tyro3*, and *Scd2*), the overlapping of the remaining 49 genes with datasets of DEGs from neurodegenerative mouse models of ALS and AD, is here reported for the first time. Only three remain to be described from the nine genes identified above (*Atp6v0a1*, *Tmem106b*, and *Tyro3*). Regarding the *Atp6v0a1* gene, it was found that the attenuation of the human microglial inflammation and suppression of the expression *IL-1 beta* and *IL-6* by the increase in *ATP6V0A1* expression with rifampicin improved the lysosomal function, which may be a novel therapeutic strategy for PD [101]. The *TMEM106B* gene was found to be involved in the pathological processes of AD, whose expression is reduced in AD brains [102]. On the other hand, it was demonstrated that the TAM (Tyro3, Axl, Mer) family of receptor tyrosine kinases limit inflammatory responses upon Toll-like receptors stimulation in microglia, with a positive impact on AD progression [103]. Another study reported that the loss of TAM receptors affects adult brain neurogenesis, which was attributed to exaggerated inflammatory responses by microglia characterized by increased mitogen-activated protein kinases (MAPK) and NF-kβ activation, as well as to an increased production of pro-inflammatory cytokines [104].

As described above, we found genes (such as the *Fos*, *Junb*, *Gsk3β*, *Acsl4*, and *Bmpr2*) that, when up-regulated, promote pro-inflammatory microglial responses. The use of inhibitors of these genes and the proteins they encode may provide a means to offer protection from inflammation-induced neuronal toxicity, i.e., these genes could be potential targets to counteract MJD. However, we also found genes (such as the *Mefc2*, *Scd2*, *Igfbp3*, *Ntn1*, *Usp11*, *Atp6v0a1*, and *Tyro3*) that promote the inhibition of inflammation in microglia through the inhibition of pro-inflammatory cytokine production, which could correspond to an endogenous neuroprotective response and explain the decrease in expression of genes encoding pro-inflammatory cytokines, such as *Il-6*, *Il-1 alpha*, *Il-1 beta*, and *Icam-1* in CMVMJD135 mice. Overall, the profile of MJD microglia is mixed regarding pro- and anti-inflammatory molecule expression, and the overlapping results suggest a higher similarity of MJD with ALS than AD, which is not unexpected, given the shared involvement of motor systems in these two disorders. Furthermore, since microgliosis was observed in MJD patients' post-mortem brains [23–25], it would be interesting to explore, in future studies, whether the genes and pathways identified in the CMVMJD135 mouse model of MJD are also altered in the brains of MJD patients, at the mRNA or protein level.

To the best of our knowledge, this is the first study to characterize the functional and morphological features of microglia in an in vivo model of MJD and to provide new insights into the transcriptomic profile of these cells in the context of this disorder. While no evidence for senescence of microglia or other brain cells was found in the CMVMJD135 mouse model, our findings revealed morphological alterations in microglia from the spinal cord of these mice, which point to an increased activation state of these cells when compared with those of WT animals. In addition, the conceived supervised machine learning model revealed key morphological features that are most affected by the disease, with the possibility of using such features to distinguish between CMVMJD135- and WT-derived microglia. Finally, the results obtained from the transcriptomic analysis provided the identification of molecular pathways that may constitute potential targets to counteract this disease, and suggest that, among others, the lipid metabolism should be further investigated in these cells.

Supplementary Materials: The following supporting information can be downloaded at: https://www.mdpi.com/article/10.3390/biomedicines10020237/s1: Supplementary Data 1—lists of cell-type-specific genes. Supplementary Data 2—Genes overlapping between published gene sets and enriched genes in CMVMJD135 and wild-type (WT)-derived microglia. Supplementary Materials and Methods—Table S1. Organization of the experimental groups to evaluate microglia phagocytic ability and morphology in culture; Table S2. List of primary and secondary antibodies used in flow cytometry and immunofluorescence; Table S3. List of primers used in reverse-transcription quantitative real-time PCR; Figure S1. The process to prepare binary (black and white) images for fractal and skeleton analysis; Figure S2. The *MorphData* and *AnalyzeSkeleton 2D/3D* plugins applied

to the skeletonized images; Figure S3. The outline images were processed using the *MorphData* and *FracLac* plugins. Supplementary Results—Figure S1. Confirmation of the high purity of microglia in culture; Figure S2. Expression of mutant *ATXN3* in microglia from CMVMJD135 mice at two different time points in culture; Figure S3. Microglia expressing *ATXN3* showed a less activated phenotype in response to lipopolysaccharides (LPS) in artificially "aged" primary cultures; Figure S4. CMVMJD135 and Wild-Type (WT)-derived microglia showed an increased phagocytic efficiency in the presence of LPS in culture; Figure S5. The ramification state of microglia in the pontine nuclei (PN) of the CMVMJD135 mice is similar to those of microglia from WT mice; Figure S6. The complexity and shape of microglia in the PN of CMVMJD135 mice are similar to those of microglia from WT mice; Figure S7. Microglia in the deep cerebellar nuclei (DCN) of CMVMJD135 mice showed no differences in features relevant to microglia ramification; Figure S8. Microglia in the DCN of CMVMJD135 mice showed no changes in the complexity and shape; Figure S9. Some parameters associated with microglia ramification were similar between CMVMJD135 and WT mice in the cervical spinal cord (CSC); Figure S10. No changes were observed in the parameters related to the complexity of ramifications and with the cylindrical shape of the cells between groups in the CSC; Figure S11. Evaluation of microglial enrichment in RNA-sequencing samples; Figure S12. Differential gene expression between microglia from CMVMJD135 and WT mice; Figure S13. Transcriptional changes seen in CMVMJD135 microglia overlap those in amyotrophic lateral sclerosis (ALS) and Alzheimer's disease (AD) mouse models.

Author Contributions: A.B.C.: conceptualization; methodology; software; formal analysis; investigation; data curation; writing—original draft; writing—review and editing; visualization. S.D.-S.: conceptualization; formal analysis; writing—review and editing; supervision; project administration. B.F.: software; validation; formal analysis; writing—review and editing. S.P.d.N.: methodology; validation. F.M.: methodology; validation. A.T.-C.: methodology; resources. A.N.-C.: investigation. D.M.-F.: investigation. C.C.P.: methodology; validation; formal analysis; investigation; writing—review and editing. R.S.: methodology; validation; formal analysis; investigation; writing—review and editing. T.S.: validation; resources; writing—review and editing. A.F.A.: conceptualization; validation; resources; writing—review and editing; supervision; project administration; funding acquisition. J.B.R.: conceptualization; validation; resources; writing—review and editing. P.M.: conceptualization; validation; resources; writing—review and editing; supervision; project administration; funding acquisition. All authors have read and agreed to the published version of the manuscript.

Funding: This work was supported by Fundação para a Ciência e a Tecnologia (FCT) (PTDC/NEU-NMC/3648/2014) and COMPETE-FEDER (POCI-01-0145-FEDER-016818). It was also supported by Portuguese funds through FCT in the framework of the Project POCI-01-0145-FEDER-031987 (PTDC/MED-OUT/31987/2017). A.B.C. was supported by a doctoral fellowship from FCT (PD/BD/127828/2016). S.P.N. was also supported by FCT (PD/BD/114120/2015). Work in the JBR laboratory was financed by FEDER—Fundo Europeu de Desenvolvimento Regional funds through the COMPETE 2020—Operational Programme for Competitiveness and Internationalization (POCI), Portugal 2020, and by Portuguese funds through FCT in the framework of the Project POCI-01-0145- FEDER-030647 (PTDC/MED-NEU/31318/2017). This work was funded by ICVS Scientific Microscopy Platform, member of the national infrastructure PPBI (Portuguese Platform of Bioimaging) (PPBI-POCI-01-0145-FEDER-022122), and by National funds, through FCT—project UIDB/50026/2020 and UIDP/50026/2020. C.C.P. and R.S. hold employment contracts financed by national funds through FCT and IP, in the context of the program contract described in paragraphs 4, 5, and 6 of art. 23 of Law no. 57/2016, of 29 August, as amended by Law no. 57/2017 of 19 July.

Institutional Review Board Statement: The animal experimentation and reporting were designed and conducted in adherence to the ARRIVE 2.0 guidelines (Animal Research: Reporting In Vivo Experiments). Animal facilities and the people directly involved in animal experiments are certified by the Portuguese regulatory entity—Direcção Geral de Alimentação e Veterinária (DGAV, license number 020317). All the performed protocols were approved by the Animal Ethics Committee of the Life and Health Sciences Research Institute, University of Minho (SECVS 120/2014).

Informed Consent Statement: Not applicable.

Data Availability Statement: The data presented in this study are available on request from the corresponding author.

Acknowledgments: We thank Dora Brites and Adelaide Fernandes for the relevant insights and helpful advice. We also acknowledge the support and assistance of Mafalda Rocha (Genomics platform) of the i3S.

Conflicts of Interest: The authors declare no conflict of interest.

References

1. He, Y.; Yao, X.; Taylor, N.; Bai, Y.; Lovenberg, T.; Bhattacharya, A. RNA sequencing analysis reveals quiescent microglia isolation methods from postnatal mouse brains and limitations of BV2 cells. *J. Neuroinflamm.* **2018**, *15*, 153. [CrossRef]
2. Schafer, D.P.; Stevens, B. Microglia Function in Central Nervous System Development and Plasticity. *Cold Spring Harb. Perspect. Biololy* **2015**, *7*, a020545. [CrossRef] [PubMed]
3. Chew, G.; Petretto, E. Transcriptional Networks of Microglia in Alzheimer's Disease and Insights into Pathogenesis. *Genes* **2019**, *10*, 798. [CrossRef] [PubMed]
4. Angelova, D.M.; Brown, D.R. Microglia and the aging brain: Are senescent microglia the key to neurodegeneration? *J. Neurochem.* **2019**, *151*, 676–688. [CrossRef] [PubMed]
5. Napoli, I.; Neumann, H. Microglial clearance function in health and disease. *Neuroscience* **2009**, *158*, 1030–1038. [CrossRef] [PubMed]
6. Fernandez-Arjona, M.D.M.; Grondona, J.M.; Fernandez-Llebrez, P.; Lopez-Avalos, M.D. Microglial Morphometric Parameters Correlate With the Expression Level of IL-1β, and Allow Identifying Different Activated Morphotypes. *Front. Cell. Neurosci.* **2019**, *13*, 472. [CrossRef]
7. Fernandez-Arjona, M.D.M.; Grondona, J.M.; Granados-Duran, P.; Fernandez-Llbrez, P.; Lopez-Avalos, M.D. Microglia morphological categorization in a rat model of neuroinflammation by hierarchical cluster and principal components analysis. *Front. Cell. Neurosci.* **2017**, *11*, 235. [CrossRef]
8. Bordeleau, M.; Lacabanne, C.; de Cossio, L.F.; Vernoux, N.; Savage, J.C.; Gonzales-Ibanez, F.; Tremblay, M.E. Microglial and peripheral immune priming is partially sexually dimorphic in adolescent mouse offspring exposed to maternal high-fat diet. *J. Neuroinflammation* **2020**, *17*, 264. [CrossRef]
9. Vargas-Caraveo, A.; Sayd, A.; Robledo-Montana, J.; Caso, J.R.; Madrigal, J.L.M.; Garcia-Bueno, B.; Leza, J.C. Toll-like receptor 4 agonist and antagonist lipopolysaccharides modify innate immune response in rat brain circumventricular organs. *J. Neuroinflammation* **2020**, *17*, 6. [CrossRef]
10. Bachiller, S.; Jimenez-Ferrer, I.; Paulus, A.; Yang, Y.; Swanberg, M.; Deierborg, T.; Boza-Serrano, A. Microglia in Neurological Diseases: A Road Map to Brain-Disease Dependent-Inflammatory Response. *Front. Cell. Neurosci.* **2018**, *12*, 488. [CrossRef]
11. Caldeira, C.; Oliveira, A.F.; Cunha, C.; Vaz, A.R.; Falcao, A.S.; Fernandes, A.; Brites, D. Microglia change from a reactive to an age-like phenotype with the time in culture. *Front. Cell. Neurosci.* **2014**, *8*, 152. [CrossRef] [PubMed]
12. Glass, C.K.; Saijo, K.; Winner, B.; Marchetto, M.C.; Gage, F.H. Mechanisms underlying inflammation in neurodegeneration. *Cell* **2010**, *140*, 918–934. [CrossRef] [PubMed]
13. Kwon, H.S.; Koh, S.H. Neuroinflammation in neurodegenerative disorders: The roles of microglia and astrocytes. *Transl. Neurodegener.* **2020**, *9*, 42. [CrossRef] [PubMed]
14. Chen, W.W.; Zhang, X.; Huang, W.J. Role of neuroinflammation in neurodegenerative diseases. *Mol. Med. Rep.* **2016**, *13*, 3391–3396. [CrossRef]
15. Bussian, T.J.; Aziz, A.; Meyer, C.F.; Swenson, B.L.; van Deursen, J.M.; Baker, D.J. Clearance of senescent glial cells prevents tau-dependent pathology and cognitive decline. *Nature* **2018**, *562*, 578–582. [CrossRef]
16. Li, W. Phagocyte dysfunction, tissue aging and degeneration. *Ageing Res. Rev.* **2013**, *12*, 1005–1012. [CrossRef]
17. Mosher, K.I.; Wyss-Coray, T. Microglial Dysfunction in Brain Aging and Alzheimer's Disease. *Biochem. Pharmacol.* **2014**, *88*, 594–604. [CrossRef]
18. Streit, W.J.; Xue, Q.S. Life and death of microglia. *J. Neuroimmune Pharmacol.* **2009**, *4*, 371–379. [CrossRef]
19. Kawaguchi, Y.; Okamoto, T.; Taniwaki, M.; Aizawa, M.; Inoue, M.; Katayama, S.; Kawakami, H.; Nakamura, S.; Nishimura, M.; Akiguchi, I. CAG expansions in a novel gene for Machado-Joseph disease at chromosome 14q32.1. *Nat. Genet.* **1994**, *8*, 221–228. [CrossRef]
20. Da Silva, J.D.; Teixeira-Castro, A.; Maciel, P. From pathogenesis to novel therapeutics for Spinocerebellar Ataxia type 3: Evading potholes on the way to translation. *Neurotherapeutics* **2019**, *16*, 1009–1031. [CrossRef]
21. Rub, U.; Brunt, E.R.; Deller, T. New insights into the pathoanatomy of spinocerebellar ataxia type 3 (Machado-Joseph disease). *Curr. Opin. Neurol.* **2008**, *21*, 111–116. [CrossRef] [PubMed]
22. Sequeiros, J.; Coutinho, P. Epidemiology and clinical aspects of Machado-Joseph disease. *Adv. Neurol.* **1993**, *61*, 139–153. [PubMed]
23. Evert, B.O.; Vogt, I.R.; Kindermann, C.; Ozimek, L.; de Vos, R.A.; Schmitt, I.; Klockgether, T.; Wullner, U. Inflammatory genes are upregulated in expanded ataxin-3-expressing cell lines and Spinocerebellar Ataxia type 3 brains. *J. Neurosci.* **2001**, *21*, 5389–5396. [CrossRef] [PubMed]

24. Duarte-Lobo, D.; Nobre, R.J.; Miranda, C.O.; Pereira, D.; Castelhano, J.; Sereno, J.; Koeppen, A.; Castelo-Branco, M.; de Almeida, L.P. The blood-brain barrier is disrupted in Machado-Joseph disease/spinocerebellar ataxia type 3: Evidence from transgenic mice and human post-mortem samples. *Acta Neuropathol. Commun.* **2020**, *8*, 152. [CrossRef] [PubMed]
25. McLoughlin, H.S.; Moore, L.R.; Paulson, H.L. Pathogenesis of SCA3 and implications for other polyglutamine diseases. *Neurobiol. Dis.* **2020**, *134*, 104635. [CrossRef] [PubMed]
26. Cunha-Santos, J.; Duarte-Neves, J.; Carmona, V.; Guarente, L.; de Almeida, L.P.; Cavadas, C. Caloric restriction blocks neuropathology and motor deficits in Machado–Joseph disease mouse models through SIRT1 pathway. *Nat. Commun.* **2016**, *7*, 11445. [CrossRef] [PubMed]
27. Silva-Fernandes, A.; Duarte-Silva, S.; Neves-Carvalho, A.; Amorim, M.; Soares-Cunha, C.; Oliveira, P.; Thirstrup, K.; Teixeira-Castro, A.; Maciel, P. Chronic treatment with 17-DMAG improves balance and coordination in a new mouse model of Machado-Joseph disease. *Neurotherapeutics* **2014**, *11*, 433–449. [CrossRef]
28. Silva-Fernandes, A.; Costa, M.C.; Duarte-Silva, S.; Oliveira, P.; Botelho, C.M.; Martins, L.; Mariz, J.A.; Ferreira, T.; Ribeiro, F.; Correia-Neves, M.; et al. Motor uncoordination and neuropathology in a transgenic mouse model of Machado–Joseph disease lacking intranuclear inclusions and ataxin-3 cleavage products. *Neurobiol. Dis.* **2010**, *40*, 163–176. [CrossRef]
29. Madeira, M.H.; Ortin-Martinez, A.; Nadal-Nicolas, F.; Ambrosio, A.F.; Vidal-Sanz, M.; Agudo-Barriuso, M.; Santiago, A.R. Caffeine administration prevents retinal neuroinflammation and loss of retinal ganglion cells in an animal model of glaucoma. *Sci. Rep.* **2016**, *6*, 27532. [CrossRef]
30. Fujita, H.; Tanaka, J.; Toku, K.; Tateishi, N.; Suzuki, Y.; Matsuda, S.; Sakanaka, M.; Maeda, N. Effects of GM-CSF and ordinary supplements on the ramification of microglia in culture: A morphometrical study. *Glia* **1996**, *18*, 269–281. [CrossRef]
31. Young, K.; Morrison, H. Quantifying Microglia Morphology from Photomicrographs of Immunohistochemistry Prepared Tissue Using ImageJ. *J. Vis. Exp.* **2018**, *136*, 57648. [CrossRef] [PubMed]
32. Campos, A.B.; Duarte-Silva, S.; Ambrósio, A.F.; Maciel, P.; Fernandes, B. MorphData: Automating the data extraction process of morphological features of microglial cells in ImageJ. *bioRxiv* **2021**. [CrossRef]
33. Fernandes, B.; Gonzalez-Briones, A.; Novais, P.; Calafate, M.; Analide, C.; Neves, J. An Adjective Selection Personality Assessment Method Using Gradient Boosting Machine Learning. *Processes* **2020**, *8*, 618. [CrossRef]
34. Holt, L.M.; Olsen, M.L. Novel Applications of Magnetic Cell Sorting to Analyze Cell-Type Specific Gene and Protein Expression in the Central Nervous System. *PLoS ONE* **2016**, *11*, e0150290. [CrossRef]
35. Li, W.; Turner, A.; Aggarwal, P.; Matter, A.; Storvick, E.; Arnett, D.K.; Broeckel, U. Comprehensive evaluation of AmpliSeq transcriptome, a novel targeted whole transcriptome RNA sequencing methodology for global gene expression analysis. *BMC Genom.* **2015**, *16*, 1069. [CrossRef]
36. Bennett, M.L.; Bennett, F.C.; Liddelow, S.A.; Ajami, B.; Zamaniam, J.L.; Fernhoff, N.B.; Mulinyawe, S.B.; Bohlen, C.J.; Adil, A.; Tucker, A.; et al. New tools for studying microglia in the mouse and human CNS. *Proc. Natl. Acad. Sci. USA* **2016**, *113*, 1738–1746. [CrossRef]
37. DePaula-Silva, A.B.; Gorbea, C.; Doty, D.J.; Libbey, J.E.; Sanchez, J.M.S.; Hanak, T.J.; Cazalla, D.; Fujinami, R.S. Differential transcriptional profiles identify microglial- and macrophage-specific gene markers expressed during virus-induced neuroinflammation. *J. Neuroinflammation* **2019**, *16*, 152. [CrossRef]
38. Hammond, T.R.; Dufort, C.; Dissing-Olesen, L.; Giera, S.; Young, A.; Wysoker, A.; Walker, A.J.; Gergits, F.; Segel, M.; Nemesh, J.; et al. Single-Cell RNA Sequencing of Microglia throughout the Mouse Lifespan and in the Injured Brain Reveals Complex Cell-State Changes. *Immunity* **2019**, *50*, 253–271. [CrossRef]
39. Itoh, N.; Itoh, Y.; Tassoni, A.; Ren, E.; Kaito, M.; Ohno, A.; Ao, Y.; Farkhondeh, V.; Johnsonbaugh, H.; Burda, J.; et al. Cell-specific and region-specific transcriptomics in the multiple sclerosis model: Focus on astrocytes. *Proc. Natl. Acad. Sci. USA* **2018**, *115*, 302–309. [CrossRef]
40. Pan, J.; Ma, N.; Yu, B.; Zhang, W.; Wan, J. Transcriptomic profiling of microglia and astrocytes throughout aging. *J. Neuroinflammation* **2020**, *17*, 97. [CrossRef]
41. Graeber, M.B.; Streit, W.J. Microglia: Biology and pathology. *Acta Neuropathol.* **2010**, *119*, 89–105. [CrossRef] [PubMed]
42. Streit, W.J.; Xue, Q.S. Alzheimer's Disease, Neuroprotection, and CNS Immunosenescence. *Front. Pharmacol.* **2012**, *3*, 138. [CrossRef] [PubMed]
43. Gorgoulis, V.G.; Pratsinis, H.; Zacharatos, P.; Demoliou, C.; Sigala, F.; Asimacopoulos, P.J.; Papavassiliou, A.G.; Kletsas, D. p53-dependent ICAM-1 overexpression in senescent human cells identified in atherosclerotic lesions. *Lab. Investig.* **2005**, *85*, 502–511. [CrossRef] [PubMed]
44. Lee, J.J.; Park, I.H.; Kwak, M.S.; Rhee, W.J.; Kim, S.H.; Shin, J.S. HMGB1 orchestrates STING-mediated senescence via TRIM30α modulation in cancer cells. *Cell Death Discov.* **2021**, *7*, 28. [CrossRef] [PubMed]
45. Socodato, R.; Portugal, C.C.; Canedo, T.; Rodrigues, A.; Almeida, T.O.; Henriques, J.F.; Vaz, S.H.; Magalhaes, J.; Silva, C.M.; Baptista, F.I.; et al. Microglia Dysfunction Caused by the Loss of Rhoa Disrupts Neuronal Physiology and Leads to Neurodegeneration. *Cell Rep.* **2020**, *31*, 107796. [CrossRef]
46. Saura, J.; Tusell, J.M.; Serratosa, J. High-yield isolation of murine microglia by mild trypsinization. *Glia* **2003**, *44*, 183–189. [CrossRef]
47. Nije, E.G.; Boelen, E.; Stassen, F.R.; Steinbusch, H.W.M.; Borchelt, D.R.; Streit, W.J. Ex vivo cultures of microglia from young and aged rodent brain reveal age-related changes in microglial function. *Neurobiol. Aging* **2012**, *33*, 195.e1–195.e12. [CrossRef]

48. Caldeira, C.; Cunha, C.; Vaz, A.R.; Falcao, A.S.; Barateiro, A.; Seixas, E.; Fernandes, A.; Brites, D. Key Aging-Associated Alterations in Primary Microglia Response to Beta-Amyloid Stimulation. *Front. Aging Neurosci.* **2017**, *9*, 277. [CrossRef]
49. Mendiola, A.S.; Rysu, J.K.; Bardehle, S.; Meyer-Franke, A.; Ang, K.K.H.; Wilson, C.; Baeten, K.M.; Hanspers, K.; Merlini, M.; Thomas, S.; et al. Transcriptional profiling and therapeutic targeting of oxidative stress in neuroinflammation. *Nat. Immunol.* **2020**, *21*, 513–524. [CrossRef]
50. Ayata, P.; Badimon, A.; Strasburger, H.J.; Duff, M.K.; Montgomery, S.E.; Loh, Y.H.E.; Ebert, A.; Pimenova, A.A.; Ramirez, B.R.; Chan, A.T.; et al. Epigenetic regulation of brain region-specific microglia clearance activity. *Nat. Neurosci.* **2018**, *21*, 1049–1060. [CrossRef]
51. Holtman, I.R.; Raj, D.D.; Miller, J.A.; Schaafsma, W.; Yin, Z.; Brouwer, N.; Wes, P.D.; Moller, T.; Orre, M.; Kamphuis, W.; et al. Induction of a common microglia gene expression signature by aging and neurodegenerative conditions: A co-expression meta-analysis. *Acta Neuropathol. Commun.* **2015**, *3*, 31. [CrossRef]
52. Sobue, A.; Komine, O.; Hara, Y.; Endo, F.; Mizoguchi, H.; Watanabe, S.; Murayama, S.; Saito, T.; Saido, T.C.; Sahara, N.; et al. Microglial gene signature reveals loss of homeostatic microglia associated with neurodegeneration of Alzheimer's disease. *Acta Neuropathol. Commun.* **2021**, *9*, 1. [CrossRef] [PubMed]
53. Srinivasan, K.; Friedman, B.A.; Etxeberria, A.; Huntley, M.A.; Brug, M.P.V.D.; Foreman, O.; Paw, J.S.; Modrusan, Z.; Beach, T.G.; Serrano, G.E.; et al. Alzheimer's Patient Microglia Exhibit Enhanced Aging and Unique Transcriptional Activation. *Cell Rep.* **2020**, *31*, 107843. [CrossRef] [PubMed]
54. Orre, M.; Kamphuis, W.; Osborn, L.M.; Jansen, A.H.P.; Kooijman, L.; Bossers, K.; Hol, E.M. Isolation of glia from Alzheimer's mice reveals inflammation and dysfunction. *Neurobiol. Aging* **2014**, *35*, 2746–2760. [CrossRef] [PubMed]
55. Wang, H.; Li, Y.; Ryder, J.W.; Hole, J.T.; Ebert, P.J.; Airey, D.C.; Qian, H.R.; Logsdon, B.; Fisher, A.; Ahmed, Z.; et al. Genome-wide RNAseq study of the molecular mechanisms underlying microglia activation in response to pathological tau perturbation in the rTg4510 tau transgenic animal model. *Mol. Neurodegener.* **2018**, *13*, 65. [CrossRef] [PubMed]
56. Chiu, I.M.; Morimoto, E.T.A.; Goodarzi, H.; Liao, J.T.; Keeffe, S.O.; Phatnani, H.P.; Muratet, M.; Carrol, M.C.; Levy, S.; Tavazoie, S.; et al. A neurodegeneration-specific gene-expression signature of acutely isolated microglia from an amyotrophic lateral sclerosis mouse model. *Cell Rep.* **2013**, *4*, 385–401. [CrossRef]
57. Noristani, H.N.; Sabourin, J.C.; Gerber, Y.N.; Teigell, M.; Sommacal, A.; Vivanco, M.D.; Weber, M.; Perrin, E. Brca1 is expressed in human microglia and is dysregulated in human and animal model of ALS. *Mol. Neurodegener.* **2015**, *10*, 385–401. [CrossRef]
58. Crapser, J.D.; Ochaba, J.; Soni, N.; Reidling, J.C.; Thompson, L.M.; Green, K.N. Microglial depletion prevents extracellular matrix changes and striatal volume reduction in a model of Huntington's disease. *Brain* **2020**, *143*, 266–288. [CrossRef]
59. Al-Dalahmah, O.; Sosunov, A.A.; Shaik, A.; Ofori, K.; Liu, Y.; Vonsattel, P.; Adorjan, I.; Menon, V.; Goldman, J.E. Single-nucleus RNA-seq identifies Huntington disease astrocyte states. *Acta Neuropathol. Commun.* **2020**, *8*, 19. [CrossRef]
60. Crotti, A.; Benner, C.; Kerman, B.E.; Gosselin, D.; Lagier-Tourenne, C.; Zuccato, C.; Cattaneo, E.; Gage, F.H.; Cleveland, D.W.; Glass, C.K. Mutant Huntingtin promotes autonomous microglia activation via myeloid lineage-determining factors. *Nat. Neurosci.* **2014**, *17*, 513–521. [CrossRef]
61. Lai, J.; Kim, J.; Jeffries, A.M.; Tolles, A.; Chittenden, T.W.; Buckley, P.G.; Yu, T.W.; Lodato, M.A.; Lee, E.A. Single-nucleus transcriptomic analyses reveal microglial activation underlying cerebellar degeneration in Ataxia Telangiectasia. *bioRxiv* **2021**. [CrossRef]
62. Zhong, J.; Tang, G.; Zhu, J.; Wu, W.; Li, G.; Lin, X.; Liang, L.; Chai, C.; Zeng, Y.; Wang, F.; et al. Single-cell brain atlas of Parkinson's disease mouse model. *J. Genet. Genom.* **2021**, *48*, 277–288. [CrossRef] [PubMed]
63. Galatro, T.F.; Holtman, I.R.; Lerario, A.M.; Vainchtein, I.D.; Brouwe, N.; Sola, P.R.; Veras, M.M.; Pereira, T.F.; Leite, R.E.P.; Moller, T.; et al. Transcriptomic analysis of purified human cortical microglia reveals age-associated changes. *Nat. Neurosci.* **2017**, *20*, 1162–1171. [CrossRef] [PubMed]
64. Keren-Shaul, H.; Spinrad, A.; Weiner, A.; Matcovitch-Natan, O.; Dvir-Szternfeld, R.; Ulland, T.K.; David, E.; Baruch, K.; Lara-Astaiso, D.; Toth, B.; et al. A Unique Microglia Type Associated with Restricting Development of Alzheimer's Disease. *Cell* **2017**, *169*, 1276–1290. [CrossRef] [PubMed]
65. Butovsky, O.; Jedrychowski, M.P.; Moore, C.S.; Cialic, R.; Lanser, A.J.; Gabriely, G.; Koeglsperger, T.; Dake, B.; Wu, P.M.; Doykan, C.E.; et al. Identification of a unique TGF-β-dependent molecular and functional signature in microglia. *Nat. Neurosci.* **2014**, *17*, 131–143. [CrossRef] [PubMed]
66. Hickman, S.; Izzy, S.; Sen, P.; Morsett, L.; Khoury, J.E. Microglia in neurodegeneration. *Nat. Neurosci.* **2018**, *21*, 1359–1369. [CrossRef] [PubMed]
67. Lecours, C.; Bordeleau, M.; Cantin, L.; Parent, M.; Paolo, T.D.; Tremblay, M.V. Microglial Implication in Parkinson's Disease: Loss of Beneficial Physiological Roles or Gain of Inflammatory Functions? *Front. Cell. Neurosci.* **2018**, *12*, 282. [CrossRef] [PubMed]
68. Si, Z.; Sun, L.; Wang, X. Evidence and perspectives of cell senescence in neurodegenerative diseases. *Biomed. Pharmacother.* **2021**, *137*, 111327. [CrossRef]
69. Martinez-Cue, C.; Rueda, N. Cellular Senescence in Neurodegenerative Diseases. *Front. Cell. Neurosci.* **2020**, *14*, 16. [CrossRef]
70. Streit, W.J. Microglial senescence: Does the brain's immune system have an expiration date? *Trends Neurosci.* **2006**, *29*, 506–510. [CrossRef]

71. Shahidehpour, R.K.; Higdon, R.E.; Crawford, N.G.; Neltner, J.H.; Ighodaro, E.T.; Patel, E.; Price, D.; Nelson, P.T.; Bachstetter, A.D. Dystrophic microglia are associated with neurodegenerative disease and not healthy aging in the human brain. *Neurobiol. Aging* **2021**, *99*, 19–27. [CrossRef] [PubMed]
72. Streit, W.J.; Sammons, N.W.; Kuhns, A.J.; Sparks, D.L. Dystrophic microglia in the aging human brain. *Glia* **2004**, *45*, 208–212. [CrossRef] [PubMed]
73. Qu, W.; Johnson, A.; Kim, J.H.; Lukowicz, A.; Svedberg, D.; Cvetanovic, M. Inhibition of colony-stimulating factor 1 receptor early in disease ameliorates motor deficits in SCA1 mice. *J. Neuroinflammation* **2017**, *14*, 107. [CrossRef]
74. Biber, K.; Block, M.L. Neuroprotection versus Neurotoxicity. In *Microglia in Health and Disease*; Tremblay, M., Sierra, A., Eds.; Springer: New York, NY, USA, 2014; pp. 145–172. [CrossRef]
75. Arganda-Carreras, I.; Fernandez-Gonzalez, R.; Munoz-Barrutia, A.; Ortiz-De-Solorzano, C. 3D reconstruction of histological sections: Application to mammary gland tissue. *Microsc. Res. Tech.* **2010**, *73*, 1019–1029. [CrossRef] [PubMed]
76. Butovsky, O.; Jedrychowski, M.P.; Cialic, R.; Krasemann, S.; Murugaiyan, G.; Fanek, Z.; Greco, D.J.; Wu, P.; Doykan, C.E.; Kiner, O.; et al. Targeting mir-155 restores abnormal microglia and attenuates disease in SOD1 mice. *Ann. Neurol.* **2015**, *77*, 75–99. [CrossRef] [PubMed]
77. Okada, S.; Obata, S.; Hatano, M.; Tokuhisa, T. Dominant-negative effect of the c-fos family gene products on inducible NO synthase expression in macrophages. *Int. Immunol.* **2003**, *15*, 1275–1282. [CrossRef]
78. Ray, N.; Kuwahara, M.; Takada, Y.; Maruyama, K.; Kawaguchi, T.; Tsubone, H.; Ishikawa, H.; Matsuo, K. c-Fos suppresses systemic inflammatory response to endotoxin. *Int. Immunol.* **2006**, *18*, 671–677. [CrossRef]
79. Li, H.; Zhang, X.; Chen, M.; Chen, J.; Gao, T.; Yao, S. Dexmedetomidine inhibits inflammation in microglia cells under stimulation of LPS and ATP by c-Fos/NLRP3/caspase-1 cascades. *EXCLI J.* **2018**, *17*, 302–311. [CrossRef]
80. Yuskaitis, C.J.; Jope, R.S. Glycogen synthase kinase-3 regulates microglial migration, inflammation, and inflammation-induced neurotoxicity. *Cell. Signal.* **2009**, *21*, 264–273. [CrossRef]
81. Jorge-Torres, O.C.; Szczesna, K.; Roa, L.; Casal, C.; Gonzalez-Somermeyer, L.; Soler, M.; Velasco, C.D.; Segundo, P.M.S.; Petazzi, P.; Saez, M.A.; et al. Inhibition of Gsk3b reduces Nfkb1 signaling and rescues synaptic activity to improve the Rett Syndrome phenotype in Mecp2-knockout mice. *Cell Rep.* **2018**, *23*, 1665–1677. [CrossRef]
82. Costa, C.; Eixarch, H.; Martinez-Saez, E.; Calvo-Barreiro, L.; Calucho, M.; Castro, Z.; Ortega-Aznar, A.; y Cajal, S.R.; Montalban, X.; Espejo, C. Expression of bone morphogenetic proteins in Multiple Sclerosis lesions. *Am. J. Pathol.* **2019**, *189*, 665–676. [CrossRef] [PubMed]
83. Fonta, C.; Barone, P.; Martinez, L.R.; Negyessy, L. Rediscovering TNAP in the Brain: A Major Role in Regulating the Function and Development of the Cerebral Cortex. *Sub-Cell. Biochem.* **2015**, *76*, 85–106. [CrossRef]
84. Kellett, K.A.B.; Hooper, N.M. The role of tissue non-specific alkaline phosphatase (TNAP) in neurodegenerative diseases: Alzheimer's disease in the focus. *Sub-Cell. Biochem.* **2015**, *76*, 363–374. [CrossRef]
85. Vardy, E.R.L.C.; Kellett, K.A.B.; Cocklin, S.L.; Hooper, N.M. Alkaline phosphatase is increased in both brain and plasma in Alzheimer's disease. *Neurodegener. Dis.* **2012**, *9*, 31–37. [CrossRef]
86. Lavin, Y.; Winter, D.; Blecher-Gonen, R.; David, E.; Keren-Shaul, H.; Merad, M.; Jung, S.; Amit, I. Tissue-resident macrophage enhancer landscapes are shaped by the local microenvironment. *Cell* **2014**, *159*, 1312–1326. [CrossRef]
87. Li, Q.; Barres, B.A. Microglia and macrophages in brain homeostasis and disease. *Nat. Rev. Immunol.* **2018**, *18*, 225–242. [CrossRef]
88. Harrington, A.J.; Bridges, C.M.; Berto, S.; Blankenship, K.; Cho, J.Y.; Assali, A.; Siemsen, B.M.; Moore, H.W.; Tsvetkov, E.; Thielking, A.; et al. MEF2C hypofunction in neuronal and neuroimmune populations produces MEF2C haploinsufficiency syndrome–like behaviors in mice. *Biol. Psychiatry* **2020**, *88*, 488–499. [CrossRef]
89. Deczkowska, A.; Matcovitch-Natan, O.; Tsitsou-Kampeli, A.; Ben-Hamo, S.; Dvir-Szternfeld, R.; Spinrad, A.; Singer, O.; David, E.; Winter, D.R.; Smith, L.K.; et al. Mef2c restrains microglial inflammatory response and is lost in brain ageing in an IFN-I-dependent manner. *Nat. Commun.* **2017**, *8*, 717. [CrossRef]
90. Zhang, X.; Liu, T.; Xu, S.; Gao, P.; Dong, W.; Liu, W.; Gao, M.; Song, L.; Cui, L.; Dong, X. A pro-inflammatory mediator USP11 enhances the stability of p53 and inhibits KLF2 in intracerebral hemorrhage. *Mol. Ther. Methods Clin. Dev.* **2021**, *21*, 681–692. [CrossRef]
91. Farmer, B.C.; Walsh, A.E.; Kluemper, J.C.; Johnson, L.A. Lipid Droplets in Neurodegenerative Disorders. *Front. Neurosci.* **2020**, *14*, 742. [CrossRef]
92. Loving, B.A.; Bruce, K.D. Lipid and lipoprotein metabolism in microglia. *Front. Physiol.* **2020**, *11*, 393. [CrossRef] [PubMed]
93. Marschallinger, J.; Iram, T.; Zardeneta, M.; Lee, S.E.; Lehallier, B.; Haney, M.S.; Pluvinage, J.V.; Mathur, V.; Hahn, O.; Morgens, D.W.; et al. Lipid-droplet-accumulating microglia represent a dysfunctional and proinflammatory state in the aging brain. *Nat. Neurosci.* **2020**, *23*, 194–208. [CrossRef] [PubMed]
94. Folick, A.; Koliwad, S.K.; Valdearcos, M. Microglial lipid biology in the hypothalamic regulation of metabolic homeostasis. *Front. Endocrinol.* **2021**, *12*, 591. [CrossRef]
95. Cui, Y.; Zhang, Y.; Zhao, X.; Shao, L.; Liu, G.; Sun, C.; Xu, R.; Zhang, Z. ACSL4 exacerbates ischemic stroke by promoting ferroptosis-induced brain injury and neuroinflammation. *Brain, Behav. Immun.* **2021**, *93*, 312–321. [CrossRef]
96. Button, E.B.; Mitchell, A.S.; Domingos, M.M.; Chung, J.H.J.; Bradley, R.M.; Hashemi, A.; Marvyn, P.M.; Patterson, A.C.; Stark, K.D.; Quadrilatero, J.; et al. Microglial cell activation increases saturated and decreases monounsaturated fatty acid content, but both lipid species are proinflammatory. *Lipids* **2014**, *49*, 305–316. [CrossRef] [PubMed]

97. Yuste, J.E.; Tarragon, E.; Campuzano, C.M.; Ros-Bernal, F. Implications of glial nitric oxide in neurodegenerative diseases. *Front. Cell. Neurosci.* **2015**, *9*, 322. [CrossRef] [PubMed]
98. Yates, S.L.; Burgess, L.H.; Kocsis-Angle, J.; Antal, J.M.; Dority, M.D.; Embury, P.B.; Piotrkowski, A.M.; Brunden, K.R. Amyloid beta and amylin fibrils induce increases in proinflammatory cytokine and chemokine production by THP-1 cells and murine microglia. *J. Neurochem.* **2000**, *74*, 1017–1025. [CrossRef] [PubMed]
99. Kielczewski, J.L.; Hu, P.; Shaw, L.C.; Calzi, S.L.; Mames, R.N.; Gardiner, T.A.; McFarland, E.; Chan-Ling, T.; Grant, M.B. Novel protective properties of IGFBP-3 result in enhanced pericyte ensheathment, reduced microglial activation, increased microglial apoptosis, and neuronal protection after ischemic retinal injury. *Am. J. Pathol.* **2011**, *178*, 1517–1528. [CrossRef]
100. Xie, Z.; Huang, L.; Enkhjargal, B.; Reis, C.; Wan, W.; Tang, J.; Cheng, Y.; Zhang, J.H. Recombinant Netrin-1 binding UNC5B receptor attenuates neuroinflammation and brain injury via PPARγ/NFkB signaling pathway after subarachnoid hemorrhage in rats. *Brain, Behav. Immun.* **2018**, *69*, 190–202. [CrossRef]
101. Liang, Y.; Zheng, D.; Peng, S.; Lin, D.; Jing, X.; Zeng, Z.; Chen, Y.; Huang, K.; Xie, Y.; Zhou, T.; et al. Rifampicin attenuates rotenone-treated microglia inflammation via improving lysosomal function. *Toxicol. In Vitr.* **2020**, *63*, 104690. [CrossRef]
102. Satoh, J.; Kino, Y.; Kawana, N.; Yamamoto, Y.; Ishida, T.; Saito, Y.; Arima, K. TMEM106B expression is reduced in Alzheimer's disease brains. *Alzheimer's Res. Ther.* **2014**, *6*, 17. [CrossRef] [PubMed]
103. Herrera-Rivero, M.; Santarelli, F.; Brosseron, F.; Kummer, M.P.; Heneka, M.T. Dysregulation of TLR5 and TAM Ligands in the Alzheimer's Brain as Contributors to Disease Progression. *Mol. Neurobiol.* **2019**, *56*, 6539–6550. [CrossRef] [PubMed]
104. Ji, R.; Tian, S.; Lu, H.J.; Lu, Q.; Zheng, Y.; Wang, X.; Ding, J.; Li, Q.; Lu, Q. TAM receptors affect adult brain neurogenesis by negative regulation of microglial cell activation. *J. Immunol.* **2013**, *191*, 6165–6177. [CrossRef] [PubMed]

Appendix D

Submitted article: MorphData: Automating the data extraction process of morphological features of microglial cells in ImageJ

bioRxiv preprint doi: https://doi.org/10.1101/2021.08.05.455282; this version posted January 4, 2022. The copyright holder for this preprint (which was not certified by peer review) is the author/funder. All rights reserved. No reuse allowed without permission.

MorphData: Automating the data extraction process of morphological features of microglial cells in ImageJ

Ana Bela Campos‡ *[a,b], Sara Duarte-Silva [a,b], António Francisco Ambrósio [c,d,e], Patrícia Maciel [a,b], Bruno Fernandes‡ [f]

[a] Life and Health Sciences Research Institute (ICVS), School of Medicine, University of Minho, Braga, Portugal

[b] ICVS/3B's, PT Government Associate Laboratory, Braga/Guimarães, Portugal

[c] University of Coimbra, Coimbra Institute for Clinical and Biomedical Research (iCBR), Faculty of Medicine, Coimbra, Portugal

[d] University of Coimbra, Center for Innovative Biomedicine and Biotechnology (CIBB), Coimbra, Portugal

[e] Clinical Academic Center of Coimbra (CACC), Coimbra, Portugal

[f] Department of Informatics, ALGORITMI Center, University of Minho, Braga, Portugal

‡ Contributed equally to the article.

* To whom correspondence should be addressed.

Ana Bela Campos. Life and Health Sciences Research Institute (ICVS), School of Medicine, University of Minho, Braga, Portugal. ana.bela.campos.88@gmail.com

Keywords: Bioinformatics, Cell Biology, Data Extraction, ImageJ, Microglia, Morphology, Neurosciences.

Abbreviations: CTR: control; EX: experimental group; GUI: Graphical User Interface; IJM: ImageJ Macro language; PBS: Phosphate-Buffered Saline; RT: room temperature.

bioRxiv preprint doi: https://doi.org/10.1101/2021.08.05.455282; this version posted January 4, 2022. The copyright holder for this preprint (which was not certified by peer review) is the author/funder. All rights reserved. No reuse allowed without permission.

Abstract

Microglial cells are the first line of defense within the central nervous system, with morphological characterization being widely used to define their activation status. Most methods to evaluate microglia status are manual, and, therefore, often biased, inaccurate, and time consuming. In fact, the process to collect morphological data starts with the acquisition of photomicrographs from where images of single cells are extracted. Then, the researcher collects the morphological features that characterize each cell. However, a manual data collection process from single cells can take weeks to complete. This work describes an open-source ImageJ plugin, *MorphData*, which automatizes the data extraction process of morphological features of single microglial cells. The plugin collects, processes, and organizes features associated with cell complexity and ramification. In a computer with limited computing power, *MorphData* was able to handle 699 single cells in less than 14 minutes. The same process, if performed manually, would take almost 19 working days. Overall, *MorphData* significantly reduces the time taken to collect morphological data from microglial cells, which can then be used to study, understand, and characterize microglia behavior in the brain of human patients or of animal models of neurological and psychiatric diseases.

bioRxiv preprint doi: https://doi.org/10.1101/2021.08.05.455282; this version posted January 4, 2022. The copyright holder for this preprint (which was not certified by peer review) is the author/funder. All rights reserved. No reuse allowed without permission.

1. Introduction

Microglial cells represent a population of macrophages-like cells in the central nervous system, with a broad range of roles in neurodevelopment, synaptic plasticity, and brain protection and repair [1]. Hence, the morphological characterization of these cells is of the utmost importance to ascertain and establish their state in particular conditions. It is known that microglia morphology and function are closely related [2]. In fact, in response to injury, microglial cells undergo morphological and functional changes, changing from a highly ramified into an amoeboid-like shape [3]. This implies that a rigorous analysis of microglia morphology data is of essence for the understanding of cellular behavior [3, 4, 5].

The collection of morphological data goes through several steps. First, one is required to obtain photomicrographs from where images of cells can be extracted. Then, ImageJ is required for image processing [6]. Being an open-source software, it is frequent to find macros and plugins, conceived by the community, that provide ImageJ with extra features. Examples include *SlideJ* [7], *aNMJ-morph* [8], and *ImageSURF* [9], and *Simple RGC* [10], among others. A different example is provided by Heindl and colleagues [11], where the authors propose a morphological analysis method outside ImageJ, using a closed and proprietary programming language and numeric computing environment.

For the morphological analysis of microglial cells, ImageJ provides two key plugins: (i) *AnalyzeSkeleton (2D/3D)* [12], which tags skeletal features relevant to cell ramification, and (ii) *FracLac* [13], which quantifies cell surface and size, soma thickness, and the cylindrical shape of cells. The use of both plugins is recommended, as cell ramification data are complementary to cell complexity [14]. However, while the latter is applied over single cell images, the former is typically applied to entire photomicrographs, thus producing results with significant noise. Hence, we aimed to develop a protocol that allowed the application of both plugins over single cells, not only reducing the amount of noise that comes from analyzing larger and noisy photomicrographs, but also solving the problem of stacked cells. This comes, however, with a significant time cost when collecting the morphological features that characterize each cell. In fact, the process to obtain such morphological features, when performed manually over each cell, is a demanding, repetitive, and laborious task, that can take several weeks to complete. Another potential issue is the human error associated with the data collection process. This sets the need for the *MorphData* plugin.

This manuscript describes the design, implementation, and use of a new plugin that automatically runs and collects morphological features for single cells in a matter of minutes, significantly reducing the time spent on the data collection process. The goal of *MorphData* is set on optimizing the data collection process of morphological features.

bioRxiv preprint doi: https://doi.org/10.1101/2021.08.05.455282; this version posted January 4, 2022. The copyright holder for this preprint (which was not certified by peer review) is the author/funder. All rights reserved. No reuse allowed without permission.

2. Materials and methods

2.1 Ethics statement

All procedures with mice were conducted in accordance with the ARRIVE 2.0 guidelines (Animal Research: Reporting *In Vivo* Experiments). Animal facilities and the people that worked directly in animal procedures were certified by the Portuguese regulatory – *Direção Geral de Alimentação e Veterinária*, license number 020317. All animal procedures were approved by the Animal Ethics Committee of the Life and Health Sciences Research Institute, University of Minho (SECVS 120/2014), and conducted in consonance with the European Union Directive 2010/63/EU. Health monitoring was performed according to the Federation of European Laboratory Animal Science Associations guidelines, where the Specified Pathogen Free health status was confirmed by sentinel mice maintained in the same animal housing room.

2.2 Animal maintenance

Two groups, control (CTR) and experimental group (EX) mice on a C57BL/6J background, were considered. Animals were maintained in a conventional animal facility and under standard laboratory conditions, which includes an artificial 12h light/dark cycle, lights on from 8:00 am to 8:00 pm, an ambient temperature of 21 ± 1ºC and relative humidity of 50–60%.

2.3 Immunofluorescence staining

CTR (n=4) and EX (n=4) mice were deeply anesthetized with a mixture of ketamine hydrochloride (150mg/kg) and medetomidine (0.3mg/kg), and transcardially perfused with phosphate-buffered saline (PBS) followed by 4% paraformaldehyde (PFA) solution (PFA, 0.1 M, pH 7.4, in PBS). Brains were removed and immersed in 4% PFA (48h), followed by 1 week in a 30% sucrose PBS buffer (at 4ºC). Coronal sections were obtained using a vibratome (VT1000S, Leica, Germany) with 40µm of thickness. For staining, the permeabilization in the free-floating sections was performed with PBS-T 0.3% (0.3% triton X-100, Sigma Aldrich, in PBS) for 10 min, followed by immersing the slices in pre-heated citrate buffer (10 mM, pH 6.0; Sigma Aldrich) during 20 min using a thermoblock (D1200, LabNet) set at 80ºC. Once cooled, slices were blocked with goat serum blocking buffer (10% normal goat serum, 0.3% triton X-100, in PBS) at room temperature (RT) for 90 min. After this, the sections were incubated with the primary antibody anti-ionized calcium binding adaptor molecule 1 (rabbit polyclonal IgG anti-Iba-1, 1:600; Wako) overnight at 4ºC. In the next day, sections were incubated with a secondary antibody (Alexa Fluor 594 goat anti-rabbit, 1:1000; ThermoFisher Scientific) during 90 min at RT, protected from light, followed with 4',6-Diamidin-2-phenylindol (DAPI, 1:1000; Invitrogen) for nuclei staining. Sections were mounted on microscope slides (Menzel-Glaser Superfrost©Plus, Thermo Fisher Scientific) and covered with a coverslip (Menzel-Glaser 24–60mm, Wagner und Munz) using aqueous mounting medium (Fluoromount TM, Sigma-Aldrich).

bioRxiv preprint doi: https://doi.org/10.1101/2021.08.05.455282; this version posted January 4, 2022. The copyright holder for this preprint (which was not certified by peer review) is the author/funder. All rights reserved. No reuse allowed without permission.

2.4 Image acquisition and preparation

Images were acquired using the Olympus Confocal FV1000 laser scanning microscope, with a resolution of 1024×1024px, using a 40× objective (UPlanSApo, N.A. 0.90; dry; field size 624.39×624.39μm; 0.31μm/px), being used to obtain Z-stacked images, which include two distinct channels (red, Iba-1; blue, DAPI). The acquisition settings were the following: scanning speed = 4μm/px; pinhole aperture = 110μm; Iba-1, excitation = 559nm, emission = 618nm; DAPI, excitation = 405nm, emission = 461nm; in a 3-dimensional scenario (X, Y, and Z axis). Four coronal brain sections per animal were imaged in both hemispheres, for a particular region of interest, to yield 4-6 digital photomicrographs per section containing the region of analysis.

The Z-stacked 3D volume images from sections of the region of interest were prepared for microglial morphology analysis using a semi-automatic method, adapted from [14], to obtain both skeleton and fractal data. However, contrary to the cited method, we went further and obtained binary (white cells on black background) single cells (one cell per file in TIFF format) to feed both the *AnalyzeSkeleton (2D/3D)* and the *FracLac* plugins.

Briefly, after stacking the 3D volume images, the double-color image was split to obtain the Iba-1 label in the red channel, which accurately mirrors the cell profile. Brightness and contrast of the red-channel were adjusted as needed and an unsharp mask was applied. Then, a despeckle filter was used to remove salt and pepper noise, with the threshold option being used and adjusted, as needed, to convert the image into a binary one. Noise was subsequently reduced using despeckle and by removing outliers. After that, random cells from both the original and the binary images were selected with the rectangle tool, using the region of interest to set the same rectangle dimensions for all the selected cells (field size 296×264). Then, after selecting the cells, the paintbrush tool was used to complete and draw the morphology of the cells (always comparing with the original image) and to clean extra signal that is not related to these cells, thus producing a single-cell image without any noise. This process is summarized in Figure 1a and 1b. Sample data are available at *MorphData*'s code repository (github.com/anabelacampos/MorphData).

699 single-cell images, for both CTR (310 single cells) and EX (389 single cells) groups, were obtained and stored in the file system, in the TIFF format. At this point, the researcher is ready to start collecting the morphological features that characterize each microglial cell using the *MorphData* plugin.

bioRxiv preprint doi: https://doi.org/10.1101/2021.08.05.455282; this version posted January 4, 2022. The copyright holder for this preprint (which was not certified by peer review) is the author/funder. All rights reserved. No reuse allowed without permission.

3. MorphData architecture and implementation

The *MorphData* plugin was developed using ImageJ Macro language (IJM), a scripting language that allows a developer to control many features of ImageJ. Plugins written in IJM can be programmed to perform sequences of actions, thus automating repetitive processes. It has a set of basic structures, including variables, conditional statements, loops, and user-defined functions. Importantly, IJM allows the developer to access ImageJ functions that are available from its Graphical User Interface (GUI). *MorphData* takes advantage of IJM to automatically collect morphological features, working on any operating system in which ImageJ can work. The plugin is open-source and available online to the community. A straightforward architectural diagram is depicted in Figure 2.

3.1 Computational requirements

The *MorphData* plugin requires basic computational resources. The experiments here described were carried out on a personal computer with an 8th generation i7 CPU with 4 cores at 1.80GHz, 8GB of RAM, a SSD disk, and the Windows 10 operating system. ImageJ 1.53c, embedded in Fiji, has been set with 6989MB of maximum heap size.

MorphData runs in any operating system compatible with ImageJ (https://imagej.nih.gov/ij/index.html), which is available, as a downloadable application, for Windows, macOS, and Linux. The plugin is reliant on ImageJ (version 1.52t, or later) and the following ImageJ plugins:

i. *AnalyzeSkeleton (2D/3D)* (version 3.4.2, or later);
ii. *FracLac* (version 2015Sep090313a9330, or later).

ImageJ/Fiji requires a system with a Java 8, or later, virtual machine. *MorphData*'s post-processing script requires Python (version 3.7.10, or later) and the following modules:

- pandas (version 1.2.3, or later);
- tkinter (version 8.6, or later).

3.2 Installation

To install the *MorphData* plugin the user is required to download ImageJ and associated bundles with preinstalled plugins, such as Fiji, prior to installation (imagej.net/Fiji/Downloads). The user is then required to add *MorphData* as a new plugin to ImageJ:

i. Download the *Morph_Data.ijm* file from the code repository;
ii. Put the file in the plugins folder of ImageJ/Fiji itself.

bioRxiv preprint doi: https://doi.org/10.1101/2021.08.05.455282; this version posted January 4, 2022. The copyright holder for this preprint (which was not certified by peer review) is the author/funder. All rights reserved. No reuse allowed without permission.

The user can then start ImageJ and the *MorphData* plugin will be available at the Plugins tab. A detailed description on how to install ImageJ plugins can be found online at https://imagej.net/plugins.

MorphData also comes with a post-processing script, which users can run if necessary. To use this script users are required to have a Python environment installed. The easiest way to have such an environment is to download and install Anaconda, a popular open-source Python distribution platform (www.anaconda.com/products/individual). To run the post-processing script the user must open the Python console/prompt and execute the command "*python MorphData_PostProcessing.py*".

3.3 Algorithm

Before detailing *MorphData*'s algorithm, it is important to clearly structure the obtained single cell images in the file system. Ideally, the user should create a structure such as the one depicted in Figure 3. To comply with the *MorphData* plugin, while the name of the folders at the two first levels is irrelevant, it is important to guarantee that the last two levels are entitled as "*Slice i*", where *i* identifies different slices, and "*Image j*", where *j* identifies different photomicrographs. Single cells should be placed inside the corresponding image folder, being entitled as "*Microgliak.tif*", where *k* identifies each cell within the image folder.

The *MorphData* plugin, when executed, starts by asking the user to indicate the folder containing the single cell images (Figure 4a). Following the file structure defined in Figure 3, the user should indicate the *CTR* folder (the root folder). The plugin then creates auxiliary folders to store the collected data and automatically starts navigating the indicated folder looking for single cell images. Then, for each image, the algorithm is summarized as follows:

i. To obtain skeletal features relevant to cell ramification:
    a) Open a single cell;
    b) Run the command "*Process* > *Binary* > *Skeletonize*" to create a skeletonized image;
    c) Run the *Analyze Skeleton (2D/3D)* plugin;
    d) Run the "*saveAs*" command to collect and store, in a csv file, skeletal data;
    e) Run the "*saveAs*" command to collect and store, in a csv file, branch information data.
ii. To obtain features relevant to cell complexity:
    a) Open a single cell;
    b) Run the "*saveAs*" command to store a shaped single cell, in TIFF format, in a folder entitled as "*Area*";
    c) Run the "*Process* > *Binary* > *Outline"* and "*saveAs*" commands to store an outlined single cell, in TIFF format, in a folder entitled as "*Perimeter*".

bioRxiv preprint doi: https://doi.org/10.1101/2021.08.05.455282; this version posted January 4, 2022. The copyright holder for this preprint (which was not certified by peer review) is the author/funder. All rights reserved. No reuse allowed without permission.

iii. Repeat steps 1. and 2. for each single cell;

iv. At the end, the algorithm indicates the total number of analyzed cells.

Finally, contrary to the *Analyze Skeleton (2D/3D)* plugin, which is automatically executed by *MorphData*, the *FracLac* plugin cannot be directly executed from within another plugin. This limitation requires the user to manually execute the *FracLac* plugin itself after the *MorphData* plugin has finished. Fortunately, since the "*Area*" and the "*Perimeter*" folders, which were automatically created by *MorphData*, already contain all shaped and outlined cells (Figure 4b and 4c), the user can execute the *FracLac* plugin in batch mode. Hence, with a batch execution of this plugin, the user obtains fractal data for all cells almost immediately (avoiding the need to execute *FracLac* for each cell individually).

3.4 Post-processing script

Up to this point, all morphological data are now available, for all single cells, in multiple csv files in auxiliary "*results*" folders. In total, the *MorphData* plugin gathers 221 features (from skeleton to fractal ones), and some of them may be irrelevant to the characterization of microglial cells. Hence, the post-processing step is useful to join all data, cleaning irrelevant features, and performing a feature engineering process to create new ones, including the *cell_area*, *cell_perimeter*, *roughness*, and *cell_circularity*, among others.

Due to the potential high number of rows (cells) and columns (morphological features), an ImageJ plugin is unsuitable for the task, as it would eventually run out of memory. Hence, a Python script, entitled as *MorphData_PostProcessing.py*, was conceived and released as part of the *MorphData* plugin. This script requires a simple python environment to execute, again asking the user to indicate the location of the root folder. It will then automatically apply the post-processing procedures, creating three final files, containing the following 46 features:

i. **skeleton_final_results.csv:**
   - *# Branches, # Junctions, # End-point voxels, # Junction voxels, # Slab voxels, Average Branch Length, # Triple points, # Quadruple points, Maximum Branch Length, animal, microglia_id*.

ii. **branch_info_final_results.csv:**
   - *Skeleton ID, Branch length, V1 x, V1 y, V1 z, V2 x, V2 y, V2 z, Euclidean distance, running average length, average intensity (inner 3rd), average intensity, animal, microglia_id*.

iii. **fraclac_final_results.csv:**
   - *fractal_dimension, lacunarity, outline_mean_fg, density, span_ratio_major_minor, convex_hull_area, convex_hull_perimeter, convex_hull_circularity, diameter_bounding_circle, mean_radius,*

bioRxiv preprint doi: https://doi.org/10.1101/2021.08.05.455282; this version posted January 4, 2022. The copyright holder for this preprint (which was not certified by peer review) is the author/funder. All rights reserved. No reuse allowed without permission.

max_span_across_convex_hull, max_min_radii, shape_mean_fg, 1_pixel_side_micron, 1_pixel_area_micron_sq, cell_area, cell_perimeter, roughness, cell_circularity, animal, microglia_id.

Figure 4d contains a graphical perspective of part of the content of the *skeleton_final_results.csv* file, which contains 11 features relevant for cell ramification. The remaining two files are similar, varying only on the quantified features. Sample input and output data are available at *MorphData*'s code repository.

bioRxiv preprint doi: https://doi.org/10.1101/2021.08.05.455282; this version posted January 4, 2022. The copyright holder for this preprint (which was not certified by peer review) is the author/funder. All rights reserved. No reuse allowed without permission.

4. Results and discussion

The performance of *MorphData* was evaluated based on the validity of the collected values and on the time it took to obtain the morphological data of all single cells of both experimental groups, when compared to a manual collection of such data.

Totally, in a computer with limited computing power, it took less than 14 minutes to collect 46 morphological features associated with 699 single cells of two experimental groups. In particular, 6.5 minutes were spent by the *MorphData* plugin, and its post-processing script, handling the CTR group. Of those, nearly 3 minutes were spent collecting skeleton data, 3.25 minutes by the *FracLac* plugin on batch mode, and 10 seconds by the post-processing script. On the other hand, 7.5 minutes were spent handling the EX group. Of those, 3.5 minutes were spent collecting skeleton data, 3.8 minutes by the *FracLac* plugin on batch mode, and 11 seconds by the post-processing script.

The same process was performed manually, by a skilled user of ImageJ, for a set of ten single cells of the CTR group. To ease the process, the same file system structure (as required by the *MorphData* plugin) was used. The goal was to mimic the processes that are automatically performed by *MorphData*, and manually collect 46 morphological features for the ten cells. The mean time to collect such morphological features was of 13 minutes per cell. Skeleton data were faster to collect (around 1.5 minutes), since the *AnalyzeSkeleton (2D/3D)* plugin only opens two results' windows that the user can immediately save in two distinct files in the file system, in csv format, and then close the opened windows. However, fractal data were considerably harder to collect (around 11.5 minutes). On the one hand, for each cell, the *FracLac* plugin must be executed twice - one for a shaped cell and one for an outlined cell, which the user must prepare. On the other hand, for each execution, this plugin opens multiple results' windows. The ones to keep opened are the “Hull and Circle Results” and the “Box Count Summary” windows. However, these windows are not user-friendly and, besides providing the user with an overwhelming amount of 173 features (most of them formulas and unwanted columns), it does not allow the user to copy only the desired features - the user must manually write each value of each desired feature to a csv, or excel, file. In fact, the process of selecting features from the *FracLac* plugin is extremely exhausting and error-prone. Finally, it is up to the user to calculate the value of non-existing features such as *cell_area*, *cell_perimeter*, *roughness*, and *cell_circularity*.

A couple more obstacles emerged with the manual process. First, the user was required to edit each stored file, for each cell, to identify the animal and the microglia of each row of data. Secondly, the user was required to copy the contents of each file to an overall file, aggregating the data for the experimental group. Since each cell is made of three files (two skeleton files and

bioRxiv preprint doi: https://doi.org/10.1101/2021.08.05.455282; this version posted January 4, 2022. The copyright holder for this preprint (which was not certified by peer review) is the author/funder. All rights reserved. No reuse allowed without permission.

one fractal file) this would require the user to open and copy 699×3 files, which would, again, be a time-consuming task that would have to be performed after collecting all data.

Overall, the manual process for ten single cells of the CTR group took more than 2 hours to complete. On the other hand, the *MorphData* plugin and its post-processing script took less than 14 minutes to collect, process, and organize the morphological features of 699 cells. Assuming a mean value of 13 minutes per cell, the manual process to collect the morphological features of all cells would take 151 hours, which corresponds to almost 19 working days (8 hours/day) collecting data without stopping.

MorphData brings obvious advantages, mainly by significantly reducing the time it takes to collect morphological data. These values could be further reduced by a computer with higher computation power. In addition, the automation of the data collection process completely removes the risk of human error. It is worth mentioning that since *MorphData* is using well established plugins to collect morphological features, it produces the same exact results as when performing the data collection process manually. In fact, *MorphData*'s collected values were further compared and validated with multiple cells data that were manually collected by multiple people, without a single collection error.

bioRxiv preprint doi: https://doi.org/10.1101/2021.08.05.455282; this version posted January 4, 2022. The copyright holder for this preprint (which was not certified by peer review) is the author/funder. All rights reserved. No reuse allowed without permission.

5. Concluding Remarks

Morphological characterization of cells is highly relevant in the sciences field, and particularly in neurosciences. However, when performed manually, the process for obtaining morphological features from single cells is a demanding, repetitive, and laborious task; it is error-prone and can take several weeks to complete.

MorphData has already been used successfully in morphological characterization studies, where several thousands of single microglial cells, from multiple experimental groups, were analyzed and characterized. The benefits were considerable - several weeks of work were spared. Even though the plugin was optimized for microglial cells, it is likely to be performant for other glial cells, such as astrocytes and oligodendrocytes, and non-glial cells, such as neurons. Likewise, *MorphData* can also be used to automate the data extraction process of morphological features of *in vitro* cells.

It is an open-source plugin. Hence, new contributors, of all experience levels, are welcome. Contributions can be proposed using the pull request feature of GitHub or by opening a new issue (github.com/anabelacampos/MorphData/issues). These contributions can, among others, focus on the data extraction process, on *MorphData* performance over different cell types other than microglial cells, improve the documentation, or be made of constructive feedback and suggestions.

Overall, *MorphData* significantly reduces the time taken to collect morphological data from microglial cells (from weeks to minutes), which can then be used to study, understand, and characterize microglia behavior in the brain of human patients or of animal models of neurological and psychiatric diseases.

bioRxiv preprint doi: https://doi.org/10.1101/2021.08.05.455282; this version posted January 4, 2022. The copyright holder for this preprint (which was not certified by peer review) is the author/funder. All rights reserved. No reuse allowed without permission.

Acknowledgements

This work is supported by *Fundação para a Ciência e a Tecnologia* (FCT) (PTDC/NEU-NMC/3648/2014) and COMPETE-FEDER (POCI-01-0145-FEDER-016818). ABC is supported by a doctoral fellowship from FCT (PD/BD/127828/2016).

Authors Contributions

ABC: Conceptualization; Methodology; Validation; Formal analysis; Investigation; Data Curation; Writing - Original Draft; Writing - Review & Editing; Visualization. SDS: Conceptualization; Resources; Writing - Review & Editing; Supervision. AFA: Conceptualization; Resources; Writing - Review & Editing; Supervision; Funding acquisition. PM: Conceptualization; Resources; Writing - Review & Editing; Supervision; Funding acquisition. BF: Methodology; Software; Validation; Formal analysis; Data Curation; Writing - Review & Editing; Visualization

Conflicts of interest

The authors declare no commercial or financial conflict of interest.

Data Accessibility

Sample input and output data are provided to the public for educational and academic research purposes, being freely available at *MorphData*'s code repository.

References

[1] Bachiller, S, Jiménez-Ferrer, I, Paulus, A, Yang, Y, Swanberg, M, Deierborg, T, Boza-Serrano, A 2018 Microglia in Neurological Diseases: A Road Map to Brain-Disease Dependent-Inflammatory Response. Frontiers in Cellular Neuroscience 12(488). DOI: https://doi.org/10.3389/fncel.2018.00488.

[2] Fernandez-Arjona, M M, Grondona, J M, Granados-Duran, P, Fernandez-Llebrez, P, Lopez-Ávalos, M D 2017 Microglia Morphological Categorization in a Rat Model of Neuroinflammation by Hierarchical Cluster and Principal Components Analysis. Frontiers in Cellular Neuroscience 11(235). DOI: https://doi.org/10.3389/fncel.2017.00235.

[3] Morrison, H W, Filosa, J A 2013 A quantitative spatiotemporal analysis of microglia morphology during ischemic stroke and reperfusion. Journal of Neuroinflammation 10(782). DOI: https://doi.org/10.1186/1742-2094-10-4.

[4] Kongsui, R, Beynon, S B, Johnson, S J, Walker, F R 2017 Quantitative assessment of microglial morphology and density reveals remarkable consistency in the distribution and morphology of cells within the healthy prefrontal cortex of the rat. Journal of Neuroinflammation 11(182). DOI: https://doi.org/10.1186/s12974-014-0182-7.

[5] Davis, B M, Salinas-Navarro, M, Cordeiro, M F, Moons, L, Groef, L 2017 Characterizing microglia activation: a spatial statistics approach to maximize information extraction. Scientific Reports 7(1576). DOI: https://doi.org/10.1038/s41598-017-01747-8.

[6] Schneider, C A, Rasband, W S, Eliceiri, K W 2012 NIH Image to ImageJ: 25 years of image analysis. Nature Methods 9(7): 671-5. DOI: https://doi.org/10.1038/nmeth.2089.

[7] Mea, V D, Baroni, G L, Pilutti, D, Loreto, C 2017 SlideJ: An ImageJ plugin for automated processing of whole slide images. PLOS ONE 12(7): e0180540. DOI: https://doi.org/10.1371/journal.pone.0180540.

bioRxiv preprint doi: https://doi.org/10.1101/2021.08.05.455282; this version posted January 4, 2022. The copyright holder for this preprint (which was not certified by peer review) is the author/funder. All rights reserved. No reuse allowed without permission.

[8] Minty, G, Hoppen, A, Boehm, I, Alhindi, A, Gibb, L, Potter, E, Wagner, B C, Miller, J, Skipworth, R J E, Gillingwater, T H, Jones, R A 2020 aNMJ-morph: a simple macro for rapid analysis of neuromuscular junction morphology. Royal Society Open Science 7: 200128. DOI: https://doi.org/10.1098/rsos.200128.

[9] O'Mara, A, King, A E, Vickers, J C and Kirkcaldie, M T K 2017 ImageSURF: An ImageJ Plugin for Batch Pixel-Based Image Segmentation Using Random Forests. Journal of Open Research Software, 5: 31. DOI: https://doi.org/10.5334/ jors.172.

[10] Cross, T, Navarange, R, Son, J-H, Burr, W, Singh, A, Zhang, K, Rusu, M, Gkoutzis, K, Osborne, A, Nieuwenhuis, B 2021 Simple RGC: ImageJ Plugins for Counting Retinal Ganglion Cells and Determining the Transduction Efficiency of Viral Vectors in Retinal Wholemounts. Journal of Open Research Software, 9: 15. DOI: https://doi.org/10.5334/jors.342.

[11] Heindl, S, Gesierich, B, Benakis, C, Llovera, G, Duering, M, Liesz, A 2018 Automated Morphological Analysis of Microglia After Stroke. Frontiers in Cellular Neuroscience 12: 106. DOI: https://doi.org/10.3389/fncel.2018.00106.

[12] Arganda-Carreras, I, Fernandez-Gonzalez, R, Munoz-Barrutia, A, Ortiz-De-Solorzano, C 2010 3D reconstruction of histological sections: Application to mammary gland tissue. Microscopy Research and Technique 73(11): 1019-29. DOI: https://doi.org/10.1002/jemt.20829.

[13] Karperien, A 2013 FracLac for ImageJ. Available online at: http://rsb.info.nih.gov/ij/plugins/fraclac/FLHelp/ Introduction.htm.

[14] Young, K, Morrison, H 2018 Quantifying Microglia Morphology from Photomicrographs of Immunohistochemistry Prepared Tissue Using ImageJ. Journal of Visualized Experiments 136: e57648. DOI: https://doi.org/10.3791/57648.

bioRxiv preprint doi: https://doi.org/10.1101/2021.08.05.455282; this version posted January 4, 2022. The copyright holder for this preprint (which was not certified by peer review) is the author/funder. All rights reserved. No reuse allowed without permission.

Figures

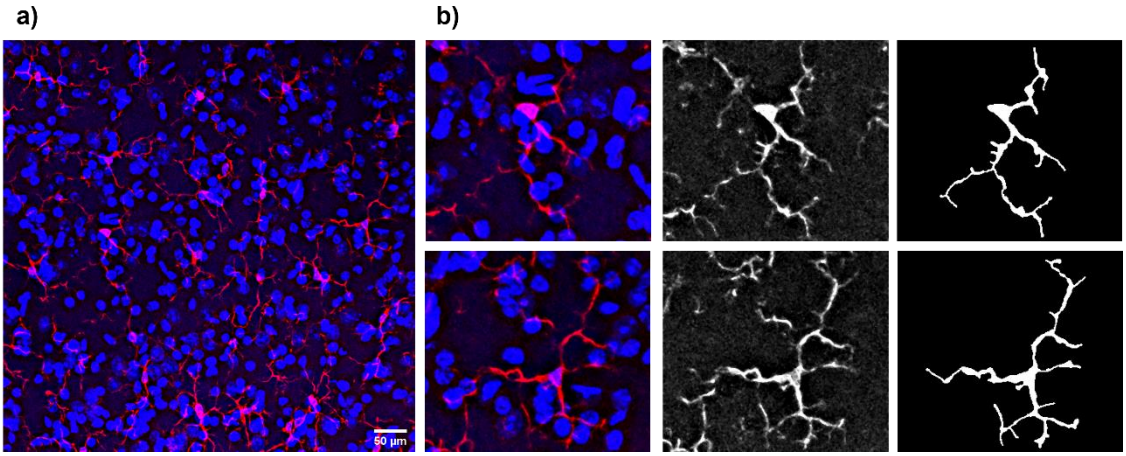

Figure 1. Representative photomicrograph from the region of interest, showing microglial cells (red) and the representation of two binary single microglial cells (gray) from a control mouse. **a)** Original Z-stacked 3D volume photomicrograph. **b)** Going from a noisy cell to a binary single cell (from the left to the right).

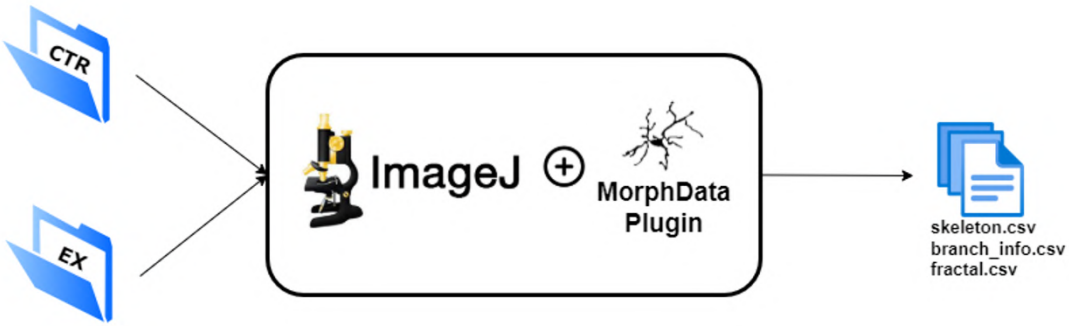

Figure 2. *MorphData*'s architectural diagram, receiving, as input, the root folders, and producing, as output, three csv files with the morphological features that characterize each single cell.

bioRxiv preprint doi: https://doi.org/10.1101/2021.08.05.455282; this version posted January 4, 2022. The copyright holder for this preprint (which was not certified by peer review) is the author/funder. All rights reserved. No reuse allowed without permission.

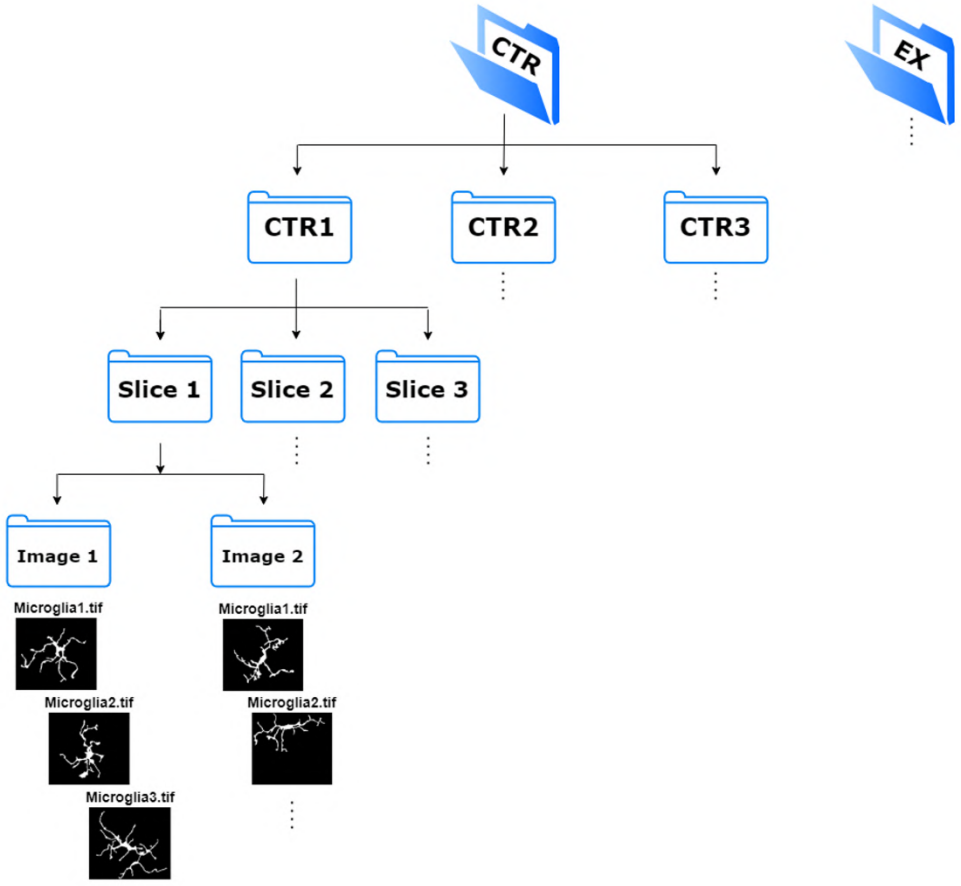

Figure 3. Recommended file system structure to store single cell images. The root folders, CTR and EX, hold the images of the corresponding experimental group.

bioRxiv preprint doi: https://doi.org/10.1101/2021.08.05.455282; this version posted January 4, 2022. The copyright holder for this preprint (which was not certified by peer review) is the author/funder. All rights reserved. No reuse allowed without permission.

a)

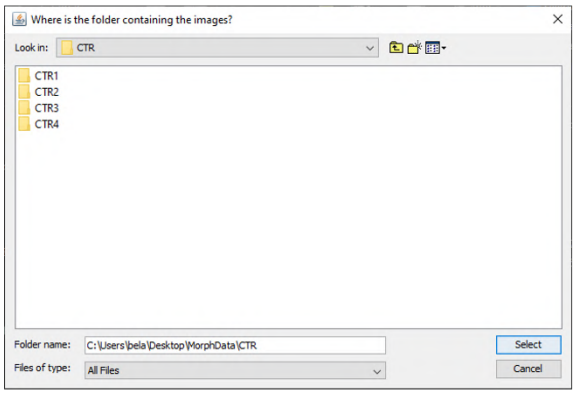

b)

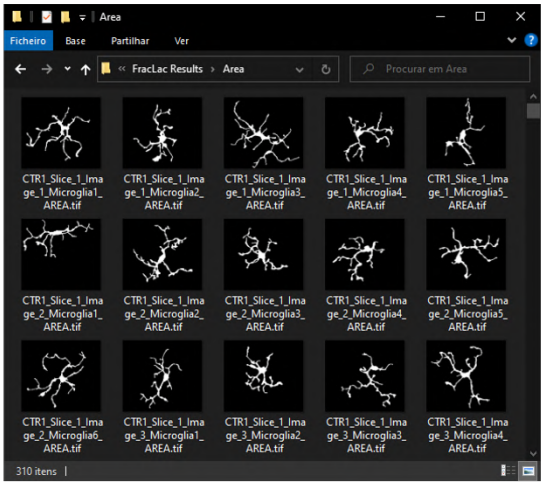

c)

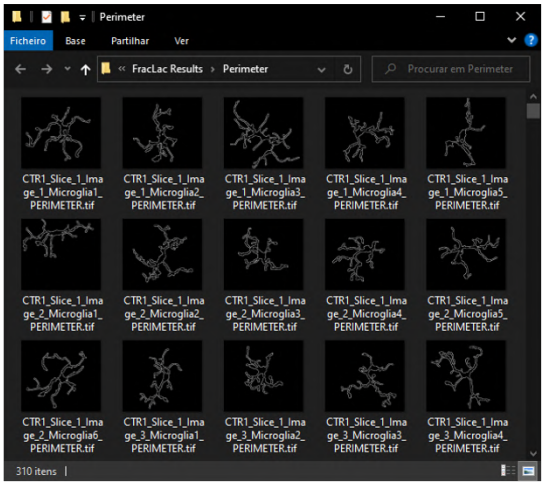

d)

# Branches	# Junctions	# End-point voxels	# Junction voxels	# Slab voxels	Average Branch	# Triple points	# Quadruple points	Maximum Branch	animal	microglia
35	17	19	51	800	17.91	17	0	73.099	CTR1	CTR1_Slice_1_Image_1_Microglia1
35	17	18	57	693	15.748	16	1	54.153	CTR1	CTR1_Slice_1_Image_1_Microglia2
47	23	24	83	1039	17.667	22	1	86.705	CTR1	CTR1_Slice_1_Image_1_Microglia3
37	18	20	58	702	14.87	18	0	47.673	CTR1	CTR1_Slice_1_Image_1_Microglia4
36	18	18	51	551	12.231	18	0	39.198	CTR1	CTR1_Slice_1_Image_1_Microglia5
33	16	17	56	692	16.333	15	1	53.98	CTR1	CTR1_Slice_1_Image_2_Microglia1
60	30	29	97	755	10.528	29	1	52.342	CTR1	CTR1_Slice_1_Image_2_Microglia2
38	19	18	54	637	13.285	18	1	39.45	CTR1	CTR1_Slice_1_Image_2_Microglia3
39	19	20	48	666	13.397	18	1	37.116	CTR1	CTR1_Slice_1_Image_2_Microglia4
33	16	18	49	686	16.07	16	0	66.034	CTR1	CTR1_Slice_1_Image_2_Microglia5

Figure 4. Execution and results of the *MorphData* plugin. **a)** *MorphData* dialog GUI asking the user where the single cell images are located. **b)** Shaped images, produced by *MorphData*, stored in the "*Area*" folder. **c)** Outlined images, produced by *MorphData*, stored in the "*Perimeter*" folder. Both shaped and outlined images are ready to be passed to the *FracLac* plugin for batch mode execution. **d)** A sample of the *skeleton_final_results.csv* file, produced by *MorphData*. This file contains 11 features relevant to cell ramification and cell identification.

Appendix E

Submitted article: Microglial depletion has no impact on disease progression in a mouse model of Machado-Joseph disease

RESEARCH

Microglial depletion has no impact on disease progression in a mouse model of Machado-Joseph disease

Ana Bela Campos[1,2], Sara Duarte-Silva[1,2], Bruno Fernandes[3], Bárbara Coimbra[1,2], Jonas Campos[1,2], Daniela M. Fernandes[1,2], Andreia Teixeira-Castro[1,2], António F. Ambrósio[4,5,6] and Patrícia Maciel[1,2*]

Abstract

Background: Machado-Joseph disease (MJD) is an autosomal dominant neurodegenerative disorder (ND). While most research in NDs has been following a neuron-centric point of view, microglial cells are now recognized as crucial in the central nervous system. Previous work revealed alterations that point to an increased activation state of microglia in the brain of CMVMJD135 mice, a MJD mouse model that replicates the motor symptoms and neuropathology of the human condition.

Methods: Here, we investigated the extent to which microglia are actively contributing for MJD pathogenesis and symptoms' progression. For this, we used PLX3397 to reduce the number of microglia in the brain of CMVMJD135 mice, which was administrated for 3 weeks beginning at a mid-stage of the disease since it is when most of the symptomatology is present and because it is difficult to treat the motor deficits observed in NDs after neuronal loss. Immunohistochemical analysis were used to validate the effects of PLX3397 on microglial density. In addition, a set of statistical and machine learning models were further implemented to analyze the impact of PLX3397 in the morphology of the surviving microglia. Then, a battery of behavioral tests was used to evaluate the impact of microglial depletion on the motor phenotype of CMVMJD135 mice.

Results: Although the PLX3397 treatment substantially reduced microglia density in the affected brain regions, it did not affect the motor deficits seen in CMVMJD135 mice. In addition to reducing the number of microglia, the treatment with PLX3397 induces morphological changes suggestive of activation in the surviving microglia, the microglia of wild-type animals becoming similar to those of CMVMJD135 animals.

Conclusions: These results suggests that, despite the morphological and transcriptomic changes seen in the microglia of CMVMJD135 mice, these cells are not key contributors for MJD progression. Furthermore, the impact of PLX3397 on microglial activation should be taken into account in the interpretation of findings of NDs modification seen upon treatment with this CSF1R inhibitor.

Keywords: Microglia depletion; Machado-Joseph Disease; Motor Phenotype; Morphology; Machine Learning

Background

Machado-Joseph disease (MJD), also known as Spinocerebellar Ataxia type 3 (SCA3), represents the most common dominantly inherited ataxia and the second most common polyglutamine disease (polyQ) worldwide [1]. This neurodegenerative disease is caused by an expansion of a cytosine-adenine-guanine (CAG) repeat tract in exon 10 of the Ataxin-3 (*ATXN3*) gene located in chromosome 14q32.1, which encodes an abnormally long polyglutamine (polyQ) segment in the ATXN3 protein, making it prone to self-assembly, and to form aggregates that are toxic to neurons [2, 3, 4]. While in healthy individuals this CAG repeat tract ranges from 12 to 44 units, in the affected patients the CAG repeat ranges from 56 to 87, the age of symptom onset being inversely correlated with the repeat length [5]. MJD symptoms reflect the involvement of multiple neurological systems, and include a wide range of progressive motor impairments such as cerebellar ataxia with abnormal gait, loss of limb coordination, impaired balance, dystonia, dysarthria, dysphagia, spasticity, and oculomotor abnormalities [6, 7]. Post-mortem analysis of MJD patients' brains reveals that the progressive motor impairment results from neuronal dysfunction and neuronal cell loss in several regions of the central nervous system (CNS), such as in the deep cerebellar nuclei (DCN), in the cerebellum, in the pontine nuclei (PN), in the brainstem, and in spinocerebellar tracts. In some patients, the involvement of the peripheral nerves may also be present [8]. Although most research in polyQ disorders has been following a neuron-centric perspective, due to the well-recognized neuronal degeneration, microglial cells are now acknowledged as vital components of the CNS that contribute to neuronal health [9].

Microglial cells are resident macrophages of myeloid origin in the CNS, being considered the first line of defense within the brain and the major orchestrators of the brain inflammatory response [10, 11, 12]. Under healthy conditions, these cells are continuously scanning their environment, pruning synapses, and regulating neuronal activity [11, 12]. Their morphology is one of its more outstanding characteristics and can change upon different situations of brain disease and pathology, including enlargement of cell bodies and thickening of their processes [13, 14]. In some neurological pathologies, microglial cells can play either a toxic or a protective role because the extent of microglial activation and, thereby, their contribution to pathogenesis depending on the type and duration of injury [14, 15, 16]. Indeed, while some studies report chronically activated microglia to be harmful and worsen the disease outcome in Huntington disease (HD) [17, 18], Parkinson disease (PD) [19], Alzheimer disease (AD) [20], and Amyotrophic lateral sclerosis (ALS) [21], other studies suggest that activated microglia may be beneficial in these diseases [22, 23, 24, 25].

Recent evidence suggested that microglial cells might also play a role in the pathogenesis of MJD. In fact, reactive microgliosis was observed in MJD patients' brains [9, 26, 27] and in a mouse model of MJD [28]. Additionally, we have recently shown morphological alterations that point to an increased activation state, as well as molecular perturbations related with oxidative stress, immune response, and lipid metabolism were seen significantly altered in microglial cells derived from CMVMJD135 mice [29], an MJD mouse model that replicates motor symptoms and neuropathology of the human condition [30]. Because most brain cells express *ATXN3*, microglial dysfunction may contribute to the disease process, due to the effects of mutant

*Correspondence: pmaciel@med.uminho.pt

[1]Life and Health Sciences Research Institute (ICVS), School of Medicine, University of Minho, Braga, Portugal

[2]ICVS/3B's, PT Government Associate Laboratory, Braga/Guimarães, Portugal

Full list of author information is available at the end of the article

ATXN3 in microglia itself or as a consequence of their interaction with neurons. However, is yet unknown whether, and how, microglia contribute to disease onset and progression in MJD. A widely used strategy to address these important questions in neurodegenerative diseases (NDs) has been the depletion of microglial cells in the brains of animal models, through pharmacological inhibition of the colony stimulating factor 1 receptor (CSF1R) signaling, which is essential for microglial survival and maintenance [15, 31, 32, 33, 34]. PLX3397, an orally bioavailable selective CSF1R inhibitor that crosses the blood-brain barrier [35], has been shown to cause microglial depletion within several days of administration [31, 36, 37, 38, 39], albeit to different extents in different studies. While depletion efficiency varies, full microglial ablation has never been reported [36, 37, 40, 41, 42, 43, 44]. In fact, it is known that a small subset of microglia in adult mouse brains can survive without CSF1R signaling [45].

In this study, we address the contribution of microglia to MJD pathogenesis through the administration of PLX3397 to the CMVMJD135 mouse model at a mid-stage of the disease and evaluate the impact of microglial depletion on the motor phenotype of this mouse model.

Materials and Methods

Transgenic mouse model and administration of PLX3397

The transgenic mouse model used in this work was the CMVMJD135 one, which, under the regulation of the CMV promoter (ubiquitous expression), expresses an expanded version of the human ATXN3 cDNA (the 3 UIMs-containing variant of ATXN3) at near-endogenous levels and manifests MJD-like motor symptoms that appear gradually and progress over time [30]. Male mice on a C57BL/6J background were used for increased homogeneity, allowing the reduction of experimental group sizes. DNA extraction, animal genotyping, and CAG repeat size analyses were performed as previously described in [46]. The mean CAG repeat size [±SD] for all CMVMJD135 mice used in this study was of 138.167 ± 4.356. Age-matched Wild-type (WT) littermate animals were used as controls. Animals (CMVMJD135 and WT, PLX3397- and vehicle treated) were housed at weaning in groups of five animals, in filter-topped polysulfone cages 267 × 207 × 140 mm (370 cm^2 floor area) (Tecniplast, Buguggiate, Italy), with corncob bedding (Scobis Due, Mucedola SRL, Settimo Milanese, Italy), in a conventional animal facility. All animals were maintained under standard laboratory conditions, which includes an artificial 12-h light/dark cycle (lights on from 8 am to 8 pm), with 21 ± 1 °C of room temperature (RT) and a relative humidity of 50–60 %. The mice were given a standard diet (4RF25 during the gestation and postnatal periods, and 4RF21 after weaning; Mucedola SRL, Settimo Milanese, Italy) and water ad libitum. A total of 81 animals (all littermates) were used in this study. Groups of 4-5 animals per genotype/treatment were used for microglia density and morphological analysis as shown in Additional file 1: Figure S1a, and groups of 14-18 animals were used per genotype/treatment for behavioral tests (Additional file 1: Figure S1b). The treatment with PLX3397 (MedChemExpress, Sollentuna, Sweden) was initiated at a mid-stage of the disease (18 weeks of age) and ended at 21 weeks of age. PLX3397 was delivered to CMVMJD135 ($n = 18$ mice) and WT ($n = 15$ mice) littermates every day via oral gavage at a dose of 40 mg/kg for 3 weeks and dissolved in 5 % dimethyl sulfoxide (DMSO) and 25 % PEG300 in ddH2O as described in [47]. Control littermate animals (CMVMJD135 ($n = 16$ mice) and WT ($n = 14$ mice)) were given vehicle (5 % DMSO and 25 % PEG300 in ddH2O), with the same frequency [47].

Immunofluorescence staining

Four experimental groups were considered for microglial cell staining: CMVMJD135 PLX3397- and vehicle-treated animals (CMVMJD135 + PLX3397 ($n = 3 - 4$ mice) and CMVMJD135 + vehicle ($n = 4$ mice)), WT PLX3397- and vehicle-treated animals (WT + PLX3397 ($n = 5$ mice) and WT + vehicle ($n = 5$ mice)). All animals were deeply anesthetized with a mixture of ketamine hydrochloride (150 mg/kg) and medetomidine (0.3 mg/kg), and transcardially perfused with phosphate saline buffer (PBS) followed by 4 % paraformaldehyde (PFA) solution (PFA 0.1 M, pH 7.4, in PBS). Brains were removed and immersed in 4 % PFA (48 h, in agitation), followed by 1 week in a 30 % sucrose PBS buffer (at 4 °C). Sagittal sections with 40 μm of thickness were obtained using a vibratome (VT1000S, Leica, Germany), and permeabilized, in free-floating sections, with PBS-T 0.3 % (0.3 % triton X-100, Sigma Aldrich, in PBS) for 10 min. Antigen retrieval was performed by immersing the slices in a pre-heated citrate buffer (10 mM, pH 6.0; Sigma Aldrich) for 20 min at 80 °C. Once cooled, slices were blocked with goat serum blocking buffer (10 % normal goat serum (NGS), 0.3 % triton X-100, in PBS) at RT for 90 min, and incubated with the primary antibody anti-ionized calcium binding adaptor molecule 1 (rabbit polyclonal IgG anti-Iba-1, 1:600; Wako) overnight at 4 °C, and with a secondary antibody (Alexa Fluor 594 goat anti-rabbit, 1:1000; ThermoFisher Scientific) for 90 min at RT, protected from light, and treat with 4',6-Diamidin-2-phenylindol (DAPI, 1:1000; Invitrogen) for nuclei staining. Sections were mounted on microscope slides (Menzel-Glaser Superfrost©Plus, Thermo Fisher Scientific), and covered with a coverslip (Menzel-Glaser 24–60 mm, Wagner und Munz) using aqueous mounting medium (Fluoromount TM, Sigma-Aldrich).

Image acquisition for evaluation of density and morphological characteristics of microglial cells

For microglial density analysis, mosaic imaging was acquired by stitching several images taken in a 3-dimensional plane (X, Y, and Z axis) using Olympus Confocal FV3000 laser scanning microscope with a resolution of 1024 × 1024 px and a 20× objective, for each region of interest (DCN and lobules of the cerebellum, and PN of the brainstem). Each image of the mosaic imaging consisted of 40-μm Z-stacks, composed of 5 μm thick image slices. 3-5 sagittal brain sections per animal were used ($n = 3 - 5$ animals per group) and one mosaic image per section of region of interest was generated. The total count of Iba-1-positive cells was obtained using the multi-point tool of ImageJ software (v1.53c; National Institute of Health, Bethesda, MD, USA) on Z-stacked 3D volume mosaic from sections of the affected brain regions. Quantification was performed on mosaic images acquired with acquisition settings described as above, normalized first to the total mosaic area and then for volume (40 μm thickness).

For the morphological analysis of microglial cells, four sagittal brain sections per animal were used ($n = 4 - 5$ animals per group) and 2 photomicrographs per section were taken in each region of interest (DCN and PN). The Olympus Confocal FV1000 laser scanning microscope with a resolution of 1024 × 1024 px and a 40× objective was used to obtain all 40-μm Z-stacked images composed of 0.31 μm thick image slices, which include two distinct channels (red, Iba-1; blue, DAPI). Using ImageJ software on Z-stacked 3D volume images from sections of the affected brain regions, a morphological analysis was performed based on a semi-automatic method adapted from [48]. Multiple steps were followed to apply commands and options to obtain binary images (white cells on black background), which are required to obtain fractal and skeleton data. At least 5 cells from both the original and the binary

images were selected with the rectangle tool, using the region of interest (ROI) to set the same rectangle dimensions for all the selected cells. Afterwards, the single-cell images without any noise were obtained by using the paintbrush tool. Then, each binary single-cell was converted into an outlined and skeletonized format, to carry out a fractal or skeleton analysis, respectively.

Features relevant to microglia ramification were obtained by the application of the *AnalyzeSkeleton 2D/3D* plugin (developed by and maintained at https://imagej.net/plugins/analyze-skeleton) over each binary single-cell. These skeletal features include the number of endpoints voxels (#/cell), number of junctions voxels (#/cell), number of junctions (#/cell), number of slab voxels (#/cell), number of branches (#/cell), number of triple points (#/cell), number of quadruple points (#/cell), Euclidean distance (μm/cell), total branch length (μm/cell), average branch length (μm/cell), and maximum branch length (μm/cell).

A fractal analysis was performed using the *FracLac* plugin (Karperien A., FracLac for ImageJ) to evaluate characteristics associated with cell surface (cell perimeter (μm) and roughness (ratio)), soma thickness (cell circularity (ratio) and density (ratio)), cell size (mean radius (μm), convex hull perimeter (μm), convex hull circularity (ratio), bounding circle diameter (μm), maximum span across the convex hull (μm), convex hull area (μm^2), and cell area (μm^2)), the cylindrical shape of cells (convex hull span ratio and the ratio of convex hull radii), the complexity of their ramifications (fractal dimension - D), and the heterogeneity of their shape (lacunarity - Λ).

MorphData plugin for data collection

The *MorphData* plugin was used to automatise the data extraction process of morphological features of single microglial cells [49]. Data were obtained from single-cells of the DCN (number of microglial cells: 263 from CMVMJD135 + PLX3397 mice, 256 from CMVMJD135 + vehicle mice, 475 from WT + PLX3397 mice, and 387 from WT + vehicle mice) and of the PN (number of microglial cells: 235 from CMVMJD135 + PLX3397 mice, 217 from CMVMJD135 + vehicle mice, 248 from WT + PLX3397 mice, and 210 from WT + vehicle mice). The total number of microglial cells used was of 1381 for the DCN and 910 for the PN.

Machine Learning setup

KNIME, a data-flow centric platform, was used to process the obtained data and to identify potential clustering of microglia concerning their morphological features. Within this platform, one workflow was conceived for each region of interest (DCN and PN). The workflows are similar, except for the used data. In fact, these are used to conceive and apply a principal component analysis (PCA) on the used data as well as to apply an unsupervised Machine Learning model, the k-means, which is a clustering method that is able to cluster data points with similar characteristics. The elbow method was used to find the ideal number of clusters, experimenting and plotting the mean squared error (MSE) associated to each cluster, with k varying between 1 to 6. The ideal k is found by picking the "elbow" of the curve as a function that minimises the error. The MSE formula is as follows:

$$\mathrm{MSE} = \frac{1}{n}\sum(y-\sigma)^2 \qquad (1)$$

where n is the number of parameters, y is the parameter value, and σ is the value of the centroid on the corresponding parameter space.

Behavioral analysis

CMVMJD135 mice and WT littermates treated with PLX3397 ($n = 15-18$ animals per group) or with ve-

hicle ($n = 14-16$ animals per group) were used for behavioral assessment (Additional file 1: Figure S1b). All behavioral tests were performed during the diurnal period. Before PLX3397 treatment, animals were tested in several motor behavioral paradigms monthly (at 6, 10, and 14 weeks of age) to make the animals get used to the tests and acquire the learning curve, and following PLX3397 administration, the behavioral assessment was conducted every two weeks until 33 weeks of age, that corresponds to an advanced disease stage, when the phenotype is fully established (Additional file 1: Figure S1b). At endpoint, at 34 weeks of age, animals were euthanized accordingly. These neurological/motor tests included (1) a general health and neurological assessment using a selection of tests from the SHIRPA protocol, namely assessment of body weight, strength to grab, spontaneous activity and gait quality, and limb clasping [50, 51]; (2) footprinting analysis and stride length measurement; (3) balance beam walk (12-*mm* square, 11-*mm* and 17-*mm* round beams); and (4) motor swimming tests. All behavioral tests used in this study were performed as previously described [30, 46, 52] and are briefly described below.

SHIRPA Protocol

A protocol for phenotypic assessment based on the primary screen of SHIRPA protocol was established in this study. This protocol mimics the diagnostic process of general neurological and psychiatric examination in humans [50]. A detailed description of the SHIRPA protocol is available online at https://www.mousephenotype.org/impress/protocol/82. A brief description of the tests follows below.

Body weight. All mice were weighed throughout the study from 6 weeks of age until the end of the trial (33 weeks of age).

Hanging wire grid test. Each animal was placed on the top of a metallic horizontal grid, which was slowly inverted and suspended at approximately 30 *cm* to the floor. The time it took each mouse to fall from the grid was recorded. After 120 seconds (the maximum time of the test), any animal still gripping the cage top was removed.

Spontaneous activity and gait quality. Mice were transferred to a 15-labelled-squares open arena ($55 \times 33 \times 18$ *cm*), and the number of squares travelled for 1 minute was counted. The gait quality was also assessed by the same researcher, where freely moving animals were scored as: normal, fluid but abnormal movement (incorrect posture of the body and tail, with decreased distance over the ground), limited (very limited movement), and unable to walk.

Limb clasping. To determine limb clasping, mice were picked by the tail and slowly descended towards a horizontal surface. The extension/contraction of the limbs was observed by the researcher and scored as absent (extension of the hindlimbs), mild (contraction in one of the hindlimbs), or severe (contraction in both hindlimbs).

Footprint analysis and stride length quantification

The footprint test was used to evaluate motor performance. To register footprint patterns of each mouse, the hind- and forepaws were coated with black or red non-toxic ink, respectively. A clean paper sheet was placed on the floor of the runway for each mouse run, and then the animals were encouraged to walk along a 100 *cm* long×4.2 *cm* width×10 *cm* height inclined runway in the direction of an enclosed safe black box. Because animals tend to run upwards to escape, an inclined runway was used, instead of a horizontal one. The stride length was obtained by measuring manually the distance between two pawprints. Three values were measured for six consecutive steps and the mean of the three values was used. To evaluate severity of footdragging, the same six consecutive steps were used,

and the dragging was scored as absent = 0, mild = 1 (up to three steps), and severe = 2 (more than three steps out of six).

Balance beam walk test

This test was performed as previously described [53] and assesses the ability of the animals to stay upright and to walk on an elevated beam (50 *cm* above the bench surface) without falling to sponges that are used to protect mice from falls. The beams (12-*mm* square, and 11-*mm* and 17-*mm* round beams) were placed horizontally with one end mounted on narrow support and the other end attached to an enclosed dark box, into which the mouse could escape. Mice were trained for 3 days (three trials per animal) in the square beam (12 *mm*), and in the fourth day, they were tested in the 12-*mm* square, and in the 11-*mm* and 17-*mm* round beams (two trials per animal were scored). The time each animal took to traverse the beams was scored and time was discounted whenever the animals stopped in the beam. The trial was considered invalid if the animal fell or turned around in the beam. Each animal was given the opportunity to fail twice.

Motor swimming test

To analyze voluntary locomotion in the water environment, each mouse was trained for two consecutive days (three trials per mouse) to traverse a clear perspex water tank (100 *cm* long) to a safe (black perspex-made) platform at the end, with the water temperature being monitored at 23 °C using a thermostat. Animals were tested for three consecutive days (two trials per mouse), and the latency to cross the tank was registered by the researcher from a 60 *cm* distance (the initiation position was marked with a blue line) [53].

Statistical Analysis

Mouse sample size was previously calculated, using the G-Power 3.1.9.2 software (University of Kiel, Germany), assuming a power of 0.95 and 0.8, for each behavioral test and histopathological analyses, respectively [52]. All statistical analyses were performed using SPSS 22.0 (SPSS Inc., Chicago, IL), and a significance level of $p < 0.05$ was used throughout this study. The assumption of normality was tested for all continuous variables through evaluation of the qualitative analysis of Q-Q plots and of the frequency distributions (z-score of skewness and kurtosis) as well as by the Kolmogorov-Smirnov and Shapiro-Wilk tests. Continuous variables with normal distributions were analysed with repeated-measures ANOVA for longitudinal multiple comparisons, using genotype and treatment as factors. The one-way analysis of variance (ANOVA), followed by Tukey HSD test, was used when data passed on the assumption of homogeneity of variances (evaluated by Levene's test). However, Dunnett T3's test was applied instead of the Tukey HSD test when the populations variances were not equal. Concerning non-normally distributed data and/or for the comparison of medians of discrete variables across time-points, a Friedman's ANOVA was carried out, with pairwise comparisons through the Kruskal-Wallis statistic test. GraphPad Prism 8 was used to create graphs, the mean being the considered measure of central tendency, while the measure of variability was the standard error of the mean (SEM).

Results

PLX3397 treatment promoted a reduction of the number of microglial cells in CMVMJD135 mice

To further understand the role of microglia in MJD, we applied a protocol to deplete microglia in the CMVMJD135 mice at a mid-stage of disease using PLX3397, an inhibitor of CSF1R signaling. Beginning at 18 weeks of age, the CSF1R inhibitor PLX3397 or vehicle were delivered to CMVMJD135 and WT littermates every day by oral gavage for three weeks, thus generating four experimental groups: WT + ve-

hicle, WT + PLX3397, CMVMJD135 + vehicle, and CMVMJD135 + PLX3397.

In accordance to our previous observations [29], at 21 weeks of age, a significant decrease in the number of microglial cells was found in the cerebellar lobules (1593 ± 536 microglia per mm^3; $p = 0.047085$) (Figure 1e,f,n) and in the PN (2743 ± 748 microglia per mm^3; $p = 0.019112$) (Figure 1i,j,o) but not in the DCN (Figure 1a,b,m) of vehicle-treated CMVMJD135 mice when compared with vehicle-treated WT mice. This suggests the possibility of mutant ATXN3 causing glia toxicity or/and a consequence of their interaction with neurons and/or other cells, which can eventually lead to microglial death processes.

The treatment of both CMVMJD135 and WT mice with PLX3397 led to a decrease in the number of microglia in the DCN, lobules, and PN when compared to vehicle-treated CMVMJD135 and WT animals, respectively. In fact, the PLX3397 treatment resulted in (1) a 59 % reduction in the number of microglial cells in the lobules of both CMVMJD135 (3285 ± 565 microglia per mm^3; $p = 0.000313$) and WT (4105 ± 536 microglia per mm^3; $p = 0.000019$) groups; (2) a 42 % reduction in the PN of both CMVMJD135 (3652 ± 748 microglia per mm^3; $p = 0.003001$) and WT (4756 ± 748 microglia per mm^3; $p = 0.000402$) groups; and (3) a 51 % reduction in microglial density in the DCN of CMVMJD135 mice (5072 ± 1086 microglia per mm^3; $p = 0.002164$) and in a 43 % reduction in WT mice (5207 ± 1030 microglia per mm^3; $p = 0.001106$). No significant differences were found in the proportion of microglial cells lost upon PLX3397 treatment between CMVMJD135 and WT mice in the affected brain regions, suggesting that microglial mutant *ATXN3* expression does not alter the dependence of these cells on CSF1R signaling for survival.

PLX3397 treatment did not promote morphological changes in microglia from CMVMJD135 mice

In addition to the observed partial depletion, we determined the effects of PLX3397 on the morphology of the remaining microglial cells in the DCN and PN of CMVMJD135 and WT mice, at 21 weeks of age.

Regarding the skeleton data of the 2291 analyzed single microglial cells, only four out of ten parameters (number of branches, junctions voxels, triple points, and quadruple points) were not found to be statistically different between the four groups (CMVMJD135 + vehicle and CMVMJD135 + PLX3397, and WT + vehicle and WT + PLX3397) in the PN (Additional file 2: Figure S1).

On the other hand, regarding the fifteen fractal parameters, only four (density, convex hull circularity, ratio of convex hull radii, and convex hull span ratio) were not found to be statistically different between the four groups in the DCN (Additional file 2: Figure S2), while two more (fractal dimension, and lacunarity) were not found to be statistically different in the PN (Additional file 2: Figure S3).

Hence, significant morphological changes were found, in both DCN and PN brain regions, in parameters relevant to cell ramification, size, surface, and soma thickness (Figure 2 and Additional file 2: Figure S4 and S5, and Figure 3 and Additional file 2: Figure S6 and S7, respectively), suggesting that microglia from CMVMJD135 + vehicle mice are more activated when compared with those from WT + vehicle mice. Indeed, when compared with microglial cells from WT + vehicle mice, those from CMVMJD135 + vehicle mice were found to (1) have less and shorter branches; (2) to be less tortuous; (3) to be less ramified; (Figure 2, Figure 3, and Additional file 2: Figure S4 and S6); (4) to have smaller size and surface; and (5) with higher soma thickness (Figure 2, Figure 3, and Additional file 2: Figure S5 and S7) and Table 1. However, these al-

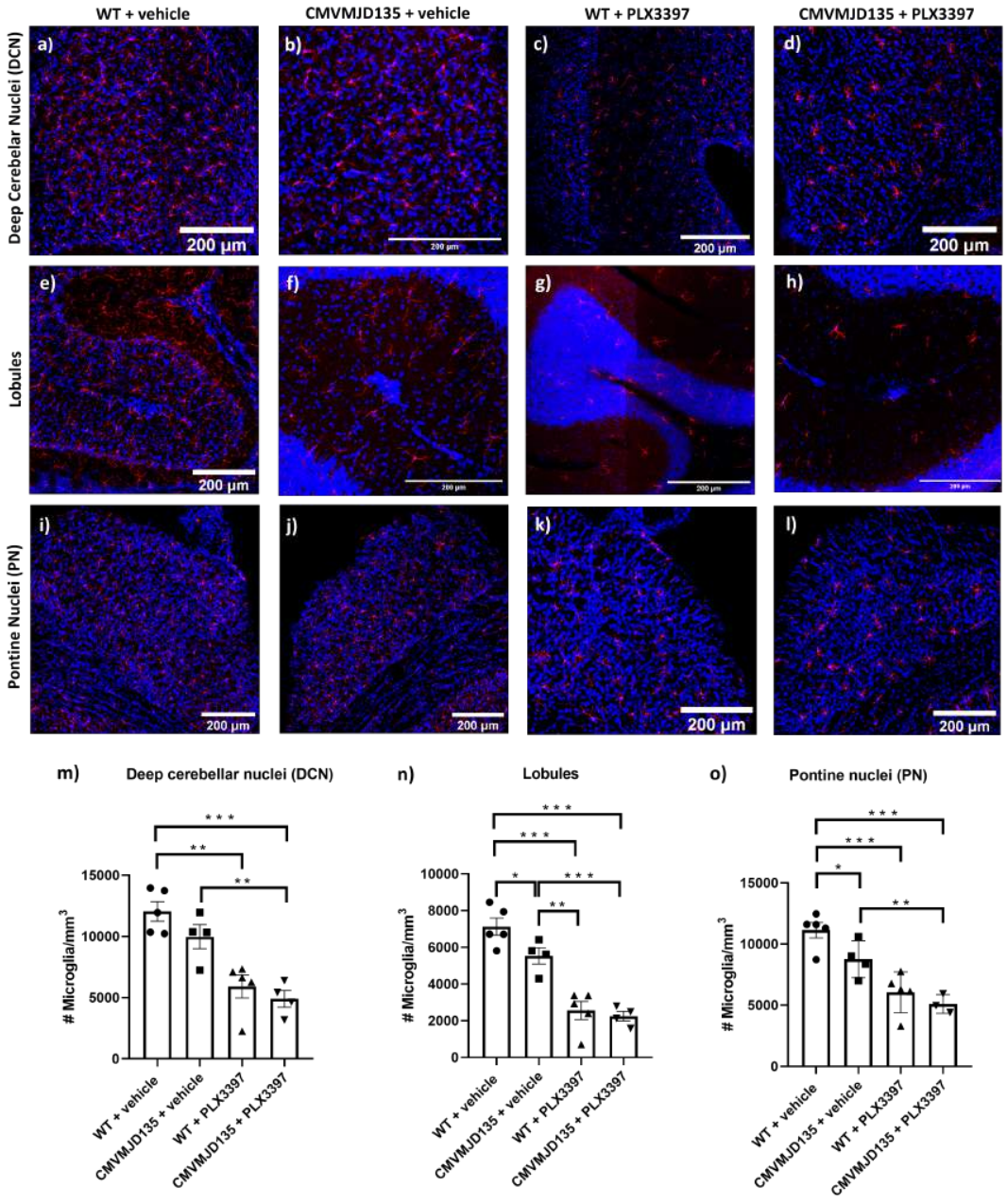

Figure 1 Microglial population halved by PLX3397 in CMVMJD135 mice. a-l) Representative images of microglial cells, using Iba-1 as a microglia marker (in red), from the DCN **a-d)** and from the lobules **e-h)**, of the cerebellum, and from the PN **i-l)**, in the brainstem of WT and CMVMJD135 mice treated with PLX3397 **c, d, g, h, k, l)** or vehicle **a, b, e, f, i, j)**. **m-o)** Quantitative analysis of the number of microglial cells per mm^3 in the **m)** DCN, **n)** lobules, and **o)** PN from PLX3397 or vehicle-treated WT and CMVMJD135 mice ($n = 3 - 5$ animals per group). Data are presented as mean+SEM (One-way ANOVA (Post hoc Tukey's test)). *, **, ***, represent the $p < 0.05$, $p < 0.01$, and $p < 0.001$, respectively. Scale bar 200 μm.

terations were not found at a late stage of the disease, in both affected brain regions, the DCN and PN. This suggests a functional adaptation of these cells to the

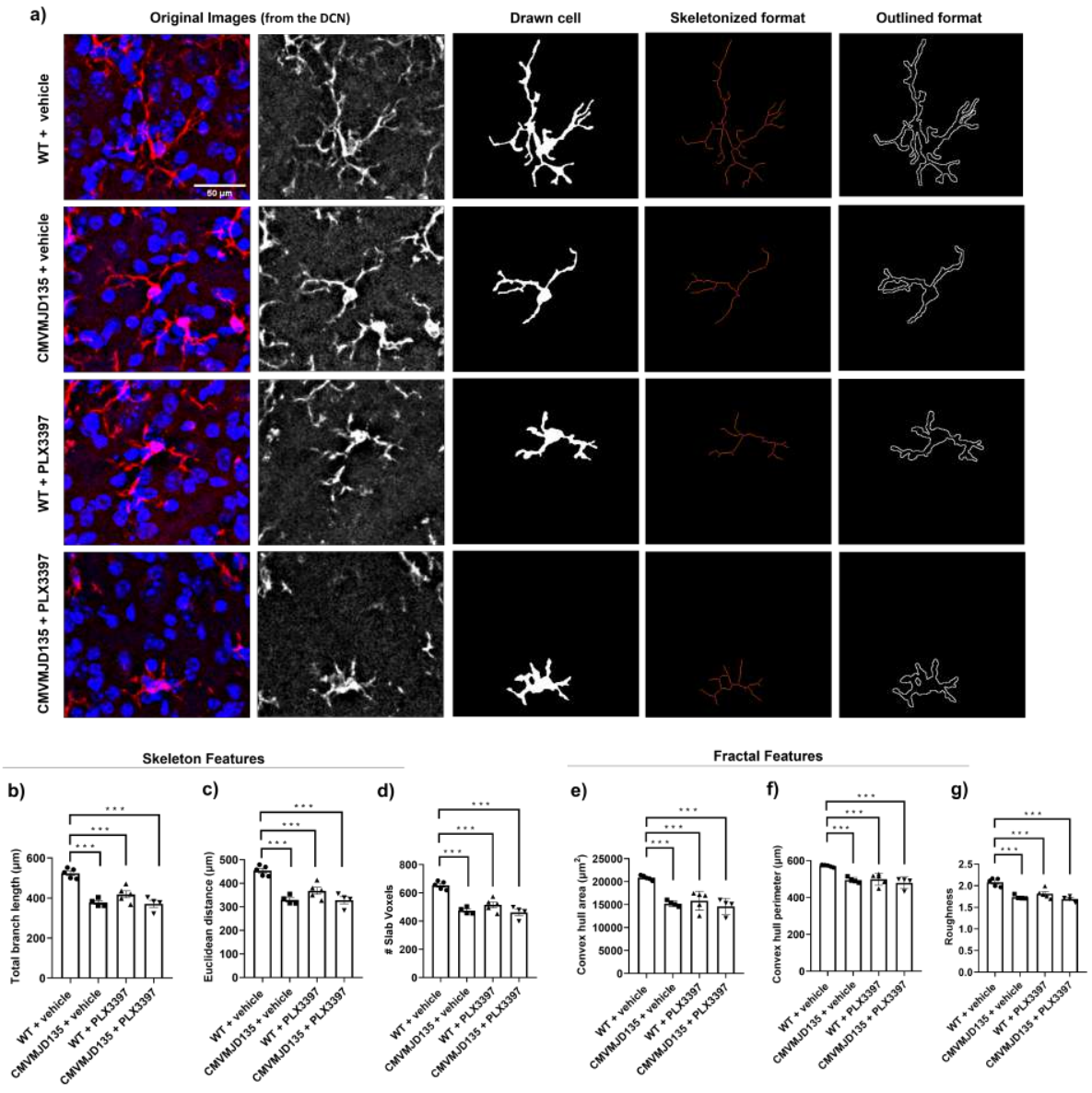

Figure 2 Treatment with PLX3397 did not induce morphological changes in the microglia in the DCN of CMVMJD135 mice at 21 weeks of age. a) Representation of the process to prepare the images for skeleton and fractal analysis of microglia morphology. These images show differences regarding the features relevant to cell ramification (from skeleton data) and relevant to cell size, surface, and soma thickness (from fractal data). Quantification of the morphometric parameters associated to microglia ramification: **b)** total branch length; **c)** euclidean distance; and **d)** # slab voxels. Associated with cell size: **e)** convex hull area; and **f)** convex hull perimeter. Associated with cell surface: **g)** roughness. Data of all these parameters were obtained from: 387 microglial cells from WT + vehicle mice ($n = 5$); 256 microglial cells from CMVMJD135 + vehicle mice ($n = 4$); 475 microglial cells from WT + PLX3397 mice ($n = 5$); and 263 microglial cells from CMVMJD135 + PLX3397 mice ($n = 4$). Data are presented as mean+SEM (One-way ANOVA (Post hoc Tukey's test)). ***, represent $p < 0.001$. Scale bar 50 μm.

characteristics of their microenvironment, which may differ according to the stage of the disease.

Curiously, CSF1R inhibition by PLX3397 treatment on CMVMJD135 mice did not induce further morpho-

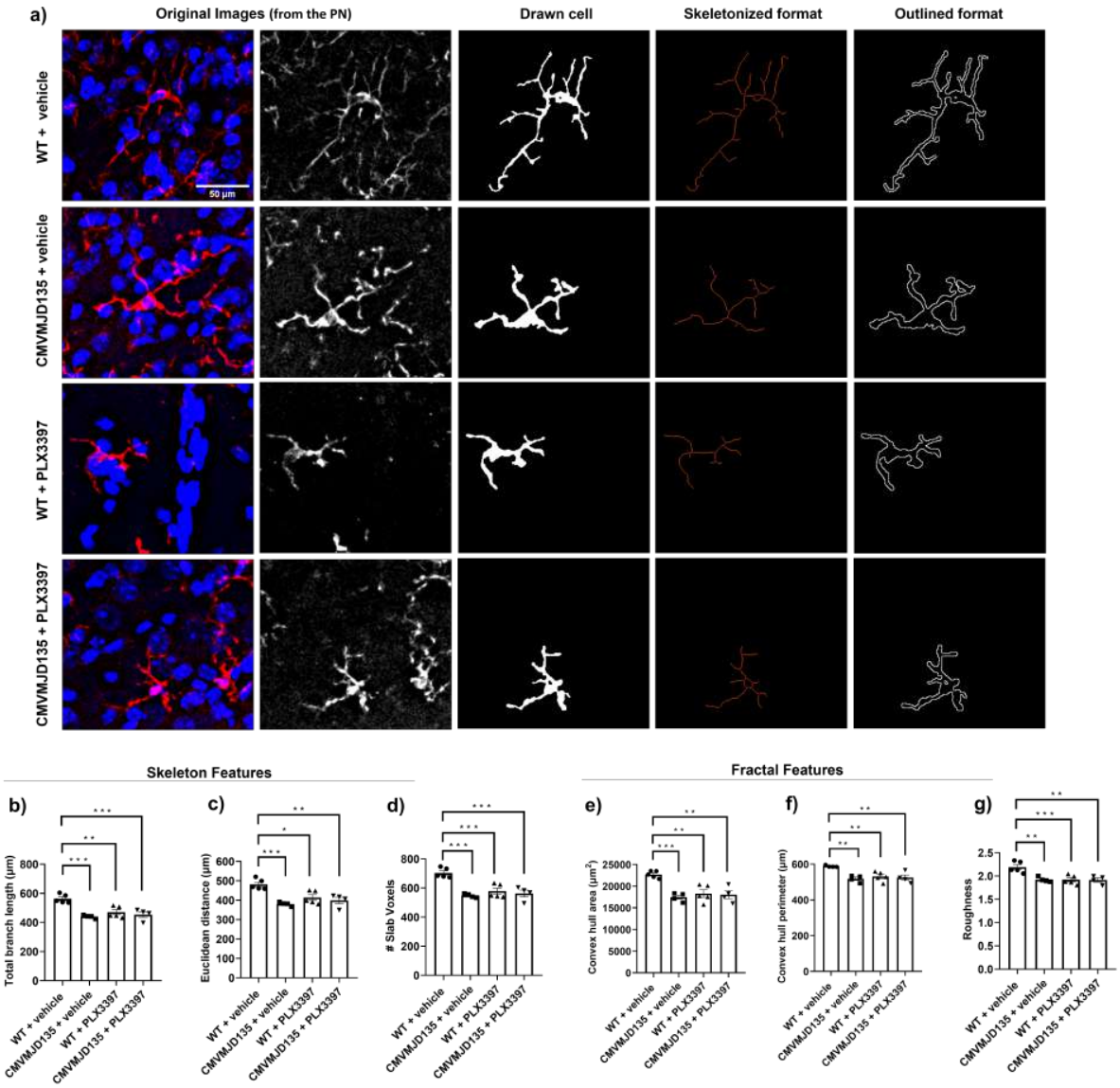

Figure 3 Microglial activation observed in the PN of CMVMJD135 mice, at 21 weeks of age, is not altered by PLX3397 treatment. a) Representation of the process to prepare the images for skeleton and fractal analysis of microglia morphology. These images show differences regarding the features relevant to cell ramification (from skeleton data) and relevant to cell size, surface, and soma thickness (from fractal data). Quantification of the morphometric parameters associated to microglia ramification: **b)** total branch length; **c)** euclidean distance; and **d)** # slab voxels. Associated with cell size: **e)** convex hull area; and **f)** convex hull perimeter. Associated with cell surface: **g)** roughness. Data of all these parameters were obtained from: 210 microglial cells from WT + vehicle mice ($n = 4$); 217 microglial cells from CMVMJD135 + vehicle mice ($n = 4$); 248 microglial cells from WT + PLX3397 mice ($n = 5$); and 235 microglial cells from CMVMJD135 + PLX3397 mice ($n = 5$). Data are presented as mean+SEM (One-way ANOVA (Post hoc Tukey's test)). *, **, ***, represent $p < 0.05$, $p < 0.01$ and $p < 0.001$, respectively. Scale bar 50 μm.

logical changes in the features associated to cell ramification, size, surface, and soma thickness, because no differences were found between CMVMJD135 + vehicle and CMVMJD135 + PLX3397 mice, in both re-

Table 1 Significant morphological changes found in both brain regions, DCN and PN, in features relevant to cell ramification, size, surface, and soma thickness. "WT VEH" stands for WT + vehicle mice; "MJD VEH" for CMVMJD135 + vehicle mice; "MJD PLX" for CMVMJD135 + PLX3397 mice; and "WT PLX" for WT + PLX3397 mice. A significance level of $p < 0.05$ was used. N. S. stands for non significant values.

	WT VEH vs MJD VEH		WT VEH vs MJD PLX		WT VEH vs WT PLX	
	DCN	PN	DCN	PN	DCN	PN
Cell ramification features (p-values)						
Nº of branches	0.000477	N.S.	0.00800	N.S.	N.S.	N.S.
Total branch length	0.000004	0.000074	0.000002	0.000074	0.000312	0.001628
Euclidean distance	0.000007	0.000174	0.000005	0.002507	0.000788	0.011000
Nº of slab voxels	0.000003	0.000027	0.000007	0.000127	0.000074	0.000298
Nº of junctions	0.000248	0.039256	0.004317	N.S.	N.S.	N.S.
Nº of junctions voxels	0.000593	N.S.	0.011179	N.S.	N.S.	N.S.
Nº of endpoints voxels	0.000361	0.025005	0.007278	N.S.	N.S.	N.S.
Nº of triple points	0.000949	N.S.	0.010280	N.S.	N.S.	N.S.
Nº of quadruple points	0.001122	N.S.	0.018000	N.S.	N.S.	N.S.
Max. branch length	N.S.	N.S.	N.S.	N.S.	0.028847	0.001628
Average branch length	N.S.	N.S.	N.S.	N.S.	N.S.	0.000738
Cell complexity and shape features (p-values)						
Convex hull area	0.000080	0.000246	0.000016	0.001212	0.000186	0.001170
Convex hull perimeter	0.000738	0.001747	0.000054	0.004893	0.000692	0.007210
Diameter bounding circle	0.004057	0.005877	0.000203	0.013184	0.002651	0.015690
Mean radius	0.003004	0.003518	0.000158	0.013447	0.002305	0.023623
Max. span across convex hull	0.004383	0.006752	0.000197	0.014309	0.002723	0.014764
Cell area	0.001454	N.S.	N.S.	N.S.	N.S.	N.S.
Cell perimeter	0.000010	0.000056	0.000001	0.000136	0.000064	0.000096
Roughness	0.000042	0.001423	0.000006	0.001110	0.000208	0.000584
Cell circularity	0.017501	N.S.	0.000001	0.002756	0.000019	0.002997
Lacunarity	N.S.	N.S.	N.S.	N.S.	0.002194	N.S.
Fractal dimension	0.007317	N.S.	N.S.	N.S.	N.S.	N.S.

gions (Figure 2, Figure 3, and Additional file 2: Figure S4-S7). Like CMVMJD135 + vehicle-derived microglia, CMVMJD135 + PLX3397-derived microglia, when compared with WT + vehicle, were also found to have less and shorter branches, to be less tortuous, to be less ramified, with smaller size and surface, and with higher soma thickness. In fact, in both regions, multiple parameters were found to be decreased in CMVMJD135 + PLX3397-derived microglia when compared with WT + vehicle, namely: total branch length; number of branches; Euclidean distance; number of slab voxels; number of junctions voxels; number of endpoints voxels; number of triple points; and the number of quadruple points (Figure 2, Figure 3, and Additional file 2: Figure S4 and S6) and Table 1. On the other hand, in contrast to the cell circularity, which was found to be increased in the CMVMJD135 + PLX3397 group when compared with the WT + vehicle group, the following features, associated with cell size and surface, were found to be decreased, namely: convex hull area; convex hull perimeter; diameter of the bounding circle; mean radius; maximum span across the convex hull; cell perimeter; and roughness (Figure 2, Figure 3, and Additional file 2: Figure S5 and S7) and Table 1. These alterations suggest that microglial cells from CMVMJD135 + vehicle and the

surviving microglia from CMVMJD135 + PLX3397 mice are similar and show an activation profile, which is not apparently dependent on CSF1R signaling.

In contrast, in both regions, treatment with PLX3397 on WT mice promoted morphological changes associated with microglial cells becoming more activated, these cells becoming similar to those of CMVMJD135 animals (PLX3397-treated and vehicle-treated) in some of the analyzed parameters, namely, the total branch length, Euclidean distance, number of slab voxels, convex hull area, convex hull perimeter, diameter of the bounding circle, mean radius, maximum span across the convex hull, cell perimeter, roughness, and cell circularity (Figure 2, Figure 3, and Additional file 2: Figure S4-S7). In fact, in both regions, skeleton data showed significant differences in microglial cells from WT + PLX3397 mice when compared with those from WT + vehicle mice. The total branch length, Euclidean distance, number of slab voxels, and maximum branch length were lower in microglial cells from WT + PLX3397 mice (Figure 2, Figure 3, and Additional file 2: Figure S4 and S6) and Table 1. Additionally, alterations in parameters associated with the heterogeneity of the shape, cell size, cell surface, and soma thickness were also observed, namely a decreased convex hull area, convex hull perimeter, diameter of the bounding circle, mean radius, maximum span across the convex hull, cell perimeter, roughness, and lacunarity (Figure 2, Figure 3, and Additional file 2: Figure S5 and S7) and Table 1. On the other hand, an increased cell circularity was observed in the WT + PLX3397 group (Additional file 2: Figure S5 and S7) and Table 1.

PLX3397-treated WT-derived microglia showed an activation profile similar to CMVMJD135-derived microglia

The morphological analysis of microglial cells from the DCN and PN of CMVMJD135 (PLX3397- and vehicle-treated) and WT (PLX3397- and vehicle-treated) mice was performed by measuring a total of twenty-six different parameters to evaluate microglia ramification, complexity, cell size, cell surface, and soma thickness. Hence, considering all statistically significant differences that were found between the four groups, in both regions, a PCA was performed to reduce the parameters' dimensionality to a two-dimensional space, obtained based on two principal components. In the DCN, the PCA preserves 96.1 % of the entire information present in the twenty-two statistically different parameters (PC0 = 76.7 % and PC1 = 19.4 %). On the other hand, in the PN, the PCA preserves 93.1 % of the entire information present in the sixteen statistically different parameters (PC0 = 71.4 % and PC1 = 21.7 %).

For both brain regions, scatter plots were designed, plotting each animal as a point in a two-dimensional space on the principal components plane. Figure 4a and Figure 5a display the two-dimensional space of WT + vehicle and CMVMJD135 + vehicle mice for the DCN and PN, respectively, a clear separation between these two groups being easily noticeable (established by the first principal component - PC0), which strengthens the assumption that microglia from CMVMJD135 + vehicle mice are different from those of WT + vehicle mice. The remaining groups (WT + PLX3397 and CMVMJD135 + PLX3397) were plotted closer to the CMVMJD135 + vehicle mice in both regions (Figure 4b,c for the DCN and Figure 5b,c for the PN), suggesting that these three groups share similarities among them. Treatment with PLX3397 had a reduced impact on the profile of microglia of CMVMJD135 mice, whereas it brings WT-derived microglia into a state of activation that resembles the one of MJD mice.

To further visualize the relationships between multiple significant parameters found to be altered in WT + vehicle mice when compared to the remain-

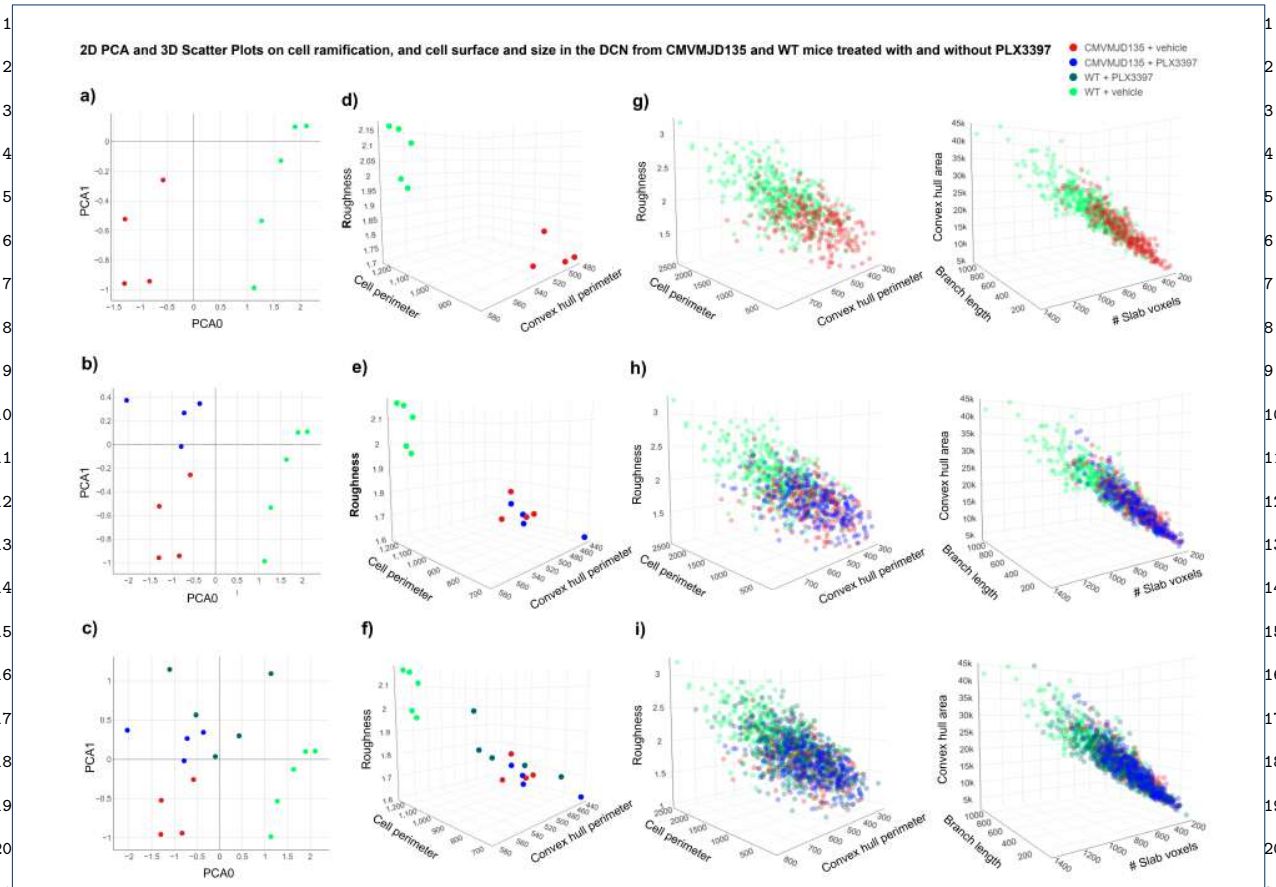

Figure 4 Separation of WT + vehicle group and all the remaining groups, including WT + PLX3397, CMVMJD135 + vehicle, and CMVMJD135 + PLX3397 mice, regarding the twenty-two significant morphological parameters found in the microglial cells from the DCN. a) 2D scatter plot showing the distribution of WT + vehicle mice (in green) and CMVMJD135 + vehicle (in red) on a principal components plane. **b,c)** 2D scatter plots showing that the remaining groups (WT + PLX3397 and CMVMJD135 + PLX3397) were plotted closer to CMVMJD135 + vehicle mice, regarding the twenty-two significant morphological parameters found in the DCN. **d,e,f)** 3D scatter plots showing a separation between WT + vehicle mice and the remaining groups regarding their roughness, cell perimeter, and convex hull perimeter. **g,h,i)** Data points of a total of 387 microglial cells from WT + vehicle mice, 256 microglial cells from CMVMJD135 + vehicle mice, 475 microglial cells from WT + PLX3397 mice, and 263 microglial cells from CMVMJD135 + PLX3397 mice were plotted on a 3D space, showing the relationship between roughness, cell perimeter, and convex hull perimeter, and between convex hull area, total branch length, and number of slab voxels.

ing groups (WT + PLX3397, CMVMJD135 + vehicle, and CMVMJD135 + PLX3397 mice), scatter plots on a three-dimensional space were designed for both regions (Figure 4d,e,f for the DCN and Figure 5d,e,f for the PN). Again, a clear separation between WT + vehicle mice and the remaining groups is noticeable, reinforcing the previous observations. Finally, scatter plots were conceived over 1381 single microglial cells for the DCN (Figure 4g,h,i) and 910 for the PN (Figure 5g,h,i), displaying all these cells on a three-dimensional space for three additional significant morphological parameters. Once more, it is possible to visualize that microglial cells from the WT + vehicle group are clustered together in higher values of convex hull area, total branch length, and number of slab voxels, whereas microglia from the three remaining groups are over-

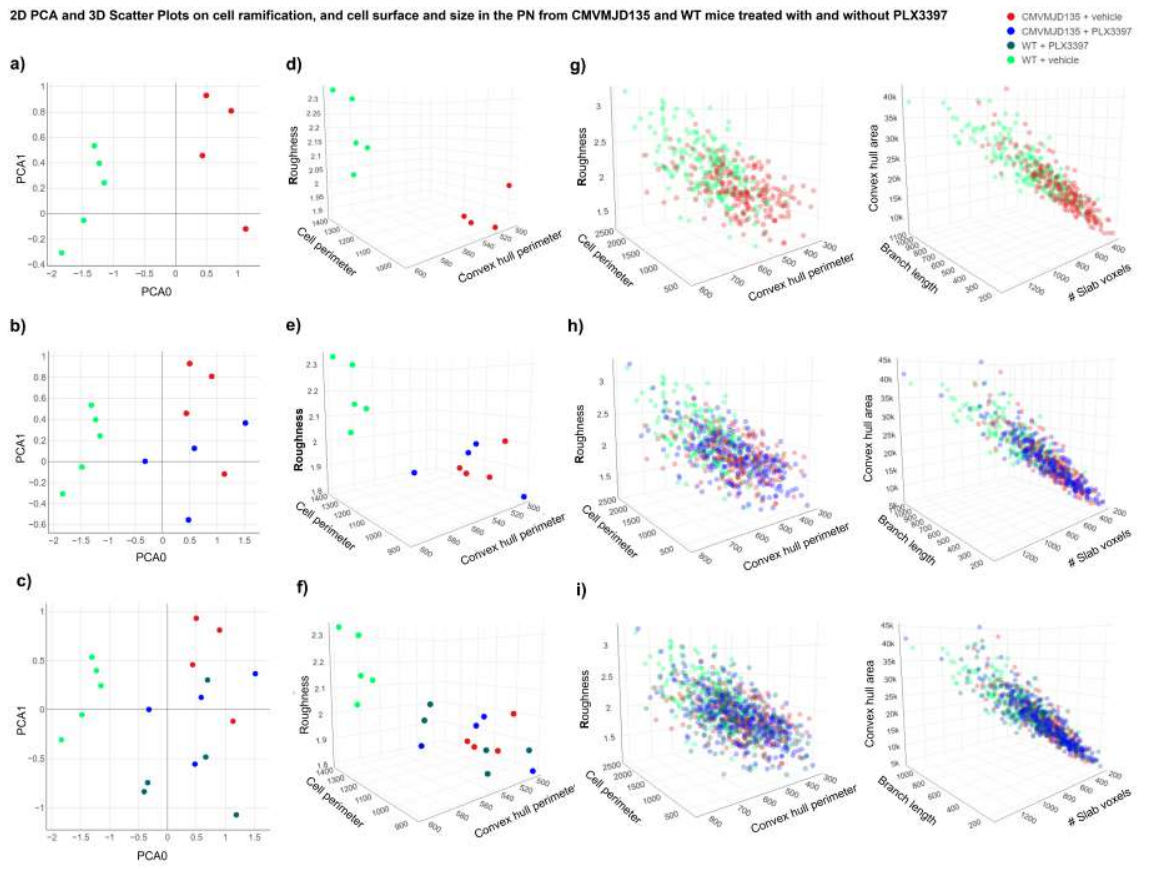

Figure 5 Separation of WT + vehicle group and all the remaining groups, including WT + PLX3397, CMVMJD135 + vehicle, and CMVMJD135 + PLX3397 mice, regarding the sixteen significant morphological parameters found in the microglial cells from the PN. a) 2D scatter plot showing the distribution of WT + vehicle mice (in green) and CMVMJD135 + vehicle (in red) on a principal components plane. **b,c)** 2D scatter plots showing that the remaining groups (WT + PLX3397 and CMVMJD135 + PLX3397) were plotted closer to CMVMJD135 + vehicle mice as a function of the sixteen significant parameters found in the PN. **d,e,f)** 3D scatter plots showing a separation between WT + vehicle mice and the remaining groups regarding their roughness, cell perimeter, and convex hull perimeter. g,h,i) Data points of a total of 210 microglial cells from WT + vehicle mice, 217 microglial cells from CMVMJD135 + vehicle mice, 248 microglial cells from WT + PLX3397 mice, and 235 microglial cells from CMVMJD135 + PLX3397 mice were plotted on a 3D space, showing the relationship between roughness, cell perimeter, and convex hull perimeter, and the relationship between convex hull area, total branch length, and number of slab voxels.

lapping with each other, assuming lower values for the referred parameters.

The PCA showing promising prospects regarding the existence of two distinct clusters, an unsupervised Machine Learning model, the k-means, was used to validate and identify clusters of data with similar characteristics within the entire dataset of microglial cells. Using all the statistically significant parameters found in microglial cells from the DCN (twenty-two parameters) and from the PN (sixteen parameters), the elbow method was implemented to identify the ideal number of clusters. As depicted in Additional file 2: Figure S8, the largest drop in the error is found when defining two clusters for both regions, which reinforces the assumption that CSF1R inhibition with PLX3397 promoted morphological changes that led to microglial cells of

WT mice becoming closer to those of CMVMJD135 mice (PLX3397-treated and vehicle-treated).

Once the ideal number of clusters was found, these clusters were plotted in a four-dimensional space, with the color, which defines the clusters, as a fourth dimension. Additional file 2: Figure S8 show the relationship between multiple significant morphological parameters for both regions. An analysis on the two conceived clusters shows that cluster 1, in green, is mainly composed of microglial cells from WT + vehicle mice, which are more ramified, have longer branches, and higher size and surface. The exception is two WT + PLX3397 mice that are clustered together with WT + vehicle mice in the DCN, and two WT + PLX3397 mice plus one CMVMJD135 + PLX3397 mouse in the PN. Conversely, cluster 0, in red, contains the majority of the animals of the remaining groups, which have typically smaller values regarding parameters associated with cell ramification, size, and surface.

Altogether, these alterations suggest that, in addition to partial microglial depletion, CSF1R inhibition by PLX3397 promotes activation of the remaining microglial cells making cells from WT + PLX3397 mice became more similar to those of CMVMJD135 animals (either PLX3397-treated or vehicle-treated), both showing an activated state.

PLX3397 treatment had no impact on the motor phenotype of CMVMJD135 mice

We have recently shown morphological alterations that point to an increased activation state, and pinpointed molecular pathways involved with oxidative stress, immune response, and lipid metabolism as significantly altered in microglia from CMVMJD135 mice [29]. However, it is unknown if and how these cells actively contributing to the disease process and symptoms progression of MJD. To study this contribution, we evaluated the impact of microglial cells depletion with PLX3397 on the motor phenotype of CMVMJD135 mice. For this, we submitted these mice (PLX3397-treated and vehicle-treated) to various tests to evaluate different components of the behavioral motor dimension, such as motor coordination and balance, muscular strength, and gait, from 6 to 33 weeks of age.

To understand whether the treatment with PLX3397 has impact on the motor (un)coordination of this animal model, we first used the motor swimming test. While, as expected, the CMVMJD135 mice (vehicle-treated) displayed swimming impairments over time given by a significant increase in the time spent to cross the 60 cm distance when compared with WT mice (vehicle-treated) (Figure 6a), no significant differences were found between CMVMJD135 + PLX3397 and CMVMJD135 + vehicle mice, and between WT + PLX3397 and WT + vehicle mice throughout age (Figure 6a), suggesting that the treatment with PLX3397 had no impact on swimming performance of CMVMJD135 or WT mice.

Because CMVMJD135 mice have difficulties in maintaining balance and show progressive impairments in fine motor control, we aimed to understand if PLX3397 treatment modified this phenotype. For this, we tested the ability of the mice to maintain balance while traversing a narrow beam to reach a safe platform. In the 12-*mm* square beam, no significant differences were found between CMVMJD135 + PLX3397 and CMVMJD135 + vehicle mice, and between WT + PLX3397 and WT + vehicle mice over time (Figure 6b), although, as expected, CMVMJD135 mice (vehicle-treated) showed a significantly worse performance traversing the 12-*mm* square beam when compared with WT mice (vehicle-treated) (Figure 6b). With disease progression, CMVMJD135 mice (PLX3397-treated and vehicle-treated) showed a worsening of the phenotype that affected their ability to perform this task, causing them to fall off the beams

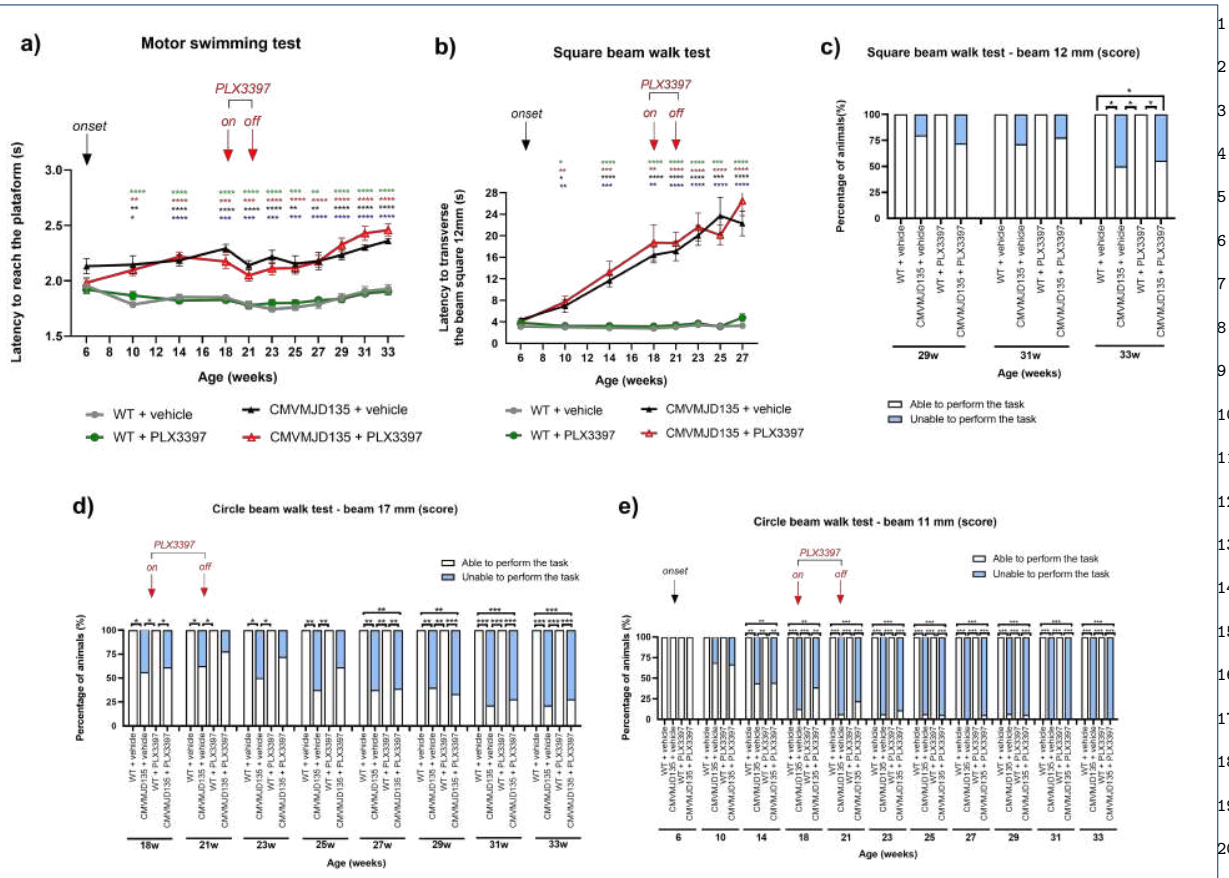

Figure 6 PLX3397 treatment had no impact on the motor coordination and balance deficits of CMVMJD135 mice. a) Motor swimming test showed that CMVMJD135 mice (PLX3397- and vehicle-treated) spent more time swimming to reach the safe platform than WT mice (PLX3397- and vehicle-treated), throughout age. No significant differences were found between PLX3397-treated and vehicle-treated mice (curve comparison over time $p > 0.05$, 6–33 weeks). *One-way ANOVA (Post hoc Dunnett T3 test)*. **b)** In the square beam test, no differences were found between CMVMJD135 + PLX3397 and CMVMJD135 + vehicle mice, and between WT + PLX3397 and WT + vehicle mice (curve comparison over time $p > 0.05$, 6–27weeks). *One-way ANOVA (Post hoc Dunnett T3 test)*. In both motor swimming and square beam tests, asterisks indicate significant differences which were found between: * WT + vehicle and CMVMJD135 + vehicle; * WT + vehicle and CMVMJD135 + PLX3397; * WT + PLX3397 and CMVMJD135 + vehicle; and * WT + PLX3397 and CMVMJD135 + PLX3397. The 12 mm-square beams walk test (at 29, 31, and 33 weeks of age) and the 17 mm-round beams walk test (from 18 weeks of age onwards), were analysed by scoring the animals. **c)** In the square beam (score) and **d)** in the circle beam of 17 mm-round (score), significant differences were found between CMVMJD135 + vehicle mice and WT + vehicle mice, but no differences were found between CMVMJD135 + PLX3397 and CMVMJD135 + vehicle mice, and between WT + PLX3397 and WT + vehicle mice. *Friedman test with Kruskal-Wallis analysis*. **e)** In the circle beam of 11 mm-round (score), results showed significant differences between WT + vehicle and CMVMJD135 + vehicle, but not between PLX3397-treated and vehicle-treated mice, from 14 weeks to 33 weeks of age. *Friedman test with Kruskal-Wallis analysis*. Values are presented as mean ± SEM or as percentage of animals (%) (for the continuous and non-continuous variables, respectively). Means were considered statistically significant at a p-value * $p < 0.05$, ** $p < 0.01$, *** $p < 0.001$, **** $p < 0.0001$.

frequently. We analyzed these data by attributing performance scores to the animals as follows: 0 – able to perform the task (can walk on the beam), and 1 – Unable to perform the task (cannot walk on the beam). Again, PLX3397 treatment had no impact on the performance of the animals traversing the 12 mm-square

beam (at 29, 31, and 33 weeks of age) and the 17 *mm*-round beam (from 18 weeks of age onwards), as no significant differences being found between CMVMJD135 + PLX3397 and CMVMJD135 + vehicle mice, and between WT + PLX3397 and WT + vehicle mice (Figure 6c,d). Once more, and as expected, significant differences were found between CMVMJD135 + vehicle mice and WT + vehicle mice, the former performing significantly worse than the latter, when traversing both the 12-*mm* square and 17 *mm*-round beams (Figure 6c,d).

Difficulties in traversing the 11 *mm*-round beam were observed in CMVMJD135 + vehicle mice from 14 weeks of age onwards when compared with WT + vehicle mice. Consistently with the previous results, the difficulty in performing this task was similar for CMVMJD135 + PLX3397 and CMVMJD135 + vehicle mice, and all animals from both WT + PLX3397 and WT + vehicle groups were able to complete the task in all timepoints analysed (Figure 6e), suggesting that motor and balance deficits observed in CMVMJD135 + PLX3397 animals can be attributed to their genotype, not being affected by microglial depletion. Of notice, PLX3397 administration to WT mice caused no overall toxicity and had no effect on their motor performance.

Microglial depletion in CMVMJD135 mouse showed no effect on gait quality

The footprint test, used to evaluate gait quality, also revealed that the treatment with PLX3397 had no impact on this aspect of the phenotype of CMVMJD135 or WT animals, as no significant differences were found between CMVMJD135 + PLX3397 and CMVMJD135 + vehicle mice, or between WT + PLX3397 and WT + vehicle mice, in the distance between the front and hind footprint (stride length) throughout age (Figure 7a). However, and in agreement with previous observations, from 14 until 33 weeks of age, CMVMJD135 mice (vehicle-treated) displayed reduced stride length when compared with WT mice (vehicle-treated) (Figure 7a). In addition, PLX3397 treatment had no impact in the severity of the footdragging phenotype observed in CMVMJD135 animals, CMVMJD135 + PLX3397 mice not differing significantly from CMVMJD135 + vehicle mice throughout age. WT mice (PLX3397- and vehicle-treated) did not show footdragging in all timepoints analysed (Figure 7b). No significant difference in spontaneous exploratory activity, was found between vehicle-treated and the PLX3397-treated transgenic mice. The gait quality was also qualitatively assessed in the open arena, onset of an abnormal gait being observed at 10 weeks in both CMVMJD135 + PLX3397 and CMVMJD135 + vehicle mice (Figure 7c,d). We also observed no beneficial or deleterious effect of the PLX3397 treatment on this parameter throughout age (Figure 7c,d).

Muscular strength and general well-being of MJD mice were not affected by microglial depletion

Some parameters of the SHIRPA protocol were also used to assess the impact of PLX3397 treatment in the motor and neurological dysfunction of CMVMJD135 mice. CMVMJD135 mice (PLX3397- and vehicle-treated) displayed significantly lower body weight gain than WT mice (PLX3397- and vehicle-treated) throughout time (Figure 8a). No differences were found among PLX3397- and vehicle-treated mice, regarding this parameter (Figure 8a).

Loss of muscular strength is a very early and severe symptom observed in CMVMJD135 mice [30, 46]. However, a similar performance in the hanging wire grid test was observed between CMVMJD135 + PLX3397 and CMVMJD135 + vehicle mice, suggesting that the PLX3397 treatment does not impact the muscular strength of CMVMJD135 animals (Figure 8b).

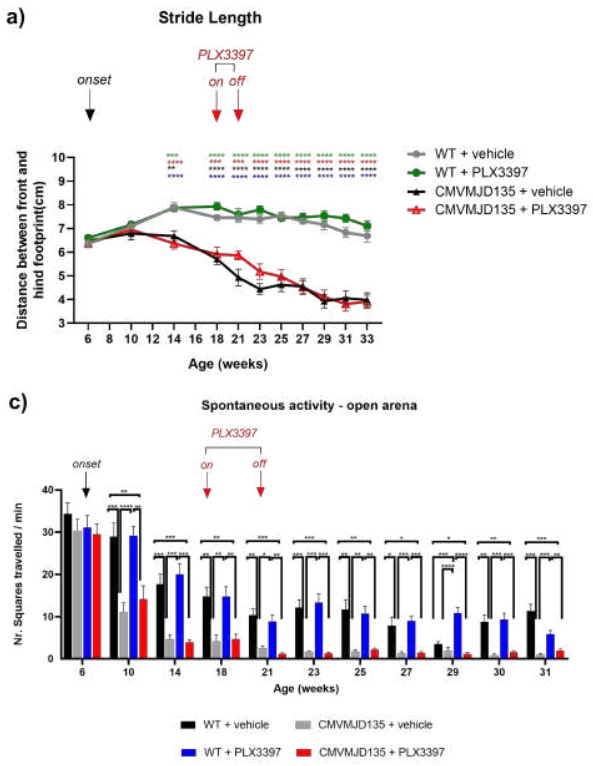

Figure 7 Abnormal stride length and footdragging phenotype observed in CMVMJD135 animals is not affected by PLX3397 treatment. a) The treatment with PLX3397 had no impact on the gait quality of CMVMJD135 mice, which displayed an abnormal stride length when compared with WT mice. Asterisks indicate significant differences which were found between: * WT + vehicle and CMVMJD135 + vehicle; * WT + vehicle and CMVMJD135 + PLX3397; * WT + PLX3397 and CMVMJD135 + vehicle; and * WT + PLX3397 and CMVMJD135 + PLX3397. *One-way ANOVA (Post hoc Tukey's test).* **b)** PLX3397 treatment had no impact on the severity of the footdragging phenotype that is observed in CMVMJD135 animals, which displayed a worsening of the footdragging phenotype with age. *Friedman test with Kruskal-Wallis analysis.* **c)** and **d)** no therapeutic effect of the PLX3397 treatment on abnormal gait observed in CMVMJD135 mice throughout age. *Friedman test with Kruskal-Wallis analysis.* Values are presented as mean ± SEM or as percentage of animals (%) (for the continuous and non-continuous variables, respectively). Means were considered statistically significant at a p-value ** $p < 0.01$, *** $p < 0.001$, **** $p < 0.0001$.

Abnormal reflexes (limb clasping) are another phenotypic characteristic of the CMVMJD135 mouse model that was detectable since 10 weeks of age in both groups of transgenic animals (CMVMJD135 + PLX3397 and CMVMJD135 + vehicle mice) (Figure 8c). However, this phenotypic characteristic was not significantly modified by PLX3397 treatment, as no differences being observed between CMVMJD135 + PLX3397 and CMVMJD135 + vehicle mice, from 10 until 33 weeks of age (Figure 8c).

Discussion

We have previously demonstrated morphological, phenotypic, and transcriptomic alterations that point to an increased activation state of microglial cells during the late stages of disease in CMVMJD135 mice [29]. Here, we aimed to understand if these alterations are, or not, actively contributing for disease onset and progression in MJD. Hence, to study the contribution of these cells during early to mid stages of disease, we evaluated the impact of microglial depletion with

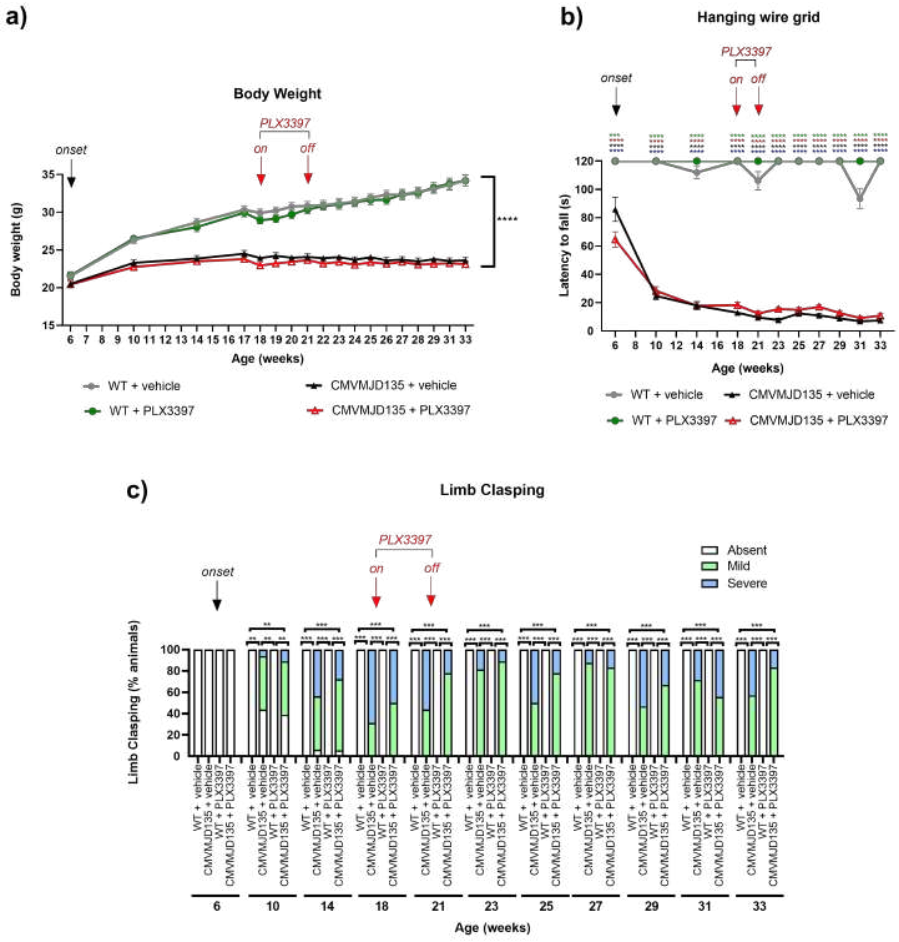

Figure 8 PLX3397-treatment did not modify the loss of muscular strength and abnormal reflexes seen in CMVMJD135 mice. a) Assessment of body weight showed significant differences between CMVMJD135 mice (PLX3397- and vehicle-treated) and WT mice (PLX3397- and vehicle-treated) throughout time. *One-way ANOVA (Post hoc Tukey's test)*. **b)** In the hanging wire grid test, in all the analysed timepoints, CMVMJD135 mice (PLX3397- and vehicle-treated) showed a significantly lower latency to fall from the grid when compared to WT mice (PLX3397- and vehicle-treated). Asterisks indicate significant differences which were found between: * WT + vehicle and CMVMJD135 + vehicle; * WT + vehicle and CMVMJD135 + PLX3397; * WT + PLX3397 and CMVMJD135 + vehicle; and * WT + PLX3397 and CMVMJD135 + PLX3397. *Friedman test with Kruskal-Wallis analysis*. **c)** Abnormal reflexes observed in the transgenic mice were not significantly improved by the PLX3397 treatment. *Friedman test with Kruskal-Wallis analysis*. Values are presented as mean ± SEM or as percentage of animals (%) (for the continuous and non-continuous variables, respectively). Means were considered statistically significant at a p-value * $p < 0.05$, ** $p < 0.01$, *** $p < 0.001$, **** $p < 0.0001$.

PLX3397 in motor phenotype of CMVMJD135 mice. The administration of PLX3397 was made at a mid-stage of the disease based on the previous observations, which suggests that (1) it is difficult to ameliorate neurodegenerative disease phenotypes, including in MJD, during late stages after neuronal loss had already occurred [15, 54] and (2) a decrease in the number of microglia during an early stage of the disease resulted in the amelioration of motor deficits in a mouse model of Spinocerebellar Ataxia type 1 (SCA1), another spinocerebellar ataxia caused by a polyQ expansion [15]. Although PLX3397 treatment was able

of substantially reduce the microglia numbers in two of the key affected regions in this disease, the cerebellum and the brainstem, it did not have an impact on the motor deficits of CMVMJD135 mice, suggesting that the contribution of microglia for MJD progression may not be relevant, and its activate state may be a consequence of the disease establishment.

In this study, CMVMJD135 and WT mice treated with PLX3397 were found to have a 42-59 % reduction in the number of microglia in the lobules and DCN, from the cerebellum, and in the PN, from the brainstem. In general, our results are similar to those obtained by [47], who reported a 55 % reduction in macrophages (CSF1R is also expressed by these peripheral monocytes [55]) between treated and untreated mice with PLX3397 using a similar experimental approach (method, dose, time of the administration, and age of treatment initiation). In fact, multiple studies have reported different results regarding the extent of depletion of microglia using PLX3397. While some have found a depletion of around 90 % of microglial cells [31, 36, 37, 40], others report depletion rates between 30 and 60 % [41, 42, 43, 44]. To the best of our knowledge, complete microglial ablation has never been reported [45]. Although it is unknown if sensitivity to CSF1R blockade changes with age [42], it is known that a small subset of microglia in adult mouse brains can survive without CSF1R signaling, which may explain the variation in depletion efficiency between different studies [45]. Therefore, additional experiments are needed to understand if the remaining microglia observed in the DCN and PN of CMVMJD135 and WT mice belong to these cell populations that are resistant to CSF1R inhibition.

A partial but significant depletion being found, we also evaluated the effects of PLX3397 on the morphology of the remaining microglial cells in the DCN and PN of CMVMJD135 and WT mice. PLX3397 treatment did not promote morphological changes in the microglia of CMVMJD135 mice in the two affected regions. Both CMVMJD135 + vehicle and CMVMJD135 + PLX3397 microglia, when compared with that of WT + vehicle, were found to have less and shorter branches, to be less tortuous, to be less ramified, with smaller size and surface, and with higher soma thickness. Decreased values of these features and increased circularity are associated with an "activated state", characterized by cells with larger cell bodies, and shorter and thicker processes [14, 13, 56]. These alterations, typically found in different situations of brain disease and pathology [14, 13, 15, 56, 57], suggest that microglia from CMVMJD135 + vehicle and CMVMJD135 + PLX3397 mice are similar and showed an activation profile, which was not dependent on CSF1R signaling. Because mutant *ATXN3* is expressed in microglia [29], we hypothesize that this activation profile may be induced by mutant *ATXN3* in microglial cells themselves or/and emerge as a consequence of their interaction with neurons undergoing degenerative processes. This, however, remains to be explored.

Interestingly, in both regions, it seems that the treatment with PLX3397 on WT mice promoted morphological changes that led to microglial cells becoming more activated, and thus more similar to those observed for CMVMJD135 animals. In fact, the PCA showed the existence of a clear structure on these morphological data, with two clusters being identified. Our analysis show that one cluster is grouping more ramified cells, with longer branches, and higher size and surface. This cluster is mainly composed of microglia from WT + vehicle mice, whereas, the second cluster is mainly composed of microglia from animals of the remaining groups, which have typically smaller values regarding parameters associated with cell ramification, size, and surface, characteristics typically found

in activated microglia. These findings are in accordance with other studies that used PLX3397, which have also found that the remaining microglia exhibited shorter and thicker processes, smaller cell size and an increased circularity [32, 58], a consequence that needs to be taken into account when interpreting the results of such experiments in the context of neurological diseases.

The neuroprotective effects of PLX3397 have been described in several models of neurodegenerative diseases [31, 34, 59, 60], and this compound was already shown to have beneficial effects in motor performance in a transgenic mouse model of SCA1, without major adverse events [15]. In this study, we submitted the CMVMJD135 mice (PLX3397- and vehicle-treated) to various tests to evaluate different components of the behavioral motor dimension, such as motor coordination and balance, muscular strength, and gait, throughout age. The general health of all animals used in this study suggests that the administration of PLX3397 is safe, as it did not cause any major behavioral alterations, weight loss, or sign of illness in mice treated with PLX3397 for 3 weeks. Since a depletion of ≈50 % of microglial cells was seen in brain regions relevant for motor function in WT mice treated with PLX3397 and this did not impact the motor phenotype of the animals, we conclude that these cells may not be highly relevant for motor performance. Additionally, and contrarily to our hypothesis, the partial reduction of microglia induced in CMVMJD135 mice had no impact on their motor phenotype. In fact, PLX3397-treated and vehicle CMVMJD135 mice displayed a similar loss of muscular strength, abnormal gait, reflexes, and stride length, and motor and balance deficits. This does not support the hypothesis that microglia is a relevant contributor for MJD pathogenesis or symptoms progression, despite the morphological, phenotypic and transcriptomic changes seen in microglia of MJD mice [29].

Conclusions

This study demonstrates that reducing the number of microglial cells, after the onset of motor deficits, is not an effective strategy to counteract disease progression in MJD: in fact, halving the microglial population did not change the phenotypic outcome in CMVMJD135 mice. While it is possible that a more severe depletion of microglia could lead to a change in neurodegeneration-related phenotype, or that the effect of microglial depletion would be more marked at earlier phases of the disease, prior to the appearance of motor symptoms, overall our data does not support a central role for microglial cells in this disease.

Supplementary Information

The online version contains supplementary material available at TBD.
Additional File 1 (.pdf): Figure S1. Schematic representation of the experimental design.
Additional File 2 (.pdf): Figure S1. Features associated with microglial ramification in the pontine nuclei (PN) were found to be similar between the four groups. **Figure S2**. Features associated with complexity and shape of microglia in the deep cerebellar nuclei (DCN) were not found to be different between the four groups. **Figure S3**. Features associated with complexity and shape of microglia in the PN were found to be similar between the four groups. **Figure S4**. Treatment with PLX3397 did not induce morphological changes in the features relevant to microglia ramification in the DCN of CMVMJD135 mice at 21 weeks of age. **Figure S5**. Treatment with PLX3397 did not induce morphological changes in the features relevant to complexity and microglia shape in the DCN of CMVMJD135 mice at 21 weeks of age. **Figure S6**. Treatment with PLX3397 did not induce morphological changes in the features relevant to microglia ramification in the PN of CMVMJD135 mice at 21 weeks of age. **Figure S7**. Treatment with PLX3397 did not induce morphological changes in the features relevant to complexity and microglia shape in the PN of CMVMJD135 mice at 21 weeks of age.**Figure S8**. In both affected brain regions, CSF1R inhibition by PLX3397 on WT mice promoted morphological changes that led to microglia becoming closer to those of CMVMJD135 mice (PLX3397- and vehicle-treated).

Funding

This work was supported by *Fundação para a Ciência e a Tecnologia* (FCT) (PTDC/NEUNMC/3648/2014) and COMPETE-FEDER (POCI-01-0145-FEDER-016818). It was also supported by Portuguese funds through FCT in the framework of the Project

POCI-01-0145-FEDER-031987 (PTDC/MED-OUT/31987/2017). A.B.C. was supported by a doctoral fellowship from FCT (PD/BD/127828/2016). This work was funded by ICVS Scientific Microscopy Platform, member of the national infrastructure PPBI (Portuguese Platform of Bioimaging) (PPBIPOCI-01-0145-FEDER-022122), and by National funds, through FCT—project UIDB/50026/2020 and UIDP/50026/2020.

Abbreviations

AD: Alzheimer disease; ALS: Amyotrophic lateral sclerosis; CAG: cytosine-adenine-guanine; CNS: central nervous system; CSF1R: colony stimulating factor 1 receptor; DCN: deep cerebellar nuclei; DMSO: dimethyl sulfoxide; HD: Huntington disease; MJD: Machado-Joseph disease; MSE: mean squared error; NDs: neurodegenerative diseases; NGS: normal goat serum; PBS: phosphate saline buffer; PCA: principal component analysis; PD: Parkinson disease; PFA: paraformaldehyde; PN: pontine nuclei; ROI: region of interest; RT: room temperature; SCA1: Spinocerebellar Ataxia type 1; SCA3: Spinocerebellar Ataxia type 3; SEM: standard error of the mean; WT: Wild-type.

Availability of data and materials

The datasets used and/or analyzed during the current study are available from the corresponding author on reasonable request.

Ethics approval and consent to participate

All procedures with mice were conducted in accordance with the ARRIVE 2.0 guidelines (Animal Research: Reporting In Vivo Experiments). Animal facilities and the people directly involved in animal procedures as well as the principal investigators were certified by the Portuguese regulatory entity *Direção Geral de Alimentação e Veterinária* (DGAV, license number 020317). All animal experiments were approved by the Animal Ethics Committee of the Life and Health Sciences Research Institute, University of Minho (SECVS 120/2014), and conducted in consonance with the European Union Directive 2010/63/EU. To minimize discomfort, stress, and pain to the animals, humane endpoints were defined and included a 20 % reduction of the body weight, inability to reach food and water, presence of wounds in the body, and dehydration. Health monitoring was performed according to the Federation of European Laboratory Animal Science Associations guidelines, where the Specified Pathogen Free health status was confirmed by sentinel mice maintained in the same animal housing room.

Competing interests

The authors declare that they have no competing interests.

Authors' contributions

A.B.C.: conceptualization; methodology; software; formal analysis; investigation; data curation; writing—original draft; writing—review and editing; visualization. S.D.S.: conceptualization; writing—review and editing; supervision; project administration. B.F.: software; validation; formal analysis; writing—review and editing. B.C.: methodology; validation. J.C.: methodology; validation. D.M.F.: investigation. A.T.C.: methodology; resources. A.F.A.: conceptualization; validation; writing—review and editing; supervision; P.M.: conceptualization; validation; resources; writing—review and editing; supervision; project administration; funding acquisition. All authors have read and agreed to the published version of the manuscript.

Author details

[1]Life and Health Sciences Research Institute (ICVS), School of Medicine, University of Minho, Braga, Portugal. [2]ICVS/3B's, PT Government Associate Laboratory, Braga/Guimarães, Portugal. [3]Department of Informatics, ALGORITMI Center, University of Minho, Braga, Portugal. [4]Coimbra Institute for Clinical and Biomedical Research (iCBR), Faculty of Medicine, University of Coimbra, Coimbra, Portugal. [5]Center for Innovative Biomedicine and Biotechnology (CIBB), University of Coimbra, Coimbra, Portugal. [6]Clinical Academic Center of Coimbra (CACC), Coimbra, Portugal.

References

1. Coutinho, P., Andrade, C.: Autosomal dominant system degeneration in portuguese families of the azores islands. a new genetic disorder involving cerebellar, pyramidal, extrapyramidal and spinal cord motor functions. Neurology **28**(7), 703–9 (1978). doi:10.1212/wnl.28.7.703
2. Maciel, P., Gaspar, C., DeStefano, A.L., Silveira, I., Coutinho, P., Radvany, J., Dawson, D.M., Sudarsky, L., Guimaraes, J., Loureiro, J.E.L., Nezarati, M.M., Corwin, L.I., Lopes-Cendes, I., Rooke, K., Rosenberg, R., MacLeod, P., Farrer, L.A., Seeiros, J., Rouleau, G.A.: Correlation between cag repeat length and clinical features in machado-joseph disease. American Journal of Human Genetics **57**(1), 54–61 (1995)
3. Kawaguchi, Y., Okamoto, T., Taniwaki, M., Aizawa, M., Inoue, M., Katayama, S., Kawakami, H., Nakamura, S., Nishimura, M., Akiguchi, I.: Cag expansions in a novel gene for machado-joseph disease at chromosome 14q32.1. Nature Genetics **8**(3), 221–8 (1994). doi:10.1038/ng1194-221
4. Da Silva, J.D., Teixeira-Castro, A., Maciel, P.: From pathogenesis to novel therapeutics for spinocerebellar ataxia type 3: Evading potholes on the way to translation. Neurotherapeutics **16**(4), 1009–1031 (2019). doi:10.1007/s13311-019-00798-1
5. Bettencourt, C., Lima, M.: Machado-joseph disease: from first descriptions to new perspectives. Orphanet Journal of Rare Diseases **6**(35), 1009–1031 (2011). doi:10.1186/1750-1172-6-35
6. Coutinho, P., Seeiros, J.: Clinical, genetic and pathological aspects of machado-joseph disease. Journal de Genetie Humaine **29**(3), 203–9 (1981)
7. Sequeiros, J., Coutinho, P.: Epidemiology and clinical aspects of machado-joseph disease. Advances in Neurology **61**, 139–53 (1993)
8. Rub, U., Brunt, E.R., Deller, T.: New insights into the pathoanatomy of spinocerebellar ataxia type 3 (machado-joseph disease). Current Opinion in Neurology **21**(2), 111–6 (2008). doi:10.1097/WCO.0b013e3282f7673d
9. McLoughlin, H.S., Moore, L.R., Paulson, H.L.: Pathogenesis of sca3 and implications for other polyglutamine diseases. Neurobiology Disease **134**(104635) (2020). doi:10.1016/j.nbd.2019.104635
10. Bachiller, S., Jiménez-Ferrer, I., Paulus, A., Yang, Y., Swanberg, M., Deierborg, T., Boza-Serrano, A.: Microglia in neurological diseases: A

road map to brain-disease dependent-inflammatory response. Frontiers in Cellular Neuroscience **12**(488) (2018). doi:10.3389/fncel.2018.00488

11. Schafer, D.P., Stevens, B.: Microglia function in central nervous system development and plasticity. Cold Spring Harbor Perspectives in Biololy **7**(10) (2015). doi:10.1101/cshperspect.a020545
12. He, Y., Yao, X., Taylor, N., Bai, Y., Lovenberg, T., Bhattacharya, A.: Rna sequencing analysis reveals quiescent microglia isolation methods from postnatal mouse brains and limitations of bv2 cells. Journal of Neuroinflammation **15**(153) (2018). doi:10.1186/s12974-018-1195-4
13. d. M. Fernández-Arjona, M., Grondona, J.M., Granados-Duran, P., Fernandez-Llebrez, P., Lopez-Avalos, M.D.: Microglia morphological categorization in a rat model of neuroinflammation by hierarchical cluster and principal components analysis. Frontiers in Cellular Neuroscience **11**(235) (2017). doi:10.3389/fncel.2017.00235
14. d. M. Fernández-Arjona, M., Grondona, J.M., Fernández-Llebrez, P., Lopez-Ávalos, M.D.: Microglial morphometric parameters correlate with the expression level of il-1b, and allow identifying different activated morphotypes. Frontiers in Cellular Neuroscience **13**(472) (2019). doi:10.3389/fncel.2019.00472
15. Qu, W., Johnson, A., Kim, J.H., Lukowicz, A., Svedberg, D., Cvetanovic, M.: Inhibition of colony-stimulating factor 1 receptor early in disease ameliorates motor deficits in sca1 mice. Journal of Neuroinflammation **14**(107) (2017). doi:10.1186/s12974-017-0880-z
16. Socodato, R., Portugal, C.C., Canedo, T., Rodrigues, A., Almeida, T.O., Henries, J.F., Vaz, S.H., Magalhaes, J., Silva, C.M., Baptista, F.I., Alves, R.L., Coelho-Santos, V., Silva, A.P., Paes-de-Carvalho, R., Magalhaes, A., Brakebusch, C., Sebastiao, A.M., Summavielle, T., Ambrosio, A.F., Relvas, J.B.: Microglia dysfunction caused by the loss of rhoa disrupts neuronal physiology and leads to neurodegeneration. Cell Reports **31**(12), 107796 (2020). doi:10.1016/j.celrep.2020.107796
17. Crotti, A., Benner, C., Kerman, B.E., Gosselin, D., Lagier-Tourenne, C., Zuccato, C., Cattaneo, E., Gage, F.H., Cleveland, D.W., Glass, C.K.: Mutant huntingtin promotes autonomous microglia activation via myeloid lineage-determining factors. Nature Neuroscience **17**(4), 513–21 (2014). doi:10.1038/nn.3668
18. Politis, M., Lahiri, N., Niccolini, F., Su, P., Wu, K., Giannetti, P., Scahill, R.I., Turkheimer, F.E., Tabrizi, S.J., Piccini, P.: Increased central microglial activation associated with peripheral cytokine levels in premanifest huntington's disease gene carriers. Neurobiology of disease **83**, 115–21 (2015). doi:10.1016/j.nbd.2015.08.011
19. McGeer, P.L., McGeer, E.G.: Glial reactions in parkinson's disease. Movement disorders **23**(4), 474–83 (2008). doi:10.1002/mds.21751
20. Lian, H., Yang, L., Cole, A., Sun, L., Chiang, A.C.A., Fowler, S.W., Shim, D.J., Rodriguez-Rivera, J., Taglialatela, G., Jankowsky, J.L., Lu, H.-C., Zheng, H.: Nfkb-activated astroglial release of complement c3 compromises neuronal morphology and function associated with alzheimer's disease. Neuron **85**(1), 101–115 (2015). doi:10.1016/j.neuron.2014.11.018
21. Boillee, S., Yamanaka, K., Lobsiger, C.S., Copeland, N.G., Jenkins, N.A., Kassiotis, G., Kollias, G., Cleveland, D.W.: Onset and progression in inherited als determined by motor neurons and microglia. Science **312**(5778), 1389–92 (2006). doi:10.1126/science.1123511
22. Beers, D.R., Henkel, J.S., Xiao, Q., Zhao, W., Wang, J., Yen, A.A., Siklos, L., McKercher, S.R., Appel, S.H.: Wild-type microglia extend survival in pu.1 knockout mice with familial amyotrophic lateral sclerosis. Proceedings of the National Academy of Sciences of the United States of America **103**(43), 16021–6 (2006). doi:10.1073/pnas.0607423103
23. Gowing, G., Philips, T., Wijmeersch, B.V., Audet, J.-N., Dewil, M., Bosch, L.V.D., Billiau, A.D., Robberecht, W., Julien, J.-P.: Ablation of proliferating microglia does not affect motor neuron degeneration in amyotrophic lateral sclerosis caused by mutant superoxide dismutase. Journal of Neuroscience **28**(41), 10234–44 (2008). doi:10.1523/JNEUROSCI.3494-08.2008
24. Streit, W.J.: Microglia as neuroprotective, immunocompetent cells of the cns. Glia **40**(2), 133–139 (2002). doi:10.1002/glia.10154
25. Parkhurst, C.N., Yang, G., Ninan, I., Savas, J.N., 3rd, J.R.Y., Lafaille, J.J., Hempstead, B.L., Littman, D.R., Gan, W.-B.: Microglia promote learning-dependent synapse formation through brain-derived neurotrophic factor. Cell **155**(7), 1596–609 (2013). doi:10.1016/j.cell.2013.11.030
26. Evert, B.O., Vogt, I.R., Kindermann, C., Ozimek, L., de Vos, R.A., Schmitt, I., Klockgether, T., Wullner, U.: Inflammatory genes are upregulated in expanded ataxin-3-expressing cell lines and spinocerebellar ataxia type 3 brains. Journal of Neuroscience **21**(15), 5389–96 (2001). doi:10.1523/JNEUROSCI.21-15-05389.2001
27. Duarte-Lobo, D., Nobre, R.J., Miranda, C.O., Pereira, D., Castelhano, J., Sereno, J., Koeppen, A., Castelo-Branco, M., de Almeida, L.P.: The blood-brain barrier is disrupted in machado-joseph disease/spinocerebellar ataxia type 3: evidence from transgenic mice and human post-mortem samples. Acta Neuropathologica Communications **8**(152) (2020). doi:10.1186/s40478-020-00955-0
28. Cunha-Santos, J., Duarte-Neves, J., Carmona, V., Guarente, L., de Almeida, L.P., Cavadas, C.: Caloric restriction blocks neuropathology and motor deficits in machado–joseph disease mouse models through sirt1 pathway. Nature Communications **7**(11445) (2016). doi:10.1038/ncomms11445
29. Campos, A.B., Duarte-Silva, S., Fernandes, B., das Neves, S.P., Marques, F., Teixeira-Castro, A., Neves-Carvalho, A., Monteiro-Fernandes, D., Portugal, C.C., Socodato, R., Summavielle, T., Ambrósio, A.F., Relvas, J.B., Maciel, P.: Profiling microglia in a mouse model of machado-joseph disease. Biomedicines **10**(2), 237 (2022). doi:10.3390/biomedicines10020237
30. Silva-Fernandes, A., Duarte-Silva, S., Neves-Carvalho, A., Amorim, M., Soares-Cunha, C., Oliveira, P., Thirstrup, K., Teixeira-Castro, A., Maciel, P.: Chronic treatment with 17-dmag improves balance and coordination in a new mouse model of machado-joseph disease. Neurotherapeutics **11**(2), 433–49 (2014). doi:10.1007/s13311-013-0255-9
31. Crapser, J.D., Ochaba, J., Soni, N., Reidling, J.C., Thompson, L.M., Green, K.N.: Microglial depletion prevents extracellular matrix changes

and striatal volume reduction in a model of huntington's disease. Brain **143**(1), 266–288 (2020). doi:10.1093/brain/awz363

32. Elmore, M.R.P., Najafi, A.R., Koike, M.A., Dagher, N.N., Spangenberg, E.E., Rice, R.A., Kitazawa, M., Matusow, B., Nguyen, H., West, B.L., Green, K.N.: Colony-stimulating factor 1 receptor signaling is necessary for microglia viability, unmasking a microglia progenitor cell in the adult brain. Neuron **82**(2), 380–97 (2014). doi:10.1016/j.neuron.2014.02.040

33. Dagher, N.N., Najafi, A.R., Kayala, K.M.N., Elmore, M.R.P., White, T.E., Medeiros, R., West, B.L., Green, K.N.: Colony-stimulating factor 1 receptor inhibition prevents microglial plae association and improves cognition in 3xtg-ad mice. Journal of Neuroinflammation **12**(139) (2015). doi:10.1186/s12974-015-0366-9

34. Spangenberg, E.E., Lee, R.J., Najafi, A.R., Rice, R.A., Elmore, M.R.P., Blurton-Jones, M., West, B.L., Green, K.N.: Eliminating microglia in alzheimer's mice prevents neuronal loss without modulating amyloid-b pathology. Brain **139**(4), 1265–81 (2016). doi:10.1093/brain/aww016

35. Lin, C.-C.: Clinical development of colony-stimulating factor 1 receptor (csf1r) inhibitors. Journal of Immunotherapy and Precision Oncology **4**(2), 105–114 (2014). doi:10.36401/JIPO-20-32

36. Elmore, M.R.P., Lee, R.J., West, B.L., Green, K.N.: Characterizing newly repopulated microglia in the adult mouse: Impacts on animal behavior, cell morphology, and neuroinflammation. PLOS ONE **10**(4) (2015). doi:10.1371/journal.pone.0122912

37. Li, M., Li, Z., Ren, H., Jin, W.-N., Wood, K., Liu, Q., Sheth, K.N., Shi, F.-D.: Colony stimulating factor 1 receptor inhibition eliminates microglia and attenuates brain injury after intracerebral hemorrhage. Journal of Cerebral Blood Flow and Metabolism **37**(7) (2016). doi:10.1177/0271678X16666551

38. Spiller, K.J., Restrepo, C.R., Khan, T., Dominique, M.A., Fang, T.C., Canter, R.G., Roberts, C., Miller, K.R., Ransohoff, R.M., Trojanowski, J.Q., Lee, C.M.-Y.: Microglia-mediated recovery from als-relevant motor neuron degeneration in a mouse model of tdp-43 proteinopathy. Nature Neuroscience **21**(3), 329–340 (2018). doi:10.1038/s41593-018-0083-7

39. Sosna, J., Philipp, S., Albay, R., Reyes-Ruiz, J.M., Baglietto-Vargas, D., LaFerla, F.M., Glabe, C.G.: Early long-term administration of the csf1r inhibitor plx3397 ablates microglia and reduces accumulation of intraneuronal amyloid, neuritic plaque deposition and pre-fibrillar oligomers in 5xfad mouse model of alzheimer's disease. Molecular Neurodegeneration **13**(11) (2018). doi:10.1186/s13024-018-0244-x

40. Jin, W.-N., Shi, S.X.-Y., Li, Z., Li, M., Wood, K., Gonzales, R.J., Liu, Q.: Depletion of microglia exacerbates postischemic inflammation and brain injury. Journal of Cerebral Blood Flow and Metabolism **37**(6), 2224–2236 (2017). doi:10.1177/0271678X17694185

41. Son, Y., Jeong, Y.J., Shin, N.-R., Oh, S.J., Nam, K.R., Choi, H.-D., Choi, J.Y., Lee, H.-J.: Inhibition of colony-stimulating factor 1 receptor by plx3397 prevents amyloid beta pathology and rescues dopaminergic signaling in aging 5xfad mice. International Journal of Molecular Sciences **21**(15), 5553 (2020). doi:10.3390/ijms21155553

42. Bennett, R.E., Bryant, A., Hu, M., Robbins, A.B., Hopp, S.C., Hyman, B.T.: Partial reduction of microglia does not affect tau pathology in aged mice. Journal of Neuroinflammation **15**(311) (2018). doi:10.1186/s12974-018-1348-5

43. Yegla, B., Boles, J., Kumar, A., Foster, T.C.: Partial microglial depletion is associated with impaired hippocampal synaptic and cognitive function in young and aged rats. Glia **69**(6), 1494–1514 (2021). doi:10.1002/glia.23975

44. Cai, Z., Ye, T., Xu, X., Gao, M., Zhang, Y., Wang, D., Gu, Y., Zhu, H., Tong, L., Lu, J., Chen, Z., Huang, C.: Antidepressive properties of microglial stimulation in a mouse model of depression induced by chronic unpredictable stress. Progress in Neuro-Pyschopharmacology and Biological Psychiatry **101**(109931) (2020). doi:10.1016/j.pnpbp.2020.109931

45. Zhan, L., Fan, L., Kodama, L., Sohn, P.D., Wong, M.Y., Mousa, G.A., Zhou, Y., Li, Y., Gan, L.: A mac2-positive progenitor-like microglial population is resistant to csf1r inhibition in adult mouse brain. Elife **9** (2020). doi:10.7554/eLife.51796

46. Silva-Fernandes, A., d. C. Costa, M., Duarte-Silva, S., Oliveira, P., Botelho, C.M., Martins, L., Mariz, J.A., Ferreira, T., Ribeiro, F., Correia-Neves, M., Costa, C., Maciel, P.: Motor uncoordination and neuropathology in a transgenic mouse model of machado-joseph disease lacking intranuclear inclusions and ataxin-3 cleavage products. Neurobiology of Disease **40**(1), 163–76 (2010). doi:10.1016/j.nbd.2010.05.021

47. Merry, T.L., Brooks, A.E.S., Masson, S.W., Adams, S.E., Jaiswal, J.K., Jamieson, S.M.F., Shepherd, P.R.: The csf1 receptor inhibitor pexidartinib (plx3397) reduces tissue macrophage levels without affecting glucose homeostasis in mice. International Journal of Obesity **44**(1), 245–253 (2020). doi:10.1038/s41366-019-0355-7

48. Young, K., Morrison, H.: Quantifying microglia morphology from photomicrographs of immunohistochemistry prepared tissue using imagej. Journal of Visualized Experiments **136**(57648) (2018). doi:10.3791/57648

49. Campos, A.B., Duarte-Silva, S., Ambrósio, A.F., Maciel, P., Fernandes, B.: Morphdata: Automating the data extraction process of morphological features of microglial cells in imagej. bioRxiv (2021). doi:10.1101/2021.08.05.455282

50. Rogers, D.C., Fisher, E.M., Brown, S.D., Peters, J., Hunter, A.J., Martin, J.E.: Behavioral and functional analysis of mouse phenotype: Shirpa, a proposed protocol for comprehensive phenotype assessment. Mammalian Genome **8**(10), 711–3 (1997). doi:10.1007/s003359900551

51. Rafael, J.A., Nitta, Y., Davies, J.P.K.E.: Testing of shirpa, a mouse phenotypic assessment protocol, on dmd(mdx) and dmd(mdx3cv) dystrophin-deficient mice. Mammalian Genome **11**(9), 725–8 (2000). doi:10.1007/s003350010149

52. Teixeira-Castro, A., Jalles, A., Esteves, S., Kang, S., d. S. Santos, L., Silva-Fernandes, A., Neto, M.F., Brielmann, R.M., Bessa, C., Duarte-Silva, S., Miranda, A., Oliveira, S., Neves-Carvalho, A., Bessa, J., Summavielle, T., Silverman, R.B., Oliveira, P., Morimoto, R.I., Maciel, P.: Serotonergic signalling suppresses ataxin 3 aggregation and

neurotoxicity in animal models of machado-joseph disease. Brain **138**(11), 3221–37 (2015). doi:10.1093/brain/awv262

53. Carter, R.J., Lione, L.A., Humby, T., Mangiarini, L., Mahal, A., Bates, G.P., Dunnett, S.B., Morton, A.J.: Characterization of progressive motor deficits in mice transgenic for the human huntington's disease mutation. The Journal of Neuroscience **19**(8), 3248–57 (1999). doi:10.1523/JNEUROSCI.19-08-03248.1999

54. Banez-Coronel, M., Ayhan, F., Tarabochia, A.D., Zu, T., Perez, B.A., Tusi, S.K., Pletnikova, O., Borchelt, D.R., Ross, C.A., Margolis, R.L., Yachnis, A.T., Troncoso, J.C., Ranum, L.P.W.: Ran translation in huntington disease. Neuron **88**(4), 667–77 (2015). doi:10.1016/j.neuron.2015.10.038

55. Lei, F., Cui, N., Zhou, C., Chodosh, J., Vavvas, D.G., Paschalis, E.I.: Csf1r inhibition by a small-molecule inhibitor is not microglia specific; affecting hematopoiesis and the function of macrophages. Proceedings of the National Academy of Sciences of the United States of America **117**(38), 23336–23338 (2020). doi:10.1073/pnas.1922788117

56. Vargas-Caraveo, A., Sayd, A., Robledo-Montana, J., Caso, J.R., Madrigal, J.L.M., Garcia-Bueno, B., Leza, J.C.: Toll-like receptor 4 agonist and antagonist lipopolysaccharides modify innate immune response in rat brain circumventricular organs. Journal of Neuroinflammation **17**(1), 6 (2020). doi:10.1186/s12974-019-1690-2

57. Bordeleau, M., Lacabanne, C., d. Cossio, L.F., Vernoux, N., Savage, J.C., Gonzalez-Ibanez, F., Tremblay, M.-E.: Microglial and peripheral immune priming is partially sexually dimorphic in adolescent mouse offspring exposed to maternal high-fat diet. Journal of Neuroinflammation **17**(264) (2020). doi:10.1186/s12974-020-01914-1

58. Kasihara, S., Shinohara, K., Tsutsui, H.: Effects of intracerebroventricular administration of colony stimulating factor 1 receptor inhibitor on microglia. Federation of American Societies for Experimental Biology **33**(S1), 621–621 (2019). doi:10.1096/fasebj.2019.33.1_supplement.lb621

59. Tahmasebi, F., Pasbakhsh, P., Mortezaee, K., Madadi, S., Barati, S., Kashani, I.R.: Effect of the csf1r inhibitor plx3397 on remyelination of corpus callosum in a cuprizone-induced demyelination mouse model. Journal of Cellular Biochemistry **120**(6), 10576–10586 (2019). doi:10.1002/jcb.28344

60. Oh, S.J., Ahn, H., Jung, K.-H., Han, S.J., Nam, K.R., Kang, K.J., Park, J.-A., Lee, K.C., Lee, Y.J., Choi, J.Y.: Evaluation of the neuroprotective effect of microglial depletion by csf-1r inhibition in a parkinson's animal model. Molecular Imaging and Biology **22**(4), 1031–1042 (2020). doi:10.1007/s11307-020-01485-w